CONF-830758--

DE84 002406

proceedings of the workshop

advanced bumpy torus concepts

July 11-13, 1983
Rancho Santa Fe, California

N. A. UCKAN
Editor

NOTICE
PORTIONS OF THIS REPORT ARE ILLEGIBLE.
It has been reproduced from the best available copy to permit the broadest possible availability.

Date Published - October 1983

SPONSORED BY

FUSION ENERGY DIVISION
OAK RIDGE NATIONAL LABORATORY
Oak Ridge, Tennessee

Operated by Union Carbide Corporation under contract W-7405-eng-26
with the Office of Fusion Energy, U.S. Department of Energy

AND

AMPC
Encinitas, California

PREFACE

The U.S.-Japan Workshop on Advanced Bumpy Torus Concepts was held at Rancho Santa Fe, California, July 11-13, 1983, under the sponsorship of the Applied Microwave Plasma Concepts (AMPC) and the Oak Ridge National Laboratory (ORNL) with the assistance of JAYCOR. About 60 participants attended the workshop (about 55 from the U.S. and 5 from Japan).

The workshop organizing committee members were:

R. L. Miller, Scientific Coordinator, AMPC

N. A. Uckan, Scientific Coordinator, ORNL

M. B. Voytilla, Administrative Coordinator, AMPC

The purpose of the workshop was to provide a forum for the presentation and discussion of recent developments on advanced bumpy torus concepts. It was hoped that the discussions would lead to: (1) identification of new configurations and ideas that might significantly enhance the performance of the present bumpy torus concept, (2) clarification of key issues entering into the evaluation of these new concepts, and (3) suggestions for further improvements to promising new concepts and directions for future studies.

The technical coverage in the workshop was very broad and included the presentation of 25 papers, followed by open forum discussions of topics selected by the workshop participants. The workshop was rich in new ideas. A large number of new names and acronyms were also introduced at the workshop, including ELMO Bumpy Racetrack (EBR) and Square (EBS), Bumpy Bean Torus (BBT), ELMO Snakey Torus (EST), Twisted Racetrack (TRT, à la Figure-8), EBT with "Andrecletti" coils (EBTEC), EBR with "Wobig" coils (called helical bumpy torus, HBT), etc.

These proceedings include (1) workshop summaries prepared by the session chairmen (N. A. Uckan, W. B. Ard, L. A. Berry, G. Gibson, H. Ikegami, and H. Weitzner), (2) the overview/summary presentation preceding the open forum discussions (N. A. Krall), and (3) the full-length manuscripts that were submitted to the workshop and presented at the following workshop sessions: Magnetics — Closed Field Line Devices (5 papers); Magnetics — Closed Flux Surface Devices (5 papers);

Interpretation and Supporting Theory (6 papers); Electric Field Enhanced Confinement (3 papers); RF Heating (3 papers); and Ring Physics (3 papers; however, 2 were withdrawn from the proceedings). An Author Index, the Attendance List, and the Agenda conclude the proceedings. (Because of the need for camera-ready copy, variations in style and format were, despite great efforts, inevitable.)

The local hosts for the workshop were AMPC and JAYCOR, and special acknowledgments are due Ray Dandl, Mike Voytilla, Bob Miller, and Barrie Alexanders of AMPC and Nick Krall and Diane Miller of JAYCOR for the excellent arrangements and warm hospitality at Rancho Santa Fe. The efforts of session chairmen provided an enthusiastic forum for discussion of papers that contributed largely to the success of the workshop. The assistance of DeLena Akers (ORNL) in the preparation and coordination of these proceedings is greatfully acknowledged. Thanks are also due the staff of the ORNL Fusion Energy Division Reports Office for handling many details of the publication.

Nermin A. Uckan

Oak Ridge, Tennessee

August 1983

DISCLAIMER

This report was prepared as an account of work sponsored by an agency of the United States Government. Neither the United States Government nor any agency thereof, nor any of their employees, makes any warranty, express or implied, or assumes any legal liability or responsibility for the accuracy, completeness, or usefulness of any information, apparatus, product, or process disclosed, or represents that its use would not infringe privately owned rights. Reference herein to any specific commercial product, process, or service by trade name, trademark, manufacturer, or otherwise does not necessarily constitute or imply its endorsement, recommendation, or favoring by the United States Government or any agency thereof. The views and opinions of authors expressed herein do not necessarily state or reflect those of the United States Government or any agency thereof.

CONTENTS

SUMMARY OF THE WORKSHOP 1

OVERVIEW 17

WORKSHOP OVERVIEW — N. A. Krall 19

MAGNETICS — CLOSED FIELD LINE DEVICES 35

DRIFT SURFACE STUDIES OF EBT CONFIGURATIONS WITH NONCIRCULAR MAGNETIC COILS — R. L. Miller, R. A. Dandl, and G. E. Guest 37

ELMO BUMPY SQUARE — L. W. Owen, D. K. Lee, and C. L. Hedrick 55

MINIMUM-B MIRRORS PLUS EBT PRINCIPLES — S. Yoshikawa 67

ORBITS ASPECT OF ADVANCED BUMPY TORUS — T. Kamimura, M. Fujiwara, and H. Ikegami 71

MAGNETICS OF INNOVATIVE BUMPY TORI — L. P. Mai and G. Gibson 73

MAGNETICS — CLOSED FLUX SURFACE DEVICES 97

OPTIMIZED APPROACHES TO EBT'S WITH SIMPLE CIRCULAR COILS — J. F. Pipkins, R. J. Schmitt, W. B. Ard, R. J. Kashuba, and F. M. Bieniosek 99

PRELIMINARY CONCEPTUAL DESIGN OF A TWISTED RACETRACK EBT DEVICE — R. J. DeBellis, H. F. Imster, J. L. Conlee, R. J. Dannenmueller, C. F. Dillow, T. J. Poteat, and R. J. Schmitt 117

ANALYTICAL STUDIES ON CHARACTERISTICS OF NEW BUMPY TORUS CONFIGURATION — A. Tsushima and M. Fujiwara 151

THE ELMO SNAKEY TORUS — A. H. Boozer 161

ENERGETIC PARTICLES IN TOKAMAKS: STABILIZATION OF BALLOONING MODES — J. W. Van Dam, M. N. Rosenbluth, S. T. Tsai, and M. G. Engquist 167

INTERPRETATION AND SUPPORTING THEORY 177

OPTIMIZED OPERATION OF BUMPY TORUS — H. Ikegami 179

NONRESONANT PARTICLE TRANSPORT FOR BUMPY FIELD LINE DEVICES WITH ARBITRARY SHAPED FLUX SURFACES — D. E. Hastings 191

COMPARISON OF MAGNETIC EQUILIBRIA AND LOW FREQUENCY STABILITY FOR EBT AND EBS — C. L. Hedrick. 217

WAVE INTERACTIONS WITH EBT PLASMAS IN THE MAGNETIC DRIFT FREQUENCY RANGE — J. B. McBride, M. Rosenberg, and N. A. Krall. 219

STABILITY BOUNDS FOR BALLOONING MODES IN EBT — K. Nguyen and T. Kammash 237

EFFECTS OF AMBIPOLAR FIELD ON LOW FREQUENCY FLUCTUATIONS IN BUMPY TORI — H. Sanuki. 261

ELECTRIC FIELD ENHANCED CONFINEMENT. 271

PLASMA CONFINEMENT IN SELF-CONSISTENT, ONE DIMENSIONAL TRANSPORT EQUILIBRIA IN THE COLLISIONLESS-ION REGIME OF EBT OPERATION — C. S. Chang and R. L. Miller 273

ICRF CONFINEMENT AND STABILIZATION OF TORUS
PART I: THEORETICAL ANALYSIS — H. Hojo, K. Hamamatsu, T. Watanabe, and K. Nishikawa 285

PART II: PARTICLE SIMULATION — K. Sakai, S. Takeuchi, and M. Matsumoto. 318

ELECTRIC FIELD BUMPY TORUS (EFBT) CONCEPT: AN ALTERNATE MEANS OF PLASMA PRODUCTION — J. R. Roth. 327

RF HEATING 363

BUILDUP AND SUSTAINMENT OF 10^{13} cm^{-3} PLASMA BY ICRF IN RFC-XX — T. Sato, S. Okamura, K. Adati, T. Aoki, D. R. Baker, H. Fujita, H. R. Garner, K. Hattori, S. Hidekuma, T. Kawamoto, R. Kumazawa, Y. Okubo, and K. Uchino. 365

EBT MICROWAVE DEPOSITION MODELING — S. Tamor. 385

THEORETICAL ASPECTS OF THROAT LAUNCH MICROWAVE HEATING IN EBT-S — D. B. Batchelor, R. C. Goldfinger, D. A. Rasmussen, and D. W. Swain 395

RING PHYSICS 415

CONTROL OF ELMO RING BY USING SURMAC COILS IN ADVANCED EBT SYSTEMS — B. H. Quon (withdrawn) 417

ON THE POSSIBILITY OF RINGS IN A MODULAR STELLARATOR — J. A. Rome, J. H. Harris, B. Masden, and V. Lynch (withdrawn). 419

REDUCTION OF MICROWAVE POWER REQUIREMENTS FOR EBT — S. Hamasaki, H. H. Klein, N. A. Krall, and J. L. Sperling 421

AUTHOR INDEX 437

ATTENDANCE LIST. 439

AGENDA 443

i/2

SUMMARY OF THE WORKSHOP

N. A. UCKAN, W. B. ARD, L. A. BERRY, G. GIBSON
H. IKEGAMI, N. A. KRALL, and H. WEITZNER

1. INTRODUCTION

The U.S.-Japan Workshop on Advanced Bumpy Torus Concepts was held at Rancho Santa Fe, California, July 11-13, 1983. It was attended by about 60 participants.

The purpose of the workshop was to provide a forum for presentation and discussion of recent developments on advanced bumpy torus concepts. It was hoped that the discussions would lead to: (1) identification of new configurations and ideas that might significantly enhance the performance of the present bumpy torus concept, (2) clarification of key issues entering into the evaluation of these new concepts, and (3) suggestions for further improvements to promising new concepts and directions for future studies.

The technical coverage in the workshop was very broad. In a total of 25 papers presented, there was a large number of creative new concepts. In addition, there were several discussion sessions for detailed discussions of classification, comparison, and potentials of these new concepts. The papers presented fell into the following categories: Magnetics — Closed Field Line Devices (5 papers), Magnetics — Closed Flux Surface Devices (5 papers), Interpretation and Supporting Theory (6 papers), Electric Field Enhanced Confinement (3 papers), RF Heating (3 papers), and Ring Physics (3 papers). It is convenient to review the workshop under these subject categories.

2. MAGNETICS — CLOSED FIELD LINE DEVICES

(Chairman: G. Gibson, Westinghouse)

The papers in this session addressed the magnetics of closed field line devices. This property of a magnetic field is found in the conventional bumpy torus, which consists of a toroidal array of circular coils. The advanced concepts discussed in this session that maintain closed field lines also consist of planar coils whose centers lie on a curve confined to a plane. However, the coils were either noncircular or not arranged in a torus, or both.

The objectives of these advanced concepts are to make the drift surfaces of the trapped and passing particles and the surfaces on which the quantity $\oint d\ell/B$ is constant more concentric and centered near the minor axis of the device so as to maximize the plasma volume utilization and minimize the neoclassical transport. They also have the objective of minimizing direct particle loss due to particles on unconfined drift surfaces, e.g., for transitional particles. These geometries depend on the "bumpiness" of the field to provide the poloidal drifts that result in closed drift surfaces and to achieve an equilibrium. The hot electron rings that characterize an ELMO Bumpy Torus (EBT) are still required to alter the field gradient in regions of bad curvature to obtain plasma stability.

Some of the advanced concepts that were presented had been under study for many months, whereas the analyses of others were preliminary in nature. In general, the analyses were based on the vacuum magnetic field only, and particle drift surfaces were obtained from the invariance of the particle's energy and the adiabatic invariants μ (magnetic moment) and J (action integral).

Three of the advanced concepts that were presented consisted of a toroidal array of noncircular coils. Each of these advanced concepts was shown to meet the desirable objectives of better centering of drift surfaces, reduced neoclassical transport, reduced direct particle losses, etc., as described earlier. The first advanced concept, presented by R. L. Miller [Applied Microwave Plasma Concepts (AMPC)], is identified as the ELMO Bumpy Torus with Enhanced Confinement (EBTEC). The EBTEC configuration consists of a toroidal array of racetrack-shaped coils ("Andreoletti coils") whose major axes are alternately oriented vertically and horizontally. By adjusting the elongation of the coils and the relative radial shift in the centers of alternate coils, it was shown that it is possible to obtain nearly concentric trapped and passing particle drift surfaces, thus greatly reducing the random-walk step size for diffusion. In addition to looking at a "next-generation-size" device, an analysis was also performed for a "reactor-size" device based on the Andreoletti coils. Because of the space requirements for a blanket and shield in a

reactor, a smaller aspect ratio results and some of the outer drift surfaces are scraped off by the blanket. However, it was still possible to produce a set of drift surfaces that would be more suitable for plasma confinement than those produced by a toroidal array of circular coils. The second alternative, presented by L. P. Mai and G. Gibson (Westinghouse), is the Bumpy Bean Torus (BBT) that consists of a toroidal array of bean-shaped ("Pacman") coils. The concave sides of the coils face the major axis of the torus. The effect of these coils is to increase the length of the field lines at the inner bore, while the field lines at the outer bore are essentially unchanged. This device, BBT, was also shown to significantly improve the plasma volume utilization and particle confinement. A third noncircular coil option, inverted D-shaped (ID) coils, was presented by M. Fujiwara and co-workers (Nagoya University, Japan). The parameters that describe the noncircularity of ID coils (ellipticity and triangularity) are similar to those of typical tokamak D-shaped, toroidal field coils. In a bumpy torus, however, the vertical "straight" leg is optimally located on the outside of the torus rather than on the inside. In a toroidal array of these coils, this orientation results in a partial cancellation of the vertical drift that arises from the toroidal effects.

Another class of advanced concepts that was presented consists of linear sections of magnetic mirrors connected by curved, high field regions. All toroidal effects are concentrated in the high magnetic field "corners." L. W. Owen et al. [Oak Ridge National Laboratory (ORNL)] have considered racetrack, triangle, and square geometries, which consist of two, three, and four linear arrays of magnetic mirrors, respectively. However, an in-depth analysis was carried out for the ELMO Bumpy Square (EBS), whose straight sides were constructed from EBT-S coils and whose high field "corners" use new coils. It was these results that were presented and compared with the present EBT-S configuration. In addition, Owen et al. have also considered replacing the circular coils in the straight sections with the Andreoletti coils. The Japanese team (Fujiwara et al.) reported on analyses of racetrack, square, and octagon geometries. Mai and Gibson (Westinghouse) proposed

the Bumpy Polygon, which is composed of single linear mirror sectors connected by short, high field, curved sections. Results were presented for a case consisting of 12 mirror sections. For all of these nontoroidal geometries, improved magnetic properties were demonstrated. In general, there is better centering of the drift surfaces and $\oint d\ell/B$ surfaces, and there are improved passing and transitional particle drift surfaces. These configurations are characterized by larger fractions of trapped particles because of the higher magnetic fields at the corners. Preliminary results reported by Owen et al. indicated that the neoclassical confinement time should be an order of magnitude larger for the EBS than for an EBT of comparable size. It was also pointed out that several heating techniques may be more practical for the geometries with linear mirror sections. For example, long path lengths would be possible for neutral beam injection. Also. ion cyclotron heating (ICH) and electron cyclotron heating (ECH) waves could be launched from the high field corner regions. The impact of the high field corners on the equilibrium and stability must still be determined.

S. Yoshikawa [Princeton Plasma Physics Laboratory (PPPL)] noted that a fundamental difficulty may exist with the use of energetic electron rings. In order for the rings to be MHD stable, tying of the field lines is apparently required. This means a cold plasma must exist along the field lines. A large neutral density will be associated with this region, and this can result in ion loss via charge-exchange processes. To avoid this problem, Yoshikawa suggested creating a minimum-B field from a combination of a toroidal field and a multipole field to confine high energy electrons stably. Three possible modes of operation were suggested. The first consists of trapping high energy ions in the azimuthally symmetric minimum-B field; the other two involve inducing currents in the electron cloud to produce magnetic surfaces.

In order to evaluate the merits of these advanced concepts relative to other concepts some form of normalization is required, e.g., keeping quantities such as the mirror ratio and the plasma size (major radius, minor radius) constant. It was recognized that although

various normalization schemes were employed, a more uniform method is desirable.

In summary, a number of advanced bumpy torus concepts having closed field lines were identified. Based on the analyses presented, better plasma volume utilization and better confinement than those of a conventional EBT are expected for these devices.

3. MAGNETICS — CLOSED FLUX SURFACE DEVICES

(Chairman: W. B. Ard, McDonnell Douglas Astronautics Company, MDAC)

In addition to the closed field line geometries discussed in the previous section, several new advanced configurations were proposed that were categorized as closed flux surface geometries. Papers presented in this session fell into two categories: the design of a new device with closed flux surfaces and the use of EBT principles in closed flux surface devices. Papers presented by J. F. Pipkins et al. (MDAC), R. J. Schmitt et al. (MDAC), and M. Fujiwara et al. (Nagoya Univ., Japan) discussed the use of rotational transform in bumpy tori to center the passing particles and to close the loss cones. A. H. Boozer (PPPL) and J. W. Van Dam [Institute for Fusion Studies (IFS)] discussed the use of high energy electrons (hot electron "rings") to enhance the stability of stellarators and tokamaks, respectively, during their start-up phase of operation.

Pipkins and Fujiwara both described racetrack geometries composed of two straight bumpy sections connected at each end by semitori with rotational transform. In these configurations the bumpiness of the field provides favorable poloidal drifts and equilibrium, and the hot electron rings (in the straight sections) provide the stability. Rotational transform in the device descibed by Pipkins is produced by twisting the racetrack to form a twisted racetrack (TRT) that is something like a "figure 8." As in the figure-8 stellarator, the flux surfaces in TRT are concentric circles with essentially no shear. The flux surfaces can therefore be matched to circular, trapped particle drift surfaces in the straight sections. Preliminary estimates of neoclassical confinement in a TRT device with the same minor plasma

radius and perimeter as the EBT Proof-of-Principle (EBT-P) indicate an improvement in confinement by a factor of roughly 20 over EBT-P and about a 3-fold improvement over a closed field line racetrack at a plasma temperature of 1 keV. A preliminary engineering study of an "EBT-P-size" device was presented by Schmitt. The estimated cost for a full super conducting, steady-state device was shown to be somewhat higher than for EBT-P; however, quasi-steady-state versions (all copper or superconducting/copper hybrid) compared favorably with EBT-P, especially when the improved confinement was taken into consideration.

Fujiwara et al. considered a helical bumpy torus (HBT), which is a racetrack geometry that uses toroidal connectors with Wobig coils (the idea of the modular coil stellarator) to produce a rotational transform in a closed field line system. The differences in loss cones between the EBT with closed flux surfaces (i.e., an HBT in this case) and tokamaks, stellarators/torsatrons, and closed field line EBTs were stressed. In an HBT, the size of the loss cones in velocity space was greatly reduced. Although a pure stellarator/torsatron cannot confine particles with high pitch angle ($V_\perp/V \sim 1$), an HBT with an $\ell = 0$ (bumpiness) field component larger than the helical field component ($\ell = 2$ or 3) has closed mod-B contours similar to a conventional bumpy torus at the midplane and therefore can confine trapped particles ($V_\perp/V \sim 1$). The HBT device described by Fujiwara had a rotational transform of 0.1 and significant shear. In this device, although one did not get a min-B, the ring requirements might be relaxed due to reduced magnetic hill and shear stabilization.

The ELMO Snakey Torus (EST) described by Boozer is a helical-axis (displaced toroidal coil) stellarator that takes advantage of a hot electron component in the initially low beta start-up plasma to provide MHD stability until the core plasma pressure becomes high enough to sufficiently perturb the flux surfaces (Shafranov shift) and produce an MHD-stable configuration. The high beta regime is similar to the second stability regime in tokamaks. The device described by Boozer becomes stable at a beta of about 10% but is unstable at lower beta without the hot electrons. The equilibrium limits the beta in the device to about 20%. The hot electrons would be produced by ECH in the

low field region on the "outside" of the torus. The sloshing hot electron distribution would lie in a band spiraled (or snaked) around the torus. The width of the band would be determined by the resonant heating zones for the electrons. Because the device would be stable at its operating beta without the hot electrons, the ECH power could be turned off and, in a reactor, not contribute to the circulating power fraction.

A similar application of hot electrons to tokamaks was discussed by Van Dam. The tokamak has a stable regime at low beta and also at high beta (second stability regime), but there is an unstable regime at intermediate beta. The hot electrons would be added to the plasma during the transition from the low beta phase to the high beta phase. The stability theory discussed by Van Dam depends on the hot electron drift frequencies and is applicable when the total beta, hot electron plus core, is not high enough to reverse the direction of the drifts. The analysis yields a sufficient condition for stability. The stability boundaries for the system depend on the hot electron temperature, beta, and distribution (i.e., the fraction of the flux surface filled by the hot electrons on the outside of the torus). Curves of stability boundaries for different conditions were shown. Again, the hot electrons are required only in the transition phase to the second stability regime and are not needed during operation at high beta.

4. INTERPRETATION AND SUPPORTING THEORY

(Chairman: L. A. Berry, ORNL)

In considering advanced configurations and concept improvements, several questions need to be answered to determine what constitutes an improvement and how to quantify these improvements. Papers presented in this session discussed possible means of optimization and/or improvement of bumpy torus plasma parameters, as well as supporting theoretical calculations in the areas of equilibrium, stability, and transport.

Discussions by H. Ikegami (Nagoya Univ., Japan) concentrated on the optimized operation of bumpy tori. Ikegami argued that any new advanced concept and/or idea that would propose to improve some of the undesirable features of the present bumpy torus concept by introducing a small variation on the basic concept would be desirable, though any "fantastic deformation" could not be justified without a definitive database. First, he noted that the relatively low density feature of the Nagoya Bumpy Torus (NBT) and EBT may be due to their steady-state operation (where particle confinement time is determined by the ionization time) as opposed to being a problem with the present bumpy torus configuration. It was pointed out that tokamaks and other devices may run into similar problems as they approach steady state. Showing some experimental results from NBT, Ikegami indicated the possibility of obtaining increased (factor of 3-4) plasma density and average ion energy ($\gtrsim$1 keV in NBT) with pulsed ICH and gas puffing. Further examples for plasma confinement, stability, and hot electron ring properties were given to indicate the near-term need for pulsed operation, better centering of drift surfaces (through magnetics; ID coils were given as an example), better understanding of the stabilization mechanism of the rings, and the need for larger plasma size for neutral shielding.

C. L. Hedrick (ORNL) examined the equilibrium and stability properties of modified EBT magnetic configurations, especially those of ELMO Bumpy Racetrack (EBR) and EBS. It was pointed out that magnetic equilibria are not a theoretical problem for closed field line systems and can be generated using an extension of Lortz-Grad theory; however, in practice these may be difficult to compute numerically. One characteristic of the equilibria of EBR and EBS is the existence of localized parallel currents in the sides (straight sections) and corners. It was shown that these currents are inversely proportional to the number of sides (corners). The effect of corners on the stability was examined using a simplified version of δW for the outside field line in the equatorial plane. The results, although preliminary, indicated stability at core betas in EBS up to 10% and in EBR only a few percent. Low frequency, coupled ring-core stability was also

reviewed by Hedrick. It was shown that the Lee-Van Dam-Nelson (LVN) core beta limit could be obtained from the kinetic term in δW. Also, a number of critical assumptions used in obtaining this mode were pointed out, such as the neglect of stabilization from the perpendicular component of the perturbed field ($Q_\perp$), etc. It was argued that these assumptions were especially questionable for low mode numbers ($m \lesssim 10$) and that more work needs to be done in examining the sensitivity of the models to approximations in this area.

D. E. Hastings (ORNL) presented a formalism for calculating nonresonant particle transport coefficients for bumpy field line devices with noncircular flux surfaces. It was found that significant changes in the transport rates could be obtained by moving the (assumed) position of the plasma center (i.e., pressure surfaces centered on mod-B or $\oint d\ell/B$ surfaces). It was clear from the results presented that the performance of bumpy torus plasmas can be substantially improved by better centering of the $\oint d\ell/B$ surfaces (through some of the magnetics designs discussed in previous sections) and by making the pressure surfaces elliptical. The improvement in the diffusion coefficient was shown to be proportional to the square of the ellipticity (a result similar to tokamaks).

J. B. McBride et al. [Science Applications, Inc. (SAI/Jaycor)] described the interaction of rf waves with plasma particles in the magnetic precessional drift frequency range ($\omega \sim \omega_\nabla$). Because strong resonant interaction occurs for $\omega \sim \omega_\nabla$ in EBT, it was shown that the transport and heating caused by this type of interaction can be substantial and in some cases can exceed neoclassical transport. It was noted that the transport is selective for a single sign of charge or energy component, thus offering the possibility of rf-enhanced confinement and ambipolar potential profile control. This active means of altering diffusion and profiles could have both near-term (improved confinement, etc.) and future (alpha particle ash removal, etc.) applications if the required wave amplitudes ($\delta B/B$) are small and waves with very specific characteristics can be excited. Although preliminary, it was argued that this type of wave-particle interaction may also be responsible for the observed changes in hot electron ring

properties (i.e., increase in ring electron temperature) during ICH experiments on EBT-S.

K. Nguyen and T. Kammash (Univ. Michigan) examined the macroscopic stability of an EBT plasma in a slab model, taking into account variations of the curvature along the field line and assuming that the hot electron rings were adiabatic. Strong line-tying stabilization was observed due to hot electron compression, and the stability boundary was quite different from that of rigid ring calculations (except at low core beta). It was shown that the LVN limit, the upper bound on the core beta, still exists and is determined by the radius of curvature at the midplane (local R_c) rather than by the average curvature. Possible application of this line tying effect to a tandem mirror with a hot electron plug was also discussed.

A paper by H. Sanuki [Univ. California Los Angeles (UCLA/Nagoya Univ., Japan)] considered the effects of ambipolar field on the electrostatic drift waves as a possible model for the low frequency fluctuations observed in the experiments (EBT/NBT). In a slab geometry, a WKB analysis is used and nonlocal properties of electrostatic drift waves in a collisionless, low beta plasma with a hot electron component are considered. It was found that a strong ambipolar field (positive or negative, independent of the sign) has a stabilizing influence. It was argued that the decrease of the low frequency fluctuation level in the T-mode operation of EBT/NBT is connected with the variations of ambipolar potential in the C-T-M mode operations.

5. ELECTRIC FIELD ENHANCED CONFINEMENT

(Chairman: H. Weitzner, New York Univ.)

Papers presented dealt with the possibility of improving the performance of EBT plasmas by maintaining a positive ambipolar potential (positive electric field), by generating rf-induced ponderomotive forces, and/or by employing an alternate start-up scenario via externally applied electric fields.

C. S. Chang (AMPC) presented a series of model, one-dimensional transport calculations of EBT steady states in the collisionless ion regime, characterized by positive ambipolar potential and positive electric field, to study the effects of the heat deposition profile on potential profile variations. The model employed relatively standard transport coefficients. The calculations showed that plasmas with positive radial electric fields could achieve densities and confinement times as much as an order of magnitude larger than plasma with negative radial electric fields. It was pointed out that in order to generate the positive potential equilibrium, the plasma heating should be concentrated in the plasma center. Although preliminary, there is some evidence that ECH is more effective than ICH. Control of the power deposition profile is believed to be a key "knob" to control the ambipolar potential in a bumpy torus.

A paper by H. Hojo et al. (Hiroshima Univ., Japan) considered the possibilities of using ponderomotive forces to confine and stabilize plasmas. The ponderomotive force in this application is generated by an rf wave at frequencies somewhat above the ion cyclotron frequency. First, it was shown that in a torus with only a toroidal magnetic field, single particles can be confined by the ponderomotive force F of an rf wave perpendicular to the magnetic field (which produces an $F \times B$ particle drift in addition to the curvature and grad-B drifts, resulting in closed particle drift orbits). Such a possibility allows a ponderomotive force to generate equilibria. Second, the stabilization possibilities of such forces were examined. The LVN stability theory was extended to include the rf-induced forces. It was shown that rf-wave amplitudes on the order of 4-5 kV/cm could stabilize EBT-like systems. Numerical simulations of such effects were shown to be in good agreement with the theoretical one.

J. R. Roth (Univ. Tennessee) reviewed the history of the NASA-Lewis Electric Field Bumpy Torus (EFBT). In that device electrodes in the plasma generated radial electric fields (up to 1 kV/cm) that confined and stabilized the plasma. Roth argued that the low density and low ion temperature results in EBT-S are due to the means selected (e.g., ECH) to generate and sustain the plasma and

proposed modification of EBT-S to add (electrodes) electrostatic confinement during the start-up phase to enhance the density. It was noted that the electrodes could be implemented in the plasma without impurity problems or other technological problems. Using the earlier results from EFBT, Roth projected that EBT-S density could be enhanced (by the EFBT technique) by a factor of 2-3 to generate a target plasma for subsequent ICH or ECH heating.

6. RF HEATING

(Chairman: H. Weitzner, New York Univ.)

Papers presented in this session also dealt with the possibility of improving performance. In this case, however, alternate heating schemes and better launching techniques were discussed.

T. Sato et al. (Nagoya Univ., Japan) described recent experiments on the RFC-20 device at Nagoya. The magnetic field configuration of the central section of RFC-20 is a mirror-like geometry. A gun plasma or ECH-generated plasma was used as a target plasma, and ICRF waves were applied (by a rotating antenna) both to build up a high density plasma and to sustain it. The rotating antenna induced either right-handed or left-handed circularly polarized waves. The right-handed wave produced higher density (up to 10^{14} cm^{-3}, peak value) and lower ion temperature (around 50 eV) than the left-handed wave (density $\sim 10^{13}$ cm^{-3}, ion temperature $\sim$ 150 eV). This plasma was sustained for the duration of the rf pulse and gas puffing ($\sim$50 ms). Sato argued that such a procedure could generate a target plasma in EBT for other heating mechanisms. As reported by Ikegami earlier, such tests on NBT have already been started.

In view of the importance of energy deposition calculations in evaluating EBT performance, S. Tamor (SAI) extended and improved a model of D. Batchelor's used to estimate the ECH energy deposition in various parts of the plasma. The partitioning of the energy into the core plasma, the ring plasma, the (cold) surface plasma, and the wall was given. The inclusion of the energy absorbed by the wall was shown to be important unless the wall reflectivity is extremely high,

$\gtrsim$98-99%. Comments by Batchelor indicated that recent experimental measurements on EBT showed this condition is satisfied. Tamor's model was in other ways more general; provided wall effects are small, the results were not significantly different from the earlier model.

D. Batchelor (ORNL) applied his energy deposition model to examine the effects of controlling the polarization and directivity of the applied ECH waves. It was argued that appropriate wave launching in the EBT-S mirror throat, high field region instead of the mirror midplane, low field region should allow varying the ratio of ring plasma to core plasma heating. This variation was shown to allow more parametric studies in EBT-S and possible improvements. Throat heating should allow more of the applied ECH power to couple into the plasma of interest (core plasma) rather than the cold surface plasma, and thus the heating should be more efficient. To implement most of these advantages, Batchelor outlined the plans for throat launch experiments on EBT-S.

7. RING PHYSICS

(Chairman: H. Ikegami, Nagoya Univ., Japan)

Highly energetic particles have been used for stabilization in various devices. In EBT and NBT (as well as STM), the hot electron rings are believed to produce a local diamagnetic well that provides the stability. Papers in this session discussed the possibility of controlling ring parameters and power losses as well as the possibility of forming hot electron rings in a modular stellarator.

B. H. Quon (Jaycor) proposed the use of Surmac coils to change the magnetic geometry and to control and modify the ring parameters. Quon argued that by using a Surmac coil coaxial with the mirror in the midplane it could be possible to modify local magnetic field scale length and to stabilize the hot electron rings by modifying or creating local mirror fields. It was noted that if the ρ/L scaling of N. Uckan holds, controlling the scale length (L) may permit operating the ring at the optimum ring energy in a reactor. However, the compatibility of this system (a current-carrying conductor near the plasma surface) with

a reactor environment was questioned. Quon also noted that the Surmac coil could provide additional stabilizing effects to "anchor" the ring by providing a favorable $\oint d\ell/B$ region between the ring and the cavity wall and confinement of a stable cold plasma at the separatrix in the vicinity of the ring.

S. Hamasaki et al. (Jaycor) presented a series of model calculations for the power requirements of ring production, based on the assumption that the ring electrons originate as runaways accelerated by the first harmonic resonance of the extraordinary mode. The required microwave power for start-up is shown to scale roughly linearly with the background core plasma density and is observed to be independent of the magnetic field strength. It was argued that because the core power requirements scale with square of the density, whereas ring power scales linearly with density, the idea of using alternative heating schemes for core plasma heating (i.e., ICH, neutral beams, etc.) would be more economical than ECH, especially for a reactor.

Combining the features of stellarators, tokamaks, bumpy tori, etc., opens new approaches to configurational optimization (some of which were discussed in previous sections), as well as introducing new questions. A paper submitted by J. A. Rome et al. (ORNL) and presented by D. Batchelor addressed one of these questions: can the hot electron rings be produced in the desired magnetic configuration? The example given was a modular stellarator with EBT-like rings, called a helical bumpy torus. In this system it was possible to obtain closed drift surfaces for energetic ($\gtrsim$100 keV) electrons with small $V_{\parallel}/V$ (deeply trapped) whose orbits reside on axis-encircling, closed mod-B surfaces. This locus (mod-B) was shown to be nearly omnigenous with the flux surfaces, thus indicating the possibility of creating a ring in a modular stellarator.

17/18

OVERVIEW

ADVANCED BUMPY TORUS CONCEPTS: WORKSHOP OVERVIEW

Nicholas A. Krall
JAYCOR
P. O. Box 85154
San Diego, CA 92138

In keeping with the theme of the workshop, Advanced Concepts, a great deal of original information was exchanged and a lot of innovative ideas exposed to scrutiny. In this overview I have tried to summarize these ideas and group the various contributions into categories.

The idea of the workshop was EBT improvements; one question is, is there a need for improvement? This question was raised and commented on by many people. As I see it there are two examples of the need to improve. One is the need for improvement in parameter performance of present experiments, the second is the need for enhancement of the attractiveness of an EBT reactor. Parameter enhancement is an obvious need; we would like to get better density, better temperature, and better confinement times. It was pointed out variously that it is important to try to get those better parameters per unit dollar because of the difficulty in obtaining funds for building experiments of increasing size and cost. However, enhancing the reactor is also important. Figures of merit in that category include dollars per kilowatt per design, unit cost, maintainability, complexity, availability, construction time, and so on.

In the category of parameter enhancement, EBT-S with parameters of 10^{12} cm^{-3}, a few hundred eV, and confinement times of order of 1 ms or less,

performs somewhat below what one might expect in terms of, for example, microwave cut off densities. EBT-S performance of 10^{13} cm^{-3} density, keV temperature, and 10 ms confinement time would be plausible if one simply took the classical arguments and did not worry about, for example, the wall interactions or possible other problems. This is such a substantial gap in parameter performance that one technique for improvement would simply be to try to induce the present devices to perform something like we thought they might. Several ideas for producing this sort of performance were discussed in the workshop, including an attempt to increase the power coupling, and an attempt to increase the filling factor in the device. It may be that in the present devices, although they have a certain size, the radius that goes into the transport calculation should be less than the device size because of the general problem of drift surfaces not exactly matching the device.

Now, how is one going to improve performance? There were at least four suggestions raised in this meeting for improving performance parameters, i.e., parameter enhancement. One was to build a new device, with different geometry. A second was to help the present device to behave as one had expected it would. A third was to build a new device, which is more likely to behave as expected, or at least to build a device that is so good that even if it doesn't behave right, it is still attractive. A fourth was to simply use the EBT techniques to help some other device to perform better.

When considering concept improvement, it is useful to relate EBT to the mainline devices. You will recall that a tokamak that performs substantially worse than classical still seems to be OK; neoclassical tokamak transport is so good that even if performance is degraded, it is still adequate. Mirrors, on the other hand, can be classical and not OK at all because classical end loss is not acceptable. EBT classical performance, on

the other hand, is OK but there is not a big margin of failure relative to classical performance before we are in trouble. This emphasizes the need either to obtain neoclassical performance, understand why not, or possibly come up with a device that has substantially better classical performance so that one could afford to have it degraded. Finally, the need for enhancing the reactor comes about despite the fact that EBT has, to begin with, a lot of advantages: steady-state, modular, modest technology, high beta. In the years since these virtues of EBT were identified, the main-stream devices have recognized and tried to incorporate these advantages. This led to the emphasis on current drive in tokamak to approach steady-state, and to modular stellarators to try to get some of the maintainability/availability advantages that come in EBT. Further, high beta is no longer unique to EBT, particularly as beta limits for EBT have been suggested. TMX's are relatively high beta machines, and both tokamaks and stellarators are looking toward (high) second beta regimes. These are reasons for needing enhancement in parameters, and also for needing enhancement in reactor performance.

In this overview, I will show what has been done at this meeting relevant to both those categories.

I. PARAMETER ENHANCEMENT

Make the Device Behave as it Should

It has been suggested by many authors that an attempt to reduce the shift of the passing particle drift surfaces compared with the trapped particle drift surfaces would have a very good effect on transport and

confinement. Coil configurations were suggested that would do this. Detailed discussions on Andreoletti coils, bean coils, and inverted-D (ID) coils all have the effect of centering the surfaces. Some of these presentations were qualitative, some were not. One thing they have in common, I think, is that none of these designs are yet optimized. On the plus side, all of these coil designs seem to center the drift surfaces and increase the area filled by them. A trouble with the work presented at the meeting is, in general, that the comparison of these designs with conventional designs lacks a detailed discussion as to how much of the effect is due to changes in mirror ratio. Also, questions of increased problems with the coil mass, fill factors, possibly engineering power density for a reactor device as you fill less and less of the device, are not yet addressed. A good feature is that in many cases it appears that the ring requirements might be relaxed. As some of the designs provide flatter $\oint d\ell/B$ profiles it might be that the ring requirements for MHD stability are less stringent. A bad feature is that we really lack quantitative documentation of the effect of centering on performance, i.e., how much does centering the surfaces actually change the diffusion coefficient? In summary, there is extensive work on coil configurations that have the apparently good effect of centering the surfaces.

A second technique for improving performance is to try to change the transport in some active way. I remind you that TMX emerged from a mirror machine that classically was not suitable for a reactor. They identified the loss regions and then in one design after another attempted to actively combat the transport, using end cells, ponderomotive forces, etc. We heard a number of works described at this meeting going in that direction and I think this is really a sound direction in which to look. One, for example, was the use of low frequency waves in the drift wave range to alter transport selectively, by

mass, by charge, and by direction (in or out). The effect of ponderomotive forces from modes which might be externally localized and provide an inward force was also discussed. It seems this is a likely area to pursue, having the advantage that this sort of thing could possibly be done on existing devices, whereas to rebuild the coil configuration might take a little longer.

Thirdly, along with improving the coils and tailoring the transport, ideas to improve the coupling of power, try to improve the density, try to reduce the atomics, reduce the control of these devices by atomic processes, were also discussed. One question that was raised was whether steady-state itself is a problem. It may be true that simply the nature of steady-state operation leads to an equilibration with the wall, and more neutrals, resulting in lower density. If that is true, then tokamaks and other devices might run into similar problems as they approach steady-state. So the question of whether a pulsed operation might be a technique for making the present devices behave was raised in a very active way. Bigger size is always stated as a way to isolate the plasma from the wall, but it is not obvious we have that option, and pulsed operation might provide similar information.

The idea of trying to direct the X-mode to resonant surfaces was discussed in an attempt to improve the power coupling as well as the power distribution, putting the power where needed so as to make both for better efficiency and possibly avoid certain instabilities. Improving confinement would raise the density and that is another figure of merit sought by pulsed operation, new coil configurations, and alternate heating and launching schemes. There is really a strong case to suggest that the actual power absorbed by this device is 10-20% of the input power. When you look at the neoclassical calculations and how they scale you find the scaling looks quite good except the amount of power absorbed does not seem to be as high as it

should be. Similarly, this morning it was pointed out that the rings at the C-T transition also scale very nicely with theory, except that the theory says less power should be required than actually is required.

Thus, alternate heating schemes or better launching techniques could have an even more dramatic effect than expected. One alternate heating scheme was discussed at this meeting, i.e., ICRF. This very exciting work showed that ICRF in the 20-30 kW range was producing kilovolt type ions of $10^{13}cm^{-3}$ density in the pulsed operation. The idea of ECH power restricted to ring heating was discussed as a method to relax power requirements, because after all, in the reactor once the thing burns only the rings need be sustained. The evidence that the ring absorption is scaling with the density even though the core is scaling with the density squared, could actually have a big effect on the reactor design. Further, the idea of alternate startup scenarios was raised. The idea raised that radial electric fields in a startup mode would lead to high densities is problematical, but I note this statement and then come back to the suggestion that pulsed operation can lead to high density. Seems like there should be more thought given to startup scenarios that might lead to a higher density regime where one can begin testing performance.

Fourthly, the idea of improving the present device by changing the ring stability with geometry was raised. Even though the ring works very nicely, nonetheless as the ring gets hotter, the walls get moved further away, beta gets bigger, and the Lee-Van Damm limits begin to come into play, the idea of changing the ring stability by changing the magnetic geometry through min-B or Surmac coils, for example, becomes a real possibility. Further, the idea in general that you might control the ring either by deposition (throat launch) or by geometry, has implications toward the reactor if not toward the present experiments.

Make a New Device

Instead of improving the present device, it was suggested that we simply make a new device. There are two types of devices that were presented in this meeting. The first type included squares, octagons, racetracks, polygons, all of which have in common that they maintain the closed field line feature of EBT but place the curvature in high magnetic field regions. This, as was the case for coil design, leads to lower drifts, better centering, possibly lower magnetic field where the rings are being formed, and increased flexibility in heating. Beam heating, for example, is enhanced in a racetrack where the path length is long. There were some evaluations of these geometries and some documentation comparing, for example, a torus having bean-shaped coil designs with a polygon having conventional coils. The results are limited, but to the extent that I saw them, the performances were comparable. Performance is generally evaluated in terms of centering, fill factor, and what percentage of the core volume is being encompassed by the surfaces of first and second invariant. Things that are missing, on the other hand, are questions as to what extent the mirror ratio is having an effect on things other than the number of bumps. Questions remain: what is the volume utilization, what about the stability requirements, to what extent are these things going to make the rings more necessary or less necessary?

Finally, the question of coil stress was raised in at least one talk and seemed to be a real question when deciding to what extent these coils are improvements. This comes back to my first point which was that improvements can be due to performance in parameters or performance in reactors. If you improve the parameter at the expense of the perceived reactor desirability, then we have not made progress, in my opinion.

A second attempt to design a new device was to not maintain the closed field line but rather to move to flux surface geometries, which might be stellarator in type. One detailed presentation discussed a twisted racetrack. That was nice in a sense because one could do a rather direct comparison between a racetrack picture (closed line) and a figure-eight racetrack picture (closed flux surfaces) and maybe try to establish some of the differences in construction if not in physics. The example given of a twisted racetrack showed that the drift surfaces passing and trapped were more centered, and less ring was required. This was because although one did not get a min-B in the device, nonetheless one did reduce the hill, seen by plotting the $\oint d\ell/B$ surfaces. The question of ambipolar potential changes is an important one, with a real difference between flux surface geometries and polygons; this was not calculated or estimated. In flux surface geometries, flux surfaces will tend to become ambipolar potential surfaces whereas in closed field line devices, field lines will tend to be constant potential surfaces.

Preliminary indications from the design as presented indicated that a twisted racetrack of the same size as EBT-P might have twenty times the confinement. The same study indicated it might have three times the confinement of the closed field line racetrack. I think that "approximate" is really to be emphasized here, as it was by the authors; nonetheless, this kind of comparison seems to be central and it has to be done in these evaluations.

The general idea of control knobs for improvement studies is a good one. There was so much complexity discussed at this meeting in terms of coil shapes, centering of coils, shapes of the torus, flux surfaces, etc., that the idea of many knobs rather than many devices is quite important; nevertheless, the only knobs that were presented at this meeting were theoretical. This is

also important, because to some extent even though you always give up rigor in order to do a more general calculation, at least the calculation doesn't have to be redone for each geometry; so this kind of knob does give guidance. We saw a detailed summary of the relative effects of $\ell = 0$ and 1 windings superimposed on weak $\ell = 2$ or $\ell = 3$ windings; that is, various types of hybrid stellarator/EBT configurations. Performance parameters that were compared were centering, shear, loss cones, etc. Some of these had more shear, which would reduce, in principle, the amount of ring needed. On the other hand, as was pointed out this morning, a little bit of shear is not a good thing in that it might introduce tearing modes and other instabilities that are simply absent in closed field line geometries. And that was not mentioned during any talk presented at the meeting; it was mentioned in the discussions. I think it is clear that just because a strong shear machine works does not mean a little bit of shear added on to the closed field line geometry is good. These are the directions in which the research will probably go. Another knob tried to analyze some of these things in terms of the number of bumps and number of twists and indicated that the more bumps the better. On the other hand, one must recognize the more bumps, the more complexity, the more microwaves, the more cavities.

Help Other Concepts

In addition to new devices that make the present concept work, the question of helping other concepts was discussed very extensively. Generically, the ideas were to enlarge the region of apparent stability. One idea was based on the fact that in addition to the low beta, stable region of tokamaks and stellarators, well documented, high beta regions of apparent

stability have been predicted theoretically, though not documented experimentally. The transition between the two might be achieved by adding the stabilizing feature of an EBT ring. This emphasizes what rings do: for EBT, the local change in B provides (permanent) stability; for Astron, field reversal provides stability, and for heliac, tokamak, stellarator, etc., transient ELMO ring population would provide transient stability. It is really important in my mind to note that in EBT and other devices, we have a lot of physics that is well documented. By contrast, when talking about going from here to there by using these ELMO techniques, the "there" is not well documented. These applications involve transport-specific calculations specific to these devices, involve geometry-specific stability calculations specific to these devices, and involve a data base that is specific to these devices. At some stage it might be very useful to the community to provide the service of hot electron rings, but I don't think we should think, just because we haven't lived with stellarators and tokamaks day after day, that they don't have their own troubles. When we talk transient stabilization to an undocumented regime, we talk about a sea of unknowns that should not be underestimated.

The general question of shear versus rings versus beans in hybrid mainline devices was raised, and is important. These other devices have shear, which reduces the ring requirements. The rings, on the other hand, can produce stability, but the coil configuration will be quite different from EBT. There might be practical advantages to this. So this point, this interplay of shear, ring, and coil shape, was actively discussed for tokamak and stellarator applications. This points out that things like the RF facility or other facilities that use bumpy torus techniques in a more general way might be of broad service to the community.

II. REACTOR PERFORMANCE ENHANCEMENT

In evaluating reactor aspects of the EBT program, some terminology definition would be useful. The discussions at the end of day one of the workshop centered on what is an advanced EBT? The average opinion around the room seemed to be that anything with a bump or hot electron was an advanced EBT. I don't agree with that. To my mind, all confinement schemes have both novel features, i.e., rings and bumps, and common features. The common features in general are transport, loss cones, stability, equilibrium, heating, and, very important, their data base. At some stage this list is going to distinguish EBT/NBT from EST (ELMO Snakey Torus), TOK, etc. There is a data base and a certain level of understanding of these items for EBT/NBT. There is a similar type of understanding of these items for tokamak and stellarator. At some stage the hybrid device is so far from EBT that the people who know about the data base for the "common features list" are not the EBT community. And therefore, just because it has a bump or an electron does not necessarily make it appropriate for EBT discussion. On the other hand, a number of other intermediate devices are not exactly closed field line devices, but might have many of the EBT common features, while being topologically very different from EBT. It seems to me those are fair game for us. I give Wendlestein and the German experiments in stellarator as an example. The question of a hybrid between a stellarator and a tokamak was addressed by a stellarator group to find improvement in their concept and they have made enormous progress, and have done their community a good service. So to simply rule out a device from our consideration because it has flux surfaces, is wrong. On the other hand, there must come a transition in which

we are so far from the EBT theoretical and experimental data base that we should not pursue it by ourselves.

What is an Improvement?

There were at least three examples of reactor improvement discussed implicitly during the meeting. First, the use of EBT to bridge a gap is an improvement in the fusion program as a whole and therefore is important to reactor physics. This use, however, has subsidiary problems such as kinks, resistive modes, technology problems which were not addressed, but nonetheless, a lot of useful effort was spent here. Second, the ideas on parameter enhancement might also constitute reactor improvement. However, we must learn to quantify the things that we hope might be practical improvements, like centering. There was some theoretical work presented in that direction, including an attempt to quantify the effect of ellipticity in the coils, in a very simple way. Never mind that the theories at this level must be simplified; in return you get a formula that gives a possible figure of merit. Similarly, work seemed to be carried out or in progress to quantify the effect of the shift in displacement of the drift surfaces and what effect that has on the diffusion and therefore reactor size. That is very much in the direction of quantifying the question of what is an improvement. The possibility, for example, that an improvement might give rise to parallel currents which instead of closing after one bump close half way around the racetrack, modifying the magnetic field, the stability and the transport, is a very good thing to keep in mind when trying to quantify what is an improvement. It might not be an improvement at all, in the same way that a little shear might not be an improvement at all. Finally, when thinking about

reactors, anything in the direction raising the beta limits would be an improvement; these, unfortunately, seem to require really gory details in the theory but some people are beginning to have the stomach to go into that.

Directions for Reactor Optimization

Reactors were not discussed specifically in this meeting. In fact, the question was raised, what's wrong with EBT as a reactor? There may be nothing wrong with EBT. It may be just how it is perceived at this particular moment by the people who are evaluating the fusion program. EBT already has done much good, including documenting all the advantages that we know about in an EBT reactor. But consider, along with the fact that there is not enough money to do everything, the following premise. Even a successful, steady-state tokamak may not be economically competitive with light-water reactors or other power sources. Once you make the premise that even a successful tokamak may not be competitive, you conclude that an EBT has to be, economically, a whale of a lot better than tokamak, in order to be what we need, particularly if you cannot afford everything. The people who show they can do a lot better than tokamak, economically, begin to make strides. This is the kind of argument that leads to the need for reactor improvement in EBT, i.e., the argument that tokamaks themselves, even if they work, may not be competitive.

There is a figure of merit in this that I would like to point out very briefly, and that is the engineering power density, defined as the output power divided by the volume of the device. This figure of merit can be used to compare fusion devices with light water reactors and has been done extensively. This shows the direction in which you want to push parameters.

Power densities are proportional to $n^2a^2/(a + \Delta)^2$ where n is the density, a the minor radius, and delta the thickness of the shield, blanket, and coils. There is a constraint on this equation, namely that the wall flux cannot be bigger than a certain amount; that gives a limit on n^2a. If the device approaches the wall flux limit, P_c, the power density is $P_c a/(a + \Delta)^2$. From this it appears that a machine whose minor radius (of the plasma) is comparable to the thickness of the blanket/shield/coil is the most economical in terms of the highest power density. It turns out that optimizing $a = \Delta$ gives power densities which are similar to those of the light water reactors.

Unfortunately, there is another constraint. This constraint is that at this size and that density, the device has to be exothermic; namely, the fusion power produced has to be bigger than the power to sustain the reaction. This is the reason we often look for improvements in confinement without quantifying what they do for a reactor. The less diffusion the more nearly one can approach the size that is desired. Beta limits also place limits on n, because there are, in general, limits on magnetic field.

I leave you with a couple of examples that I have taken from various reports. Starfire is a tokamak reactor design with a minor radius of 7.5 m, and has an engineering power density (EPD) of 0.3. One particular fusion engineering device (FED) design has a minor radius of 5 m and an EPD of 0.1. TRACT is an example of a small reactor based on a field reversed theta pinch, which has a size a lot less than the 1 m required for blanket and shield, and therefore smaller than optimum. It has a power density of 1.7. The compact reversed field pinch design was optimized with respect to this figure of merit as stated, and so had a 1.5 m minor radius, nearly matching delta and would have an EPD of 14, <u>transport losses permitting</u>. Folded into this, of course,

is the question of how much you are willing to pay for the wall, and this compact reversed field pinch had a wall loading of 20 MW/m^2, which may be too high a price. But the fact that this design came out near to a light water reactor in EPD has resulted in some gains for its proponents. Therefore, the original EBT reactor, similar to the original reversed field pinch reactor, is more comparable to Starfire. The direction for improvement is increasing n and optimizing a, or increasing $A^2B^2R^2_T$.

So, in summary, there are ideas for improving the present devices, making new devices, and helping old devices. Some of those things have been quantified, but none of the studies have gone in the direction of optimizing the reactor; although it is really premature to do so, this is in fact one of the present motivations for the search for an advanced concept.

35/36

MAGNETICS-CLOSED FIELD LINE DEVICES

DRIFT SURFACE STUDIES OF EBT CONFIGURATIONS WITH NONCIRCULAR MAGNETIC COILS*, **

R.L. Miller, R.A. Dandl and G.E. Guest
AMPC Inc.
Encinitas, California 92024

ABSTRACT

We have carried out a systematic comparison of the drift surface properties of a number of noncircular magnetic coil geometries for EBT. The most promising configuration we have identified is the shifted Andreoletti coil set (racetrack coils which are alternately positioned horizontally and vertically). By adjusting height-to-width ratios and a radial shift parameter, it is possible to make trapped and passing particle orbits nearly coincide indicating greatly enhanced confinement. Furthermore, at large aspect ratio, even the resonant particle drift orbits are closed and nearly circular. Thus resonant particle losses should be greatly reduced as well.

1. INTRODUCTION

The particle and energy confinement observed in the ELMO Bumpy Torus experiments have been interpreted as due to neoclassical processes[1,2]. In that model, transport rates are ultimately determined by the Coulomb scattering of particles from one guiding center drift orbit to another. The drift orbits of particles with different energies or pitch angles are not concentric and thus a Coulomb scattering leads to a spatial excursion or "step-size" whose size is determined by the extent of the non-overlap of the two drift orbits. With proper averaging over energy

*Work supported by Department of Energy Contract No. DE-AC03-82ER51030
**A portion of this work related to an EBT-P scale device has been submitted for publication to Phys. Rev. Letters and may be subject to an APS transfer of coypright agreement.

and pitch angle, these step-sizes can be used together with collision frequency information to determine transport rates.

One class of particles which leads to very large spatial excursions is the set of resonant particles which reside in a narrow range of pitch angle space near the trapped-to-passing transition region. These particles have nearly zero azimuthal drift because they sample nearly equal amounts of positive and negative field curvature. Thus they drift primarily vertically and execute eccentric and, in many cases, unclosed orbits. The role of these resonant particles in determining the overall confinement properties of the ELMO Bumpy Torus is not adequately understood at present, but in a nearly collisionless plasma the resulting loss of particles scattering slowly through the resonant interval in pitch angle seems likely to have serious consequences.

Strictly speaking, the above picture of confinement applies only for high energy particles. For particles of moderate energy ($\varepsilon \sim e\phi \sim kT$), the radial ambipolar potential can significantly modify the drift surfaces. However, previous work[3] has shown that the vacuum field drift surfaces, when compared with more accurate ambipolar results, provide a good measure of relative confinement properties among various coil configurations.

Noncircular coils[3,4] offer the possibility of improved confinement by modifying the single particle drift orbits in such a way that Coulomb scatterings lead to smaller step-sizes. Here we report a remarkable improvement in the drift-surface geometry for trapped, passing and resonant particles in a bumpy torus made up of a toroidal array of racetrack-shaped coils whose major axes are alternately oriented vertically and horizontally. Because of the resemblance of one sector of this torus to straight, magnetic-mirror coils analyzed by Andreoletti[5], the coils may appropriately be described as "Andreoletti-shaped". But the elongations discussed here are only 2:1 or 3:1, in contrast to the extreme elongations required for the magnetic well of interest in the early mirror studies.

The basic parameters that define the ELMO Bumpy Torus/Enhanced Confinement (EBTEC) configuration are as follows: (1) the elongation of the racetrack-shaped coils, H/W; the major radius of the torus, R, relative to the minor radius in which plasma is confined, a; the position of the "limiter", which can be either a material limiter or the surface on which the stabilizing ELMO ring is located; the relative shift in the centers of alternate coils, ΔR; and the mirror ratio in each sector, M.

In this report, two EBTEC configurations are discussed, each with mirror ratio, M, equal to 2.25. The first has overall dimensions similar to the EBT-P conceptual device[6] with R = 500 cm, a = 20 cm, H/W = 2, and ΔR chosen to align the centers of the trapped- and passing-particle drift surfaces (~ 25 cm). The second configuration is "reactor-size" with R = 35 m, a = 1.25 m, H/W = 3, and again ΔR chosen to align drift orbit centers (~ 7.5 m).

All drift surfaces presented here are calculated numerically using the magnetic field geometry code EFFI[7] and the entire technique is described in Ref. 3.

2. R = 500 CM CASE

In Fig. 1, one quadrant of the equitorial plane of the R = 500 cm case is shown. The two field lines denote the boundary of the plasma. It is qualitatively clear from the two field lines that EBTEC achieves a magnetic configuration somewhat reminiscent of that studied by Meyer and Schmidt[8].

In Fig. 2, we compare midplane sections of surface of the drift surfaces of deeply-trapped ($V_{\parallel}/V \to 0$) and fully-passing ($V_{\parallel}/V \to 1$) particles for EBTEC (Fig. 2a) and the corresponding elementary bumpy torus, (Fig. 2b). $(V_{\parallel}/V)^2$ is defined as $(\varepsilon - \mu B_{oo})/\varepsilon$, where ε and μ are the energy and magnetic moment of the particle and B_{oo} is the maximum magnetic intensity in the midplane between two successive coils. For the deeply-trapped particles,

the center of the section of surface is indicated by the symbol 0 ($V_{||}/V = 0$). The largest section of surface for fully-passing particles contained within the surface for trapped particles is also shown in these figures, and the center is indicated by the symbol * ($V_{||}/V = 1$). Note that in EBTEC the two surfaces are nearly concentric, whereas in the elementary bumpy torus the centers are separated by 7 cm. It is this separation that is usually taken as the basic step size in a random walk picture of neoclassical diffusion in the absence of any ambipolar field. Also shown in these two figures are the projections of the outline of a material limiter, along magnetic lines-of-force, onto the reference plane. The position of the limiter was dictated by considerations of shielding the magnetic coils. It is clear that EBTEC renders the limiting drift surfaces concentric. The circular coil drift surfaces do not touch the limiter points because they are constrained to be within $|B| \lesssim 0.6\ B_{oo}$ to insure that particles are adiabatic. The EBTEC configuration has a larger magnetic field scale length (~ 4/3 the circular value) and thus is limited by the first material wall rather than adiabaticity considerations.

The cross-sectional area (in the reference plane) of drift surfaces of particles with pitch angles intermediate to those of Fig. 2 are shown in Fig. 3, where the resonant particles are clearly visible in the elementary bumpy torus case. Note that closed drift surfaces with nearly the full cross-sectional area exist for <u>all</u> pitch angles in EBTEC, whereas particles with $V_{||}/V \sim 0.8$ are not confined in any region of the elementary bumpy torus. The nature of the near-resonant drift surfaces is further clarified in Figures 4a and 4b, for EBTEC and the elementary bumpy torus, respectively. Again, the figures show sections of surface nested inside the outermost confined surface. Note that in EBTEC, the <u>outermost</u> surfaces retain their nearly concentric and circular cross sections, while the resonant phenomena is apparent in the distortion of the <u>inner</u> surfaces. Exact resonance cannot be illustrated for the elementary case, since no closed surfaces of finite cross-sectional area exist at this toroidal aspect ratio.

Resonant-particle drift surfaces for an alternating racetrack configuration without shifted centers are found to be qualitatively similar to the circular coil case although the confinement is improved. The apparant reason for the improved resonant particle behavior in the shifted configuration is a loss of symmetry such that the resonance condition cannot be maintained over large distances. Thus a particle quickly drifts out of a resonance region and executes a nearly circular orbit.

Figure 5 illustrates one aspect of this loss of symmetry in the shifted Andreoletti case by plotting the $|B|$ contours between two coils. Note that, unlike the standard bumpy torus, the minimum field value no longer occurs in the midplane. Figure 6 considers the effect of aspect ratio, R/a, on the area enclosed by resonant drift orbits (A(res)), the shift required to align trapped and passing drift orbit centers, and the magnetic field scale length, L_B, normalized to the corresponding circular coil case. L_B is calculated in the midplane from $[\frac{1}{B}\frac{\partial B}{\partial R}\Big)_{R_{ref}}]^{-1}$ and from the maximum curvature along the field line by K_{max}^{-1}. As R increases, the necessary shift decreases while A(res) remains nearly constant. L_B, which may influence ring properties, maximum stable beta values and ECH processes, decreases with increasing R/a relative to the circular coil case.

3. REACTOR CASE, R = 35 M

For a reactor, we must include the effects of a blanket and shielding which for a fixed geometry will reduce the plasma radius. To recover the desired plasma radius at fixed R and M, we must increase the coil size and decrease the number of sectors, N. A smaller aspect ratio results and some outer drift surfaces are scraped off by the shielding. Figure 6 shows that smaller R/a requires a larger shift and creates a larger L_B. However, we can reduce ΔR and L_B by choosing a larger H/W; for the reactor case, we take H/W = 3 and an $L_B \sim 2$ results. In Fig. 7, one quadrant of the equitorial plane is shown. The coil cross sections are 70 cm x 240 cm and the shielding (which is not shown) is assumed to be one meter thick.

Figure 8 shows that even with reactor shielding it is possible to make the trapped- and passing-particle orbits concentric. $R(V_{\parallel}/V = 1)$ is the location of the passing-particle orbit center, while $R(V_{\parallel}/V = 0)$ is the center of the trapped particle orbit. The figure indicates that a shift, ΔR, of ~ 750 cm is necessary to achieve nearly concentric orbits. This ΔR is evident in Fig. 7.

A plot of area enclosed by a drift surface in the midplane vs. $V_{\parallel}/V$ is shown in Fig. 9 for an EBTEC reactor and a standard EBT reactor with the same R, a and M. We see that, once again, the EBTEC has nearly concentric orbits for all $V_{\parallel}/V$, however, the area for the resonance particles is small due to shielding scrapeoff. It may be possible to alleviate this scrapeoff by proper shaping or parameter optimization. In any case, a very significant improvement in resonant particle behavior over the circular case is evident from Fig. 9.

4. SUMMARY

In conclusion, we have shown that an EBTEC configuration (racetrack coils which are alternately positioned horizontally and vertically), with properly chosen parameters, exhibits nearly concentric drift surfaces and large-area, closed resonant drift surfaces. As a result, neoclassical transport should be greatly reduced. In fact, previous estimates of random-walk step-size can be reduced to zero.

As the aspect ratio, R/a, incresses, we find: (1) a smaller shift, ΔR, is required to achieve concentric drift orbits; (2) the magnetic field scale length, L_B, decreases; and (3) the area enclosed by resonant drift orbits is nearly constant. However, circular resonant orbits occur at smaller radii as R/a is increased.

Reactor systems differ from "next-device" size machines due to the scrapeoff of field lines by blankets and shielding. Nevertheless, a preliminary study of an R = 35 m reactor suggests that most of the above transport advantages of EBTEC are still present.

ACKNOWLEDGEMENT

It is a pleasure to thank L.W. Owen for useful discussions of related numerical results.

REFERENCES

1. R.A. Dandl and G.E. Guest, "The ELMO Bumpy Torus", in Fusion, ed. E.A. Teller (Academic Press, N.Y., 1981) Vol. 1, Part B, p. 79ff.
2. F.W. Baity, et al., Plasma Physics and Controlled Nuclear Fusion Research, IAEA, 1982, paper CN-41/L-1.
3. R.L. Miller, submitted to Nucl. Fusion.
4. L.W. Owen and N.A. Uckan, J. Fusion Energy 1, 341 (1981); R.A. Dandl, et al., "The ELMO Bumpy Torus Experiment", Oak Ridge National Laboratory Report ORNL/TM-3694, November 1971; M. Fujiwara, et al., 9th International Conference on Plasma Physics and Controlled Nuclear Fusion Research, IAEA-CN-41/L2, Baltimore, 1982.
5. J. Andreoletti, Comptes Rendus 257, 1235 (1963).
6. W.R. Hamilton and H.F. Imster, Proceedings of the Symposium on Engineering Problems of Fusion Research, 47-50 (1981) (Conf.-811040). See also ORNL/Sub--81-21099/1-01.
7. S.J. Sackett, "EFFI - A Code for Calculating the Electromagnetic Field, Force, and Inductance in Coil Systems of Arbitrary Geometry", Lawrence Livermore Laboratory Report UCRL-52402, Rev. 1 (1981).
8. F. Meyer and H.U. Schmidt, Z. Naturforsch 13a, 1005 (1958).

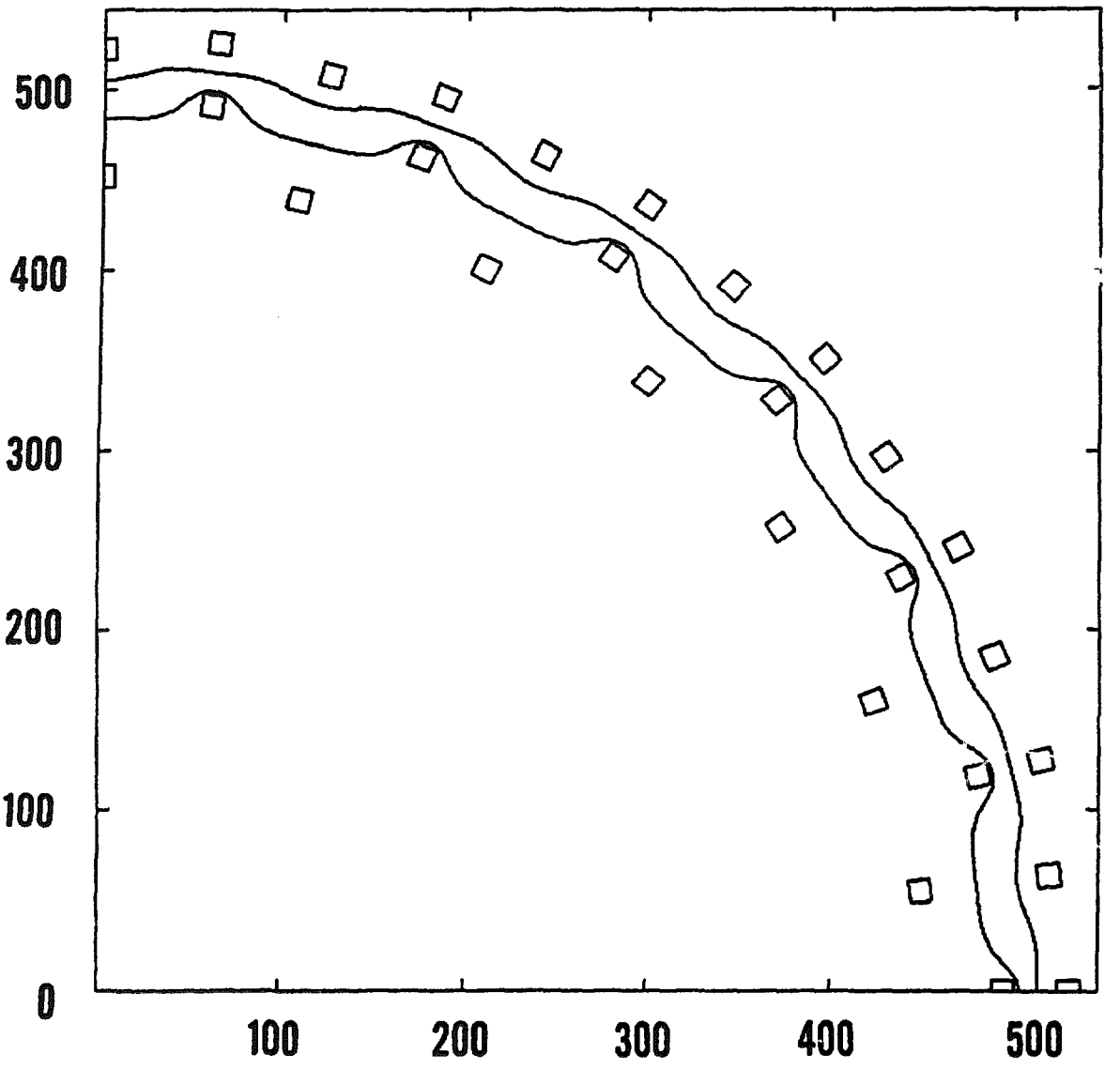

1. One quadrant of an R = 500 cm EBTEC projected onto the equatorial plane, with two magnetic lines of force shown.

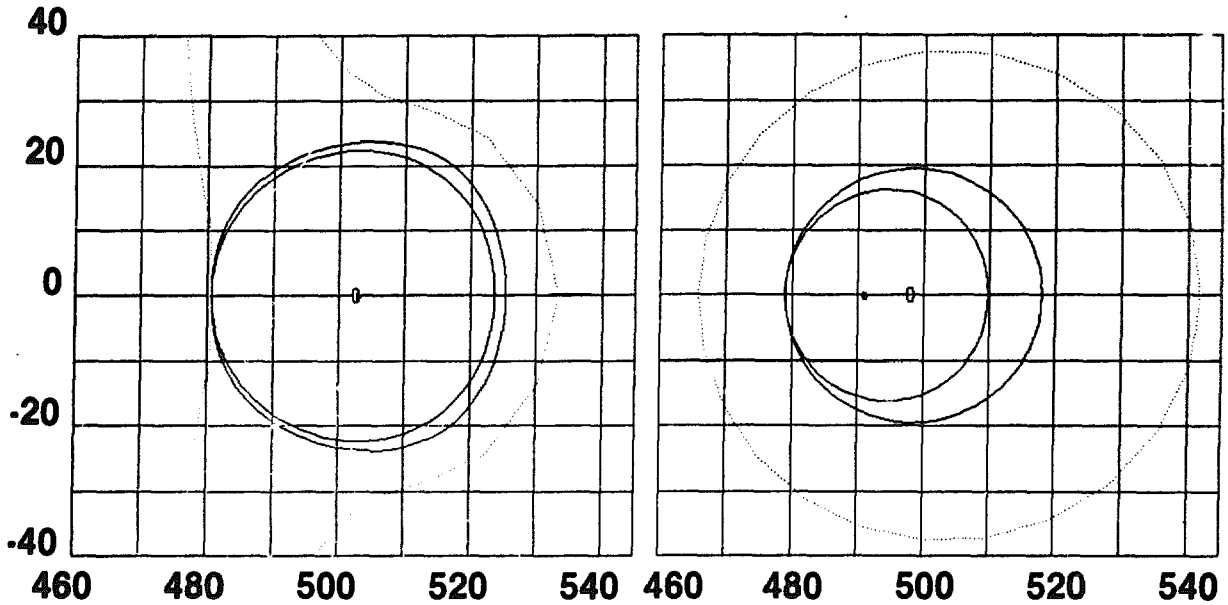

2a. Sections of surface of deeply-trapped and fully-passing particles in an R = 500 cm EBTEC (solid curves) and the projection of the material limiter onto the reference plane.

2b. Sections of surface of deeply-trapped and fully-passing particles in a simple bumpy torus of equal R, a and M.

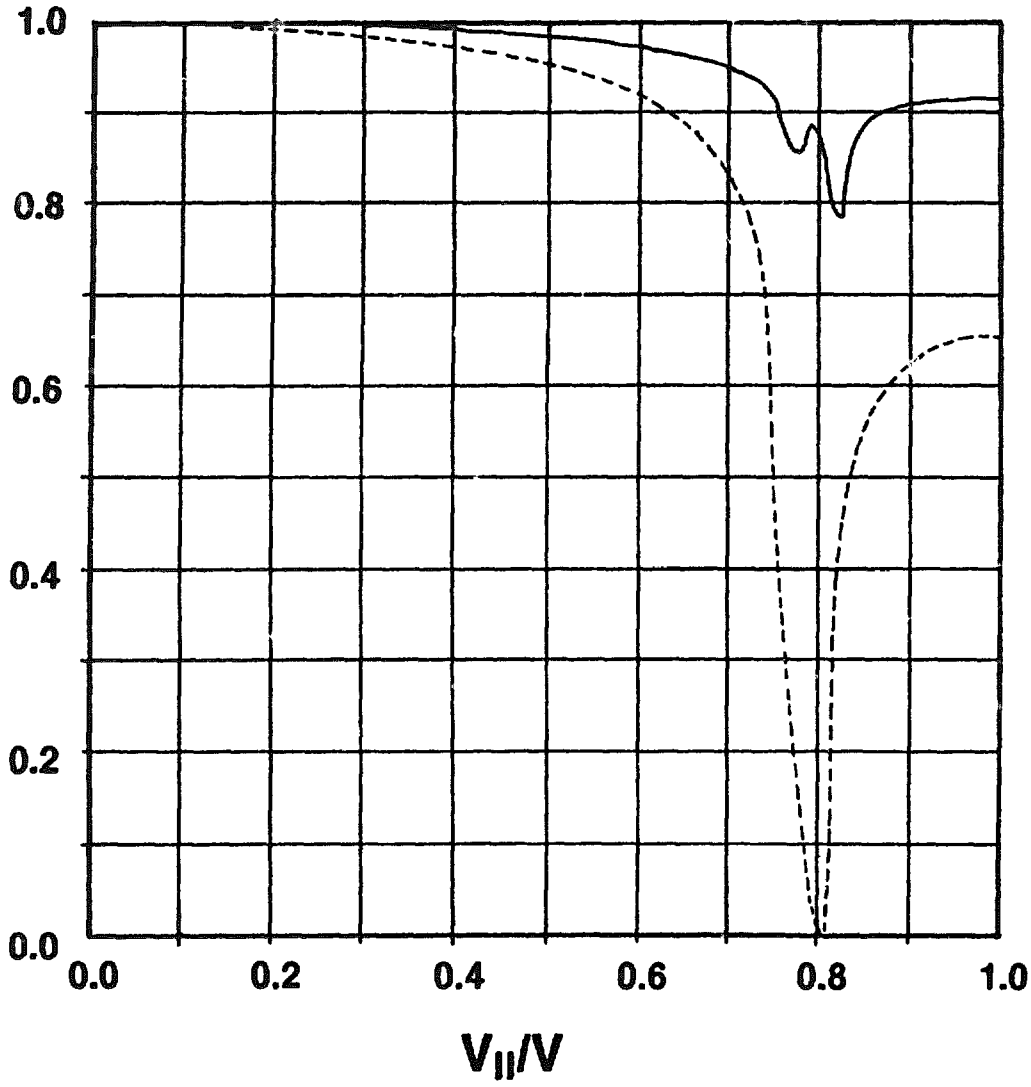

3. The fraction of cross-sectional area occupied by closed drift surfaces for varying pitch angle in an R = 500 cm EBTEC (solid curve) and the corresponding simple bumpy torus (dashed curve).

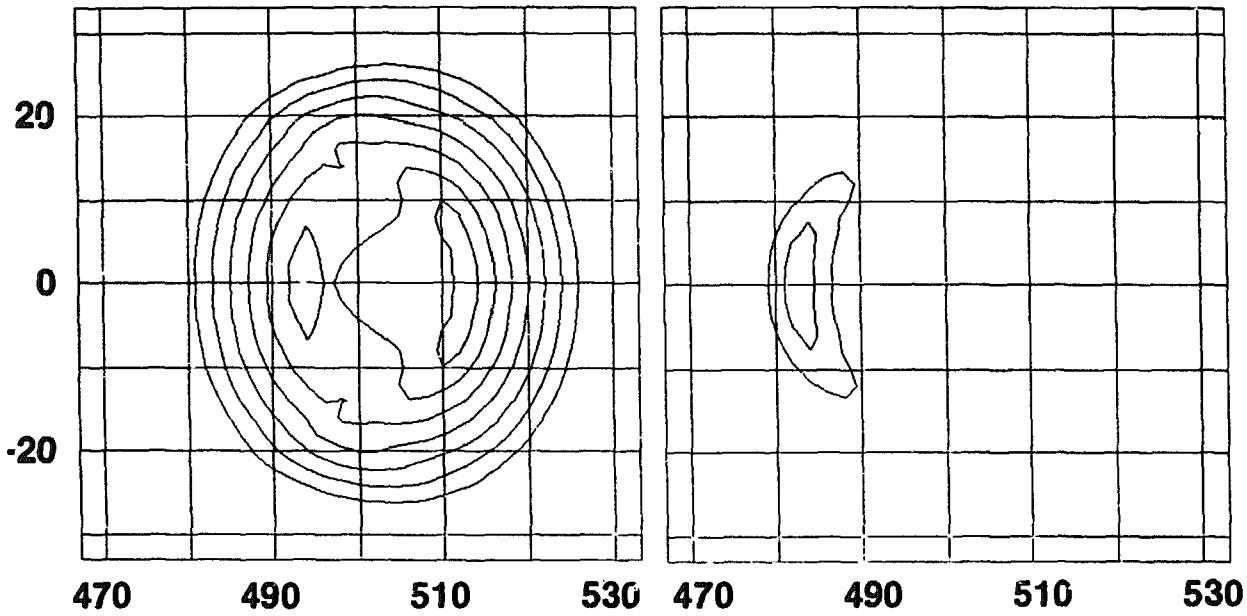

4a. Sections of surface for resonant particles in an R = 500 cm EBTEC ($V_{||}/V = 0.8$).

4b. Sections of surface for nearly resonant particles in a simple bumpy torus of equal R, a and M ($V_{||}/V = 0.8$).

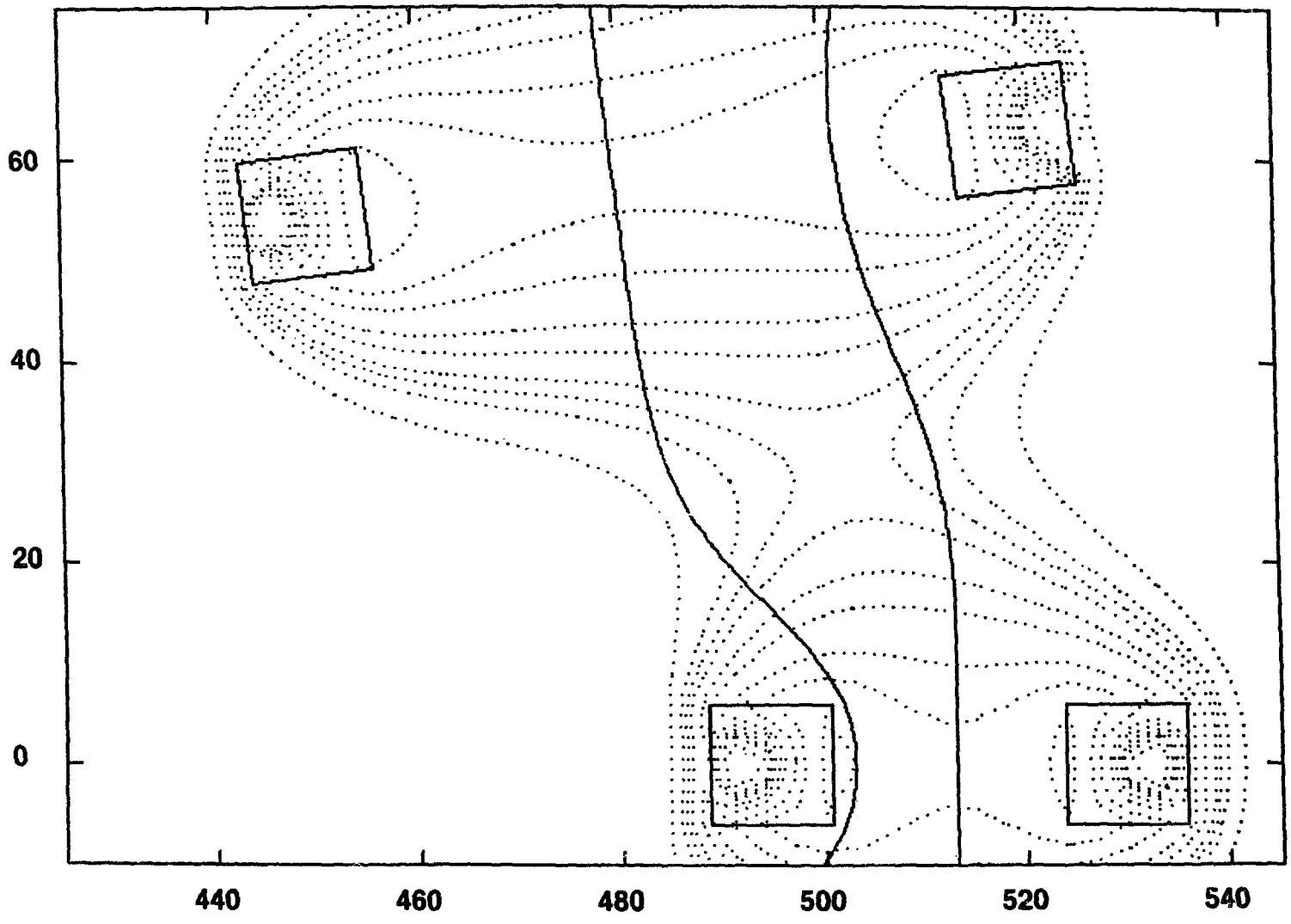

Fig. 5. |B| contours in the equatorial plane for an R = 500 cm EBTEC.

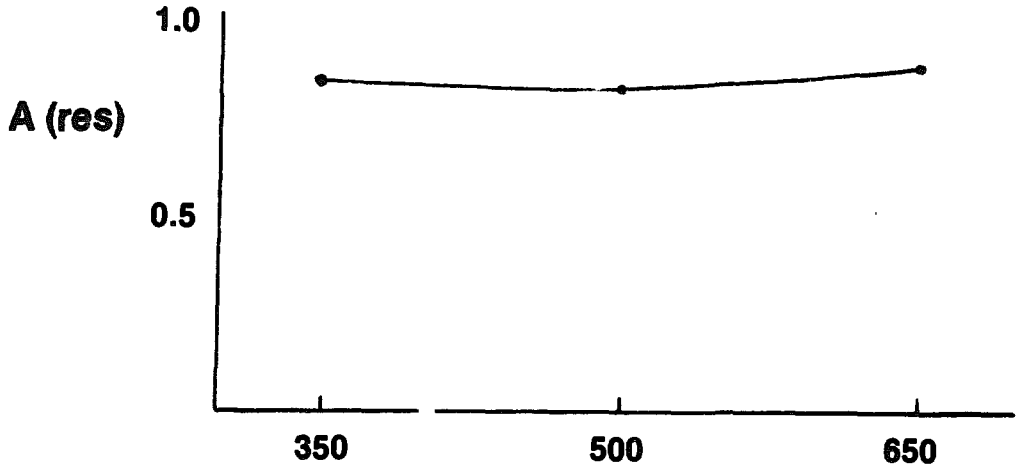

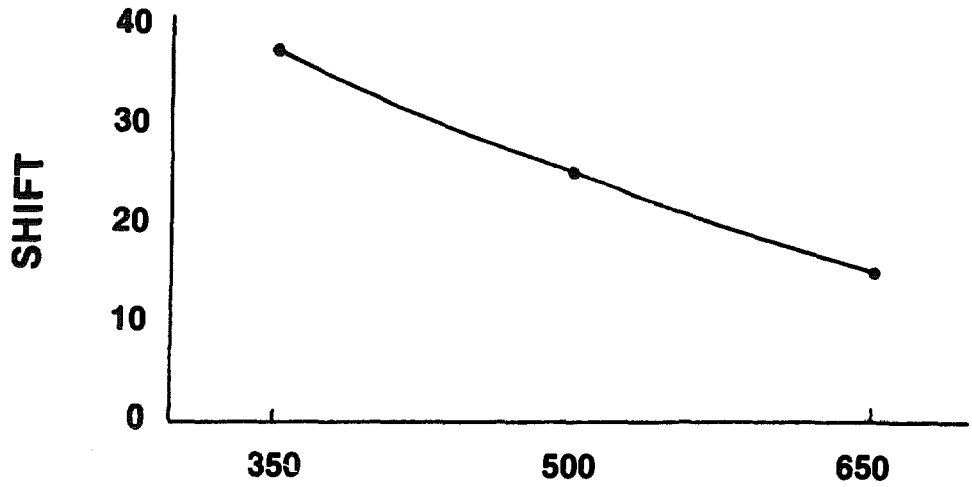

6a. Maximum area enclosed by resonant drift surfaces vs. major radius, R, for EBTEC's. a = 20 cm, M = 2.25.

6b. Optimal shift required to align trapped- and passing-particle drift orbits vs. R for EBTEC's.

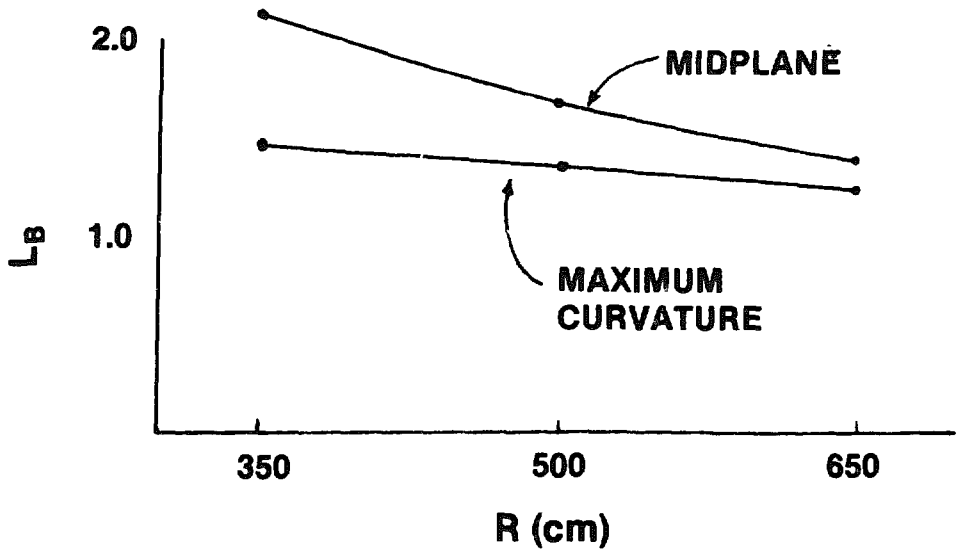

6c. The magnetic field scale length, L_B, normalized to the corresponding circular coil case, vs. R for EBTEC's.

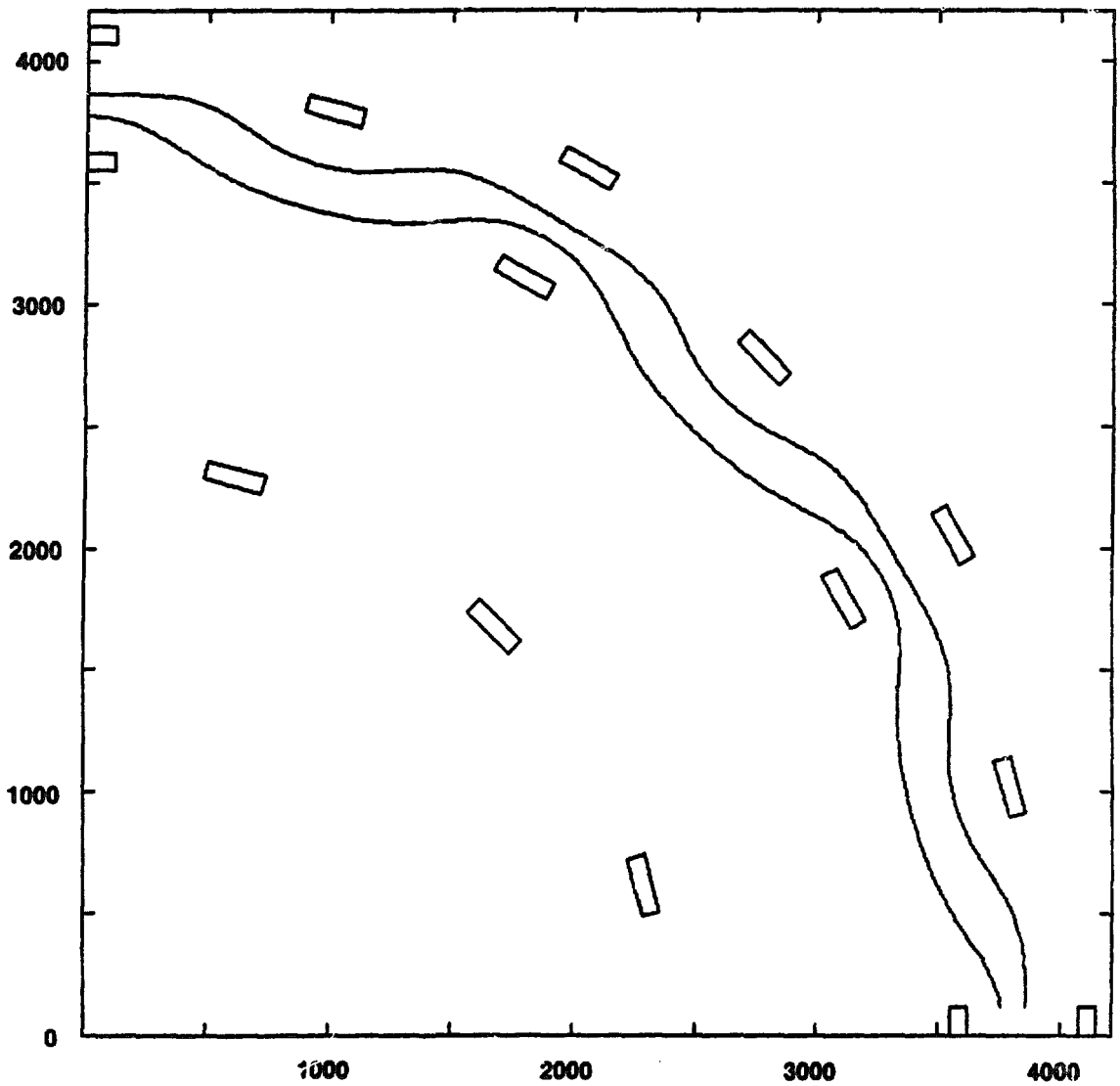

7. One quadrant of an R = 35 m EBTEC projected onto the equatorial plane, with two magnetic lines of force shown.

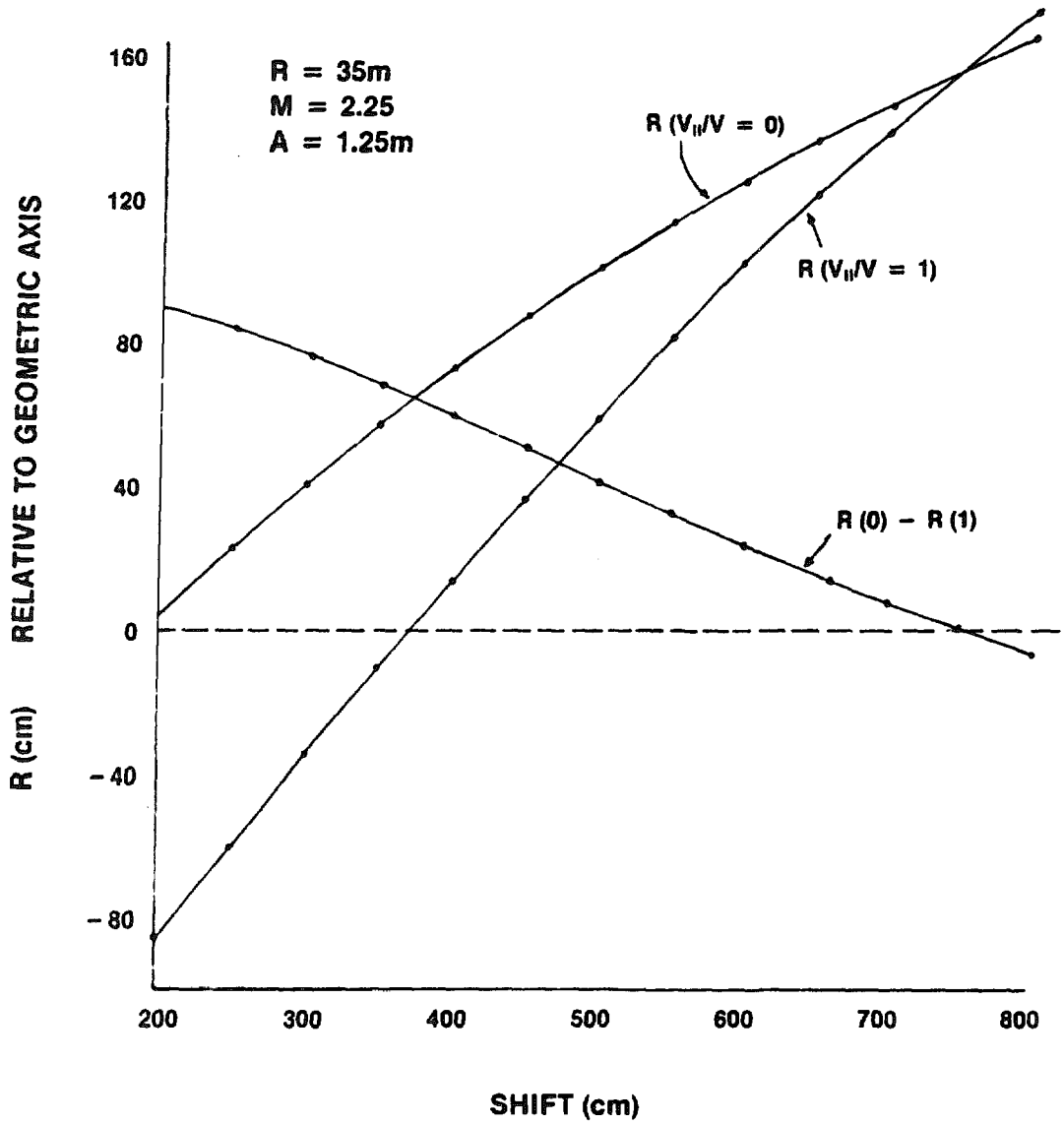

8. The location of the passing-particle drift orbit center, $R(V_{||}/V = 1)$, and the location of the trapped-particle drift orbit center, $R(V_{||}/V = 0)$, vs. coil shift, ΔR, for an R = 35 m EBTEC.

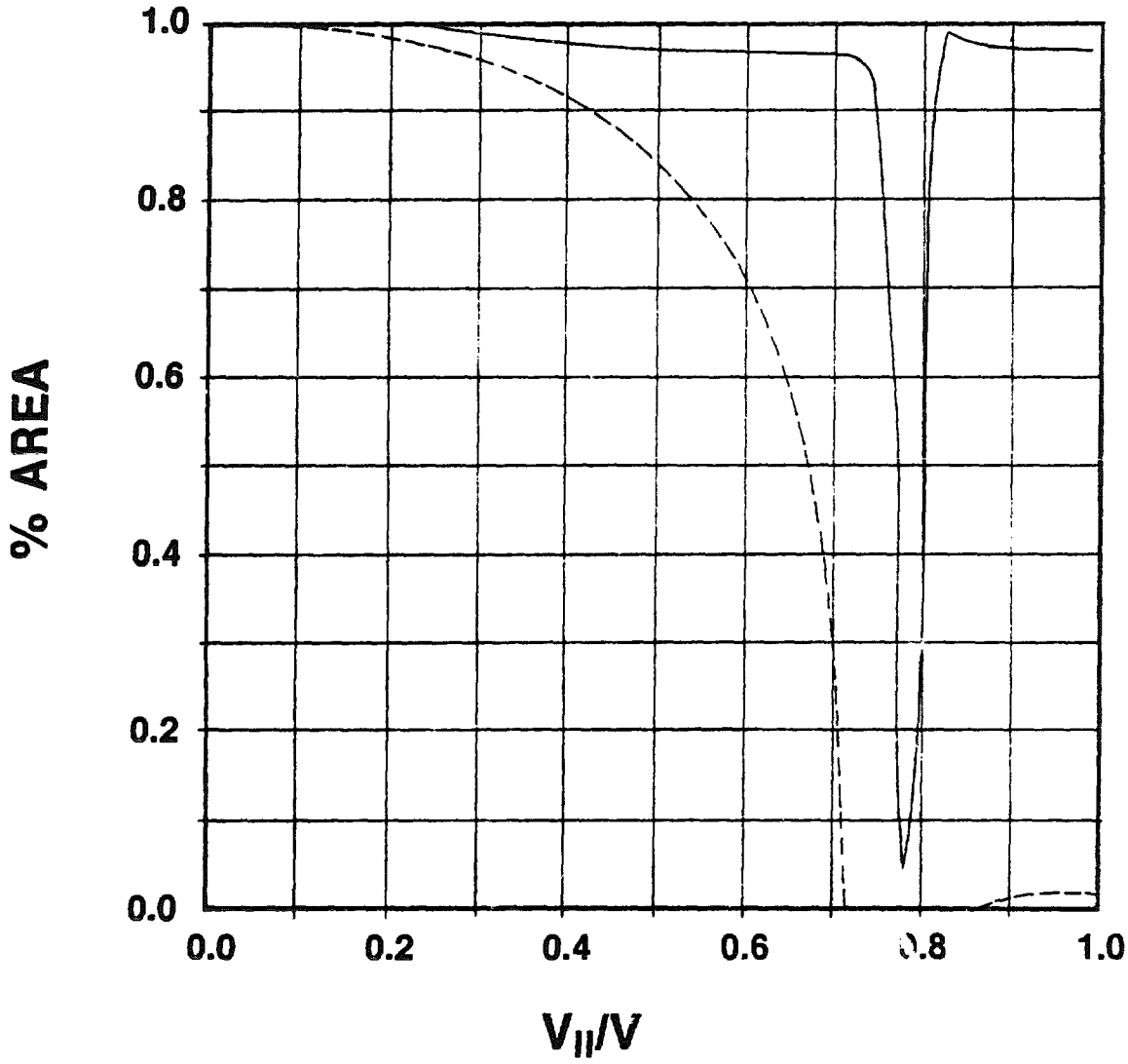

9. The fraction of cross-sectional area occupied by closed drift surfaces for varying pitch angle in an R = 35 m EBTEC (solid curve) and the corresponding simple bumpy torus (dashed curve).

ELMO BUMPY SQUARE*

L. W. Owen and D. K. Lee
Computer Sciences at Oak Ridge National Laboratory

and

C. L. Hedrick, Jr.
Fusion Energy Division
Oak Ridge National Laboratory
Oak Ridge, Tennessee 37830

New magnetics configurations based on the ELMO Bumpy Torus (EBT) confinement concept have been developed. The ELMO Bumpy Racetrack, Triangle or Square is formed by two, three, or four linear arrays of magnetic mirrors linked by sections of a high field toroidal solenoid. (The focus of this work is on the ELMO Bumpy Square (EBS).) These configurations localize the unavoidable toroidal curvature in regions in which the magnetic field is much stronger than the average field in the mirror sections, and thereby minimize its effect on single particle drift orbits, plasma volume utilization, etc. As in EBT, the central core plasma is stabilized by the presence of hot electron rings in the mirror cavities. High field solenoid sections (corner of the square in EBS) of circular and elliptical cross section have been analyzed. The elliptical shape is found to give the best passing particle confinement. Single particle drift orbits, the radial position of the minimum of the longitudinal invariant J, and a crude measure of the diffusion step size for particles near the hot electron rings are presented for EBS and compared to those for EBT-I/S. These results suggest that the neoclassical confinement time in EBS should be an order of magnitude larger than that in a standard bumpy torus of comparable size. In addition, the core and ring pressure surfaces and the ambipolar potential are much better centered because toroidal

---

*Research sponsored by the Office of Fusion Energy, U.S. Department of Energy, under contract W-7405-eng-26 with Union Carbide Corporation.

effects in $\oint d\ell/B$ occur in regions of high magnetic field. A number of interesting heating techniques may be more practical in an EBS than in an EBT. Access at the corners permits a long path length for near-parallel neutral beam injection and lack of magnetic moment conservation should quickly isotropize the hot ion distribution. In an EBS that utilizes an EBT-S-like magnetic field ($\approx$ 1 Tesla in the mirror cavities), slow-wave ICRH and 60-GHz ECRH can be launched from the high field corners, with the rings sustained by 28-GHz second harmonic heating.

I. Introduction

Various methods have been proposed for improving single particle confinement in the vacuum magnetic field of a standard bumpy torus consisting of a toroidally linked array of circular mirror coils.[1] These include the use of axis-encircling aspect ratio enhancement (ARE) coils, field symmetrization (SYM) coils, and circular split-wedge mirror coils. Particle confinement in toroidal arrays of inverse dee coils has also been examined.[2] Generally, the objective is to achieve better centering of the plasma in the magnetic field and vacuum chamber, reduced neoclassical losses by reducing dispersion in drift orbits, and reduced direct particle losses on unconfined drift surfaces (particularly for high energy passing and transitional particles that are least affected by finite ring beta and the ambipolar electric field).

In these studies the N-fold symmetry (with N the number of mirror sectors) of the basic EBT was preserved. The ELMO Bumpy Polygon, in which the magnetic axis is not circular but shaped like a racetrack, triangle, square, pentagon, etc., represents a departure from the philosophy of maintaining the maximum possible degree of symmetry in the magnetic field. The focus of the work reported in this paper is on the ELMO Bumpy Square (EBS), which has four vertical planes of mirror symmetry in addition to the horizontal symmetry plane (equatorial plane). (Reflection symmetry about the equatorial plane and at least

one vertical plane is required for a device to have closed field lines.) In the following sections it is shown that the advantage of the bumpy polygon configuration lies in constructing the sides of the polygon with axisymmetric, or nearly axisymmetric, simple mirrors and isolating the unavoidable toroidal curvature at the vertices of the polygon where its effects can be minimized. In EBS the corners are 90° sections of a high field toroidal solenoid.

The arrangement of the magnetic field coils in EBS and the resultant magnetic field geometry are discussed in Sect. II. Results of single particle drift orbit calculations for the EBS vacuum magnetic field are presented in Sect. III and compared to those of EBT-I/S. Summarizing remarks, conclusions, and directions for future work are found at the end of Sect. III.

II. The EBS Vacuum Magnetic Field

For concreteness we will compare the present EBT-I/S with an EBS whose sides are constructed from EBT-I/S mirror coils and whose corners are 90° sections of a high field toroidal solenoid. In Fig. 1 the central, innermost, and outermost magnetic field lines in the equatorial plane are displayed for (a) EBT-I/S and (b) EBS. The inner and outer field lines are defined by the clear bore in the throat of a mirror coil. The central field line defines a minor axis or magnetic axis for the device. Although the equivalent major radius (circumference/2π) of EBS is 2.44m, compared to 1.524m for EBT-I/S, the plasma volume is only about 25% larger than that of EBT-I/S. The coil spacing in the sides of EBS is such that the mirror ratio in each sector is the same as that in EBT-I/S (M=1.88).

Since high energy passing particles with $V_{\parallel}/V=1$ drift on contours of constant $\oint d\ell$, the most efficient way of optimizing passing particle confinement in EBS is by vertically fanning the field lines so as to minimize the difference in field line length across the minor axis. This is done in Fig. 1 with toroidal solenoid sections (corners) having

elliptical cross section with a height to width ratio of 3 and a mean minor diameter of 26cm. This is slightly smaller than the mean diameter (33.2cm) of the circular EBT-I/S mirror coils.

A major feature of EBS is the high field corners in which all toroidal effects are concentrated. In Fig. 2(a) the normalized magnetic field strength is plotted for one field period as a function of arc length along the magnetic axis. The on-axis mirror ratio in the sides is seen to be 1.88 and the "global" mirror ratio (B at the corners/B at the reference midplane) for this particular case is 4.2. From the shape of the curve in Fig. 2(a), one can classify particles in the EBS vacuum magnetic field as being mirror trapped in a single sector, mirror trapped between the high field corners, or passing. (There will also be transitional particles that turn or barely pass near the various field maxima.) Since the different classes of particles have different drift motion, it should be possible to vary the vacuum field confinement properties of the system by varying the ratio of the coil currents in the sides and corners of the square. For example, if the field in the sides were set at the EBT-I-like value of 0.5 Tesla (midplane) and the corners were operated at the maximum field, global mirror ratios of approximately 6 can be obtained. This could prove to be a convenient "knob" for varying the effective aspect ratio of the device.

Magnetic field lines and the locations of the current filaments that approximate the mirror coils and the toroidal solenoid sections are displayed in the equatorial plane of EBS in Fig. 2(b). As in EBT-I/S, the core plasma in an EBS would be stabilized by the presence of hot electron rings in each of the mirror cavaties; the corners would not have rings. In Fig. 2(b) the radial position of the solenoid section has been adjusted, relative to the axis of the straight section, in such a way that the electron ring in the "transition" sector is formed on the same flux lines as in the axisymmetric mirror cavities. (The transition sector is that sector between the solenoid and an adjacent mirror coil.) If it were desireable to maintain the ring in the same position in an actual EBS experimental device, a

"trim" coil in the midplane of the transition sector would be necessary in experiments in which the relative currents in the corners and sides were varied.

III. Single Particle Confinement in EBS

Single particle drift orbits and $\oint d\ell/B$ contours (core plasma pressure surfaces) for EBT-I/S and the EBS configuration of Figs. 1 and 2 are displayed in a reference midplane in Fig. 3. The selected orbits (dashed curves) and $\oint d\ell/B$ contours (solid curves) pass through the point $(R - R_T) = -17$cm in the equatorial plane. For EBT-I/S the worst confined drift orbit does not close within a minor radius of 17cm and is not shown. For EBS the drift orbits of deeply trapped particles and the $\oint d\ell/B$ surfaces are almost exactly centered on the minor axis. In addition the extreme passing particle orbit is much better centered than in the standard torus and the worst confined transitional particle orbit is shifted inward by only about 6cm. This dramatic reduction in the dispersion of drift orbits about the pressure surfaces means that both diffusive and direct particle losses in EBS should be correspondingly reduced.

A useful measure of single particle confinement and drift orbit dispersion in the plasma interior is afforded by the quantity R_{JMIN}, defined in Fig. 4(a). In Fig. 4(b) R_{JMIN} curves for EBT-I/S and two EBS configurations are plotted as functions of $V_{\parallel}/V$ defined at the center of the reference midplane. The solid EBS curve is for the device displayed in Figs. 1 and 2, in which the corner sections are elliptical in cross section. The dashed curve is for an EBS device in which the corner sections have circular cross section with a mean coil diameter of 26cm. The corner section coil current is chosen so that the total required DC power for the magnets is the same in the two cases. The slight dip in the EBS curves near $V_{\parallel}/V = 0.7$ is due to an outward shift in transitional particle drift orbits in the transition sector that joins the corners and the sides of the square. In this sector the field is, of course, not axisymmetric because of the strong

1/R solenoidal field in the corners. In Fig. 5 the transitional particle peak, associated with particles that turn in the corners of EBS, is seen to be much smaller, narrower and to occur at larger $V_{\parallel}/V$ than in EBT-I/S. The radial distance in the equatorial plane from the minor axis to the minimum of $\oint d\ell/B$ is denoted by arrows labeled by U_{min}.

An approximate measure (for the vacuum magnetic field) of the diffusion step size and drift orbit dispersion about a pressure surface ($\oint d\ell/B$ contour) for particles near the hot electron rings is plotted in Fig. 5 for standard EBT's and for the EBS configuration discussed in Sect. II. The dashed curve is for EBT-I/S and the dot-dash curve is for a device that has exactly four times the aspect ratio of EBT-I/S, i.e., 96 sectors and major radius of 6.1m. It is seen that the EBS step size for trapped and passing particles is comparable to those for the 96 sector standard EBT. Equally important is the large reduction in the step size and in the width of the resonance region associated with transitional particles. It is also observed that the dip in the R_{JMIN} curves, discussed above and shown in Fig. 4(b), does not appear for particles in the ring region.

Results of the work reported here demonstrate that a bumpy polygon having a small number of sides, in particular EBS, has single particle confinement properties and plasma volume utilization that are distinctly superior to those of a standard bumpy torus of comparable size. The hot electron rings are exceedingly well centered since they are formed in a near-axisymmetric magnetic field. The core plasma pressure surfaces and the ambipolar equipotentials can be very nearly centered on the magnetic axis because toroidal effects in $\oint d\ell/B$ occur in regions of high B. Because of high "global" mirror ratio, a larger fraction of the particles are trapped and move on the best centered drift surfaces. The confinement of high energy passing and transitional particles is dramatically improved due to high B and vertical fanning in the corners of EBS. The geometry of the EBS, or bumpy polygon configuration, suggests the possibility of using very interesting heating techniques that would not be practical in a

standard EBT. Access at the corners permits a long path length for neutral beam injection, and lack of magnetic moment conservation at typical beam energies should quickly isotropize the hot ion distribution. In an EBS that utilizes EBT-S-like magnetic fields ($\approx$ 1 Tesla in the mirror cavities), slow wave ICRH and 60-GHz ECRH can be launched from the high field corners with the rings sustained by 28-GHz second harmonic heating.

Further work is planned (1) to study the effects of field ripple introduced when the toroidal solenoid sections are modified to allow experimental access at the corners, (2) to investigate confinement in an EBS in which the relative currents in the corners and sides are varied and the field in the transition sector is tailored with one or more "trim" coils, and (3) to optimize an EBS reactor magnetics system subject to constraints imposed by superconducting magnet technology and by required coil shielding and blanket breeding ratio.

References

1. L. W. Owen and N. A. Uckan, J. Fusion Energy 1, 341 (1981).

2. M. Fujiwara, et al., 9th International Conference on Plasma Physics and Controlled Nuclear Fusion Research, IAEA-CN-41/L2, Baltimore, 1982.

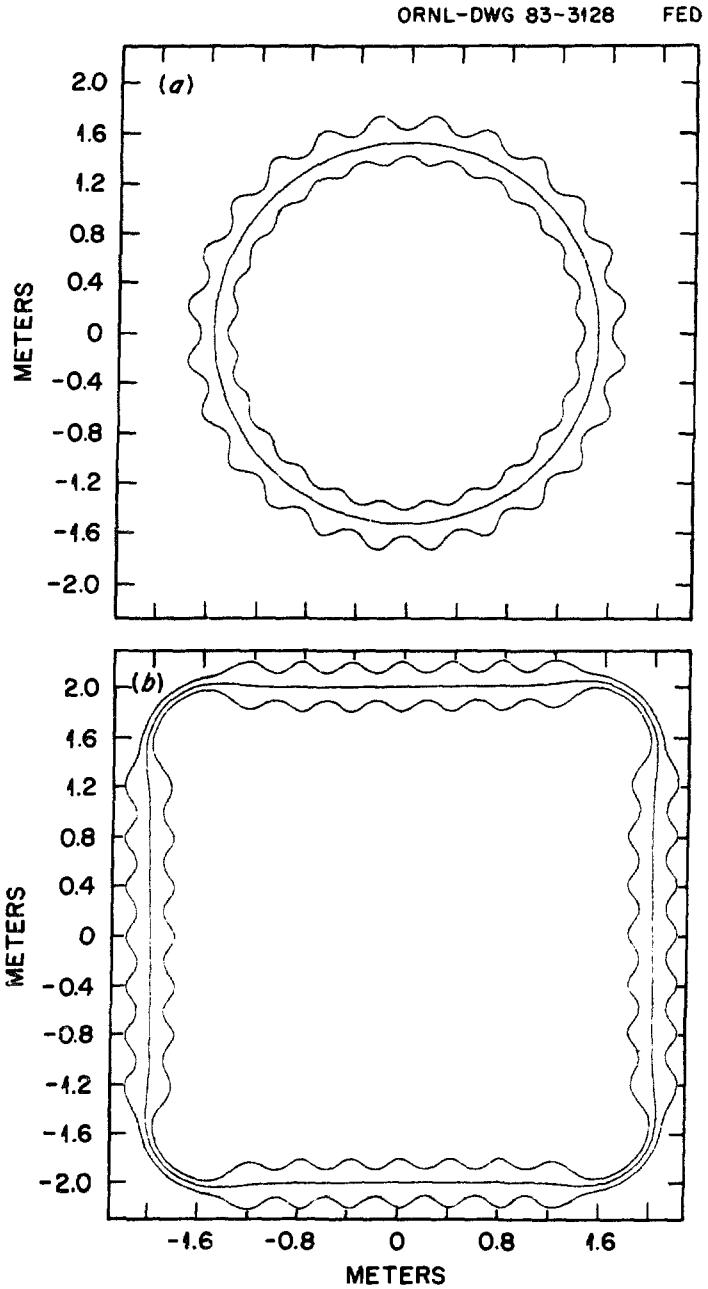

Fig. 1. The central, innermost and outermost (as defined by the clear bore in the coil throat) magnetic field lines in the equatorial plane are displayed for (a) EBT-I/S and (b) an EBS. Each side of the EBS configuration consists of a linear array of six EBT-I/S mirror coils and the corners are formed by 90° - sections of a toroidal solenoid of elliptical cross section.

ORNL-DWG 83-3127 FED

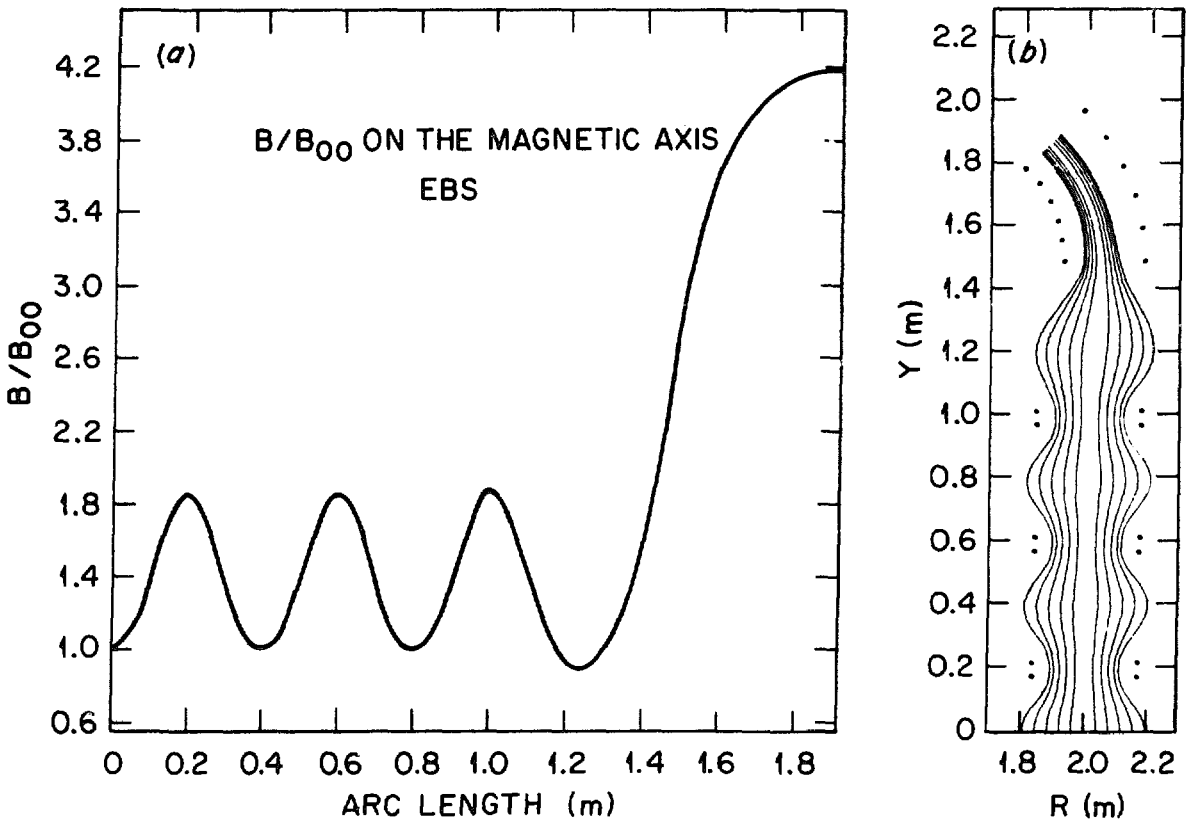

Fig. 2. (a) The magnetic field is plotted for one field period as a function of arc length along the central field line that forms the magnetic axis of the EBS configuration.
(b) Magnetic field lines and the locations of the current filaments that approximate the mirror coils and the toroidal solinoid section are displayed in the equatorial plane of EBS.

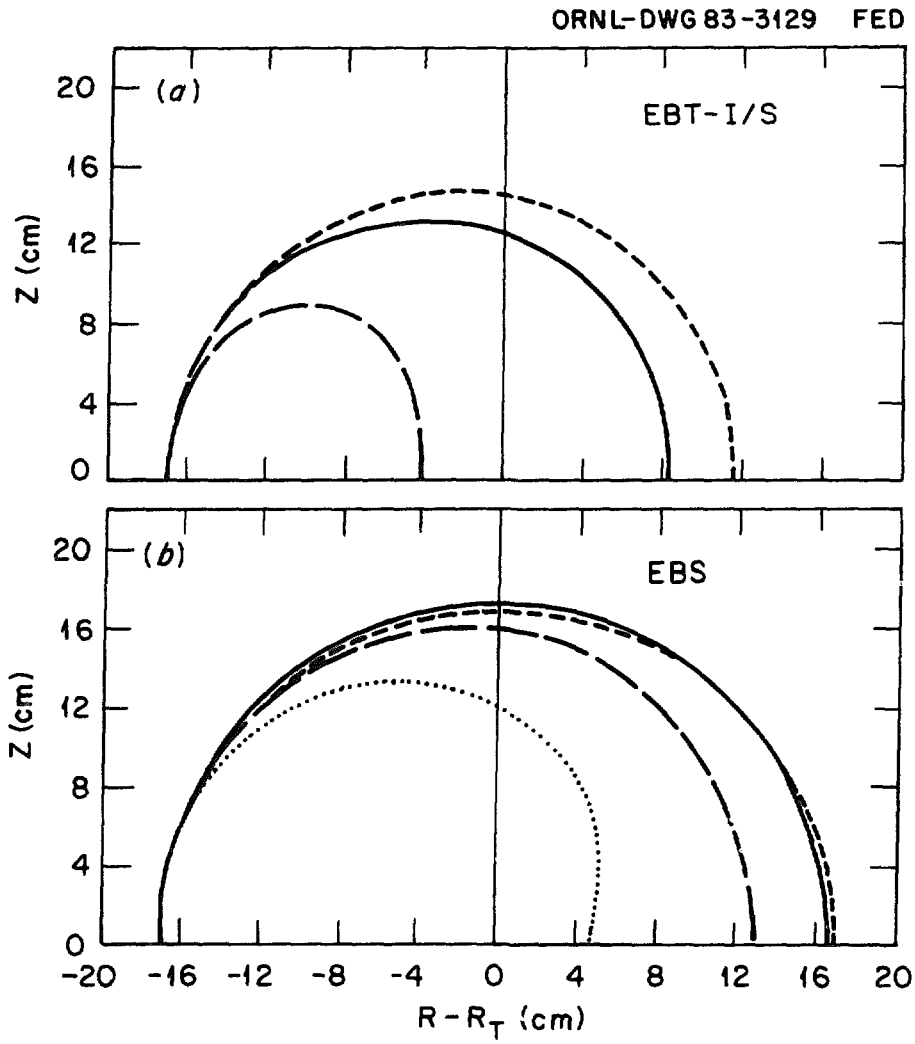

Fig. 3. Single particle drift orbits (dashed lines) and $\oint d\ell/B$ contours (solid lines) for (a) EBT-I/S and (b) the EBS configuration of Figs. 1 and 2 are displayed in a reference midplane. Orbits for deeply trapped ($V_{\parallel}/V=0$) and extreme passing ($V_{\parallel}/V=1$) particles are denoted by the short-dash and long-dash curves, respectively. The transitional particle orbit near the boundary between trapped and passing that represents the worst confined drift orbit in the vacuum magnetic field is denoted by the dotted curve. The absence of this curve for EBT-I/S means that the worst orbit does not close within a minor radius of 17cm.

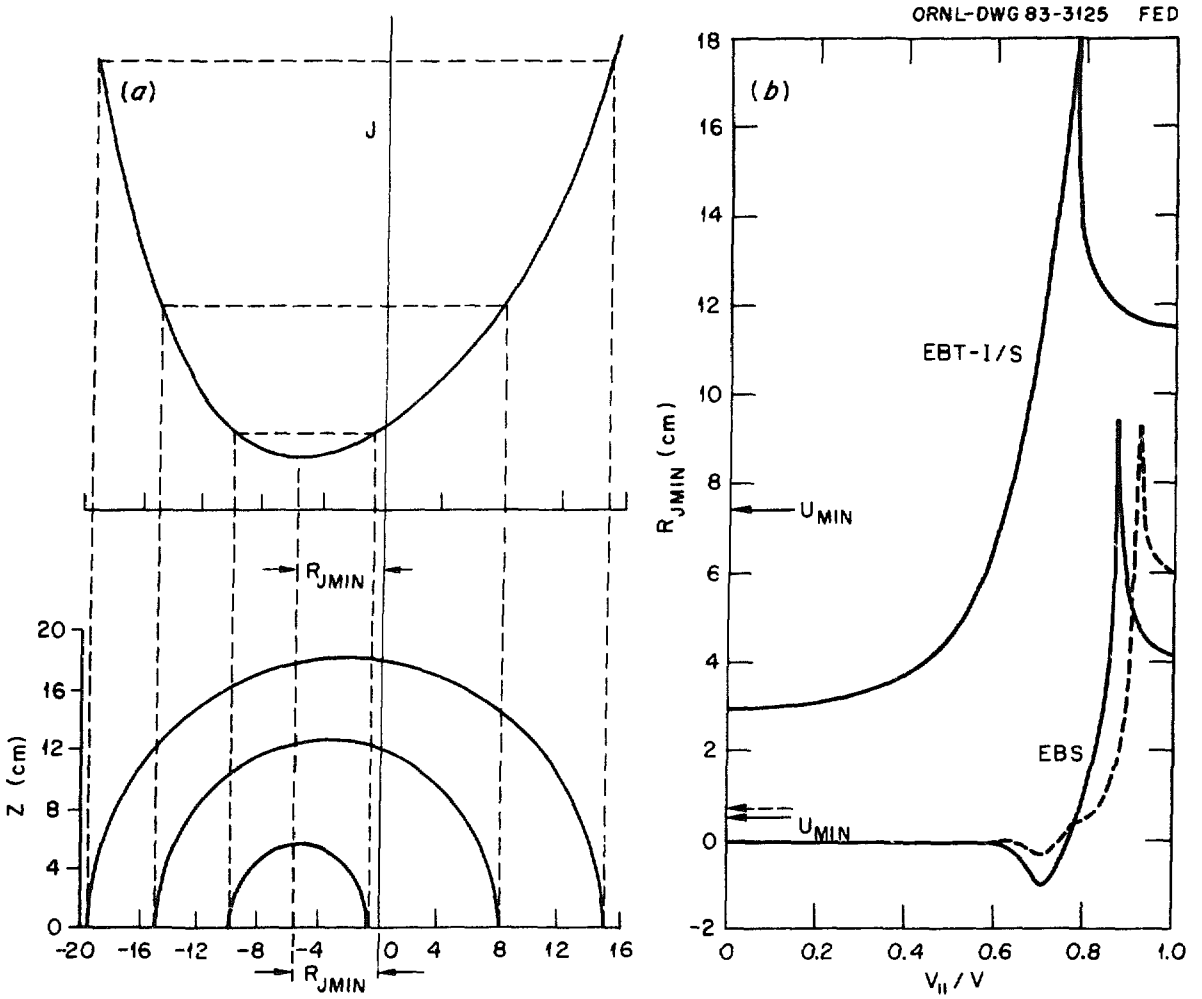

Fig. 4. (a) A useful measure of single particle confinement and drift orbit dispersion near the plasma center is afforded by the quantity R_{JMIN}. It represents the radial distance from the minor axis of the center of that drift orbit (for a particular pitch angle) which has the largest inward shift toward the major axis of the torus.

(b) R_{JMIN} curves for EBT-I/S and two EBS configurations are plotted as functions of $V_{\parallel}/V$ at the center of the reference midplane. The solid (dashed) EBS curve corresponds to a device in which the cross section of the high field corners is elliptical (circular). The radial distance from the minor axis to the minimum of $\oint d\ell/B$ is denoted by arrows labeled by U_{min}.

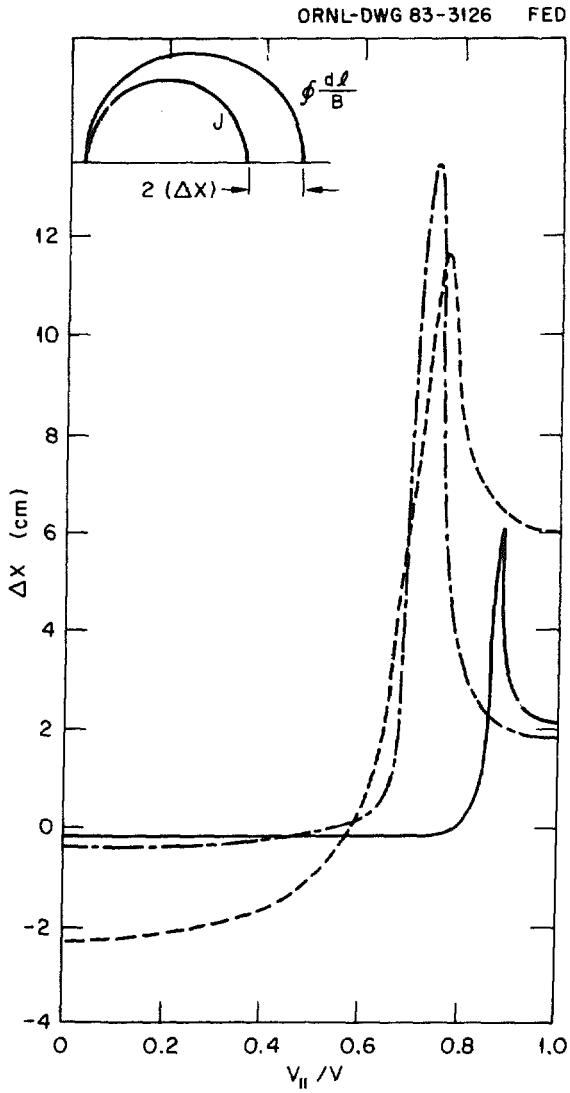

Fig. 5. An approximate measure (for the vacuum magnetic field) of the neoclassical diffusion step size and drift orbit dispersion about a pressure surface ($\oint d\ell/B$ contour) for particles near the hot electron ring is plotted for standard EBT's and for EBS (solid curve). The dashed curve is for EBT-I/S and the dot-dash curve is for a device which has exactly four times the aspect ratio of EBT-I/S (96 sectors, major radius = 6.1m). ΔX is defined in the inset at the top of the figure, where J represents the single particle drift orbit having a given $V_{\parallel}/V$ that is tangent to the pressure surface on the inboard side of the torus.

MINIMUM-B MIRRORS PLUS EBT PRINCIPLES

Shoichi Yoshikawa
Princeton Plasma Physics Laboratory
Princeton, New Jersey 08544

Electrons are heated at the minimum B location(s) created by the multipole field and the toroidal field. Resulting hot electrons can assist plasma confinement by (i) providing mirror, (ii) creating azimuthally symmetric toroidal confinement, or (iii) creating modified bumpy torus.

The EBT E-ring is a remarkable device that is used to stabilize toroidal plasmas. Present rings are created at regular mirrors. Thus rings are subject to the MHD interchange instabilities. These instabilities are apparently cured by the line tying. It is immaterial whether actual cold plasmas are present or some other mechanisms such as ionization of neutrals plays the role of the line tying. The fact remains that stabilization of rings requires the presence of particles near the periphery which apparently causes the need for high-neutral pressure. Hence the ion confinement (through charge exchange) is bad.

One possible solution is to create the electron ring in minimum-B geometry. As shown in Fig. 1, toroidal octupole coupled with toroidal field creates an azimuthally symmetric minimum-B geometry. This configuration has a vacuum minimum-B property and creation of an electron ring should be easy.

There are several ways to use this electron cloud. We note that, as it is, electrons create far a deeper minimum-B well than that created by the vacuum field. Thus high-energy ions could be mirror trapped, and we have the possibility of an azimuthally symmetric, minimum-B mirror device.

Actually it is better to create a toroidal device. If a toroidal current is induced in the electron cloud, the octupole magnetic field could be shielded.[1] When the electron cloud carries at the center a current equal to that of each conductor of octupole, magnetic field lines are closed in more than the half area (see Fig. 2).

If the current flows within the electron cloud, the configuration is similar to that of a tokamak. Thus purists in the EBT community might object to this configuration. Furthermore, the aspect ratio must be reasonably small in order to confine high-β plasmas.

The third approach to creating an EBT-like configuration with minimum-B mirror is to vary the toroidal field strength toroidally. In the absence of poloidal field due to octupole and the magnetic field by electron cloud, the toroidal field variation would create $\int d\ell/B$ equilibria. The electron cloud will carry a small toroidal current to shield out the poloidal field of the octupole. The electron cloud, which is now rings, is contained in the sections of weak toroidal field. The MHD stability must be investigated. The current distribution within the rings is crucial for stability of the overall system.

Three different configurations for the plasma confinement using the EBT technique have been proposed here. The first two are azimuthally symmetric — the first one utilizes the mirror principle for plasma confinement and the second allows the current to flow toroidally. The configuration in the second case is a tokamak with high-energy electrons.

The third configuration is more complex. Azimuthally symmetry was violated, and the current in the electron cloud and/or plasmas shielded out the poloidal field. Plasma equilibria are maintained by variation of the toroidal field, á la $\int d\ell/B$. Since rotational exists, the equilibria are determined by both $\int d\ell/B$ and by rotational transform.

Acknowledgment

This work was supported by United States Department of Energy Contract No. DE-AC02-76-CHO-3073.

Reference

[1]S. Yoshikawa, Phys. Fluids 15, 1683 (1972).

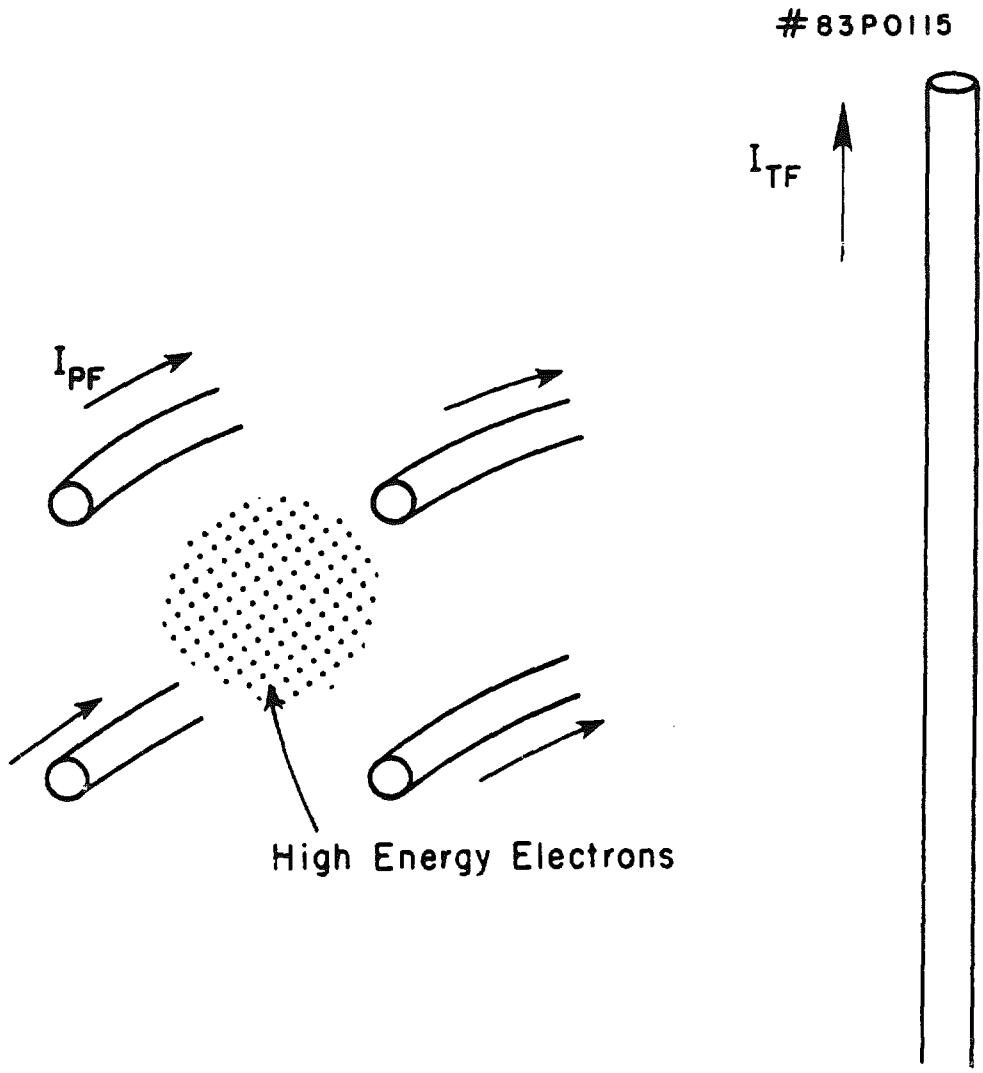

Fig. 1. Minimum-B configurations with octupole and toroidal field.

#83P0116

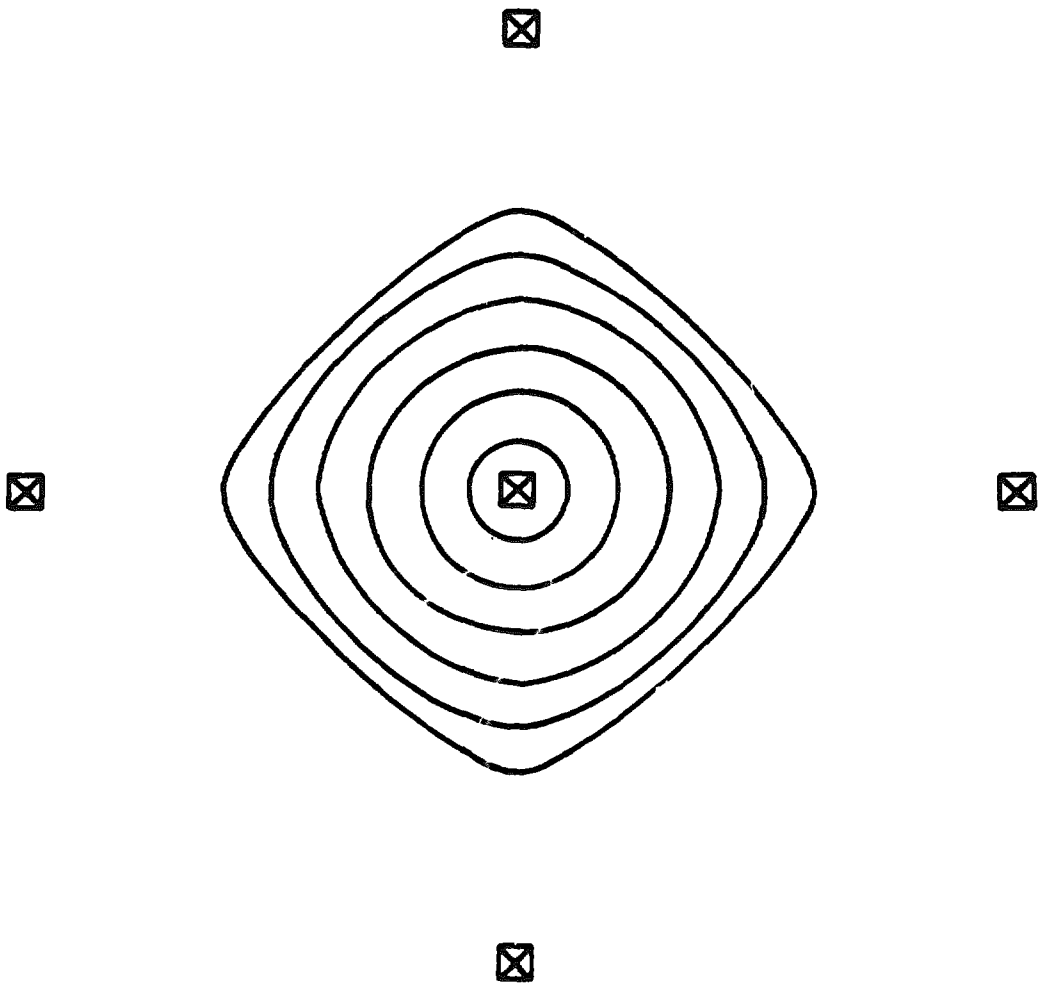

Fig. 2. Shielding of external field by the current flowing inside the electron clouds. See also Fig. 1 of Ref. 1.

ORBITS ASPECT OF ADVANCED BUMPY TORUS

T. Kamimura, M. Fujiwara and H. Ikegami
Institute of Plasma Physics, Nagoya University, Nagoya 464, Japan

ABSTRACT

Racetrack, square, octagon geometries of modified bumpy torus, and noncircular inverted Dee shape coils are studied for enhancement of particle orbits confinements. Comparisons are made of the advantage and disadvantage of these geometries. We have also tested helical magnetic field effects on the passing particle orbits by using modular stellarator coils for bumpy configuration. One important aim of this work is to understand how to manipulate and control passing particles separately from trapped particles.

****

Editor's Note: The manuscript that was received for this paper included an abstract, no text, and copies of 15 figures without figure captions. Although this editor could have prepared some representative figure captions, it would not be fair to the authors if the intended meanings were to change with the editor's interpretation of their results. The requested full manuscript for this paper did not arrive in time to be included in these proceedings. The abstract submitted to the workshop is included here for the purpose of completeness. — N. A. Uckan

****

MAGNETICS OF INNOVATIVE BUMPY TORI*

L. P. Mai and G. Gibson
Westinghouse Advanced Energy Systems Division
Madison, Pennsylvania 15663

ABSTRACT

The Bumpy Bean Torus consists of a conventional bumpy torus coil arrangement except that the coils are bean-shaped rather than circular. The indentations of the bean coils face the major axis of the torus. A second concept is identified as a Bumpy Polygon and it is composed of a closed array of linear mirror devices connected by short high field regions where particle trapping will be minimized. The particles are confined primarily in the system of linear mirror regions. For both of these closed-flux-line geometries the flux lines in the inner bore area are comparable in length to the outer bore region. The volume for good single particle confinement is expected to be increased, and the neoclassical transport loss is expected to be reduced relative to the conventional bumpy torus. Energetic electron rings similar to those used in the Elmo Bumpy Torus (EBT) are required for plasma stability. Preliminary results from calculations of magnetics properties such as flux shapes, mod-B surfaces, particle drift surfaces, and plasma pressure surfaces $\oint \frac{d\ell}{B}$, will be presented.

1.0 INTRODUCTION

Preliminary results for two advanced bumpy torus geometries are presented. One of the advanced geometries is a toroidal array of non-circular coils. The minor axis of the torus lies in a plane perpendicular to the major axis. The coils are bean-shaped and the concave side of the coils face the major axis. The plane of each coil contains the major axis. This geometry is referred to as the Bumpy Bean Torus. The second advanced concept consists of an array of simple linear mirror segments connected by short high field corner regions. Circular coils have been employed. The high field region is achieved by adding a trimming coil between each adjacent pair of mirror regions. Toroidal effects are confined to the high field corner sections.

---

*Supported in part by UCC/ND under Basic Ordering Agreement No. E-13820C.

Care is taken in the design to avoid introducing new mirrors in the high field regions. The major radius vector drawn from the major axis to the center of any of the liner mirror sections is perpendicular to the minor axis. This configuration is referred to as the Bumpy Polygon.

In a simple linear mirror geometry, the intersection of a charged particle's drift surface with the mid-plane, i.e., the vertical plane midway between adjacent coils, is a circle centered on the axis of the device independent of the pitch angle of the velocity vector. The intersection of the plasma pressure surfaces defined by constant u surfaces where $u = \oint d\ell/B$ with the mid-plane are also circles. In order to eliminate the end losses defined by the loss cones in velocity space, a toroidal array of mirrors was conceived, i.e., the bumpy torus. However, the degeneracy in the drift surfaces is removed in the toroidal configuration and drift-surface, or neoclassical transport across the magnetic field can occur. That is, as the pitch angle of the particles velocity vector changes due to collisions the particle can make large excursions across the magnetic field as it drifts on new surfaces independent of its larmor radius. The advanced concepts presented in this paper have closed flux lines similar to the conventional bumpy torus, but the shape of the field is such that the drift surfaces for both passing and trapped particles and constant u surfaces are more concentric. This results in better plasma volume utilization and particle confinement.

Plasma stability is assumed to be achieved with high energy electron rings as is done in the conventional Elmo Bumpy Torus, EBT. The effect of the high field regions in the Bumpy Polygon geometry on equilibrium and stability must be analyzed. In this paper, preliminary magnetics properties such as the drift surfaces including the Mod-B surfaces, and contours of equal flux line lengths, and constant-u surfaces are presented for the advanced concepts.

2.0 CONVENTIONAL EBT (EBT-S)

As a base case, the magnetic properties of the experimental device, EBT-S, at ORNL have been investigated. The EBT-S parameters are listed in Table I and the coil configuration is shown in Figure 1. To the extent possible, the same parameters are being used to study the advanced concepts. Figure 2 shows the flux lines and the surfaces of constant magnetic field strength, i.e., Mod-B surfaces, in the equatorial or horizontal symmetry plane of one cell of the EBT-S device. Note that the flux lines at the inner bore are shortened and

those at the outer bore are lengthened as a result of the toroidal arrangement of the coils. In order to determine the boundary of the plasma the limiting flux lines, i.e., the ones that just touch the walls in passing through the throat of the coils must be identified. Since surfaces are shifted to smaller major radii, the limiting flux lines at the inner bore are of interest. Figure 3 shows the structure surrounding the coils in the EBT-S. Although the inner radius of the coil conductor is at R ≈ 137 cm, the inner bore of the structure lies at ≈139 cm. If this limiting flux line in the equatorial plane is followed to a mid-plane, the flux line lies at a major radius of ≈132 cm.

To determine a particle's drift surfaces three quantities: the total kinetic energy, W, the magnetic moment, μ, and the action integral J, are assumed to be invariant. In a static magnetic field the kinetic energy of a charged particle is constant if its radiation is ignored. The other two quantities are adiabatic invariants that remain approximately constant provided the relative change in magnetic field across the larmor orbit is much less than unity. Although drift surfaces having arbitrary values for the adiabatic invariants are being studied, only two limiting cases will be discussed in this preliminary paper. The magnetic moment is expressed as

$$\mu = \frac{p_\perp^{\,2}}{2MB}$$

where p is the component of momentum perpendicular to the magnetic field, m is the particle's mass and B is the magnetic induction. The action integral is expressed as

$$J = \oint p_{\parallel}\, d\ell$$

where $p_{\parallel}$ is the component of momentum parallel to the magnetic field and $d\ell$ is an increment of length along the flux line. The integration is performed over a period of motion of the particle. One limiting case is for:

$$\mu = \frac{p_\perp^{\,2}}{2MB} = \frac{p^{\,2}}{2MB} \quad \text{and } J = 0$$

i.e. for particles confined to the plane midway between adjacent coils. The guiding centers of these particles drift on curves where B = constant since μ and p are constants. The second limiting case is for:

$$J = \oint p_{\parallel}\, d\ell = p \oint d\ell, \quad \mu = 0$$

i.e., for particles traversing the entire torus. The guiding centers of particles rear this limiting case drift on surfaces that are covered with flux lines of equal length.

Figure 4a shows the mod-B contours in the mid-plane of EBT-S, i.e., the vertical plane midway between adjacent coils. The contours are fairly concentric, but shifted inside the minor axis by approximately 2.5 cm. In Figure 4b some additional curves are superimposed on these mod-B contours. The flux lines that just touch the walls in passing through the throat of the coils pass through the curve-L in the mid-planes. Flux lines within the closed curve L pass around the torus without intercepting a wall whereas flux lines outside of L do pass through a wall. The point C is where the minor axis crosses the mid-plane, and the point t is the center of the drift curves for the trapped particles, i.e. the center of the mod-B curves. The circle-P is the boundary for the extreme passing particles.
Flux lines passing through the curve-P are of equal length. Particles whose momentum essentially lies in the direction of the magnetic field must lie within the curve-P when passing through a mid-plane otherwise their drift surfaces will intercept a wall. It can be seen that the volume utilization is not good since a fully trapped particle can become a traversing particle after scattering events change the particles pitch angle by 90°. The point-p is the center of the passing particle confinement volume. The distance between the points t and p is 7.5 cm; this is a measure of the neoclassical transport. As the aspect ratio approaches infinity the points c, t, and p should coincide. The advanced concepts tend to approach this condition for devices having the same aspect ratio as the EBT-S. Figure 5 shows a plot of three functions along the intersection of the equatorial plane with a vertical plane midway between adjacent coils. The functions are the magnetic field strength (B) in Figure 5a, the length of the flux lines (ℓ) in Figure 5b, and the quantity $u = \oint d\ell/B$ in Figure 5c. The vertical line to the left of these plots identifies the boundary of the good confinement region (at R=132 cm as described earlier). Drawing a horizontal line allows one to identify the outer boundary on which the particular quantity is conserved. These curves can also be used as a measure of the plasma confinement and volume utilization in a bumpy torus.

3.0 THE BUMPY BEAN TORUS

The Bumpy Bean Torus has been described in the introduction. Figure 6 shows the geometry of the coils, and Figure 7 shows the arrangement of twenty-four of them into a torus. If the coils were circular the major radius of the torus would be 150 cm and the coil mean radius 16.4 cm, the same as for EBT-S. By making the coils bean-shaped the flux lines at the inner bore should be moved to larger major radii as they pass through the throat of the coil and consequently be lengthened. Since the coils are circular at the outer bore, the flux lines there should not be significantly perturbed from those obtained in EBT-S.

Figure 8 shows the flux lines and mod-B surfaces in the equatorial plane of the Bumpy Bean Torus. The flux lines are indeed lengthened at the inner bore. Figure 9 shows the mod-B curves in a mid-plane; the curves are fairly concentric and are centered at a major radius of ≈152 cm. Figure 10 shows the quantities: magnetic field strength, length of flux line, and $\oint d\ell/B$ as a function of distance from the major axis along the intersection of the equatorial plane with a vertical plane located midway between adjacent mirror coils. The boundary at the inner side of this particular torus is located at R ≈ 130 cm. It can be seen by comparing Figure 10 with Figure 5 that the curves are much more concentric than those for the standard bumpy torus. Essentially the full volume available to the plasma can be utilized, and the neoclassical transport should be greatly reduced since the drift surfaces for the passing and trapped particles tend to be concentric and centered near the minor axis. The pressure surfaces are also centered near the minor axis.

4.0 THE BUMPY POLYGON

The Bumpy Polygon has also been described in the Introduction. Using the twenty-four EBT-S coils would allow a twelve sided polygon consisting of 12 linear mirror sections to be formed. Figure 11 shows the coil model for the Bumpy Polygon. In order to shape the high field corner sections an additional coil is added between each mirror section as shown in Figure 12. The total arrangement of coils is shown in Figure 13. By keeping the high field regions short and fairly symmetric more concentric drift and plasma pressure surfaces typical of linear mirror geometries should be attainable. Because of the high mirror ratio there is a larger fraction of trapped particles, and the passing particles spend relatively little time in the corner sections. Figure 14 shows the shape of the flux lines and the mod-B curves in the equatorial

plane. By calculating the magnetic field strength along the flux lines it has been found that the field increases monotonically until the maximum field is reached. The ampere turns in the smaller trim coils are two times larger than the ampere turns in the mirror coils. From Figure 15 it can be seen that the plots of the magnetic field strength and the quantity $\oint d\ell/B$ are concentric and centered about R ≈ 147 cm. However, the plot of the length of the flux lines is symmetric about R ≈ 142 cm. Although the volume utilization and suppression of neoclassical transport is improved compared to the conventional EBT, further optimization of the Bumpy Polygon is required.

5.0 SUMMARY

The preliminary analyses that have been performed indicate a significant improvement in volume utilization and in making the drift surfaces and plasma pressure surfaces more concentric in the advanced configurations. Table II is a comparison of the maximum radial intervals in the equatorial plane defined by the limiting surfaces. These values were obtained from Figures 5, 10, and 15. It can be seen that the boundary surfaces for the advanced concepts more nearly fill the available volume. Also, the spacing between the centers of the trapped particle and the passing particle confinement regions is reduced from 7.5 cm for the standard EBT device (the EBT-S device) to 5 cm for the Bumpy Polygon and to 1 cm for the Bumpy Bean Torus. Optimization studies are currently underway. Drift surfaces for the transitional particles are also being studied. Transitional particles are particles that are trapped between adjacent mirrors, but as they drift reach a point where they begin traversing the torus then subsequently are trapped in some other mirror region.

For quantitative comparisons, the calculations for the different concepts must be normalized. Thus far, the number of coils and the device size have been held constant to the extent possible. Currently, the impact of keeping the mirror ratio the same for the Bumpy Bean Torus and the Standard EBT is being studied. In the calculations reported in this paper the mirror ratio for the Standard EBT was 1.9, for the Bumpy Bean Torus 3.0, and for the Bumpy Polygon 12.

TABLE I

REFERENCE EBT-S DEVICE PARAMETERS

Torus Parameters

Major Radius	1.5 M
Mirror Coil Mean Radius	16.4 CM
Aspect Ratio	9:1
Number of Coils	24
Angular Spacing of Coils	15°
Distance Between Coils (Circumferential)	39.2 CM
Magnetic Field on Axis	1.36T; 0.728 T
Mirror Ratio	1.87
Torus Volume	1350ℓ

TABLE II

ΔR(CM) INTERVALS IN THE EQUATORIAL PLANE DEFINED BY THE BOUNDARY SURFACES

	Standard Bumpy Torus	Bumpy Bean Torus	Bumpy Polygon
$u = \oint \frac{d\ell}{B}$	29	47	52
MUD-B	34	47	55
$\oint d\ell$	18	46	45

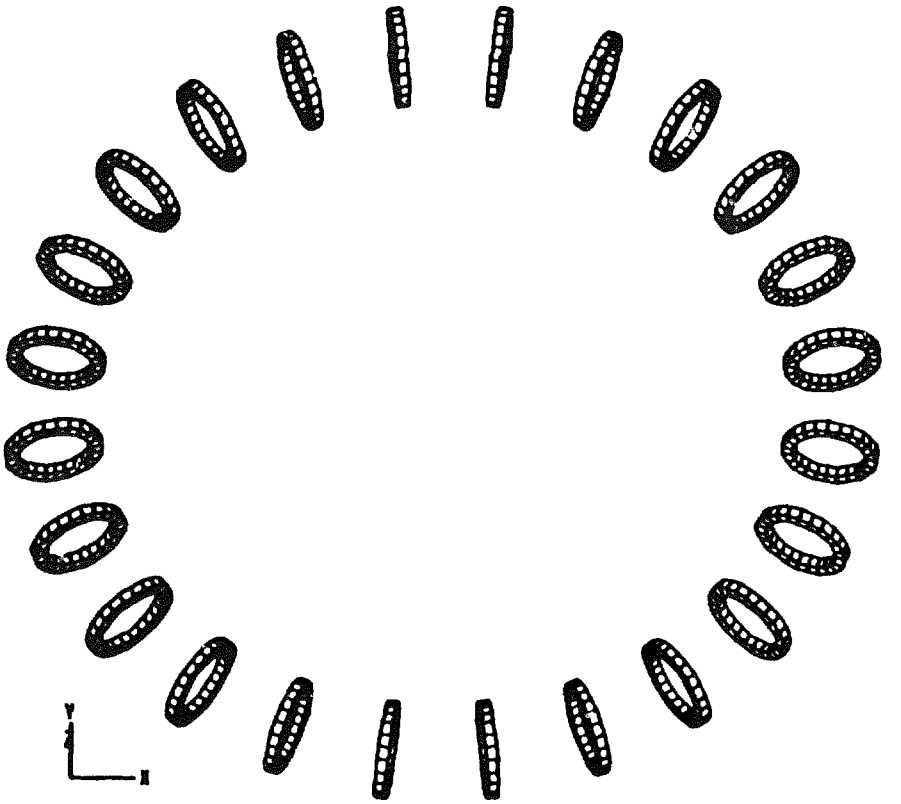

FIGURE 1 THE EBT-S COIL CONFIGURATION

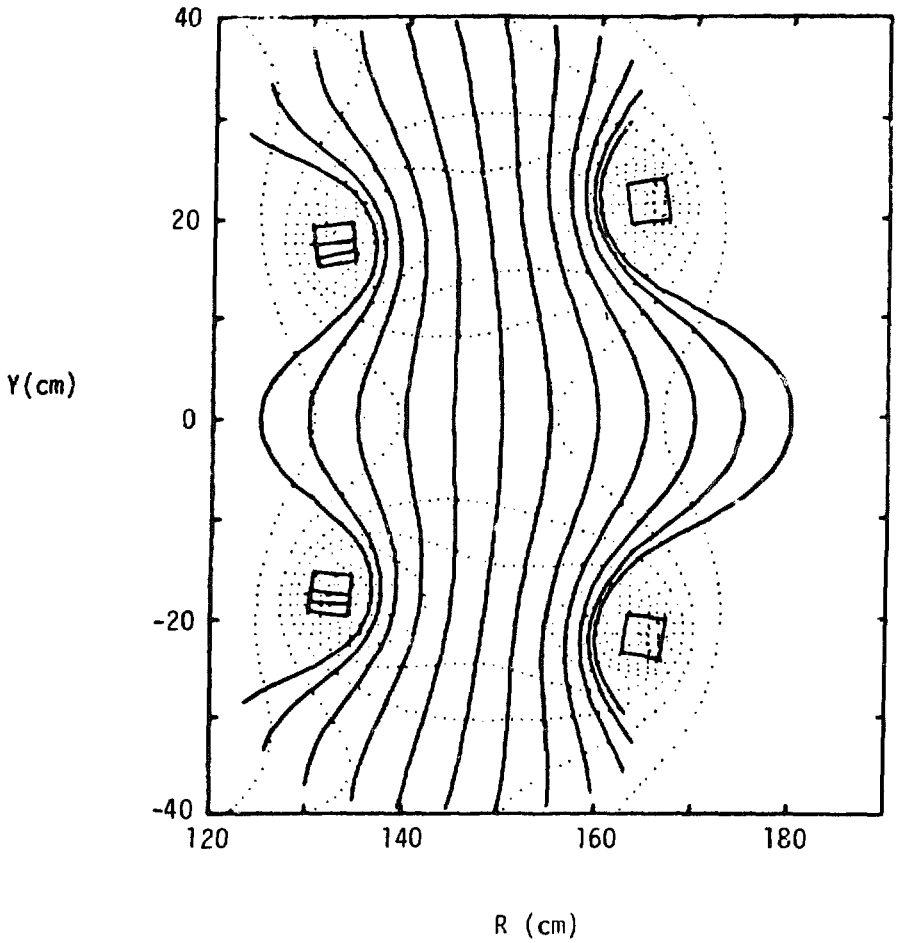

FIGURE 2 FLUX LINES AND MOD-B SURFACES IN THE HORIZONTAL SYMMETRY PLANE OF EBT-S

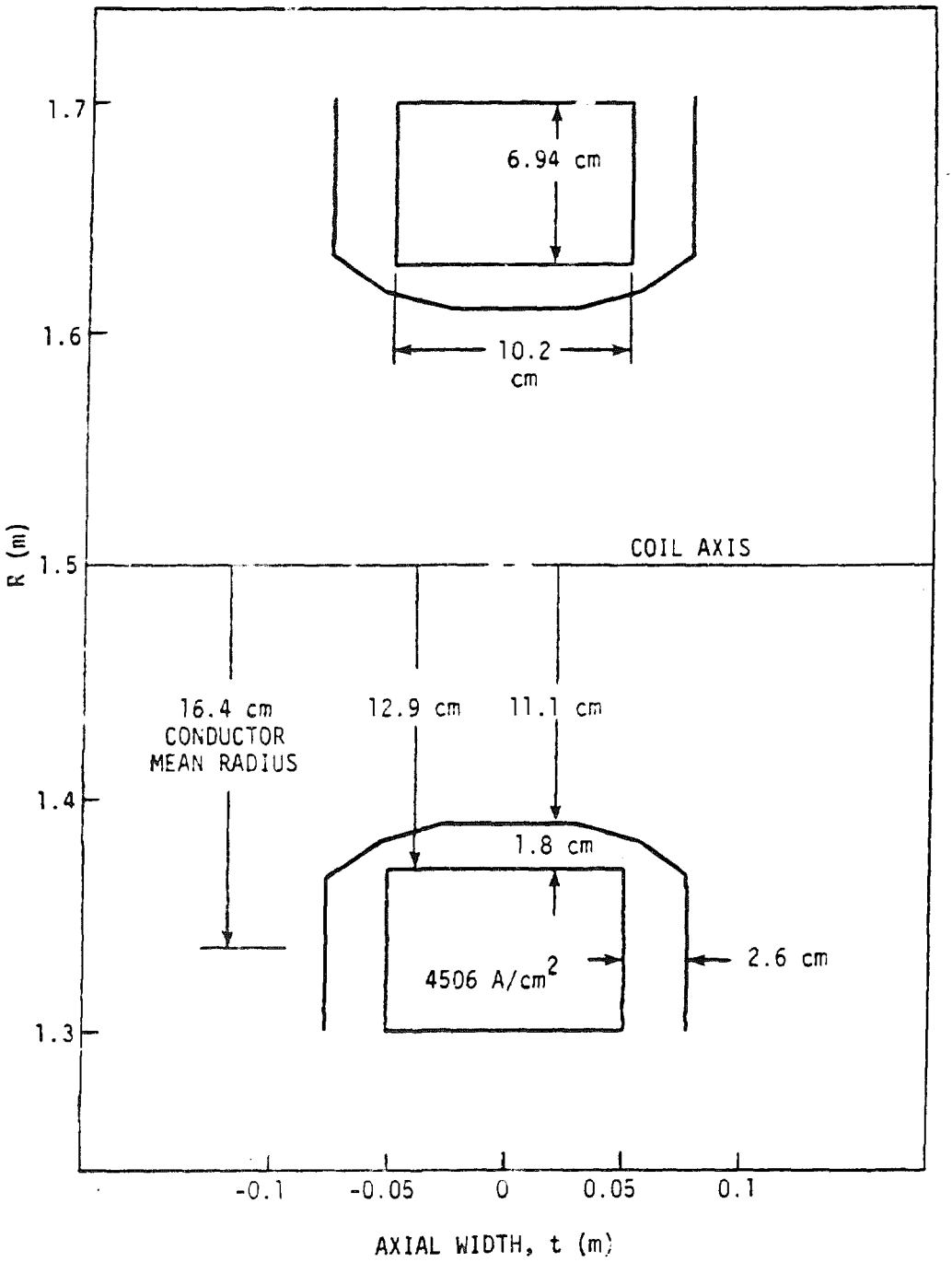

FIGURE 3 MODEL USED FOR THE MIRROR COILS IN PERFORMING THE MAGNETIC FIELD AND DRIFT-SURFACE ANALYSES FOR EBT-S

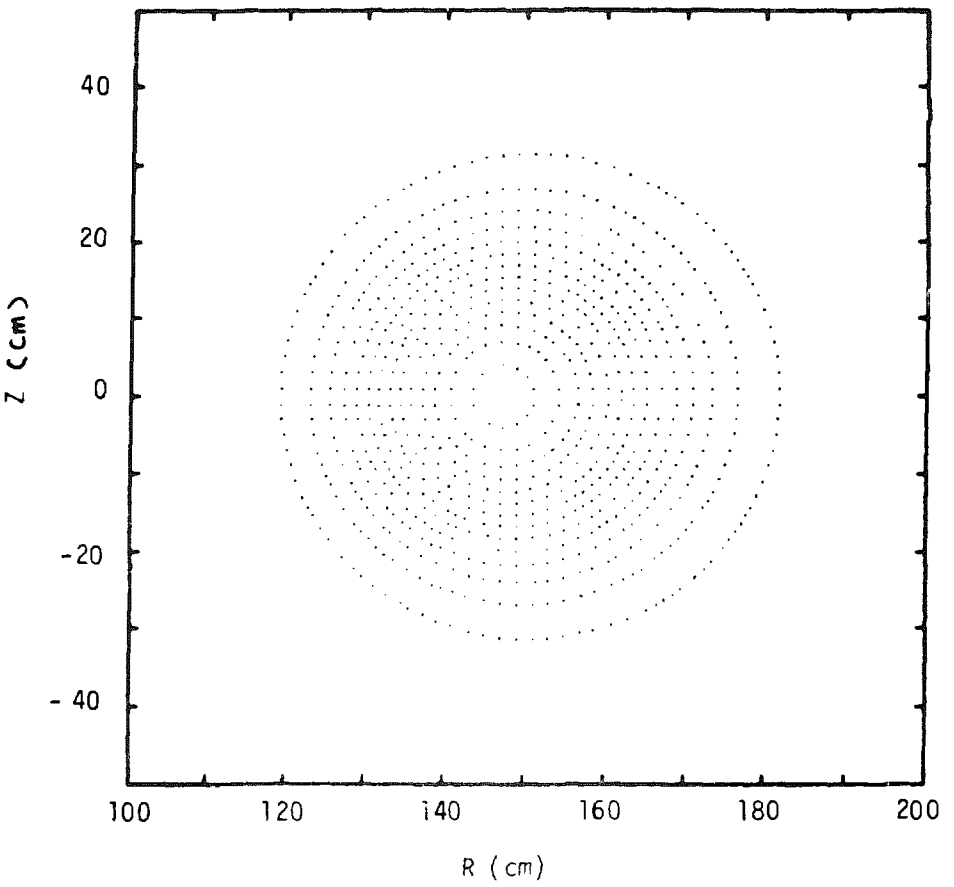

FIGURE 4a MOD-B SURFACES IN A VERTICAL PLANE MIDWAY BETWEEN ADJACENT MIRROR COILS OF EBT-S

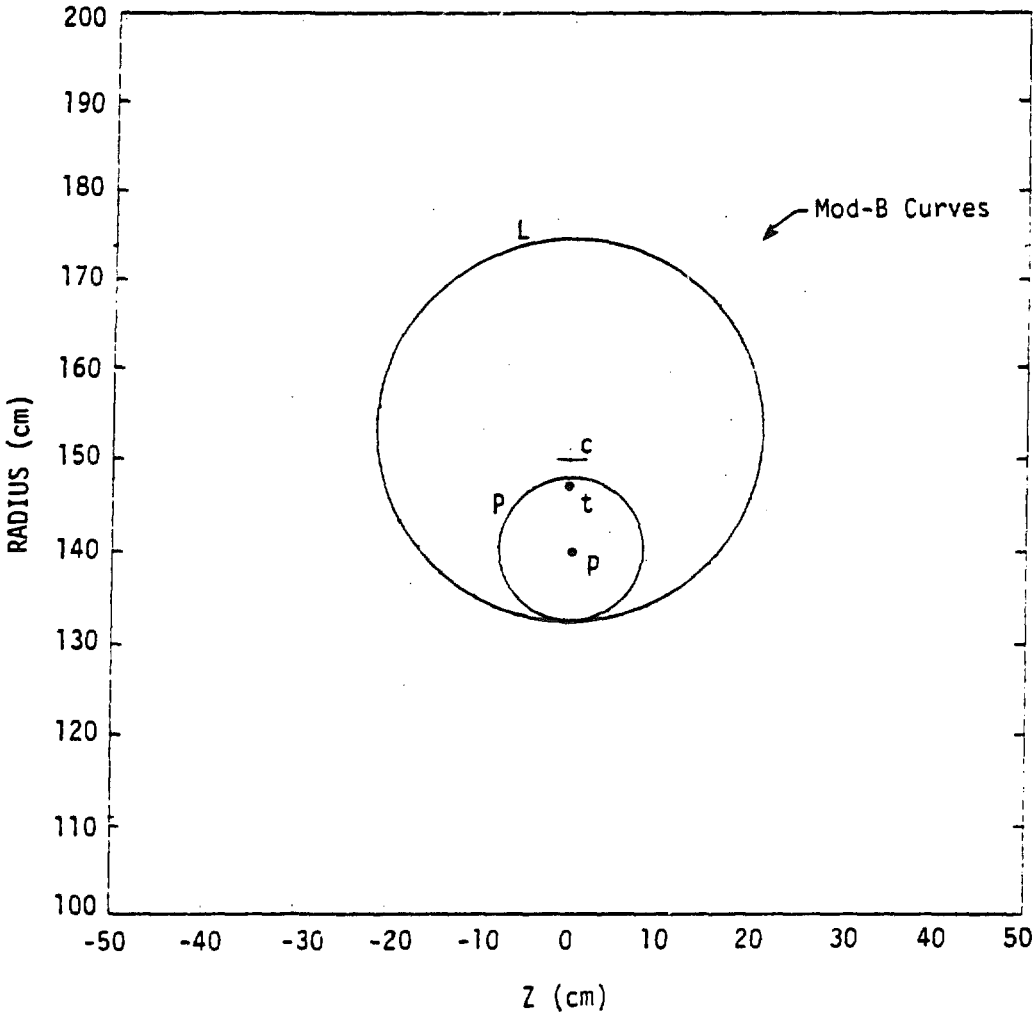

FIGURE 4b CONFINEMENT REGIONS FOR THE TRAPPED AND PASSING PARTICLES IN EBT-S

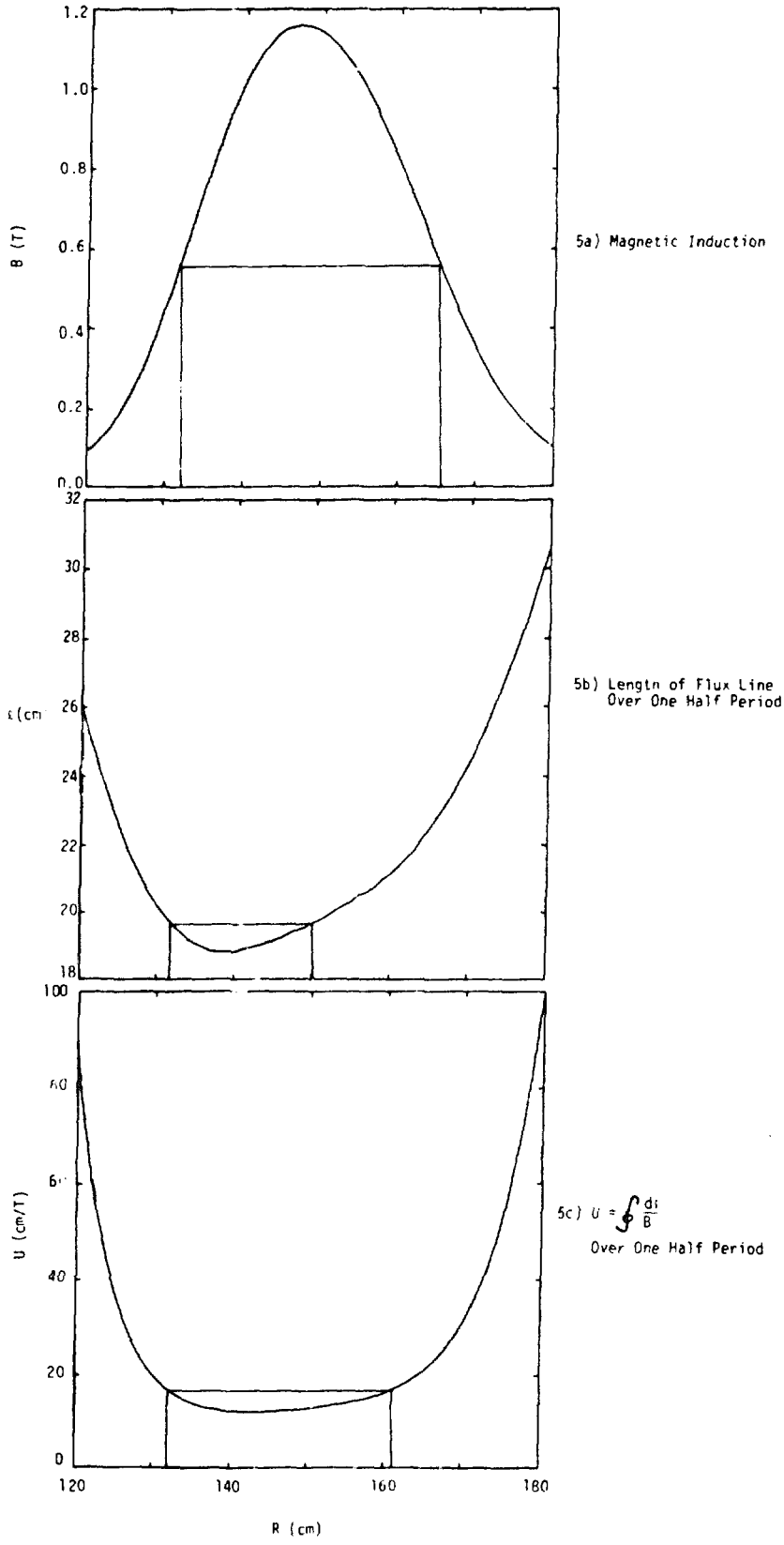

FIGURE 5 STANDARD BUMPY TORUS (EBT-S)

Quantities as a Function of Distance from the Major Axis Along the Intersection of the Equatorial Plane with a Vertical Plane Located Midway Between Adjacent Mirror Coils

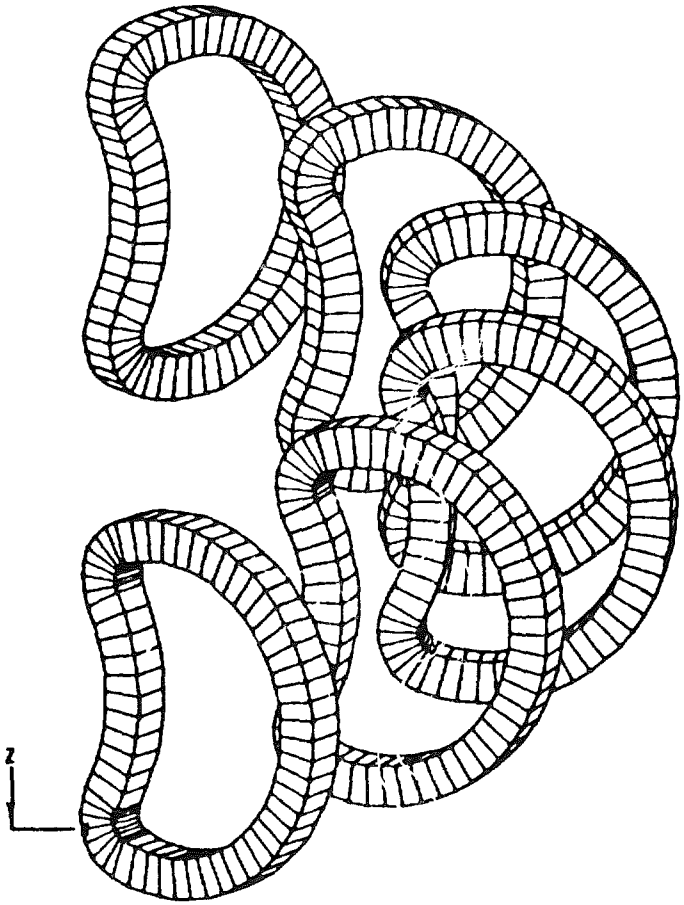

FIGURE 6

COIL GEOMETRY FOR BUMPY BEAN TORUS

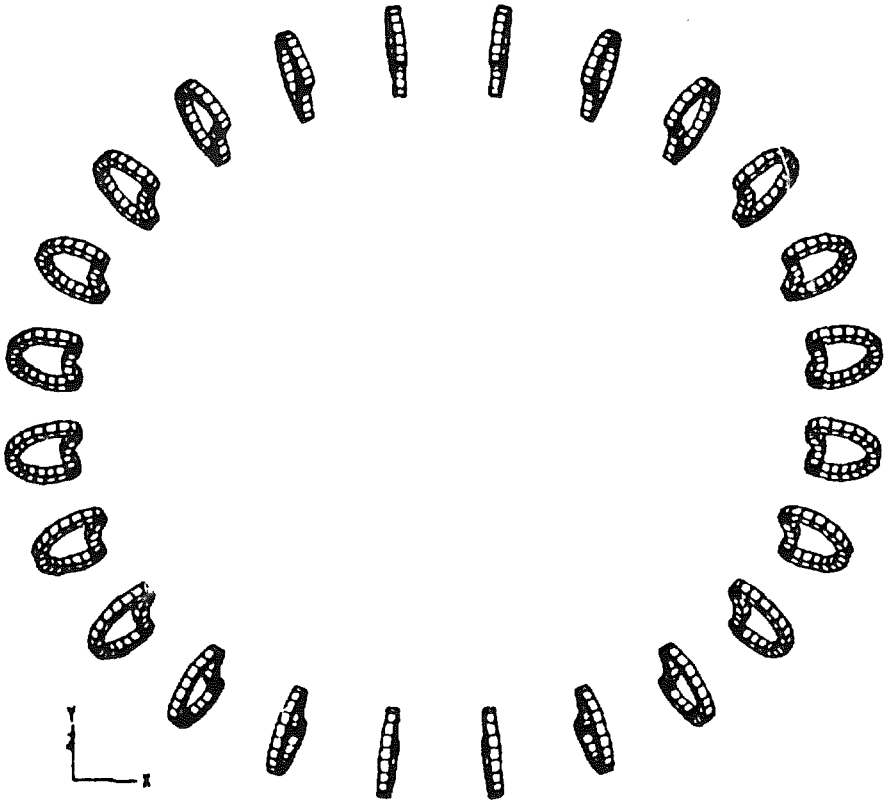

FIGURE 7 COIL ARRANGEMENT FOR BUMPY BEAN TORUS

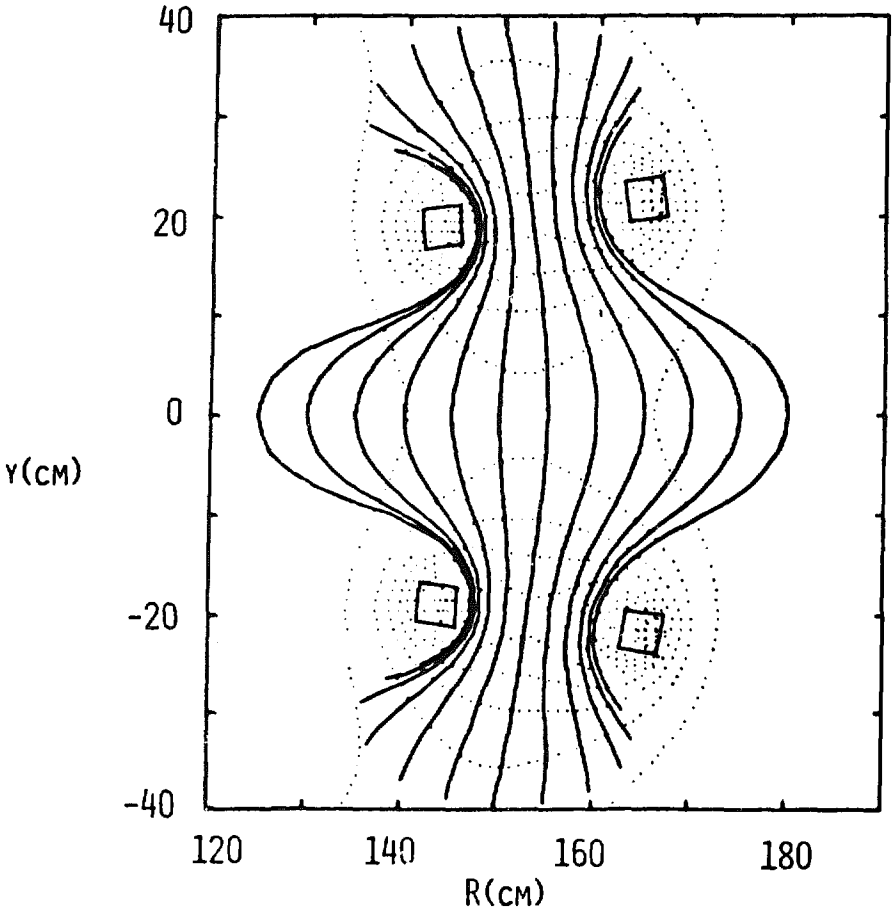

FIGURE 8 FLUX LINES AND MOD-B SURFACES IN THE EQUATORIAL PLANE OF THE BUMPY BEAN TORUS

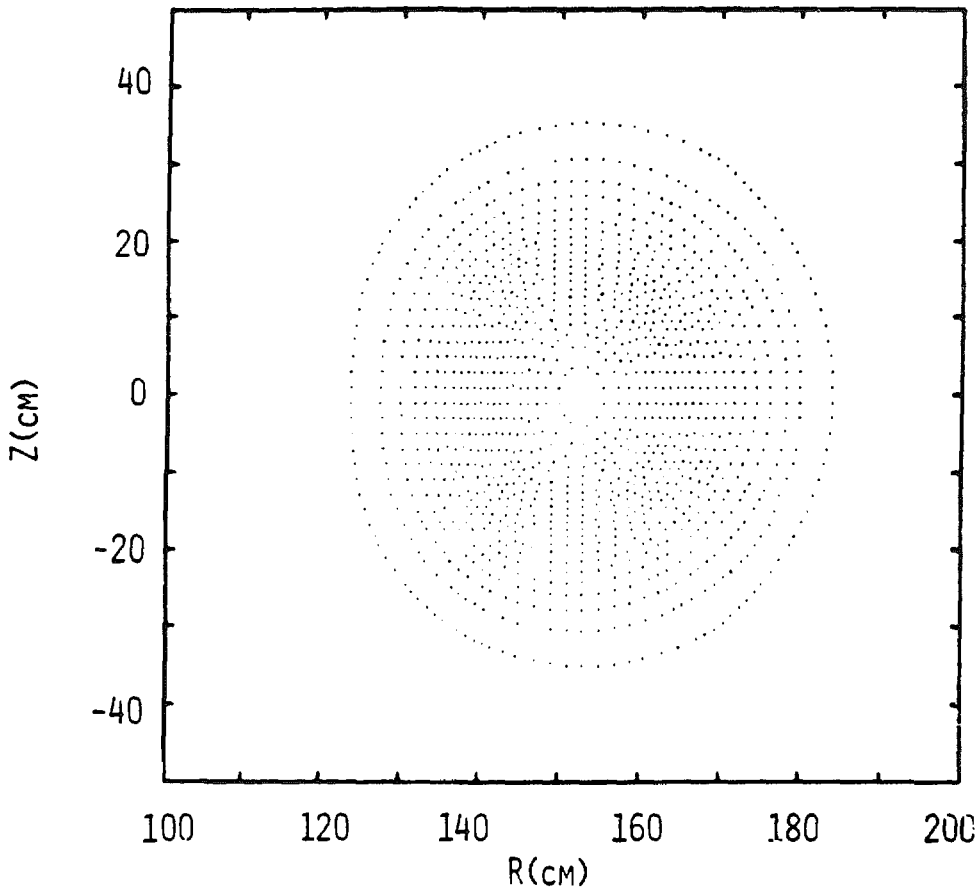

FIGURE 9 MOD-B SURFACES IN A VERTICAL SYMMETRY PLANE OF THE BUMPY BEAN TORUS

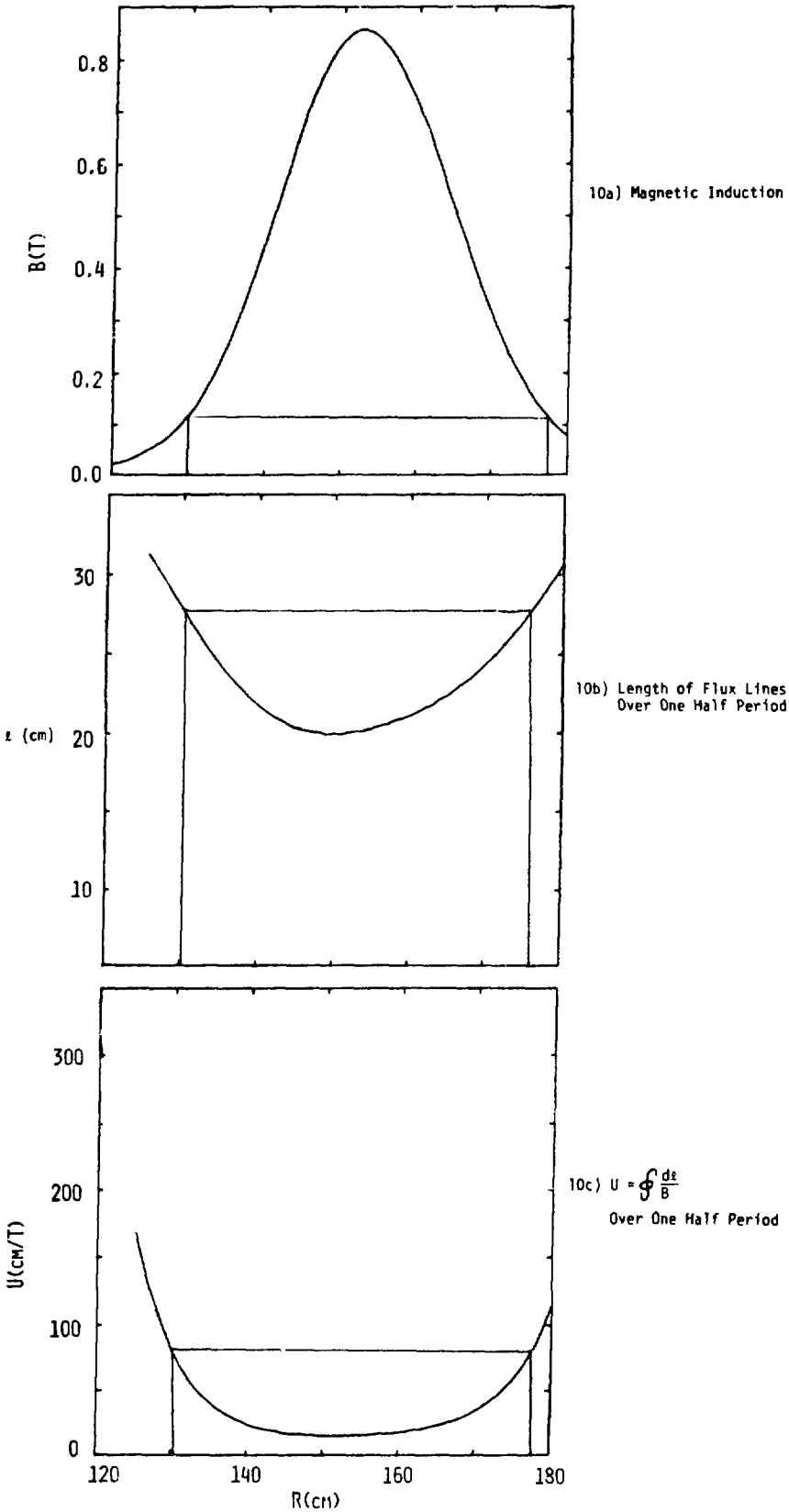

FIGURE 10 BUMPY BEAN TORUS

QUANTITIES AS A FUNCTION OF DISTANCE FROM THE MAJOR AXIS ALONG THE INTERSECTION OF THE EQUATORIAL PLANE WITH A VERTICAL PLANE MIDWAY ADJACENT MIRROR COILS

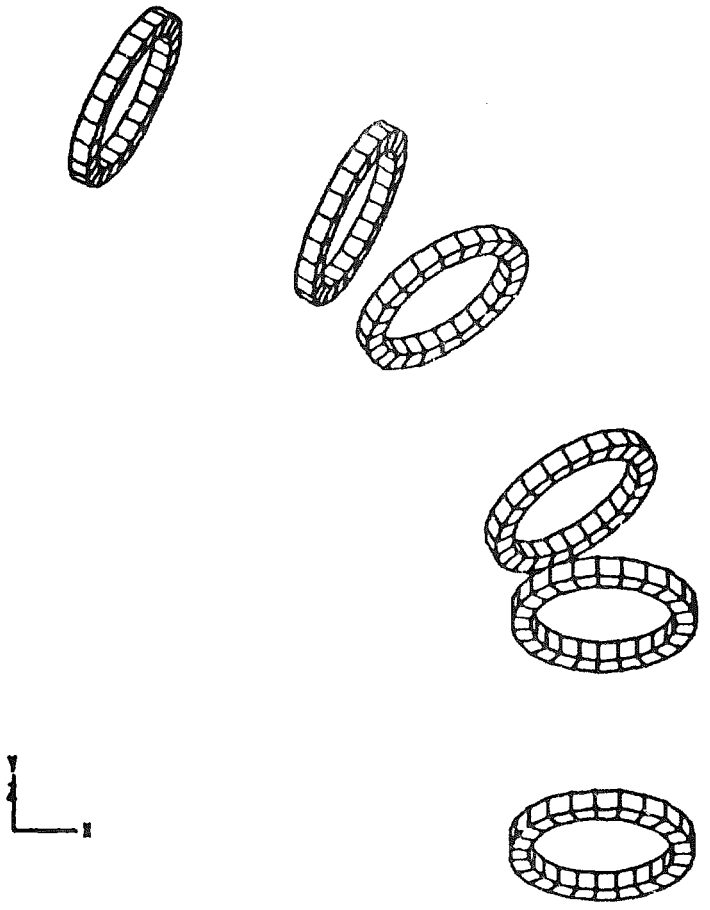

FIGURE 11 COIL MODEL OF BUMPY POLYGON

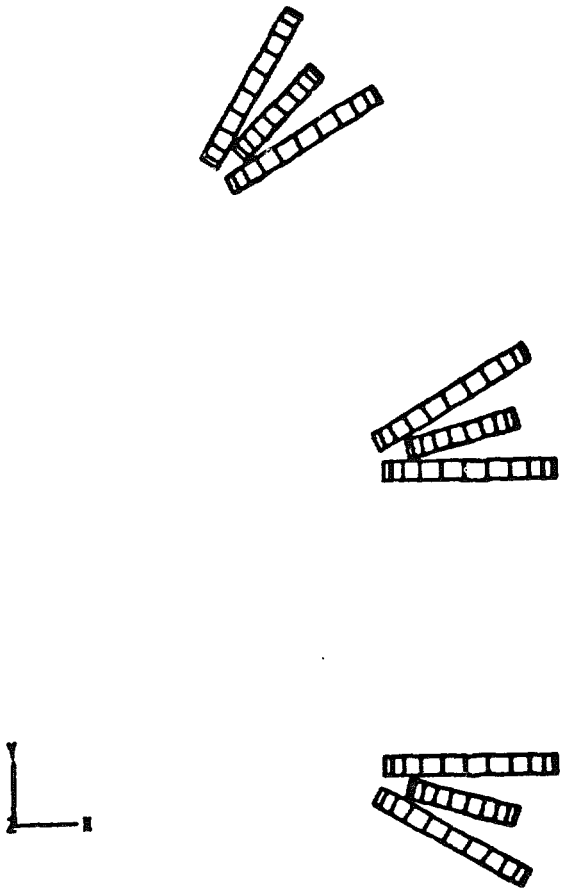

FIGURE 12 COIL MODEL OF BUMPY POLYGON WITH FIELD TRIMMING COILS

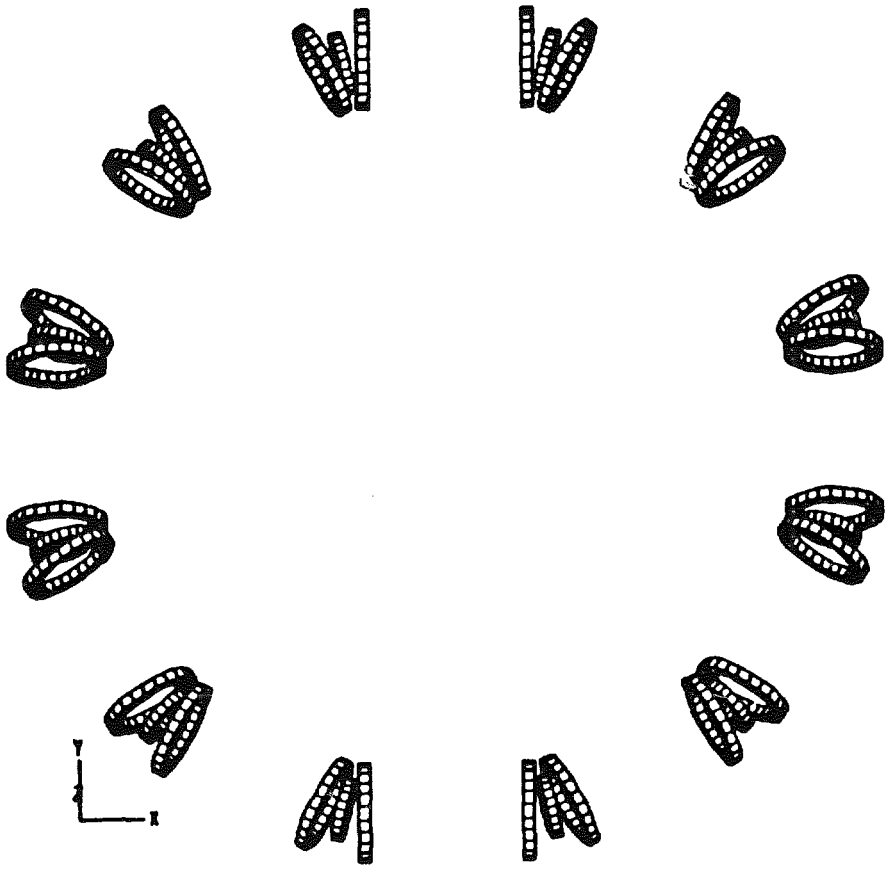

FIGURE 13 BUMPY POLYGON WITH FIELD TRIMMING COILS

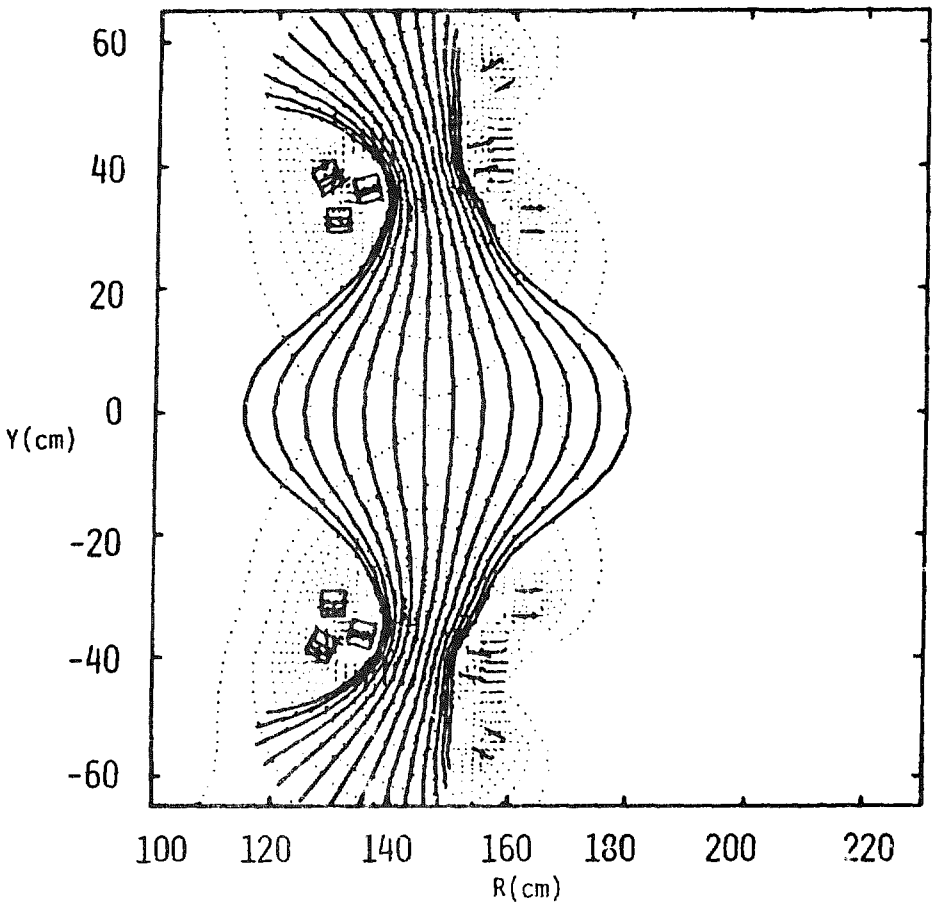

FIGURE 14 FLUX LINES AND MOD-B SURFACES OF BUMPY POLYGON IN THE EQUATORIAL PLANE

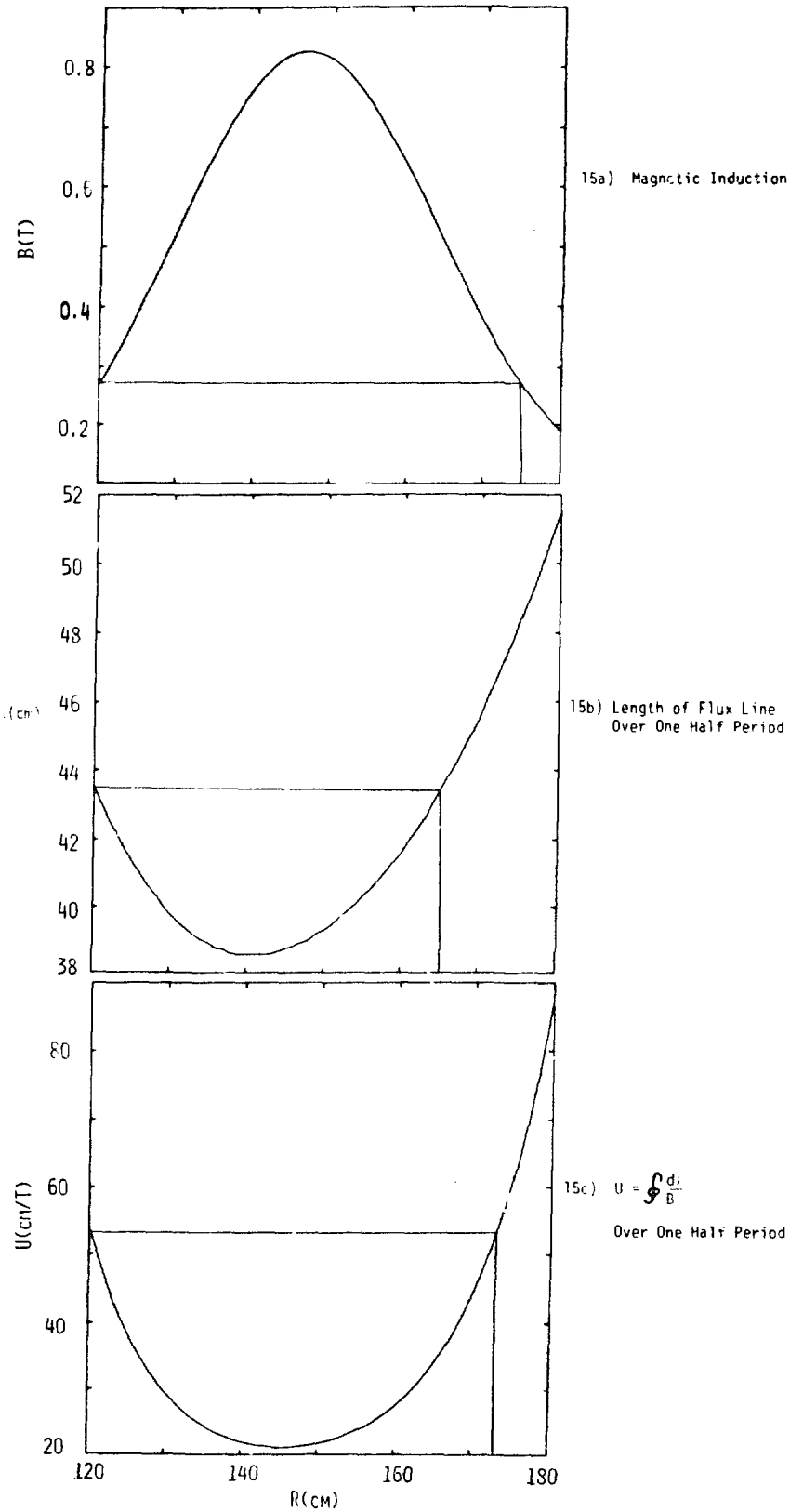

FIGURE 15 BUMPY POLYGON

QUANTITIES AS A FUNCTION OF DISTANCE FROM THE MAJOR AXIS ALONG THE INTERSECTION OF THE EQUATORIAL PLANE WITH THE VERTICAL PLANE MIDWAY BETWEEN MIRROR COILS OF A LINEAR MIRROR SECTION

97/98

MAGNETICS-CLOSED FLUX SURFACE DEVICES

OPTIMIZED APPROACHES TO EBT'S WITH SIMPLE CIRCULAR COILS

J.F. Pipkins, R.J. Schmitt, W.B. Ard,
R.J. Kashuba and F.M. Bieniosek
McDonnell Douglas Astronautics Company, St. Louis, MO

Several approaches have been proposed for magnetic configurations for EBT that reduce the dispersion in drift orbits and increase the fraction of orbits confined in the device over those in a simple bumpy torus. In this paper we qualitatively compare two approaches using simple circular coils, with and without rotational transform. The devices we compare consist of two linear segments of simple mirrors connected at the ends with segments of a torus. In one device the two linear segments do not lie in the same plane so that the toroidal connection results in the establishment of flux surfaces rather than closed field lines. The projection of the resulting flux surfaces are concentric circles that coincide with the drift surfaces of particles trapped in the mirror segments. Both devices are EBT's in that they require magnetic mirrors for the equilibrium and high beta rings to provide MHD stability for both low and high core beta. Devices based on the twisted racetrack approach offer advantages over circular EBT's for reactor applications as well as for experimental devices.

INTRODUCTION

In addition to its steady-state operation a very attractive feature of the EBT concept as a commercial fusion power reactor is that it is a high aspect ratio device that can be constructed from simple circular coils. In the form employed in present devices it can be completely modular, that is, made of N identical sections that can be connected to form a complete torus. In looking for variations that might improve plasma confinement and thereby, reduce the minimum size of the reactor it would be desirable to retain as many of the advantages of the present configuration as possible. In this paper we consider variations of the EBT that retain the feature of simple circular coils with modular construction.

The devices considered include a closed field line device and a device with flux surfaces, both stabilized by high β annuli. Comparisons are made with EBT-P, a circular EBT with simple mirror coils only, as a reference.

As an example of non-simple-circle closed line devices we consider a racetrack version of the "square" (Ref. 1). Transport in the racetrack should be representative of that in squares and circular EBT's with circular ARE coils. However, equilibria in these devices could be quite different. The racetrack is two straight elements, consisting of a number of simple mirror segments, connected together at the ends

with high magnetic field simple semi-tori. This approach will be referred to as the simple or planar racetrack (RT).

If the racetrack is twisted so that the two straight sections do not lie in the same plane and the ends are again connected with tori, the field lines no longer close and flux surfaces are produced. In this twisted ractrack device (TRT) the flux surfaces can be made to coincide with the concentric circular drift surfaces in the straight mirrors. It is similar to the DRACON (Ref. 2) concept and can be, in principle, made equivalent since the connecting toroidal sections can be made into a form of CREL. The CREL is a toroidal connector that matches both $\int dl/B$ and flux surfaces to the drift surfaces. Another flux surface device with circular coils is the helical axis stellerator, Elmo Snakey Torus (Ref. 3). This device also requires hot electrons for stability at low beta but it may be stable without rings at high beta.

We make no real attempt to optimize the configurations. In fact we make all the devices the same size and magnetic field strength in the mirror sections. That is, the plasma mirror radius in the coil throats is 20 cm, the distance around the device is 900π cm = 28 m, the same as EBT-P, and the average magnetic field in the mirror section is 2T (1T at the ring location). This is done to provide a common point of comparison and not an optimum.

Figure 1 is a schematic of the simple racetrack showing a number of the closed magnetic field lines. Figure 2 is a schematic of the twisted racetrack showing the projections of a typical field line followed several times around the device. At low beta both the $\int dl$ and the $\int dl/B$ surfaces are centered on the magnetic axis in this device. The rotational transform of the device is 2.86 radians per revolution resulting in a $q = 2.2$ device. q is the number of times a particle must transit the device to experience a 360° rotation around the minor axis.

Figures 3 and 4 are plots of $\int dl$ and $\int dl/B$ as a function of minor radius in a coil throat at the center of a straight section for both the planar and twisted racetracks. The values for EBT-P are also plotted for comparison. The curves for the twisted racetrack are centered on the minor axis because of the rotational transform. Although the planar racetrack has only two thirds as many mirror sections as EBT-P, the curves are better centered than EBT-P because all the toroidal curvature in the device occurs in the high magnetic field connection.

The different devices are principally compared on the basis of transport. However, because transport will depend on the equilibri-

um at finite beta, we give some discussion of equilibrium in the different devices.

EQUILIBRIUM AND STABILITY

The interpretation that a principal loss process for EBT is the collisionless loss on open drift surfaces (open meaning drift surfaces that intersect the vacuum wall) eventually led to the introduction of rotational transform, to provide better centering of the drift orbits. The approach to generate the rotational transform was to use straight bumpy sections and twist the ends. This allows rings to be generated in the bumpy sections to stabilize the device. As is well known, a simple figure-eight stellerator has an unfavorable $\int dl/B$, and the bumpy section further adds to the unfavorable $\int dl/B$.

Equilibrium in the planar and twisted racetracks has the good feature that the $\int dl/B$ curves for both devices are better centered on the magnetic axis than in EBT-P. Finite beta in the toroidal connecting sections of both devices will cause the center of the pressure surfaces to shift outward (away from the major toroidal axis). However, in the planar racetrack, the $\int dl/B$ surfaces in the vacuum field are shifted inward due to the effect of toroidicity, and hence finite beta will tend to center the plasma. In the twisted racetrack, the vacuum $\int dl/B$ surfaces are already centered due to the rotational transform. In this device, finite beta will shift the flux surfaces outward and separate the flux surfaces from the drift surfaces of particles trapped in the mirrors of the straight sections. The effect will be to produce plasma transport similar to that in closed line EBT devices.

In both planar and twisted racetrack devices, the shift of the pressure surfaces is limited by the variation in $\int dl/B$ produced by the mirrors in the straight sections. If the straight sections were simple straight solenoids, the planar racetrack would have no equilibrium by analogy with the simple torus, and the twisted racetrack would have an equilibrium only at very low beta by analogy with the figure-eight stellerator. The outward shift in the twisted racetrack can be reduced by increasing the rotational transform. The shift can be reduced to zero if the rotational transform in each of the connecting sections is greater than 2π (i.e., effectively a $q \leqslant 1/2$ device). This is the basis of the DRACON device, whose long uniform-field straight sections require a large rotational transform.

Further analysis will be required to fully assess the sensitivity of the bumpy twisted racetrack equilibrium to the core plasma beta. However analysis shows that the shift in the center of the flux surfaces at high beta is limited to the displacement of the minimum in

$\int dl/B$ integrated around one-half of the device. The maximum shift can be reduced by increasing the rotational transform in each connector or by increasing the magnetic field in the connectors as in the planar racetrack.

The variation in $\int dl/B$ across the minor radius is much smaller in the planar and twisted racetrack than EBT-P; therefore, a lower annulus β is required to stabilize the system against interchange modes. Because the connecting ends of the racetrack are physically separated from the stabilizing rings, both devices are subject to localized modes in the connecting sections at finite beta. Stability against such modes has not been analyzed at this point. However, preliminary es timates indicate that the core plasma beta limit due to these modes is comparable to the beta limit due to ring-core coupling in the mirror segments.

TRANSPORT

In order to estimate the confinement scaling of the different devices we will consider some simplified transport estimates. We will do this by ignoring the electric field and concentrate on the scaling of electron confinement. This is done even through electric fields will almost certainly arise from equilibrium and ambipolarity requirements because including these effects would require extensive model calculations. However, estimates based on magnetic considerations only should be a measure of the relative efficiency of the different devices for confining a plasma.

Initially we will consider closed field line devices EBT-P and RT. Two plasma loss process are important. The first is due to the fact that these devices have a rather large fraction of passing particles that are not on drift surfaces that close in the device. The second loss process is due to dispersion of the closed drift surfaces with particle pitch angle. We consider each of these processes in turn.

<u>OPEN DRIFT ORBIT TRANSPORT:</u> Particles on open drift orbits have an average drift that is dominated by the drift due to the toroidal curvature. The step size for diffusion for these particles is given by the average toroidal drift speed, $\bar{v}_T$, times the collision time, $1/\nu_e$, where ν_e is the electron collision frequency. For squares and racetracks the particles spend only a fraction of their time in the curved section so that the average drift speed is:

$$\bar{v}_T = v_T f = \frac{cT}{eB_T R_T}\left(\frac{2\pi R_T}{L+2\pi R_T}\right) = \frac{2\pi\, cT}{eB_T\,(L+2\pi R_T)} \,. \qquad (1)$$

Here, R_T, is the radius of curvature of the toroidal section, taken to be equal to the magnetic radius of curvature, and L is the total length of the straight sections. Note that the average vertical drift is inversely proprotional to the magnetic field in the curved sections and to the total perimeter of the device, $L + 2\pi R_T$.

The diffusion coefficient for particles on open drift orbits is

$$D_o = \Delta x^2 \nu_e = \frac{\bar{v}_T^2}{\nu_e} , \tag{2}$$

We define for comparison of different devices a lifetime, τ_o

$$\tau_o = \frac{a^2}{D_o} = \frac{a^2 \nu_e}{v_T^2} , \tag{3}$$

where a is the plasma radius. The lifetime is

$$\tau_o = 10^{-23} a^2 B_T^2 \left(\frac{L+2\pi R_T}{2\pi}\right)^2 nT^{-7/2} , \tag{4}$$

where we have used for the electron collision frequency $\nu_e = 10^{-9}$ $nT^{-3/2}$. In this paper the temperature is in keV, the magnetic field is in Tesla and distances are in cm. This expression is the same as that for stellerators in the collisional regimes. However, it applies to stellerators only when the collision time is less than the transit time through a full rotational transform

$$\nu_e > \frac{v_{th}}{2\pi q R_T} \tag{5}$$

where v_{th} is the thermal velocity and q is the number of transits of the device required to experience a rotational transform of 2π. For devices without rotational transform this collisional scaling applies as long as the particle drift during a collision time is less than the plasma radius, $\nu_e > v_T/a$. For $\nu_e < v_T/a$ the lifetime becomes the scattering time and the confinement is mirror like.

<u>CLOSED DRIFT ORBIT TRANSPORT:</u> Diffusion of particles on closed drift surfaces forms the basis for the neoclassical transport theory for EBT. Although there is an extensive body of literature on neoclassical transport in EBT, for comparison of different devices we define a neoclassical lifetime, τ_N, as

$$\tau_N = A^{*2} \left(\frac{\nu_e^2 + \Omega_p^2}{\nu_e \Omega_p^2}\right), \tag{6}$$

where A^* is the effective aspect ratio and is defined by the expression

$$\Delta r = a/A^* \tag{7}$$

where Δr is the displacement of the center of passing particle drift surfaces from trapped particle drift surfaces. In the above expression Ω_p is the poloidal drift frequency. For a simple circular EBT, $A^* = R_T/R_c$ and $\Omega_p = cT/eaBR_c$, where R_c is effectively the coil mean radius.

We estimate A^* for a racetrack or square EBT by calculating Δr. The quantity Δr is the distance a particle drifts toroidally during a poloidal drift time,

$$\Delta r = \frac{\bar{v}_T}{\bar{\Omega}_p} \tag{8}$$

where averages are again calculated since particles are not always drifting vertically or poloidally. The quantity $\bar{v}_T$ is given in Eq. (1) and the average poloidal drift frequency is given by

$$\bar{\Omega}_p = \Omega_p f' = \left(\frac{cT}{e\, B_m R_c}\right) \left(\frac{L}{L + 2\pi R_T}\right), \tag{9}$$

where B_m is the average magnetic field in the straight mirror sections. Substituting Eqs. (1) and (9) into Eq. (8) yields

$$\Delta r = \left(\frac{B_m}{B_T}\right) \left(\frac{2\pi R_c}{L}\right) a, \tag{10}$$

from which we can obtain the effective aspect ratio

$$A^* = \left(\frac{B_T}{B_m}\right) \left(\frac{L}{2\pi R_c}\right). \tag{11}$$

We note that the confinement time scales with the square of A^* and thus the square of the ratio of toroidal to mirror magnetic field. In addition A^* is directly proportional to the length of the straight section.

The net confinement for a simple EBT or RT depends on which of the process, either open or closed drift orbit transport, is largest. However, before we discuss specific cases, we want to obtain the scaling for the twisted racetrack.

TRANSPORT IN A TRT: The twisted racetrack device has rotational transform so that at low beta transport is dominated by particles that do not experience the full rotational transform. These are either passing particles that undergo collisions before experiencing a full 2π transform or particles that get trapped because of this toroidal field variation on the flux surfaces in the curved sections.

Confinement in the collisional regime scales in the TRT the same as in the RT. However, this regime is limited to cases where the collision time is less than the transit times or

$$\nu_e > \frac{v_{th}}{q\,(L + 2\pi R_T)} \,. \tag{12}$$

For the twisted racetrack described in this paper with $q \approx 2$ and $(L + 2\pi R_T) = 2800$ cm, Eq. (12) implies $T < 5.5 \times 10^{-8}\, n^{1/2}$. For a nominal operating density of 2×10^{13} cm^{-3} this regime only applies to $T < .25$ keV.

At low collisionality the dominant loss is due to ions trapped because of the toroidal field variation. These ions are in banana orbits and the diffusion step size is the banana width, i.e.,

$$\Delta x = \frac{\bar{v}_T}{\nu_b} \,, \tag{13}$$

where ν_b is the bounce frequency. For a low q device the bounce frequency can be approximated by

$$\nu_b = \frac{1}{(L + 2\pi R_T)} \left(\frac{T_{\|}}{M_i}\right)^{1/2} . \tag{14}$$

In the above expression we take $T_{\|} \approx a/R_T T$ for those ions trapped in the weak mirrors. In order to estimate the confinement time we use Eq. (2) with Δx from Eq. (13) but with an effective collision frequency $\nu_{eff} = \sqrt{a/R_T}\, \nu_i$, thus

$$\tau_B = 2 \times 10^{10}\, a^2\, B_T^2 \left(\frac{a}{R_T}\right)^{1/2} \frac{T^{1/2}}{n} \,. \tag{15}$$

The collisional and banana regimes are connected by a plateau regime (Ref. 4) where the scaling is given by

$$\tau_p = 3.5 \times 10^{-6}\, a^2\, B_T^2 \frac{R_T}{q}\, T^{-3/2} \,. \tag{16}$$

From Eqs. (15) and (16) we see for the case studied in this paper that the confinement time would decrease rapidly to a minimum for a temperature around 1 keV and then rise with $T^{1/2}$.

As the plasma beta increases the Pfirsch-Schluter currents produce a vertical magnetic field in the device that will displace the flux surfaces from the trapped particle drift surfaces in the mirrors. This separation between the flux and drift surfaces will result in transport similar to neoclassical transport in closed line devices. Thus

$$\tau_N = A^{*2}/\nu_e \tag{17}$$

where $A^* \propto a/\Delta x$ and $\Delta x \propto \beta$ is the displacement of the flux surfaces from the drift surfaces.

<u>COMPARISON OF CONFINEMENT</u>: The confinement times based on the different loss processes for EBT-P, RT and TRT are plotted in Figure 5 as a function of electron temperature. An electron density of 2×10^{13} cm^{-3} is assumed in all three of the devices. Figure 4 is a plot of the confinement times for EBT-S based on the same scaling relations we have used for EBT-P and RT. We assume a density of 1×10^{12} cm^{-3} in EBT-S. The EBT-S confinement scaling is included only for reference. The table summarizes the basic parameters of the devices and their relative confinement properties. It should be emphasized that the confinement times estimated from the simple scaling relations are intended to represent only the relative effectiveness of the devices.

PARAMETERS OF DEVICES

	R_T	$L/2\pi$	R_C	a	B_T	B_M	A^*	τ_O (1 keV)	τ_N (1 keV)
EBT-P	450	—	30	17	2	2	15	50	55
EBT-RT	150	300	30	17	5	2	25	300	350
EBT-TRT	210	240	30	17	3	2	—	—	900
EBT-S	150	—	15	12	1	1	10	1.0	100

It can be seen from the scaling relations, and from the EBT-S plots, confinement scales with size, especially a, R_T and B. In the closed line devices, EBT-S, EBT-P and EBT-RT with some open drift surfaces, confinement of particles on both the open and the closed drift surfaces must be good for the device to exhibit good confinement. In particular confinement of particles on closed surfaces in EBT-S is quite good at modest density, however, the confinement of particles on open surfaces is very poor even at only modest electron temperature.

EBT-P and EBT-RT are both large enough to have good confinement into the kilovolt electron temperature range. EBT-RT is significantly better than EBT-P because A* is larger and the greatly improved confinement on open surfaces, due to the higher magnetic field in the curved section, and larger size allows confinement to remain good up to fairly high electron temperature. Both devices should exhibit neoclassical confinement over a reasonable range of electron temperature. However, the rapid scaling of confinement on open surfaces ($a^2B^2R_T^2n$) would preclude operation in the neoclassical regime in any significantly smaller or lower magnetic field device. This is particularly true of a steady-state EBT in which n scales with B^2.

Neoclassical confinement in the twisted racetrack at low beta is very good because the passing particles are confined on the closed flux surfaces that are coincident with the drift surfaces of particles trapped in the mirrors. Because at finite beta the Pfirsch-Schluter currents will displace the flux and drift surfaces the confinement will approach that of a closed line device at sufficiently high beta. It will always remain somewhat better than the simple closed line racetrack because that device also has an equilibrium high beta shift in its passing and closed drift surfaces. It appears however that a signifi-

cant beta is required for this effect to play a major role in confinement in the either device.

To determine the quantitative scaling of confinement with beta in these devices will require further analysis of equilibria. However, because neoclassical confinement in the twisted racetrack is so good it is likely that, even at low beta, the confinement will be determined by the shift in flux surfaces. Because the shift in flux surfaces is proportional to beta, confinement would scale in the device as $\beta^{-2}T^{3/2} \propto T^{-1/2}$.

POTENTIAL OF THE TRT AND RT FOR EBT RESEARCH

Both the racetrack devices offer significant advantages over conventional EBT's for resolving EBT physics issues. These advantages arise from both potentially lower device cost and experimental flexibility. The lower device cost for both types of racetrack results because only a part of the total device must have hot electron rings and therefore, requires quasi-steady state operation. The toroidal connecting section can be operated in a pulsed mode without limiting the ability of the device to be used for addressing toroidal confinement issues.

The simple racetrack is an extremely powerful device for addressing toroidal confinement in closed line systems. The ability to change the magnetic confinement properties of the device by changing the magnetic field in the curved sections without affecting the rings directly is unique to this approach. For example, if the device we describe is operated with hot electron rings at 0.5 Tesla field, the effective aspect ratio of the device can be changed continuously from 10 to 50, changing the neoclassical confinement by a factor of 25.

The change in aspect ratio is effected by changing the center of the drift surfaces for passing particles in the straight sections where the trapped particle drift surfaces and therefore, the rings are axisymmetric. This provides a direct approach for connecting the neoclassical confinement properties of the EBT with electrostatic potential profiles experimentally.

The twisted racetrack has the same advantage of lower device cost as the racetrack. The added complication of a non-planar device will certainly increase structural costs but these would probably be more than offset by the lower magnet and power cost because of the considerable lower field required in the curved sections. A very important advantage of the twisted racetrack is that a somewhat smaller and lower field device could be built that has significant confine-

ment. However, as with all confinement experiments, small plasma radius and low plasma density make it very difficult to intrepret results in the face of wall and atomic physics effects.

A relatively small device could, however, address questions of basic stability of the concept at low beta. The question of stability at high beta requires significant plasma density and minor radius. If the toroidal confinement is as good as expected, this could be accomplished with significantly lower plasma heating power than in the simple racetrack or in EBT-P.

REACTOR IMPLICATIONS OF RACETRACK EBT'S

Devices based on the racetrack approach offer advantages over circular EBT's for reactor applications as well as for experimental devices. Both the planer and twisted racetrack approaches retain the basic construction and maintainability aspects of the conventional EBT. Both can be of modular construction but require more than a single type of module and therefore, more flexible remote maintenance equipment.

The greatly improved confinement of the simple racetrack over the conventional EBT may not be fully realizable for reactor scale devices because of the very high magnetic fields required in the curved sections. Also, a sizable fraction of the plasma volume will be at low beta which will not fully utilize the magnetic energy in the curved sections.

The twisted racetrack does not require high field in the curved section to enhance the confinement. It does require the EBT rings and its maximum stable beta is the same as a conventional EBT. The degradation of confinement due to the Pfirsch-Schluter currents from the curved section at high beta can, in principle, be controlled by increasing the rotaional transform in the curved section. This can be done while retaining the simple coil construction by alternating the curvature in the connecting sections as in the DRACON approach.

Considerably more analysis is required to optimize the twisted racetrack as a reactor. In particular it is not clear at this point how many rings are required to stabilize the system. It may be feasible to replace many of the bumps in the straight section with a uniform field region.

Acknowledgement: We would like to thank C.L. Hendrick Jr. and A. Boozer for very helpful discussions and J.W. VanDam for invaluable assistance with the preparation of the paper.

References:

[1] L.W. Owen, D.K. Lee, C.L. Hedrick Jr., "Elmo Bumpy Square," this conference.

[2] V.V. Arsenin, V.M. Glagolev, B.B. Kadomstev, V.P. Pastukhov, B.A. Trubnikov, and V.D. Shafranov, "Closed Magnetic Traps with Rectilinear Sections," paper IAEA-CN-41/073 presented at the 9th IAEA Conference on Plasma Physics and Controlled Nuclear Fusion Research, Baltimore, 1-8 September 1982.

[3] A.H. Boozer, "ELMO Snakey Torus," this conference.

[4] J.W. Conner and R.J. Hastie, Phys. of Fluids 17, 118 (1974).

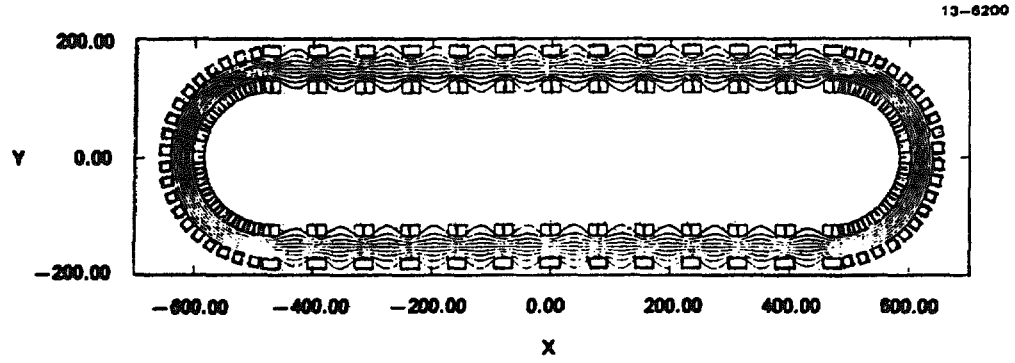

Figure 1. Schematic of the closed field line planar racetrack showing several magnetic field lines.

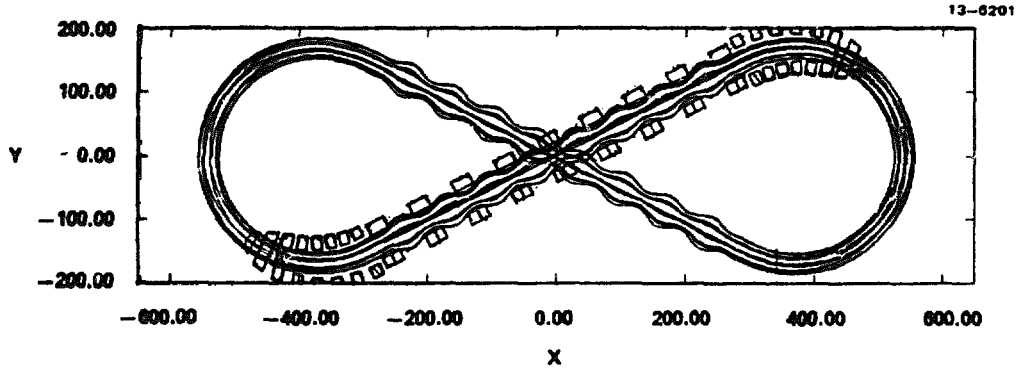

Figure 2. Schematic of the twisted racetrack projected on a horizontal plane showing a field line at a particular radius followed several times around the device.

13-6217

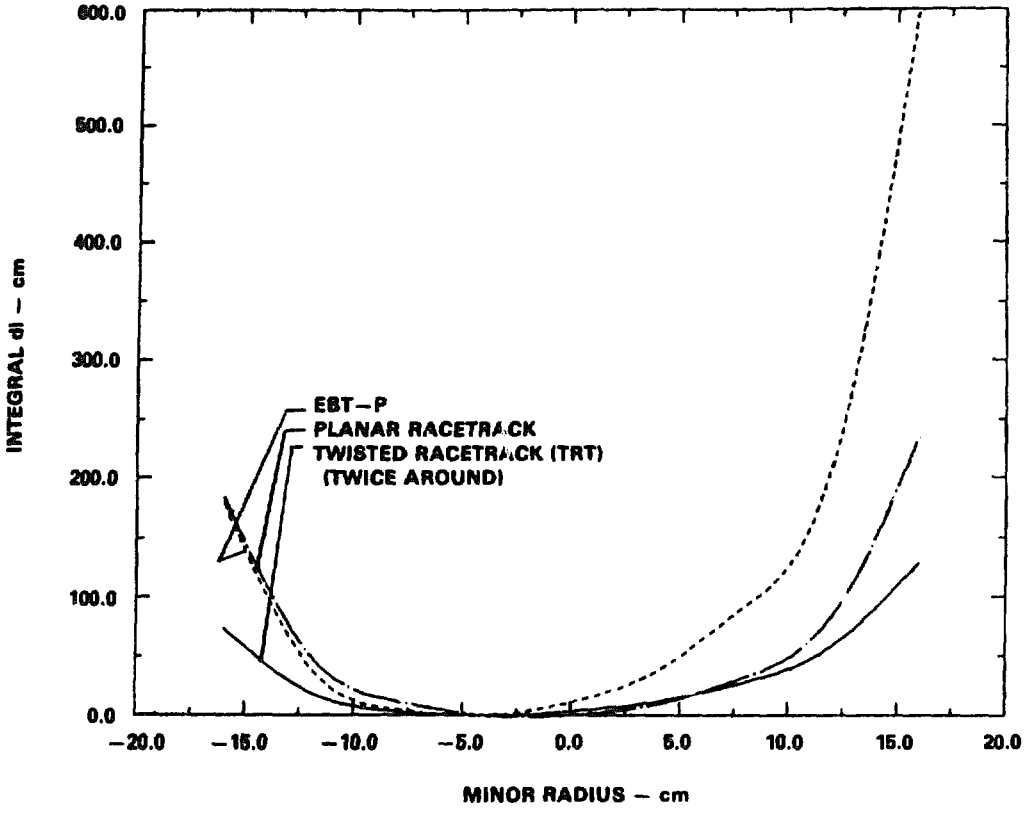

Figure 3. Plots of $\int dl$ for EBT-P, RT and TRT versus minor radius at the coil throat in the center of the straight sections. For the TRT the integral is taken twice around the device and includes the effect of essentially the full rotational transform.

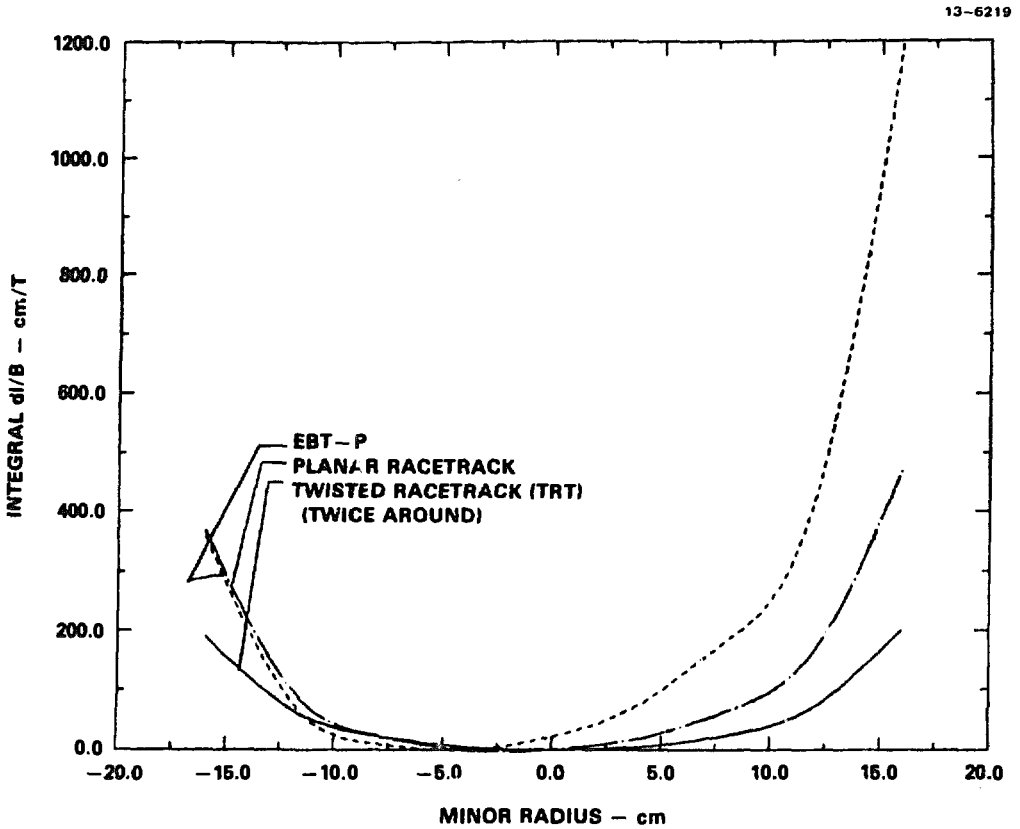

Figure 4. Plots of ∫dl/B for EBT-P, RT and TRT versus minor radius. Again the TRT is integrated twice around the device.

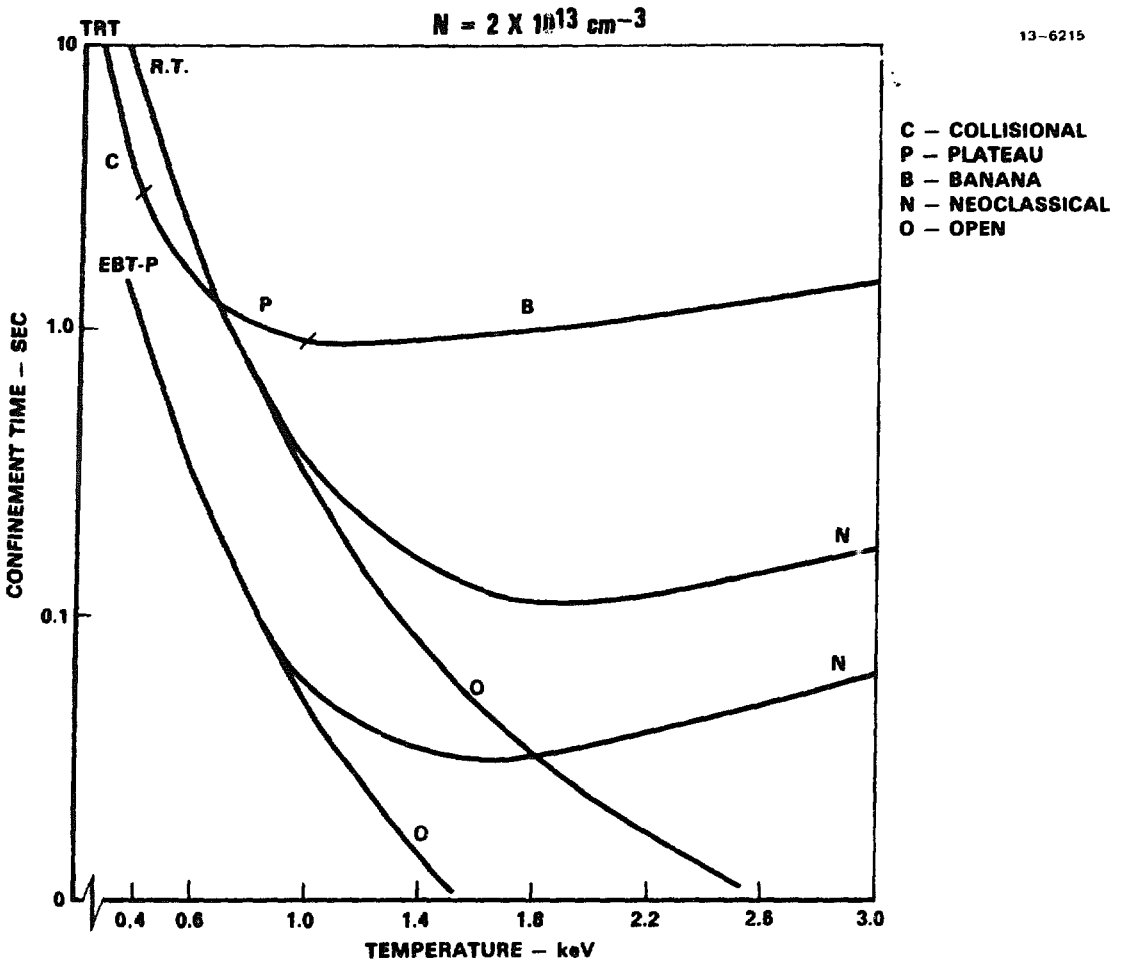

Figure 5. Plots of τ_N(N) and τ_O (O) for EBT-P and RT and τ for the three collisionality ranges of the TRT, collisional (C), plateau (P) and banana (B). A plasma density of 2 x 10^{13} cm^{-3} is assumed for all three devices. Note that in the collisional limit differences in confinement in the device is due only to differences in the magnitude of the magnetic field in the curved sections. For EBT-P, a circular device, this is the average field in the device.

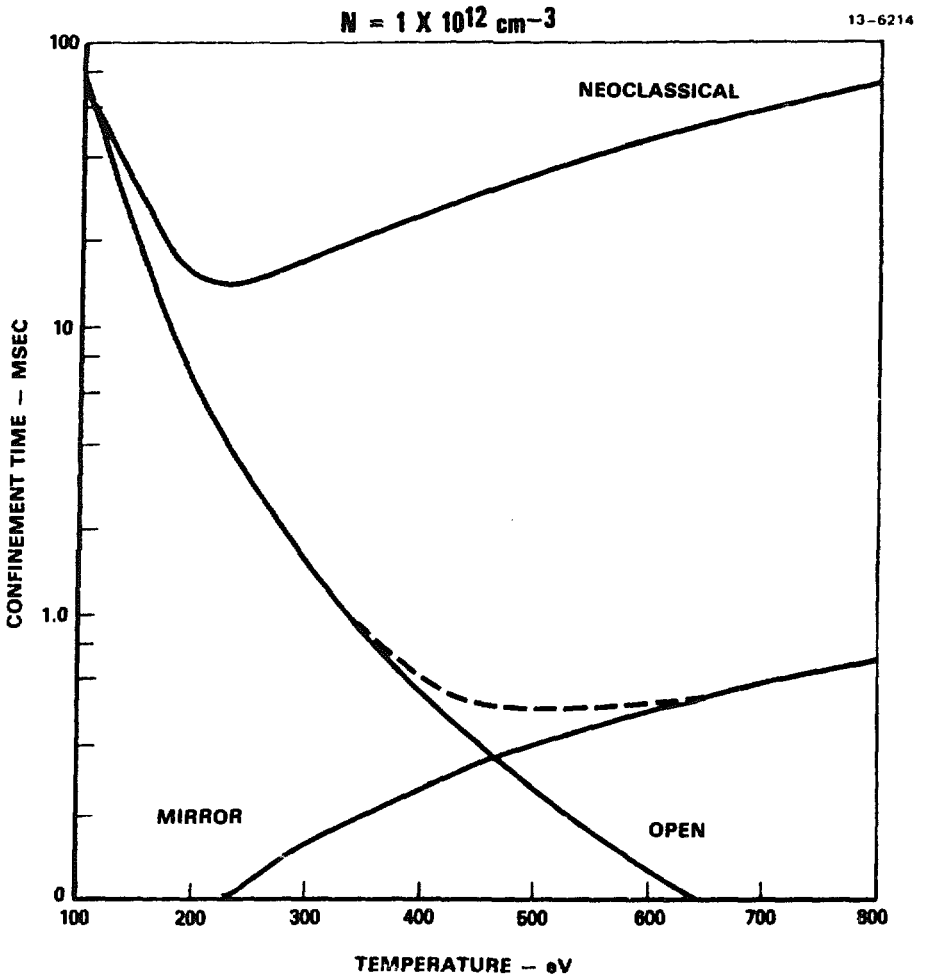

Figure 6. Plots of τ_N, τ_O and confinement time in the mirror (90° scattering time) for EBT-S. A density of 10^{12} cm^{-3} is assumed for EBT-S.

PRELIMINARY CONCEPTUAL DESIGN OF A TWISTED RACETRACK EBT DEVICE

R. J. DeBellis, H. F. Imster, J. L. Conlee,
R. J. Dannenmueller, C. F. Dillow, T. J. Poteat
R. J. Schmitt

McDonnell Douglas Astronautics Company - St. Louis, Missouri 63166

ABSTRACT

A twisted racetrack alternative to the usual type of EBT device consists of two straight sections with EBT mirrors connected by two end segments in the form of simple toroidal solenoids. The straight sections are separated vertically by several meters to produce a non-planar device with a rotational transform. The engineering aspects of a twisted racetrack device are considered in this paper, with emphasis on magnet, vacuum vessel and main support structure. Three configurations are discussed, a steady state concept with superconducting coils, a pulsed concept with copper coils and a hybrid concept with both copper and superconducting coils. Areas of unusual or difficult design aspects are identified and preliminary cost estimates are presented and compared to cost estimates generated previously for EBT-P.

1. DESIGN METHODOLOGY AND GENERAL DEVICE CONFIGURATION

This paper describes a preliminary concept for an improved EBT device called the Twisted Racetrack (TRT). The TRT device is an EBT since it requires EBT hot electron rings for both start-up and steady-state operation. Another paper[1] provides plasma physics data for the TRT; this paper considers the TRT from the engineering viewpoint. Design and cost data generated for the EBT-P device have been used as starting points for the TRT work both to capitalize on the investment already made in EBT-P and to provide a reference from which TRT costs can be estimated.

This work was performed under Subcontract 22X-21099C to Union Carbide Corporation, Nuclear Division, for the Oak Ridge National Laboratory, and the U.S. DOE.

This work has relied on a number of computer codes some of which were in existence and several of which were developed specifically for the TRT study (Table I). The EFFI code (maintained by LLNL on the MFE network) is used to trace field lines around the TRT device and to compute magnetic forces on selected coils. An EFFI pre-processor code (TRTSET) was developed to iteratively determine the pitch and radius of the helical space curve which defines the centerline of the solenoids required to complete the TRT device for a given configuration of coils on the straight sections. Pre-processor runs are made until an arrangement is established having a sufficiently large vertical separation between the straight sections (ZDIFF = 245.5 cm). Several meters of vertical separation are needed to accommodate magnet and support structure requirements. The XPLOTTER and Unigraphics codes use EFFI output data files to generate cross-sectional magnetic surface plots and to provide basic device configuration data for support structure, ports and for dimensional analysis.

Figure 1 shows the general magnetic field and magnet configuration of the TRT device provided by the EFFI code. For purposes of discussion, this configuration roughly approximates EBT-P (see Table II). In particular, the mirror coils on the straight sections are identical to EBT-P coils and the perimeter of this TRT design (measured on the geometric space curve defined by the coil centers) is equal to the circumference of EBT-P (2827 cm). The solenoid coils which interconnect the straight sections are modeled for B-field calculations using thirty (30) half-width EBT-P coils for each solenoid. For this preliminary work each coil is modeled as a single filamentary current loop. Figure 2 shows a representation of the TRT device generated by the Unigraphics code used to define the basic device dimensions.

Figure 3 shows mod-B as a function of distance along the field line corresponding to the space curve defined by the coil centers. The mirror fields are adjusted for 60 GHz operation ($\sim$3.3T in the mirror coil throats) at the EBT-P mirror ratio = 2.2 on the centerline. This results in a separation of 74.67 cm between mirror coils. The current density in the solenoid is adjusted to produce $\sim$3.4T on the centerline.

The typical field line in the TRT device is infinitely long, i.e., it defines a magnetic surface. Figure 4 shows one such line followed for a distance of 45000 cm (approximately 13 times around the device). As Figure 5 shows, this field line defines a circular magnetic surface that is well-centered within the machine. The rotational transform q is approximately 2.2. The vacuum field in the TRT device defines nested, concentric, circular-cross-section magnetic surfaces. Displacements of the magnetic surfaces in the presence of plasma pressure are not considered in this paper.[1]

2. MAGNET SYSTEM

The magnetic system for the TRT device is illustrated in Figure 6. Each straight section consists of nine mirror coils which produce magnetic fields similar to that for 60 GHz EBT-P operation. The 1.4×10^6 amp turns produce the field strength required for second harmonic heating of the electron rings at 60 GHz. The axial separation distance is selected to provide a mirror ratio of 2.2. The straight sections are connected by twisted solenoidal end sections. The twist gives the magnetic field lines a rotational transform to enhance plasma characteristics in the curved solenoidal sections. The solenoidal or turning coils must produce a relatively constant magnetic field along the axis which is equal to or slightly greater than the field in the throat of the mirror coils to prevent the trapping of particles in the curved solenoid section. The turning coils are modeled as one-half the cross sectional area of the mirror coils, but with a 33 cm mean coil radius. Thirty turning coils are required at each end of the device.

The magnetic system concept for the twisted racetrack configuration presents some interesting design problems due to the geometry of the device and the asymmetry of loads from coil to coil in the solenoid section. The coil support system must be capable of handling the high in-plane and out-of-plane loads with minimal deflections due to anticipated magnetic field error requirements.

Three magnetic system concepts were considered during the study for conceptual and cost analysis.

1. An all superconducting magnet system operating steady state;
2. An all copper coil system operating in a pulse mode; and
3. A hybrid or combination using steady state superconducting mirror coils and pulsed copper coils at the ends.

Although these systems have not been optimized for power and cooling cost considerations, they can provide a comparative basis for conceptual evaluation.

All Superconducting Magnet System

Mirror Coils - The superconducting magnet system concept makes full use of the design and development test program for EBT-P. The mirror coils require only minor modifications with the exception of the end mirror coil next to the solenoid coils. The cold mass support system in the end coils must be modified for the higher steady state loads and to minimize cold mass deflections. The mirror coil mounting base and cryogenic connections are modified to facilitate mounting and to provide improved diagnostic access at each side of the mirror cavities. The horizontal orientation of the mirror sections allows use of the flooded LHe cooling concept being developed for EBT-P. The center seven mirror coils are connected via a superconducting bus in series electrically through a single set of vapor cooled leads. The mirror coil at each end of the straight section is powered independently but in series such that trim power supplies may be used in this transition region.

Turning Coils - The turning coils for the solenoid ends of the device are configured as wedge coils, as shown in Figure 7. Placing two cold mass assemblies within the same dewar alleviates some of the load problems and provides a larger envelope for the cold mass support system. Three or possibly four configurations with different wedge angles may be required. The winding configuration is identical to the EBT-P mirror coils except that the cross-sectional area is one-half that of the mirror coils and the mean coil radius is 33 cm, (4 cm larger). Five wedge coil assemblies are connected in series by a superconducting bus similar to that proposed for EBT-P.

All Copper Magnet System

Mirror Coils - The conceptual design at the copper coils for the TRT is based on the conceptual design which evolved for the MDAC/ORNL EBT-X study of October 1982. These coils were sized to fit within the envelope for the EBT-P superconducting magnets and maintain the same approximate mirror ratio and mean coil radius. The coils were designed for steady-state operation at 60 GHz heating field levels. Operation of these coils on the TRT device at 60 GHz fields comparable to the superconducting system requires a current density of approximately 2500 amps/cm^2 which is well within the state-of-the-art for copper coil design, especially for pulsed systems. The total peak power dissipation per mirror coil is approximately 2 MW at 60 GHz. The conceptual winding assembly for the mirror coils is 10 pancakes with 4 turns in hand.

Turning Coils - The turning coils for the solenoid ends are one-half the cross sectional area of the mirror coils, i.e., five pancakes with 4 turns in hand. All turning coil winding assemblies are identical. The configuration differences are limited to the wedge supports and structure between the coils. The peak power consumption of the turning coils is approximately 1 MW per coil during 60 GHz operation.

Hybrid Magnet System Concept

Mirror Coils - The superconducting mirror coils retain the EBT-P design as modified for the flooded LHe cooling concept with minor changes to the support base and placement of the cryogenic servicing lines. The EBT-P design has been under development for over three years. Except for the verification of the flooded LHe cooling system performance, this magnet/conductor design is ready to commit to a TRT production program. The hybrid concept for the TRT utilizes 14 S/C mirror coils and 4 all copper steady state mirror-transition coils. These copper coils at the ends of each straight section reduce the out-of-plane loads on the end S/C mirror coils and prevent load reversals during pulse operation of the solenoid turning coils. Therefore, with all S/C coils in a straight section connected in series, and with the transition coils reducing the out-of-plane loadings, no further development testing is required on the EBT-P design

for loads verification. The copper mirror-transition coil configuration is the same as the mirror coil described for the all copper magnet concept, except that the mean coil radius is increased to provide clearance for vacuum vessel contouring along the field lines. Trim coils may be required on all concepts in the transition region between the mirror and solenoid section to facilitate these contours.

Turning Coils - The turning coils are identical to the turning coils for the all copper device, except that they are not pulsed from zero current to operating current. If the turning coils are turned off completely, thermal stress problems can be expected in the vacuum vessel where magnetic field lines from the mirror coils cut through it in a local area. Significant vacuum vessel design problems may be avoided by pulsing the turning coils from a low current rather than from zero. The low to intermediate current may be varied from coil to coil to achieve a maximum distribution of plasma impingement on the vacuum vessel wall.

Magnet Power Supply Requirements

The power supplies for the copper coils of the all-copper and hybrid concepts are off-the-shelf solid-state power supplies except that additional current regulation is required. The current is regulated to $\pm 0.1\%$ compared to the standard value of $\pm 1\%$. These supplies can be operated at 200% of rated output for periods up to one minute. Therefore during pulsed 60 GHz operation, only one-half of the power requirements from Table III is needed in power supply capacity. This amounts to 48 MW of power supplies for the all-copper and 34 MW for the hybrid concept.

3. TRT MAGNET COOLING

The magnet cooling system for the TRT S/C coils requires a 2000 watt refrigerator/liquefier, 6000 liter LHe storage dewar, GHe storage tanks with a capacity of 160,000 SCF, 6-600 liter phase separators, 12,000 gallon LN_2 storage dewar, 18 vapor cooled lead pods and associated super

insulated vacuum-jacketed piping. These elements are shown schematically in Figure 8. LHe for the superconducting TRT coils is supplied by 6 parallel natural convective loops. Two parallel natural convective loops supply LN_2 to the coil dewar insulation shields.

The liquid helium head pressure provided by the elevated phase separator in conjunction with the decreasing fluid density in the direction of flow establishes a natural convective flow between the coil packs and the phase separator. Each coil pack receives approximately 800 liters per hour of LHe. Fluid quality in the coil packs is less than 2 1/2 percent.

The 9 mirror coils in each straight section are supplied with liquid helium from an elevated phase separator as shown in Figure 8. Liquid flows from the phase separator down through the feed header to the LHe feed manifold. The feed manifold supplies LHe to each magnet through a flexible inlet feed line. The LHe flows through the coil pack and out a flexible return line to a return manifold. Liquid from the return manifold is returned to the phase separator via a LHe return header. All lines in the system are superinsulated and vacuum jacketed. The total pressure drop in the LHe feed header, LHe feed manifold, individual flexible inlet lines and individual flexible return lines, return manifold, return header is low relative to the pressure drop in the coil packs to minimize flow maldistribution between the coil packs.

The solenoid coils in each end of the TRT are supplied with LHe in a manner similar to the straight section. Two phase separators and associated piping are utilized to establish LHe flow in the coils in each end of the device. Thus 15 coil packs are fed from each phase separator. Fluid flow rates and fluid quality in each solenoid coil are approximately the same as for the mirror coils. However, the flow rate through each coil is different from those adjacent to it as a result of the different static head available at each coil.

LN_2 for the coil dewar insulation shields is provided by two natural convective loops. Each loop supplies LN_2 to the coils in one half of the device. The LN_2 loops are similar to the LHe loops.

No major problems are anticipated in implementing the TRT cryogenic magnet cooling system. However, further analysis is required to fully

appreciate the implications of the variable static head on the flow in the solenoid coils. The design of the solenoid coil LHe feed manifold, flexible feed lines and flexible return lines and LHe return manifold is a challenge.

The magnet cooling system for the copper coils consists of a 20 MW cooling tower, batch process demineralized water system, and stainless steel distribution system. This system is sufficient for cooling both the all copper and hybrid concepts. For pulse operation water is circulated continuously through the coil during device operation. The flow is sufficient to maintain the coil peak temperature within acceptable limits during pulse operation up to 10 seconds. The pulsed duty cycle allows the cooling tower capacity to be reduced significantly below the steady state heat rejection rate of the copper coils.

The magnet cooling system for the hybrid device consists of a 800 watt refrigerator/liquefier and the other components associated with the all S/C device in addition to 35 MW of cooling tower capacity and those components associated with the copper coil machine.

4. VACUUM VESSEL

The TRT vacuum vessel consists of two crossing, 6 meter long straight sections, their centers separated vertically by 2.45 meters. Two curved helical sections connect the straight section ends as shown in Figure 9. Each helical section has a 1.7 meter radius and is 7.46 meters long. The vacuum vessel geometry is the same for either a continuous operation superconducting magnet device or for a pulsed device with copper coils in the helical end sections, though the water cooling requirements are different, as discussed below.

A typical portion of the TRT straight section is shown in Figure 10. Two mirror cavities are shown attached to vacuum liners which pass through the bores of the superconducting magnets. Eight mirror cavities are provided in each straight section. Each mirror cavity is a cylindrical section 76 cm diameter and 30 cm long, with nine penetration for vacuum ports, as shown in Figure 11. Four small ports (3 shown) are provided for limiters. Large racetrack ports

are located at the top and bottom for diagnostic access. A small port for an ion gage is located on the bottom diagnostic port extension. A large vacuum pumping port is located on one side of the mirror cavity and an ECRH heating port is on the opposite side. The mirror cavity shell is a double-walled, stainless steel structure with hydrostatically formed water coolant passages, as in EBT-P. Vacuum liners pass through each magnet in the straight section and connect adjacent mirror cavities. The vacuum liners are 76 cm diameter at the interface to the mirror cavities and reduce to 37 cm diameter through the magnet bore. The vacuum liners are double-wall hydrostatically formed shells identical to those developed for EBT-P.

Each helical end section consists of two 40 cm diameter pipe sections approximately 3 meters long connecting three diagnostic cavities. Diagnostic cavities are located in the helical end sections near each transition between the straight and helical sections as shown in Figure 9. A diagnostic cavity is also located near the center of each helical end section. The diagnostic cavities at the transitions are connected via high vacuum flanges and 40 cm pipe to those at the centers. Shown in Figure 12 is a plan view and side view of the diagnostic cavities. The racetrack ports, located 180 degrees apart, are approximately 5 cm wide and 50 cm long. The close spacing between magnets in the end sections impacts the design of the diagnostic cavities. As seen in Figure 12 the racetrack vacuum flanges are located outside the magnet envelopes and the circular end flanges are located between adjacent magnets.

The cooling requirements for the TRT vacuum vessel have also been investigated. As discussed below, the continuous operation superconducting TRT requires full water cooling and the pulsed copper coil TRT requires water cooling only in the straight sections.

The total input power for TRT to achieve comparable plasma properties to an upgraded EBT-P is 1.0 MW. For purposes of this analysis the power loss is divided between the helix and straight sections at 75% to the helixes and 25% to the straights. For the helixes, .75 MW is assumed to be distributed uniformly over the inside vessel surface

area, resulting in a 5 W/cm^2 flux. Design heat fluxes are assumed to be 50% greater resulting in a uniform flux on the helix sections equal to 7.5 W/cm^2.

The power loss in the straight sections is divided between the mirror cavity and the corner, throat and sidewall of the vacuum liner. as shown in Figure 10. The corner flux is calculated using the same scrape off relationship used for EBT-P,[2] resulting in a 15 W/cm peak flux, decreasing around the bend and down the sidewall. The sidewall and throat fluxes are calculated by assuming 1/4 of the power in the straight sections is deposited on the area of each section uniformly, resulting in 1.73 W/cm^2 on the sidewall and 1.65 W/cm^2 on the throat. The mirror cavity flux is assumed to be the ring energy, 1/2 the power in the straight sections, distributed uniformly over the area of the 16 mirror cavities. This results in a flux of 1.0 W/cm^2. Again the design fluxes are assumed to be 50% greater than the calculated values. To summarize, the design heat fluxes are:

- o Vacuum Liner Corner 23 W/cm^2
- o Vacuum Liner Throat 2.5 W/cm^2
- o Vacuum Liner Sidewall 2.6 W/cm^2
- o Mirror Cavity 1.5 W/cm^2
- o Helical Section Surfaces 7.5 W/cm^2

Steady state operation of TRT with the incident fluxes shown above requires active water coolant on both the helix and straight sections. The helical ends may be cooled with tubes spaced 2.8 cm apart to keep the peak temperatures below 150°C. This spacing is close though, so integral (double wall) cooling may be desired for cost and fabrication ease.

The straight sections require integrally cooled walls due to the high heat flux on the vacuum liner corner and the small clearance between the vacuum liner and the magnet, which prevents use of coolant tubes. Figure 13 shows calculated temperatures for worst case heating on the corner section of an integrally cooled vacuum vessel wall. A coolant capacity of 900 gpm is required to remove 1.0 MW of input power, achieve adequate flow and maintain a coolant temperature rise of 10°C or less for steady state operation.

Limiters are necessary only to prevent local hot spots on the walls or for plasma shaping. The probable locations are at the entrance and exits of the helixes. Assuming the entire 1 MW impinges on a 2.54 cm wide strip of 8 half moon limiters, the resulting flux is comparable to the EBT-S limiter design flux of 300 W/cm^2 on the edge.

For pulsed operation, the vacuum vessel heat fluxes are identical to those assumed for continuous operation. A 2 second on/10 minute off duty cycle is assumed for the helix sections, and a 10 second on/10 minute off duty cycle for the straight sections. The helixes' short pulse, good clearance between vessel and magnet, and open space between magnets, allows for natural convection cooling. The 7.5 W/cm^2 uniform flux pulsed for 2 seconds produces a maximum equilibrium temperature of 85°C. This assumes a natural convection heat transfer coefficient of 5.67 W/m^2c over the entire helix outer wall surface. Variations to the pulse, such as increasing "on" time or shortening "off" time, may require the wall to be actively cooled.

The straight sections of the TRT have a 10 second "on" time, close clearance between vessel and magnets and high peak fluxes on the corner. These conditions, therefore, require the straight sections to be actively cooled even during pulsed operation.

5. MAIN SUPPORT STRUCTURE

Several structural support concepts are being analyzed to provide adequate load paths for the magnets, support for the vacuum vessel and ancillary device equipment, and provide good accessibility to the plasma for diagnostic and heating purposes.

A preliminary loads analyses was made to determine the magnitude and orientation of the magnet loads for establishing the required support structure. Magnetic loads were determined for magnets at various locations around the twisted racetrack. These loads are shown in Table IV. The maximum out-of-plane load of 119100 lbs occurs at the last magnet in the straight section. The maximum in-plane resultant load of 41200 lbs occurs at the fourth solenoid magnet.

A plan view of the TRT device is shown in Figure 14. The structural concept used is to base-mount all the magnets on beams which are supported by reinforced concrete. The radial load from the solenoid magnets are reacted by a vertical bucking column centered at each end. The magnet out-of-plane loads are reacted by struts which connect adjacent magnets on both upper sides of the magnets and by the base of the magnet dewar.

A concrete support platform extends beyond both sides of the magnets to allow for personnel work platforms and to provide for support of device diagnostics and instrumentation (Figures 15 and 16). Magnet alignment is accomplished by adjustment of the base attachment mechanism and the out-of-plane struts. Penetrations through the concrete support platform allow vertical plane access to the plasma for diagnostics.

A superstructure supported on top of the two bucking columns provides support for device ancillary equipment such as cryogenic manifolds and equipment, magnet protection equipment, and water coolant manifolds.

In the straight sections the vacuum vessel is supported, independent of the magnets, by struts which attach between the support fittings of the vacuum vessel and the support platform, Figure 17.

6. COST COMPARISONS

Cost analyses were performed in order to provide a basis for evaluating each of the different TRT configurations and to provide a basis for comparison of the TRT with other approaches for the "next step" EBT experimental device.

EBT-P cost data were used as the baseline for performing the TRT cost comparison analysis. An abundant data bank of EBT-P cost information is available from many EBT-P cost analysis exercises that have been conducted since Phase II of the project was initiated in October 1980. The EBT-P baseline cost data selected for comparison purposes were for the current "descoped" EBT-P configuration, i.e., the convectively cooled magnet configuration.

In performing the TRT cost comparison study, only those cost bearing items that are highly device configuration dependent were analyzed. These cost items were for the fabrication, installation, and associated sustaining engineering costs for the magnet system, magnet cooling (cryogenic or water), vacuum vessel, device support structure, microwave distribution system (for 400 kW of 28 GHz CW heating, same as current EBT-P baseline), and facility cost impacts associated with the magnet and magnet cooling systems. Cost bearing items such as project management, systems integration, and Title I and Title II engineering were excluded from the cost comparison, since these cost items are not highly device configuration dependent.

Table V shows a summary of the fabrication and installation costs of three TRT configurations (all superconducting, all copper, and hybrid superconducting/copper magnetic configurations) as compared to the reference, "descoped" EBT-P baseline. Included in the fabrication and installation costs are the costs of the associated sustaining engineering. In terms of fabrication and installation costs, the pulsed TRT-Cu (all copper magnets) is the least expensive of the three TRT configurations and is about the same as the EBT-P cost. The next least expensive is the pulsed TRT-hybrid (superconducting/copper magnet combination), and the highest cost configuration is the steady-state TRT-S/C (all superconducting configuration). The cost difference between the two directly comparable configurations, the steady-state EBT-P and the TRT-S/C, is due to: (a) the 50% higher ampere-turns in the TRT-S/C magnet coils, (b) the differences in design between the mirror and superconducting magnets for TRT-S/C, and (c) associated impacts on the magnet cooling (cryogenics) costs for TRT-S/C. The total cost of each of the TRT configuration's vacuum vessel, support structure, and microwave distribution is about the same as the total cost of these systems for EBT-P. Relative to EBT-P, the TRT's cost difference for each of these systems is due to:

- Vacuum Vessel - TRT's cost is lower because of the reduced number of vessel ports and reduced number of vacuum vessel flanged joints.

- o Support Structure - TRT's cost is higher due to increased structure complexity with the over-under bridges and large, non-symmetrical operating structural loads.
- o Microwave Distribution - TRT's cost is lower because of the reduced number of rings required to be heated (16 versus 36), which reduces the cost of the distribution manifold, waveguides, and vacuum windows.

Development costs are based on the costs to finish development from where the EBT-P development testing status will stand at the end of GFY 1983. They are not the total costs of the development program. Most of the development work already performed for EBT-P would remain valid for subsequent continuation of EBT-P or directly applicable for a TRT alternate concept. Also, these cost estimates assume that test equipment and fixtures available for EBT-P would remain available for any alternate concept.

In analyzing the development costs for the magnets for EBT-P, only the costs associated with conducting the flooded, prototype magnet test program were considered. The fabrication cost of the prototype magnet was excluded in the cost comparisons. Also, it was assumed that the currently available EBT-P magnet development test data and the ORNL magnet test facility would be utilized appropriately in the TRT-S/C and TRT-hybrid development programs for the mirror magnets. Table VI shows a comparison of the development costs of the four configurations. The footnotes to the table explain the scope of the development programs. The large magnet development cost for the TRT-S/C configuration is due to the new development required for the superconducting solenoid coils due to the new wedge type coil configuration and new magnet structural supports.

In the vacuum vessel development activities the existing EBT-P Toroidal Vessel/Seal Development Test Article would be used to qualify all of EBT-P's vacuum vessel or the straight sections of the vacuum vessel for the TRT. For both cases the vacuum liners and the installation tooling are the same. Continuation of development testing using the EBT-P wedge shape mirror cavities is justified since the straight cavities for the TRT concept will be simpler to fabricate and install.

However, for the TRT there needs to be additional development work for the diagnostic cavities in the solenoid ends. The cost estimates assume that the EBT-P test article fabrication procedure will be fully developed and the test article fabricated and paid for prior to the end of GFY 1983. Table VI shows the results of the vacuum vessel development cost analyses.

A summary of the cost comparison study is shown in Table VII. Note that the total of fabrication, installation, and development costs for the TRT-SC is considerably higher than for either of the other two TRT configurations. The cost of the pulsed TRT-Cu is slightly lower than the cost of the steady-state EBT-P. However, one must remember that the cost comparison excludes Title I and Title II engineering and associated project management costs. For EBT-P Title I engineering is complete and Title II engineering is approximately 75% complete.

Table VII also shows the estimated annual operating costs for magnet electrical power. The extremely high operating costs for the TRT-Cu and TRT-hybrid machines are due to the high peak power demands for the Cu magnets even though they are operated in a pulse mode. This large peak demand requires the utility to amortize the costs of large, new power substations with annual power charges. In these estimates the amortization period was assumed to be 7 years. When annual operating costs are considered in addition to fabrication, installation, and development costs, the TRT-SC configuration is a better investment for a TRT device with a 2-Tesla field bulk plasma and an EBT-P equivalent plasma volume. "Up front" costs, as well as initial operating costs, for the TRT-Cu and TRT-hybrid configurations could be reduced greatly by machine start-up with copper magnet power supplies necessarily sized only to produce a one-Tesla field bulk plasma with later upgrade to a 2-Tesla field, if desired. Also, the copper magnet systems hardware and operations cost could be reduced by optimization of the coil design to reduce power consumption and by use of motor-generators or motor-generator/solid-state power supply combinations to reduce peak electrical load demands. In this study there was insufficient time to investigate these approaches.

7. RECOMMENDATIONS FOR NEAR TERM EFFORT

The work discussed in this paper is preliminary and has served to explore a number of difficult or unusual features of the TRT concept. In particular, the following items appear to require immediate attention in order to advance the TRT concept further:

a) More work is required to optimize the TRT magnetics. A parametric study is required to establish the optimum way to splice the straight sections to the helical end segments. This study should also address configurations somewhat smaller than EBT-P in overall size, while retaining the capability for 60 GHz magnetic fields. The aim here is to attempt to reduce the initial cost of the TRT device.

b) The three magnetic configurations discussed above should be studied further in an attempt to choose the optimum performance mode (steady-state, pulsed, hybrid) in light of proof-of-principle requirements and available budgets both for construction and for operation of a TRT device. Stored energy magnet power systems such as motor-generator-flywheels need to be investigated to reduce peak electrical loads and hence, annual operating costs of the copper and hybrid TRT magnetic configurations.

c) More work is needed on the solenoid end magnetics, both in superconducting and in copper versions. The aim here is to reduce the number of individual coils required to produce an acceptable low-ripple solenoidal field.

d) Refined estimates are needed for TRT ECRH ring heating power requirements. This parameter influences vacuum vessel cooling requirements as well as requirements for radiation shielding.

e) Existing cost codes require modification to allow rapid and accurate cost estimates to be generated during parametric studies of the TRT concept.

f) Further work is required to determine how much of the investment already made in the EBT-P design can be applied to the TRT concept.

g) A TRT reactor study should be started.

ACKNOWLEDGEMENT

The contributions to this paper of W. B. Ard, D. Bowers, R. Busam, M. Delaney, D. Driemeyer, A. Hartmann, T. Hellwig, D. Lieurance, T. Mann, A. McMahon, J. Pipkins, D. Ruester, J. Stika, G. Taylor, and J. Wolverton are gratefully acknowledged by the authors.

REFERENCES

1. J. F. Pipkins, et al., "Optimized Approaches to EBT's with Simple Circular Coils," presented at this Workshop.

2. C. F. Dillow et al., "Vacuum Vessel Seals and Wall Material Trade Study," EBT-P-TN-001, 1 June 1981.

TABLE I - TRT STUDY METHODOLOGY

TRTSET CODE

- o Input: Mirror ratio, number of coils, mirror/solenoid fields, mean coil radii, coil cross-section dimensions
  Condition: TRT length = EBT-P length
- o Output: Helix pitch, helix radius, vertical separation, current densities, coil X, Y, Z, Euler angles

Result: EFFI input file

EFFI CODE

- o Output: B-Line parameters, $\int^{ds}/B$ vs S, B-mod contours
  Plots of B-lines and coils
  Forces on selected coils

XPLOTTER CODE

- o Input: EFFI output data files
- o Output: Magnet surface plots, $\int^{ds}/B$ vs S plots

  $\frac{d}{d\Theta} \int \frac{ds}{B}$ vs S plots, rotational transform/shear

CAD CODES - UNIGRAPHICS SYSTEM

- o Input: TRTSET output data, EFFI B-line data

  Output: B-Line trimetric layouts
  TRT coil geometry
  Support structure, port details
  Dimensional analysis

TABLE II - TRT/EBT-P SPECIFICATIONS

ITEM	TRT	EBT-P
PERIMETER	2827 cm	2827 cm
HELIX LENGTH (ONE HELIX)	746 cm	N/A
HELIX PITCH	30.65 cm/radian	N/A
HELIX RADIUS	170.0 cm	N/A
EBT-P MAJOR RADIUS	N/A	450.0 cm
ZDIFF = VERTICAL SEPARATION OF STRAIGHT SECTIONS	245.5 cm	N/A
NO. OF MIRROR COILS	18	36
NO. OF SOLENOID COILS	60	N/A
MIRROR RATIO	2.2	2.2
MIRROR COIL FIELD (60 GHz)	3.3 T	3.3 T
SOLENOID FIELD	3.4 T	N/A
MIRROR COIL SEPARATION	74.67 cm	78.74 cm
NO. OF ELECTRON RINGS	16	36
ROTATIONAL TRANSFORM q	2.2	N/A

TABLE III - POWER CONSUMPTION OF COPPER COILS AT 60 GHZ FIELD

MAGNET SYSTEM CONCEPT	TYPE OF COIL	POWER PER COIL (MW)	NO. OF COILS	TOTAL POWER PER TYPE (MW)	TOTAL POWER FOR DEVICE (MW)
ALL COPPER DEVICE	MIRROR COILS	2	18	36	96
	SOLENOID COILS	1	60	60	
HYBRID DEVICE	TRANSITION COILS	2	4	8	68
	SOLENOID COILS	1	60	60	

TABLE IV — TYPICAL OPERATING MAGNETIC LOADS

MIRROR COIL MEAN RADIUS = 29 cm MIRROR COIL WEIGHT = 4000 lb

SOLENOID COIL MEAN RADIUS = 33 cm SOLENOID COIL WEIGHT = 2500 lb

VERTICAL BETWEEN STRAIGHT SECTIONS IS 2.46 m

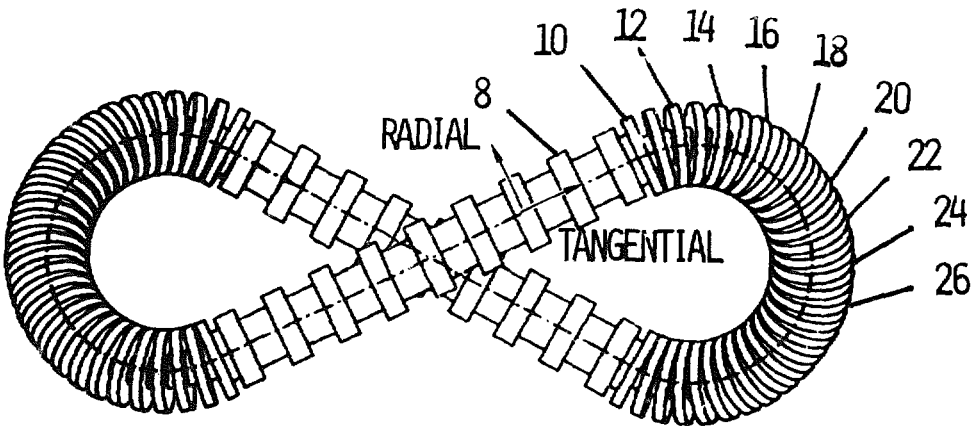

COIL NUMBER	RADIAL FORCE (LB)	TANGENTIAL FORCE (LB)	VERTICAL FORCE (LB)
8	-300	-1000	-100
9	-3700	119100	-1400
10	-21100	90500	-7800
11	-33500	27600	-12000
12	-37300	10100	-14400
13	-38300	4700	-15100
14	-38200	2200	-14700
15	-37700	800	-13900
16	-36800	500	-12600
17	-35700	0	-11200
18	-34800	0	-10000
19	-33800	0	-8100
20	-32900	0	-6600
21	-32200	0	-5000
22	-31700	0	-3500
23	-31300	0	-2200
24	-31200	0	-700
25	-31200	0	700

TABLE V - FABRICATION AND INSTALLATION COST COMPARISON

(GFY 83 $ M)

ITEM	EBT-P (S/C)	TRT (S/C)	TRT (Cu)	TRT (HYBRID)
MAGNETS[a]	12.1	20.5	8.5	12.7
MAGNET POWER SUPPLIES	0.2	0.3	4.6	3.1
MAGNET DEWAR PUMPING	1.0	1.2	0.0	0.4
MAGNET COOLING	4.3	9.1	3.5	6.9
VACUUM VESSEL	3.0	1.8	1.8	1.8
SUPPORT STRUCTURE	1.0	2.6	2.6	2.6
MICROWAVE DISTRIBUTION	1.6	1.0	1.0	1.0
FACILITY IMPACT[b]	0.0	0.0	1.2	0.9
TOTAL	23.2	36.5	23.2	29.4

a INCLUDING POWER DISTRIBUTION AND COIL PROTECTION COSTS

b DELTA RELATIVE TO EBT-P FACILITY COSTS FOR POWER SUPPLY PADS, SWITCHGEAR, EQUIPMENT BUILDING, ETC.

TABLE VI- DEVELOPMENT COST COMPARISON

(GFY 83 $ M)

ITEM	EBT-P (S/C)	TRT (S/C)	TRT (Cu)	TRT (HYBRID)
MAGNET DEVELOPMENT	1.5[a]	4.1[b]	0.5[c]	0.8[d]
VACUUM VESSEL DEVELOPMENT	0.3	0.4[e]	0.4[e]	0.4[e]
TOTAL DEVELOPMENT	1.8	4.5	0.9	1.2

a COST OF COMPLETING "FLOODED" PROTOTYPE TESTING AND 3-MAGNET STRUCTURAL TEST

b COST OF COMPLETING "FLOODED" PROTOTYPE TESTING AND S/C SOLENOID MAGNET DEVELOPMENT

c COST OF TESTING FIRST PRODUCTION Cu MIRROR MAGNET AND FIRST TWO PRODUCTION Cu SOLENOID MAGNETS

d COST OF COMPLETING "FLOODED" PROTOTYPE TEST, TEST OF FIRST PRODUCTION Cu TRANSITION MAGNET, AND FIRST PRODUCTION Cu SOLENOID MAGNET.

e SAME AS EBT-P DEVELOPMENT COST PLUS COST OF DEVELOPMENT OF SOLENOID SECTION DIAGNOSTIC CAVITY

TABLE VII - COST COMPARISON SUMMARY

(GFY 83 $ M)

	EBT-P (S/C)	TRT (S/C)	TRT (Cu)	TRT (HYBRID)
FABRICATION AND INSTALLATION	23.2	36.5	23.2	29.4
DEVELOPMENT	1.8	4.5	0.9	1.2
TOTAL	25.0	41.0	24.1	30.6
ANNUAL MAGNET OPERATING COST[a] ($/YR)	<1	<1	11	8

a ANNUAL COST OF ELECTRICAL POWER FOR OPERATING MAGNET POWER SUPPLIES AND MAGNET COOLING.

b ANNUAL OPERATING COSTS FOR THE CRYOGENIC MAGNET OPTIONS ARE LESS THAN THE ESTIMATE ACCURACY OF THE OPERATING COSTS FOR THE OPTIONS WITH COPPER MAGNETS.

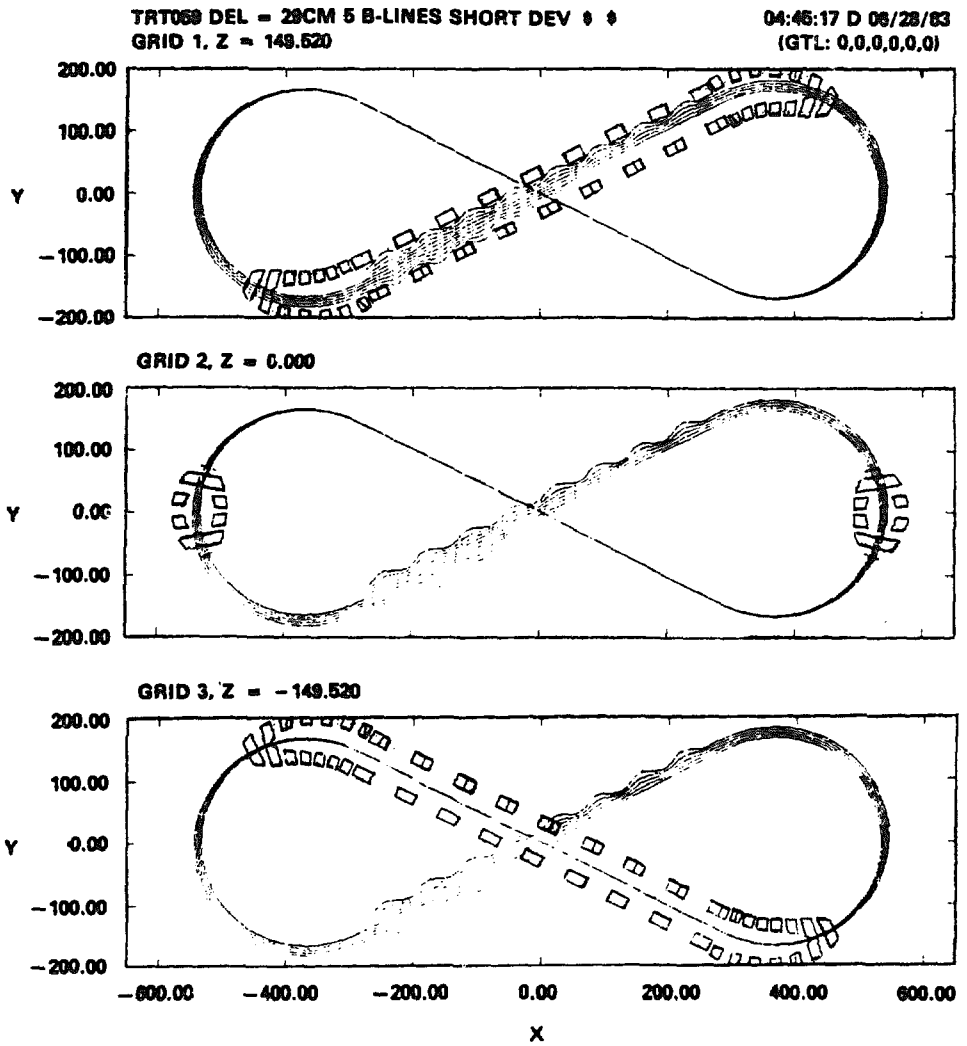

Figure 1 - TRT Device Configuration - EFFI Plots (Dim. in cm.)

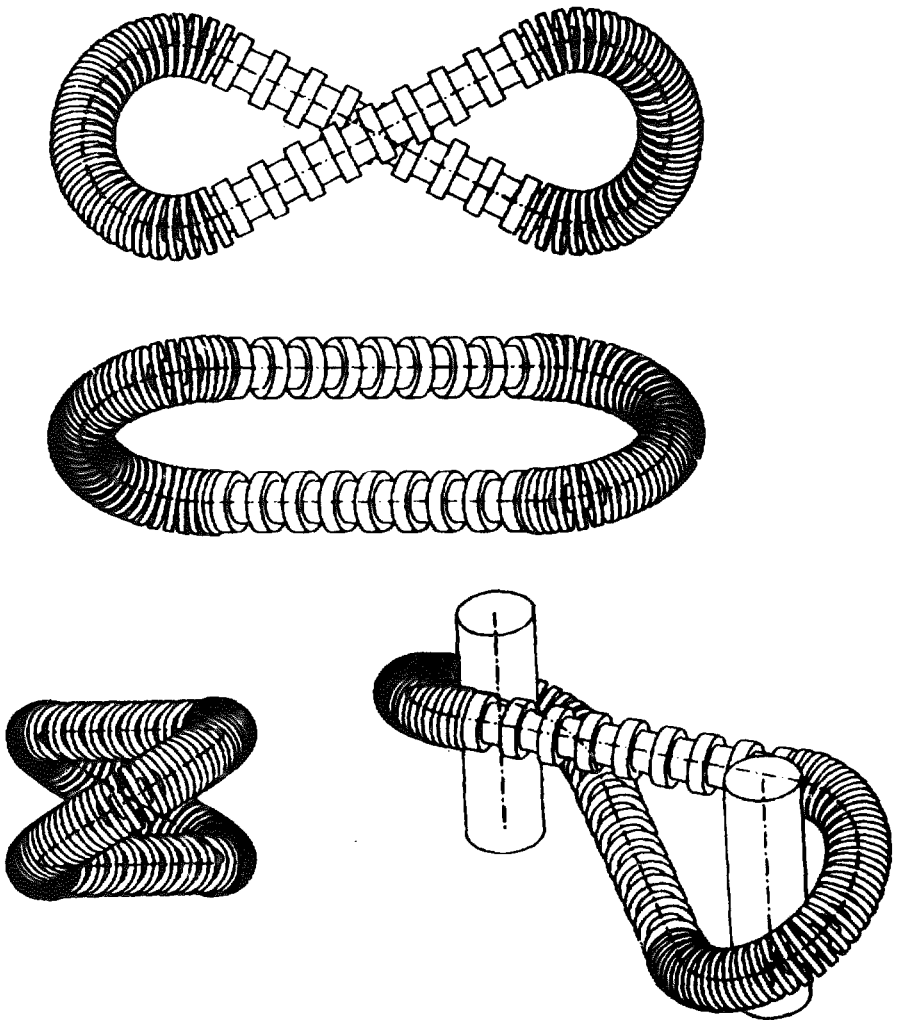

Figure 2 - TRT Device External Configuration - Unigraphics Plots

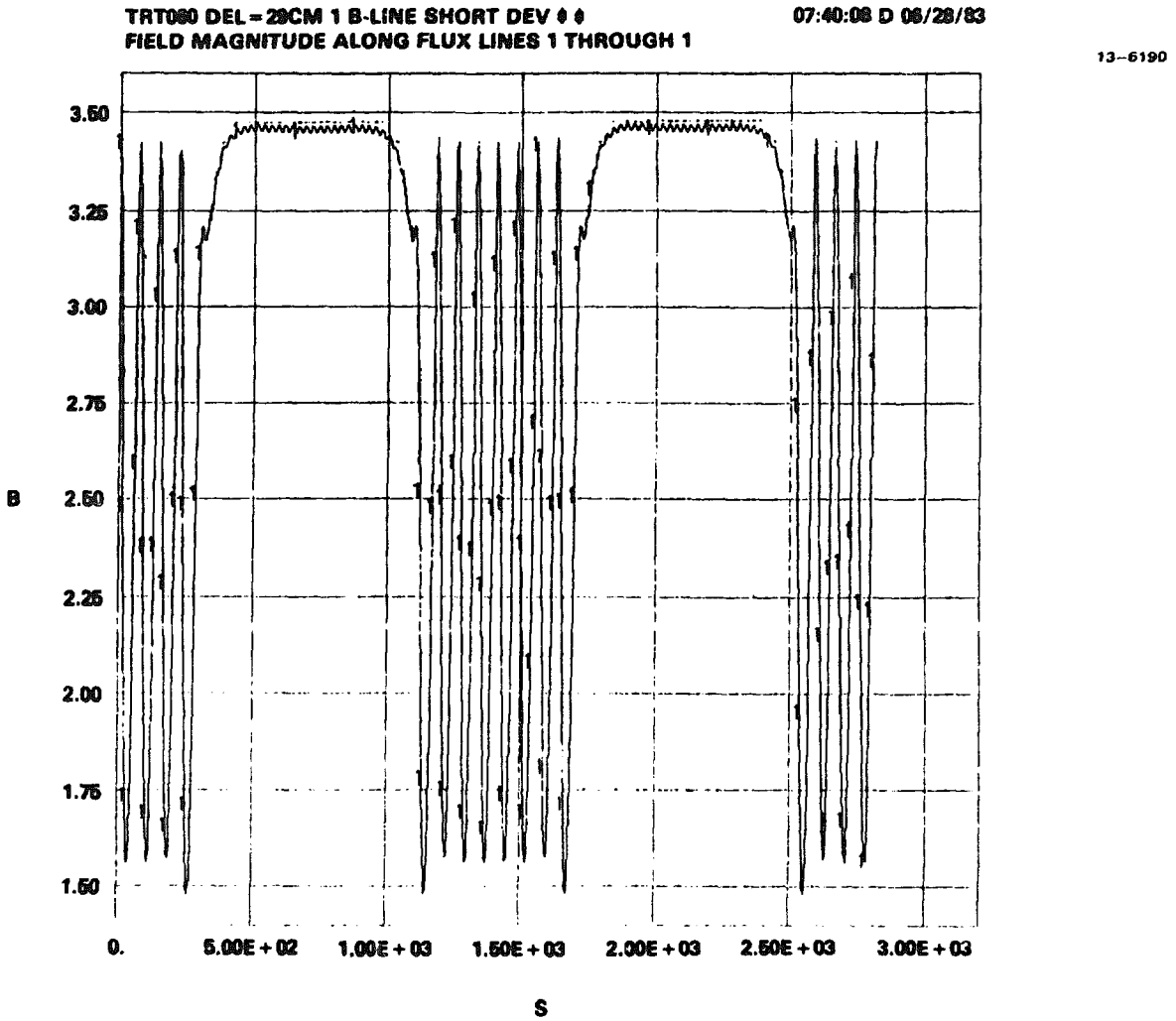

Figure 3 - TRT Device - Mag B vs S Curve - Typical (B in Tesla, S in cm.)

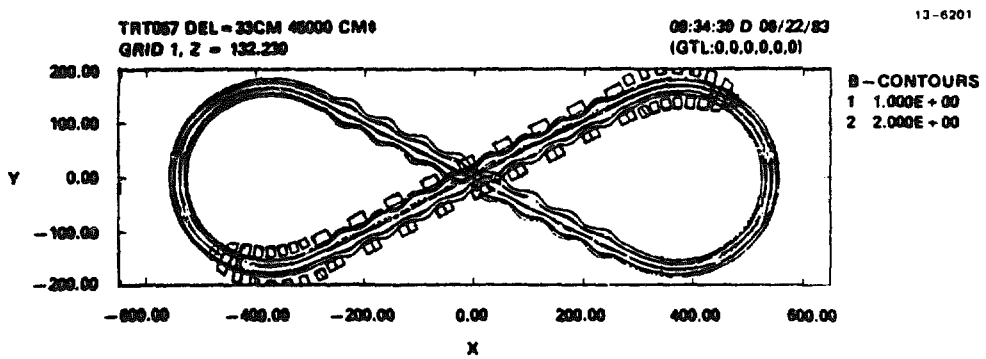

Figure 4 - TRT Device 45000 cm. B-line - Typical

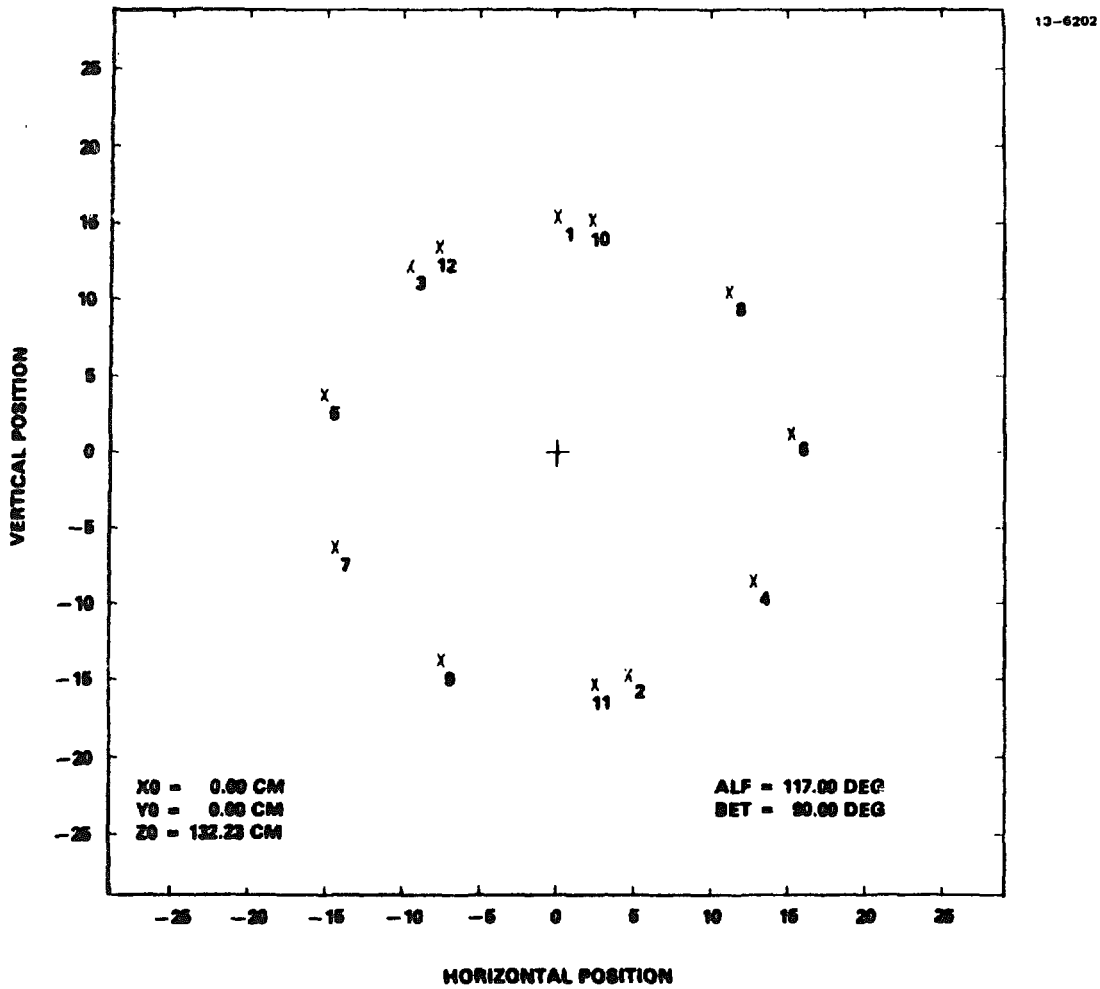

Figure 5 - TRT Device Magnetic Surface in Plane of Middle Mirror Coil (Dim. in cm.)

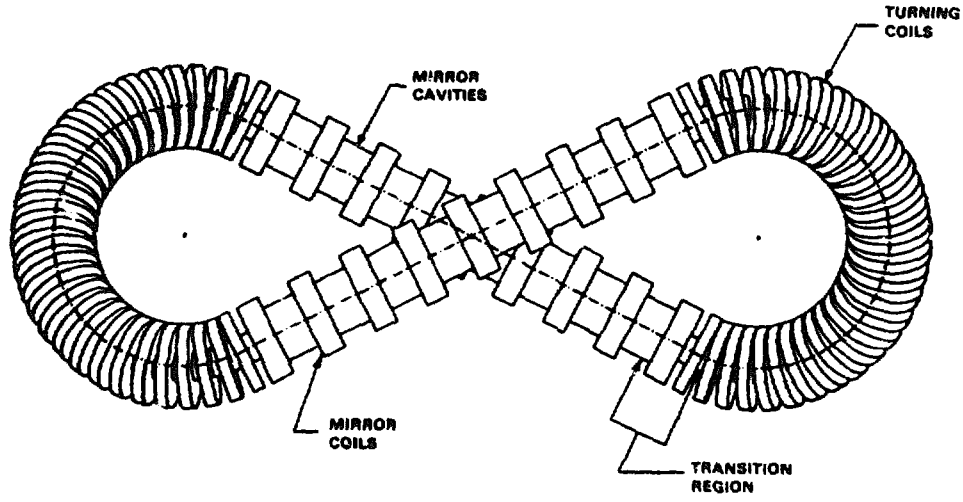

Figure 6 - TRT Magnet System Arrangement - Plan View

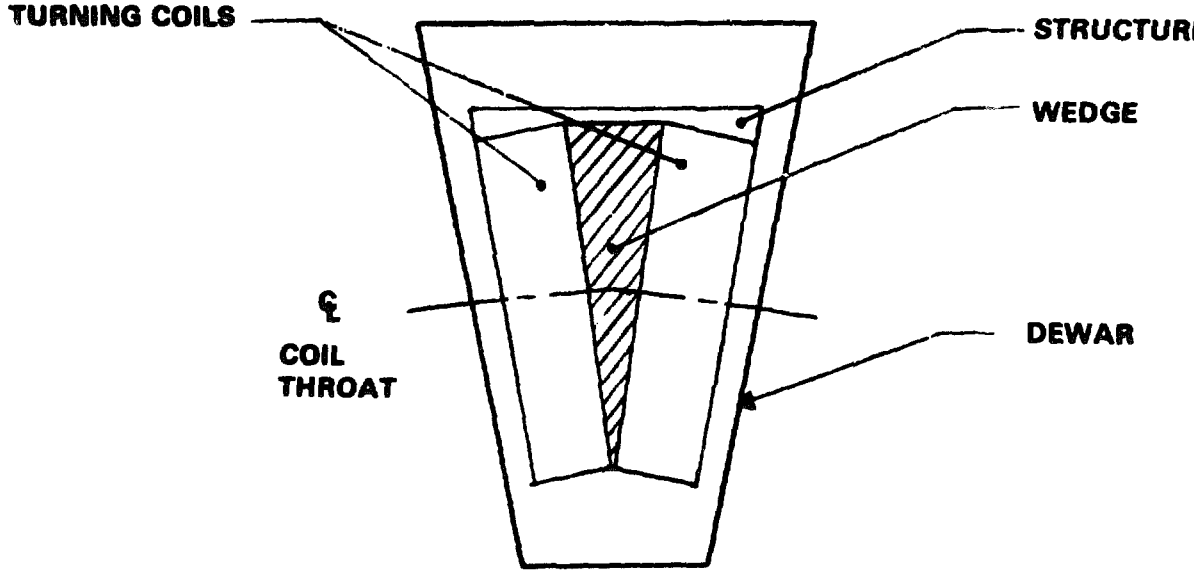

Figure 7 - Wedge Coil Concept for Superconducting Turning Coils

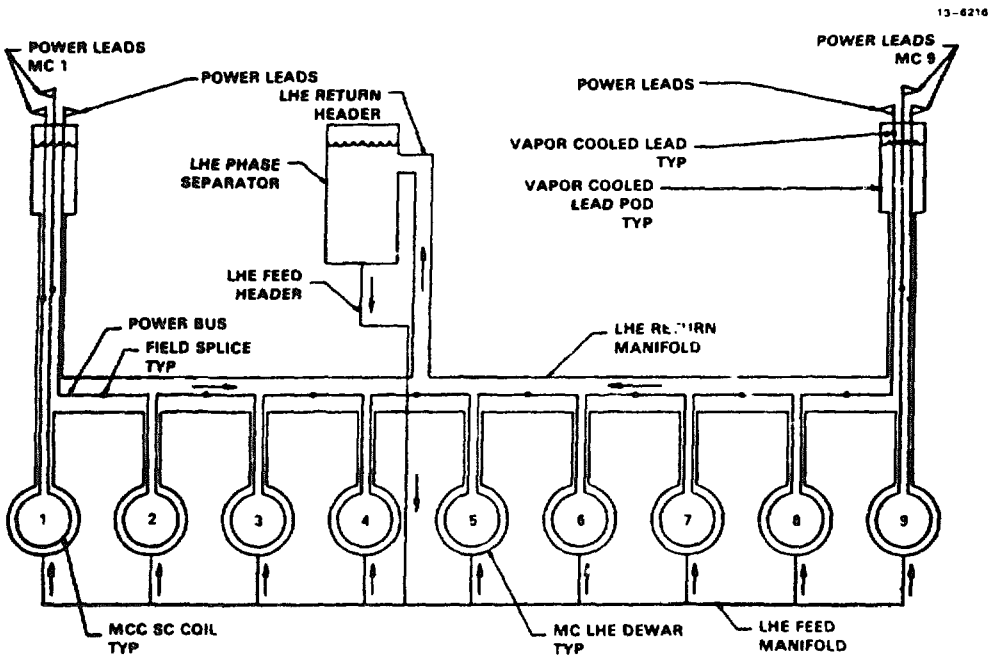

Figure 8 - TRT Straight Section Cryo and Power Bus Arrangement

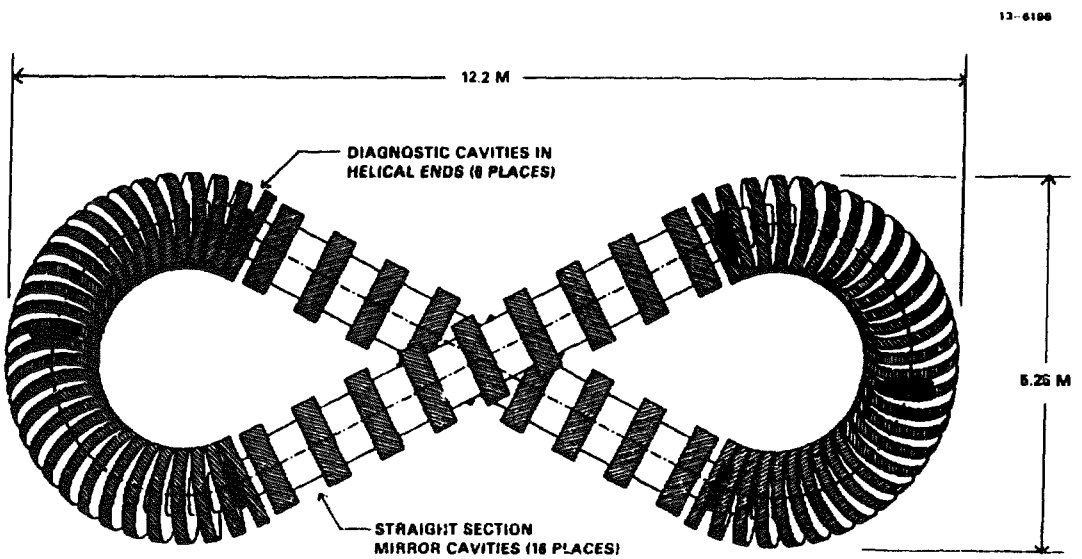

Figure 9 - TRT Vacuum Vessel Layout

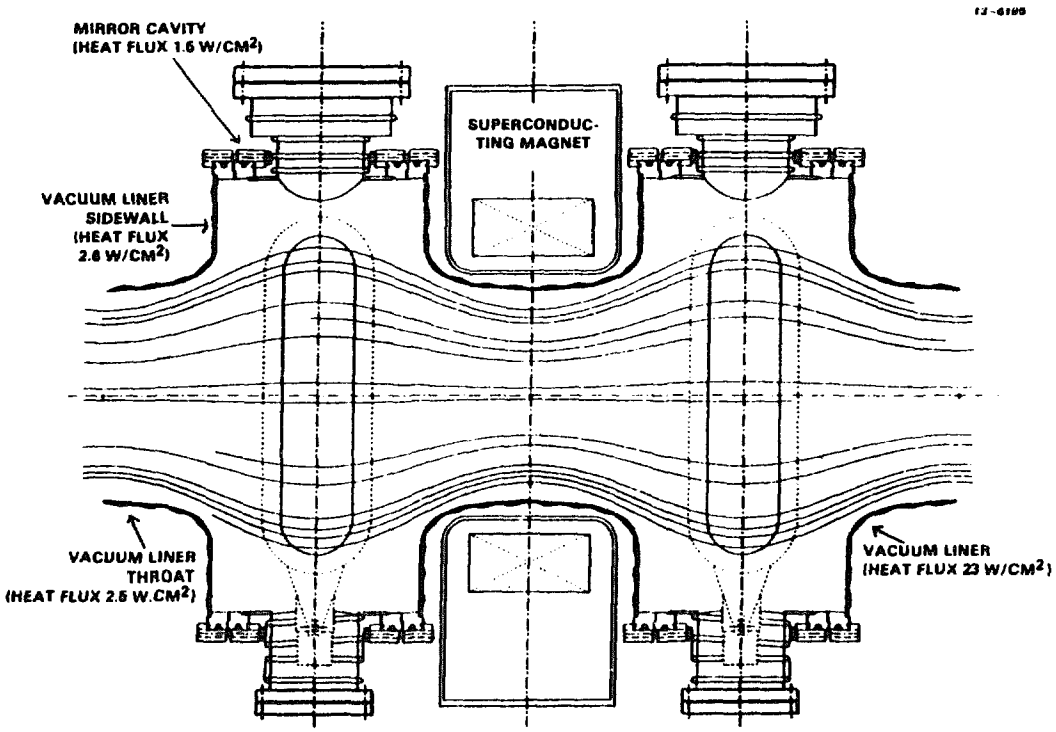

Figure 10 - Typical TRT Vacuum Vessel Straight Section

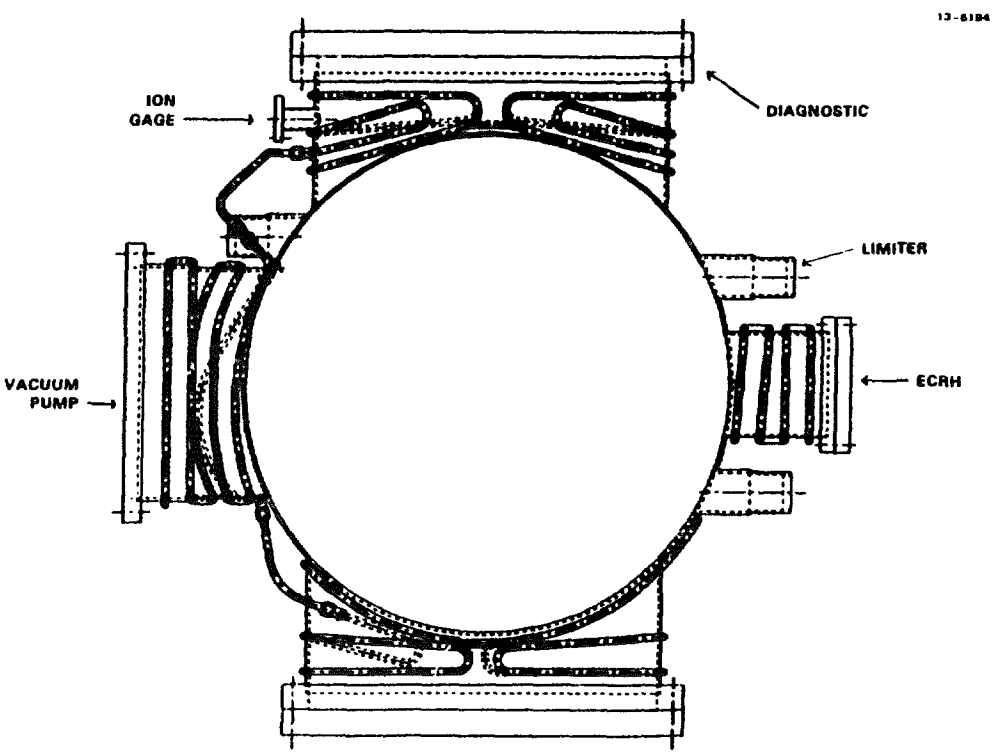

Figure 11 - TRT Mirror Cavity

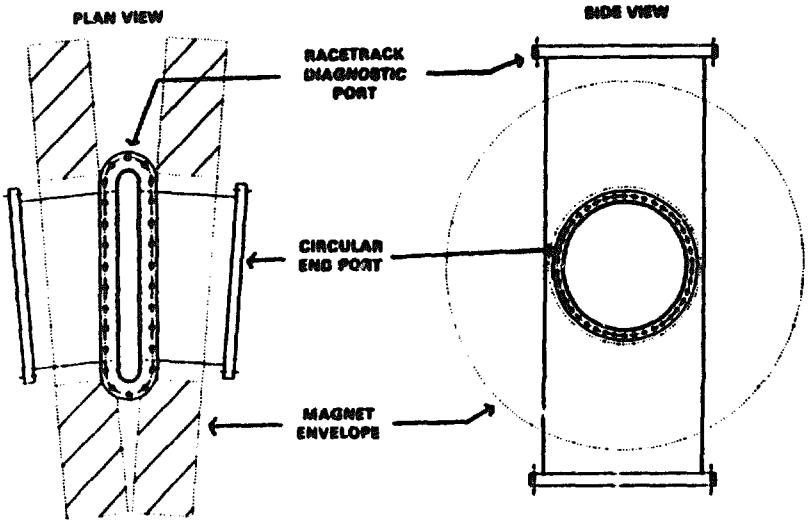

Figure 12 - Diagnostic Cavity in TRT Helical End Section

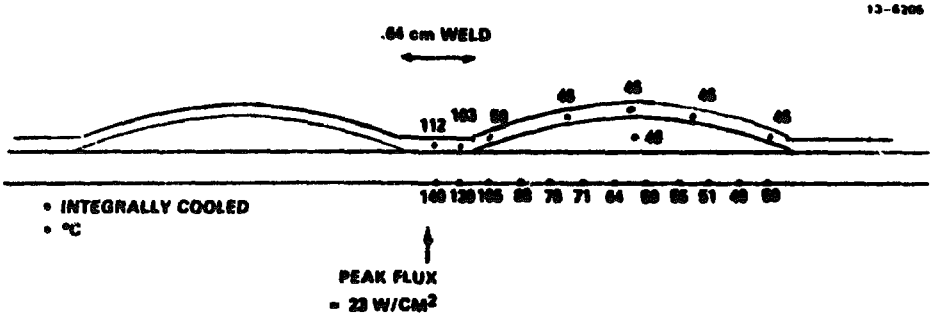

Figure 13 - Temperatures Due to Peak Heating on TRT Corner Region

13 6211

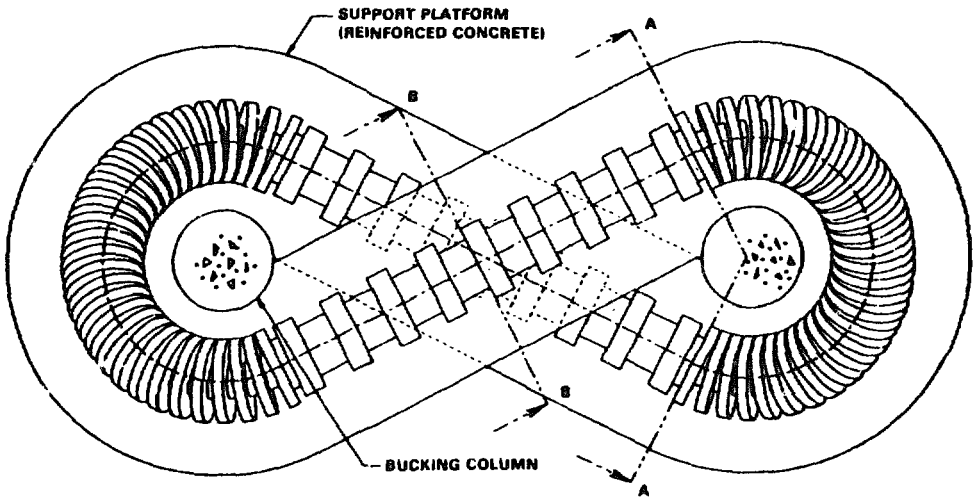

Figure 14 - Device Support Structure - Plan View

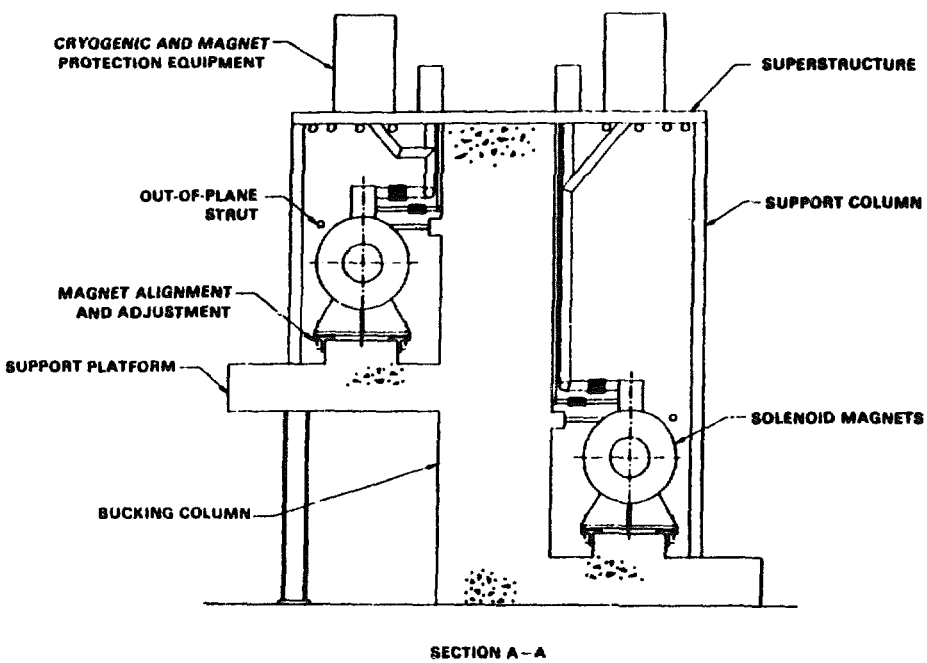

Figure 15 - Structural Arrangement - Solenoid Section

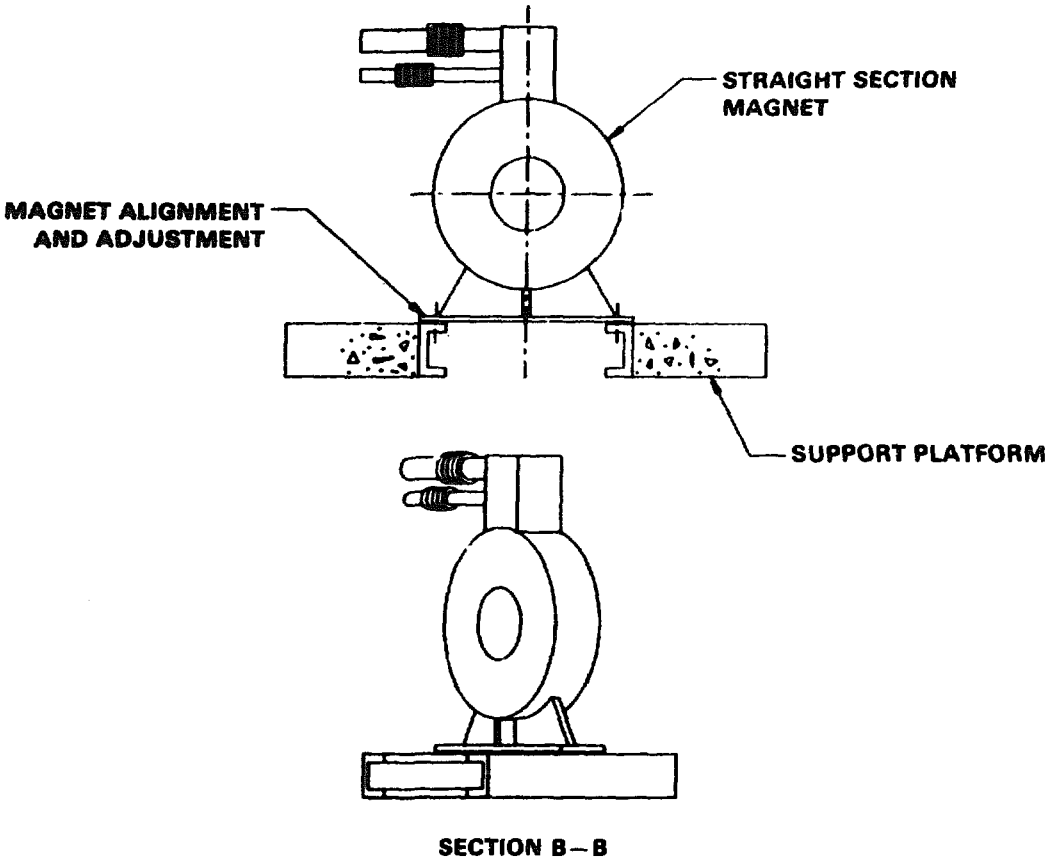

Figure 16 - Magnet Support - Straight Section

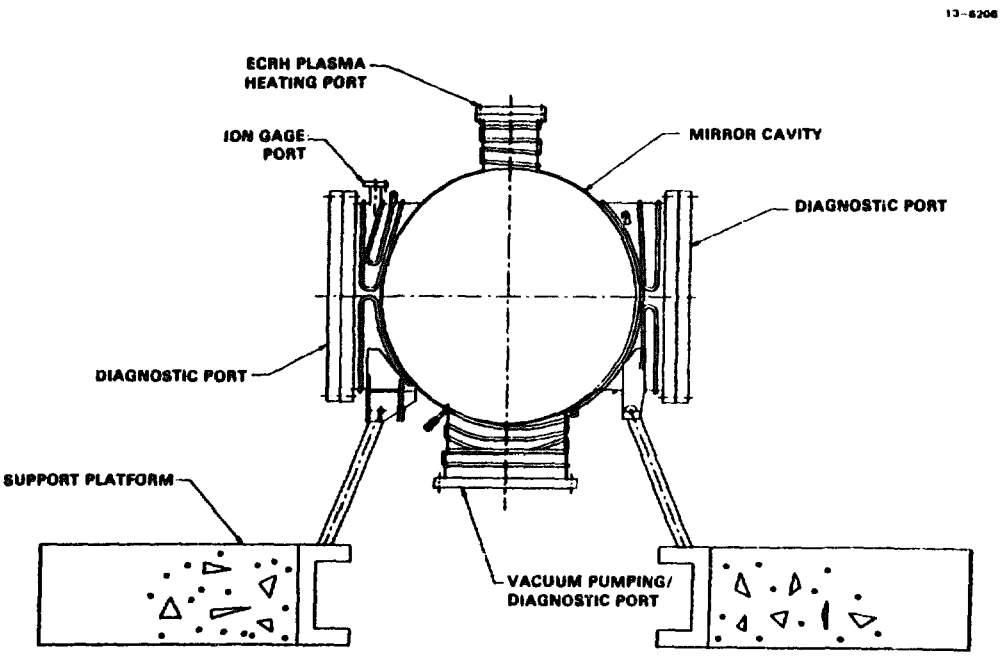

Figure 17 - Diagnostic Access - Straight Section

ANALYTICAL STUDIES ON CHARACTERISTICS OF NEW BUMPY TORUS CONFIGURATION

A. Tsushima and M. Fujiwara
Institute of Plasma Physics, Nagoya University, Nagoya 464, Japan

ABSTRACT

Theoretical studies are carried out to develop a new bumpy torus configuration without deterioration of its various advantages against other fusion devices such as tokamaks, stellarators and so on. In this configuration plasmas are confined by finite magnetic rotational transform which is localized in the central core region and stabilized by hot electron annulus at the peripheral region. By using expansion method around the magnetic axis, necessary field components and various magnetic surface quantities are investigated to evaluate the confinement characteristics of this configuration. Coil structures to provide such fields are also examined.

1. INTRODUCTION

ECH bumpy tori such as NBT-1/1M, EBT-I/S realize stable plasma confinement by MHD stabilization due to energetic electron plasma rings and by closed drift surfaces due to combination of grad B poloidal drift and $E_r \times B$ drift, where E_r is an ambipolar electric field. Recent experimental and theoretical studies clarified that the plasma is actually stabilized by high β electron annuli and confinement can be scaled by neoclassical diffusive losses. But as is discussed in Ref.1, we have a serious difficulty in the confinement of high energy particles like α particles in a simple, conventional bumpy torus. Various methods such as ARE coil, wedge coil, symmetrizing coil and ID coil system are presented to solve this problem, but a future bumpy torus reactor using any method descrbied above may be a large size facility with the aspect ratio $A \geq 15$ compared with other type of toroidal devices (tokamaks, stellarators, etc.). The aspect ratio A of tokamak and stellarator or

torsatron reactor are 2-5 and 10, respectively as shown in Fig.1. The other difficulty lies in a more elementary level, that is, the bumpy torus confinement is easily deteriorated by error field whose critical level is the order of 10^{-3}-10^{-4} for NBT-1/1M and EBT-1/S. The critical level of error field is evaluated preliminary as $\delta B/B \sim \rho_i/R$ where ρ_i and R are ion Larmor radius and the major radius of the torus, respectively. If this estimation is assumed to be correct, a severe problem appears in a future large size and high magnetic field device. To solve difficulties discussed above, we present the new concept of helical bumpy torus, which employed special coils used in the idea of a modular coil stellarator. The guiding principle of helical bumpy torus discussed by one of the authors, M. Fujiwara, a few years ago is as follows:

1. To reduce difficulties of error field level scaled by ρ_i/R which is 10^{-5} in the low temperature plasma at build up phase of a bumpy torus reactor.

2. To improve high energy particle confinement and to demonstrate the feasibility of a smaller size bumpy torus reactor.

3. To improve the confinement scaled as $\tau_p \sim A^2\tau_c(1 + \frac{e\phi}{\kappa T})^2$ and $\tau_E \sim 10^{-1}\tau_p$ in a pure bumpy torus by replacing $D \sim \nu\rho^2 q^2$ in usual tokamak or stellarators.

2. ANALYSIS OF SURFACE QUANTITIES

We investigate the magnetic field structure of bumpy torus with various kind of helical fields, which are produced by Rehker-Wobig type coils.[2] This type coil give the two sets of helical lines, i.e., the helical lines and the antihelical line. The field corresponding to the helical lines is

$$\mathbb{B}_+ = \nabla \Phi_+ = B_0 \nabla \left[\epsilon_+ I_\ell\left(\frac{mr}{R}\right) \sin(\ell\theta - m\phi)\right]$$

and the antihelical field is

$$\mathbb{B}_- = \nabla \Phi_- = B_0 \nabla \left[\epsilon_- I_\ell\left(\frac{nr}{R}\right) \sin(\ell\theta + n\phi)\right]$$

where we use the toroidal coordinate (r, θ, φ). The relation between these two field are as follows,

$$n = N - m \qquad (m \neq N/2)$$

$$\left(\frac{\epsilon_-}{\epsilon_+}\right)^2 = \frac{1 + \left(\frac{ma}{\ell R}\right)^2 \cdot \left(\frac{N}{m} - 1\right)^2}{\left[1 + \left(\frac{ma}{\ell R}\right)^2\right]\left(\frac{N}{m} - 1\right)^4}$$

where N is the numberof coils and a is the radius of the coil. We define R/a as aspect ratio A, but the aspect ratio is used to calculate the ratio of helical and antihelical field only. This ratio can be controlled by changing the modification of the coil. Since we consider the case in which the coil number of the torus is N, the bumpy field is given by

$$\mathbb{B}_b = \nabla \Phi_b = B_0 \nabla \left[\epsilon_b I_0\left(\frac{Nr}{R}\right) \sin N\phi \right]$$

We calculate the surface quantities without toroidal effect at first, and then we solve the magnetic surfaces and drift surfaces with toroidal effect.[3)]

Averaged magnetic surface without toroidal effect are functions of r only,

$$\frac{\epsilon_+^2}{R} \cdot \frac{I_\ell\left(\frac{mr}{R}\right) I_\ell'\left(\frac{mr}{R}\right)}{r} - \frac{\epsilon_-^2}{R} \frac{I_\ell\left(\frac{nr}{R}\right) I_\ell'\left(\frac{nr}{R}\right)}{r} = \text{const.}$$

The longitudinal and azimuthal flux in this surface are

$$\bar{\Phi} \simeq \pi B_0 \left\{ r^2 - \epsilon_0^2 \frac{Nr}{R} I_0\left(\frac{Nr}{R}\right) I_0'\left(\frac{Nr}{R}\right) - \epsilon_+^2 \frac{mr}{R} I_\ell\left(\frac{mr}{R}\right) I_\ell'\left(\frac{mr}{R}\right) - \epsilon_-^2 \frac{nr}{R} I_\ell I_\ell' \right\}$$

$$\chi \simeq \pi B_0 R \left\{ \epsilon_+^2 \frac{\ell}{r} I_\ell\left(\frac{mr}{R}\right) I_\ell'\left(\frac{mr}{R}\right) - \epsilon_-^2 \frac{\ell}{r} I_\ell\left(\frac{nr}{R}\right) I_\ell'\left(\frac{nr}{R}\right) \right\}$$

Then, rotational transform of magnetic field lines

$$\iota = d\chi/d\Phi$$

$$\simeq \frac{1}{2}\frac{R}{r}\left\{\epsilon_+^2\frac{d}{dr}\left[\frac{\ell}{r}I_\ell\left(\frac{mr}{R}\right)I_\ell'\left(\frac{mr}{R}\right)\right]-\epsilon_-^2\frac{d}{dr}\left[\frac{\ell}{r}I_\ell\left(\frac{nr}{R}\right)I_\ell'\left(\frac{nr}{R}\right)\right]\right\}$$

The volume in this surface is

$$V = 2\pi^2 R\left\{r^2+\frac{1}{2}\epsilon_0^2 I_0'^2\left(\frac{Nr}{R}\right)+\frac{1}{2}\epsilon_+^2 I_\ell'^2\left(\frac{mr}{R}\right)+\frac{1}{2}\epsilon_-^2 I_\ell'^2\left(\frac{nr}{R}\right)\right\}$$

and the specific volume is

$$U = \frac{dV}{d\Phi}$$

$$\simeq \frac{2\pi R}{B_0}\frac{1}{1-\frac{1}{2}\epsilon_0^2\frac{1}{r}\frac{d}{dr}\left[\frac{Nr}{R}I_0 I_0'\right]-\frac{1}{2}\epsilon_+^2\frac{1}{r}\frac{d}{dr}\left[\frac{mr}{R}I_\ell I_\ell'\right]-\frac{1}{2}\epsilon_-^2\frac{1}{r}\frac{d}{dr}\left[\frac{nr}{R}I_\ell I_\ell'\right]}$$

where B_0 is the averaged toroidal magnetic field.

Now we take toroidal effect into the calculation of magnetic surfaces. Since the first order of the magnetic surface is ε^2, we must consider the magnetic field with the order of $\varepsilon\frac{r}{R}$.

$$\mathbb{B} \simeq \mathbb{B}_0\left(1-\frac{r}{R}\cos\theta\right)\mathbb{e}_\phi + \nabla(\Phi_b+\Phi_++\Phi_-)$$

$$\Phi_b \simeq B_0\epsilon_b\left(1-\frac{1}{2}\frac{r}{R}\cos\theta\right)I_0\left(\frac{Nr}{R}\right)\sin N\phi$$

$$\Phi_+ \simeq B_0\epsilon_+\left(1-\frac{1}{2}\frac{r}{R}\cos\theta\right)I_\ell\left(\frac{mr}{R}\right)\sin(\ell\theta-m\phi)$$

$$\Phi_- \simeq B_0\epsilon_-\left(1-\frac{1}{2}\frac{r}{R}\cos\theta\right)I_\ell\left(\frac{nr}{R}\right)\sin(\ell\theta+n\phi)$$

Because the toroidal component of averaged vector potential $\bar{A}_\phi$ is zero, averaged magnetic surface can be obtained by

$$\psi = \frac{R^3\left(1+\frac{r}{R}\cos\theta\right)^3}{B_0}\,\overline{\left(\hat{B}_r\cos\theta - \hat{B}_\theta\sin\theta\right)\left(B_r\sin\theta + B_\theta\cos\theta\right)}$$

$$= \text{const.}$$

where

$$\bar{f} = \frac{1}{2\pi}\int_0^{2\pi} f\, d\phi$$

$$\hat{f} = \widetilde{\int_0^{\phi} \tilde{f}\, d\phi} \qquad \left(\tilde{f} = f - \bar{f}\right)$$

Then, averaged magnetic surface is

$$\left[\frac{\epsilon_+^2}{R}\,\frac{I_\ell\left(\frac{mr}{R}\right)I_\ell'\left(\frac{mr}{R}\right)}{r} - \frac{\epsilon_-^2}{R}\,\frac{I_\ell\left(\frac{nr}{R}\right)I_\ell'\left(\frac{nr}{R}\right)}{r}\right]$$

$$+\frac{r}{R}\cos\theta\left\{2\left[\frac{\epsilon_+^2}{R}\,\frac{I_\ell\left(\frac{mr}{R}\right)I_\ell'\left(\frac{mr}{R}\right)}{r} - \frac{\epsilon_-^2}{R}\,\frac{I_\ell\left(\frac{nr}{R}\right)I_\ell'\left(\frac{nr}{R}\right)}{r}\right]\right.$$

$$\left. - \left[\frac{\epsilon_+^2 I_\ell^2\left(\frac{mr}{R}\right)}{2mr^2} - \frac{\epsilon_-^2 I_\ell^2\left(\frac{nr}{R}\right)}{2nr^2}\right]\right\} = \text{const.}$$

The drift equation[4)] is given by

$$\frac{d\mathbf{r}}{dt} = v_\parallel\frac{\mathbf{B}}{B} + \frac{m\left(2v_\parallel^2 + v_\perp^2\right)}{2qB^3}\left[\mathbf{B}\,\nabla B\right]$$

$$\frac{d\mathbb{r}}{dt} = \frac{v_{\parallel}}{B}\,\mathbb{B}^*$$

$$\mathbb{B}^* = B_0\left\{\frac{\mathbb{B}}{B_0} + g\,\frac{[\mathbb{B}\,\nabla B]}{B^2}\right\}$$

$$g = \frac{m(2v_{\parallel}^2 + v_{\perp}^2)}{2qB_0}$$

or

$$\frac{dr}{\mathbb{B}^*} = \frac{r\,d\theta}{B_\theta^*} = \frac{R\,d\phi}{B_\phi^*} = \frac{v_{\parallel}}{B}\,dt$$

which are very similar to the equation of field line

$$\frac{dr}{B_r} = \frac{r\,d\theta}{B_\theta} = \frac{R\,d\phi}{B_\phi} = \frac{dl}{B}$$

The drift surface of passing particles in the B field is considered to be the magnetic surface of the B* field. Giving care to the fact that $\overline{A_\phi^*} = B_0 g \frac{r}{R}\cos\theta$, the drift surface can be obtained:

$$\left\{\epsilon_0^2 F_0(r) + \epsilon_+^2 F_+(r) + \epsilon_-^2 F_-(r)\right\}\left(1 + 3\frac{r}{R}\cos\theta\right)$$
$$+ \left\{g + \epsilon_+^2 f_+(r) + \epsilon_-^2 f_-(r)\right\}\frac{r}{R}\cos\theta = \text{const.}$$

$$F_0(r) = \frac{1}{2R^2}\,g\,N^2 I_0'^2\left(\frac{Nr}{R}\right)$$

$$F_+(r) = \frac{1}{2R^2}\left[I_\ell'\left(\frac{mr}{R}\right) + g\frac{\ell}{r/R}I_\ell\left(\frac{mr}{R}\right)\right]\left[\frac{\ell}{r/R}I_\ell + g^2 m^2 I_\ell'\right]$$

$$F_-(r) = -\frac{1}{2R^2}\left[I_\ell'\left(\frac{nr}{R}\right) - g\frac{\ell}{r/R}I_\ell\left(\frac{nr}{R}\right)\right]\left[\frac{\ell}{r/R}I_\ell - g^2 n^2 I_\ell'\right]$$

$$f_+(r) = -\frac{1}{2R^2}(1-m^2g^2)\frac{\ell}{r/R}\, I_\ell\left[I_\ell' + \frac{1}{2}\frac{1}{mr/R}\, I_\ell\right]$$

$$f_-(r) = \frac{1}{2R^2}(1-n^2g^2)\frac{\ell}{r/R}\, I_\ell\left[I_\ell' + \frac{1}{2}\frac{1}{nr/R}\, I_\ell\right]$$

3. DISCUSSION ON NUMERICAL RESULTS

Representative samples of numerical results are listed up in Table I. Prior to the evaluation for each case, we discuss on the guiding principle of a helical bumpy torus using modular coils. (1) A helical bumpy torus with a finite magnetic rotational transform can confine passing particles well. (2) As is well known, pure stellarators or torsatrons can not confine particles with high pitch angle ($V_\perp/V \sim 1$). A helical bumpy torus, in which $\ell = 0$ (bumpiness) field component $b_0/B_0 \simeq 0.2$-0.3 is larger than helical field component b_h/B_0, has closed Mod$|B|$ contours similar to conventional bumpy torus at the midplane and can confine trapped particles ($V_\perp/V \sim 1$). So, RF heatings such as ECH or ICH, which deposit the energy to the perpendicular direction primarily, can be used more efficiently compared with the case of stellarators or torsatrons. (3) In this configuration, energetic electron annulus is not used only to stabilize various MHD activities due to bad curvature effect of bumpy field, but high β ($\beta \sim 20$-30 %) electron plasmas have also the possibility to increase β limit of pure stellarators or of torsatrons. According to the viewpoint described above, the numerical results listed up in Table 1 are characterized as follows.

(1) $\ell = 1$ Helical Bumpy Torus:

- (1)-a Ψ_M = const surface (magnetic surface) coincides well with the drift surface Ψ_D of passing particles in wide energy ranges from 100 eV $\sim$ 3.5 MeV.
- (1)-b Shear stabilization can not be expected.
- (1)-c $b_0/B_0 \lesssim b_i/B_0$ means that mod B contour is dominated by $\ell = 1$ helical field.

(2) $\ell = 2$ H.B.T.

(2)-a Ψ_M agrees well with Ψ_D in the range 0.1 keV $\sim$ 3.5 MeV.

(2)-b Low shear.

(3)-c $b_2/B_0 << b_0/B_0$.

(3) $\ell = 3$ H.B.T.

(3)-a Ψ_M agrees well with Ψ_D.

(3)-b $\iota \sim 0$ in the central region of the plasma and ι is finite at the periphery (surface confinement).

(3)-c $b_3/B_0 << b_0/B_0$.

(3)-d Shear stabilization.

Here we discuss the characteristics of H.B.T. configuration by using averaged magnetic surface only, but the other important feature is the real shape of the magnetic surfaces which are shifted circle for $\ell = 1$, ellipse ($\ell = 2$) and triangle ($\ell = 3$). Since the deformation factor increases with b_ℓ/B_0 and ι, the difference between magnetic surfaces and Mod|B| contours must be studied.

Loss cone in H.B.T. can be predicted to exist in some pitch angle region between $V_\parallel/V \sim 0$ and $V_\parallel/V \sim 1$, but the width of loss cone angle, energy dependence and the effect of ambipolar potential must be studied.

References

1) M. Fujiwara et al., Proc. Spring College on Fusion Energy, Trieste (1981) p.193.

2) T. K. Chu et al., PPPL-1796.

3) A. I. Morozov and L. S. Solovev, in Review of Plasma Physics, Vol.II.

4) P. A. Poprydukhin, Sov. Atomic Energy 18 (1965) 118.

Table 1. Summary of numerical results

No.	R_o (A)	N	$\ell=0$ b_o	ℓ	m	n	$\varepsilon_+ \frac{m}{R_o}$	$b_{\ell z+}$ $b_{\ell r+}$ $b_{\ell\theta+}$	$\varepsilon_- \frac{m}{R_o}$	$b_{\ell z-}$ $b_{\ell r-}$ $b_{\ell\theta-}$	
1	10	24	0.3								pure bumpy M = 1.86
10	10	24	0.0	1	6	18	1.0	0.15 0.5	0.1962	0.663	ℓ=1 pure stellarator
12	10	24	0.2	1	8	16	1.0	0.2 0.5	0.3683	0.73	ℓ=0 + ℓ=1 H.B.T. High +
14	10	24	0.3	2	6	18	0.5	5×10^{-3} 3.7×10^{-2}	0.071	0.09	ℓ=0 + ℓ= 2 weak H.B.T.
18	10	24	0.2								pure bumpy M = 1.5
22	10	24	0.2	2	8	16	1.0	2×10^{-2} 7.5×10^{-2}	0.29	0.42	ℓ=0 + ℓ=2 H.B.T. High +
23	10	24	0.0	2	8	16	1.0	2×10^{-2} 7.5×10^{-2}	0.29	0.42	ℓ=2 pure stellarator
31	10	24	0.0	3	6	18	12.0	5×10^{-4} 5×10^{-3}	1.52	0.32	ℓ=3 pure stallarator
33	10	24	0.2	3	6	18	12.0	5×10^{-4} 5×10^{-3}	1.52	0.32	ℓ=3 H.B.T. High +

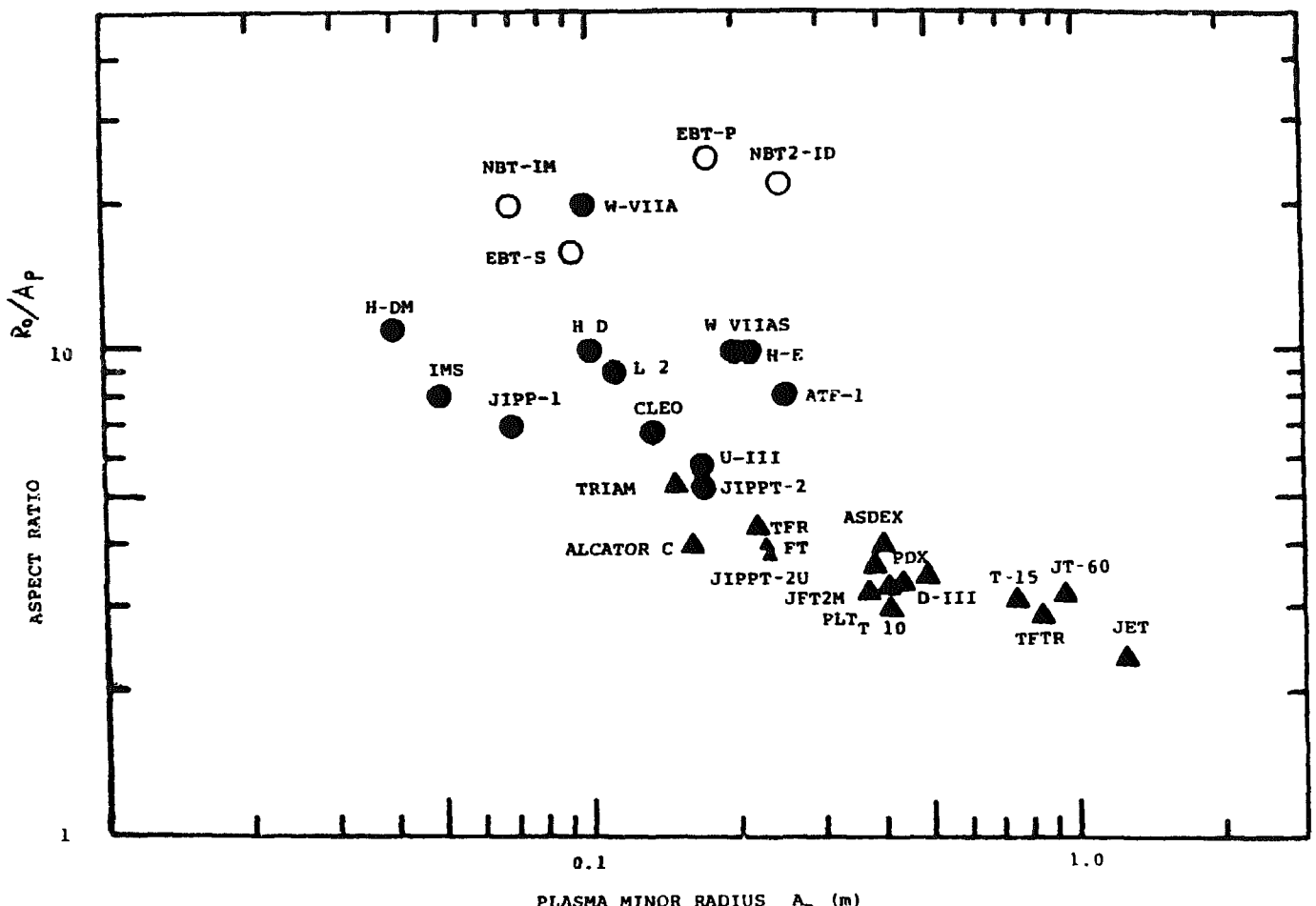

Fig. 1. Aspect ratio vs plasma minor radius for various fusion devices

THE ELMO SNAKEY TORUS

Allen H. Boozer
Princeton Plasma Physics Laboratory
Princeton, New Jersey 08544

In the Elmo Snakey Torus (EST), circular toroidal field coils are displaced along a helical path to produce a magnetic configuration with surfaces. One such surface is illustrated in Fig. 1. A hot electron annulus is used to overcome the pressure driven instabilities, which are predicted for EST plasmas, during the start-up phase. After the beta value is raised above about 10%, the Shafranov shift has a strong stabilizing effect on the pressure driven modes and the electron annulus should not be required at the operating beta value which is about 20%. The EST concept was originated with the suggestion of Harold Furth. Donald Monticello and Allan Reiman have also made important contributions.

Traditional EBT designs raise two power balance issues. The first is the bulk plasma energy confinement time, which is closely related to the dependence of the particle drift orbits on pitch angle. The second is the maintenance of the high energy electrons of the annulus, which is required to maintain the bulk plasma stability. Both issues are sensitive to the magnetic field design. This is particularly true, if by the EBT program, we mean the study of net current free toroidal plasmas which require stabilization by energetic particles.

Of the modified EBT designs, the Snakey Torus is one of the few which retains the attractive feature of simple circular coils. The near vacuum pressure surfaces in the EST are also nearly circular in cross section although they become significantly dee-shaped at high beta, $\langle\beta\rangle \gtrsim 10\%$.

The existence of magnetic surfaces in the Snakey Torus implies that passing particle orbits remain close to the pressure surfaces. In closed magnetic field line devices, there is no natural constraint. In both closed line devices and devices with magnetic surfaces, the trapped particle drift orbits can stray significantly from the pressure

surfaces. Consequently, careful design and analysis is required in both types of devices to insure adequate bulk plasma confinement.

The Snakey Torus has the unfortunate feature, as does the traditional EBT design, that the near vacuum pressure surfaces are shifted inward giving an average maximum B configuration. However, the Snakey Torus has several advantages in this regard. The inward shift is smaller, the magnetic hill is much lower, and the shift becomes outward giving a magnetic well at reasonable operating beta values. Although energetic particle stabilization is required in EST, it is required only for start-up. Consequently, the energetic particles do not raise a reactor power balance question in EST as they do in traditional EBT designs. The high power required to maintain the energetic particles during EST start-up also provides some of the required heating of the bulk plasma.

The basic features of the Snakey Torus can be understoood in a symmetric helix of length $2\pi R$, just as a traditional EBT can be understood in a circularly symmetric but bumpy cylinder of the same length. In a bumpy cylinder, the field strength is approximately

$$B = B_o[1 + \varepsilon_b \cos(N_p \phi)]$$

with B_o and ε_b approximately constant. N_p is the number of periods and ϕ is the distance along the cylinder divided by R. In usual EBT designs $\varepsilon_b \sim 1/3$. The equivalent expression for a Snakey Helix is

$$B = B_o[1 + \varepsilon_s \cos(N_p \phi - \theta)]$$

with θ the poloidal angle. Unlike in a Bumpy Cylinder ε_s is approximately proportional to the minor radius, r. If toroidal field coils of radius a_c must be displaced by a distance r_o to be centered on a helical rather than a circular path around the torus, then

$$\varepsilon_s \simeq \frac{r}{r_o} \frac{N_p^2 r_o^2}{R^2 + N_p^2 r_o^2} \quad .$$

In practice, $R \simeq N_p r_o$ and at the plasma edge $r \simeq r_o/2$ so that $\varepsilon_s \lesssim 1/4$. The inward shift Δ_s of the Snakey Helix magnetic surfaces, along the direction of helical curvature, is approximately

$$\Delta_s \simeq \frac{\varepsilon_s}{4} a_c \quad .$$

The rotational transform of the Snakey Helis is

$$\iota \simeq N_p \left[1 + \left(\frac{R^2}{R^2 + N_p^2 r_o^2}\right)^{1/2}\right] \quad .$$

In practical designs, $\iota/N_p \simeq 1/3$ and the number of periods is $N_p \simeq 5$. At finite beta, the surfaces shift outward due to the Pfirsch-Schluter currents. This Shafranov shift Δ_β is roughly

$$\Delta_\beta \simeq \langle\beta\rangle r_o \quad .$$

The shift becomes excessive for $\langle\beta\rangle \gtrsim 20\%$. Toroidal effects on the basic Snakey Torus equilibrium are modest if the transform is significantly greater than one. Of course, toroidal effects, which break the helical symmetry, cause both the dominate bulk plasma energy transport at low collisionality and also the breakup of the magnetic surfaces if the helical shift Δ_β becomes too large. Toroidal effects

in traditional EBT designs are stronger leading to an inward shift, along the major radius, of

$$\Delta_{BT} \simeq \frac{8}{3} \frac{R}{N_p^2 \epsilon_b^2}$$

which is often quite large.

The inward shifts of both the Bumpy and Snakey Torus lead to a magnetic hill in the vacuum configuration. In the simple Bumpy Torus the height of this hill is

$$\frac{\delta\langle B\rangle}{\langle B\rangle} \simeq \frac{3}{4} N_p^2 \epsilon_p^2 \left(\frac{r}{R}\right)^2$$

which in practice is about 30%. The magnetic hill in the Snakey Torus is

$$\frac{\delta\langle B\rangle}{\langle B\rangle} \simeq \frac{1}{2} \epsilon_b^2 \quad .$$

At low beta, both the Bumpy Torus and the Snakey Torus require energetic particles to obtain stable plasmas. The required beta for the hot component is roughly

$$\beta_h \gtrsim 2 \frac{\delta_h}{a} \frac{\delta\langle B\rangle}{\langle B\rangle}$$

with δ_h the annulus width and a the plasma radius. In EST the plan would be to make $\delta_h \simeq a$, which is in contrast to traditional EBT reactor designs in which $\delta_h \simeq 0.05$ a. The factor of ten between the

$\delta\langle B\rangle/\langle B\rangle$ in EST and traditional EBT designs implies the actual annulus beta values are comparable.

An important feature of using high energy electrons for stabilization only during start-up is that it is not necessary to heat the annulus while the plasma beta is being raised. The point is that the n_τ for the annulus to give up energy to the background plasma is about 10^{13}. At a plasma density of $10^{14}/cm^3$, the annulus will last about 100 msec without additional power. The importance comes from the difficulty of obtaining accessibility for the electron cyclotron waves, traditionally used to form the annulus, when the plasma beta is high.

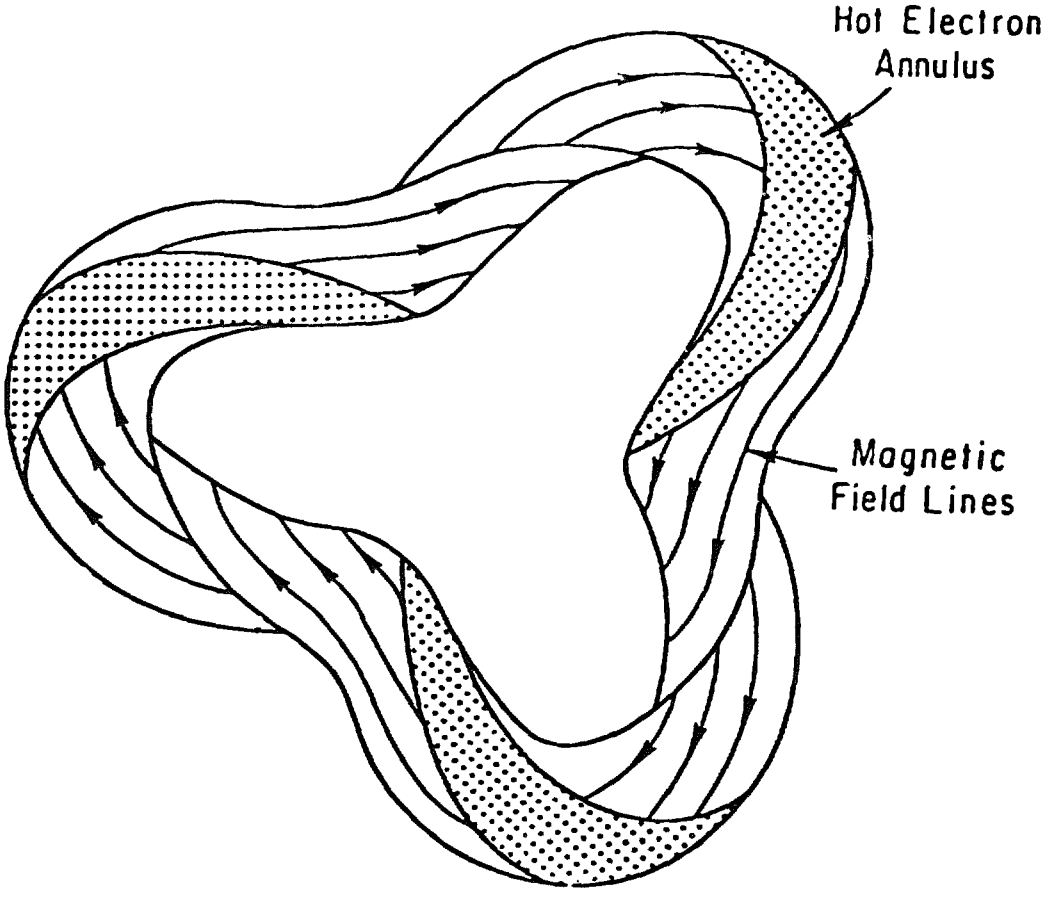

Fig. 1. Illustration of surfaces in ELMO Snakey Torus Number of periods equals 3.

ENERGETIC PARTICLES IN TOKAMAKS: STABILIZATION OF BALLOONING MODES

J.W. Van Dam[a]

McDonnell-Douglas Astronautics Company

St. Louis, MO 63166

and

M.N. Rosenbluth, S.T. Tsai[b], M.G. Engquist

Institute for Fusion Studies, University of Texas
Austin, TX 78712

ABSTRACT

The introduction of an ELMO-type superhot particle species trapped in the unfavorable curvature region of a tokamak has recently been shown to provide the possibility of stable access to high-beta confinement. The energetic particles stabilize high-mode-number ballooning modes up into the regime of second stability, after which they are no longer required. A summary is given of stability estimates calculated for a model shifted-circle, large-aspect-ratio equilibrium.

INTRODUCTION

The idea of using highly energetic particles to provide stable confinement of a plasma is a generic one and has been the basis for several types of devices, including the ELMO Bumpy Torus (EBT), symmetric tandem mirrors, and the Astron and ion ring devices. The latter are somewhat different from the first two since in the Astron and ion ring experiments, energetic electrons or ions were employed in an effort to reverse the magnetic field, whereas in the EBT concept, the hot particles only produce a local minimum or well in the field strength. Then, because the hot electrons in EBT precess so rapidly, they are "rigid" in the sense that they do not respond to interchange-type fluid displacements in the usual frozen-in manner, but instead behave so as to conserve the magnetic flux through their precessional orbit (i.e., third adiabatic invariant). Consequently, the minimum-B well produced by the diamagnetic current of a sufficient

---

(a) Permanent address: Institute of Fusion Studies, University of Texas, Austin, TX 78712.

(b) Permanent address: Institute of Physics, Chinese Academy of Sciences, Beijing, The People's Republic of China

number of these suprathermal particles can stabilize the rest of the plasma against instabilities driven by unfavorable curvature.

The major thrust in applying the principle of hot particle stabilization in recent years has been and is now in the EBT program. Future planning for the EBT concept has recently diversified into several new directions. One direction is to explore whether there may be better designs than the standard bumpy torus. Some of the ideas[1] that have been developed are for advanced design coils, for reconfiguring the bumpy torus into bumpy straight sections with high field corners, and for hybrid combinations of EBT with rotational transform as in stellerators. These novel concepts may have significant potential for improving particle confinement, and therefore they are being vigorously investigated as possibilities for a next-stage device.

As another direction to explore, we would point out that ELMO physics, i.e., the physics of plamas containing a superhot component, can have a broad applicability to currently existing devices other than EBT. As an example of such an application, consider the situation where one introduces ELMO-type energetic particles (either ions or electrons, by microwave heating or beam injection) into a standard tokamak[2]. Just as in EBT where the hot species digs a diamagnetic well and thereby provides stabilization, the idea is that the same thing will occur in a tokamak.

In addition, there may be extra advantages. In EBT, the hot particles are essential for stability and must be continuously supplied. Tokamaks, on the other hand, already possess certain stability properties, which could be augmented by the presence of a very hot particle species. In particular, tokamaks are predicted to have a parameter regime of stability at high beta[3, 4]. This so-called second zone of stability is separated from the usual stable regime (first stability) by an unstable gap. Introducing energetic particles could open up an avenue for direct stable access from first to second stability. The other advantage is that once the plasma is in the second stable regime, the high energy component is no longer needed. In this regime, plasma confinement is predicted to improve as beta increases, at least with respect to ballooning and kink mode stability. Since the hot particles would then be used only during the start-up phase of the tokamak, their production would constitute only a temporary energy drain on the overall reactor economics of such a system. The corresponding application of hot particles in stellerators or heliacs ("ELMO Snakey Torus") would have similar merits[5].

In the next section, Sec. II, we will describe the theoretical approach used in Ref. 2 to demonstrate enhanced stability of tokamaks containing ELMO-type energetic particles. Section III presents the results obtained for a model equilibrium, which show that ballooning modes can be stabilized up into the second stability regime for reasonable values of the shear. A discussion of the potential usefulness of this scheme is given in Sec. IV.

II. THEORETICAL METHOD

We investigated the situation of an isotropic plasma of pressure P_c, with a fairly anisotropic population of energetic particles mirror trapped on the unfavorable-curvature outer side of the tokamak. The hot particles are assumed to drift across field lines so rapidly that their average magnetic drift frequency $\bar{\omega}_{dh}$ is much larger than the frequency ω of a typical fluctuation:

$$\bar{\omega}_{dh} >> |\omega| . \tag{1}$$

For example, $|\omega|$ may be on the order of the interchange mode growth rate. Condition (1) means that the hot particles possess "rigidity" in that they do not participate in the usual E×B motion. To satisfy condition (1) requires fairly high energies, as will be quantified in Sec. IV. However, since the energetic species is trapped on the outside and its pressure is assumed to be not so high as to cause drift reversal, the hot particle drift is on average unfavorable, i.e., in the same direction as the diamagnetic drift:

$$\bar{\omega}_{dh}\, \omega_{*h} > 0. \tag{2}$$

Condition (2) also eliminates the magnetic compressional instability with trapped particles[6].

For the sake of simplicity, a model equilibrium was adopted. In this model, the aspect ratio is large: $r/R << 1$, with r and R the minor and major radii. Furthermore, the flux surfaces are approximately shifted circles, with pressure gradients localized in a thin layer: hence the ordering $\beta_{\perp h} \approx \beta_c << 1$, but $R\,(d\beta/dr) \approx 0(1)$. A convenient pressure distribution in poloidal angle θ is $P_{\perp h}$ = const. for $|\theta| \leqslant \theta_0$ and zero elsewhere. The toroidal magnetic field is approximately $B_T \propto 1 - (r/R)\cos\theta$. Although a simplified model, this equilibrium does contain the poloidal variation of the local shear and therefore yields the characteristic features of second stability.

The MHD stability of high-mode-number ballooning mode perturbations was studied by means of the low-frequency kinetic-type energy principle[7, 8]. This energy principle is valid when condition (1) is satisfied and when the bounce motion of the hot particles is rapid compared to their drift motion. It was previously applied to EBT stability in the reversed-drift case[7]. A lower bound to the kinetic part of this energy principle can be derived by means of the Schwarz inequality. Employing this lower bound enables us to deal with line integrals of macroscopic quantities such as the pressure, instead of a more complicated velocity integral of bounce-averaged quantities involving the microscopic particle distribution function. Minimization of the lower bound to the energy than leads to an inhomogeneous ballooning mode equation:

$$\frac{d}{d\theta}[1 + h^2(\theta)]\frac{d\Phi}{d\theta} + (\alpha_c + \frac{1}{2}\alpha_h)\, D(\theta)\, \Phi(\theta) = \frac{1}{2}\alpha_h D \frac{\int d\theta\, D\Phi}{\int d\theta\, (D - \alpha_c/2q^2)} . \quad (3)$$

Here, Φ is the electrostatic potential, $D(\theta)$ is proportional to the field line curvature, α_c and α_h are proportional to the plasma and hot component pressure gradients, and $1 + h^2(\theta)$ is proportional to the square of the transverse wavenumber of the mode. Equation (3) is numerically solved for Φ in each successive trapped/untrapped particle θ-interval, where θ now represents the extended poloidal variable of the ballooning representation, ranging over an infinite domain along a field line. This procedure eventually yields an underestimate of the marginal stability boundaries. More details may be found in Ref. 2.

III. RESULTS

The stability results obtained with the model equilibrium described previously are presented in Figs. 1-3. In these figures, the abscissa is the normalized plasma beta value $\alpha_c = -(2q^2 R/B_T^2)(dP_c/dr)$; the ordinate is the average shear $S = d(\ln q)/d(\ln r)$, where $q = rB_T/RB_p$ is the safety factor. The angle θ_0 determines how localized the energetic species is about the midplane (located at $\theta = 0$). The angular quantity θ_k is the zero point for the local shear and, hence, indicates approximately where the mode amplitude is peaked poloidally. Also, $\alpha_h = -(2q^2R/B_T^2)(dP_{\perp h}/dr)$ is proportional to the beta value of the hot species.

Figure 1 shows various stability boundaries, with θ_0 as a parameter. We set $q = 2$ and $\theta_k = 0$ in this figure. The dashed curves are the well-known boundaries for first and second stability (without any hot particles). There is an unstable gap separating these two stable

regions. The dotted lines indicate where drift reversal occurs without hot particles. Our stability analysis is valid only when the bounce-averaged magnetic drift is not reversed. For the limiting particles whose turning points are at $\theta = \pm\theta_0$, the condition $\bar{\omega}_{dh}(\theta_0) = 0$ can be expressed as

$$\alpha_c A_1(\theta_0) + \alpha_h A_2(\theta_0) = S A_3(\theta_0) + A_4(\theta_0), \tag{4}$$

where the A_j are given in terms of elliptic integrals. For a given θ_0, the corresponding dotted line indicates where the presence of even an infinitesimal amount of hot pressure will cause reversal. Thus, our theoretical analysis is able to predict stability only to the left of each such line. The solid curves in Fig. 1 are the marginal stability boundaries in the presence of hot particles, with α_h chosen, for each (α_c, S) point on the curves, to have its maximum value as allowed by the non-drift-reversal condition.

Although this analysis yields a pessimistic estimate of stability, the results in Fig. 1 nevertheless indicate that energetic particles trapped between $\theta = \pm\pi/4$ are able to stabilize ballooning modes for shear values up to S = 0.9 and for beta values up to and beyond the second stability limits.

Figure 2 shows the stability diagram for the optimal angle $\theta_0 = \pi/4$ when the pressure gradient layer is taken to correspond to various values of the safety factor q. For q = 4, stabilization is seen to extend up to S = 1.9, appropriate near the edge of the plasma.

Also, the value of θ_k was varied, in order to consider the stability of modes peaked off the midplane. Figure 3 compares the stability of modes peaked at $\theta_k = 0$ and at $\theta_k = 3\pi/8$; the latter value can be shown to be approximately the most unfavorable θ_k value at large α_c. In this figure, q = 2 and $\theta_0 = \pi/4$ were chosen again. The two stability boundaries have virtually the same broad minimum at S = 0.9, although the $\theta_k = 3\pi/8$ curve then dips down to S = 0.6 near the point where its second stability and drift reversal limit curves intersect.

IV. DISCUSSION

From the preceding results, we conclude that it may be possible to bridge the ballooning unstable gap between first and second stability in a tokamak by means of the introduction of ELMO-type energetic particles. After the plasma reaches the high-beta second stable regime, no further injection or heating of hot particles would be required.

There are several issues that remain to be investigated. For one thing, the second stability regime in tokamaks has not yet been experimentally verified. Also, the stability of internal or global ideal kink modes and resistive modes in the presence of energetic particles and in the predicted second stable zone needs to be considered. Moreover, microinstabilities such as whistlers or modes near the ion cyclotron frequency may be associated with the introduction of suprathermal particles. The decoupling condition for interchange stability of the hot species becomes more difficult to satisfy at finite plasma pressures. In fact, when the drift frequency $\overline{\omega}_{dh}$ is not large enough to decouple the dynamics of the hot particles from those of the plasma, the mode tends to acquire an oscillation frequency approximately equal to $\overline{\omega}_{dh}$ near the onset of instability. (A similar feature is observed for the so-called fishbone fluctuations in the PDX experiment.) Finally, the technological requirements of schemes for injecting or heating the superhot particles, the power balance, etc., deserve study.

We can estimate the energy required for the hot particles as follows. The decoupling condition $\overline{\omega}_{dh} >> |\omega|$ can be more precisely expressed in the form $\gamma_h/\overline{\omega}_{dh} < 0.5$. If this inequality is satisfied, then our energy principle analysis provides a valid sufficient condition for stability. Here, γ_h is the hot particle interchange growth rate: $\gamma_h \approx 0.25\ (N_h T_h/N_i M_i rR)^{1/2}$ for $m \geqslant 2$, with N_h and T_h the density and temperature of the energetic component and m the poloidal mode number. Then, with $\overline{\omega}_{dh} \approx (m/r)\ (cT_h/eB_T R)$ and if we take $\beta_h \approx \beta_i$, the requirement becomes

$$\frac{T_h}{T_i} > \frac{(rR)^{1/2}}{2m\rho_i}\ , \tag{5}$$

where ρ_i is the plasma ion Larmor radius. For example, if we consider D-T reactor-like parameters ($r = 1.5$ m, $R = 5$ m, $T_i = 10$ keV, and $B = 5$ T), this condition requires a minimum energy of $T_h \simeq 2.1$ MeV (for $m = 2$), which is high but not unreasonable.

In conclusion, we have specifically demonstrated the enhanced stability of tokamaks containing highly energetic particles like those in EBT. More generally, this exercise illustrates the broad applicability of EBT physics to other devices.

ACKNOWLEDGEMENTS

The work described in Ref. 2 was supported by the U.S. Department of Energy. One of the authors (JVD) gratefully acknowledges support from McDonnell-Douglas Corp. for the preparation and presentation of this manuscript.

References:

1. See, for example, other papers presented at this workshop.

2. M.N. Rosenbluth, S.T. Tsai, J.W. Van Dam, and M.G. Engquist, Institute for Fusion Studies Report #98 (1983).

3. B. Coppi, A. Ferreira, J. Mark, and J. Ramos, Nucl. Fusion 19, 715 (1979).

4. J.M. Greene and M.S. Chance, Nucl. Fusion 21, 453 (1981).

5. H.P. Furth and A.H. Boozer, memorandum (1982); A.H. Boozer, paper presented at this workshop.

6. M.N. Rosenbluth, Phys. Rev. Lett. 46, 1525 (1981).

7. J.W. Van Dam, M.N. Rosenbluth, and Y.C. Lee, Phys. Fluids 25, 1349 (1982).

8. T.M. Antonsen and Y.C. Lee, Phys. Fluids 25, 132 (1982).

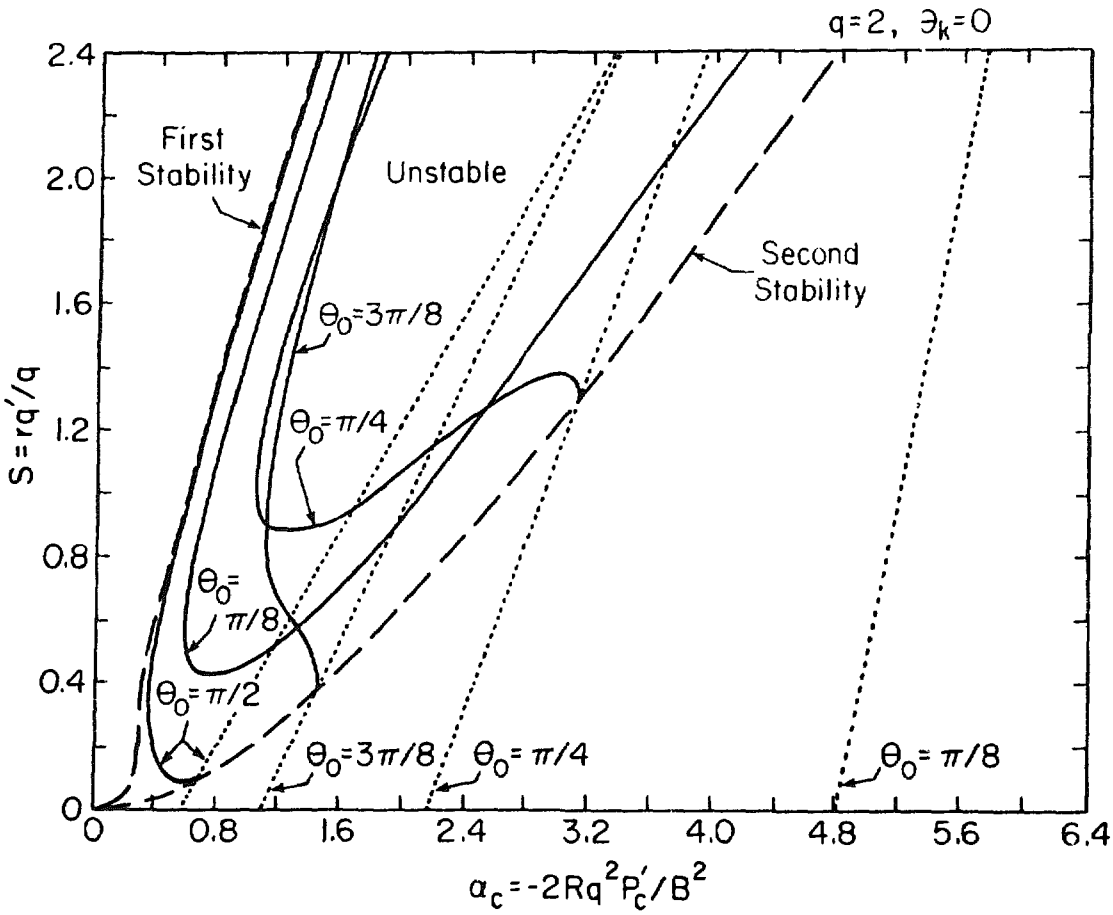

Fig. 1. Stability boundaries in shear S and core beta α_c, for maximal hot beta and various degrees of localization θ_0, with q = 2 and $\theta_k = 0$.

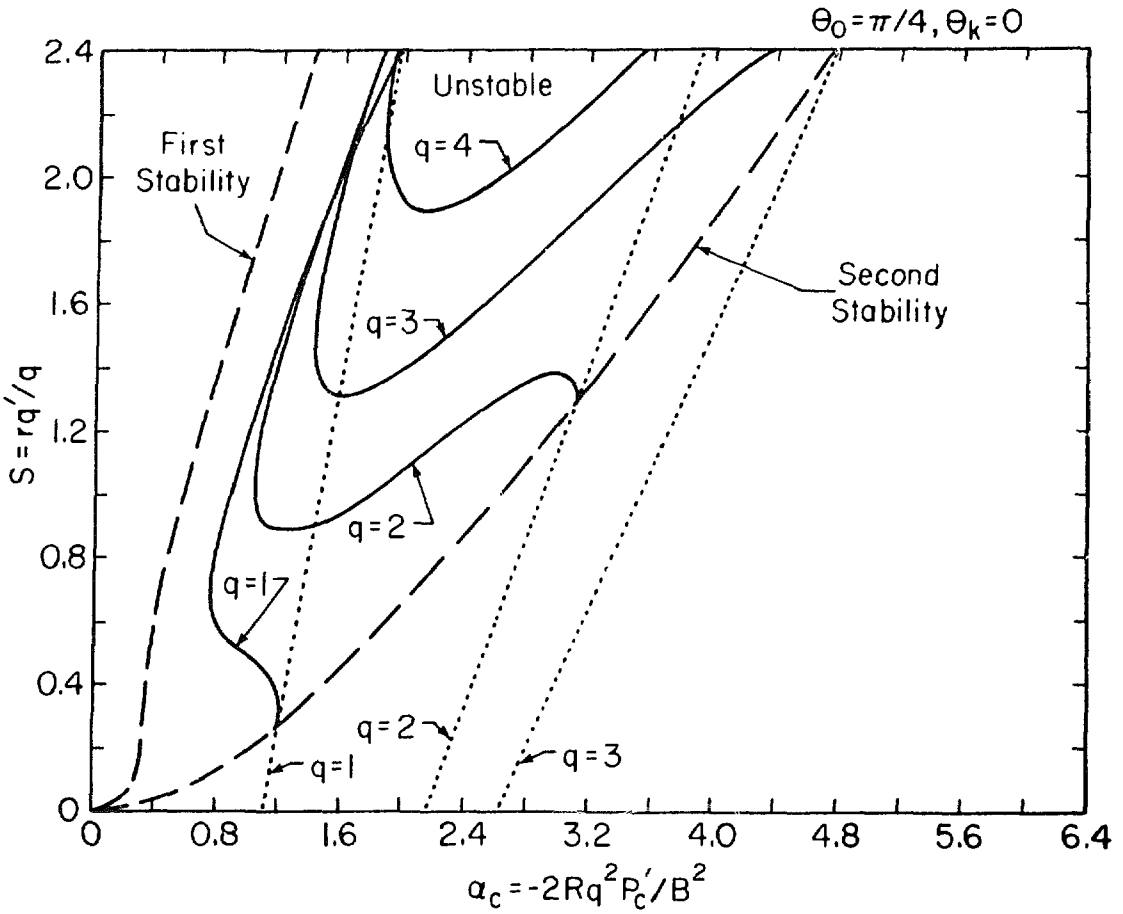

Fig. 2. Stability boundaries for various q values, with $\theta_0 = \pi/4$ and $\theta_k = 0$.

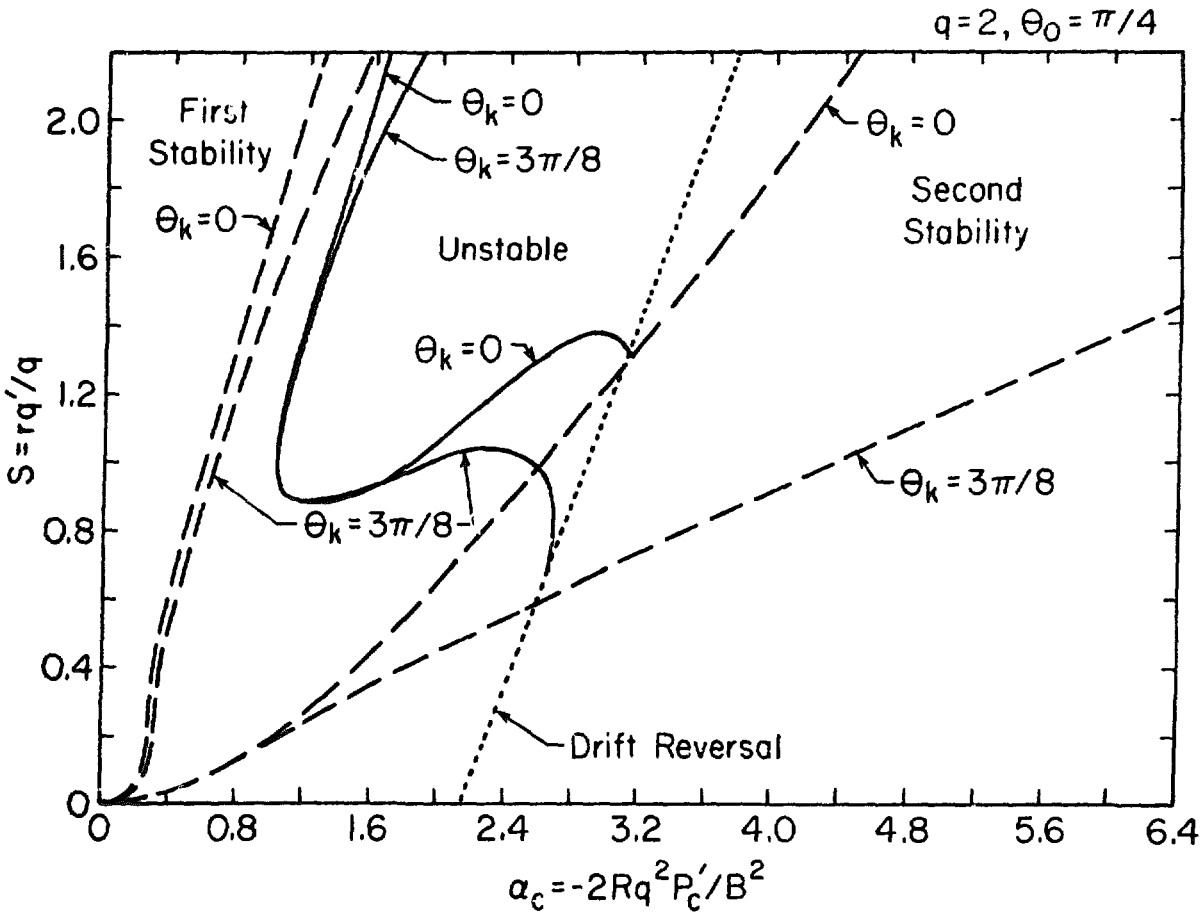

Fig. 3. Stability boundaries for centered ($\theta_k = 0$) and off-centered ($\theta_k = 3\pi/8$) modes, with $q = 2$ and $\theta_0 = \pi/4$.

177/178

INTERPRETATION AND SUPPORTING THEORY

OPTIMIZED OPERATION OF BUMPY TORUS

Hideo Ikegami
Institute of Plasma Physics, Nagoya University, Nagoya 464, Japan

On developing a new concept for the bumpy torus, one is supposed to have a clear understanding of plasmas in the currently operation two bumpy tori, Nagoya Bumpy Torus (NBT) and Elmo Bumpy Torus (EBT). Any new concepts would propose to improve some of the undesirable features of the present bumpy torus concept in exchange of introducing a little bit of gimmick hopefully harmless.

To the author's understanding, however, the two bumpy tori, NBT and EBT, have never been operated to produce enough materials to ask for a help with exotic and fantastic deformation.

From a conservative viewpoint of experimentalist, some strange and disregarded, but maybe new and important, data will be discussed, which may lead to a re-evaluation of the bumpy torus concept.

Density

The line integrated density measured by a microwave interferometer is found to be nearly proportional to the square root of rf power for discharge under similar ambient gas pressures as shown in Fig.1. The fact may lead to that the plasma temperature depends weakly on the rf power like $T \propto P^{1/3}$ and that the particle confinement time is almost constant as one may anticipate from the particle balance in the steady state operation which equates the particle confinement time to the ionization time.

This rather low density feature of NBT and EBT may be due to their steady state operation rather than the concept of bumpy torus configuration. Any fusion device has never operated in a steady state except NBT and EBT.

Quite interesting experimental results are shown in Fig.2, where the plasma density is observed to increase 3-4 times with an impose of pulsed rf power of 10 msec and the density increment depends strongly on the rf power absorbed which shows a resonance as shown in Fig.3. Pulsed opera-

tion of those bumpy tori would produce quite satisfactory plasmas, however, this is to turn the face from what other fusion concepts are going to meet with sooner or later.

Temperature

Experiments on NBT indicates that ion cyclotron heating is apparently more efficient than electron cyclotron heating. As shown in Figs.4 and 5 the ICH heating rate with a small input power reaches 500 eV/kW or 5 eV/kW/10^{14} cm^{-3}, which is superior to those ICH experiments on tokamaks and other devices. It must be noted that the plasma density does not decrease with the ICH power.

The NBT plasma is still dominated by charge exchange processes, so that the observed heating rate does not reflect the energy confinement time that can evaluate the bumpy torus concept. Also as shown in Fig.4, the heating rate levels off as the input power is further increased, to which several reasons may be considered responsible.

Confinement

The plasma confinement in the bumpy torus cannot be discussed without introducing the effect of radial electric field. Experimentally, however, no evidence was detected so far as to the enhanced confinement due to the radial electric field.

In the steady state operation, the particle confinement time is essentially equal to the ionization time. Most experiments on NBT and EBT were carried out with the so-called T-mode plasma, which exists for a narrow filling gas pressure range, so that any drastic change cannot be anticipated in the particle confinement time. In other words, it may be correct to say that both NBT and EBT have never operated properly to study the confinement scaling. In order to decide whether the confinement is neoclassical or not, it may be necessary to have a pulsed, bumpy torus operation.

The other concern is whether we can depend upon the radial electric field for the confinement or not (Figs.6 and 7). Probably not. So that better magnetic configuration, like the inverse dee (ID) coil system, must be developed.

Plasma Beta

The radial distribution of the hot electrons are quite instructive. They are composed of three groups, that is, hot electron ring, toroidal hot electrons, and core hot electron, as clearly shown in Fig.8.

Two origins of the core hot electrons will be considered. One is the fundamental cyclotron resonance heating which works off the midplane. The other is the hot electron ring, which decays inward generating the core hot electrons. In the latter case, however, it is difficult to explain a rather sharp boundary between the core hot electron and the ring. Furthermore, the core hot electron appears to have its maximum intensity somewhere near the center and does not disappear by skimming off the ring.

Comparing the intensity of core hot electrons and the ring, we must admit that the core hot electron carries a plasma beta of several per cent which must be the bulk plasma beta itself, so that the plasma beta of several per cent has been achieved already in the present bumpy torus configuration.

Stability

To the bumpy torus concept, the most important and serious question is if the hot electron ring can really work for the stabilization of MHD instabilities. In each mirror sector, the plasma surface is forced to contact with the cavity throat and the plasma appears to stay quite stable even without the hot electron ring. For example, in the C-mode operation, large amplitude MHD instabilities have never been observed.

Since the stabilization by the hot electron ring is the key issue of the bumpy torus concept, the stabilization functioning must be confirmed.

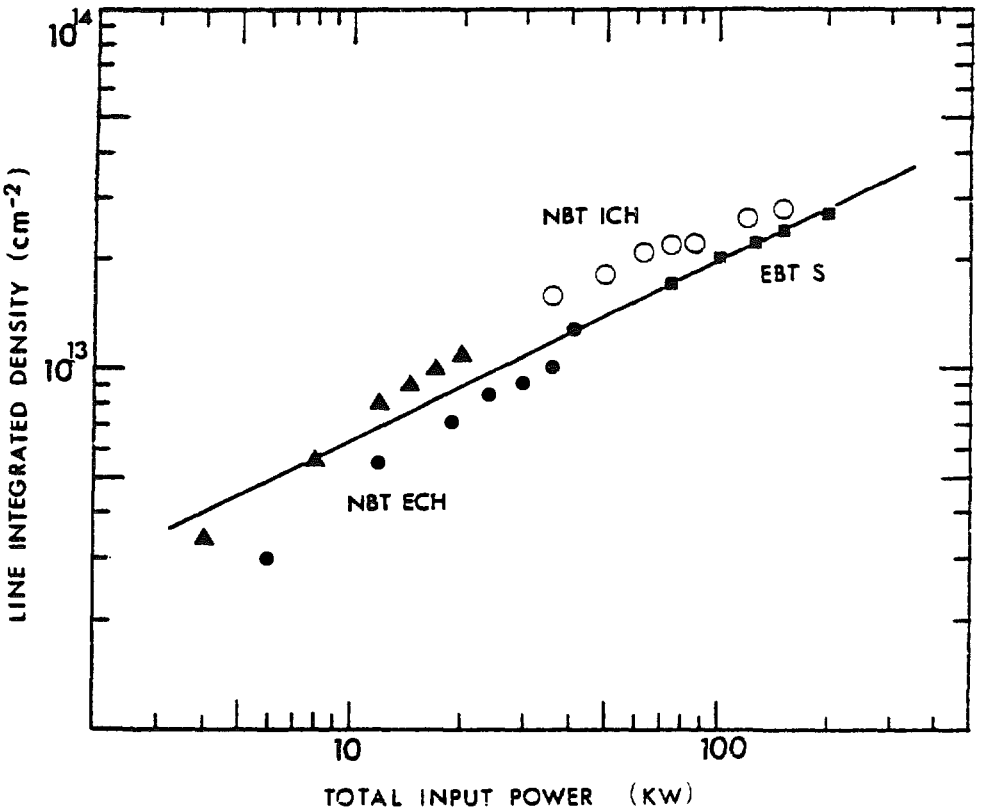

Fig.1 Line integrated density against total rf input power for plasma production in the T-mode operation of NBT and EBT.

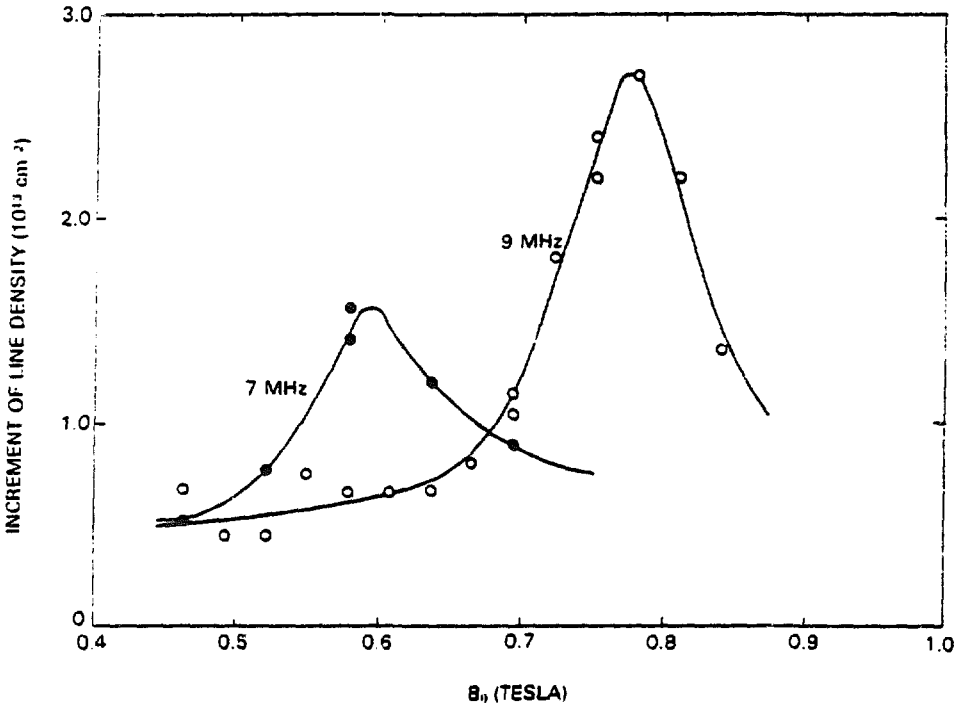

Fig.2 Line integrated density as a function of additional rf power at 9 MHz with 9 msec pulse width.

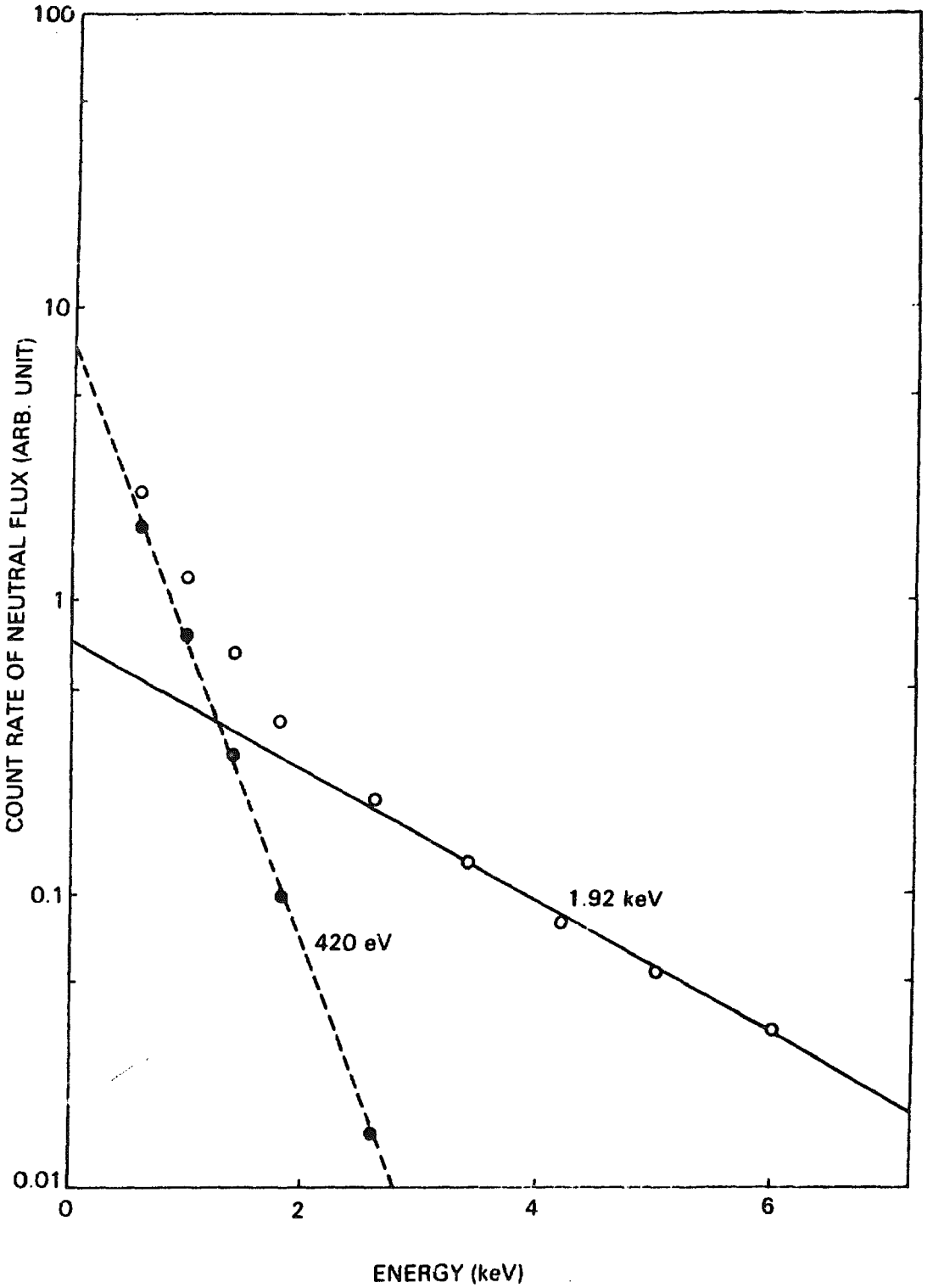

Fig.5 Ion energy distribution composed of 50% 1.92 keV ions and 50% 0.42 keV ions. The rf power level is 25.7 kW at 7 MHz.

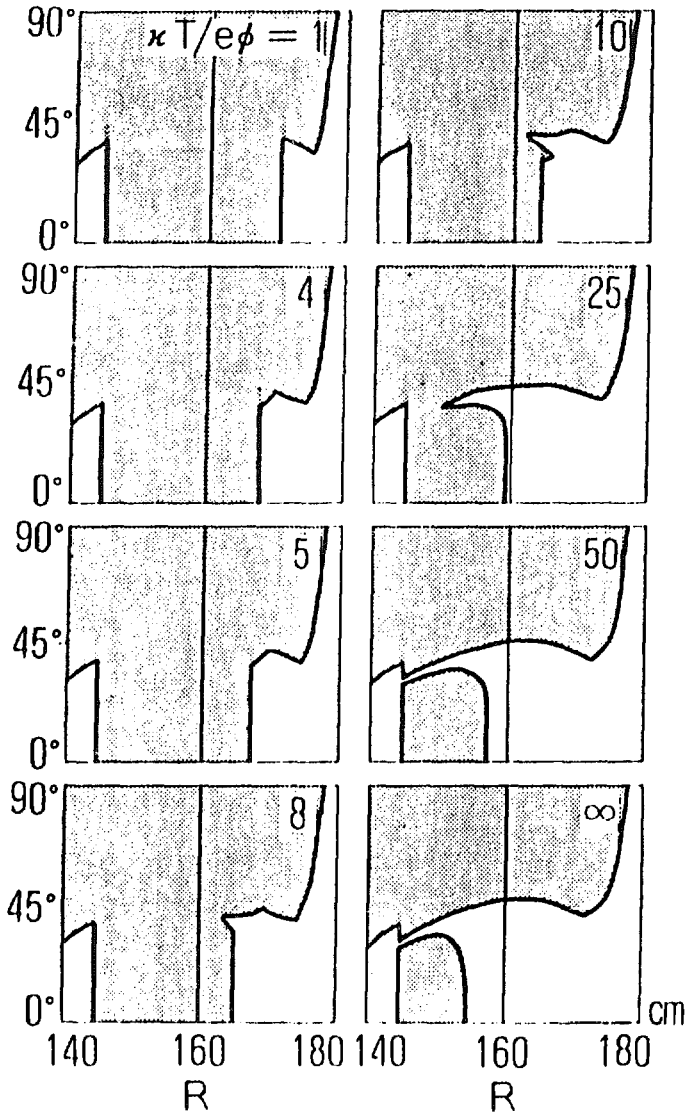

Fig.6 Distribution of direct loss area (blank) in NBT (ions for convex potential or electrons for concave potential) with kinetic energy as a parameter. The maximum/minimum potential measured from the wall is given by eφ. Ordinate is pitch angle of gyrating particles and abscissa is the location along the major radius in cm.

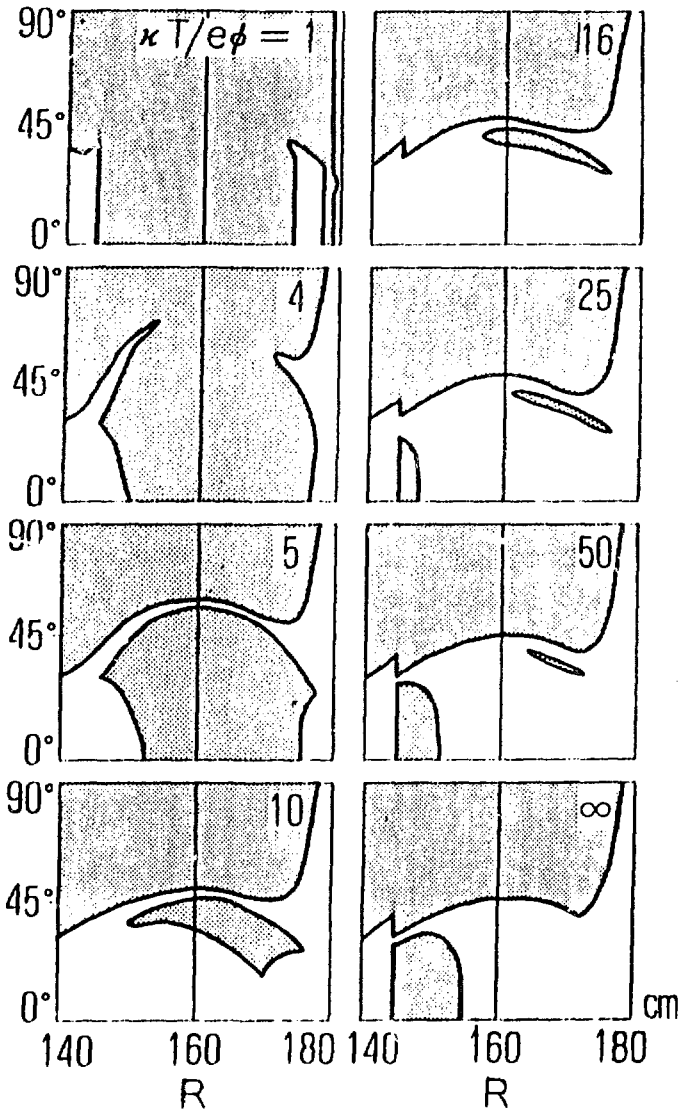

Fig.7 Distribution of direct loss area (blank) in NBT (ions for concave potential or electrons for convex potential) with kinetic energy as a parameter. The maximum/minimum potential measured from the wall is given by eφ. Ordinate is the pitch angle of gyrating particles and abscissa is the location along the major radius in cm.

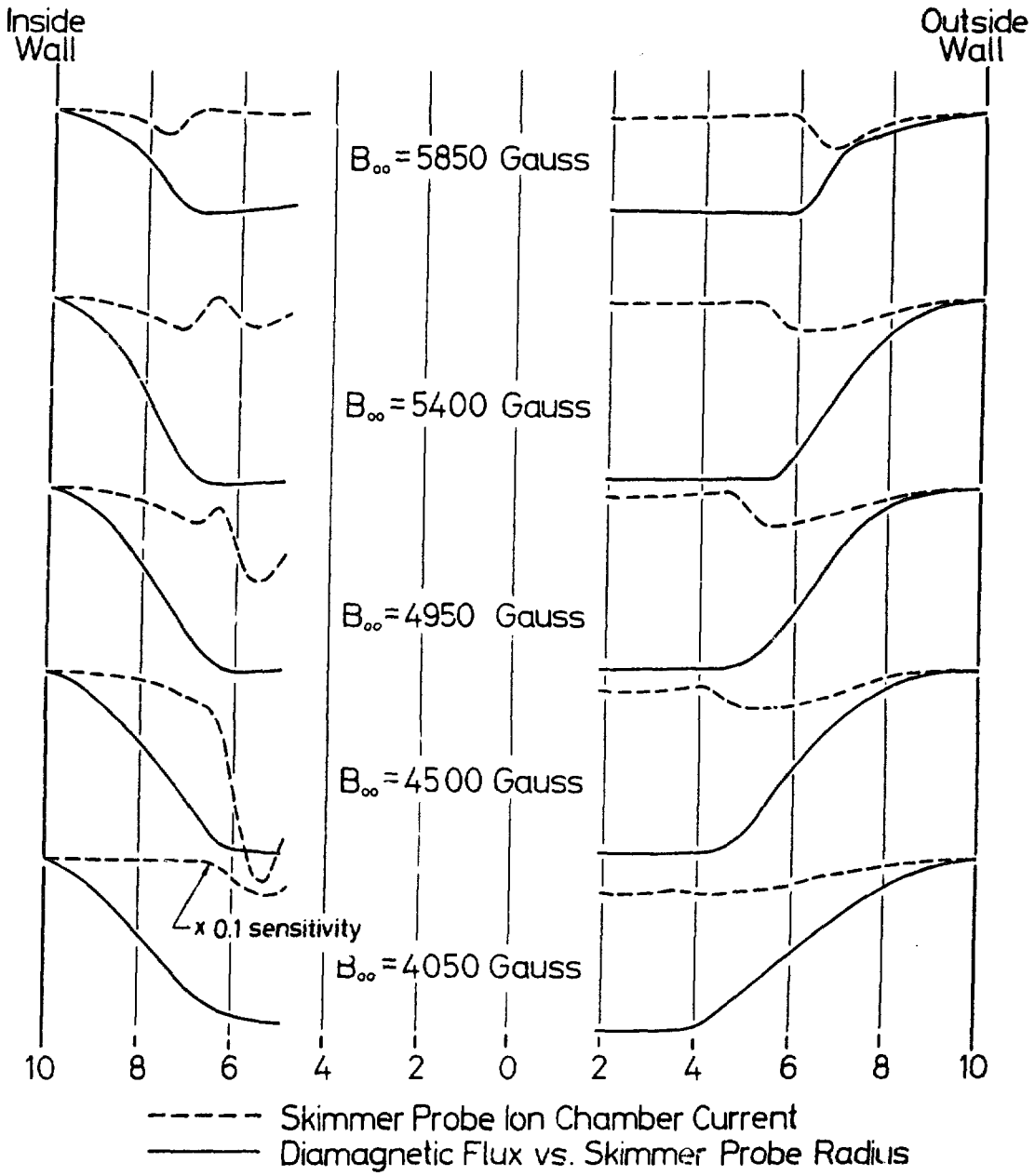

Fig.8 Signals of ionization chamber in EBT-I. Abscissa is the minor radial position. The signals reveal the existence of three different hot electron group; hot electron ring, toroidal hot electrons, and core hot electrons which mixed up with the bulk plasma with an implication that the core plasma beta must have reached several percent already.

NONRESONANT PARTICLE TRANSPORT FOR BUMPY FIELD LINE DEVICES WITH ARBITRARY SHAPED FLUX SURFACES*

D. E. Hastings
Oak Ridge National Laboratory
Oak Ridge, Tennessee 37830

ABSTRACT

In a bumpy closed field line device, the radial drift through the pressure surfaces is the sum of the ∇B, curvature, and poloidal electric field drifts. Since the ∇B and curvature drifts are determined by the magnetic field geometry, which for low beta plasmas are independent of the plasma, the radial drift is a function of plasma position. This may enhance the vertical drift that a particle sees and hence neoclassical diffusion. Another way the vertical drift may be enhanced is if the magnetic field has a poloidal structure beyond that caused by the toroidal effects (e.g., if the mod-B surfaces are slightly elliptical in shape). We shall explore the changes in the diffusion coefficients caused by both of these effects.

*Research sponsored by the Office of Fusion Energy, U. S. Department of Energy, under contract No. W-7405-eng-26 with the Union Carbide Corporation.

1. INTRODUCTION

Recently there has been renewed interest in obtaining nonresonant diffusion coefficients for bumpy torus plasmas in devices like ELMO Bumpy Torus-Scale (EBT-S) and NBT-1M. The first work was done by Kovrizhnykh[1] and was recently extended in to include the finite and small electric field regimes. All of these pieces of work have assumed that the plasma center was at the position of the average magnetic axis and that the mod-B surfaces were circular. If these two assumptions are not true, then the nonresonant diffusion coefficients could be substantially changed since both of these assumptions affect the radial drift through the pressure contours. In Ref. 4, the effect of taking the plasma center to be off the average magnetic axis was considered along with a self-consistent poloidal electric field. It was found that significant changes in the transport rates could be obtained by moving the (assumed) position of the plasma center.

In this work we follow the basic structure of Ref. 4 and consider the effect of taking the pressure surfaces to be noncircular and centered on the $\oint d\ell/B$ center. In Sect. 2, we derive expressions for the mod-B and $\oint d\ell/B$ surface using the analytic equilibrium of Hazeltine and Catto.[5] In Sect. III we obtain the radial drift through the pressure surfaces. In Sect. IV, we use this radial drift to get the perturbed distribution function, the self-consistent poloidal electric field, and finally the diffusion coefficients. In Sect. V, we discuss our results and conclusions.

2. MOD-B AND $\oint d\ell/B$ SURFACES

For the magnetic field in the low beta core plasma, we follow the analytic analysis of Ref. 5. Hence, we choose to label the constant pressure surfaces by the contained magnetic flux $2\pi\alpha$. The magnetic field is written as

$$\underline{B} = \underline{\nabla}\alpha \times \underline{\nabla}\beta \ , \tag{1}$$

where beta is a generalized poloidal angle.

If we take the magnetic field B as $B = B(\alpha, \beta, \ell)$, where ℓ is the distance along a field line, and the electrostatic potential as $\phi = \phi(\alpha, \beta)$, then the particle velocity across the pressure surfaces due to the poloidal electric field is

$$\underline{v}_{d_e} \cdot \underline{\nabla}\alpha = -\frac{\partial\phi}{\partial\beta}(\alpha, \beta) \ , \tag{2}$$

and the particle velocity across the pressure surfaces due to the ∇B and curvature drifts is

$$\underline{v}_{d_B} \cdot \underline{\nabla}\alpha = -\frac{(mv^2/2)}{ZeB}\left(1 + \zeta_p^2\right)\frac{\partial B}{\partial\beta}(\alpha, \beta) \ , \tag{3}$$

where ζ_p is the pitch angle $(v_\parallel/v)$.

In the notation of Ref. 5, the core magnetic field is given by

$$\underline{B} = \left[\underline{e}_r \frac{\partial\hat{\phi}_o}{\partial r} + \underline{e}_\zeta \left(\bar{B} + \frac{\partial\hat{\phi}_o}{\partial\zeta}\right)\right](1 - \varepsilon r \cos\theta)$$

$$- \frac{\varepsilon}{2}\cos\theta \left\{\underline{e}_r\left[r^2 \frac{\partial^2\hat{\phi}_o}{\partial r^2} + \frac{\partial}{\partial r}\left(r\hat{\phi}_o\right)\right] + \underline{e}_\zeta\left(r^2 \frac{\partial^2\hat{\phi}}{\partial r\,\partial\zeta} + r\frac{\partial\hat{\phi}_o}{\partial\zeta}\right)\right\}$$

$$+ \underline{e}_\theta \frac{\varepsilon}{2}\sin\theta \frac{\partial}{\partial r}\left(r\hat{\phi}_o\right) + \varepsilon\underline{\nabla}_o h \ , \tag{4}$$

where ε is the inverse aspect ratio given by

$$\varepsilon \equiv a/R_o \tag{5}$$

with a being the maximum minor radius of the plasma and R_o the average major radius of the magnetic axis. The variables r and θ are defined by

$$R = R_o(1 + \varepsilon r \cos \theta) , \tag{6}$$

$$Z = ar \sin \theta , \tag{7}$$

where R is the major radius and Z is the vertical distance from the toroidal midplane. The toroidal angle ζ is defined so that $\zeta = 0$ is the midplane of a mirror sector and $\zeta = \pi/N\varepsilon$ is the coil plane. Here, N is the number of mirror sectors. The magnetic potential $\hat{\phi}_o$ is given by

$$\hat{\phi}_o = \sum_k a_k \sin k\zeta I_o(kr) , \tag{8}$$

where

$$k = \varepsilon n N, \quad n = 1,2 \ldots , \tag{9}$$

and the function h, which corresponds to an $O(\varepsilon)$ distortion of the flux surfaces (due to coil geometry) beyond that required by toroidicity, is given by

$$h(r,\theta,\zeta) = \sum_{k,m} \left(b_{km} e^{im\theta} + b^*_{km} e^{-im\theta}\right) I_m(kr) \sin(k\zeta) , \tag{10}$$

where the sum over m is for $m \geq 0$ and b^*_{km} is the complex conjugate of b_{km}.

For positions close to the average magnetic axis ($r \ll 1$) it can be shown that

$$\hat{\phi}_o \simeq a_1 \sin(k_1\zeta) I_o(k_1 r) , \tag{11}$$

where

$$a_1 = -\frac{\varepsilon_o B_{m_o}}{(1 - \varepsilon_o)} \frac{1}{k_1} , \tag{12}$$

$$k_1 = \varepsilon N , \tag{13}$$

$$\varepsilon_o = \frac{M - 1}{M + 1} , \tag{14}$$

and M is the mirror ratio on the average magnetic axis while B_{m_o} is the value of the magnetic field at $r = 0$, $\theta = 0$, and $\zeta = 0$ or on the midplane at the center.

We shall assume that the following ordering holds:

$$\varepsilon_o^2 << \varepsilon << \varepsilon_o << 1 . \tag{15}$$

We note that for EBT-S parameters $\varepsilon \simeq 0.1$ and $\varepsilon_o \simeq 0.3$ so this is marginally satisfied. To determine B we work to first order in small quantities:

$$B \simeq B_\zeta \simeq \frac{B_{m_o}}{1 - \varepsilon_o} \{1 - \varepsilon r \cos\theta - \cos(k_1\zeta) [\varepsilon_o I_o(k_1 r)$$

$$- k_1 \varepsilon \sum_m (b_{1m} e^{im\theta} + b_{1m}^* e^{-im\theta}) I_m(k_1 r)]\} . \tag{16}$$

In the midplane ($\zeta = 0$), for $r << 1$ the contours of constant B are given by (for $x = r \cos\theta$, $y = r \sin\theta$)

$$\text{const} = B = \frac{B_{mo}}{1 - \varepsilon_o} \left\{1 - \varepsilon x - \varepsilon_o\left(1 + \frac{k_1^2 x^2}{4} + \frac{k_1^2 y^2}{4}\right) + \frac{k_1^3 \varepsilon}{8}\left[2b_{12}(x^2 - y^2)\right]\right\}$$

$$= \frac{B_{mo}}{1 - \varepsilon_o}\left[(1 - \varepsilon_o) - \varepsilon x - x^2\left(\frac{\varepsilon_o k_1^2}{4} - \frac{\varepsilon k_1^3 b_{12}}{4}\right) - y^2\left(\frac{\varepsilon_o k_1^2}{4} + \frac{\varepsilon k_1^3 b_{12}}{4}\right)\right]. \tag{17}$$

In Eq. (17), for simplicity we have taken $b_{1m} = 0$ for $m \neq 2$ and $b_{12} = b_{12}^*$. The $|B|$ contours for this choice of b's are ellipses with the center at $x = x_b$, $y = 0$, where

$$x_b \simeq -\frac{2\varepsilon}{\varepsilon_o k_1^2}\left(1 - b_{12}\frac{\varepsilon}{\varepsilon_o} k_1\right), \tag{18}$$

and the elongation e_ℓ (in the y direction) is given by

$$e_\ell \simeq 1 - b_{12}\frac{\varepsilon}{\varepsilon_o} k_1 \quad . \tag{19}$$

In a closed field line device like a bumpy torus there are no surfaces that are ergodically covered by the magnetic field lines. However, it can be shown that the pressure is constant on the $\oint d\ell/B$ contours for such devices. To determine $U = \oint d\ell/B$ we work to $O(\varepsilon^2)$:

$$U = \oint \frac{d\ell}{B} = \int_0^{\pi/N\varepsilon} \varepsilon R_o \frac{d\zeta}{B_\zeta}$$

$$= \left(\frac{R_o}{N}\right) \frac{(1 - \varepsilon_o)}{B_{m_o}} \{1 + \varepsilon r \cos\theta + \varepsilon^2 r^2 \cos^2\theta + \frac{\varepsilon_o^2 I_o^2(k_1 r)}{2}$$

$$+ \frac{\varepsilon^2 k_1^2}{2} \left[\sum_m (b_{1m} e^{im\theta} + b_{1m}^* e^{-im\theta}) I_m(k_1 r)\right]^2$$

$$- \varepsilon_o \varepsilon I_o(k_1 r) k_1 \sum_m (b_{1m} e^{im\theta} + b_{1m}^* e^{-im\theta}) I_m(k_1 r)\} \quad . \tag{20}$$

We can proceed as for Eq. (17) and write

$$\text{const} = U = \left(\frac{R_o}{N}\right) \frac{(1 - \varepsilon_o)}{B_{m_o}} \{1 + \varepsilon x + \varepsilon^2 x^2 + \frac{\varepsilon_o^2}{2} \left(1 + \frac{k_1^2 x^2}{2} + \frac{k_1^2 y^2}{2}\right)$$

$$+ \frac{\varepsilon^2 k_1^2}{2} \left[2b_{12} \frac{k_1^2}{8} (x^2 - y^2)\right]^2 - \varepsilon_o \varepsilon k_1 2b_{12} \frac{k_1^2}{8} (x^2 - y^2)\} \ . \tag{21}$$

Equation (21) is the equation of an ellipse with center at $x = x_p$, $y = 0$, where

$$x_p = - \frac{2\varepsilon}{\varepsilon_o^2 k_1^2} \left[1 + b_{12} k_1 \frac{\varepsilon}{\varepsilon_o} - \frac{4}{k_1^2} \left(\frac{\varepsilon^2}{\varepsilon_o^2}\right)\right] \tag{22}$$

and with elongation e_ℓ given by

$$e_\ell = 1 + \frac{2\varepsilon^2}{k_1^2\varepsilon_o^2} - b_{12}k_1\frac{\varepsilon}{\varepsilon_o} . \tag{23}$$

We note that in the midplane the pressure surfaces are shifted inwards from the $|B|$ surfaces. If the $|B|$ surfaces are elliptical with $b_{12} < 0$ (i.e., the major axis in the y direction), then the pressure surfaces are also elliptical in the same direction but their ellipticity is larger. This has been observed numerically.[6]

3. RADIAL AND POLOIDAL DRIFT VELOCITIES

In Eq. (3), we showed that to evaluate $\underline{v}_{dB} \cdot \underline{\nabla}\alpha$ we need $\partial B(\alpha,\beta)/\partial\beta$. From the chain rule this is given by

$$\frac{\partial B}{\partial\beta}(\alpha,\beta) = \frac{\partial\theta}{\partial\beta}(\alpha,\beta)\,\frac{\partial B}{\partial\theta}(r,\theta) + \frac{\partial r}{\partial\beta}(\alpha,\beta)\,\frac{\partial B}{\partial r}(\theta,r) \quad . \tag{24}$$

We evaluate Eq. (24) up to $O(\varepsilon/\varepsilon_o)^2$. It is easy to show through use of the sine and cosine rules that

$$\beta \simeq \theta + \left(\frac{\Delta}{r}\right)\sin\theta + \ldots , \tag{25}$$

where

$$\Delta = \frac{2\varepsilon}{\varepsilon_o^2 k_1^2} , \tag{26}$$

and we have assumed that $(\Delta/r) \ll 1$. Since Δ is the offset of the pressure surfaces, this implies that we are conisdering radial locations in the plasma far from the plasma center. To $O(1)$, $\beta \simeq \theta$, and from Eq. (16), we may write

$$\frac{\partial B}{\partial \theta}(r,\theta) = \frac{B_{mo}}{1-\varepsilon_o}\left[\varepsilon r \sin\theta + \varepsilon k_1 \cos(k_1\zeta)\frac{\partial \hat{h}}{\partial \theta}\right], \tag{27}$$

where we have defined $\hat{h}(r,\theta)$ by

$$\hat{h}(r,\theta) = \sum_{m=o}^{\infty} \left(b_{1m}e^{im\theta} + b_{1m}^{*}e^{-im\theta}\right)I_m(k_1 r) \quad . \tag{28}$$

To write Eq. (27) as a function of (α,β) we must express r as a function of (α,β). The flux α is defined by

$$\alpha(U) = \frac{1}{2\pi}\int_o^{2\pi} d\beta \int_o^{r(\beta;U)} dr\; rB_\zeta(\zeta = 0) \tag{29}$$

$$= \frac{B_{m_o}}{2\pi}\int_o^{2\pi} d\beta\, \frac{1}{2}\, r^2(\beta;U) + O(\varepsilon_o) \quad . \tag{30}$$

To obtain $r = r(\beta;U)$ we expand $I_o^2(k_1 r)$ to $O(k_1^2 r^2)$ in Eq. (20) and obtain

$$r^2(\beta;U) = \frac{4}{\varepsilon_o^2 k_1^2}\left[\left(\frac{N}{R_o}\right)\frac{B_{m_o}}{1-\varepsilon_o}U - 1 - \frac{\varepsilon_o^2}{2}\right]$$

$$- \frac{4}{\varepsilon_o^2 k_1^2}\left\{\varepsilon r(\beta;U)\cos\beta - \varepsilon_o \varepsilon k_1 \hat{h}\left[r(\beta;U),\beta\right]\right\} \quad . \tag{31}$$

Since the terms in the second set of brackets on the right side of Eq. (31) are smaller than the terms in the first set we can construct an iteration scheme by

$$r_{n+1}^2(\beta;U) = \frac{4}{\varepsilon_o^2 k_1^2}\left[\left(\frac{N}{R_o}\right)\frac{B_{m_o}}{1-\varepsilon_o}U - 1 - \frac{\varepsilon_o^2}{2}\right]$$

$$- \frac{4}{\varepsilon_o^2 k_1^2}\left\{\varepsilon r_n(\beta;U)\cos\beta - \varepsilon_o \varepsilon k_1 \hat{h}[r_n(\beta;U],\beta)\right\} . \tag{32}$$

If we take $r_o = 0$, then we have

$$r_1^2 = \frac{4}{\varepsilon_o^2 k_1^2}\left[\left(\frac{N}{R_o}\right)\frac{B_{m_o}}{1-\varepsilon_o}U - 1 - \frac{\varepsilon_o^2}{2} + \frac{4}{k_1}\left(\frac{\varepsilon}{\varepsilon_o}\right)b_{10}\right] , \tag{33}$$

and using Eq. (30) we have the first iterate on the flux given from

$$r_1 = \left(\frac{2\alpha_1}{B_{m_o}}\right)^{1/2} . \tag{34}$$

The second iterate on $r(\beta;U)$ written in terms of α_1 is

$$r_2 = r_1\left[1 - \frac{\Delta}{r_1}\cos\beta + \left(\frac{\varepsilon}{\varepsilon_o}\right)\frac{2\hat{h}(r_1,\beta)}{k_1 r_1^2}\right] . \tag{35}$$

We use Eqs. (34) and (35) to obtain $r(\alpha,\beta)$.

For the second term on the right-hand side of Eq. (24) we need $\partial B/\partial r$ and $\partial r/\partial\beta$. The radial gradient of B can be obtained from Eq. (16),

$$\frac{\partial B}{\partial r}(r,\theta) = -\frac{B_{m_o}}{1-\varepsilon_o}\left[\varepsilon_o\cos(k_1\zeta)k_1 I_1(k_1 r) + \varepsilon\cos\theta - k_1\varepsilon\cos(k_1\zeta)\frac{\partial\hat{h}}{\partial r}\right]; \tag{36}$$

$\partial r(\alpha,\beta)/\partial\beta$ can be obtained by differentiating Eq. (35). Then, $\partial B(\alpha,\beta)/\partial\beta$ to $0\left[(\varepsilon/\varepsilon_o)^2\right]$ is obtained from Eqs. (36), (35), (27), and (26) as

$$\frac{\partial B}{\partial\beta}(\alpha,\beta) = -\frac{B_{mo}}{1-\varepsilon_o}r\sin\beta\left[\left(\frac{\varepsilon}{\varepsilon_o}\right)\cos(k_1\zeta) + 2\left(\frac{\varepsilon}{\varepsilon_o}\right)^2\frac{\cos\beta}{k_1^2 r_1}\right.$$

$$\left. - 2\left(\frac{\varepsilon}{\varepsilon_o}\right)^2\frac{\cos(k_1\zeta)}{k_1 r_1}\frac{\partial\hat{h}}{\partial r}\right]. \tag{37}$$

The radial drift through the pressure contours is then

$$\underline{v}_{d_B}\cdot\underline{\nabla}\alpha = \frac{(-mv^2/2)}{Ze}(1+\zeta_p^2)\varepsilon r\sin\beta\left[-\frac{\cos(k_1\zeta)}{\varepsilon_o} - 2\left(\frac{\varepsilon}{\varepsilon_o}\right)\frac{\cos\beta}{\varepsilon_o k_1^2 r_1}\right.$$

$$\left. + \left(\frac{\varepsilon}{\varepsilon_o}\right)\frac{2}{k_1 r}\frac{\partial\hat{h}}{\partial r}\frac{\cos(k_1\zeta)}{\varepsilon_o}\right]. \tag{38}$$

We can interpret Eqs. (24)-(38) physically in the following manner. The first term on the right-hand side of Eq. (24) is the well-known radial drift driven by toroidal effects although we see in Eq. (28) that there is a contribution due to the ellipticity of the $|B|$ surfaces. The second term on the right-hand side of Eq. (24) is a correction to the first term due to the fact that the pressure center may not coincide with the average magnetic axis. This too has a contribution from the noncircularity of the pressure surfaces.

Since the bounce time is smaller than the drift time, we average $\underline{v}_d \cdot \underline{\nabla}\alpha$ over the bounce time by defining the integral operator

$$\langle \ldots . \rangle = \oint \frac{d\ell}{v_\parallel} \ldots . \tag{39}$$

The bounce time τ_b

$$\tau_b = \oint \frac{d\ell}{v_\parallel} , \tag{40}$$

so on bounce averaging Eq. (2), we obtain

$$\langle \underline{v}_{d_e} \cdot \underline{\nabla}\alpha \rangle = - \tau_b \frac{\partial\phi}{\partial\beta} . \tag{41}$$

For $r \ll 1$, it is easy to show that

$$v_\parallel = v\zeta_m [1 - \kappa^2 \sin^2(k_1\zeta/2)]^{1/2} , \tag{42}$$

where ζ_m is the pitch angle ζ_p in the midplane and κ^2 is given by

$$\kappa^2 = \frac{1 - \zeta_m^2}{\zeta_m^2} \left(\frac{2\varepsilon_o}{1 - \varepsilon_o}\right) . \tag{43}$$

When we bounce average Eq. (38) using Eq. (42) and integrating from $\zeta = 0$ to $\zeta = 2/k_1 \sin^{-1}(1/\kappa)$ we obtain

The total poloidal drift Ω is given in Ref. 4 and is

$$\Omega = \langle \underline{v}_d \cdot \underline{\nabla}\beta \rangle = \tau_b \Omega_{th} \left[x^2 \bar{h}(\zeta_m) + w_o \right] , \tag{47}$$

where

$$\Omega_{th} = - \frac{k_b T}{Ze B_{m_o} a^2} \frac{1}{r_1 R_c} , \tag{48}$$

$$x^2 = \frac{(1/2) m v^2}{k_b T} \tag{49}$$

$$w_o = - \frac{Ze}{k_b T} \frac{\partial \phi_o}{\partial \alpha} r_1 R_c B_m , \tag{50}$$

$$R_c = - \left. \frac{\partial \ln B}{\partial r_1} \right|_{\varepsilon=0} , \tag{51}$$

and

$$\bar{h}(\zeta_m) = \begin{cases} 2 \zeta_m^2 \kappa^2 \left[\dfrac{E(1/\kappa^2)}{K(1/\kappa^2)} - \dfrac{1}{2} \right] , & \kappa^2 > 1 \\ 2 \zeta_m^2 \left[\dfrac{E(\kappa^2)}{K(\kappa^2)} - 1 + \dfrac{\kappa^2}{2} \right] + \varepsilon_o^2 \left(\dfrac{\zeta_m - 1/\sqrt{M}}{1 - 1/\sqrt{M}} \right) , & \kappa^2 < 1 . \end{cases}$$

$$\langle \underline{v}_{d_B} \cdot \underline{\nabla}\alpha \rangle = -\frac{(1/2)mv^2}{Ze}\left(\frac{\varepsilon}{\varepsilon_o}\right) r_1 \sin\beta\left[1 - \left(\frac{\varepsilon}{\varepsilon_o}\right)\frac{2}{k_1 r}\frac{\partial \hat{h}}{\partial r}\right]$$

$$\times \left[g_1(\zeta_m) - g(\zeta_m)\right]\tau_b + \frac{(1/2)mv^2}{Ze}\left(\frac{\varepsilon}{\varepsilon_o}\right)^2 r_1 \sin 2\beta\left(\frac{1}{k_1^2 r_1}\right) g(\zeta_m \tau_b) \ , \qquad (44)$$

where

$$g(\zeta_m) = \begin{cases} 1 + \zeta_m^2\left\{\kappa^2\left[\frac{E(1/\kappa^2)}{\kappa(1/\kappa^2)} - \left(1 - \frac{1}{\kappa^2}\right)\right]\right\} , & \kappa^2 > 1 \\ 1 + \zeta_m^2 \frac{E(\kappa^2)}{K(\kappa^2)} , & \kappa^2 < 1 \end{cases} \qquad (45)$$

and

$$g_1(\zeta_m) = \begin{cases} 2\left[1 - \frac{E(1/\kappa^2)}{K(1/\kappa^2)}\right] + 2\zeta_m^2\left\{\frac{1-\kappa^2}{3\kappa^2} + \frac{2\kappa^2 - 1}{3}\left[\frac{E(1/\kappa^2)}{\kappa(1/\kappa^2} - \left(1 - \frac{1}{\kappa^2}\right)\right]\right\} , & \kappa^2 > 1 \\ \frac{2}{\kappa^2}\left[1 - \frac{E(\kappa^2)}{K(\kappa^2)}\right] + 2\zeta_m^2\left[\frac{1-\kappa^2}{3\kappa^2} + \frac{2\kappa^2 - 1}{3\kappa^2}\frac{E(\kappa^2)}{\kappa(\kappa^2)}\right] , & \kappa^2 > 1 . \end{cases} \qquad (46)$$

The total radial drift $V = \langle \underline{v}_d \cdot \underline{\nabla}\alpha \rangle$ is the sum of Eqs. (44) and (41). Equation (44) contains both the effect of taking the plasma center to be off the geometric center [in the function $g_1(\zeta_m)$] and the effect of noncircularity of the pressure surface (through the function $\hat{h}$).

4. THE COLLISIONLESS DISTRIBUTION FUNCTION AND THE ASSOCIATED DIFFUSION COEFFICIENTS

The steady-state bounce-averaged drift kinetic equation is

$$V \frac{\partial f}{\partial \alpha} + \Omega \frac{\partial f}{\partial \beta} = \nu(f) \ , \tag{53}$$

where

$$\nu(f) = \langle C(f) \rangle \tag{47}$$

and C(f) is the Fokker-Planck collision operator.

If we expand Eq. (46) to first order in $(\varepsilon/\varepsilon_o)$ and then to zeroth order in the collisionality ($\nu_{ei}/\Omega_{th} << 1$), we obtain

$$f = -\frac{1}{\Omega} \int V d\beta \frac{\partial F_M}{\partial \alpha} \ , \tag{55}$$

where F_M is a Maxwellian distribution.

We define the generalized forces A_1 and A_2 by

$$A_1 = \frac{1}{n} \frac{dn}{d\alpha} + \frac{1}{T} \frac{dT}{d\alpha} + \frac{Ze}{T} \frac{d\phi_o}{d\alpha} \ , \tag{56}$$

$$A_2 = \frac{1}{T} \frac{dT}{d\alpha} \ , \tag{57}$$

and expand the potential $\phi(\alpha, \beta)$ as

$$\phi(\alpha,\beta) = \phi_o(\alpha) + \phi_1(\alpha,\beta) \ , \tag{58}$$

where $\phi_1 << \phi_o$. From Eqs. (55), (47), (44), and (41), we obtain

$$\frac{f}{F_M} = (r_1 R_c B_{m_o}) \left[r_1 \left(\frac{\varepsilon}{\varepsilon_o}\right) a^2\right] \left\{\frac{x^2}{w_o} \left[g_1(\zeta_m) - g(\zeta_m)\right]\left[1 - \frac{x^2}{w_o} \bar{h}(\zeta_m)\right]\right\}$$

$$\times \left[\cos\beta - \left(\frac{\varepsilon}{\varepsilon_o}\right) \frac{2}{r_1} h_2(r_1,\beta)\right] \left(A_1 - \frac{5}{2} A_2 + x^2 A_2\right)$$

$$+ \frac{a^2 \phi_1(\alpha,\beta)}{\Omega_E} \left[1 - \frac{x^2}{w_o} \bar{h}(\zeta_m)\right]\left[A_1 - \frac{5}{2} A_2 + x^2 A_2\right] \ , \tag{59}$$

where

$$\Omega_E = a^2 \Omega_{th} w_o \ , \tag{60}$$

and

$$h_2(r_1,\beta) = 2b_{10} \cos\beta I_1(k_1 r_1) + \frac{b_{11}}{2} \cos 2\beta \left[I_2(k_1 r_1) + \frac{I_1(k_1 r_1)}{k_1 r_1}\right]$$

$$+ \frac{1}{2} \left\{ \sum_{m=2}^{\infty} \left[\frac{b_{1m} e^{i(m+1)\beta} + b_{1m}^* e^{-i(m+1)\beta}}{(m+1)}\right] - \left[\frac{b_{1m} e^{i(m-1)\beta} + b_{1m}^* e^{-i(m-1)\beta}}{(m-1)}\right]\right.$$

$$\times \left.\left[I_{m+1}(k_1 r) + \frac{m I_m(k_1 r_1)}{k_1 r_1}\right]\right\} \tag{61}$$

Note that in Eq. (59), we have taken the large electric field approximation ($w_o >> 1$).

The first-order potential ϕ_1 can be computed from the requirement of first-order quasi-neutrality. The total first-order density is given by

$$n_{1_j} = \frac{1}{\int d\ell/B} \int \frac{d\ell}{B} \int d^3v \; f - \frac{nZ_j e\phi_1}{k_b T} , \tag{62}$$

where we assume that both the ions and electrons are collisionless. In Eq. (62) the first term arises from the displacement of the particle orbits due to toroidal effects and the second term comes from the density perturbation induced by the first-order potential. When we impose quasi-neutrality in the above manner, we obtain for the self-consistent potential

$$\phi_1 = r_1^2 B_{m_o} \left(\frac{\varepsilon}{\varepsilon_o}\right) \left(R_c \frac{\partial\phi_o}{\partial\alpha}\right) \left\{ \left(\frac{a_{001} - a_{010}}{a_{100}}\right) \left[\cos\beta - \left(\frac{\varepsilon}{\varepsilon_o}\right) \frac{2}{r_1} h_2(r,\beta)\right] \right.$$

$$\left. + \left(\frac{\varepsilon}{\varepsilon_o}\right) \frac{a_{010}}{a_{100}} \frac{\cos 2\beta}{2k_1^2 r_1} \right\} , \tag{63}$$

where

$$a_{kmn} = \int_0^1 d\zeta_m \left(\frac{v\zeta_m \tau_b}{\int d\ell \, B_m/B}\right) \bar{h}^k(\zeta_m) g^m(\zeta_m) g_1^n(\zeta_m) . \tag{64}$$

We define the pressure surface average of a function F by

$$\langle F \rangle_v = \frac{1}{V'_\ell} \oint d\beta \int \frac{d\ell}{B} F , \tag{65}$$

where

$$V'_{\ell}(\alpha) = \oint d\beta \oint \frac{\delta \ell}{B} \ . \tag{66}$$

Then the surface-averaged particle and energy fluxes are given by

$$\Gamma = \langle \int d^3v \ \underline{v}_d \cdot \underline{\nabla}\alpha f \rangle_v \ , \tag{67}$$

$$Q = \langle \int d^3v \ (\frac{1}{2} mv^2)(\underline{v}_d \cdot \underline{\nabla}\alpha) f \rangle_v \ . \tag{68}$$

If we define the rate of irreversible entropy production

$$\Theta = - \langle \int d^3v (\frac{f}{F_m}) \ C(f) \rangle_v \ , \tag{69}$$

then we can write[4]

$$\Theta = L_{11}A_1^2 + 2L_{12}A_1A_2 + L_{22}A_2^2 \ , \tag{70}$$

and the fluxes can be written as

$$\Gamma = -L_{11}A_1 - L_{12}A_2 \ , \tag{71}$$

$$(Q - \frac{5}{2} \Gamma T)/T = -L_{12}A_1 - L_{22}A_2 \ . \tag{72}$$

For a collision operator we choose the differential collision operator of Hirshman and Sigmar[7] and specialize it for electrons and ions. Hence we have

$$C(f) = \frac{\nu_D^e}{2} \frac{\partial}{\partial \zeta_p} \left(1 - \zeta_p^2\right) \frac{\partial f}{\partial \zeta_p}$$

$$+ \frac{1}{v^2} \frac{\partial}{\partial v} \left[\frac{v^4}{2} \left[\nu_{\parallel}^{ee} F_{M_e} \left(\frac{\partial}{\partial v} n_{e_1} - 2q_{ee} \frac{v}{v_{the}^2}\right)\right]\right] , \tag{73}$$

where

$$\nu_D^e(v) = \nu_{ei} \left[1 + \mathrm{erf}\left(\frac{v}{v_{the}}\right) - G\left(\frac{v}{v_{the}}\right)\right] / \left(\frac{v}{v_{the}}\right)^3 \tag{74}$$

with v_{the} being the electron thermal velocity, $G(x) = [\mathrm{erf}(x) - 2x/\sqrt{\pi}e^{-x^2})/2x^2$ and $\nu_{\parallel}^{ee} = 2\nu_{ee}G(v/v_{the})/(v/v_{the})^3$. The 90° scattering time ν_{ab} is given by

$$\nu_{ab} = \frac{4\pi n_b (e_a e_b)^2 \ln \Lambda}{(2T_a)^{3/2} m_a^{1/2}} \tag{75}$$

and n_{e_1} and q_{ee} are

$$n_{e_1} = \frac{1}{2} \int_{-1}^{1} d\zeta_p \frac{f}{F_{M_e}} , \tag{76}$$

$$q_{ee} = \int \frac{1}{2} m v^2 \nu_E^{ee}(v) f \, d^3v / \int \frac{1}{2} m v^2 \left(\frac{v}{v_{the}}\right)^2 \nu_E^{ee} F_{M_e} \, d^3v \quad , \tag{77}$$

with

$$\nu_E^{ee}(v) = 2\nu_s^{ee}(v) - 2\nu_D^{ee}G(v/v_{the})/(v_{the}) \ , \tag{78}$$

$$\nu_s^{ee}(v) = 4\nu_{ee}G(v/v_{the})/(v/v_{the}) \ . \tag{79}$$

The derivative $\partial n_{e1}/\partial r$ is the energy scattering term while q_{ee} is the energy restoring term necessary for energy to be conserved in a collision. The momentum restoring terms are neglected since it can be shown that when the full collision operator is bounce averaged these terms will vanish.

When this operator is used in Eq. (69), for L_{11}, L_{12}, and L_{22} we obtain

$$L_{11} = n(r_1B_{mo})^2R_c^2 \frac{(r\varepsilon a^2)}{w_o^2} \frac{\nu_{ei}}{\sqrt{\pi}} \{M_{00}(1 + \frac{1}{\sqrt{2}}) - \frac{1}{w_o}[(4 + \frac{9}{2\sqrt{2}})M_{02}$$

$$+ \frac{B_{1001}5}{2\sqrt{2}}]\} \ \overline{P}(r;\varepsilon_o) \ , \tag{80}$$

$$L_{12} = n\ (r_1B_{mo})^2R_c^2\frac{(r_1\varepsilon a^2)^2}{w_o^2} \frac{\nu_{ei}}{\sqrt{\pi}} \{M_{00}(\frac{3}{2} + \frac{7}{4\sqrt{2}}) - \frac{5}{4}\ C_2\ \frac{B_{1000}}{\sqrt{2}}$$

$$- \frac{1}{w_o}[M_{02}(2 + \frac{25}{8\sqrt{2}}) + \frac{7}{8}\ \frac{B_{1001}}{\sqrt{2}} + \frac{11}{4\sqrt{2}}\ B_{0110}]\} \ \overline{P} \ , \tag{81}$$

$$L_{22} = n(r_1B_{mo})^2R_c^2 \frac{(r_1\varepsilon a^2)^2}{w_o^2} \frac{\nu_{ei}}{\sqrt{\pi}} \{M_{00}(\frac{9}{4} + \frac{35}{16\sqrt{2}}) + \frac{25}{4}\ C_2\ \frac{B_{1000}}{\sqrt{2}}$$

$$+ \frac{11}{2}\ \frac{B_{0101}}{\sqrt{2}} - \frac{1}{w_o}[M_{02}(13 + \frac{491}{64\sqrt{2}}) + \frac{1839}{32\sqrt{2}}\ B_{1001} + \frac{235}{8\sqrt{2}}\ B_{0110}\ ]\} \ \overline{P} \ , \tag{82}$$

where

$$C_2 = \left(\frac{a_{001} - a_{010}}{a_{100}}\right)\frac{1}{\varepsilon_o} , \tag{83}$$

$$M_{00} = \{N[(g_1')^2] - N[(g')^2]\}\frac{1}{\varepsilon_o^2} + C_2^2 N[(\bar{h}')^2]$$

$$- \frac{2C_2}{\varepsilon_o} N(g_1'\bar{h}') - \frac{2}{\varepsilon_o^2} N(g_1' g') + \frac{C_2}{\varepsilon_o} g N(g'\bar{h}') \tag{84}$$

$$M_{02} = \frac{1}{\varepsilon_o^2}\{N[(g_1')^2\bar{h}] + N(g_1' g_1 \bar{h}')) - 2N[(g_1' g'\bar{h}])$$

$$+ N(g_1 g'\bar{h}') + N(g_1' g\bar{h}') - N((g')^2\bar{h}) + N(\bar{h}' g' g)\}$$

$$+ \frac{C_2}{\varepsilon_o}\{N(g'\bar{h}'\bar{h}) + N[(\bar{h}')^2 g] - N(g_1'\bar{h}'\bar{h}) - N[g_1(\bar{h}')^2]\} \tag{85}$$

$$N[f] = \int_0^1 d\zeta_m \, (1 - \zeta_m^2)\frac{\sqrt{2}}{2}\,\bar{Q}(\zeta_m) f(\zeta_m) , \tag{86}$$

with

$$\tilde{Q}(\zeta_m) = \frac{2}{\sqrt{2}}\frac{1}{2v\zeta_m}\,\frac{1}{\int d\ell/B}\int \frac{d\ell}{B} v_{\parallel}, \tag{87}$$

$$B_{kmnp} = \frac{1}{\int d\ell \, B_{mo}/B}\int_0^1 d\zeta_m \zeta_m b_{km}(\zeta_m) H^n(\zeta_m) G_1^p(\zeta_m), \tag{88}$$

$$G_1(\zeta_m) = \frac{1}{\varepsilon_o}[g_1(\zeta_m) - g(\zeta_m)] - C_2\bar{h}(\zeta_m) , \tag{89}$$

$$H(\zeta_m) = \frac{\bar{h}(\zeta_m)}{\varepsilon_o} \left[g_1(\zeta_m) - g(\zeta_m)\right] , \tag{90}$$

$$b_{km}(\zeta_m) = \int \frac{d\ell}{v_\parallel/v} \int \frac{d\zeta_m \zeta_m}{(v_\parallel/v)(B_m/B)} H^k(\zeta_m) G_1^m(\zeta_m) . \tag{91}$$

Finally, in L_{ij} geometrical function $\bar{P}(r;\varepsilon_o)$ is to $O(\varepsilon/\varepsilon_o)$

$$\bar{P}(r;\varepsilon_o) = \frac{2}{2\pi} \int_0^{2\pi} d\beta \left[\cos^2\beta - 4\left(\frac{\varepsilon}{\varepsilon_o}\right) \frac{1}{r_1} h_2(r_1,\beta)\cos\beta\right]$$

$$= 1 - 4\left(\frac{\varepsilon}{\varepsilon_o}\right) b_{10} + 4\left(\frac{\varepsilon}{\varepsilon_o}\right) \frac{b_{12}}{r_1} \left[I_3(k_1 r_1) + \frac{2I_2(k_1 r_1)}{k_1 r_1}\right] . \tag{92}$$

The function $\bar{P}(r;\varepsilon_o)$ contains the effect of averaging the diffusion coefficients over the noncircular pressure surfaces.

For definition, if we choose $\varepsilon_o = 1/3$ $(M = 2)$ and write

$$\Gamma = -D_n \frac{dn}{d\alpha} - D_T \frac{dT}{d\alpha} - \mu_n n \frac{d\phi_o}{d\alpha} ,$$

$$Q = -K_n \frac{dn}{d\alpha} - K_T \frac{dT}{d\alpha} - \mu_T n \frac{d\phi_o}{d\alpha} ,$$

where μ_n and μ_T are the well-known Einstein mobilities, then

$$D_n = (r_1 B_{mo})^2 R_c^2 \frac{(r_1 \varepsilon a^2)^2}{w_o^2} \nu_{ei} \left(8.308 + \frac{0.018}{w_o}\right)\bar{P} , \tag{93}$$

$$D_T = (r_1 B_{mo})^2 \; R_c^2 \frac{(r_1 \varepsilon a^2)^2}{w_o^2} \; \nu_{ei} \frac{n}{k_b T} \left(20.725 + \frac{0.024}{w_o}\right)\overline{P} \; , \tag{94}$$

$$K_n = (r_1 B_{mo})^2 R_c^2 \frac{(r_1 \varepsilon a^2)^2}{w_o^2} \; \nu_{ei} \; k_b T \left(33.187 + \frac{0.051}{w_o}\right)\overline{P} \; , \tag{95}$$

$$K_T = (r_1 B_{mo})^2 \; R_c^2 \frac{(r_1 \varepsilon a^2)^2}{w_o^2} \; \nu_{ei} n \; \left(87.291 - \frac{0.761}{w_o}\right)\overline{P} \; . \tag{96}$$

For comparison the diffusion coefficients in Ref. 2 are

$$D_n = (r_1 B_{mo})^2 R_c^2 \frac{(r_1 \varepsilon a^2)^2}{w_o^2} \; \nu_{ei} \; \left(0.274 + \frac{1.824}{w_o}\right) \; , \tag{97}$$

$$D_T = \frac{n}{k_b T} \; R_c^2 (r_1 B_{mo})^2 \frac{(r_1 \varepsilon a^2)^2}{w_o^2} \; \nu_{ei} \; \left(0.548 + \frac{3.624}{w_o}\right) \; , \tag{98}$$

$$K_n = k_b T (r_1 B_{mo})^2 R_c^2 \frac{(r_1 \varepsilon a^2)^2}{w_o^2} \; \nu_{ei} \; \left(0.958 + \frac{5.76}{w_o}\right) \; , \tag{99}$$

$$K_T = n R_c^2 (r_1 B_{mo})^2 \frac{(r_1 \varepsilon a^2)^2}{w_o^2} \; \nu_{ei} \; (14.07). \tag{100}$$

5. DISCUSSION AND CONCLUSIONS

We note that the expressions in Eqs. (93)-(96) are substantially larger than those in Eqs. (97)-(100). This difference arises mainly due to the fact that the plasma center, is at the $\oint d\ell/B$ center, which for ε_o =

1/3 is highly shifted from the geometric center. Mathematically, we can see that the expansion parameter in the distribution function is $(\varepsilon/\varepsilon_o)$ and not ε, which it would be if the plasma center coincided with the geometric center. Since the diffusion coefficients scale as $\varepsilon^2/\varepsilon_o^2$, this should increase them by almost an order of magnitude. Some of this increase is tempered by the fact that the differential collision operator correctly includes the falloff in velocity space of the collision frequency and the BGK operator used in Ref. 2 does not.

We also note that the effect of noncircularity is to mulitply the diffusion coefficients by a geometrical factor of O(1). In Eq. (92), we can take $b_{10} = 0$ since from Eq. (33) it is clear that b_{10} will only change the U surface value. Then, on comparing $\bar{P}$ and e_ℓ as given in Eq. (23), we see that for $r \ll 1$ and to $O(\varepsilon/\varepsilon_o)$ $\bar{P} = 1/e_\ell^2$. Therefore, the diffusion coefficients can be written as $D_{noncir} = D_{cir}/e_\ell^2$, where D_{cir} is the diffusion coefficient associated with circular pressure surfaces and D_{noncir} is the diffusion coefficient associated with noncircular pressure surfaces. This result is well known in tokamak neoclassical theory and occurs here for the same reason. That is, it is the vertical drift through the pressure surfaces which determines the magnitude of the diffusion coefficients, and for surfaces with $e_\ell > 1$ there is less vertical drift through the pressure surfaces than for $e_\ell = 1$. Conversely, for $e_\ell < 1$ there is more and the diffusion coefficients are increased. We speculate that the above conclusion holds even outside the range of our approximations and hence bumpy torii with ellipitical-shaped surfaces with $e_\ell > 1$ will have intrinsically less diffusion than bumpy torii with circular coils.

From the above results, it is clear that the performance of bumpy torii can be substantially improved by centering the $\oint d\ell/B$ surfaces and by making the pressure surface elliptical.

In conclusion, we have shown the importance of treating the shift of the plasma in the diffusion coefficients and that noncircular pressure surfaces can have less diffusion for a bumpy torus than circular pressure surfaces.

REFERENCES

[1]L. M. Kovrizhnykh, Sov. Phys. JETP 29, 475 (1969).

[2]D. E. Hastings and D. A. Spong, Phys. Fluids 26, 1551 (1983).

[3]D. E. Hastings, J. S. Tolliver, and C. L. Hedrick, "Nonresonant EBT Transport Coefficients in the Small Electric Field Regime," submitted to Physics of Fluids.

[4]D. E. Hastings, "Electron Transport in EBT in the Low Collisionality Frequency Limit," submitted to Physics of Fluids.

[5]R. D. Hazeltine and P. J. Catto, Phys. Fluids 25, 2022 (1982).

[6]L. W. Owen, Oak Ridge National Laboratory, private communication.

[7]S. P. Hirshman and D. J. Sigmar, Phys. Fluids 19, 1532 (1976).

COMPARISON OF MAGNETIC EQUILIBRIA AND LOW FREQUENCY STABILITY FOR EBT AND EBS*

C. L. Hedrick
Oak Ridge National Laboratory
Oak Ridge, TN 37830

ABSTRACT

Analytic approximations are developed for the magnetic equilibria of both a standard EBT and ELMO Bumpy Square (EBS) or Racetrack (EBR). Sufficient toroidal effects are included to distinguish the low frequency stability properties of the two classes of devices. To illustrate the application of the equilibrium quantities, simple analytic results based on the so-called rigid ring stability model are presented. Examination of more detailed stability theories which include effects leading to the Lee-Van Dam-Nelson limit will be presented as time permits.

---

*Research sponsored by the Office of Fusion Energy, U.S. Department of Energy, under contract W-7405-eng-26 with the Union Carbide Corporation.

****

Editor's Note: The manuscript for this paper did not arrive in time to be included in these proceedings. The abstract submitted to the workshop is included here for the purpose of completeness. — N. A. Uckan

****

WAVE INTERACTIONS WITH EBT PLASMAS IN THE MAGNETIC DRIFT FREQUENCY RANGE*

J. B. McBride
Science Applications, Inc.
La Jolla, California 92038

M. Rosenberg and N. A. Krall
JAYCOR
San Diego, California 92138

ABSTRACT

We calculate the particle and energy transport and heating that results from the resonant, quasilinear interaction of EBT plasma particles with waves in the magnetic drift frequency range. Substantial transport can occur even for relatively small wave field amplitudes. For example, for flute perturbations of relative amplitude $\delta B/B$, the wave induced diffusion can exceed neoclassical diffusion in the collisionless regime for $\delta B/B \sim (\nu/\omega_\nabla)^{1/2} A^{-1}$, where A^{-1} is the inverse aspect ratio and ν, ω_∇ are the collision and thermal grad B drift frequencies, respectively. The diffusion is selective and can cause preferential transport of a single sign of charge or energy component. Possible applications include plasma pressure and ambipolar potential profile modification, instability induced transport arising from curvature or drift modes and α-ash removal. In addition, this type of wave-particle interaction may play a role in the observed changes in EBT-S electron ring parameters during ICH experiments.

1. INTRODUCTION

This paper describes the initial results of a study of transport and heating of EBT plasmas due to the resonant, quasilinear interaction of waves with plasma particles in the magnetic precessional drift frequency range. The primary motivation for this study is to examine the possibility

---

*This work was supported by the U.S. Department of Energy.

of altering the plasma and potential profiles by means of low frequency RF. Other applications of the transport calculations presented here are to the heating of ring electrons during ICH experiments on EBT-S, instability transport from curvature driven modes and drift waves when the magnetic and density gradients are comparable, and α-ash removal.

In Section 2 we use a slab model which treats the essential resonant interaction of waves with the particle grad B drift motion, to write an equation for the quasilinear rate of change of the particle distribution function. By taking moments of this equation, we generate expressions for the resonant particle and energy fluxes and the wave heating. In Section 3 we include the parallel velocity dependence of the curvature drifts in the so-called "z-pinch" model[1] of EBT to calculate the radial transport for comparison. Section 4 describes the general features of the results, and Section 5 contains a summary.

2. TRANSPORT EQUATIONS IN SLAB GEOMETRY

In this section we use the well known slab model[2] to derive a set of transport equations for particle and energy diffusion and heating due to the resonant quasilinear interaction of waves in the gradient B drift frequency range in EBT plasmas. The slab model contains the essential feature of the gradient B drift resonance which gives rise to the plasma transport and heating, but includes curvature effects simply through an assumed constant gravity. In the next section, we discuss the effects of including the parallel velocity dependence of the curvature drifts.

Using standard techniques[2], the solution to the linearized Vlasov equation in slab geometry is[3]

$$\delta f = -\frac{q}{m}\sum J_p \frac{\exp[i(p-\ell)(\phi-\pi/2)]}{\omega' - kV_B - \ell\omega_c}\left\{\frac{v_\perp}{kc}\left[2\omega'\frac{\partial F_0}{\partial v_\perp^2} + \frac{k}{\omega_c}\frac{\partial F_0}{\partial x}\right] J_\ell' \delta B\right.$$

$$\left. - \frac{i}{k}\left[2(\ell\omega_c + kV_B)\frac{\partial F_0}{\partial v_\perp^2} + \frac{k}{\omega_c}\frac{\partial F_0}{\partial x}\right] J_\ell \delta E\right\} \quad . \tag{1}$$

The equilibrium distribution function in Eq. (1) is

$$F_0 = n \left(\frac{m}{2\pi T}\right)^{3/2} \exp\left[-\frac{m(v_\perp^2 + v_\parallel^2)}{2T}\right]$$

The wave vector has been chosen to be in the y (poloidal) direction, x corresponds to the radial direction and z corresponds to the toroidal direction in EBT. Flute perturbations of the magnetic field have been assumed, i.e., $\delta\underset{\sim}{B}$ is in the z-direction and δE is the wave electrostatic field component in the y direction. The grad B drift speed is $V_B = v_\perp^2/2\omega_c L_B$ where $L_B = [(1/B)(dB/dx)]^{-1}$ and $\omega_c = qB/mc$. The argument of the Bessel functions is $k\, v_\perp/\omega_c$ and $\omega' = \omega - kV_E - kV_g$, where V_E and V_g are the equilibrium $\underset{\sim}{E}\times\underset{\sim}{B}$ and curvature drifts. Since V_E and V_g are constant, independent of particle velocity, the equilibrium electric and curvature drifts do not affect the transport calculations other than through ω'.

Transport coefficients can be calculated directly from Eq. (1) by taking moments of the Vlasov equation to generate a coupled set of fluid equations in the usual way. Perturbation theory is then applied to the fluid equations to generate a set of fluid-transport equations to quasilinear (second) order in the perturbations. The method has been described in detail by Krall and McBride[4] and by Tange et al.[5]. For example, the "radial" (x-component) particle flux calculated in this way is

$$\Gamma_x = \frac{c}{B} \langle \delta n \delta E_y - \delta\Gamma_x \delta B_z/c \rangle \tag{2}$$

where $\delta n = \int d^3v \delta f$ and $\delta\Gamma_x = \int d^3v\, v_x \delta f$. Using the delta function representation of $(\omega' - kV_B)^{-1}$ to write

$$(\omega' - kV_B)^{-1} = -\frac{i\pi v_0^2}{|\omega_\nabla|}\, \delta\left(\frac{v_\perp^2}{2} - \frac{\omega' v_0^2}{\omega_\nabla}\right) \tag{3}$$

the resonant contribution to the particle flux is readily evaluated to give

$$D = \frac{2\sqrt{2\pi}}{|\omega_\nabla|} \frac{e^{-\omega'/\omega_\nabla}}{B^2} \int_0^{x_0} dx\ |\delta W|^2\ G(x) \tag{4}$$

We have defined

$$\delta W = J_0 \delta E - i \frac{v_\perp}{c} J_0'\ \delta B$$

$$G(x) = e^{-x^2/2} \left[1 - \frac{\omega'}{\omega_*} - \eta_T\left(\frac{3}{2} - \frac{x^2}{2} - \frac{\omega'}{\omega_\nabla}\right)\right]$$

and δW is evaluated at $v_\perp = (2\omega' v_0{}^2/\omega_\nabla)^{1/2}$. Note that the existence of resonant particles requires $\omega'/\omega_\nabla > 0$. Also we have introduced a cutoff to the $v_\parallel$ integral ($x = v_\parallel/v_0$) recognizing that since, in fact, the curvature drift depends on $v_\parallel$, resonance can occur only for particles with $v_\parallel$ below a certain value. As we shall see in the next section, the value of x_0 that emerges from a proper treatment of the $v_\parallel$ dependence of the curvature drift is $x_0 = \omega R_c/\omega_\nabla L_B$. We have defined $\Gamma_x = -D dn/dx$, $\omega_\nabla = kv_0{}^2/\omega_c L_B$, $\omega_* = kv_0{}^2/\omega_c L_n$, $v_0{}^2 = T/m$, $\eta_T = L_n/L_T$, $L_n = [(1/n)(dn/dx)]^{-1}$, $L_T = [(1/T)(dT/dx)]^{-1}$.

In principle the transport effects associated with the higher order moment equations can also be calculated using similar procedures, e.g., the energy flux. However, the algebraic complexity associated with generating the full transport matrix makes it desirable to use, as a general starting point, an equation for the slow, quasilinear evolution of the distribution function, f, directly. Thus, using Eq. (1) for δf, we have used the standard procedure[6] for obtaining the quasilinear rate of change of f. The result is (see Appendix A for a brief outline of the derivation)

$$\frac{\partial f}{\partial t} = -\,2\mathrm{Im} \sum_{k>0} \left(\frac{q}{m}\right)^2 \left(\frac{1}{\omega_c}\frac{\partial}{\partial x} + 2V_B \frac{\partial}{\partial v_\perp{}^2}\right) \frac{|J_0 \delta E - i\,\frac{v_\perp}{c} J_0{}' \delta B|^2}{\omega' - kV_B}$$

$$\bullet \left(\frac{1}{\omega_c}\frac{\partial}{\partial x} + 2V_B \frac{\partial}{\partial v_\perp{}^2}\right) F_0 \tag{5}$$

We have retained only the $\ell = 0$ term in the Bessel series summation since we are interested in resonant transport for $\omega \sim \omega_\nabla$.

The effects of the waves on particle and energy confinement and plasma heating can now be obtained by calculating $\int d^3v\, \partial f/\partial t \equiv \partial n/\partial t$ and $\int d^3v\, (m/2)(v_\parallel{}^2 + v_\perp{}^2)\, \partial f/\partial t \equiv (3/2)(\partial nT/\partial t)$ directly from Eq. (5). Using Eq. (3), we obtain

$$\frac{\partial n}{\partial t} = \frac{\partial}{\partial x} D \frac{\partial n}{\partial x} \tag{6}$$

$$\frac{3}{2}\,\frac{\partial nT}{\partial t} = -\frac{\partial}{\partial x} Q + P \tag{7}$$

where D is given by Eq. (4), and Q, P are the wave induced energy flux and the effective wave heating, respectively, given by

$$Q = -\frac{2\sqrt{2\pi}}{|\omega_\nabla|}\,\frac{nT^{-\omega'/\omega_\nabla}}{L_n B^2} \int_0^{x_0} dx\left(\frac{\omega'}{\omega_\nabla} + \frac{x^2}{2}\right) |\delta W|^2\, G(x) \tag{8a}$$

$$P = -\frac{\omega'}{\omega_\nabla}\,\frac{nT\,D}{L_B L_n} \tag{8b}$$

Eqs. (6) and (7) are in a form suitable for incoporation into 1-D transport codes[7,8] to study the effects of waves near $\omega \sim \omega_\nabla$ on the confinement of EBT plasmas, in addition to the classical and neoclassical transport terms already included in these codes.

3. TRANSPORT EQUATIONS IN THE Z-PINCH MODEL

In this section we present the transport equations analogous to Eqs. (6) and (7) for the so-called "z-pinch" model used by Berk et al.[1] to study linear stability of curvature driven modes. In this model the magnetic field lines are circular so that the field line curvature is present in a natural way, albeit simplified to avoid having to perform field line integrations (bounce averages) in the more complicated geometry of EBT. We use the Berk et al.[1] small Larmor radius solution to the linearized drift kinetic equation, i.e.,

$$\delta f = \frac{i}{(\omega' - kV_B - kV_c)} \left[\left(\frac{i\,k\,\mu\delta B}{qB} - \frac{\delta E}{B} \right) \frac{\partial F_0}{\partial r} + \left(i\omega'\mu\delta B + q\delta E(V_B + V_c) \right) \frac{\partial F}{\partial H} \right] \tag{9}$$

$$\omega' = \omega - kV_E$$

$$V_B \equiv \frac{\mu}{qL_B} \quad , \quad \mu = \frac{mv_\perp^2}{2B}$$

$$V_c \equiv \frac{-mv_\parallel^2}{qBr}$$

The equilibrium distribution is a function of H, μ, r. We will use the Maxwellian

$$F_0 = n\left(\frac{m}{2\pi T}\right)^{3/2} \exp(-H/T) \quad ,$$

as we did in Section 2. Using this linear solution to the drift kinetic equation, the slow, quasilinear rate of change of the distribution function is

$$\frac{\partial f}{\partial t} = -2\ \mathrm{Im} \sum_{k>0} \frac{1}{B}\left(\frac{\partial}{\partial r} + 2qBV_c \frac{\partial}{\partial v_\parallel{}^2}\right) \frac{\left|\delta E - \frac{ik\mu\delta B}{q}\right|^2}{\omega' - kV_B - kV_c}\left(\frac{\partial}{\partial r}\right.$$

$$\left. + 2qBV_c \frac{\partial}{\partial v_\parallel{}^2}\right) F_0 \tag{10}$$

We have changed variables from H,μ,r to $v_\parallel{}^2,\mu,r$ using $H = \mu B + mv_\parallel{}^2/2$.

The resonant transport equations analogous to Eqs. (6) and (7) may be obtained from Eq. (10) by defining $(2\pi/m)\int B d\mu dv_\parallel\ \partial f/\partial t = \partial n/\partial t$ and $(2\pi/m)\int B d\mu dv_\parallel\ (\mu B + mv_\parallel{}^2/2) = (3/2)\partial nT/\partial t$. The μ-integration is readily performed using

$$(\omega' - kV_B - kV_c)^{-1} = \frac{-i\pi v_0{}^2}{|\omega_\nabla| B}\,\delta\left[\,\mu - \frac{v_0{}^2}{\omega_\nabla B}\,(\omega' - \eta_c\omega_\nabla x^2)\,\right] \tag{11}$$

to give

$$\frac{\partial n}{\partial t} = \frac{1}{r}\,\frac{\partial}{\partial r}\, rD\,\frac{\partial n}{\partial r} \tag{12}$$

$$\frac{3}{2}\,\frac{\partial nT}{\partial t} = -\frac{1}{r}\,\frac{\partial}{\partial r}\, rQ + P \tag{13}$$

$$D = \frac{2\sqrt{2\pi}}{|\omega_\nabla|} \frac{e^{-\omega'/\omega_\nabla}}{B^2} \int_0^{x_0} dx\ |\delta W|^2\ G(x) \tag{14a}$$

$$Q = -\frac{2\sqrt{2\pi}}{|\omega_\nabla|} \frac{nTe^{-\omega'/\omega_\nabla}}{L_n B^2} \int_0^{x_0} dx\left[\frac{\omega'}{\omega_\nabla} + \frac{x^2}{2}(1-2\eta_c)\right]\ |\delta W|^2\ G(x) \tag{14b}$$

$$P = -\frac{\omega'}{\omega_\nabla} \frac{nT\ D}{L_B L_n} \quad . \tag{14c}$$

We have made the following definitions

$$\delta w = \delta E - i\omega' L_B(1-x^2/x_0{}^2)\delta B$$

$$G(x) = \exp\left[\ x^2(\eta_c - \frac{1}{2})\right]\ \ 1 - \frac{\omega'}{\omega_*} - \eta_T\left(\frac{3}{2} - \frac{\omega'}{\omega_\nabla} + \frac{x^2}{x_0{}^2}\left(\frac{\omega'}{\omega_\nabla} - \frac{x_0{}^2}{2}\right)\right)\ ]$$

$$x = v_\parallel/v_0$$

$$x_0 = \omega'/\eta_c\omega_\nabla$$

$$\eta_c = \frac{L_B}{R_c} > 0 \qquad (R_c = -r \text{ in this model})$$

Note that contact between the "z-pinch" model and the EBT magnetic geometry is made by replacing r by $-R_c$ in the transport coefficients, where R_c is the average radius of curvature of a field line. From Eq. (11) we see that $\omega'/\omega_\nabla > 0$ and $x^2 < x_0{}^2 \equiv \omega'/\eta_c\omega_\nabla$ are required for resonant particles ($\mu>0$). Note that Eqs. (12)-(14) are identical to Eqs. (6)-(8) for $R_c \to \infty$ and for finite R_c the differences are non essential.

4. DISCUSSION OF RESULTS

Equations (12)-(14) can be incorporated into 1-D EBT transport codes. This will be required to study the effects of wave induced transport on the details of EBT plasma dynamics and steady state profiles. In this section we will discuss some general features of the transport properties calculated in the previous section and indicate some potential applications.

We first note that the diffusion is selective. Resonant transport requires $\omega/\omega_\nabla > 0$. (We drop the prime on ω in what follows but must remember that $\omega \to \omega - kV_E$ for the radial electric fields of EBT.) Thus for a given wave mode, $\omega(k)$, resonance is possible only for one sign of the charge, since ω_∇ depends on the charge of a species. Since the diffusion is peaked around $\omega \sim \omega_\nabla$, it is also selective with respect to energy. Thus a single species with two separated energy components, or two different positively charged species with separated energies, e.g., the α-particles and thermal fuel ions of a reacting EBT plasma, would be subject to selective diffusion. Due to the selective nature of the process, this means of altering diffusion might be used to control the ambipolar potential profile.

We further note that the diffusion coefficient in Eq. (14a) can be negative if $G(x)$ is negative. For weak temperature gradients, this condition is

$$1 - \frac{\omega}{\omega_*} < 0 \tag{15}$$

Since $\omega/\omega_\nabla > 0$, wave induced inward diffusion could occur, in principal, if $\omega \sim \omega_\nabla$ and $L_n > L_B$, as it would be in the core EBT plasma for neoclassical transport. If the magnitude of the induced diffusion can be made larger than neoclassical (a condition for this to occur is given below), substantial improvement in confinement and control over the shape of the

plasma profiles may be possible if Eq. (15) can be satisfied. We emphasize that it must be possible to propagate waves with precisely the right characteristics to exert this degree of control. Whether this is theoretically possible remains to be shown. Thus a study of linear wave excitation and propagation in EBT for $\omega \sim \omega_\nabla$ and $L_B \lesssim L_n$ must be performed before the utility of this process can be assessed.

In order for the wave induced transport to be important in practice, it would have to be comparable to or larger than the residual neoclassical transport. A condition on the amplitude of the wave fields for the quasilinear diffusion to exceed neoclassical can be obtained from Eq.(14). In the case of Kovrizhnykh neoclassical transport[9] (e.g., electrons for $E < 0$, as in EBT-S), we may write

$$\frac{|\delta B|}{B} > \frac{1}{(12\sqrt{2\pi})^{1/2}} \frac{1}{\eta_c} \frac{r}{R_T} \left(\frac{\nu|\omega_\nabla|}{\omega^2}\right)^{1/2}$$

$$\frac{(1 + 2\eta_T - qEL_n/T)^{1/2}}{[\nu^2/\Omega_0{}^2 + (1 - qER_c/T)^2]^{1/2}} \frac{e^{\omega/2\omega_\nabla}}{|I_1|^{1/2}} \tag{16}$$

as the condition on the flute perturbation of the equilibrium magnetic field. We have defined

$$I_1 = \int_0^{x_0} dx(1 - x^2/x_0{}^2)^2 \; G(x)$$

$$\Omega_0 = T/qBR_c r$$

For collisionless plasmas and $\omega \sim \omega_\nabla$, this condition is roughly

$$\frac{|\delta B|}{B} \sim \sigma \left(\frac{\nu}{|\omega_\nabla|}\right)^{1/2} A^{-1} \quad ; \quad (A = R_T/a) \tag{17}$$

where σ is a number which depends upon details of the profiles, but is less than unity. Thus the induced diffusion can exceed neoclassical even for very small perturbations (wave amplitudes) to the equilibrium magnetic field. In steady state the RF induced flux and the neoclassical flux of the one (resonant) species must balance the neoclassical flux of the other species for charge neutrality. The ambipolarity condition will determine the consistent profile shapes and ambipolar fields for a given operating density and temperature. For wave amplitudes satisfying Eq. (16) in the initial plasma steady state, i.e., before the application of RF, we would expect significant changes in the final operating state (ambipolar electric field, plasma profiles).

It is also interesting to write the condition for wave induced transport to dominate neoclassical in terms of the electrostatic component of the wave field. Using Poisson's equation and Eq. (14), the condition on the size of the density fluctuations required to induce diffusion greater than neoclassical is

$$\frac{|\delta n|}{n} > \frac{1}{(12\sqrt{2\pi})^{1/2}} \frac{k^2\lambda_D^2}{|\chi|\eta_c} \frac{r}{R_T} \left(\frac{\nu}{|\omega_\nabla|}\right)^{1/2}$$

$$\bullet \frac{(1 + 2\,\eta_T - qEL_n/T)^{1/2}}{[\nu^2/\Omega_0^2 + (1 - qR_cE/T)^2]^{1/2}} \frac{e^{\omega/2\omega_\nabla}}{(|I_2|)^{1/2}} \tag{18}$$

where

$$I_2 \equiv \int_0^{x_0} dx G(x)$$

and χ is the linear susceptibility. For a wave with poloidal mode number ℓ, we may take $k = \ell/r$ in Eq. (18). Thus this condition may be useful in

conjunction with stability theory of intermediate to high ℓ-number curvature driven modes to determine the practical importance of these modes from the standpoint of the transport they can be expected to cause (the quantity $|\delta n|/n$ is measured in EBT experiments). For the hot electron rings the meaningful measure of $\delta n/n$ is the level above which instability induced losses exceed those due to the dominant classical ring power loss mechanism, e.g., hot electron drag on the background in EBT-S, i.e., $D > \Delta^2 \tau_d^{-1}$ (D is given by Eq. (14a), Δ is the ring halfwidth and τ_d^{-1} is the drag rate). The condition is approximately

$$\frac{|\delta n|}{n} \sim \frac{k^2 \lambda_D^2}{(|\omega_\nabla| \tau_d)^{1/2}} \frac{\Delta}{|L_B|} \frac{1}{|\chi|} \quad .$$

For completeness we also give the conditions corresponding to Eqs. (16)-(18) for particles diffusing according to neoclassical plateau transport[10]. These conditions are

$$\frac{|\delta B|}{B} > \frac{1}{(2\pi)^{1/4}} \frac{\omega_\nabla}{\omega} \frac{1}{\sqrt{\eta_c}} \frac{r}{R_T} \frac{1}{(kr)^{1/2}} \frac{\exp(qER_c/2T)\ e^{\omega/2\omega_\nabla}}{|I_1|^{1/2}}$$

$$\bullet\ [1 + \eta_T(1 + qER_c/T) - qEL_n/T]^{1/2} \tag{19}$$

$$\frac{|\delta n|}{n} > \frac{k^2 \lambda_D^2}{(2\pi)^{1/4}} \frac{1}{|\chi|\sqrt{\eta_c}} \frac{r}{R_T} \frac{1}{(kr)^{1/2}} \frac{\exp(qER_c/2T)\ e^{\omega/2\omega_\nabla}}{|I_2|^{1/2}}$$

$$\bullet\ [\ 1 + \eta_T(1 + qER_c/T) - qEL_n/T\ ]^{1/2} \quad . \tag{20}$$

Equation (19) for typical cases gives roughly

$$\frac{|\delta B|}{B} \sim \frac{A^{-1}}{\ell^{1/2}} \exp(qER_c/2T) \quad ; \quad qER_c < 0$$

In addition to the possible applications of the above results to bulk plasma transport modification, this type of resonant wave particle interaction may play a role in the observed changes of the hot electron ring properties during ICH experiments on EBT-S where the ring stored energy is observed to nearly double[11] for modest ICH input power (~ 10-15 kW). In these experiments, the input wave power is in the frequency range of the average hot electron gradient B drift frequency. An estimate of the power absorption in the ring electrons can be obtained from Eq. (14c) by taking $\omega = \omega_\nabla$, $L_B = -L_n$, $n(\text{ring}) = 3\text{x}10^{11}$ cm^{-3}, T(ring) = 400 keV, $V(\text{ring}) \simeq 4\pi a^2 N\Delta$, a = 10 cm, Δ = 2 cm, N = 24 (sectors), consistent with experiment[11]. The result is

$$P\text{x } V(\text{ring}) \sim 10^{11} \frac{|\delta B|^2}{B^2} \text{ Watts}$$

Thus for $|\delta B|/B = 2\text{x}10^{-4}$, which corresponds to a wave magnetic field of only 1 gauss, a total of ~ 4 kW of ICH power is absorbed by the ring electrons. This is a sizeable fraction of the ECH power that is estimated to be absorbed by the ring electrons, and is evidence that the process described here may be responsible for the observed increase in ring electron temperature. A more accurate assessment of these effects on ICH of ring electrons would require a detailed knowledge of the ring structure and wave characteristics in the ring region for input to Eqs. (12)-(14).

5. SUMMARY

We have calculated quasilinear plasma transport (particle and energy fluxes and heating) due to the resonant interaction of plasma particles

with waves in the magnetic precessional drift frequency range in EBT. Slab model results were presented to demonstrate the essential grad B drift resonance effects, followed by "z-pinch" model results to illustrate the main effects of curvature in a model where the proper $v_{\parallel}$ dependence of the curvature drifts is included. These results are suitable for use in 1-D transport codes. The transport and heating caused by this type of interaction can be substantial and can exceed neoclassical transport for relatively small wave field amplitudes

$$\delta B/B \sim \left(\frac{\nu}{\omega_\nabla}\right)^{1/2} A^{-1}$$

in collisionless EBT plasmas. The transport is selective and can in principle cause preferential diffusion of a single sign of charge or energy component. In certain situations diffusion may be induced up a density gradient, offering the possibility for improved confinement and profile shaping. However this would require that it be possible to excite waves with very specific characteristics. Inoue and Itoh[12] have shown the possibility of sizeable wave induced inward diffusion in tokamak due to Landau resonance with waves having a nonzero value of $k_{\parallel}$ ($\sim v_0/\omega$). Their results are valid for $\omega \gtrsim \omega_* \gg \omega_\nabla$. When $\omega \sim \omega_* \sim \omega_\nabla$ the inclusion of $k_{\parallel}$ effects (now in progress) in our calculations for EBT will allow application to a wider class of waves. Thus deailed application of the results must await a study of waves in EBT geometry for $L_n \sim L_B \sim L_T$ that could be used in practice to cause this type of transport. It will also require detailed knowledge of the wave field amplitudes in space. Due to the variety of possible applications to EBT (profile/transport modification, α-ash removal, ring electron heating during ICH and instability induced transport) the continued study of this topic seems worthwhile.

ACKNOWLEDGMENT

This work was supported by the U.S. Department of Energy under contract DE-AC01-82-ER53126. One o. the authors (J. McBride) was also partially supported under subcontract 85B-13861/85x60 with Union Carbide Corporation.

REFERENCES

1. H. L. Berk et al., Phys. Fluids 26, 201 (1983).

2. N. A. Krall, in Advances in Plasma Physics, edited by A. Simon and W. B. Thompson (Wiley, New York, 1968), Vol. 1.

3. R. C. Davidson et al., Phys. Fluids 20, 301 (1977).

4. N. A. Krall and J. B. McBride, Nuclear Fusion 17, 713 (1977).

5. T. Tange et al., J. Phys. Soc. Japan 46, 266 (1979).

6. H. L. Berk, J. Plasma Phys. 20, 205 (1978).

7. E. T. Jaeger et al., Nuclear Fusion 19, 1627 (1979).

8. H. H. Klein et al., Science Applications, Inc. Report No. SAI-78-744-LJ/ LAPS-41 (June 1978).

9. L. M. Kovrizhnykh, Sov. Phys. JETP 29, 475 (1969); see also Ref. 7 for a summary of the transport coefficients.

10. R. D. Hazeltine et al., Nuclear Fusion 19, 1597 (1979).

11. F. W. Baity et al., Proc. of the 2nd Hot Electron Ring Workshop, San Diego, CA (December 1-3, 1981) p. 587, and T. L. Owens et al., Nuclear Fusion 23, 49 (1983).

12. S. Inoue and K. Itoh, Proc. 8th Int. Conf. on Controlled Nuclear Fusion Research (Brussels 1980), paper IAEA-CN-38/Z-2.

13. P. J. Catto et al., Plasma Phys. 23, 639 (1981).

APPENDIX A

The quasilinear equation for the slow time evolution of the distribution function f is

$$\frac{\partial f}{\partial t} = \frac{-q}{m} \sum \left(\delta E_{-k} + \frac{v x \delta B_{-k}}{c} \right) \bullet \frac{\partial}{\partial v} \delta f_k \quad , \tag{A-1}$$

where δf_k is given by Eq. (1) in the text. The solution for f is obtained by the method of characteristics. Following Berk[6], (A-1) is integrated over a cyclotron period $\tau_0 = 2\pi/\omega_c$ to obtain

$$f(v_\perp^2, v_\parallel^2, X, t + \tau_0) - f(v_\perp^2, v_\parallel^2, X, t) = \frac{-q}{m} \sum \int_t^{t+\tau_0} dt' \left(\delta E_{-k}(x', t') + \frac{v(t') x \delta B_{-k}(x', t')}{c} \right) \bullet \frac{\partial}{\partial v(t')} \delta f_k(x', v', t') \quad . \tag{A-2}$$

The left-hand side of (A-2) is approximately

$$\tau_0 \frac{\partial f(t)}{\partial t} \quad ,$$

because

$$f(t + \tau_0) = f(t) + \tau_0 \frac{\partial f(t)}{\partial t} \quad .$$

Using[13] $\delta f_k(x',v',t') = \delta f_k(X,v',t')e^{iL'}$, where $L' = \omega_c^{-1}\, k\cdot\hat{z}xv' = \omega_c^{-1}\, kv_\perp\cos(\phi-\omega_c t')$, and approximating the perturbed fields as $\delta A(x',t') \approx \delta A(X,t)$, gives

$$\frac{\partial f}{\partial t} = -\tau_0^{-1}\,\frac{q}{m}\sum_k \int_t^{t+\tau_0} dt'\left(\delta E_{-k}(X,t) + \frac{v(t')x\delta B_{-k}(X,t)}{c}\right)\bullet\frac{\partial}{\partial v(t')}$$

$$\exp(iL')\delta f_k(X,v(t'),t') \qquad \text{(A-3)}$$

where

$$\frac{\partial}{\partial v(t')} = \hat{e}_x\left(2v_x(t')\frac{\partial}{\partial v_\perp{}^2} - \frac{1}{\omega_c}\frac{\partial}{\partial X}\right) + \hat{e}_y\left[2\left(v_y(t') - v_g\right)\frac{\partial}{\partial v_\perp{}^2} + \frac{1}{\omega_c}\frac{\partial}{\partial X}\right]$$

$$+\ \hat{e}_z\, 2v_z(t')\frac{\partial}{\partial v_z{}^2} + \frac{\hat{\phi}}{v_\perp}\frac{\partial}{\partial\phi'} \quad .$$

The solution for the unperturbed orbits $v(t')$ is standard[3]. In the quantity $f_k(X,v(t'),t')$, the rapidly varying phase terms are evaluated at t' while the slowly varying amplitude is evaluated at t. Performing the time integration in (A-3), and using the Bessel function identity

$$\exp(-i\mu\cos\theta) = \sum_{\ell=\infty}^{\infty} J_\ell(\mu)\,\exp[i\ell(\theta - \pi/2)]$$

to do manipulations similar to those which are done to obtain δf_k, yields Eq. (5) of the text.

Stability Bounds for BALLOONING MODES IN EBT*

K. Nguyen and T. Kammash
The University of Michigan
Ann Arbor, Michigan 48109

Most recent studies of EBT stability have produced beta values based on the stability of the interchange mode in which variations of the field curvature along the field are ignored. In this paper we examine the macroscopic stability of an EBT plasma in a slab model taking into account variations of the curvature along the field. A quasi-kinetic approach is followed in which the interaction of the hot electron component with the plasma as well as the finite Larmor radius (FLR) effects of the background ions are included. It is shown that in the absence of FLR a critical hot electron beta must be achieved in order for the ballooning modes to be stable and that this threshold value agrees very well with an MHD rigid ring result deduced by an energy principle. The analysis also shows that when the compression term has a pole inside the ring the background ballooning mode becomes stable for any value of the hot electron beta due to strong line tying which would not arise if the hot electrons were not allowed to be perturbed. Finally it is shown that the upper bound on the core beta is in agreement with the Van Dam and Lee limit if the radius of curvature at the midplane rather than the average curvature is used in the "local" stability analysis.

---

*Work supported by DOE

I. Introduction

Because of its unique properties as a plasma confinement device the Elmo Bumpy Torus (EBT) has been receiving increasing attention in recent years. Its potential as a fusion reactor, however, depends critically on the beta (ratio of plasma to magnetic pressure) value it can support and this in turn depends on the stability properties of the configuration. Several investigations have, in the past few years, attacked the problem of macroscopic stability of EBT and have generated values for the maximum beta of the core plasma that are still subject to further refinement. These different beta values are in effect a reflection of the models used, e.g. whether the hot electron component is treated as a rigid ring that only contributes to the stabilizing magnetic well, or whether its interaction with the background plasma is adaquately accounted for. For the interchange modes where the field curvature is taken normal to the field, studies[1,2] have yielded core betas, β_c , of about 6-8%. Such beta values have been shown[3] to be substantially reduced when new instabilities arising from coupling between the high frequency compressional Alfven wave and the low frequency flute interchange modes are taken into account. In most of these studies variations of the magnetic curvature along the field have been ignored, and when they were incorporated[4], rigid ring representation of the hot electron component was considered. In this paper we address the problem of ballooning stability in EBT using a quasi-kinetic approach in which we include the interaction of the hot electrons with the background plasma as well as the finite Larmor

radius effects of the plasma ions. We obtain the stability boundary and the critical β_c and β_h (of the hot electron) values which reduce to those based on the interchange analysis when variations along the field are ignored. An energy principle is also used to predict the stability boundary when the hot electrons are taken to be rigid and non-interacting, and these results agree with those previously obtained numerically[5].

II. Basic Equations and Analysis

The ballooning interchange equation is derived by starting with the equilibrium force equation given by

$$\frac{\underline{J} \times \underline{B}}{c} = \nabla \cdot \underline{\underline{P}} + \underline{F} \tag{1}$$

where $\underline{J}$ is the current density, $\underline{B}$ is the magnetic field, c is the speed of light, $\underline{\underline{P}}$ is the pressure tensor and $\underline{F}$ is a general force. If $\underline{b}$ denotes the unit vector along the field, and the Chew-Goldberger-Low (CGL) form of the pressure tensor is used then

$$\underline{\underline{P}} = P_\perp \underline{\underline{I}} + (P_\parallel - P_\perp)\underline{b}\,\underline{b}$$

The perpendicular component of the current density can readily be shown to read

$$\tau \underline{J}_\perp = \frac{c\,\underline{b}}{B} \times \left[\nabla P_\perp + \frac{(P_\parallel - P_\perp)}{B} \nabla B + \underline{F} \right] \tag{2}$$

where

$$\tau = 1 + \mu_0 \frac{(P_\perp - P_\parallel)}{B^2}$$

It should be noted at this point that if the background plasma in EBT is taken to be isotropic then τ will only pertain to the

hot electron component which is generally taken to be highly anisotropic. We now invoke the quasi neutrality condition $\nabla \cdot \vec{J} = 0$ which allows us (See Appendix A) to write Eq. (1) as

$$\nabla \cdot (\tau \vec{J}_{\parallel}) + c\, \nabla_{\perp} \cdot \left(\frac{\vec{b}' \times \vec{F}}{B} \right) + \frac{c}{B} \left(\vec{b}' \times \hat{\vec{b}} \cdot \nabla \vec{b}' \right) \cdot \nabla (P_{\parallel} + P_{\perp})$$

$$+ \frac{\mu_0}{B^2} \left(\vec{F} \cdot \vec{J}_{\perp} - \vec{F} \cdot \vec{J}_{\parallel} \right) = 0 \tag{3}$$

The geometry to be used in this analysis is that of an equivalent bumpy cylinder[5] with z taken along the axis of the cylinder and θ to represent the azimuthal angle. In equilibrium it is assumed that the current density along the field, $J_{\parallel}^{0}$, and the force $F_{\perp}^{0}$ to be identically zero; and that the perturbed force normal to the field is that which is associated with the polarization drift arising from the perturbed electric field, which for low frequency can be expressed as

$$\hat{\vec{b}} \times \vec{F}' \simeq - c \frac{n_{0i} m_i}{B} \frac{d}{dt} \nabla \varphi \tag{4}$$

In writing Eq. (4) the electron contributions have been ignored due to their small mass. Moreover, if we express the perturbed electric and magnetic fields in terms of the vector and scalar potentials i.e.,

$$\vec{E}' = -\nabla \varphi - \frac{1}{c} \frac{\partial \vec{A}}{\partial t}$$
$$\vec{B}' = \nabla \times \vec{A} \tag{5}$$

then using Ampere's law (with the displacement current ignored):

$$\nabla \times \vec{B}' = \frac{\mu_0}{c} \vec{J}' \tag{6}$$

together with the ideal magnetohydrodynamic (MHD) condition:

$$\underset{\rightarrow}{b}' \cdot \underset{\rightarrow}{E}' = 0 \tag{7}$$

the parallel component of the current density can be written as

$$\underset{\rightarrow}{J}'_{\parallel} = \left(\frac{m}{r}\right)^2 \frac{c}{\mu_0} A_{\parallel} = \left(\frac{m}{r}\right)^2 \frac{c^2}{i\mu_0 \omega} \underline{b}' \cdot \nabla \varphi \tag{8}$$

In arriving at the above result use was made of the assumption that the perturbed quantities are of the form

$$\varphi = \varphi(z) \exp i \left[\frac{m}{r} \theta - \omega t \right] \tag{9}$$

where m is the azimuthal mode number. With these facts the linearized form of Eq. (3) can be put in the form

$$B \underline{b}' \cdot \nabla \left[\frac{c^2 \left(\frac{m}{r}\right)^2 \tau}{i \omega \mu_0 B} \underline{b}' \cdot \nabla \varphi \right] + \frac{c^2 n_{0i} m_i}{q_i B^2} \left(\frac{m}{r}\right)^2 \frac{d\varphi}{dt} + \frac{c}{B} \nabla (P'_{\parallel} + P'_{\perp}) \cdot (\underline{b}' \times \underline{b}' \cdot \nabla \underline{b}') = 0 \tag{10}$$

with q_i being the charge of the ions. We note further that we can write

$$\frac{d}{dt} = \frac{\partial}{\partial t} + \underset{\rightarrow}{v}_i \cdot \nabla$$
$$= -i (\omega - \omega_{*i})$$

where ω_{*i} is the ion diamagnetic frequency. If we now introduce the Alfven speed, V_A, and the radius of curvature through their usual forms, namely

$$V_A^2 = \frac{B^2}{\mu_0 n_{0i} m_i}$$

$$\frac{m}{r R_c} = i\left(\underline{b}^{\circ} \times \underline{b}^{\circ} \cdot \nabla \underline{b}^{\circ}\right) \cdot \nabla$$

then Eq. (10) becomes

$$B\, \underline{b}^{\circ} \cdot \nabla \left(\frac{\tau}{r^2 B} \underline{b}^{\circ} \cdot \nabla \varphi \right) + \frac{1}{r^2 V_A^2} \omega (\omega - \omega_{*i}) \varphi + \frac{\mu_0 \omega}{m c B} \frac{(p_{\parallel}' + p_{\perp}')}{r R_c} = 0 \tag{11}$$

It is interesting to note that when $\underline{b}^{\circ} \cdot \nabla (\quad) = 0$ i.e. when we neglect the ballooning effect embodied in the left hand side of Eq. (11) then the equation in question reduces to that obtained by VanDam and Lee[1] for the study of the interchange modes.

In applying this analysis to EBT plasma we invoke the familiar approximation of limiting the analysis to the outer region of the hot electron ring and thus assume that the perpendicular wave length is much smaller than the parallel wave length or any other equilibrium scale length i.e., the long thin approximation. Moreover, we take the background plasma and the hot electrons to have the same radial density profile, and further assume that the bulk plasma is isotropic and responds basically to the $\underline{E} \times \underline{B}$ motion. The hot electrons, on the other hand, due to their large perpendicular energy $(T_{\perp h} \gg T_{\parallel h})$ respond poorly to the $\underline{E} \times \underline{B}$ drifts and exhibit primarily an adiabatic behavior. In that case we can write the perturbed pressure for the core species as[1]:

$$p_c' \simeq -q\, n_{0i} \frac{\omega_{*i}}{\omega} \left(1 + \frac{T_e}{T_i}\right) \varphi + \frac{\beta_c}{4\pi} B B_{\parallel}' \tag{12}$$

and for the hot electrons

$$p_{\perp h}' = \frac{1}{8\pi} \beta_h \frac{\omega_{*h}}{\omega_{bh}} B B_{\parallel}' \tag{13}$$

These two equations together with the quasi-static pressure balance, namely

$$4\pi p_{\perp}' + B B_{\parallel}' = 0 \tag{14}$$

yield

$$D B B_{\parallel}' - 4\pi q\, n_{0i} \frac{\omega_{*i}}{\omega} \left(1 + \frac{T_e}{T_i}\right) \varphi = 0 \tag{15}$$

or

$$p_{\parallel}' + p_{\perp}' \simeq -q\, n_{0i} \frac{\omega_{*i}}{\omega} \left(1 + \frac{T_e}{T_i}\right)\left(1 + \frac{1}{D}\right) \varphi \tag{16}$$

where

$$D = 1 + \beta_c + \frac{1}{2} \beta_h \frac{\omega_{*h}}{\omega_{bh}}$$

$$\omega_{*s} = \frac{T_s}{m_s \Omega_s} \vec{k}_{\perp} \cdot \underline{b}' \times \ln n \simeq -\left(\frac{m}{r}\right) \frac{T_s}{m_s \Omega_s R_p} \tag{17}$$

$$\omega_{bh} = \frac{T_h}{m_e \Omega_e} \vec{k}_{\perp} \cdot \underline{b}' \times \ln B \simeq \left(\frac{m}{r}\right) \frac{T_h}{m_e \Omega_e R_b}$$

with β_c denoting the core beta, β_h the hot electron beta and ω_{bh} the frequency associated with the magnetic gradient drift. From the force balance equation it can be shown that the magnetic gradient can be expressed as

$$\frac{1}{R_b} = \frac{\beta_t}{2r_p} - \frac{\tau}{R_c} \; ; \; \tau = 1 + \frac{\beta_h}{2} \; ; \; \beta_t = \beta_c + \beta_h \tag{18}$$

In view of the above relations Eq. (1) can be put in the form

$$B\,\underline{b}'\cdot\nabla\left(\frac{\tau}{r^2 B}\,\underline{b}'\cdot\nabla\varphi\right) + \left\{\frac{1}{V_A^2}\,\omega\,(\omega-\omega_{*i}) + \frac{\beta_c}{2r_p R_c}\left(1+\frac{1}{D}\right)\right\}\frac{\varphi}{r^2} = 0 \tag{19}$$

where we recall that R_c represents the radius of curvature of the field. It might be noted at this juncture that the first term in the above equation (the shear Alfven wave) represents the communication between regions of different curvature along the field line, the second term arises from the polarization drift of the ions and the finite gyroradius effects of the ions, while the last term arises from the field line curvature drift. In the absence of the hot electrons term i.e., $\beta_h = 0$ Eq. (19) reduces to the standard ballooning equation with finite Larmor radius corrections.

With the hot electrons, however, Eq. (19) with the aid of Eq. (17) can be further written as

$$\frac{d}{dz}\left(\frac{\tau B_z}{r^2 B^2}\frac{d\varphi}{dz}\right) + \left\{\frac{1}{V_A^2}\,\omega\,(\omega-\omega_{*i}) + \frac{\beta_c}{2r_p R_c}\left(2 + \frac{\beta_h(1-\beta_c)}{\beta_c(1+\beta_h) - 2r_p\tau/R_c}\right)\right\}\frac{\varphi}{r^2 B_z} = 0 \tag{20}$$

where we have let

$$\underline{b}'\cdot\nabla \equiv \frac{B_z}{B}\frac{d}{dz}$$

In order to solve Eq. (20) we will assume that the background plasma is uniform along z (so that P_c is also independent of z) and situated inside a bumpy cylinder with a mirror ratio M , and a distance L between the mirrors. The hot electrons are taken to occupy symmetrically a length ℓ at the center of the mirror so that we choose to write

$$\beta_h = \begin{cases} \beta_{h_0}\left[1-\left(\frac{2z}{\ell}\right)^2\right] & ; \quad |z| \le \ell/2 \\ 0 & ; \quad |z| > \frac{\ell}{2} \end{cases} \tag{21}$$

The vacuum magnetic field is expressed as

$$\underline{B} = B_z \hat{z} + B_r \hat{r}$$

with

$$\begin{aligned} B_z &\simeq B_0\left[1 - b\, I_0(sr)\cos(sz)\right] \\ B_r &\simeq -B_0\, b\, I_1(sr)\sin(sz)\Big] \end{aligned} \tag{22}$$

where

$$s = \frac{2\pi}{L} \quad ; \quad b = \frac{M-1}{M+1}$$

and I_0 , and I_1 , are the familiar modified Bessel functions. The above relations allow us to approximately write for the radius of curvature the expression (see Appendix B)

$$\frac{1}{R_c} \simeq \frac{r}{a R_0}\left[\Delta + \alpha\cos(sz)\right] \tag{23}$$

where

$$\frac{1}{R_0} = \frac{\pi^2 a}{L^2} \quad ; \quad \alpha = 2b$$

$$\Delta = b^2\left[\frac{1}{2} + \left(\frac{\pi r}{L}\right)^2\right]$$

and "a" is the radial location of the ring at midplane. Consistent with these relations we can write for the variation of the radial distance with z at the ring the following relation

$$r^2 = a^2 \left[\frac{1 - b\left\{1 + \left(\frac{\pi a}{L}\right)^2/2\right\}}{\left\{1 - b\cos(sz)\right\}\left\{1 + \left(\frac{\pi r}{L}\right)^2/2\right\}} \right] \tag{24}$$

With the aid of the above expressions Eq. (20) can be solved numerically to produce the lowest eigenvalues utilizing the following boundary conditions:

$$\frac{d\varphi(0)}{dz} = \frac{d\varphi(\pm L/2)}{dz} = 0 \tag{25}$$

These conditions represent the fact that the most unstable mode in the system possesses even symmetry with respect to the midplane and is periodic with period L.

Due to the presence of the hot electrons, however, there are values of β_c for which D in Eq. (19) may vanish at points $\pm z_p$. When this occurs, it can be readily seen from Eq. (15) that the perturbed potential must vanish at these points or

$$\varphi(\pm z_p) = 0 \tag{26}$$

As a result, each sector is now decoupled into two regions in which the ballooning equation must be solved subject to the appropriate conditions which can be stated as

$$\frac{d\varphi(0)}{dz} = 0 \qquad \varphi(|z_p|) = 0 \qquad |z| \le |z_p|$$

and

$$\varphi(|z_p|) = 0 \qquad \frac{d\varphi(L/2)}{dz} = 0 \qquad |z_p| \le z \le \frac{L}{2} \tag{27}$$

The requirement that φ vanish at these points (line tying) represents a strong stabilizing effect due to the tension created by field line bending. This is a new effect that would not exist if the hot electrons were not allowed to be perturbed.

III. MHD (Rigid Ring) Analysis

If the hot electron ring is not allowed to be perturbed (i.e., be considered rigid) but intended only to reverse the ∇B drift, then a ballooning equation can be derived directly from an energy principle which we can write as

$$\delta K + \delta W = \frac{1}{2} m_i \omega^2 \int n_{0i} \vec{\xi}^2 \, dV$$
$$+ \frac{1}{2\mu_0} \int \Big[\vec{B}_1^2 + \vec{J}_0 \cdot \vec{\xi} \times \vec{B}_1 + \mu_0 \gamma p_0 (\nabla \cdot \vec{\xi})^2 \tag{28}$$
$$+ \mu_0 \vec{\xi} \cdot \nabla p_0 (\nabla \cdot \vec{\xi}) \Big] dV$$

where
$$\vec{B}_1 = \nabla \times (\vec{\xi} \times \vec{B})$$
$$\vec{\xi} = \vec{B} \times \nabla \varphi / B^2$$

are the perturbed magnetic field and displacement respectively. Quantities in Eq. (28) with subscript "o" represent equilibrium quantities e.g. the equilibrium pressure p_0 and γ denotes the ratio of specific heats. In view of the above relations it can easily be shown that

$$\nabla \cdot \vec{\xi} = \frac{i m}{r} \frac{\varphi}{B^2} \left[\frac{1}{R_b} - \frac{1}{R_c} \right]$$
$$\vec{B}_1 = \frac{i m}{r} \frac{d\varphi}{d\zeta} \vec{b}' \times \vec{\theta}' \tag{29}$$

which leads to

$$\vec{J}_0 \cdot (\vec{\xi} \times \vec{B}_1) = 0 \tag{30}$$

For a long thin plasma we can neglect the third term in δW in comparison to the fourth and the energy integral reduces to

$$\delta K + \delta W = \frac{m^2}{2\mu_0} \int \left[\left(\frac{1}{r} \frac{d\varphi}{d\zeta} \right)^2 - \frac{\omega^2 \varphi^2}{r^2 V_A^2} + \frac{\beta_c}{2 r^2 r_p} \left(\frac{1}{R_b} - \frac{1}{R_c} \right) \varphi^2 \right] dV \tag{31}$$

where, as before, V_A denotes the Alfven speed, and r_p represents the density gradient scale length. Upon optimization, Eq. (31) becomes upon replacing ζ with z ;

$$\frac{d}{dz} \frac{B_z}{r^2 B^2} \frac{d\varphi}{dz} + \frac{\omega^2}{r^2 V_A^2} \frac{\varphi}{B_z} + \frac{\beta_c}{r_p} \left[\frac{1}{R_c} - \frac{\beta_h}{4 r_p} \right] \frac{\varphi}{r^2 B_z} = 0 \tag{32}$$

where in the process of minimization we have utilized the boundary condition

$$\frac{d\varphi(0)}{dz} = \frac{d\varphi(\pm L/2)}{dz} = 0 \tag{33}$$

Eq. (32) together with (33) can then solved numerically as was done in the previous section.

IV. Discussion and Results

If the finite Larmor stabilization of the background ions is ignored then the stability boundary for ballooning modes in EBT can be displayed as shown in Figs. 1-3. In the three cases it is shown that at low β_c , the hot electron beta, β_h , must exceed a certain critical value for the system to achieve stability, and this threshold value agrees very well with the MHD rigid ring result represented by the dashed lines. It should be noted

that the β_h value referred to in this discussion as well as in the graphs refers to the maximum hot electron beta at the midplane. Moreover, it can be seen from Figs. 1 and 2 that the threshold value in question becomes much smaller when the hot electron ring is made longer since in this case the magnetic well dug by these electrons extends further along the magnetic field towards the throats of the mirror. Such improvements in stability arising from longer rings have been noted qualitatively by Nelson and Hedrick[5]. It may also be observed that as β_c increases the threshold value for β_h decreases further with the improvement resulting from the enhancement in the compression term $1/D$.

However, as β_c increases even further D may vanish at some point inside the ring and the boundary conditions given by Eq. (27) then apply. In this case, the background ballooning mode becomes generally stable for any given value of β_h (as indicated by the horizontal line in Figs. 1-3) due to the strong line-tying stabilization which would not occur if the hot electrons were not allowed to be perturbed.

The upper bound on β_c represents the effect of the interacting interchange ballooning mode. It is interesting to note that this mode will be unstable when D is positive everywhere along the field line i.e., when

$$\beta_c \gtrsim \frac{2 r_p}{R_{MP}}$$

where R_{MP} is the radius of curvature at the midplane. This suggests that the radius of curvature at the midplane rather than the average curvature should be used in "local" stability analysis.

A comparison of Figs. 1 and 3 reveals that the upper bound on β_c can be dramatically increased by increasing the mirror ratio; however this happens at the expense of destabilizing the background ballooning mode. Increasing the mirror ratio results in a decrease in the radius of curvature and a corresponding enhancement in β_c . Similar results have been predicted by Nelson[2] even though the stability of the ballooning modes was not addressed in his analysis.

Finally, Fig. 4 shows examples of typical eigenfunctions for different values of β_c . It is seen that for low β_c (e.g curve a) the strong effect of the magnetic well dug by the hot electrons stabilizes the mode by forcing the peak of the eigenfunction towards the mirror throat where the curvature is good. As β_c increases, the quantity D may vanish inside the ring and this in turn forces the eigenfunction to vanish at that point thereby decoupling the mirror into two regions. This line tying effect is shown in Fig. 4 where curves ($b1$) and ($b2$) meet. But the modes in this case are generally stable due to the tension created by the magnetic field line bending. However, if β_c crosses a certain threshold where D is everywhere positive the eigenfunction becomes highly peaked at the center of the ring (thus justifying the use of the midplane radius of curvature in local analysis) and the interacting ballooning mode becomes unstable.

Acknowledgement

This work is supported by the Department of Energy. The authors are grateful to Professors J.C. Lee and W. Martin of the University of Michigan for making available the ONED code, and

Acknowledgement (cont.)

and for helpful hints in the numerical solutions of the equations.

References

1. J.W. VanDam and Y.C. Lee, Proc. Workshop on EBT Ring Physics, Oak Ridge, CONF-7911228, Dec. 1979, p. 471.
2. D.B. Nelson, Phys, Fluids 23, 1850 (1980).
3. K.T. Tsang and C.Z. Cheng, Proc. Workshop on EBT Stability Theory, Oak Ridge, CONF-81052, May 1981, p. 141.
4. H. Sanuki and M. Fujiwara, Proc. Workshop on EBT Ring Physics, Oak Ridge, CONF-7911228, Dec. 1979, p. 453.
5. D.B. Nelson and C.L. Hedrick, Nuclear Fusion, 19, 283 (1979).

Appendix A

In this appendix the derivation of Eq. (3) is presented starting from the basic equations that characterize the system. With the pressure tensor given by

$$\underline{\underline{P}} = P_\perp \underline{\underline{I}} + (P_\parallel + P_\perp)\,\underline{b}\,\underline{b} \;;\quad \underline{b} = \frac{\underline{B}}{B}$$

and the equilibrium equation

$$\frac{\underline{J} \times \underline{B}}{c} = \nabla \cdot \underline{\underline{P}} + \underline{F}$$

we can readily obtain

$$\underline{J}_\perp = \frac{c\,\underline{b}}{B} \times \left[\nabla_\perp P_\perp + (P_\parallel - P_\perp)\,\underline{b} \cdot \nabla \underline{b} \right] + \frac{c\,\underline{b} \times \underline{F}}{B} \tag{A.1}$$

$$\underline{b} \cdot \nabla P_\parallel - \frac{P_\parallel - P_\perp}{B}\,\underline{b} \cdot \nabla B = -F_\parallel \tag{A.2}$$

In obtaining the above results we have made use of

$$(\nabla\cdot\underline{\underline{P}})_{\parallel} = \underline{b}^{\wedge}\cdot\nabla P_{\parallel} - \frac{P_{\parallel}-P_{\perp}}{B}\,\underline{b}^{\wedge}\cdot\nabla B = -F_{\parallel} \tag{A.3}$$

$$(\nabla\cdot\underline{\underline{P}})_{\perp} = \nabla_{\perp}P_{\perp} + (P_{\parallel}-P_{\perp})\,\underline{b}^{\wedge}\cdot\nabla\underline{b}^{\wedge} \tag{A.4}$$

Utilizing the relation

$$\mu_0\,\frac{\underline{J}\times\underline{B}}{c} = \nabla\times\underline{B}\times\underline{B}$$

$$= -B\nabla B + B^2\,\underline{b}^{\wedge}\cdot\nabla\underline{b}^{\wedge}$$

the perpendicular component of the current density is found to be

$$\underline{J}_{\perp} = \frac{c}{\mu_0}\,\underline{B}\times\left(\underline{b}^{\wedge}\cdot\nabla\underline{b}^{\wedge} - \frac{\nabla B}{B}\right) \tag{A.5}$$

Upon combining Eqs. (A.1) and (A.5) we obtain

$$\underline{\Lambda} = \tau\underline{J}_{\perp} = \frac{c\,\underline{b}^{\wedge}}{B}\times\left(\nabla P_{\perp} + \frac{P_{\parallel}-P_{\perp}}{B}\nabla B + \underline{F}\right) \tag{A.6}$$

where

$$\tau = 1 + \frac{\mu_0\,(P_{\perp}-P_{\parallel})}{B^2}$$

Invoking the quasi-neutrality conditions

$$\nabla\cdot\underline{J} = \frac{c}{\mu_0}\,\nabla\cdot\nabla\times\underline{B} - \frac{1}{\epsilon_0\mu_0}\frac{\partial\rho}{\partial t} = 0 \tag{A.7}$$

where ρ is the charge density, we can write

$$\nabla\cdot\underline{J}_{\parallel} = -\nabla\cdot\underline{J}_{\perp} = -\nabla\cdot\frac{\underline{\Lambda}}{\tau}$$

$$= -\frac{1}{\tau}\nabla\cdot\underline{\Lambda} + \frac{\underline{J}_{\perp}}{\tau}\cdot\nabla\tau$$

or simply

$$\tau \, \nabla \cdot \vec{J}_{\parallel} = -\nabla \cdot \vec{\Lambda} + \vec{J}_{\perp} \cdot \nabla \tau \tag{A.8}$$

From (A.6) it can be seen that

$$\begin{aligned} \nabla \cdot \vec{\Lambda} = {} & c \, \nabla \cdot \left(\frac{\underline{b}' \times \vec{F}}{B} \right) + \mu_0 \left(\frac{\nabla P_{\perp}}{B^2} + \frac{P_{\parallel} - P_{\perp}}{B^3} \nabla B \right) \cdot \vec{J} \\ & + \nabla (P_{\parallel} + P_{\perp}) \cdot \frac{c \, \underline{b}' \times \nabla B}{B^2} \end{aligned} \tag{A.9}$$

and that

$$-\vec{F} \cdot \vec{J}_{\perp} = \left(\nabla P_{\perp} + \frac{P_{\parallel} - P_{\perp}}{B} \nabla B \right) \cdot \vec{J}_{\perp} \tag{A.10}$$

On the other hand Eq. (A.3) allows us to write

$$\begin{aligned} \vec{J}_{\parallel} \cdot \nabla \tau &= \mu_0 \vec{J}_{\parallel} \cdot \left[\frac{\nabla (P_{\perp} - P_{\parallel})}{B^2} - 2 (P_{\perp} - P_{\parallel}) \frac{\nabla B}{B^3} \right] \\ &= \mu_0 \left[\frac{\nabla P_{\perp}}{B^2} - \frac{P_{\parallel} - P_{\perp}}{B^3} \nabla B \right] \cdot \vec{J}_{\parallel} \end{aligned} \tag{A.11}$$

If we now substitute Eqs. (A.10 and (A.11) in (A.9) we obtain

$$\begin{aligned} \nabla \cdot \vec{\Lambda} = {} & c \, \nabla \cdot \left(\frac{\underline{b}' \times \vec{F}}{B} \right) - \frac{\mu_0}{B^2} \vec{F} \cdot \vec{J}_{\perp} + \vec{J}_{\parallel} \cdot \nabla \tau \\ & - \frac{\mu_0 \vec{F} \cdot \vec{J}_{\parallel}}{B^2} + \nabla (P_{\parallel} + P_{\perp}) \cdot \frac{c \, \underline{b}' \times \nabla B}{B^2} \end{aligned} \tag{A.12}$$

With the aid of (A.10) and (A.5) we can also write

$$\vec{J}_{\perp} \cdot \nabla \tau = -2 \mu_0 \vec{F} \cdot \vec{J}_{\perp} - c \, \nabla (P_{\parallel} + P_{\perp}) \cdot \frac{\underline{b}' \times}{B} \left(\underline{b}' \cdot \nabla \underline{b}' - \frac{\nabla B}{B} \right) \tag{A.13}$$

Substituting (A.12) and (A.13) into (A.8) we find

$$\nabla \cdot \tau \vec{J}_{\parallel} = -c\,\nabla \cdot \left(\frac{\underline{b}' \times \vec{F}}{B} \right) - \frac{\mu_0}{B^2} \left(\vec{F} \cdot \vec{J}_{\perp} - \vec{F} \cdot \vec{J}_{\parallel} \right) \tag{A.14}$$

$$- \frac{c}{B} \nabla (p_{\parallel} + p_{\perp}) \cdot \underline{b}' \times \underline{b}' \cdot \nabla \underline{b}'$$

which is Eq. (3) in the text.

Appendix B

In this appendix we provide the mathematical basis for Eq. (23) in the text. The magnetic field in a simple mirror geometry can be expressed by

$$B_z \simeq B_0 \left[1 - b\, I_0(sr) \cos(sz) \right]$$

$$B_r \simeq - B_0\, b\, I_1(sr) \sin(sz) \tag{B.1}$$

where

$$s = 2\pi / L$$

"L" is the distance between the mirrors, and I_0 and I_1, are the familiar modified Bessel functions. For $sr \lesssim 1.5$ these functions can be approximated by

$$I_0(sr) \simeq 1 + \left(\frac{sr}{2} \right)^2$$

$$I_1(sr) \simeq sr/2 \tag{B.2}$$

In view of these relations Eq. (1) assumes the form

$$B_z \simeq B_0 \left[1 - b \left\{ 1 + \left(\frac{sr}{2} \right)^2 \right\} \cos(sz) \right] \tag{B.3}$$

$$B_r \simeq - B_0\, b \left(\frac{sr}{2} \right) \sin(sz)$$

where we now observe that

$$b \simeq \frac{M-1}{M+1}$$

with M being the mirror ratio. The radius of curvature is given by

$$\frac{1}{R_c} = -\frac{1}{2B^2}\frac{\partial}{\partial r} B^2$$
$$= -\frac{1}{B^2}\left(B_z \frac{\partial B_z}{\partial r} + B_r \frac{\partial B_r}{\partial r} \right) \tag{B.4}$$

so that if we keep terms of order b^2 or less then we readily find that

$$\frac{B_z}{B^2}\frac{\partial B_z}{\partial r} \simeq -\frac{S^2 r}{4}\left[b^2 \left\{ 1 + \left(\frac{Sr}{2}\right)^2 \right\} + 2b \cos(Sz) \right] \tag{B.5}$$

and

$$\frac{B_r}{B^2}\frac{\partial B_r}{\partial r} \simeq \frac{B_r}{B_0^2}\frac{\partial B_r}{\partial r} \simeq \frac{b^2 S^2 r}{8} \tag{B.6}$$

where we have utilized the approximation

$$\cos^2(Sz) \simeq \sin^2(Sz) \simeq 1/2$$

Combining Eqs. (B.4), (B.5), and (B.6) we obtain

$$\frac{1}{R_c} \simeq \frac{S^2 r}{4}\left[b^2 \left\{ \frac{1}{2} + \left(\frac{Sr}{2}\right)^2 \right\} + 2b \cos(Sz) \right]$$

or

$$\frac{1}{R_c} \simeq \frac{1}{R_0}\left[\Delta + \alpha \cos\frac{2\pi z}{L} \right] \tag{B.7}$$

where we have let

$$\frac{1}{R_0} = \frac{\pi^2 r}{L^2}$$

$$\Delta = b^2 \left[\frac{1}{2} + \left(\frac{\pi r}{L} \right)^2 \right]$$

$$\alpha = 2b$$

If we specify the curvature at the ring location i.e., $r = a$ then (B.7) yields Eq. (23) in the text.

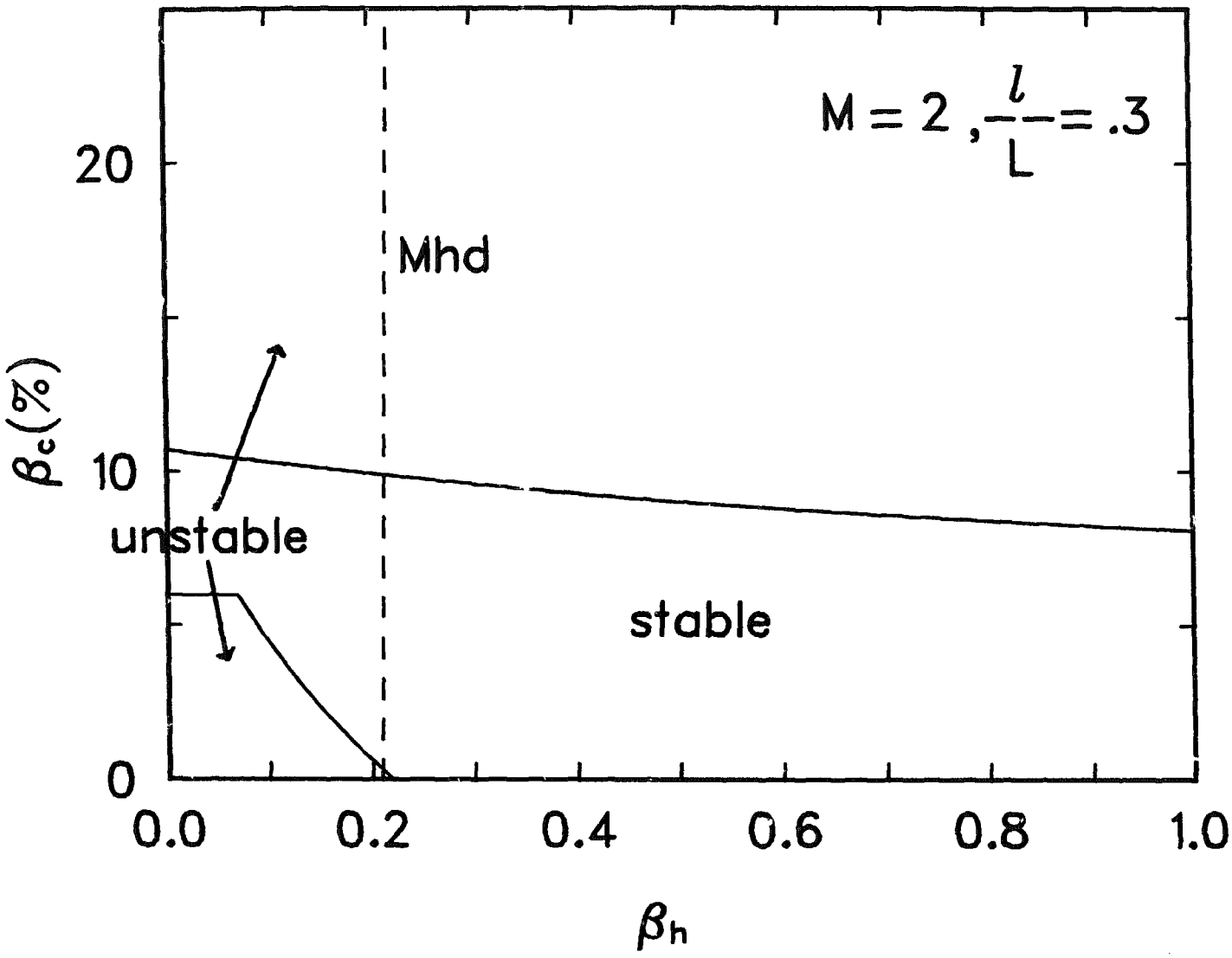

Figure 1 Stability boundary for ballooning modes in EBT with $r_p/R_0 = 0.07$, $R_0/L = 0.5$

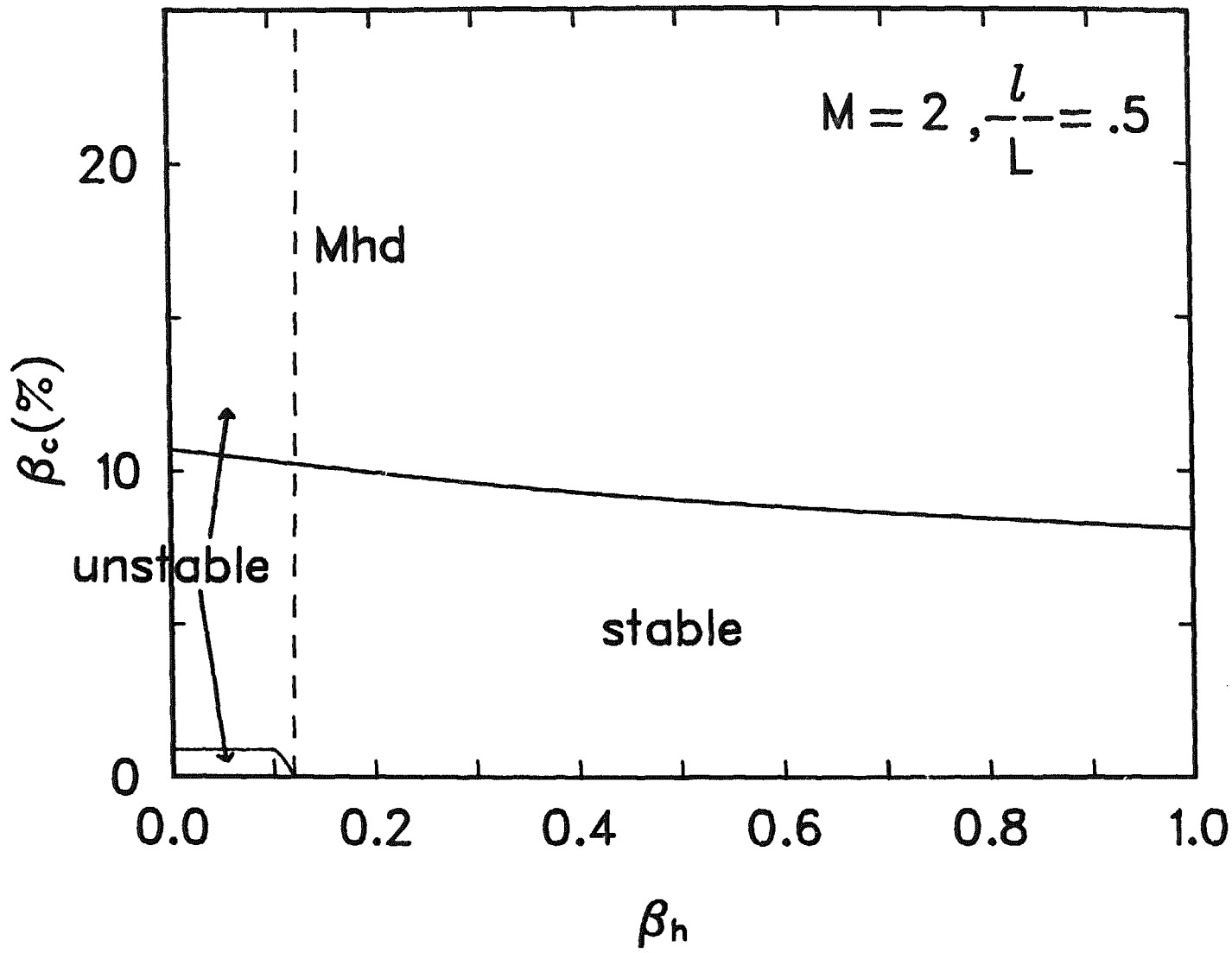

Figure 2 Effect of increasing ring length on stability of ballooning mode

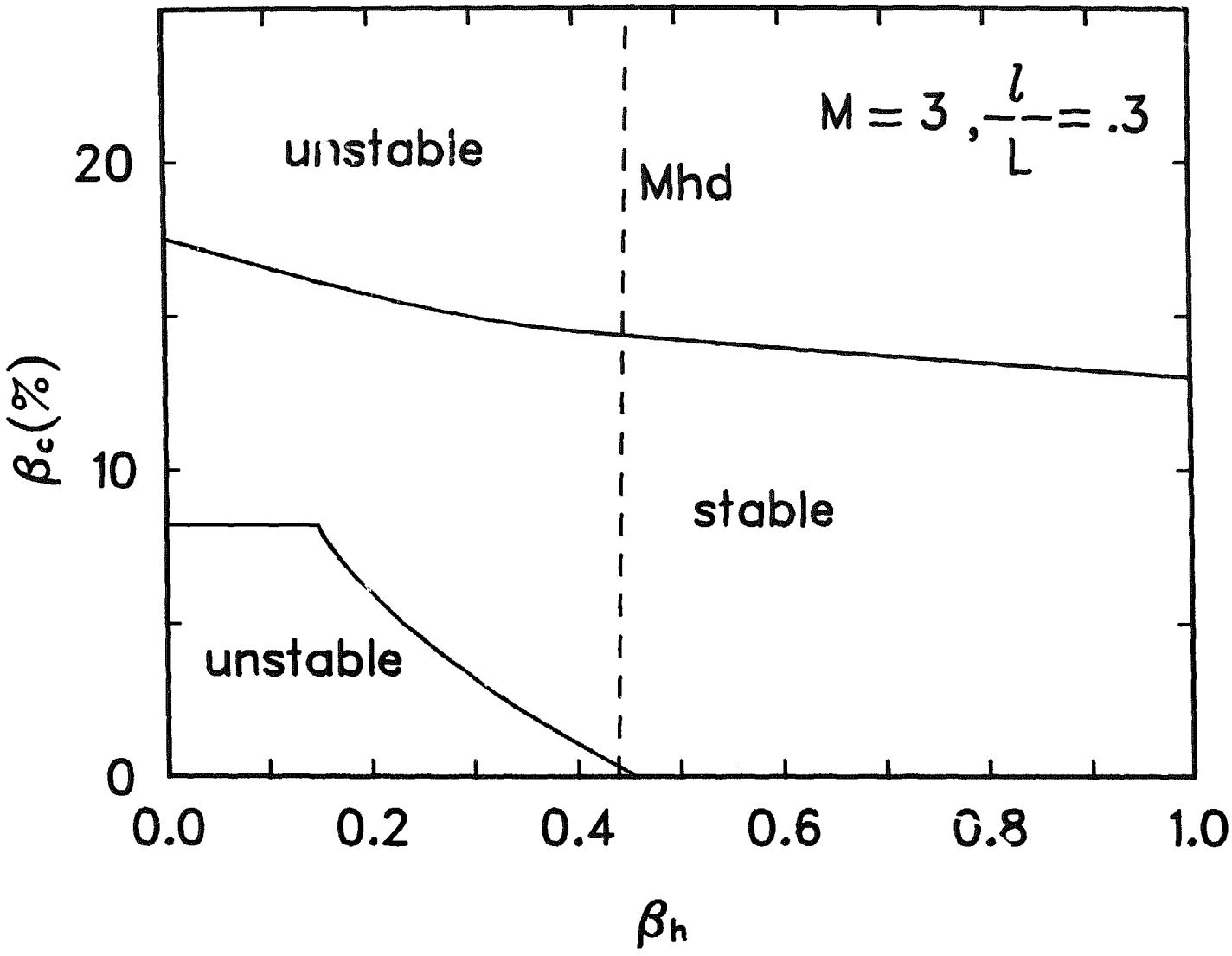

Figure 3 Stability enhancement due to larger mirror ratio

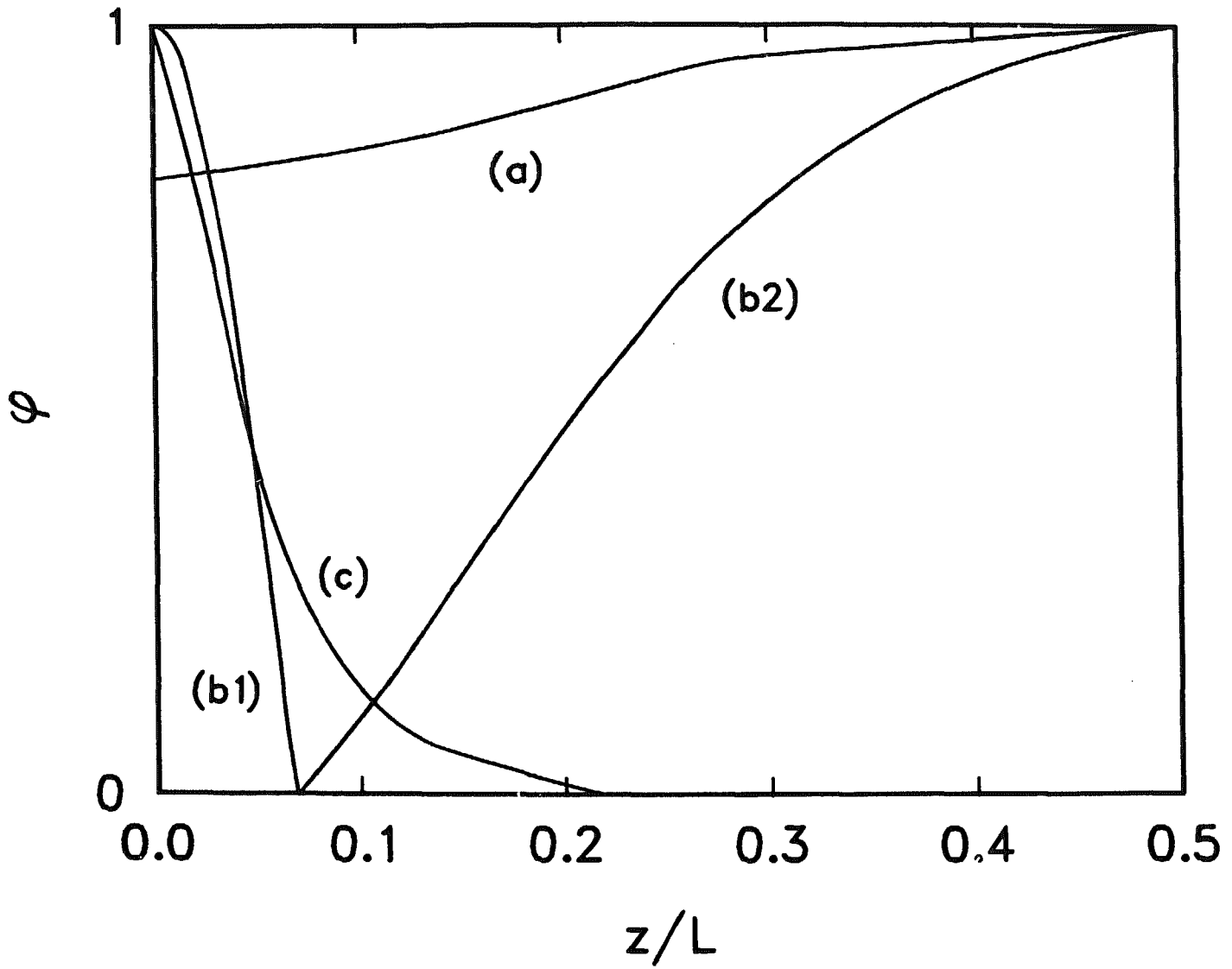

Figure 4 Typical eigenfunctions with $r_p/R_0 = 0.07$, $R_0/L = 0.5$, $\ell/L = 0.3$, M = 2, $\beta_h = 0.6$ for different core betas. (a) $\beta_c = 5.5\%$, (b1) and (b2) $\beta_c = 8.0\%$, (c) $\beta_c = 8.7\%$

EFFECTS OF AMBIPOLAR FIELD ON LOW FREQUENCY FLUCTUATIONS IN BUMPY TORI

Heiji Sanuki*

Department of Physics
University of California, Los Angeles
405 Hilgard Avenue
Los Angeles, California 90024

ABSTRACT

Nonlocal properties of electrostatic drift waves in a straight magnetic field in a collisionless and low-β plasma with a hot electron component are discussed analytically in detail. Interesting drift wave features such as eigenfrequency, growth rate, radial wavenumber, and position of localization are clarified. Effects of the ambipolar potential on the stability of drift waves are also studied and related to low frequency fluctuations measured in EBT/NBT experiments. It is found that a strong ambipolar field has a stabilizing influence on unstable drift waves.

The stability aspects associated with fluctuations have been investigated in EBT and NBT experiments. A large effort is currently aimed at correlating the fluctuation behavior with the ambipolar potential in those experiments. These observations[1,2] generally indicate that:

[1] The transitions from the T mode of operation to the C and M modes are clearly correlated with changes in plasma fluctuation activity.

[2] Most of the fluctuation energy is at low frequencies ($\approx$ 100 KHz).

*Permanent Address: Institute of Plasma Physics
Nagoya University
Nagoya, 464, Japan

[3] High frequency fluctuations appear at low pressures and high microwave power, and are generally observed outside the ring.

[4] Low frequency fluctuations are slightly enhanced near the C-T transition.

[5] Enhanced fluctuations near the T-M transition are correlated with increased ion-tail densities and deep potential wells.

There is a considerable diagnostic effort currently aimed at studying fluctuation phenomena. These observations indicate that the low frequency fluctuations are localized around the region with large density gradient and the direction of rotation is that of the electron diamagnetic drift. Therefore, the low frequency fluctuations may be related to the density gradient drift wave. We here consider the effects of an ambipolar field on the electrostatic drift waves as a possible model for the low frequency fluctuation phenomena seen in EBT/NBT experiments. A new approach to the analysis of electrostatic eigenmodes in an inhomogeneous Vlasov plasma using a WKB approximation in K space was developed in a previous paper[3]. This systematic nonlocal stability analysis in an inhomogeneous Vlasov plasma is quite general and is applicable to any electrostatic modes with $k\lambda \gg 1$ (k is the wavenumber in the direction of the density gradient and λ is the density gradient scale length). This technique provides useful information about localized modes such as the position of localization and the typical radial wavenumber associated with a given mode.

We consider a collisionless low-β plasma having a density gradient perpendicular to a uniform and straight magnetic field B_o and a parabolic ambipolar potential

$$\Phi_o = \frac{E_o}{2\lambda_o} x^2 = \frac{m_j}{2q_j} \omega_{Ej}^2 x^2. \tag{1}$$

Here we use a slab geometry with z axis along the uniform magnetic field. The plasma density and the ambipolar potential are assumed to vary only in the x direction. In Eq. (1), q_j and m_j are the charge and mass of the j-th species, λ_o is the inhomogeneity scale length of

the ambipolar potential and $\omega_{Ej}^2 \equiv q_j E_o/\lambda_o m_j$. The plasma is composed of three species: bulk ions and electrons, and hot electrons. The equilibrium is represented by Maxwellian distributions for each species, with spatially uniform temperatures, isotropic in the case of the bulk species and anisotropic ($T_\parallel \neq T_\perp$) for the hot electrons. Following Ref. (3), we consider the density distribution

$$n_{oj}(x) = N_{oj} \{\varepsilon + \exp[-(x-x_{oj})^2/2\lambda_j^2]\}, \tag{2}$$

where ε is an arbitrary constant and εN_{oj} is the uniform background plasma density, which may be related to the surface plasma component in the bumpy torus experiment. For simplicity, we assume the quasi-neutrality condition. In Eq. (2), N_{oi}, N_{oe}, and N_{oh} are the bulk ion, electron, and hot electron densities given by $N_{oi} = N_o$, $N_{oe} = (1-\alpha)N_o$, and $N_{oh} = \alpha N_o$, respectively. Here, α characterizes the percentage of hot electron component. We assume $\lambda_i = \lambda_e = \lambda >> \lambda_h$ and also $T_{\perp j} = T_{\parallel j}$ for the bulk plasma components, while $T_{\perp h} \neq T_{\parallel h}$. The bulk plasma is assumed to be centered at the origin (χ_{oi}, $\chi_{oe} = 0$) while the hot electrons are also assumed to be centered about $\chi_{oh} \neq 0$. The radial profiles of these densities and the ambipolar potential are shown schematically in Fig. (1).

As noted in a previous paper[3], without magnetic shear effects, the drift waves may be localized in the following two cases: (1) the drift frequency ω_* has a peak at a critical position of plasma density, and (2) the drift frequency ω_* does not have a peak, namely, $\partial\omega_*/\partial\chi \neq 0$ for all x, but the quasi-neutrality condition is not imposed because this condition is invalid at the periphery of a plasma. For the density distribution [Eq. (2)], the drift frequency has a peak; then drift waves are localized around this peak whose location depends on the parameter ε.

After lengthy calculations following Ref. (3), we finally obtain the eigenfrequency ω_o, the radial wavenumber $\hat{k}$, and the growth rate Γ as follows:

$$\omega_o = \omega_c \left[1 - \frac{(2N+1)}{2\omega_c a_4} \frac{\rho_i}{\lambda} (a_1 a_3)^{1/2} \right], \tag{3}$$

$$k = \left[\frac{\rho_i}{\lambda} \left(\frac{a_3}{a_1} \right)^{1/2} (2N+1)\Pi \right]^{1/2}, \tag{4}$$

$$\Gamma = - \frac{1}{a_4} \left(\frac{\pi}{2} \right)^{1/2} \left(\frac{T_i}{T_e} \right)^{3/2} \left(\frac{m_e}{m_i} \right)^{1/2} \frac{\omega_o}{\omega_{ci}} \frac{(1-\alpha)}{\hat{k}_{ze}} (F_1+F_2+F_3), \tag{5}$$

where ρ_i is the ion cyclotron radius, N the radial mode number, ω_c the eigenfrequency at the localization center (g_{oc}), and $\hat{k}_{ze} \simeq k_z \rho_i$. While we can determine self-consistently the radial wavenumber (k), the location (g_{oc}), and the eigenfrequency (ω_c) at the localization center, and the coefficients a_1 through a_4, and F_1 through F_3, we here omit these exact expressions. The second term in the brackets of Eq. (3) comes from the finiteness of ρ_i/λ for localized drift waves, and the frequency ω_o decreases as the radial mode number N increases. Equation (4) shows that the wavelength decreases as N increases because $\hat{k}$ is proportional to $[(2N+1)\rho_i/\lambda]^{1/2}$. The terms F_1, F_2, and F_3 in Eq. (5) represent the contributions from the bulk electrons, ions, and the hot electrons, respectively. Equation (5) indicates that Landau damping due to the bulk electrons results in the instability, but Landau damping due to ions tends to decrease the growth rate of the instability. As for the hot electron contribution, we note that Landau damping due to the hot electrons may enhance the instabiltiy if $g_{oi} > x_{oh}$ (x_{oh} is the position of hot electron ring), and may decrease the growth rate of the instability if $g_{oc} < x_{oh}$. In general, the growth rate of drift waves increases as the frequency ω increases in the region of small ω and has a maximum at a certain value of $\omega(\omega \sim \omega_{*e}/2)$; with further increase of ω the growth rate decreases gradually and approaches zero near $\omega \sim \omega_{*e}$. We note that the growth rate becomes large (small) as ω_o decreases (increases) when ω_o is bigger than the critical frequency corresponding to the maximum of the growth rate, but the growth rate becomes small (large) as ω_o decreases (increases) when the frequency ω_o is smaller than the critical frequency.

We now study the characteristics of drift waves on the basis of Eqs. (3), (4), and (5). We restrict ourselves to the low frequency fluctuations with typical frequencies of 100 KHz associated with electrostatic drift waves. We consider the electrostatic drift waves, which are located inside the ring. The parameters are $B_o = 0.3T$, $T_i = 100$ eV, $T_e \simeq (200 \sim 400)$eV, $T_{\perp h} \simeq (100 \sim 200)$KeV, $T_{\parallel h} < 40$ KeV, $\lambda_h = 1$cm, $\lambda = 6.7$cm, $x_{oh} = 11.4$cm, $m_i/m_e = 1836$, and $\varepsilon = 0.2$. Using these parameters, we obtain the scaled quantities: $T_e/T_i = (2 \sim 4)$, $T_{\perp h}/T_i = (10^3 \sim 2 \times 10^3)$, $T_{\perp h}/T_{\parallel h} = (5 \sim 15)$, $\lambda/\lambda_h = 6.7$, and $\delta_i = \rho_i^2/\lambda^2 = 2 \times 10^{-3}$.

One of the key elements in the bumpy torus is the ambipolar potential. It is known from experiments that the sign of the ambipolar potential depends upon the operating region, being positive for the C-mode, negative for the T-mode and slightly positive in the C-T transition region. We study the effect of the ambipolar potential on the stability of drift waves. The frequency, the growth rate, and the position of localization center of the fundamental mode (N = 0) versus $k_y\rho_i$ are shown in Figs. (2a) -(2c) for several values of γ_i, which is defined by $\omega_{Ei}^2/\omega_{ci}^2$. We used $k_z\rho_i = 6 \times 10^{-3}$, $T_e/T_i = 4$, $T_{\perp h}/T_i = 10^3$, $T_{\perp h}/T_{\parallel h} = 5$, and $\alpha = 0.1(10\%)$. Figure (2a) shows the dependence of the frequency on γ_i; the frequency increases if the ambipolar potential is negative ($\gamma_i > 0$) and decreases when it is positive. Figure (2b) indicates the growth rates for several values of negative ambipolar potential. We note that the growth rate decreases with increasing $\gamma_i > 0$. The case of positive ambipolar potential is also considered. Although the most unstable mode is the mode with slightly positive potential ($\gamma_i \simeq -2 \times 10^{-4}$) in this case, the result is qualitatively similar to the result for negative potentials: the growth rate of the drift waves decreases with increasing amplitude of the ambipolar field regardless of the sign of the potential. The effects of ambipolar potentials on the position of the localization center for drift waves are shown in Fig. (2c). The localization center g_{oc} exhibits a small shift outside for negative potentials and a large shift towards the inside for positive potentials. The maximum of frequencies and growth rates of the N = 0 (solid line) and N = 2 (dotted

line) modes versus both the positive and negative ambipolar potentials ($\pm\gamma_i$) are shown in Fig. (3). This figure shows that the N = 2 mode has a stronger suppression due to the ambipolar potential than the fundamental mode, and a weak positive ambipolar potential slightly destabilizes the drift waves, but the unstable drift waves may be stabilized by a large ambipolar potential regardless of the sign of the potential, provided $|\gamma_i| \gtrsim 10^{-3}$ corresponding to a critical value of the ambipolar field, $E_A \simeq 12$V/cm.

The fluctuation measurements in EBT/NBT experiments[4] indicate that there exists a relatively large positive ambipolar potential in the C-mode operation which decreases but is still positive in the C-T transition, and a large negative ambipolar potential has been measured in the T-mode operation. From the comparison between the present theoretical results and these experimental measurements, we may conclude that the enhancement of the low frequency fluctuations in the C-T transition and the decrease of the fluctuation level in the T-mode operation are strongly connected with the variations of ambipolar potential in the C-T-M mode operations and the formation of the hot electron ring. Finally, we note that large ambipolar potentials may stabilize the electrostatic drift waves but may enhance the flute modes in the bumpy torus plasma, which has been discussed recently[5].

Acknowledgments

The author would like to acknowledge Drs. M. Fujiwara, A. Kamori, and T. Shoji for their useful comments and discussions on the experimental observations. Also, he would like to thank Professor B. D. Fried and Dr. G. J. Morales for their stimulating discussions. This research is sponsored by the U.S. Department of Energy under contract DOE DE-AM03-SF7600010 PA26, Task VIA.

References

[1] L. Bighel, G. Haste, and A. Komori, Proc. of the EBT Stability Theory Workshop, Oak Ridge, Tennessee, May 13, 1981, p. 75.

[2] S. Hiroe, A. Komori, D. Rasmussen, and J. Wilgen, Proc of the US-JAPAN Workshop on Hot Electron Physics, Austin, Texas, January 10, 1983, p.87.

[3] H. Sanuki, T. Watanabe, and M. Watanabe, Phys. Fluids 23, 158 (1980).

[4] T. Shoji, F. Tsuboi and NBT Group, Proc. of the Ambipolar Potential Formation and Control in Bumpy Tori and Mirror Workshop, Oak Ridge, Tennessee, May 12, 1981, P. 423.

[5] H. Sanuki, J. Phys. Soc. Japan 52, 511 (1983).

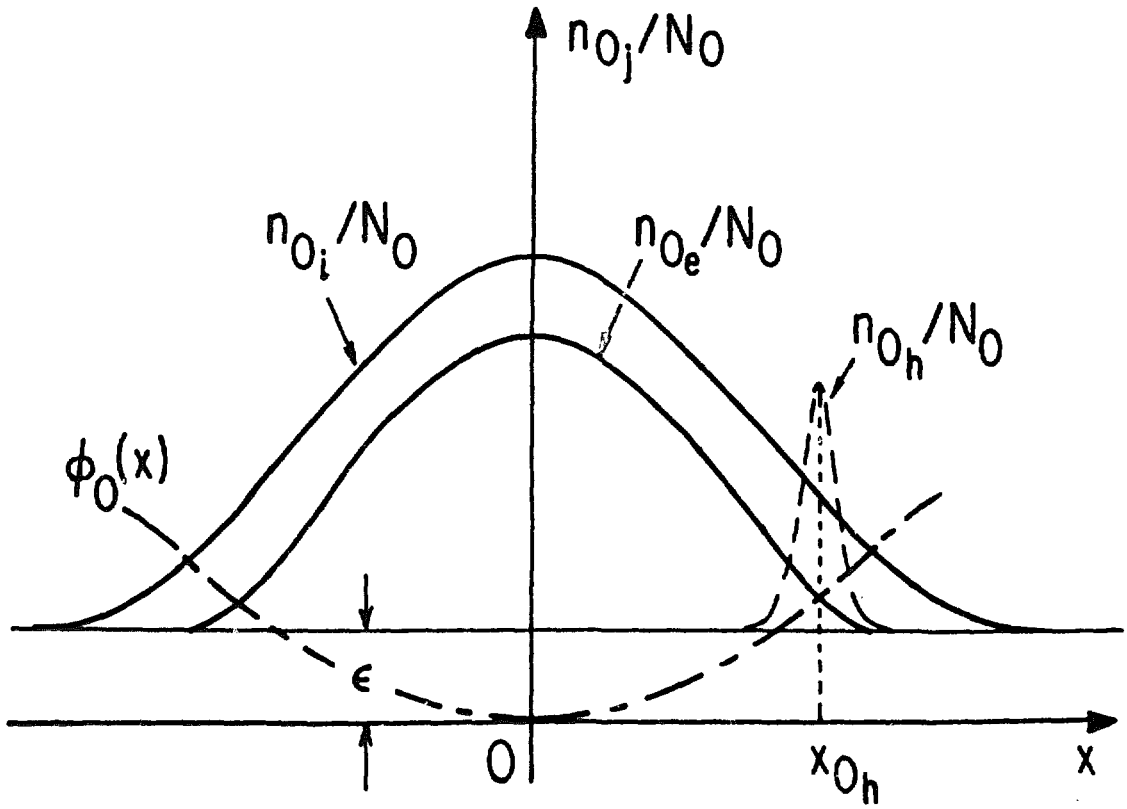

Fig. (1) The radial profiles of the bulk electrons (n_{oe}/N_o), ions (n_{oi}/N_o), the hot electrons (n_{oh}/N_o), and the ambipolar potential are shown. Here, ϵ is an arbitrary constant.

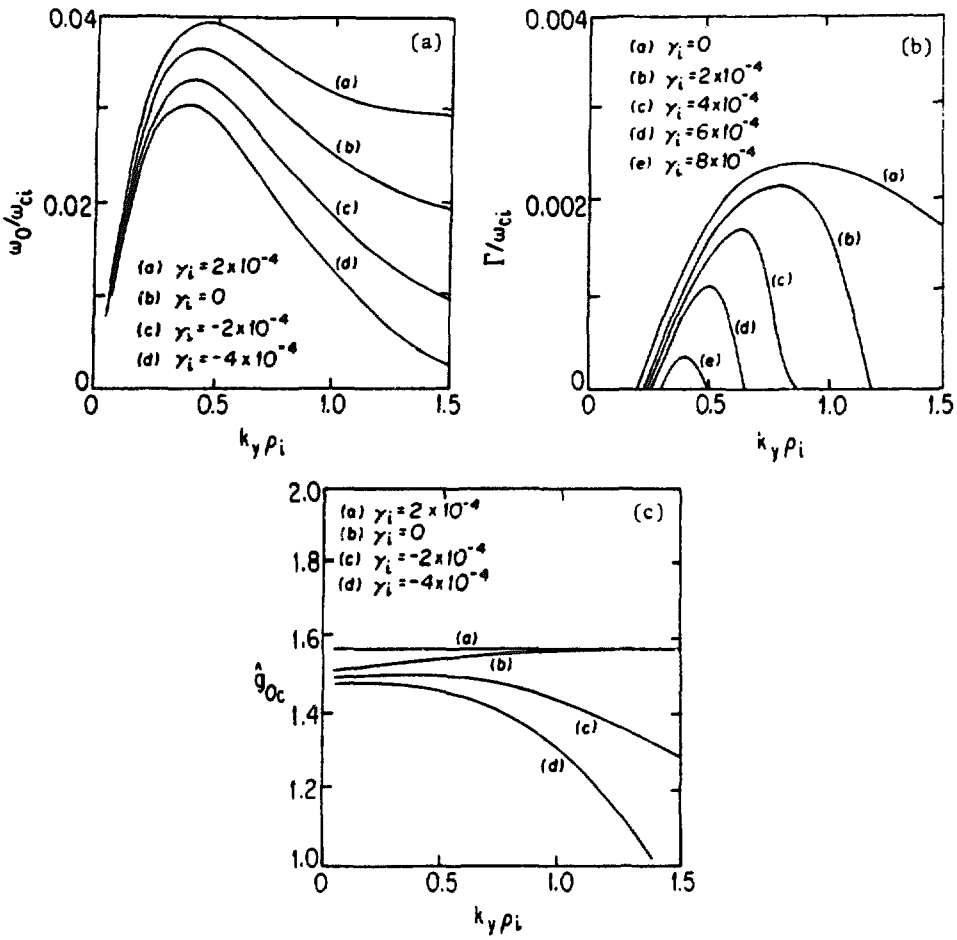

Fig. (2) Effects of the ambipolar potentials on the frequency (Fig. (2a)), the growth rate (Fig. (2b)), and the position of the localization center (Fig. (2c)) of the fundamental mode (N = 0). The parameters as $\gamma_i = 2 \times 10^{-4}$, 0, $-2 \times 10-4$, and -4×10^{-4} are used in Figs. (2a) and (2c). The parameters as $\gamma_i = 0$, 4×10^{-4}, 6×10^{-4}, and 8×10^{-4} are used in Fig. (2b). The parameter $\alpha = 0.1$ is used.

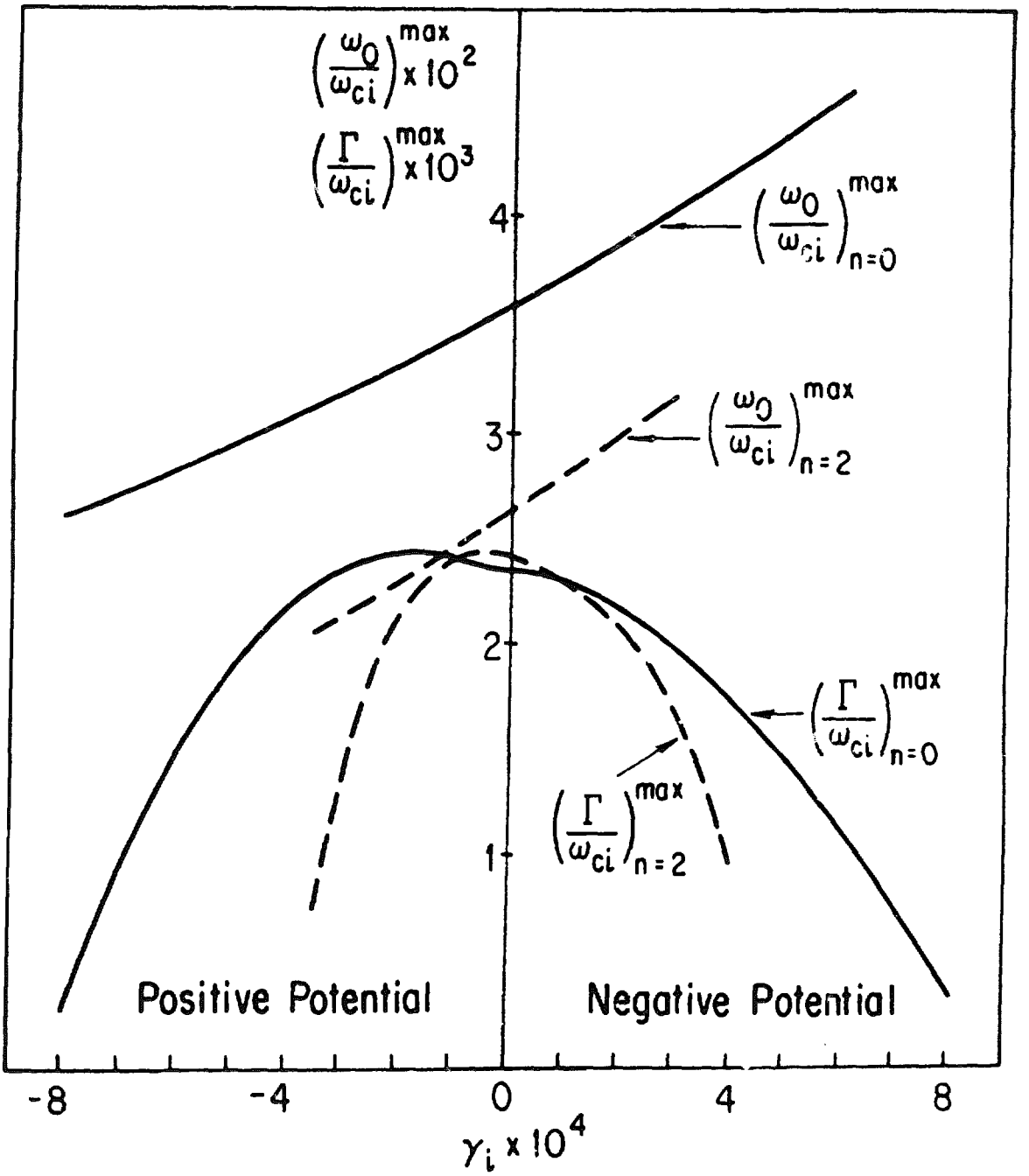

Fig. (3) The maximum values of frequencies and growth rates of the N = 0 (solid line) and N = 2 (dotted line) modes versus both the positive and negative ambipolar potentials ($\pm\gamma_i$). The parameters used are the same as in Fig. (2).

271/272

ELECTRIC FIELD ENHANCED CONFINEMENT

PLASMA CONFINEMENT IN SELF-CONSISTENT, ONE-DIMENSIONAL TRANSPORT EQUILIBRIA IN THE COLLISIONLESS-ION REGIME OF EBT OPERATION*

C.S. Chang and R.L. Miller
AMPC Inc.
Encinitas, California 92024

ABSTRACT

It has long been recognized that if an EBT-confined plasma could be maintained in the collisionless-ion regime, characterized by positive ambipolar potential and positive radial electric field, the particle loss rates could be reduced by a large factor. The extent to which the loss rate of energy could be reduced has not been as clearly determined, and has been investigated recently using a one-dimensional, time-dependent transport code developed for this purpose.

We find that the energy confinement can be improved by roughly an order of magnitude by maintaining a positive radial electric field that increases monotonically with radius, giving a large ExB drift near the outer edge of the core plasma.

The radial profiles of heat deposition required to sustain these equilibria will be presented, and scenarios for obtaining dynamical access to the equilibria will be discussed.

1. INTRODUCTION

It is well known that the quiescent mode (T-mode) of present ELMO Bumpy Torus (EBT) operation is characterized by a negative electrostatic potential in the core plasma region. It is also well known that if the electrostatic potential can be made positive in the core plasma region,

* Work supported by Department of Energy Contract No. DE-AC03-82ER51030.

the particle confinement time should improve substantially[1] in T-mode operation. What are not yet well known are what gives rise to the negative ambipolar potential in the T-mode regime of present EBT experiments and how can the ambipolar potential be controlled. It is the purpose of the present work to study active means of controlling the ambipolar potential profile in the T-mode regime, which can be incorporated into the design of a next generation EBT device.

A one-dimensional transport code was developed specifically for this work and the full set of one-dimensional time dependent transport equations was solved. Unlike the negative potential regime, where resonant behavior enhances the ion transport to the level of electrons and the details of the ambipolar mechanism are not yet known, in the positive potential regime a self-consistent radial electric field profile can be unambiguously obtained from well-known diffusion coefficients. Hence the ambipolar transport problem is much better defined in the positive potential regime.

The possibility of also improving the energy confinement by positive ambipolar potential operation has been in question for some time. We find that it is indeed possible to have significantly enhanced energy confinement (by an order of magnitude) due to the large radial electric field at the edge of the core plasma, which may be an intrinsic property of the positive potential regime (collisionless ion regime).

In Section 2, the radial transport equations are defined and solved numerically to show the enhancement in the confinement times and to show the required heating profiles to achieve equilibrium in the positive potential regime. The physics behind the confinement-enhancement and required heating profiles is presented in Section 3, and a summary appears in Section 4.

2. RADIAL TRANSPORT EQUATIONS AND THE SOLUTIONS

Assuming charge neutrality, the transport equations we solve consist of the ambipolarity, particle conservation, ion energy conservation, and electron energy conservation equations:

$$\Gamma_{er} = \Gamma_{ir} \quad , \tag{1}$$

$$\frac{\partial n}{\partial t} = n_o \langle\sigma v\rangle_i n - \frac{1}{r}\frac{\partial}{\partial r}(r\Gamma_r) \quad , \tag{2}$$

$$\frac{\partial}{\partial t}\left(\frac{3}{2} nkT_i\right) = Q_{i\mu} + Q_{ei} - \frac{1}{r}\frac{\partial}{\partial r}(rQ_{ir}) - n_o\langle\sigma v\rangle_{cx}\frac{3}{2} nk(T_i - T_o) + e\Gamma_{ir}E_r + n_o\langle\sigma v\rangle_i \frac{3}{2} nkT_o \quad , \tag{3}$$

$$\frac{\partial}{\partial t}\left(\frac{3}{2} nkT_e\right) = Q_{e\mu} - Q_{ei} - \frac{1}{r}\frac{\partial}{\partial r}(rQ_{er}) - n_o\langle\sigma v\rangle_i nE_I - e\Gamma_r E_r \tag{4}$$

where $n \equiv n_e \cong n$, $\Gamma_r \equiv \Gamma_{er} \cong \Gamma_{ir}$, $Q_{e\mu}(Q_{i\mu})$ is the microwave power absorbed by the electrons (ions), E_I is the ionization energy, and the rest of the notations are standard.

The ion species are nonresonant since the electric field points radially outward (positive). For simplicity, we assume that the constant electrostatic potential surfaces are concentric circles whose centers coincide with the machine's geometric center; and use the nonresonant diffusion coefficients given by Kovrizhnykh[2] for the ion transport.

The electrons are resonant. We combine Kovrizhnykh diffusion coefficients with the resonant banana diffusion coefficients to obtain a uniformly valid expression:

$$D_e = D_e^B \exp\left[-\frac{1}{3}\frac{\nu_e}{\Omega_e}\left(\frac{R}{a}\right)^{3/2}\right] + D_e^K \quad , \tag{5}$$

where D_e^B represents banana diffusion coefficients and D_e^K denotes Kovrizhnykh coefficients for electrons. The factor $\frac{1}{3}$ in the exponent is chosen for a simple fitting to the plateau values, and the results of Ref. 3 are used for D_e^B.

A set of typical solutions are shown in Fig. 1, using EBT-I(S) parameters with a ring beta value of 20%. One interesting observation made during the numerical study was that all the solutions we obtained required good heating at the plasma center and an equilibrium was not possible with a hollow power deposition profile in the core plasma. We also found that the profile of the ambipolar potential is sensitive to the profile of the power deposition and vice versa. From these observations, we may argue that the negative ambipolar potential observed in the T-mode operation of present EBT devices could result merely from the lack of microwave power deposition at the center of the plasma (hollow power deposition profile) and the positive potential regime operation may be attained with good penetration of the microwave power to the center of the plasma. Simple analytic arguments to support this will be presented in the next section.

The confinement times are most sensitive to the background neutral density as shown in Fig. 2. As we can see from the figures, the confinement times in the positive potential regime are superior to those from the negative potential regime (not shown in the plots). The superiority of the particle confinement time has been known for some time[1], but the improvement in the energy confinement time is new. We find that the improvement in the energy confinement time is due to the intrinsic large electric field of the positive potential regime, which will be explained in the following section. We should point out here that the decrease in the energy confinement time at lower neutral density in Fig. 2 is due to the stronger resonance behavior in the particle motion (banana transport) at lower neutral density.

3. PHYSICAL INTERPRETATION

The two most significant results from the last section are the enhancement (from the negative potential case) in the energy confinement time and the necessity of good core heating for positive potential equilibria. In this section, we present simple physical interpretations of these results.

Let's first consider the enhancement in the energy confinement time. The energy confinement is controlled mostly by the electrons for both positive and negative electrostatic potential cases. The banana diffusion of the electrons is negligibly small (the resonance location is at very high energy) in the positive potential case, except for the very low neutral density cases ($n_o \sim 10^7$). Thus, we may use Kovrizhnykh's coefficients for electron diffusion for both the positive and negative potential cases. Then we can easily show, for the same electron temperatures, that the ratio in the energy confinement times is given as

$$\frac{\tau_E^+}{\tau_E^-} \approx \left(\frac{E_r^+}{E_r^-}\right)^2 , \qquad (6)$$

where E_r^+ (E_r^-) is the representative radial electric field in a positive (negative) potential regime plasma. For a rough confinement estimate, we compare the radial electric fields at the edge of the core plasma.

In the negative electrostatic potential case, the potential well depth is roughly the electron thermal energy. The electric field strength increases as the minor radius, r, increases, but it reaches a maximum value and then decreases again toward the edge of the core plasma and vanishes near the hot electron ring center (see Fig. 3). Thus the electric field magnitude at the edge of the core plasma is smaller than kT_e/ea, where a is the minor radius of the plasma at the midplane.

In the positive potential case, the electric field is determined from the ambipolarity condition, $\Gamma_e = - D_{ne} (n' + nT_e'/T_e + neE_r/kT_e) \cong 0$, which yields $eE_r = kT_e(n'/n)$, assuming $T_e' = 0$ for simplicity. Near the edge of the core plasma, the particle confinement gets better and the density gradient becomes steeper. Hence the magnitude of n'/n becomes larger than a, and we have $E_r > kT_e/ea$.

From the above simple argument, we obtain $E_r^+/E_r^- > 1$ and thus $\tau_E^+/\tau_E^- \simeq (E_r^+/E_r^-)^2 >> 1$, explaining why we should get improved energy confinement by operating in the positive potential regime. The superiority of the particle confinement in the positive potential regime is not discussed here because it is rather well known. But the possibility of enhancement in the energy confinement has been in question for some time and the present work shows that the energy confinement is indeed enhanced significantly (but not as dramatically as the particle confinement).

The second result, the positive potentail equilibrium is maintained only with good heating of the plasma center, can be understood with a simplified electron energy conservation equation. The two main terms in the electron energy conservation equation with $T_e \cong T_i$ are the microwave heat input and the diffusion term. The energy loss through atomic process is insignificant in the positive potential regime because of the low background neutral density. We thus have the following simplified energy conservation equation:

$$\nabla \cdot q_{er} \cong Q_{e\mu} \quad , \tag{7}$$

where $q_{er} \cong - K_{T_e} T_e'$, $K_{T_e} = (V_{ye}^2/6)(\nu_e/\Omega_e^2)(101/2)n$, $\Omega_e \equiv cE_r/Br$, and $V_{ye} \equiv cT_e/eBR_T$. Assuming a parabolic function for $\phi(r)$ and using $\nu_e \propto nT^{-3/2}$, we obtain $q_{er} \propto n^2 T^{\frac{1}{2}} T'$. Due to the large electron heat conduction, T_e is a slowly varying function of r in the core region of the plasma. Hence the main dependence of q_{er} is through n. We now substitute this q_{er} into Eq. (7) and differentiate to obtain $\frac{\partial}{\partial r} \nabla \cdot q_{er} = \frac{\partial}{\partial r} Q < 0$. Therefore, the heat deposition profile should be monotonically decreasing as r increases in the central region of the plasma.

A similar argument can be made for the negative potential case to show that a hollow power deposition profile may be required to maintain a negative potential equilibrium. In the negative potential regime, the ion transport is enhanced by the resonance behavoir and $D_i > D_e$ is obtained (this part is not well understood theoretically). The ambipolarity is then maintained by detailed adjustment of the ion radial flow. If D_i becomes bigger than D_e due to the resonance behavior, then we have $\Gamma_i \simeq 0$ as the ambipolarity condition. Hence, $n' = neE_r/T_i$ is obtained and the electric field has the same value as the positive potential case except for the sign. This different sign in the electric field yields a different sign in the gradient of the power deposition profile and therefore it could be concluded that the negative electric field equilibrium requires a hollow power deposition profile. We must caution here that the requirement of a hollow $Q_{e\mu}$ profile for a negative potential equilibrium is merely from the preceding hand waving argument, whereas the requirement of good central heating for the positive potential equilibrium is obtained from a rigorous numerical study.

4. DISCUSSIONS

Using a one-dimensional transport code, we have shown that, by maintaining positive ambipolar potential in a bumpy torus, we can obtain plasmas with good confinement times ($\tau_E \simeq 30$ msec for EBT-S) and that we may be able to achieve a positive potential equilibrium by good heating of the plasma center. Simple arguments have also been presented in an attempt to understand the physics behind these results.

Electron heating has been used as the main power source in the present study, and only small amounts of direct ion heating power have been tried. A limited study of the positive potential equilibrium has been done with high power ICH heating power and preliminary results indicate that an equilibrium is possible only at very high neutral density, thus yielding low confinement times. Further study is now underway.

The present study indicates that control of the power deposition profile may be a key "knob" to control the ambipolar potential in a bumpy torus. Having the ability to control the power deposition profile, and thus the ambipolar potential profile, may be an essential feature for the success of present and future bumpy tori experiments.

REFERENCES

1. R.A. Dandl and G.E. Guest, "The ELMO Bumpy Torus", in Fusion, Vol 1, Part B, Ed., E. Teller.
2. I.M. Kovrizhnykh, Ah. Ehksp. Teor. Fiz., 56, 877 (1969), (Sov. Phy.-JETP 29, 475 (1969).
3. D.E. Hastings, E.F. Jaeger, C.L. Hedrick and J.S. Tolliver, Phys. Fluids 6, 1516 (1983).

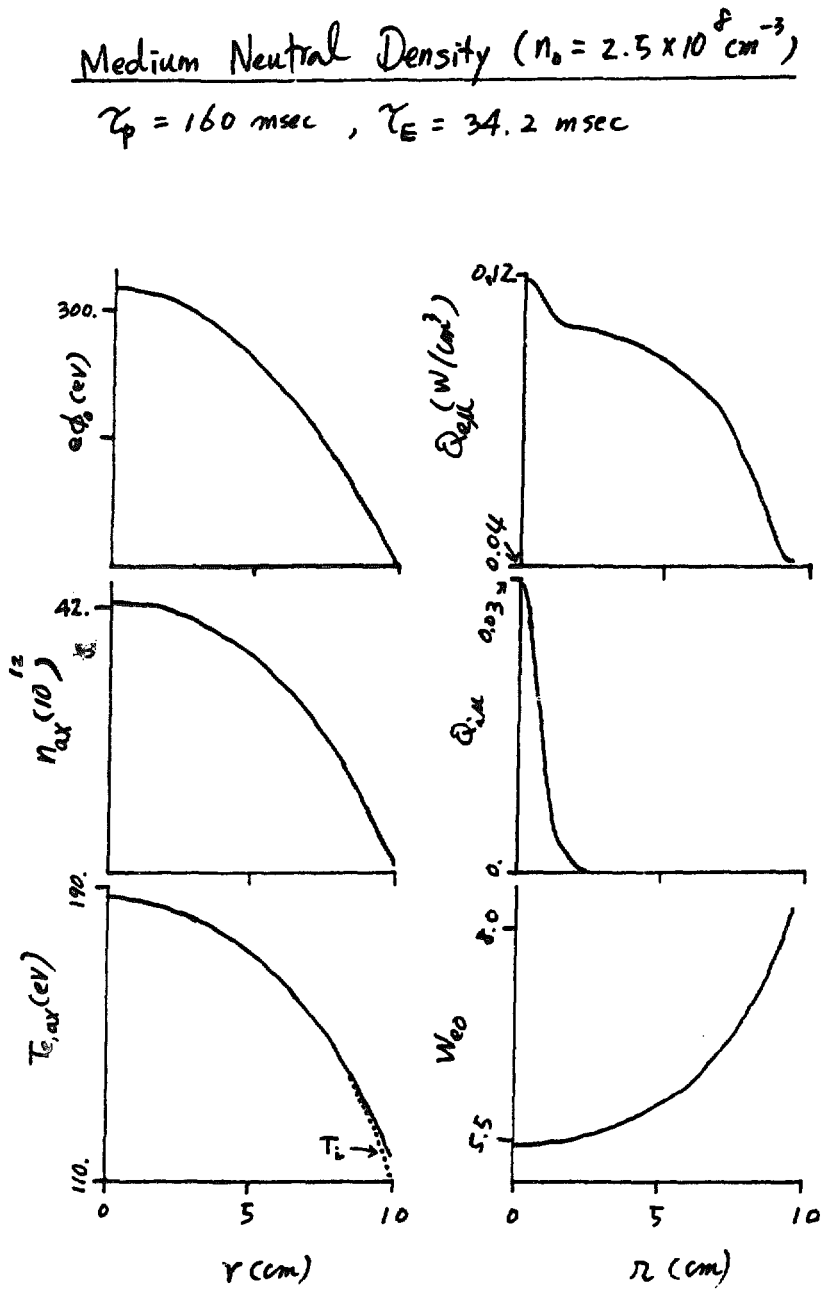

Fig. 1. A typical equilibrium in the positive ambipolar potential regime with ECH power deposition comparable to that of present EBT-S experiments (50 MW). Background neutral density is 2.5 x 10^8 cm^{-3}. τ_E = 160 msec and τ_p = 34 msec.

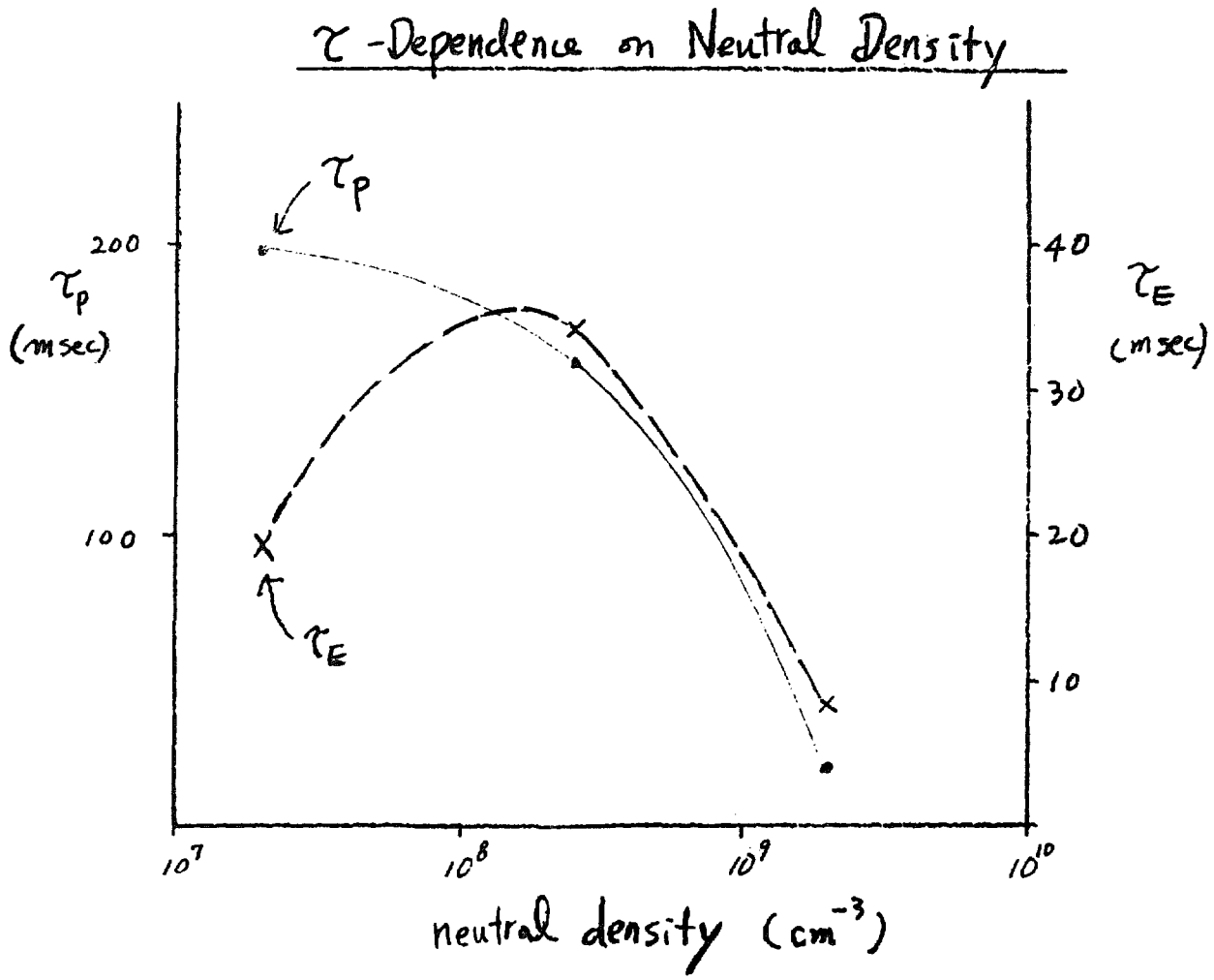

Fig. 2. Dependence of the confinement times on the background neutral density.

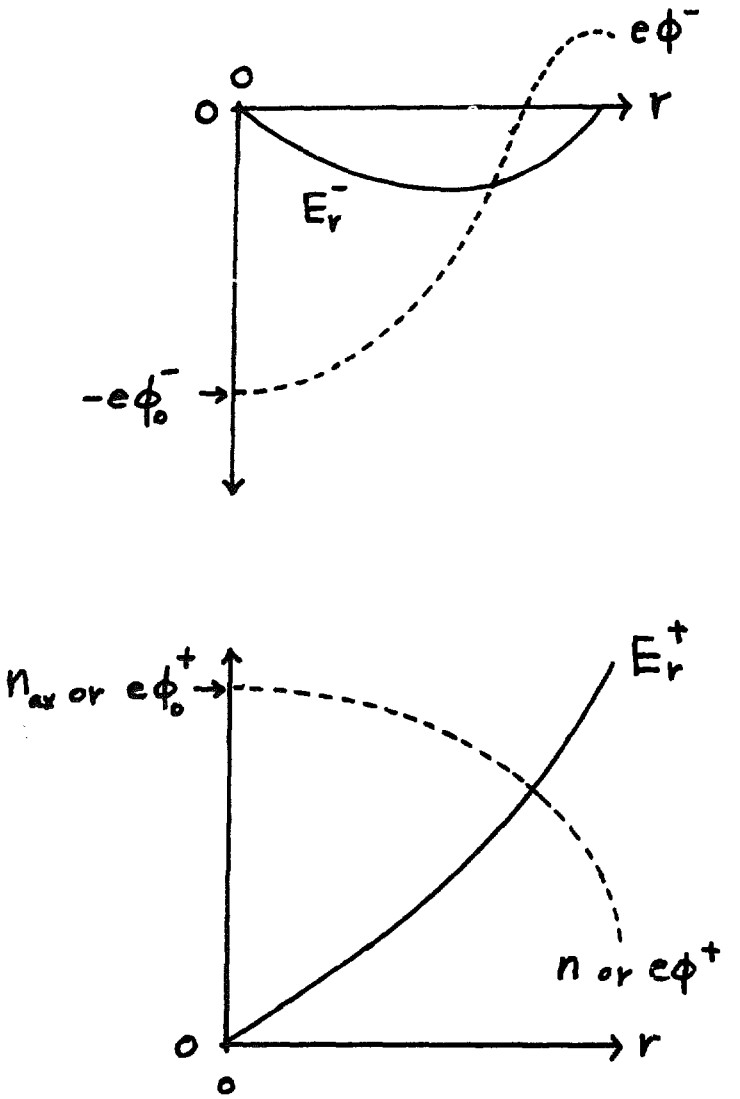

Fig. 3. Comparison of the ambipolar electric field for the positive and negative potential regimes.

ICRF Confinement and Stabilization of Torus Plasma

H. Hojo, K. Hamamatsu, T. Watanabe and Kyoji Nishikawa

(Part I Theoretical Analysis)

and

K. Sakai†, S. Takeuchi† and M. Matsumoto†

(Part II Particle Simulation)

Faculty of Science and Institute for Fusion Theory
Hiroshima University, Hiroshima 730, Japan
†*Faculty of Engineering, Yamanashi Univ. Yamanashi 400, Japan*

Abstract

Possibility for improving confinement and MHD stability of torus plasma by the ponderomotive force of rf field in the ion cyclotron range of frequencies is studied.

The ponderomotive force perpendicular to the magnetic field produces cross-field drift in addition to the curvature and gradient-B drifts. As a result, closed particle drift orbits can be formed. Numerical calculation of particle orbits in a simple torus with strong rf field is carried out to show the ICRF confinement of plasma. Vlasov equilibrium of torus plasma with rf field is also studied for a simplified model.

When the drift due to the ponderomotive force perpendicular to the magnetic field cancels the curvature drift, the MHD instability such as curvature-driven interchange modes can be suppressed. ICRF stabilization of a hot electron plasma due to the ponderomotive force effect is studied theoretically. A particle simulation is carried out for a gravity-driven mode analogous to the interchange mode and the stabilization by ponderomotive force of ICRF field is shown .

Part I Theoretical Analysis

§ 1 Introduction

Bumpy torus is receiving increasing attention both experimentally and theoretically in fusion research. One of the recent interests in the bumpy torus is in developing new advanced concepts to improve the confinement and MHD stability of the plasma .

In the bumpy torus, there exists no magnetic surface and the gradient-B drift by the bumpy field produces the rotational transform for plasma particles to form closed drift orbits[1]. The radial electric field due to the ambipolar plasma potential can also improve the particle confinement, though the strong ambipolar potential will not be appropriate from the viewpoint of plasma stability. The MHD stability of the bumpy torus plasma is owing to a hot electron ring created by ECRH. Recent theoretical studies[2,3,4] have, however, shown that when the hot electron ring is allowed to be perturbed, various instabilities can appear and the hot electron stabilization of the core plasma may not be optimistic .

We here propose a new approach for improving the confinement and MHD stability of torus plasmas. Our basic idea is the control of the plasma by ponderomotive force effects of a strong rf field . The rf field considered is in the ion cyclotron range of frequencies , where a strong coupling between ions

and rf fields is expected . The ponderomotive force along the magnetic field is often used to suppress the end loss of plasma particles in open-ended systems [5, 6] For the present purpose, the ponderomotive force perpendicular to the magnetic field is of importance, which can modify the confinement and stability.

First, the cross field drift by the ponderomotive force produce the rotational transform for particles to be confined. This implies the possibility of plasma confinement by an rf field even if no other rotational transform is present such as in a simple torus.

Secondly, the cross field drift by the ponderomotive force is possible to cancel the bad curvature drift. The curvature driven interchange modes can then be suppressed. The rf stabilization of flute modes in mirror-confined plasmas has been shown in several experiments[7 - 9]

The content of the present paper is as follows. We first show an elementary derivation of the general expression for the time averaged force (ponderomotive force) of a strong rf field. The results are compared quantitatively with the direct numerical computation of particle orbits in a simple torus with strong ICRF field. The equilibrium of ICRF sustained torus is analyzed in § 3 with a simplified model. The ICRF stabilization of the curvature-driven modes is studied in § 4 based on the energy principle. Particle simulation on ICRF stabilization of the gravity-driven modes analogous to the curvature-driven modes is summarized in § 5.

§ 2 Ponderomotive Force of RF Field

Time averaged force of a strong rf field (i.e., ponderomotive force) has been studied theoretically and numerically[10 - 12]. Here, we show that the ponderomotive force is a potential force independent of the specific structure of the magnetic and rf fields.

Particle orbits under the rf field are determined by

$$d\mathbf{x}/dt = \mathbf{v}, \tag{1}$$

$$d\mathbf{v}/dt = (q/M)[\ \mathbf{E}_0 + \mathbf{E}_s \sin(\omega t) + \mathbf{E}_c \cos(\omega t) + \mathbf{v} \times (\mathbf{B}_0 + \mathbf{B}_s \sin(\omega t) + \mathbf{B}_c \cos(\omega t))/c\ ], \tag{2}$$

where q and M are the charge and mass of the particle and $\mathbf{E}_0$ and $\mathbf{B}_0$ are the static electric and magnetic fields . $\mathbf{E}_s$, $\mathbf{E}_c$, $\mathbf{B}_s$ and $\mathbf{B}_c$, which are assumed to be real functions of space variable $\mathbf{x}$ alone, represent amplitudes of the rf electromagnetic field. These amplitudes are related through Maxwell's equations:

$$\omega \mathbf{B}_s = -c\,\nabla \times \mathbf{E}_c, \tag{3}$$

$$-\omega \mathbf{B}_c = -c\,\nabla \times \mathbf{E}_s. \tag{4}$$

We analyze eqs. (1) and (2) by the Bogoliubov method[13]. To this end, we first introduce the following normalizations:

$$\omega t = \tilde{t} \tag{5}$$

$$\mathbf{x}/a = \tilde{\mathbf{x}}, \tag{6}$$

$$\mathbf{E}_s = E_{rf}\,\tilde{\mathbf{E}}_s, \tag{7}$$

$$\mathbf{E}_c = E_{rf}\,\tilde{\mathbf{E}}_c, \tag{8}$$

$$\mathbf{v} / (R / a)^{1/2} (q E_{rf} / M \omega) = \tilde{\mathbf{v}}, \tag{9}$$

$$\mathbf{E}_0 = (q E_{rf}^2 / M \omega^2 a) \tilde{\mathbf{E}}_0, \tag{10}$$

$$\mathbf{B}_0 = B_0 \tilde{\mathbf{B}}_0, \tag{11}$$

where the wigle '~' represents the normalized quantities and a and R are the minor and major radii of the torus. E_{rf} and B_0 are the typical intensities of the rf electric field and the static magnetic field, respectively. The electrostatic field $\mathbf{E}_0$ is normalized by the intensity of the ponderomotive potential which is assumed to be the origin of the electrostatical potential in the plasma. The normalization factor of the particle velocity $\mathbf{v}$ is determined from the condition of confinement by the ponderomotive force: i.e.

centrifugal force $\simeq$ ponderomotive force,

$$M \mathbf{v}^2 / R \simeq q^2 E_{rf}^2 / M \omega^2 a.$$

The equations of motion of particles (1), (2) are rewritten as

$$d \mathbf{x} / d t = \epsilon \mathbf{v}, \tag{12}$$

$$\begin{aligned} d \mathbf{v} / d t = {} & (a/R)^{1/2} [\mathbf{E}_s \sin(t) + \mathbf{E}_c \cos(t)] \\ & + \epsilon(a/R) \mathbf{E}_0 + \Omega_c \mathbf{v} \times \mathbf{B}_0 \\ & + \epsilon(a/R)^{1/2} \mathbf{v} \times [- \nabla \times \mathbf{E}_c \sin(t) + \nabla \times \mathbf{E}_s \cos(t)], \end{aligned} \tag{13}$$

where $\mathbf{x}$, $\mathbf{v}$, t, $\mathbf{E}$, $\mathbf{B}$ are all normaiized quantities and the wigle is omitted hereafter. The quantity Ω_c represents the normalized cyclotron frequency defined by

$$\Omega_c = (q B_0 / M c) / \omega, \tag{14}$$

and ϵ is defined by

$$\epsilon = (R / a)^{1/2} (q E_{rf} / M \omega^2) / a, \tag{15}$$

$$= (\text{ aspect ratio })^{1/2} (\text{ excursion length / minor radius }),$$

and is assumed to be small:

$$\epsilon < 1 .$$

When the above condition is satisfied, the equation of motion, (12) and (13) can be analyzed by the Bogoliubov's method [13]. The quantity **x** and **v** are composed of the averaged parts and the oscillating parts as

$$\mathbf{x} = \mathbf{y} + \mathbf{x}_1, \tag{17}$$

$$\mathbf{v} = \mathbf{w} + \mathbf{v}_1, \tag{18}$$

where **y** and **w** are the averaged parts of the position **x** and the velocity **v**. The oscillating parts due to the rf field are represented by $\mathbf{x}_1$ and $\mathbf{v}_1$.

At the lowest order of expansion, we have, after straightforward calculations,

$$\mathbf{x}_1 = \mathbf{x}_s \sin(t) + \mathbf{x}_c \cos(t), \tag{19}$$

$$\mathbf{v}_1 = \mathbf{v}_s \sin(t) + \mathbf{v}_c \cos(t), \tag{20}$$

$$\begin{aligned} \mathbf{x}_s &= \epsilon\, \mathbf{v}_c \\ &= \epsilon\, (a/R)^{1/2} [-(\mathbf{B}_0\mathbf{E}_s)\, \mathbf{B}_0 \\ &\qquad + (\mathbf{E}_s \times \mathbf{B}_0) \times \mathbf{B}_0 / (1 - \Omega_c^2 \mathbf{B}_0^2) \\ &\qquad - \Omega_c \mathbf{B}_0^2\, \mathbf{E}_c \times \mathbf{B}_0 / (1 - \Omega_c^2 \mathbf{B}_0^2)] / \mathbf{B}_0^2 , \end{aligned} \tag{21}$$

$$\begin{aligned} \mathbf{x}_c &= -\epsilon\, \mathbf{v}_s \\ &= -\epsilon\, (a/R)^{1/2} [(\mathbf{B}_0\mathbf{E}_c)\, \mathbf{B}_0 \\ &\qquad - (\mathbf{E}_c \times \mathbf{B}_0) \times \mathbf{B}_0 / (1 - \Omega_c^2 \mathbf{B}_0^2) \\ &\qquad - \Omega_c \mathbf{B}_0^2\, \mathbf{E}_s \times \mathbf{B}_0 / (1 - \Omega_c^2 \mathbf{B}_0^2)] / \mathbf{B}_0^2 . \end{aligned} \tag{22}$$

Equation of motion for the averaged parts reduces to

$$d\,\mathbf{y}/dt = \epsilon\,\mathbf{w}, \tag{23}$$

$$\begin{aligned} d\,\mathbf{w}/dt = {} & (a/R)^{1/2}\,[\,(\mathbf{x}_c\nabla)\,\mathbf{E}_c + (\mathbf{x}_s\nabla)\,\mathbf{E}_s\,]/2 \\ & + \Omega_c[\,\mathbf{v}_s \times (\mathbf{x}_s\nabla)\mathbf{B}_0 + \mathbf{v}_c \times (\mathbf{x}_c\nabla)\mathbf{B}_0\,]/2 \\ & + \epsilon\,(a/R)^{1/2}\,[\,-\mathbf{v}_s\times(\nabla\times\mathbf{E}_c) + \mathbf{v}_c\times(\nabla\times\mathbf{E}_s)\,]/2 \\ & + \epsilon\,(a/R)\;\mathbf{E}_0 + \Omega_c\,\mathbf{w}\times\mathbf{B}_0\,. \end{aligned} \tag{24}$$

In the above expression, the electromagnetic field **E** and **B** should be evaluated at the position **y** (the averaged position of particle motion) and ∇ represents the derivative with respect to **y**.

The equation of motion for the averaged position **y**, eq.(24), can be reduced to a simple form (see appendix 1),

$$d\,\mathbf{w}/dt = \Omega_c\,\mathbf{w}\times\mathbf{B}_0 + \epsilon\,(a/R)\,\mathbf{E}_0 - \epsilon\,(a/R)\,\nabla\,\Psi_{rf}\,, \tag{25}$$

where Ψ_{rf} is the ponderomotive potential and is given by

$$\begin{aligned} \Psi_{rf} = {} & \tfrac{1}{4}\,\epsilon\,(a/R)\,[\,(\mathbf{B}_0\mathbf{E}_c)^2 + (\mathbf{B}_0\mathbf{E}_s)^2 \\ & + (\,(\mathbf{E}_c\times\mathbf{B}_0)^2 + (\mathbf{E}_s\times\mathbf{B}_0)^2)\,/\,(1 - \Omega_c^{\,2}\mathbf{B}_0^{\,2}) \\ & + 2\,\Omega_c\mathbf{B}_0^{\,2}\,(\mathbf{E}_s\times\mathbf{E}_c)\,\mathbf{B}_0\,/\,(1 - \Omega_c^{\,2}\mathbf{B}_0^{\,2})\,]. \end{aligned} \tag{26}$$

The averaged force of the rf filed is reduced to a potential force independent of the specific structure of the rf field or the magnetic field. The expression for the ponderomotive force is essentially the same as the results of ref. 10). The 'ponderomotive magnetic field' derived in ref. 10) is not appeared in the present situation. The validity of the ponderomotive potential (26) and the possibility of ICRF sustaining of torus plasma by the ponderomotive force are examined by the direct numerical computation of eqs. (1) and (2) for a given appropriate form of the electromagnetic field. Typical example are shown

in Figs. 1 - 4. These results are in good agreement with the above analysis.

§ 3 Steady State Equilibrium Distribution Function and a Simple Model of ICRF Sustained Torus

When a strong rf field is applied, the distribution function of the plasma will be separated to a sum of the steady part and the rf oscillating part. The rf oscillating part determines the selfconsistent profile of the rf field in a plasma. Here we do not consider this problem.

The steady state part of the distribution function should be a function of the constants of motion. Here we restrict ourselves to the case of ICRF sustained simple torus.

In the present paper, we make the following assumptions:

1) Electromagnetic field is a travelling wave in the toroidal direction, namely,

$$\mathbf{E}_{rf}(\mathbf{x}, t) = \mathbf{E}_s \sin(t) + \mathbf{E}_c \cos(t)$$
$$= \mathbf{E}_1(r,z) \sin(m\theta - t) + \mathbf{E}_2(r,z) \cos(m\theta - t).$$
$$(m : \text{integer}) \qquad (27)$$

2) Static magnetic field $\mathbf{B}_0$ is present only in the toroidal direction and assumed to be

$$\mathbf{B}_0 = (0, B_0 R/r, 0). \qquad (28)$$

In this case the ponderomotive potential becomes axisymmetric and the equa-

tion of motion (23) and (25) have the two constants of motion, energy E and angular momentum P_θ in the θ direction ,

$$E = \tfrac{1}{2} M (d \mathbf{y} / d t)^2 + q \Psi_0 + \Psi_{rf}, \tag{29}$$

$$P_\theta = M (y_x w_y - y_y w_x) , \tag{30}$$

where and hereafter we express all quantities without normalization. The ponderomotive potential Ψ_{rf} is given by

$$\begin{aligned}\Psi_{rf} = \tfrac{1}{4} q^2 / M^2 \omega^2 [& (\mathbf{B}_0\mathbf{E}_1)^2 + (\mathbf{B}_0\mathbf{E}_2)^2 \\ & + ((\mathbf{E}_1 \times \mathbf{B}_0)^2 + (\mathbf{E}_2 \times \mathbf{B}_0)^2) / (1 - \Omega_c^2 \mathbf{B}_0^2) \\ & - 2 \Omega_c \mathbf{B}_0^2 (\mathbf{E}_1 \times \mathbf{E}_2) \mathbf{B}_0 / (1 - \Omega_c^2 \mathbf{B}_0^2)].\end{aligned} \tag{31}$$

The steady state distribution function f_0 ($\mathbf{x}$, $\mathbf{v}$) should be a function containing only E and P_θ . If we express the averaged quantities $\mathbf{y}$ and $\mathbf{w}$ by $\mathbf{x}$ and $\mathbf{v}$ using eqs. (17) and (18), the steady state distribution function $f_0(\mathbf{x},\mathbf{v})$ is given by

$$\begin{aligned} f_0(\mathbf{x},\mathbf{v}) = F_0 [& \tfrac{1}{2} M (\mathbf{v} - \mathbf{v}_1)^2 + q \Psi_0(\mathbf{x} - \mathbf{x}_1) + \Psi_{rf}(\mathbf{x} - \mathbf{x}_1) , \\ & (x - x_1)\times(v_y - v_{1y}) - (y - y_1)\times(v_x - v_{1x})] . \end{aligned} \tag{32}$$

In general, the distribution function will have a dependency on P_θ , but we assume here for simplicity that the steady state distribution depends only on the energy. If the rf field is in the frequency range of the ion cyclotron and the rf electric field is almost perpendicular to the magnetic field, the ponderomotive force gives a significant effect only on ions and will give little effect on electrons. We can then consider the situation that the ion is confined by the ponderomotive force while the electron is confined by the ambipolar electric field. As the simplest model we assume the following form of distribution

functions:

$$f_{0j} = n_0 (M_j / 2\pi T_j)^{3/2}$$
$$\times \exp[- [\tfrac{1}{2} M_j (\mathbf{v}-\mathbf{v}_{1j})^2 + q_j \Psi_0 (\mathbf{x}-\mathbf{x}_{1j}) + \Psi_{rfj} (\mathbf{x}-\mathbf{x}_{1j})]/T_j], \quad (33)$$

where suffix ' $_j$ ' represents the ion (j = i) or the electron (j = e). The ponderomotive potential for the electron, $\Psi_{rf\,e}$ is neglected.

Steady state of the current and the density profile is obtained by the distribution function (33). Selfconsistent spacial distribution of the plasma and the spacial profiles of $\mathbf{E}_0$, $\mathbf{B}_0$ are determined by the Poisson and Ampere equations:

$$(\partial / r\partial r) (r \partial \Psi_0 / \partial r) + (\partial^2 \Psi_0 / \partial z^2)$$
$$= -4\pi e (n_i - n_e)$$
$$= -4\pi e\, n_0 (\exp[- (e\Psi_0 + \Psi_{rf\,i}) / T_i] - \exp[e\Psi_0 / T_e]) . \quad (34)$$

Here we have neglected the small difference between the actual particle position and the time averaged particle position. In the present model the diamagnetic plasma current is zero, then the magnetic field (28) is self consistent.

In the region in which the plasma density is sufficiently high, the Poisson equation (34) can be replaced by the quasi-neutrality condition;

$$n_i \simeq n_e .$$

In this case, the steady state density distribution and the ambipolar potential are given by

$$n_i = n_e = n_0 \exp[- \Psi_{rf\,i} / (T_i + T_e)] , \quad (35)$$

$$\Psi_0 = - \Psi_{rf\,i} T_e / (T_i + T_e) . \quad (36)$$

In the periphery of the plasma, the plasma density becomes low and the quasineutral condition breaks down. To study the structure near the plasma edge, we have solved the Poisson equation (34) neglecting the z - dependence. with the condition that $\partial \Psi_0 / \partial r = 0$ at the boundaries. The results are summarized in Figs. 5 - 7 .

§ 4 RF Stabilization of Curvature-Driven Modes

We study **rf** stabilization of curvature-driven modes in a bumpy torus plasma in this section. The **rf** stabilization of flute modes in a mirror-confined plasma has been studied by several authors[14 - 16) , but their theories are applicable only to a sufficiently low-β plasma. The present analysis of **rf** stabilization, which allows arbitary beta, is based on the energy principle. A guiding center energy principle which takes into account the effects of rf fields is obtained by Hojo[17) , which is analogous to the theory of Antonsen and Lee[18) .

We here consider a cylinder plasma model and the magnetic field is given by

$$\mathbf{B} = B\,\mathbf{b} = \nabla \psi \times \nabla \chi , \qquad (37)$$

where ψ is the magnetic flux and χ the poroidal angle. When the perturbations are expressed in terms of displacement ξ of a field line ($\xi \cdot \mathbf{b} = 0$) and the perturbed magnetic field $\mathbf{Q}$ defined by

$$\mathbf{Q} = \nabla \times (\xi \times \mathbf{B}) . \qquad (38)$$

The energy integral ΔW including the effects of the rf field is written as

$$\Delta W = \Delta W_F + \Delta W_{rf} + \Delta W_K \,. \tag{39}$$

$$\begin{aligned}\Delta W_F = \frac{1}{2}\int d\tau \,\{ & \frac{\sigma}{4\pi} Q_\perp^2 + \frac{\tau_*}{4\pi} Q_\parallel \\ & - \frac{\sigma}{c} J_\parallel b\cdot(Q_\perp\times\xi) - (\xi\cdot\kappa)(\xi\cdot\hat{\nabla}p_\parallel) \\ & - \frac{1}{B}(2Q_\parallel+\xi\cdot\nabla B)[\xi\cdot\hat{\nabla}P_\perp + \frac{P_{\perp\psi_0}}{-\rho_{\psi_0}}\xi\cdot\hat{\nabla}\rho]\} \,,\end{aligned} \tag{40}$$

$$\begin{aligned}\Delta W_{rf} = \frac{1}{2}\int d\tau \sum_{e,i} \{ & \frac{n}{B}\frac{\partial}{\partial B}(\psi_{rf}+\nu_{rf})Q_\parallel^2 \\ & + n[\xi\cdot\nabla\psi_{rf}+\frac{Q_\parallel}{B}(\nu_{rf}+B\frac{\partial}{\partial B}\psi_{rf})](\xi\cdot\nabla\ell nB+\xi\cdot\kappa-\xi\cdot\nabla\ell nn) \\ & - (\xi\cdot\kappa)Q_\parallel n\frac{\partial}{\partial B}\psi_{rf} \\ & - (\xi\cdot\nabla\psi_{rf})[(\xi\cdot\kappa)P_{\parallel\psi_{rf}} + \frac{1}{B}(2Q_\parallel+\xi\cdot\nabla B)\times(P_{\perp\psi_0}+\frac{P_{\perp\psi_0}}{-\rho_{\psi_0}}\rho_{\psi_{rf}})]\} \,,\end{aligned} \tag{42}$$

$$\Delta W_K = -\frac{1}{2}\int d\tau \sum_{e,i}\int d\Gamma\, H(H-\langle q\hat{\phi}_L+\xi\cdot\nabla\psi_{rf}\rangle)\frac{\partial F_0}{\partial\varepsilon} \,, \tag{41}$$

$$H = \langle mv_\parallel^2(\xi\cdot\kappa) + (\mu+\frac{q\rho_B}{-\rho_{\psi_0}})(Q_\parallel+\xi\cdot\nabla B)\rangle \,,$$

$$\sigma = 1 + \frac{4\pi}{B^2}(P_\perp - P_\parallel) \,, \qquad \tau_* = 1 + \frac{4\pi}{B}P_{\perp B} + \frac{4\pi\rho_B^2}{-\rho_{\psi_0}} \,,$$

$$(\phi+\xi\cdot\nabla\psi_0-\hat{\phi}_L)\rho_{\psi_0} + (Q_\parallel+\xi\cdot\nabla B)\rho_B = 0 \,,$$

where $\boldsymbol{\kappa} = (\mathbf{b} \cdot \nabla)\,\mathbf{b}$ is the curvature, n the density, $P_\perp$ and $P_\parallel$ the perpendicular and parallel pressure, respectively, ρ the charge density, Ψ_0 the electrostatic potential, ϕ the perturbed electrostatic potential, $J_\parallel$ the parallel plasma current ($J_\parallel = 0$ in an axisymmetric system), Ψ_{rf} the ponderomotive potential and ν_{rf} the quantity being related to the rf-induced magnetization M ($\mathbf{M} = M\mathbf{b}$) through $M = -n\,\nu_{rf} / B$, E and μ the energy and magnetic moment of a particle, respectively, defined by

$$E = \tfrac{1}{2}\, m\,(v_\perp^2 + v_\parallel^2) + q\Psi_0 + \Psi_{rf} \qquad (43)$$

and

$$\mu = m\, v_\perp^2 / (2B) , \qquad (44)$$

ω_* the diamagnetic drift frequency, ω_d the guiding center drift frequency composed of the curvature drift, gradient-B drift, $E \times B$ drift and $F_{rf} \times B$ drift by the ponderomotive force $\mathbf{F}_{rf}$, and F_0 the equilibrium guiding center distribution function. We note that all quantities in eq.(39) are defined in the oscillation center coordinates, which provide a convenient description of the plasma in the presence of rf field[10]. The bracket < > in eq.(42) denotes the bounce average along the field line defined by

$$< \ldots > = \int (\ldots)\, ds/|v_\parallel| / [\int ds/|v_\parallel|] .$$

In eq.(39), ΔW_F is the fluid-like part, ΔW_K the kinetic part and ΔW_{rf} the part explicitly dependent on the rf field.

We now study rf stabilization of flute interchange modes driven by the bad magnetic curvature in a hot electron plasma. We here restrict ourselves to the local stability analysis. For simplicity, we assume that all species (the core

ion, core electron and hot electron) are Maxwellian and neglect the effect of the ambipolar potential. The analysis is also restricted to the axisymmetric system and high-m modes. We shall consider only the outer region of the ring.

We first analyze the electrostatic interchange modes and neglect the effect of the parallel perturbed magnetic field $Q_{\parallel}$. The stability condition in this case is given by

$$(\beta_c + \beta_h)(\beta_c + \beta_h - \beta_*) + 2\delta_{rf} > 0 , \qquad (45)$$

$$\beta_* = 4\Delta / R$$

$$\delta_{rf} = (\Delta / \Delta E)(8\pi n \psi_{rf} / B^2)$$

$$\Delta = 1 / |\nabla \ln(n)| \simeq 1 / |\nabla \ln(p)| ,$$

$$\Delta E = 1 / |\nabla \ln(\Psi_{rf})| ,$$

where β_c and β_h are the core and hot electron betas, and R is the curvature radius. In the derivation of eq.(45), the force balance equation expressed as

$$p' + B B' / 4\pi \simeq B^2 \kappa / 4\pi - n \Psi'_{rf} ,$$

is used, where the prime $'$ denotes the derivative with respect to Ψ. Without rf field, we have the usual stability criterion $\beta_h + \beta_c > \beta_*$, which expresses the condition for the reversing of the ion drift. With rf fields, the stability condition is changed as

$$\beta_c + \beta_h > \beta_* / 2 + [(\beta_*/2)^2 - 2\delta_{rf}]^{1/2} ,$$

or

$$\beta_c + \beta_h > \beta_* / 2 - [(\beta_*/2)^2 - 2\delta_{rf}]^{1/2} , \qquad (46)$$

and we have the complete rf stabilization of the electrostatic interchange modes when $\delta_{rf} > (\beta_*)^2 / 8 = 2 (\Delta / R)^2$.

We next analyze the interacting interchange modes of the core plasma. We assume that the ring electron is so hot as to satisfy $| \omega_{dc} | << \omega << | \omega_{dh} |$ and the sufficient diamagnetic well is created by the hot electron ring. From the minimization of the energy integral ΔW with respect to $Q_{\parallel}$, we have the stability condition given by

$$2\delta_{rf} - (\beta_c + \beta_h) \times \{ \beta_* + \beta_h (\beta_c + \beta_h) / [\beta_c (1 + \beta_h) - \delta_{rf} - \beta_*] \} > 0 . \qquad (47)$$

This equation provides the Nelson-VanDam-Lee criterion in the absence of rf fields.

The stability condition eq.(47) is satisfied for weaker rf fields when

$$\beta_c < (\beta_* + \delta_{rf}) / (1 + \beta_h) . \qquad (48)$$

Eq.(48) gives the upper boundary of β_c and the lower boundary becomes that obtained for electrostatic modes, that is, eq.(46) if the estimation $| \beta_c (\beta_h + 1) - \delta_{rf} - \beta_* | \simeq \beta_h$ is adopted in eq.(47). The stability boundary in this case is shown in Fig.8. If we require stronger rf fields, we obtain the stability even for

$\beta_c(1+\beta_h) > \delta_{rf} + \beta_*$. In this case, the ponderomotive potential, thereby electric field required for the stability is given by

$$\delta_{rf} > \tfrac{1}{2}\,(\beta_c + \beta_h)\,(\beta_c + \beta_h + \beta_*)\,, \qquad (49)$$

except for the region $\beta_c(1+\beta_h) - \delta_{rf} - \beta_* < \beta_h$

We here studied the effects of the ponderomotive force on curvature - driven interchange modes of the core plasma in a hot electron plasma and obtained the increase of stability boundaries by the ponderomotive force effects of rf fields. The nonlocal analysis and examinations of the ponderomotive force effect on other modes are left to our future problems.

Acknowledgements

The authors wish to express their sincere thanks to Prof. H. Ikegami and NBT group of Institute of Plasma Physics, Nagoya university for the motivation and encouragement of the present studies. They are also grateful to Prof. T. Hatori for valuable comments. This work was partially supported by the Grant in Aids for the Scientific Research of the Ministry of Education, Science and Culture of Japan, and the Nissan Science Foundation.

Appendix **Derivation of Ponderomotive Potential**

The time averaged force $\mathbf{F}_{rf}$ (ponderomotive force) of the rf field is given by the right hand side of eq. (24):

$$\mathbf{F}_{rf} = \tfrac{1}{2} (a / R)^{1/2} [(\mathbf{x}_c \nabla) \mathbf{E}_c + (\mathbf{x}_s \nabla) \mathbf{E}_s]$$
$$+ \tfrac{1}{2} \Omega_c [\mathbf{v}_s \times (\mathbf{x}_s \nabla) \mathbf{B}_0 + \mathbf{v}_c \times (\mathbf{x}_c \nabla) \mathbf{B}_0]$$
$$+ \tfrac{1}{2} \epsilon (a/R)^{1/2} [-\mathbf{v}_s \times (\nabla \times \mathbf{E}_c) + \mathbf{v}_c \times (\nabla \times \mathbf{E}_s)] . \qquad (A - 1)$$

To simplify the manipulation, we calculate the ponderomotive force in the typical direction, i.e. in the x-direction. If we represent the $\mathbf{x}_c$, $\mathbf{x}_s$ by $-\epsilon \dot{\mathbf{x}}_s$, $\epsilon \mathbf{x}_c$, the ponderomotive force in the x-direction $F_{rf\,1}$ reduces to

$$F_{rf\,1} = \tfrac{1}{2} \epsilon (a / R)^{1/2} [- (v_{s\,1} \partial_1 + v_{s\,2} \partial_2 + v_{s\,3} \partial_3) E_{c\,1}$$
$$+ (v_{c\,1} \partial_1 + v_{c\,2} \partial_2 + v_{c\,3} \partial_3) E_{s\,1}]$$
$$- \tfrac{1}{2} \epsilon \Omega_c [v_{s\,2} (v_{c\,1} \partial_1 + v_{c\,2} \partial_2 + v_{c\,3} \partial_3) B_{0\,3}$$
$$- v_{c\,2} (v_{s\,1} \partial_1 + v_{s\,2} \partial_2 + v_{s\,3} \partial_3) B_{0\,3}$$
$$- v_{s\,3} (v_{c\,1} \partial_1 + v_{c\,2} \partial_2 + v_{c\,3} \partial_3) B_{0\,2}$$
$$+ v_{c\,3} (v_{s\,1} \partial_1 + v_{s\,2} \partial_2 + v_{s\,3} \partial_3) B_{0\,2}]$$
$$- \epsilon (a / R)^{1/2} [- v_{s\,2} (\partial_1 E_{c\,2} - \partial_2 E_{c\,1})$$
$$+ v_{c\,2} (\partial_1 E_{s\,2} - \partial_2 E_{s\,1})$$
$$+ v_{s\,3} (\partial_3 E_{c\,1} - \partial_1 E_{c\,3})$$
$$- v_{c\,3} (\partial_3 E_{s\,1} - \partial_1 E_{s\,3})] , \qquad (A\ 2)$$

where suffixes ' $_1$ ', ' $_2$ ', ' $_3$ ' represent the ' x ', ' y ', ' z ' and

$\partial_i = \partial / \partial y_i$, (i = 1 , 2 , 3) .

The above relations reduce to a simple form due to the relation $\nabla \mathbf{B}_0 = 0$,

$$F_{rf\,1} = \tfrac{1}{2}\,\epsilon\,(a/R)^{1/2}\,[\,-\mathbf{v}_s\,\partial_1\,\mathbf{E}_c + \mathbf{v}_c\,\partial_1\,\mathbf{E}_s\,]$$
$$+\ \tfrac{1}{2}\,\epsilon\,\Omega_c\,(\mathbf{v}_c \times \mathbf{v}_s)\,\partial_1\,\mathbf{B}_0\,. \qquad (A-3)$$

If we replace $\mathbf{E}_s$ and $\mathbf{E}_c$ by $\mathbf{v}_c$ and $\mathbf{v}_s$ using the following relations ,

$$-\mathbf{v}_c = (a/R)^{1/2}\,\mathbf{E}_s + \Omega_c\,\mathbf{v}_s \times \mathbf{B}_0\,, \qquad (A-4)$$

$$\mathbf{v}_s = (a/R)^{1/2}\,\mathbf{E}_c + \Omega_c\,\mathbf{v}_c \times \mathbf{B}_0\,, \qquad (A-5)$$

which are the relations between the rf oscillating parts ,

the ponderomotive force (A - 3) reduces to

$$F_{rf\,1} = \tfrac{1}{2}\,\epsilon\,\partial_1\,[\,-\tfrac{1}{2}\,(\mathbf{v}_s^{\,2} + \mathbf{v}_c^{\,2}) + \Omega_c\,(\mathbf{v}_s \times \mathbf{v}_c)\,\mathbf{B}_0\,)\,]\,. \qquad (A-6)$$

The above relation holds for any directions , though for simplicity we considered the one along the x-direction. The ponderomotive force is proved to be a potential force. The ponderomotive potential Ψ_{rf} is given by

$$\Psi_{rf} = \tfrac{1}{4}\,\epsilon\,(\mathbf{v}_s^{\,2} + \mathbf{v}_c^{\,2}) - \tfrac{1}{2}\,\epsilon\,\Omega_c\,(\mathbf{v}_s \times \mathbf{v}_c)\,\mathbf{B}_0\,,$$
$$= -\tfrac{1}{4}\,(a/R)^{1/2}\,(\mathbf{x}_c\,\mathbf{E}_c + \mathbf{x}_s\,\mathbf{E}_s)\,, \qquad (A-7)$$

where we have again used the relations (A - 4), (A - 5) .

The result (A - 7) is essentially the same as the result of ref 10), though the ''ponderomotive magnetic field '' does not appear in the present situation. If we substitute the expressions (21) and (22) into eq. (A - 7) we can express the ponderomotive potential in terms of the amplitude of the rf field as shown in eq. (26).

Referencies

1) E. R. Jeager, C. L. Hedrick, and J. S. Tolliver, *A kinetic Transport Model for the Elmo Bumpy Torus* , Oak Ridge National raboratory report ORNL/TM-6313, Oak Ridge National Raboratory, Oak Ridge, Tennessee (1978)

2) H. L. Berk, J. W. Van Dam, Rosenbluth and D. A. Spong: phys. Fluids **26** (1983) 201

3) Adel. El-Nadi: Phys. Fluids **25** (1982) 2019.

4) K. T. Tsang and P. J. Catto: Phys. Fluids **25** (1982) 1260

5) K. Adatti, T. Watari, T. Aoki, S. Hidekuma, S. Hiroe, M. Ichimura, K. Kawamoto, R.Kumazawa, Y. Okubo, S. Okamura, T. Sato, C. M. Singh, K.Takayama, M.Sugawara, H. Akiyama, H. Takeda, R. Itatani, Y. Yasaka: *Plasma Physics and Controlled Nucrear Research*, **vol 1**, IAEA Vienna, (1981) 143

6) T. Watanabe, H. Hojo and Kyoji Nishikawa: *Theoretical and Computational Plasma Physics* , IAEA, Vienna (1978) 441

7) H. Akimune, I. Ikeda, T. Hirata and F. Okamoto: J. Phys. soc. Japan **50** (1981) 2729

8) Y. Yasaka, H.Imaizumi and R. Itatani: Proc. Int. Conf. Plasma Physics (Nagoya, 1980 ½ **vol. 1**, p. 327

9) Breun et al., : Japan - US Work Shop on Tandem Mirrors (Tsukuba , 1983)

10) H. Hatori and H. Washimi: Pys. Rev. Letters, **46**, (1981) 243

11) J. R. Cary and A. N. Kaufman; Phys. Rev. Letters, **39**, (1977) 402

12) T. Watanabe, A. Oda, H.Hojo and Kyoji Nishikawa: J. Phys. Sos. Japan, **49** (1980) 1988.

13) N. Krylov and N.N. bogoliubov: *Introduction to Nonlinear Mechanics* (Princeton Univ. Press, 1947).

14) H. Hojo: Kakuyugo-Kenkyu (1982) [in Japanese]

15) K Itoh and S. I. Itoh: Japanese J. Applied Phys. **21** (1982) L 203

16) H.Sanuki: J. Phys. Soc. Japan **52** (1983) 511.

17) H. Hojo: in preparation.

18) T. M. Antonsen, Jr. and Y. C. Lee: Phys. Fluids **25** (1982) 132

Figure Captions

Fig. 1 The drift surface $W(r, z) = const.$ in (r,z) plane. The drift surface $W(r, z)$ is defined by the angular momentum and the ponderomotive potential as

$$W(r, z) = \tfrac{1}{2} P_\theta^2 / r^2 M + \Psi_{rf}(r, z).$$

Rf electric field is assumed to be given by the rf vector potential $\mathbf{a}(\mathbf{x}, t)$,

$$\mathbf{a}(\mathbf{x}, t) = (E_{rf} / c\omega)[-z, 0, r - R] \times \rho^2 \exp(-\rho^2 / a^2) \sin(m\theta - t),$$

$$\rho = ((r - R)^2 + z^2)^{1/2},$$

$R = 100$ cm, $a = 20$ cm,

$B_0(r = R) = 1$ T, $E_{rf} = 3$ kV/cm,

$\omega / \omega_{c0} = 1.4$, $m = 1$,

$\tfrac{1}{2} M (r v_\theta)^2 = (115.0)^2 \times 50 \text{ cm}^2 \times \text{eV}$.

Fig. 2 Particle orbit in (r,z) plane calculated from the equation of motion (1) and (2) with the same parameters as those given in Fig. 1. Initial conditions of the particle are as follows:

$\mathbf{x}(t = 0) = (115, 0, 0)$,

$\mathbf{v}(t = 0) = (v_0, v_0, v_0)$,

$\tfrac{1}{2} M v_0^2 = 50$ eV.

The initial conditions for Figs. 3 and 4 are also the same as those given in the above table.

The particle orbits are in accordance with the prediction of the drift surface shown in Fig. 1 .

Fig. 3 Variation of kinetic energy of the ion. The result shows that the particle motion is almost completely adiabatic.

Fig. 4 Time evolution of the angular velocity v_θ. Due to the time averaged conservation of the angular momentum, the value v_θ changes periodically with the period of the rotational motion of particle in (r,z) plane.

Fig. 5 Spatial structure of the electrostatic potential created by the ponderomotive potential Ψ_{rf}, which is assumed to be given by

$$\Psi_{rf} = \frac{1}{4} (q^2 / M \omega^2) [E_{rf}^2 (1 - \cos(\pi (r-R)/2a))]^2 / [1 - (R - a)^2 / 1.44 \times \rho^2] .$$

The typical plasma parameters are as follows;

$T_i = T_e = 938$ eV, $n_{center} = 3.4\ 10^9$ cm $^{-3}$,

$R = 100$ cm, $a = 20$ cm, $B_0 = 1$ t ,

$\omega = 1.2\ \omega_c (r = R - a)$,

a) $E_{rf} = 1.5$ kV / cm .

b) $E_{rf} = 6$ kV / cm .

c) $E_{rf} = 9$ kV / cm .

The ponderomotive force increases the ambipolar potential inside the plasma. When the ponderomotive force becomes strong, the potential

height exceeds the ion temperature T_i (case b , c) .

Fig. 6 Density profile of the ion (solid lines) and the electron (dashed lines) . The plasma parameters are the same as those shown in Fig. 5. Strong rf field can confine the plasma in a torus (case c) .

Fig. 7 The potential height inside the plasma as a function of the intensity of the ICRF field.

Fig. 8 The marginal stability boundary for the interacting interchange mode in the presence of the ponderomotive force effect of rf field, where β_c and β_h are the core and ring betas, respectively, $\Delta / R = 0.05$ and $\delta_{rf} = 0.05$. The dashed lines show the Nelson - Van Dam - Lee stability boundaries.

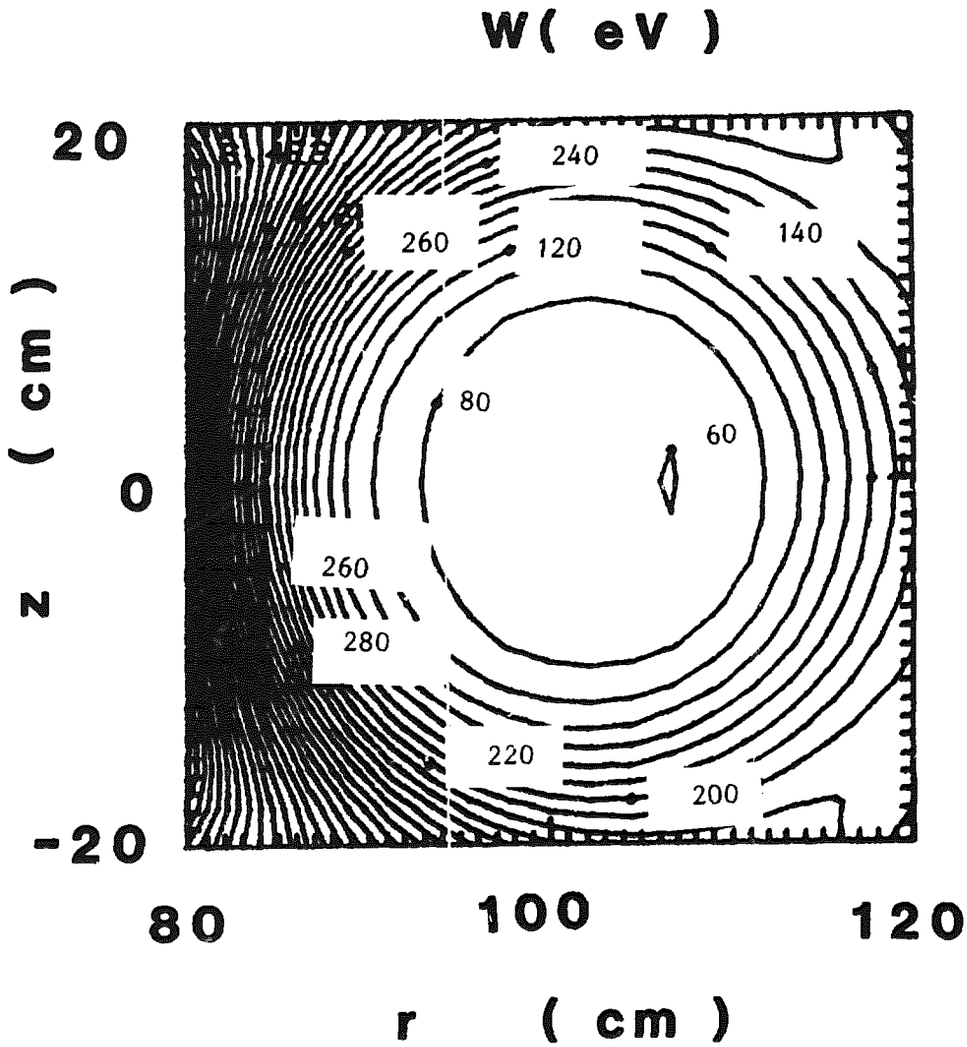
W(eV)
20
0
-20
z (cm)
80
100
120
r (cm)
240
260
120
140
80
60
260
280
220
200

Fig. 1

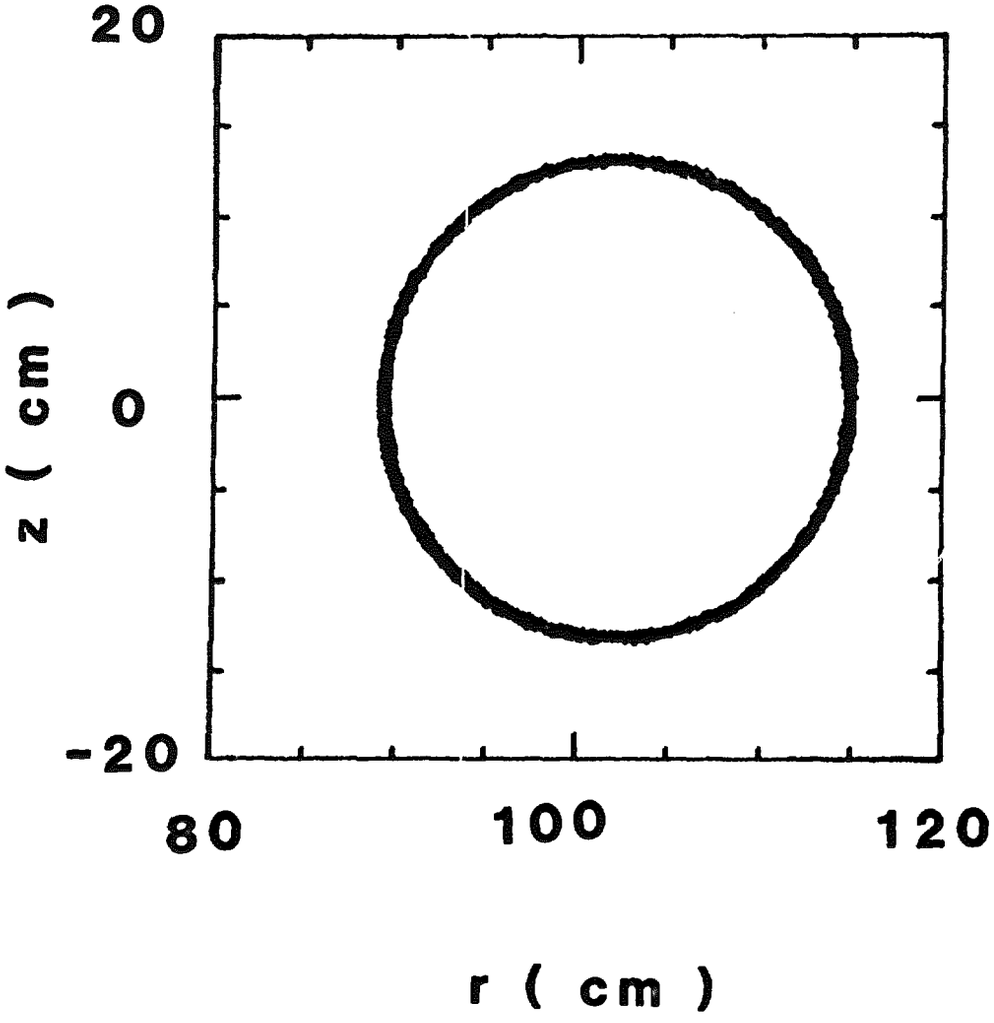

Fig. 2

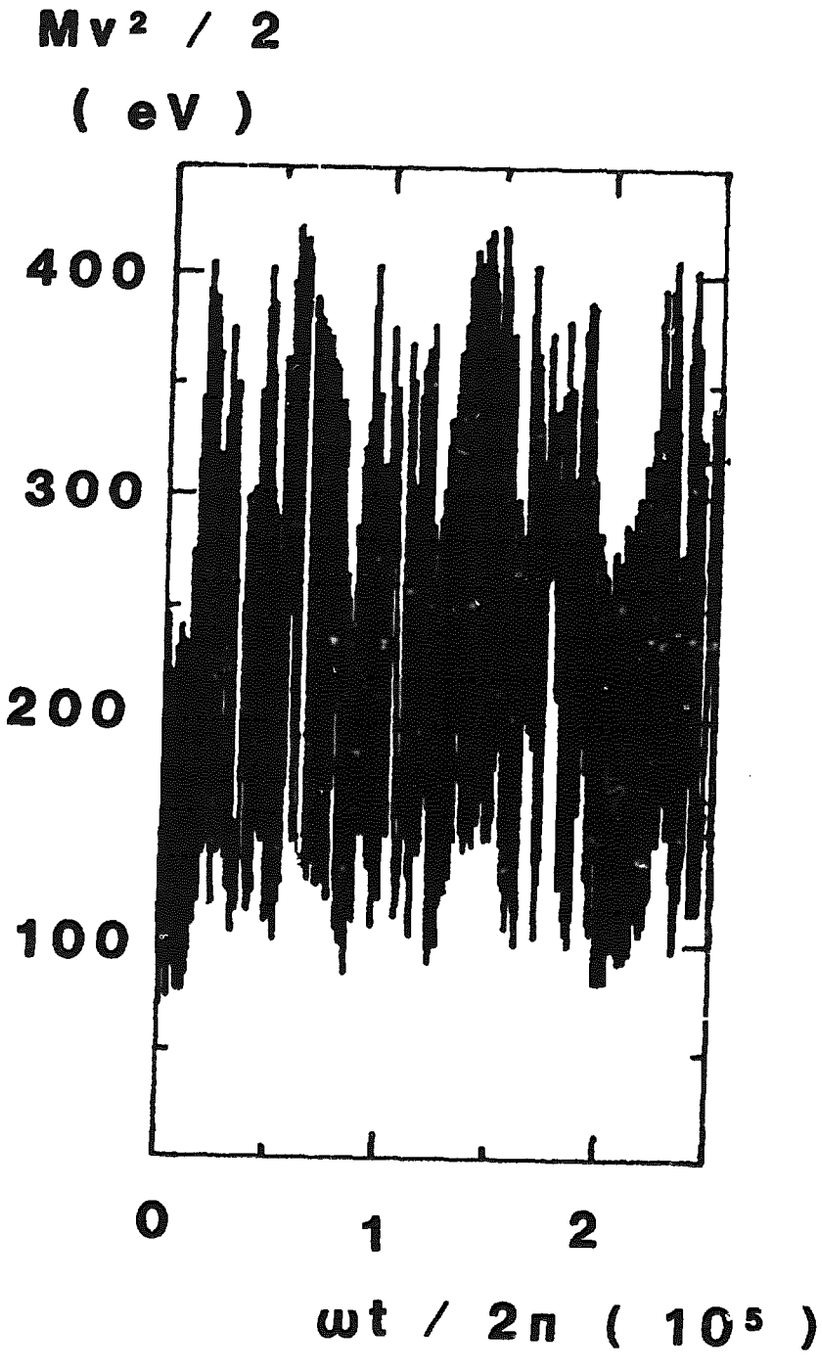

Fig. 3

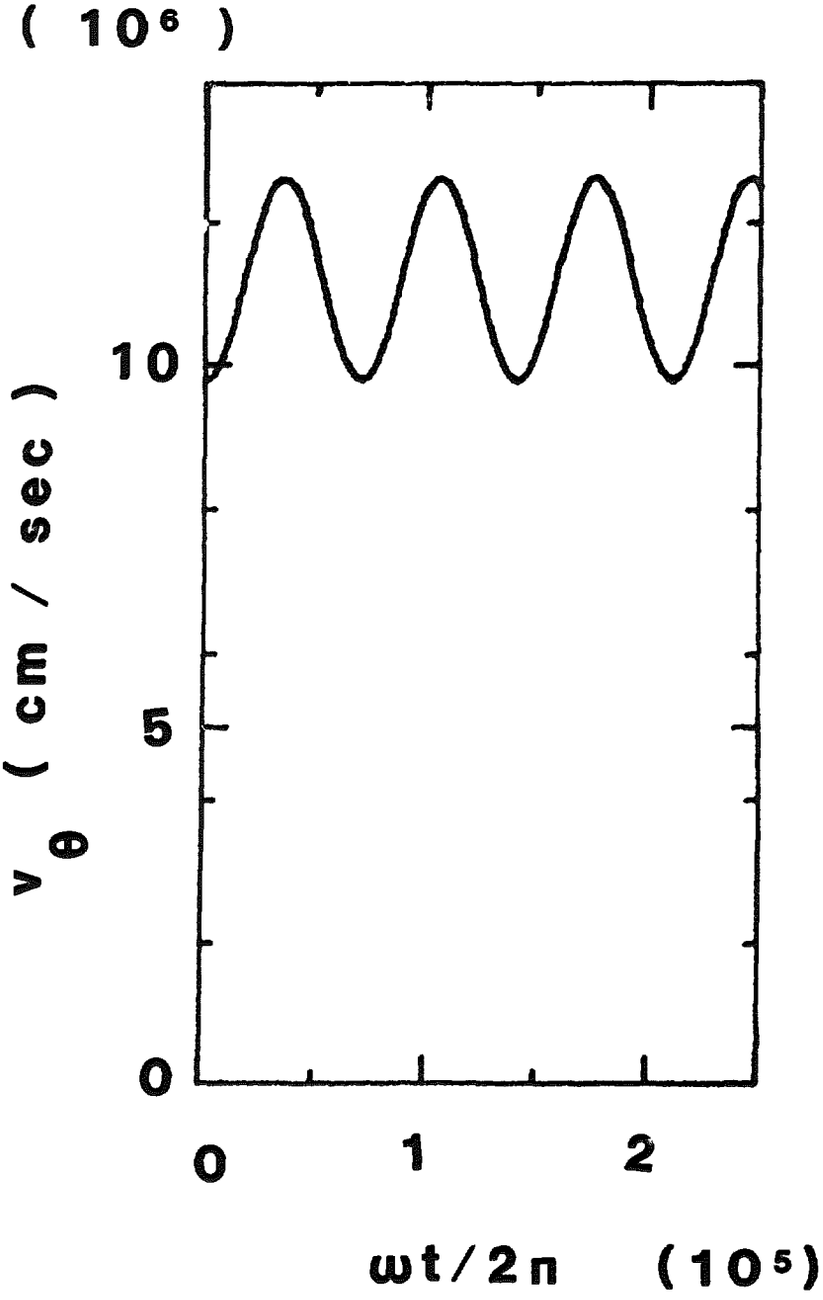

Fig. 4

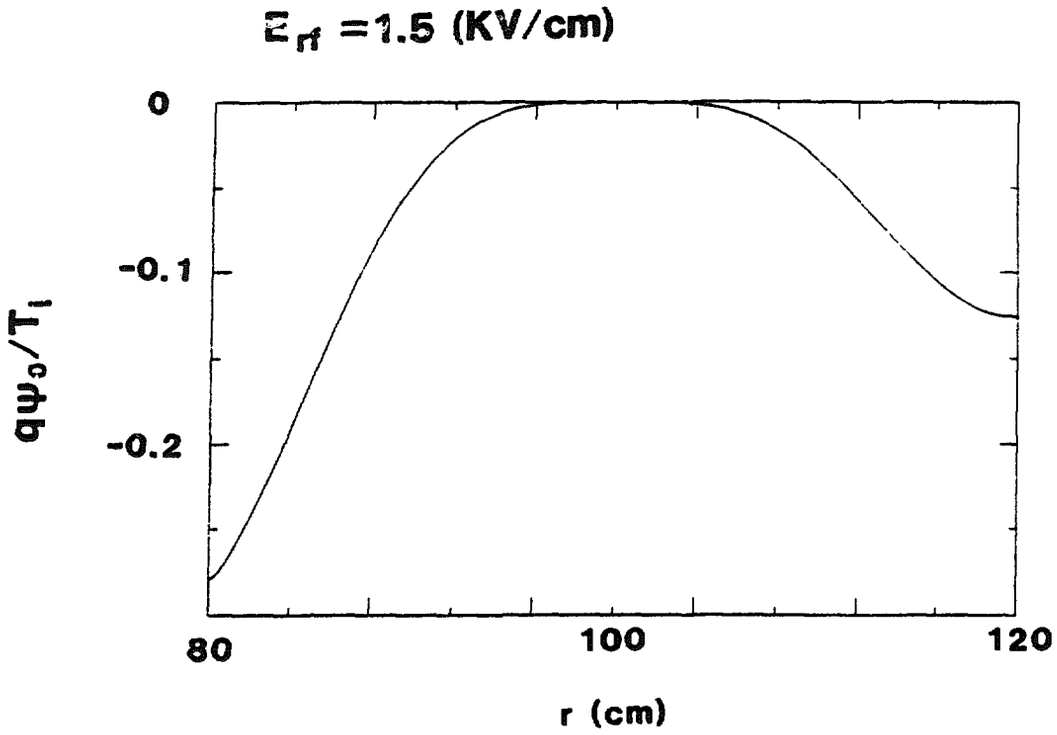
E_rf =1.5 (KV/cm)
0
-0.1
-0.2
qψ₀/T_i
80
100
120
r (cm)

Fig. 5(a)

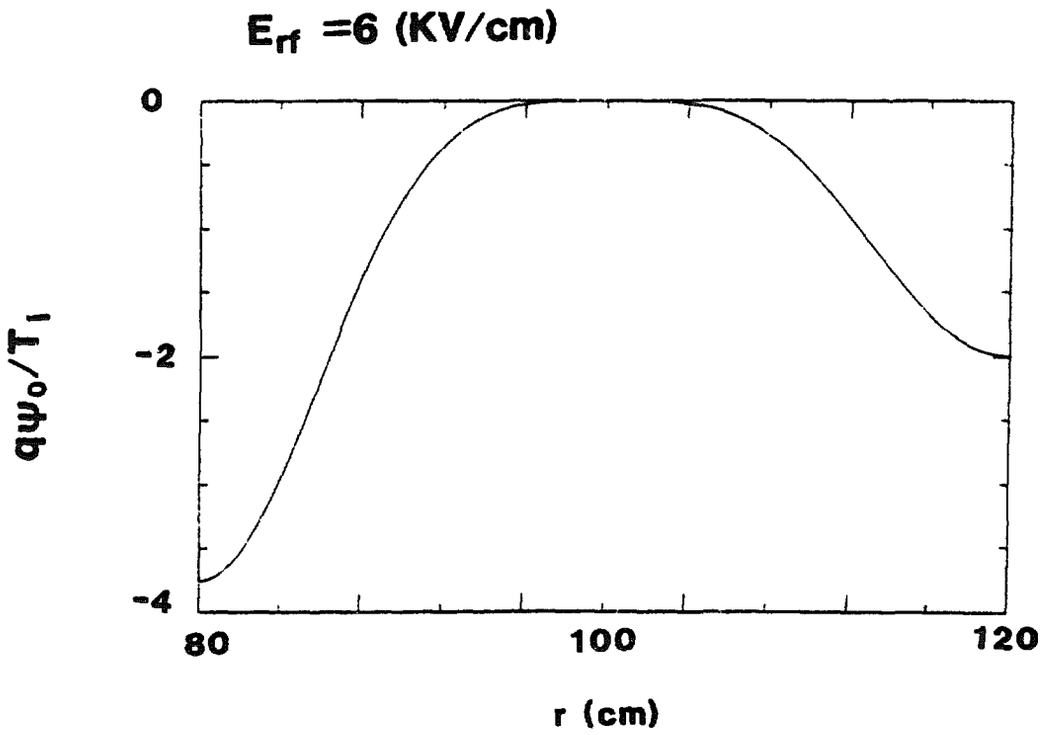
E_rf =6 (KV/cm)
0
-2
-4
qψ₀/T_i
80
100
120
r (cm)

Fig. 5(b)

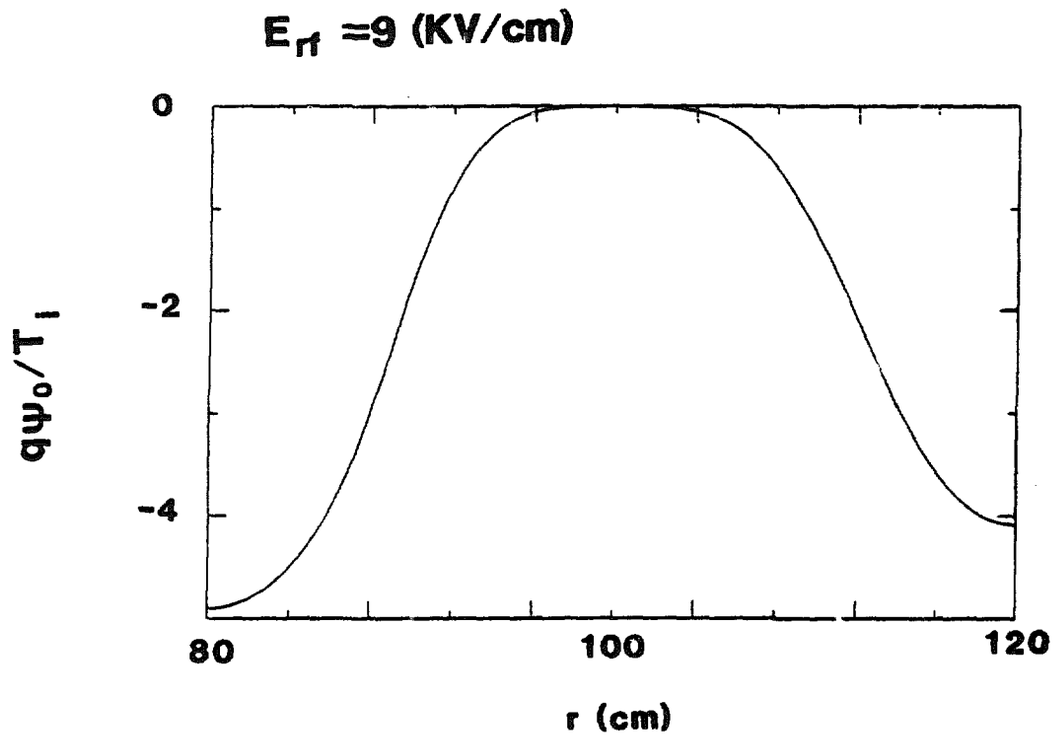

Fig. 5(c)

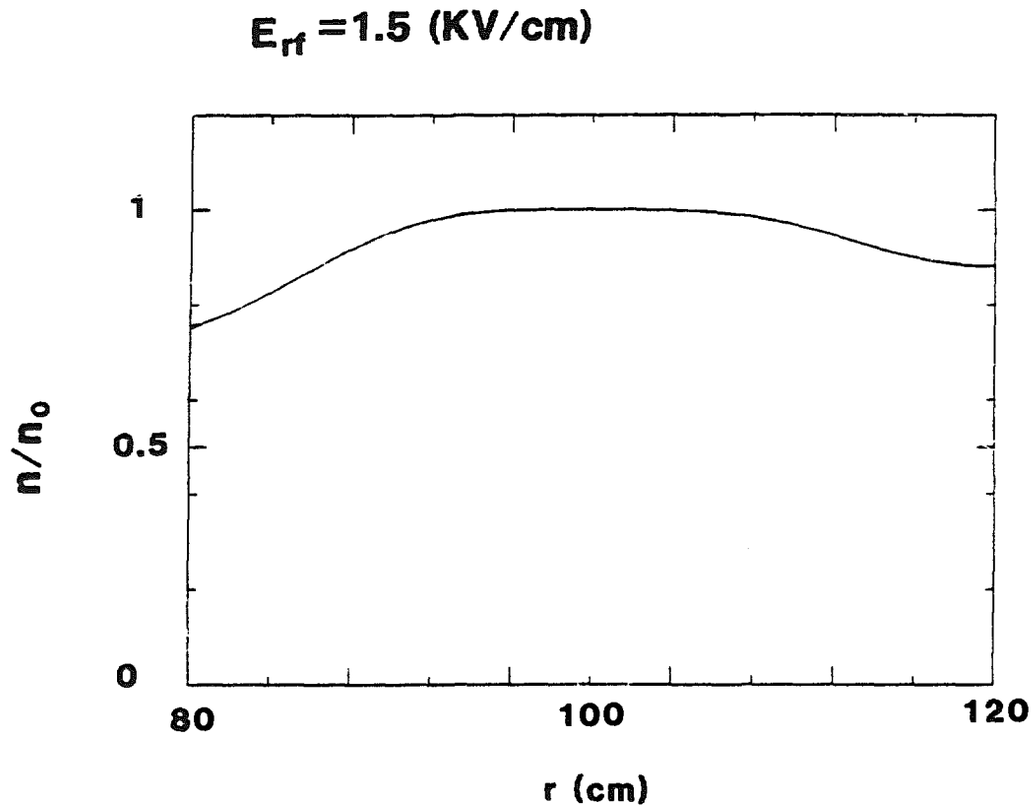
E_{rf} =1.5 (KV/cm)
1
0.5
0
n/n$_o$
80
100
120
r (cm)

Fig. 6(a)

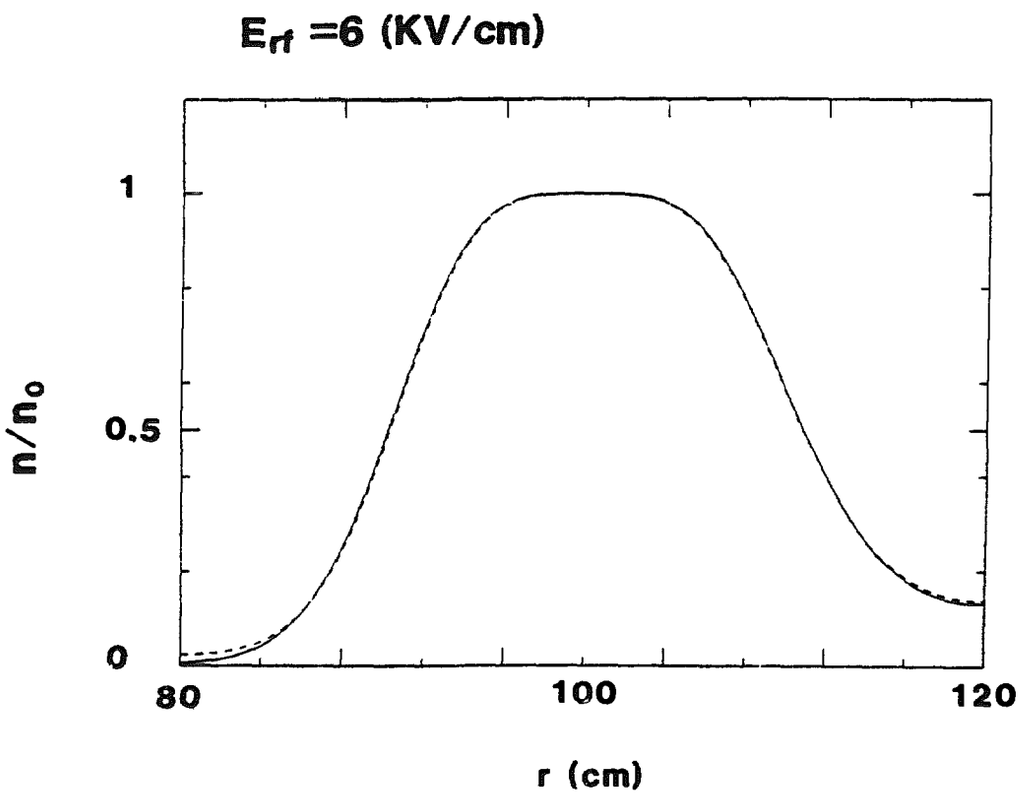
E_{rf} =6 (KV/cm)
1
0.5
0
n/n$_o$
80
100
120
r (cm)

Fig. 6(b)

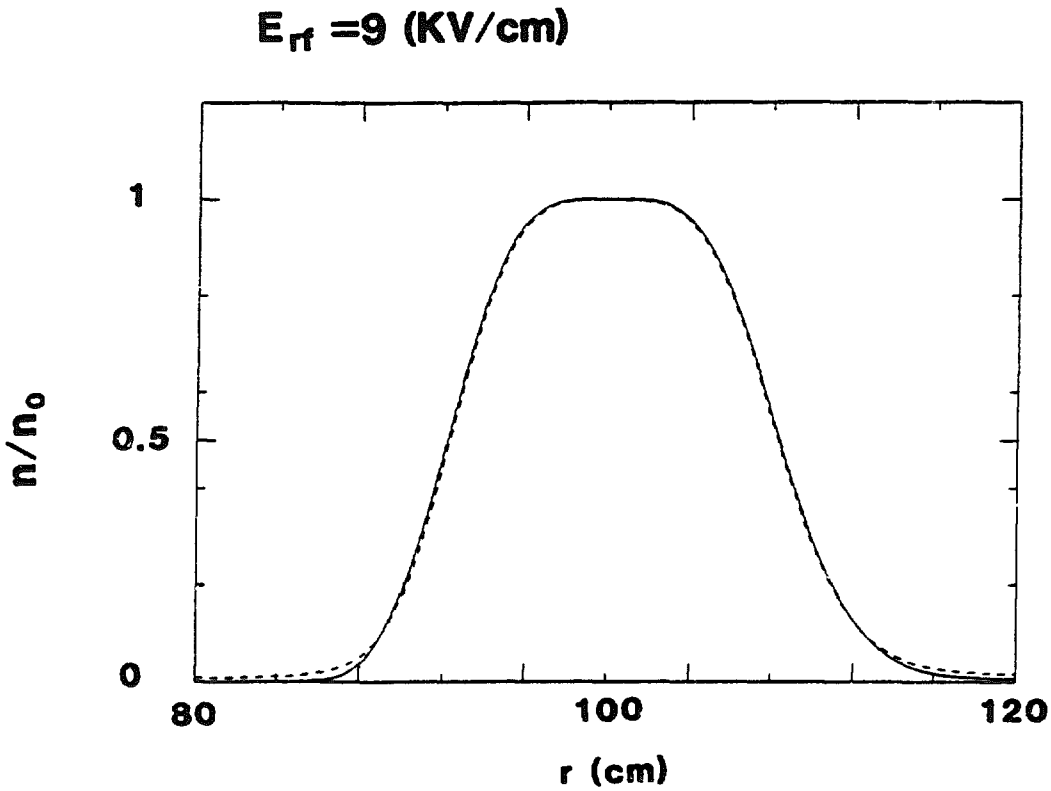

Fig. 6(c)

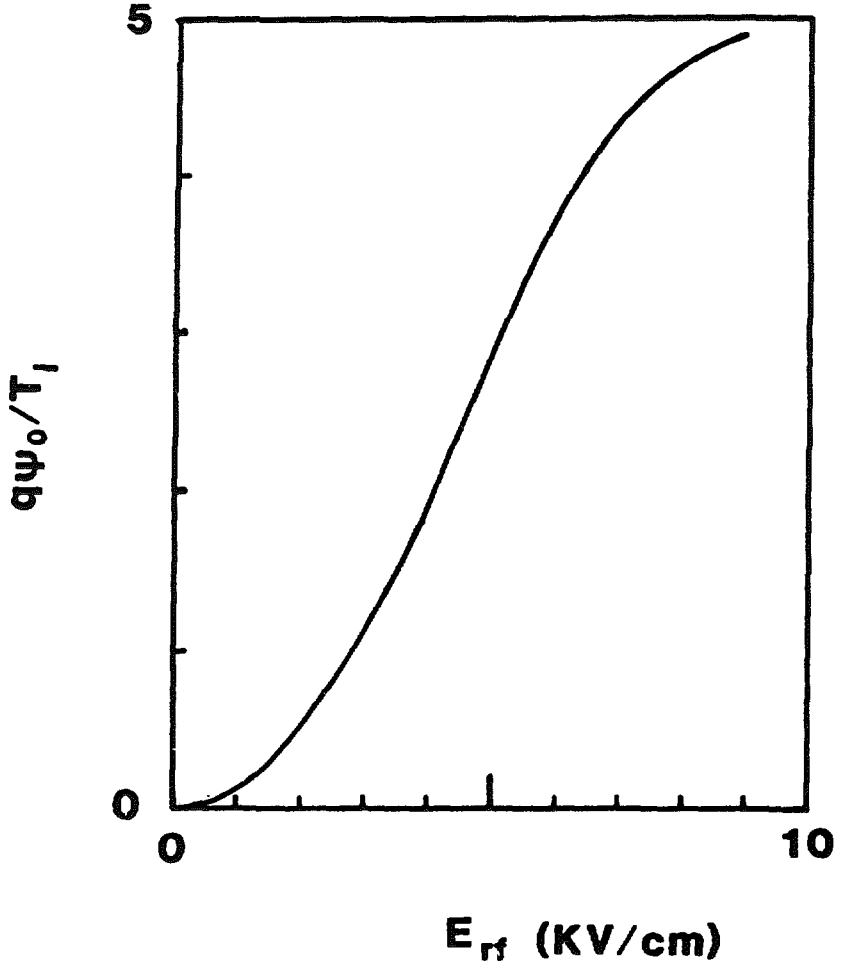

Fig. 7

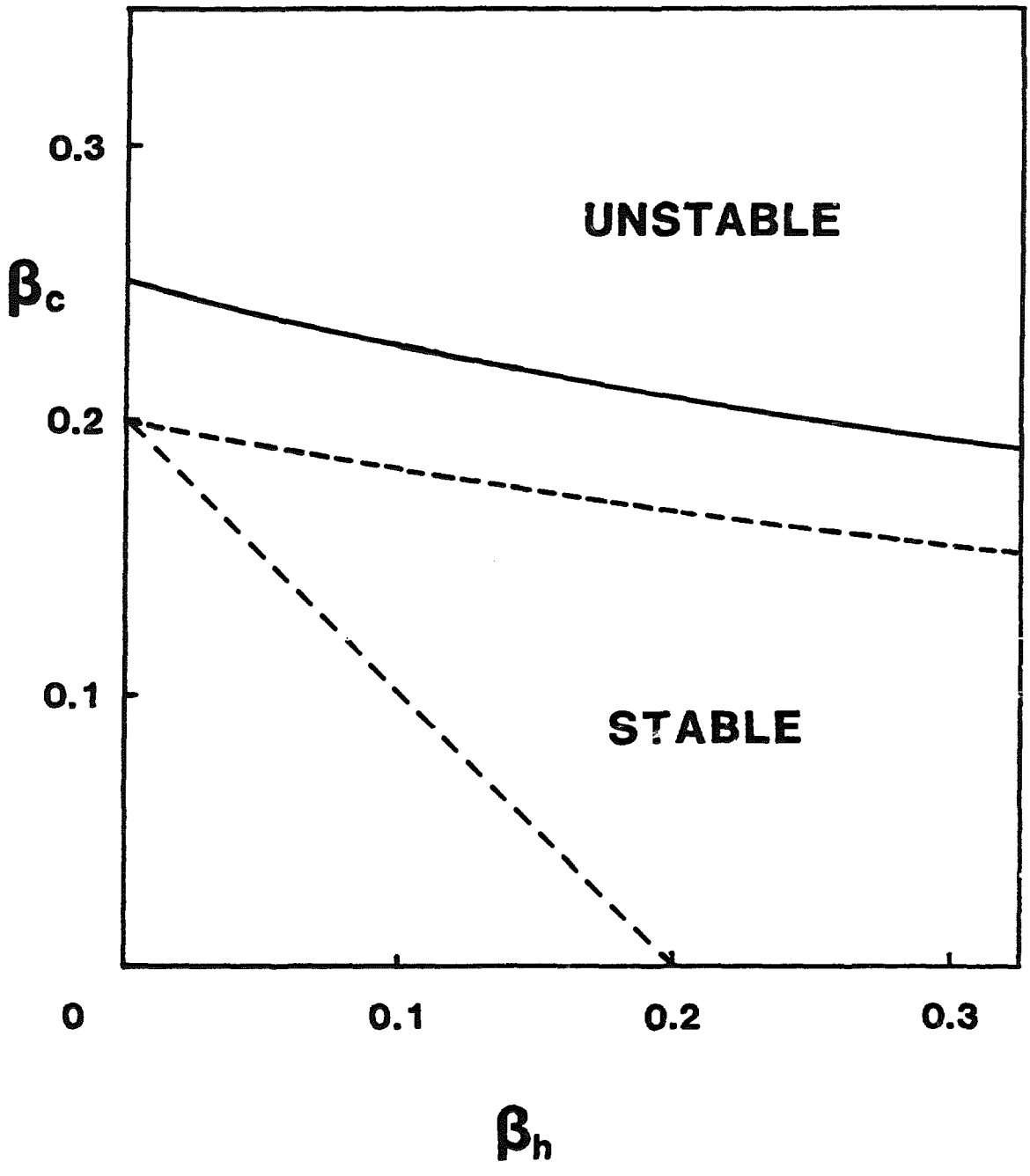

Fig. 8

Part II Particle Simulation

PARTICLE SIMULATIONS OF RF STABILIZATION OF THE FLUTE INSTABILITIES

K. Sakai, S. Takeuchi and M. Matsumoto
Department of Applied Science, Yamanashi University
Kofu 400, Japan

A 2-1/2 dimensional fully electromagnetic particle code used to study RF stabilization of the flute instabilities. It is graphically shown that a suitablly applied Rf electromagnetic field of a frequency $\omega > \omega_{ci}$ effectively stabilizes a flute instability, where ω_{ci} is the ion cyclotron frequency.

1. INTRODUCTION

The recent experiments[1,2] have shown that the flute instabilities are stabilized by RF electric fields of perpendicular to magnetic fields in the simple axisymmetric mirrors. It is considered that the ponderomotive force[3,4] of RF electric field compensates the centrifugal force arizing from the bad curvature of magnetic fields. The purpose of this paper is to give a plane evidence of the RF stabilization of the flute instabilities by particle simulations.

The simulations were performed by using a 2-1/2 dimensional fully electromagnetic particle code with finite size particle technique and fast Fourier transform.

2. SIMULATIONS

In the present simulations, the spatial region of the system concerned is rectangular in x-z plane, the origin of

which are taken in the center of the rectangle as shown in Fig. 1.

A homogeneous magnetic field B is parallel to the y axis. As shown in Figs. 1 and 2, the plasma density n has, at initial, the parabolic distribution

$$n = n_0 \left\{ 1 - \left(\frac{x}{\ell} + \frac{\xi}{\ell} \sin \frac{2\pi z}{L_z} \right)^2 \right\}$$

with the small perturbation $(\xi/\ell)\sin(2\pi z/L_z)$, where L_z is the length of the side parallel to z of the rectangle. The velocity distributions are Maxwellians of temperatures T_i and T_e for ions and electrons, respectively.

The centrifugal acceleration $\vec{g}$ from the bad curvature of magnetic field in a real mirror machine are replaced in the simulations by the step function of x : $\vec{g} = (g,0,0)$ with $g = \pm g_0$ $(x \gtrless 0)$, where g_0 is a constant.

The RF electromagnetic fields are excited by the external currents $\vec{j} = (0,0,j_0 x \sin\omega t)$ with frequencies $\omega \simeq \omega_{ci}$, where j_0 is a constant and ω_{ci} is the ion cyclotron frequency.

The simulations were performed for the hydrogen plasma of the following parameters : the initial particle density at the maximum $n_0 = 1.8 \times 10^{12} cm^{-3}$ for both ions and electrons ; the initial temperature of plasma $T_e = T_i = 2 KeV$; the strength of the static magnetic field B = 4 Tesla ; the centrifugal acceleration $g_0 = 2.7 \times 10^{14} cm\ s^{-2}$. Under these conditions the typical Debye length $\lambda_D = 0.033 cm$; the ion cyclotron frequency $\omega_{ci} = 3.8 \times 10^8\ s^{-1}$; the ion gyroradius $\rho_i = 0.12 cm$.

The simulational conditions were chosen as follows : the system size $L_x = 256\lambda_D$ and $L_z = 64\lambda_D$; the width of the plasma $2\ell = 200\lambda_D$; the density perturbation $\xi/\ell = 0.01$; the ion-electron mass ratio $m_i/m_e = 4$; the number of particles $N_i = N_e = 25600$. The periodic boundary conditions

are imposed for both x and z. The all quantities are assumed to be uniform in the y direction.

Runs were executed in the four cases :

(1) in the absence of both the acceleration g and RF field

(2) in the presence of g and the absence of RF

(3) in the presence of g and RF of frequencies $\omega > \omega_{ci}$

(4) in the presence of g and RF of frequencies $\omega < \omega_{ci}$

The total run time $\omega_{ci}t = 126$ for a run. The main results of these runs are graphically shown by the contour maps of ion density in Figs. 3 and 4.

2.1 IN THE ABSENCE OF g AND RF

In this case, the plasmas were stable and almost static in the course of runs, except that weak surface waves were slowly propagating in perpendicular to the magnetic fields.

2.2 IN THE PRESENCE OF g AND THE ABSENCE OF RF

In this case, there arises a growing mode of density wave at the surface of plasma as clearly shown in Fig. 3. The features of the mode are characteristic of the flute instabilities. It was found that the growth rate of the mode $\gamma = 8 \times 10^6\ s^{-1}$; it quite well accords with the theoretical one $\gamma = (-g_0 n'/n)^{1/2} = 9 \times 10^6\ s^{-1}$.

2.3 IN THE PRESENCE OF g AND RF OF $\omega > \omega_{ci}$

As shown in Fig. 4, the flute instability caused by the acceleration g was effectively stabilized by the applied RF field. One of the profiles of the RF field is shown in Fig. 2. From the typical value of the RF electric field energy $E^2/16\pi nT = 0.1$, it is roughly estimated that the ponderomotive acceleration of the RF field

$$g_p = \frac{v_{thi}^2}{\ell^2}\left(\frac{\omega_{pi}}{\omega_{ci}}\right)^2 \frac{1}{(\omega/\omega_{ci})^2 - 1} \cdot \frac{E^2}{16\pi nT}$$

is egual to 1×10^{15} cms^{-2}.

2.4 IN THE PRESENCE OF g AND RF OF $\omega < \omega_{ci}$

In the present simulations, the RF fields of $\omega < \omega_{ci}$ hardly gave any effects to the behaviors of the contour maps of ion density. The further investigations are necessary to say something about the RF stabilization in this frequency region.

3. SUMMARY AND DISCUSSIONS

The RF stabilization of the flute instabilities are effective at least in the frequency region $\omega > \omega_{ci}$. It seems that the value of RF electric field energy $E^2/16\pi nT$ is too large, but it has origin in our setting the large, value of the acceleration g. It is expected that RF electric field energy necessary for stabilization will reduce to the extent of two order of magnitude in real systems.

The author would like to thank Dr. H. Hojo and Dr. T. Watanabe for the useful discussions. This work was supported by the Grand in Aids for the Scientific Research of the Ministry of Education, Science and Culture of Japan.

REFERENCES

1) H. Akimune, I. Ikeda, T. Hirata and F. Okamoto, J. Phys. Soc. Japan 50 (1981) 2729.
2) Y. Yasaka, H. Imaizumi and R. Itatani, Proc. Int. Conf. Plasma Physics (Nagoya, 1980) Vol. I, p.327.
3) H. Washimi and V. I. Karpman, Zh. Eksp. Teor. Fiz. 71 (1976) 1010 [Sov. Phys. JETP 44 (1976) 528].
4) T. Hatori and H. Washimi, Phys. Rev. Letters 46 (1981) 240.

Figure Captions

Fig. 1 : Spacial configuration of the system in the present simulations.

Fig. 2 : Profiles of the density n of plasma at initial and the RF electric field energy E^2 at a typical moment.

Fig. 3 : Time development of the contour map of the ion density in the presence of the bad acceleration g and the absence of RF field ; T stands for the time measured in the unit of ion cyclotron period.

Fig. 4 : Time development of the contour map of the ion dendity in the presence of the bad acceleration g and the RF field of $\omega = 1.7\,\omega_{ci}$.

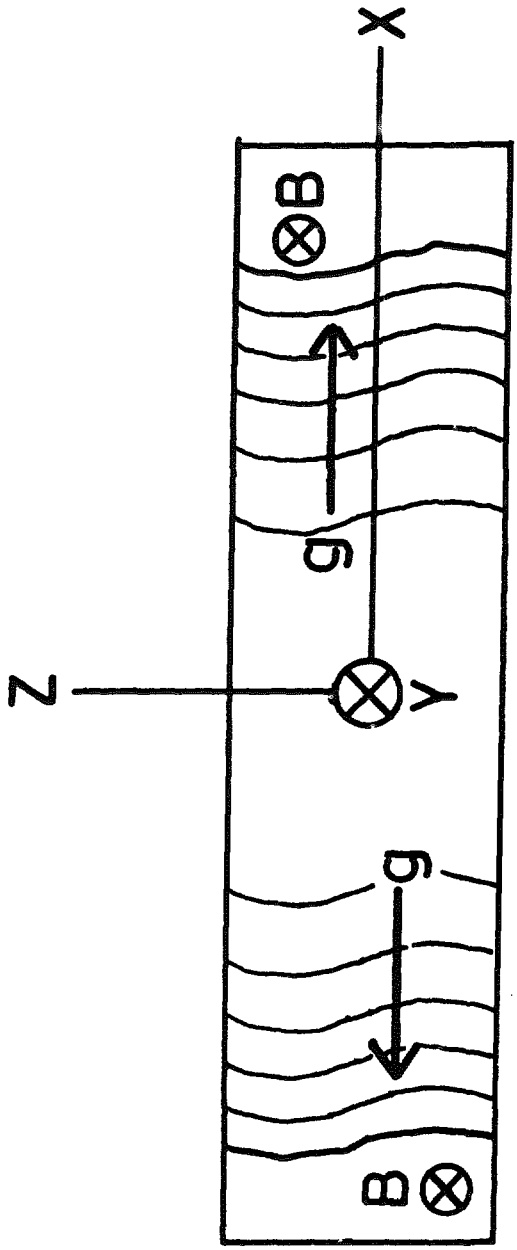

Fig. 1

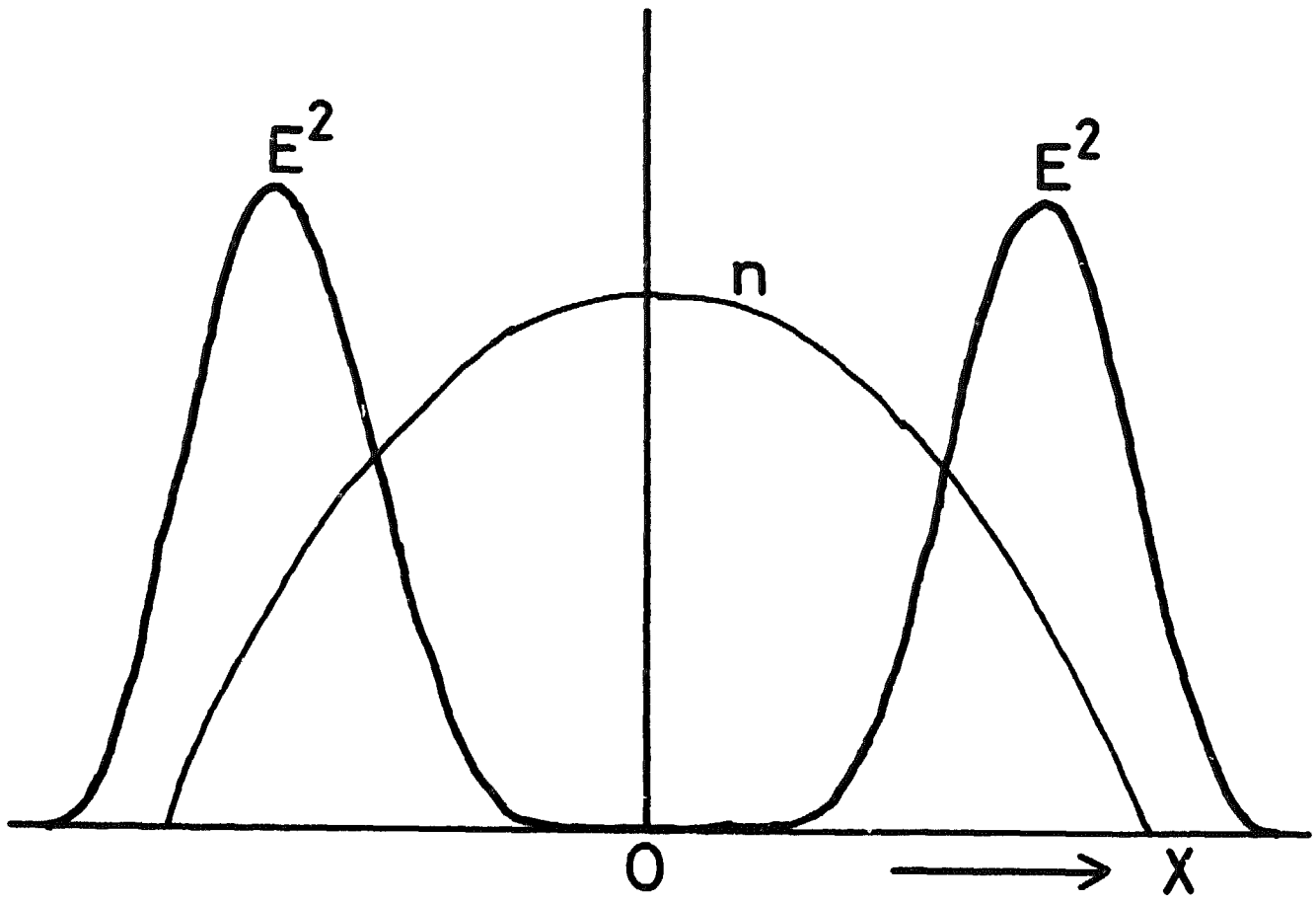

Fig. 2

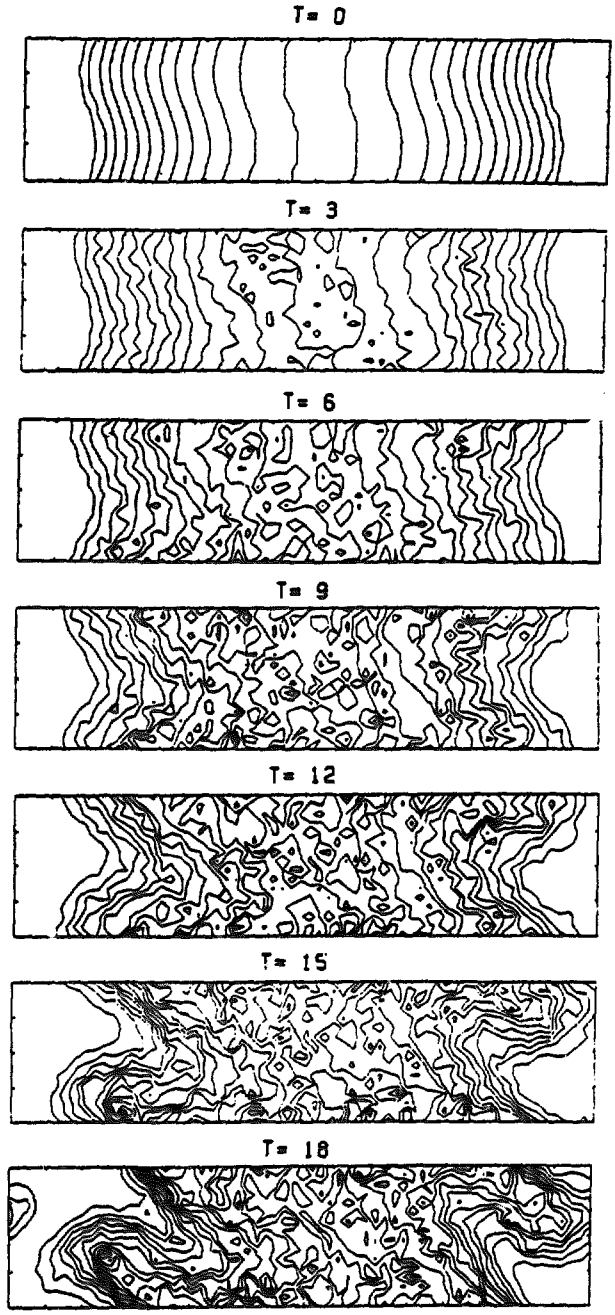

Fig. 3

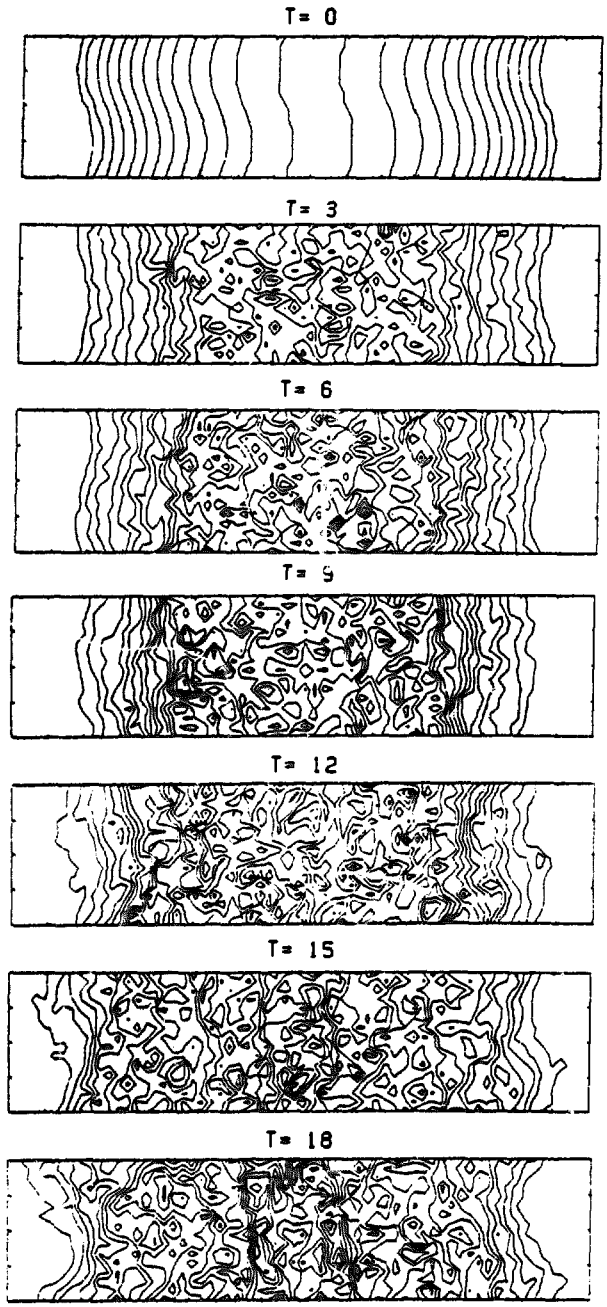

Fig. 4

THE ELECTRIC FIELD BUMPY TORUS (EFBT) CONCEPT: AN ALTERNATE MEANS OF PLASMA PRODUCTION

J. Reece Roth
University of Tennessee
Knoxville, Tennessee 37996-2100
(615) 974-4446

ABSTRACT

It is very probable that the EBT approach to plasma confinement and heating in a bumpy torus geometry has gone as far as it can with the existing mechanism for plasma production. If the average plasma number density could be increased by a factor of 2 to 4 above the $10^{12}/cm^3$ recently reported for the EBT-S experiment, this would allow greatly increased coupling and absorbtion of ICRH power to the toroidal plasma; a factor of 5 to 10 increase in number density above EBT-S levels would reach the "burnout" regime, in which the neutral mean free paths are smaller than the plasma radius. In the burnout regime, the interpretation of physical processes in the plasma would be greatly simplified, and the energy balance of the toroidal plasma would no longer be charge-exchange dominated. The Electric Field Bumpy Torus (EFBT) approach has demonstrated the production of a steady-state plasma in a bumpy toroidal magnetic field with average numer densities up to $3.2 \times 10^{12}/cm^3$ and maximum number densities greater than $6 \times 10^{12}/cm^3$ on the plasma axis. These number densities should be sufficient to increase the coupling of ICRH power above levels characteristic of the EBT-S experiment. Simple modifications of the EFBT approach should allow the higher densities required for plasma burnout to be achieved. In the original EFBT experiment conducted at the NASA Lewis Research Center, gross confinement was provided by a bumpy torus magnetic field. Plasma heating, macroscopic stabilization, and enhanced confinement were provided by externally applied radial electric fields which reached values up to 1.5 kV/cm at the plasma boundary. The ions and electrons in the EFBT received energy from external power supplies through this radial electric field, and the E/B ion drift velocities thermalized to kinetic temperatures which reached several kilovolts. In the NASA-Lewis EFBT experiment, the enhancement of confinement provided by negative plasma bias made possible, simultaneously, the number densities cited above, ion kinetic temperatures of 300-500 eV, and a particle containment time of τ = 2.5 milliseconds in an 82 liter

plasma. It should be possible to apply the EFBT to approach to the EBT-S apparatus at Oak Ridge with relatively minor modifications.

INTRODUCTION

From an outsider's perspective, it appears that bumpy torus research has arrived at a crossroads. The recent revision downward of the EBT-S data base has resulted in plasma parameters which are almost certainly too low to justify proceeding with the EBT-P program, or any other scale-up of this concept. Indeed, the plasma parameters of the EBT-S experiemnt are so low that the future viability of the EBT-S approach is open to serious question. If means are not found to greatly improve bumpy torus plasma parameters over those achieved by the EBT-S experiment, a very elegant plasma containment geometry and a very attractive alternate fusion reactor concept may prematurely fall by the wayside.

In attempting to identify the reason for the poor performance of the EBT-S experiment, it is useful to distinguish between the basic bumpy torus magnetic containment configuration, and the means selected to generate and sustain a plasma in that configuration. For reasons discussed below, I believe that the basic difficulty does not lie with the bumpy torus magnetic field configuration itself, but with the means selected in the EBT approach to generate and sustain the plasma. I propose to leave the basic bumpy torus magnetic field configuration intact, and replace the EBT plasma production mechanism with another which has demonstrated the ability to produce plasma of higher number densities and ion kinetic temperatures, and containment times at least as long as those reported from the EBT-S experiment.

THE BUMPY TORUS CONFIGURATION

It is important to keep in mind that the bumpy torus configuration is both simple and elegant. Its large aspect ratio, modest requirements on superconducting magnet technology, simple coil configuration, and modularity are in sharp contrast with the characteristics of mainline and many alternate plasma confinement configurations. These advantages were extensively documented in a 1977 science court-like review of 11 alternate confinement concepts sponsored by the DoE.[1] This review considered 11 plasma containment concepts, each of which was advanced by advocates and attacked

by critics on the basis of the existing physics data, and reactor design studies done especially for the review. The review panel adjudicated the claims of the advocates and critics, and produced overall scores in three major areas; confidence in physics, confidence in technology, and reactor desirability. The numerical scores resulting from this procedure allowed the 11 concepts to be ranked.

TABLE I

RANKING OF ALTERNATE CONCEPTS
BY DOE REVIEW PANEL, 1977

Confidence in Technology		Reactor Desirability	
Concept	Score*	Concept	Score
Elmo Bumpy Torus	6.7	LINUS	770
LINUS	5.0	Fast Liner Reactor	760
Fast Liner Reactor	3.8	Elmo Bumpy Torus	690
Tormac	3.4	Tormac	560
Laser Heated Solenoid	2.2	SURMAC	560
Ion Rings	2.1	e-Beam Solenoid	550
Theta Pinch	1.6	Reversed Field Pinch	520
e-Beam Heated Solenoid	1.5	Laser Heated Solenoid	500
Reversed Field Pinch	0.85	Ion Rings	480
Multiple Mirror	0.46	Multiple Mirror	420
SURMAC	0.27	Theta Pinch	420

*The overall technology score has been multiplied by 10^{-5}.

On Table I is the ranking of alternate concepts by the DoE review panel for confidence in technology and reactor desirability. It is notable that the Elmo Bumpy Torus approach ranked 1st of the 11 in confidence in technology, and 3rd of the 11 concepts in reactor desirability. These high rankings were due largely to the simplicityof the bumpy torus confinement configuration. Because of this perceived advantage of the bumpy torus configuration, it seems clear that the bumpy torus magnetic containment configuration should not be altered except for very specific and well-documented reasons. It is my contention that at present no such clear and well-documented reasons have been put forward to justify the abandonment of the basic

bumpy torus magnetic containment configuration. This magnetic field configuration should be preserved because of its reactor advantages, while research for other ways to generate a denser, hotter plasma in this containment geometry should be pursued.

PLASMA PRODUCTION MECHANISMS FOR BUMPY TORI

Let us consider some plasma production mechanisms for bumpy tori. We will see if we can identify why the Elmo approach, using electron cyclotron resonance heating (ECRH) has not been adequate, then proceed to consider other plasma production and heating mechanisms, and finally, to assess their advantages and disadvantages for the generation of plasmas in a bumpy torus confinement configuration.

ECRH and the EBT Mechanism

There are at least two serious drawbacks to the use of the Elmo approach to heating toroidal plasmas. One of these is that the required high levels of RF power at the ECRH frequency is pushing the state-of-the-art in radio frequency power generation. The second difficulty is that the chain of energy flow from the DC electrical power supply to the toroidal plasma ion population has many lossy links, which make it difficult to achieve a high number density in the toroidal plasma, or to achieve burnout of the background neutral gas.

On Table II is a schematic energy flow for the EBT-S plasma. The DC electrical power provided to the gyrotrons is converted to ECRH microwave power with efficiencies that are typically somewhat below 50%. A portion of the ECRH power is lost in waveguides and vacuum windows before entering the plasma containment volume, where some is also lost on walls and absorbing structures. The remaining microwave power is absorbed by the plasma, some of it directly by the toroidal plasma, but apparently most of it by the hot electron ring population in the midplane of each sector. The power absorbed by the hot electron population is partly lost in the form of bremsstrahlung and x-radiation, and some of this power is transferred to the toroidal electron and/or ion population.

One can identify at least five separate steps at which power can be lost before it reaches the toroidal plasma. This probably limits the plasma parameters of which the Elmo approach is capable. The average plasma number densities achieved thus far, about 1×10^{12} particles per cubic centimeter, are too low to allow effective coupling of

TABLE II

SCHEMATIC ENERGY FLOW IN EBT-S PLASMA

DC ELECTRICAL POWER

↓

GYROTRON → LOSSES

↓

ECRH MICROWAVE POWER

↓

WAVEGUIDES & VACUUM WINDOWS → LOSSES

↓

ABSORBTION BY PLASMA → LOSSES

↓

HOT ELECTRON POPULATION → LOSSES

↓

TOROIDAL ELECTRON POPULATION → LOSSES

↓

ION POPULATION

neutral beam heating, ICRH, and probably lower hybrid heating to the toroidal plasma. A less lossy production and heating scheme would be desirable to achieve average plasma number densities from 5 to 7 x 10^{12} particles per cubic centimeter, at which point the mean free paths of the background neutral gas would be smaller than the plasma radius, and the toroidal plasma would no longer be charge-exchange dominated, as it is now.

Neutral Beam Heating

Neutral beam heating does not appear to be a realistic alternative for the generation of a dense bumpy torus plasma. A serious limitation of neutral beam heating, not confined to this application, is that existing neutral beam sources are capable of operating only in a pulsed mode, rather than being available for steady-state heating. Neutral beam heating with existing technology would give up the significant advantage of being able to operate in the steady-state.

In addition to this technological limitation, the product of the plasma number density and the minor plasma diameter is not high enough to provide a reasonably large probability of an energetic neural being ionized before it exits the opposite side of the plasma. To overcome this limitation of the EBT-S plasma would require a major developmental program to produce energetic neutrals in a high enough state of ionization to interact before traversing the minor plasma diameter. Another limitation of netural beam heating is the steady state gas load which it would impose on the vacuum system.

Ion Cyclotron Resonance Heating (ICRH)

Ion cyclotron resonance heating has many advantages for heating bumpy torus and other toroidal plasmas. Large amounts of steady-state RF power are available at reasonable cost with technology which is readily available. Moreover, the ICRH power is fed directly into the ion population of the plasma, the species which one must heat for fusion applications. A limitation of ICRH power is that the free space wavelength is much larger than the dimensions of the plasma which one wishes to heat. In order to achieve a reasonable degree of coupling from the antenna to the plasma, the antenna must be located very near the plasma boundary, thus presenting problems of sputtering and erosion. The index of refraction of the plasma must be sufficiently high to lower the wavelength within the plasma to dimensions that are comparable to the plasma size.

The theory which describes the coupling between the current generation of ICRH antennas and the plasma is not complete. It appears that at or below densities of around 1 to 2 x 10^{12} particles per cubic centimeter, the index of refraction of the plasma is not sufficiently high to bring the ICRH wavelength in the plasma down to values comparable to the plasma dimensions, and the resulting coupling efficiency is relatively low. The coupling of ICRH power to the plasma apparently is a very sensitive function of number density in the low 10^{12} particle per cubic centimeter range, and it would appear that ICRH would be a much more attractive plasma heating scheme if only the background plasma density of the EBT-S could be increased by a factor 2 to 4 above present levels.

Lower Hybrid Heating

Lower hybrid heating would appear to offer many of the same advantages as ion cyclotron resonance heating, without the necessity of an antenna structure close to the plasma. It is probable that higher background plasma densities would greatly improve the coupling of lower hybrid heating power to the plasma, just as in the case of ICRH. Probably the factor most detrimental to lower hybrid heating is the practical consideration that the funds required to provide large amounts of steady-state lower hybrid power for the EBT experiment are not likely to be available until the EBT-S experiment can demonstrate plasma parameters to justify the funds.

The Electric Field Bumpy Torus (EFBT) Mechanism

The EFBT mechanism is described more fully below, and the details of its physics are summarized in ref. 11. This mechanism of plasma production and heating was developed at the NASA-Lewis Research Center in Cleveland, Ohio over the period from 1965 to 1978. It provides a remarkably simple way of coupling a dc power supply to the plasma ion population, and has demonstrated the capability of generating a steady-state toroidal plasma with parameters which equal or significantly exceed those reported from the EBT-S experiment.

TABLE III

SCHEMATIC ENERGY FLOW IN EFBT PLASMA

DC ELECTRICAL POWER

↓

BIASING ELECTRODE

↓

RADIAL ELECTRIC FIELD → LOSSES

↓

ION POPULATION → LOSSES

↓

TOROIDAL ELECTRON POPULATION

A schematic of the energy flow in an EFBT plasma is shown on Table III. Raw dc elecrical power is used to bias the toroidal plasma by means of an electrode. When this electrode is negatively biased, the toroidal plasma forms a toroidal electrostatic potential well for ions, and the negative electrode acts like a Langmuir probe in ion saturation. The resulting plasma has radial electric fields as high as one kilovolt per centimeter, which produce a crossed-field configuation with the strong radial electric field pointing inward, at right angles to the toroidal magnetic field. Both ions and electrons drift in these crossed fields with a velocity which is, to a first approximation, equal, and thus the radial electric field deposits most of its energy in the ion population. Since the electrons acquire an energy in the crossed fields that is smaller than that of the ions by the electron-ion mass ratio, the more energetic ion population will impart some of its energy to the toroidal electron population, as well as suffer radial transport losses and/or charge-exchange losses on the neutral background gas.

The relatively few links in the chain of energy flow in the EFBT plasma might reasonably be expected to lead to higher background number densities, as well as higher ion kinetic temperatures than are possible in the Elmo approach. Indeed, this appears to be the case. On Table IV are shown the simultaneously observed plasma

TABLE IV

SIMULTANEOUSLY OBSERVED PLASMA PARAMETERS

PARAMETER	EBT-S PLASMA	EFBT PLASMA
AVERAGE DENSITY, CM^{-3}	$1\text{-}1.5 \times 10^{12}$	3.2×10^{12}
HOT ELECTRON TEMPERATURE, KEV	200-400	—
TOROIDAL " " , EV	~200	5 - 30
PARTICLE CONTAINMENT TIME, MSEC	~1.0	2.5
ENERGY CONTAINMENT TIME, SEC	~1.0	?
ION ENERGY, (TEMPERATURE), EV	20-50	(300-500)
BMAX, TESLA	1.0	2.4
RADIAL ELECTRIC FIELD, V/CM	~30	1500
TYPE OF GAS	H_2(?)	D_2
NEUTRAL PRESSURE, TORR	$\sim 5 \times 10^{-5}$	3×10^{-5}

parameters for the EBT-S plasma, and the best set of simultaneously measured plasma parameters for the EFBT experiment at NASA-Lewis. The numbers shown for the EBT-S experiment are believed to represent the latest revision of the EBT-S data set. The average number density for the EFBT plasma refers to an approximately triangular radial density profile, with central values that were approximately 6 x 10^{12} particles per cubic centimeter. The very low electron kinetic tempertures are characteristic of the EFBT approach, and are a consequence of the fact that the ion and electron energies tend to be proportional to the mass of the individual species. The conditions illustrated on Table IV for the EFBT plasma involved approximately 30 to 50 kilowatts of dc electrical power input to the plasma. Under other operating conditions, up to 150 kilowats of dc electrical power was fed into the plasma. The particle containment time for the conditions shown was about 2.5 milliseconds, and the highest value ever observed was approximately 6 milliseconds. The EFBT plasma was charge-exchange dominated, and this limited the energy containment time to values somewhat less than the particle containment time, perhaps as low as one millisecond. In both plasma production concepts, the particle and energy containment times would be expected to improve markedly as the densities are raised to values that would allow burnout of the neutral gas from the containment volume.

THE ELECTRIC FIELD BUMPY TORUS (EFBT) MECHANISM

In the electric field bumpy torus (EFBT), gross confinement is provided by a bumpy torus magnetic field, and plasma heating, macroscopic stabilization, and enhanced confinement by externally applied electric fields. In this magnetoelectrically confined plasma, the radial electric field has exceeded one kilovolt/centimeter at the plasma boundary and has penetrated inward to at least one half the plasma radius. These high dc radial electric fields drive strong low frequency fluctuations of the density and potential, and cause radially inward fluctuation-induced transport against the radial plasma density gradient. With negative electrode polarity the particle confinement was a balance of two processes; radial infusion of ions in sectors of the plasma not containing electrodes, resulting from fluctuation-induced transport in the radially inward dc electric fields; and ion losses to the electrodes, each of which acted like a Langmuir probe in ion saturation to extract ions from the plasma. A simple model predicts that the particle containment time is proportional to the plasma volume, and this was experimentally observed. The ions and electrons

receive energy from external dc power supplies through the imposed radial electric field, and the E/B drift velocities thermalize to kinetic tempertures which can reach several kilovolts. In the steady-state NASA-Lewis EFBT experiment, the enhancement of confienement provided by negative plasma bias made possible simultaneously an average number density of $n_e = 3.2 \times 10^{12}$ per cubic centimeter, an ion kinetic temperature of 300 - 500 eV, and a particle containment time of $\tau = 2.5$ milliseconds in an 82 liter plasma.

The NASA-Lewis EFBT Experiment

The history of the NASA-Lewis Bumpy Torus project is summarized on Table V. In December 1964 the superconducting Pilot Rig was placed into operation. This was the first superconducting magnet facility to be used in plasma physics or fusion research. This was a modified Penning discharge, which formed the basis for the electric field bumpy torus experiment. From June, 1965 to June, 1971 turbulence and the ion heating process in the modified Penning discharge were investigated, and the results documented in references 2 through 6. On April 21, 1972 the bumpy torus facility first became superconducting, and was the first superconducting facility to generate a toroidal magnetic field. On December 5, 1972 the first plasma was

TABLE V

HISTORY OF LEWIS ELECTRIC FIELD BUMPY TORUS PROJECT

DECEMBER 1964:	SUPERCONDUCTING PILOT RIG IN OPERATION - FIRST SC FACILITY TO BE USED IN PLASMA PHYSICS OR FUSION RESEARCH
JUNE 1965 - JUNE 1971:	STUDY OF ION HEATING IN MODIFIED PENNING DISCHARGE
APRIL 21, 1972:	BUMPY TORUS FACILITY FIRST SUPERCONDUCTING - FACILITY TO GENERATE A TOROIDAL MAGNETIC FIELD
DECEMBER 5, 1972:	FIRST PLASMA IN BUMPY TORUS
JANUARY 1973 - JUNE 1976:	STUDY OF ION HEATING IN TOROIDAL GEOMETRY
JUNE 1976 - MARCH 1978:	STUDY OF FLUCTUATION - INDUCED TRANSPORT SCALING OF PARTICLE CONTAINMENT TIME, AND RF PLASMA EMISSIONS
MARCH 31, 1978:	LAST DAY OF EXPERIMENTAL OPERATION AT NASA LEWIS

generated in the bumpy torus facility. In the period from January, 1973 to June, 1976 the ion heating process was studied in the electric field bumpy torus. From June, 1976 through March, 1978, the dominant research topic was the study of fluctuation-induced transport in the EFBT plasma. On March 31, 1978 the EFBT experiment was shut down as the result of changing research priorities within NASA.

An isometric cutaway drawing of the NASA-Lewis EFBT experiment is shown in Figure 1. The superconducting coils of this magnet facility were capable of operating at magnetic fields of $B_{max} = 3.0$ tesla. There was a 2.5:1 mirror ratio along the magnetic axis, with 12 superconducting coils in the toroidal array. The entire confinement volume was immersed in a large vacuum tank. On Figure 2 is shown a photograph of the EFBT plasma. The vertical element in the center is an electrode ring which was used to bias the toroidal plasma. This photograph illustrates the excellent visual and experimental access to the plasma volume which was possible in this experiment. Because there were no hot electron rings or energetic electrons in the experiment, it was possible to observe the plasma from one meter away, outside the glass viewports in the equaltorial plane.

TABLE VI

DOCUMENTATION OF THE ELECTRIC FIELD BUMPY TORUS (EFBT) PLASMA PRODUCTION MECHANISM

Topic	References
A) The NASA-Lewis EFBT Experiment	7-13
B) Electrostatic Potential Control	14-16
C) Plasma Heating and Thermalization	2-6; 9-11
D) Plasma Transport	17-23
E) Macroscopic Plasma Stability	24-25
F) Scaling of Plasma Production Mechanism	9-11

The physics of the EFBT plasma has been extensively documented elsewhere. On Table VI is shown some of the more important physical processes that have been identified in the EFBT plasma, and the archival references in which they are described. The characteristics of the NASA-Lewis superconducting bumpy torus magnet facility are described in refs. 7 and 8. A survey of the physical processes and characteristics of the EFBT plasma are described in refs. 9 through 13. Of these, ref. 11 is the most complete description of the work done at NASA-Lewis.

The documentation of the radial electric fields and the electrostatic potential characteristic of the EFBT plasma are summarized in refs. 14 to 16. On Figure 3 is shown a schematic drawing of the electric field structure in the EFBT with negative midplane electrodes. It was found during the course of the the NASA-Lewis experiments that the entire toroidal plasma could be biased to negative potentials with a single negative electrode ring at one of the magnetic mirror midplanes. Strong radial electric fields, often exceeding one kilovolt per centimeter, then pointed into the plasma forming an electrostatic potential well for ions. The penetration of these electric fields into the plasma, and their dependence on the plasma operating parameters are documented in refs. 14 through 16.

The high ion kinetic temperatures and the thermalization of the ion E/B drift velocities to maxwellian distributions are documented in refs. 2 to 6 for the simple axisymmetric modified Penning discharge; and in refs. 9 to 11 for the electric field bumpy torus plasma. A characteristic example of these ion energy distribution functions is shown on Figure 4, which includes data taken with a charge exchange neutral energy analyzer under three sets of plasma operating conditions which yielded ion kinetic temperatures from 220 to about 700 electron volts. These distributions are characteristically maxwellian, and in some cases the tail of the distribution function can be followed for 7 or 8 e-folding lengths down into the maxwellian tail. An important issue in this kind of measurement is to assure that there is not a large population of low temperature ions to which the charge exchange neutral energy analyzer is blind. This was confirmed under plasma operating conditions more energetic than that shown in Figure 4, in which a deuterium plasma was sufficiently hot and dense enough to produce steady-state neutrons. It was found that the neutron flux predicted from the ion kinetic temperatures observed with the charge-exchange neutral detector, and the number densities obtained from the microwave interferometer agreed to within a factor of 2 of the neutron fluxes actually observed with a neutron counter.

The radial transport of this plasma was dominated by fluctuation-induced transport, which resulted from the high levels of electrostatic turbulence in the plasma. This made possible, under the right conditions, the inward transport of ions against a density gradient as they stochastically fell down the toroidal electrostatic potential well for ions. The radially inward ion transport, and other aspects of the fluctuation-induced transport in the EFBT plasma, are documented in refs. 17 to 23.

The EFBT plasma was observed to be macroscopically stable. it operated in the steady-state and, under a wide range of normal operating conditions, exhibited no flutes, no peaks in the spectrum of density or potential fluctuations, and a Gaussian distribution of amplitudes for the probability density function for both density and potential fluctuations. In addition to the rather clear-cut experimental evidence for the absence of flute instabilities, it can be shown, and is shown in refs. 24 and 25, that the strong radially inward electric field can counter-balance the centrifugal forces which result from particle motion along the field lines: Moreover, shear along the axis in the magnitude of the electric field can give rise to stabilization of flute instabilities in an electric field bumpy torus[25].

Finally, the scaling of the plasma parameters with the operating variables of the NASA-Lewis EFBT plasma are discussed in refs. 9 to 11. An important aspect of the scaling of this plasma production mechanism is illustrated on Figure 5. The average plasma number density is shown as a function of electrode current in the EFBT plasma for a biasing electrode consisting of a tungsten wire across the minor diameter of the plasma, and also two water-cooled 0.63 in diameter stainless steel tubes across the minor diameter of the plasma. These biasing electrodes resulted in an average plasma number density which was almost directly proportional to the electrode current. This is what one would expect from a Langmuir probe in ion saturation; the plasma number density is directly proportional to the current drawn. An important feature of these curves is that they are a straight line on log-log graph paper for an order of magnitude or more. There is no tendency of these curves to become asymptotic as the number density reaches about 3×10^{12} particles per cubic centimeter. Two factors kept the number density at or below the numbers shown; the power supply available was capable of no more than 20 amperes, and at the currents and plasma number densities shown, overheating of some of the sheet metal surrounding the containment volume occured. With better water cooling of the walls of the containment vessel and more current capability, higher number densities should easily be reached.

In Figure 6 is shown the particle containment time as a function of the average electron number density for the same negative biasing electrodes illustrated on Figure 5. These curves are important from a confinement point of view, because they indicate that there is very little particle containment time penalty for going to higher average number densities. The functional dependence of particle containment time on average number density is either independent, or possibly very slightly decreasing, with increasing average number density.

The strong axial and radial electric fields, and the processes responsible for ion heating and thermalization seem to be the same in modified Penning discharges as they are in the electric field bumpy torus. In the UTK Plasma Science Laboratory we are studying the turbulence, transport, ion heating, and RF emission of electric field dominated plasmas generated in classical and modified Penning discharges. Some characterisitc data from a Penning discharge plasma is shown on Figures 7a and 7b. Figure 7a is a retarding potential energy analyzer curve which was taken of ions lost along the magnetic field lines from a magnetic mirror configuration. Figure 7b shows the best fitting maxwellian distribution to the raw experimental data. The best fitting maxwellian distribution had a floating potential for the plasma of 1.17 kilovolts, and an ion kinetic temperature of about 440 electron volts. Data from retarding potential energy analyzer traces such as this also reveal clearly that there is no population of low energy ions inn these elecric field dominated plasmas. Other aspects of the Penning discharge plasmas studied in the UTK Plasma Science Labortatory may be found in ref. 26.

ISSUES RELATED TO BIASING ELECTRODES

The use of high voltage electrodes to bias a plasma is really no different from the issues associated with the use of limiters in tokamaks, divertors in any toroidal confinement configuration, antenna structures for ion cyclotron resonance heating, or plasma diagnostics with perturbing probes. The EFBT approach requires that the toroidal plasma be biased to high potential, and the presence of the biasing electrode is sometimes perceived as a unique disadvantage, even though the problems which it presents are really no worse than the other forms of plasma-surface interaction just discussed.

The use of a radiation or water-cooled electrode is the simplest way to bias a toroidal plasma for study. It has been shown to operate satisfactorily at average number densities up to 3×10^{12} particles per cubic centimeter, and there is good reason to believe that number densities as high as 10^{13} particles per cubic centimeter can be obtained using biasing electrodes and the EFBT mechanism. The presence of a negative biasing electrode will, of necessity, remove ions from the plasma volume in the manner of a Langmuir probe in ion saturation. If the drift surfaces and the operating conditions of an EFBT plasma are adjusted so that essentially all plasma ions are lost on the negatively biased electrode, however, the particle containment time

becomes proportional to the plasma volume. This occurs because if the volume of the EFBT plasma is doubled, it will take the average ion twice as long to impact on the negative biasing electrode. It also follows that the particle containment time is inversely proportional to the surface area of the negative biasing electrode. The smaller the electrode, the longer it takes an ion to impact on it. The removal of ions from the plasma volume by this mechanism is not really a disadvantage, and for sufficiently large volume plasmas results in a scaling law superior to that for classical diffusion.

Three other issues are potentially serious, and under certain conditions can limit the use of biasing electrodes. These include possible introduction of impurities into the plasma as a result of sputtering of electrode material by energetic ions impacting the electrode surface; electrode erosion; and the difficulty of cooling the biasing electrodes for the high power fluxes that are to be expected at fusion reactor conditions. These difficulties have been examined quantitatively in ref. 27. Because the use of biasing electrodes is unfamiliar to those who have not worked with an EFBT plasma, and because this is widely regarded as one of the most serious issues involved in EFBT plasmas, we will discuss this at some length, depending on refs. 11 and 27 for detailed documentation.

Impurity Introduction by Electrodes

A natural concern in appying the EFBT approach is the possible introduction of impurities into the plasma from sputtered electrode material. It appears reasonable to assume the impurities will have confinement times which are no longer, and which will probably be shorter, than the particle containment time of the plasma ions. If this is the case, and if every sputtered atom from the electrode surface is ionized and remains in the plasma with the average particle containment time, then the impurity fraction will build up to levels which are no longer than the sputtering yield for the electrode material. The sputtering yield gives an impurity fraction which is an upper bound to the impurity fraction. If the impurities are confined for shorter times than the plasma ions, the impurity fraction will be less. Candidate electrode materials are available for which the maximum sputtering yields are between 1% and 0.1%, and can be even less if the ion energies are far away from the maximum of the sputtering yield curve. The impurity fraction also will be reduced by the electric fields which point into a negatively biased electrode. These fields will tend to re-implant the impurity

atoms once they become ionized in the sheath surrounding the electrode. Also, in the crossed electric and magnetic fields existing in the electrode sheath, impurity ions will acquire large gyroradii and be lost from the plasma volume before contributing to the impurity fraction of the confined plasma itself.

Electrode Erosion

Heat transfer considerations aside, the time required to erode the walls of a biasing electrode can be surprisingly long. Long enough, in fact, to allow easy electrode replacement during the course of a steady-state experiment. The rate at which the electrode material is eroded by energetic deuterium ion bombardment is a complicated function of the sputtering yield, the ion energy, the impinging ion mass, and the density of the electrode material. If one makes the pessimistic assumption that the impinging ions have energies at the maximum of the sputtering yield curve for each material, the time to erode one millimeter of material in hours can be plotted as a function of ion number density on Figure 8. The time required to erode through the walls of various electrode materials is measured in hours to hundreds of hours, depending on the local ion number density above the electrode surface. It should be noted that this ion number density may not be the average number density in the containment volume. If, as was done in the NASA-Lewis experiment, the toroidal plasma is biased by a circular electrode at the outer circumference of the plasma, the local ion number densities can be a factor of 5 to 10 below the average number density.

The time to erode through the wall of an electrode will in general be much longer than that shown on Figure 8, since the impinging ions are not usually at or near the energy corresponding to the maximum of the sputtering yield curve. At NASA-Lewis, the electrodes were made of 0.95 cm diameter water-cooled copper tubing. On a very few occasions, theses electrodes were used long enough for the tubing wall to become eroded through and allow cooling water to escape in the vacuum vessel. This occurred after about 60 ampere-hours of operation with deuterium. An important point to be made is the fact that the time scale for erosion of the electrode material is long enough to allow replacement before the electrodes erode through.

Electrode Cooling

The power flux resulting from energetic ions bombarding a water-cooled electrode has been calculated in reference 27. On Figure 9 is shown the combinations

of ion kinetic temperature for deuterium ions and ion number densities which will yield power deposition rates on the electrodes of 1 to 5 kilowatts per square centimeter. These two power fluxes span a range, which gives the upper limit at which it is reasonable to consider water-cooled tubular electrodes. They place an upper limit on the ion kinetic temperature and number density which an electrode can withstand in an EFBT plasma. These calculations indicate that an EFBT plasma with ion kinetic tempertures of 1 keV can be biased with an electrode at number densities up to about 2 x 10^{12} particles per cubic centimeter; if the ions have kinetic temperatures of only 100 eV, densities ranging from 10^{13} to 5 x 10^{13} should be possible. Again, it should be kept in mind that the number densities shown here are the number densities in the vicinity of the electrode, and if the electrode surrounds the plasma minor circumference rather than penetrating along the minor diameter of the plasma, the effective number densities can be much below the average number density in the containment volume.

Some of the electrodes used in the NASA-Lewis EFBT experiment are shown in Figure 10. Electrode "A" is a water-cooled electrode made of 0.63 cm stainless steel tubing and was inserted along a minor radius of the plasma to the equatorial plane, rather than along a minor plasma diameter. Electrode "B" was also of water-cooled 0.63 cm stainless steel tubing, and was inserted along a minor diameter of the plasma. Electrode "C" had approximately half the surface area of electrode "B" and again was water-cooled with a counter-current heat transfer arrangement with the cold water flowing downward along the outside of an annulus and back up along the axis along an inside tube.

On Figure 11 are shown some more conservative electrode designs which do not necessitate penetrating the minor diameter of the plasma. On the right-hand side is one of the "standard" D-shaped electrodes which encircled the minor circumference of the plasma. It was this watercooled design which allowed us to achieve the highest plasma number densities and steady-state power inputs to the plasma, up to 150 kilowatts. On the left-hand side is what might be called the "conservative electrode" which biases the toroidal plasma with a thin filament of tungsten wire at the outer circumference of the plasma, without exposing the bulk of the plasma to water-cooled electrode tubing.

APPLICATION OF THE EFBT MECHANISM TO THE EBT-S EXPERIMENT

If the EBT-S experiment is to recover lost ground, it will almost certainly require that a plasma production mechanism other than the Elmo approach be applied to the EBT-S facility at Oak Ridge. The EFBT experiment at NASA-Lewis has demonstrated the production of a steady-state toroidal plasma, the number density and ion kinetic temperature of which are substantially higher than has been observed thus far in the EBT-S experiment, and the particle and energy containment times of which are comparable. Moreover, the EFBT approach appears capable of being scaled up by straightforward means to higher number densities and to higher ion kinetic temperatures than those achieved in the NASA-Lewis experiment.

TABLE VII

REQUIRED EQUIPMENT

1.) D.C. POWER SUPPLY
   . MINIMUM SPECIFICATIONS: 10kV @ 10 AMP.
   . AVAILABLE ON LOAN FROM UTK: 50kV @ 20 AMPS

2.) EBT-S FACILITY

3.) SINGLE BIASING ELECTRODE IN MIDPLANE OF ONE SECTOR

4.) CAPABILITY FOR ± 30 GAUSS VERTICAL FIELD

Table VII lists equipment that would be required to apply the EFBT approach to the existing EBT-S experiment at Oak Ridge. An essential requirement is a dc power supply - very minimal filtering would be required - to energize the EFBT electrode. Because the EBT-S facility has a containment volume at least twice as large as the EFBT experiment at NASA-Lewis, the achievement of a given number density will probably require a smaller electrode current than was the case at NASA-Lewis.

Probably the minimum power supply characteristics required to produce an interesting plasma in the EBT-S facility would be a supply capable of 10 kilovolts at 10 amps. As it happens, the UTK Plasma Science Laboratory has available for loan a 50 kilovolt, 20 ampere power supply if this is needed.

Also needed would be the EBT-S facility, with its diagnostic equipment and vacuum pumping equipment. We would not need the gyrotrons or the ECRH power to test the creation of an EFBT plasma, and these could be valved off or removed from the vacuum system during the EFBT test.

An additional requirement is a single biasing electrode across the minor diameter of the plasma in the midplane of one of the sectors. By starting the plasma in the right way, we were able at NASA-Lewis to generate an EFBT plasma with a single negatively biased electrode ring in a 12-sector plasma. There appears to be no reason why the same should not be possible in the 24 sector EBT-S facility.

During the experimental investigations of the EFBT plasma, it was found that a weak vertical magnetic field of only a few 10's of Gauss had a very important effect on the plasma containment and radial transport in the EFBT plasma. The adjustment of this vertical magnetic field over only a few Gauss would change the phase angle betwen the density and potential fluctuations, and hence the radial transport and confinement in that plasma. Accordingly, the EBT-S facility should be fitted, if it does not already possess the capability, with vertical field coils which are capable of producing plus or minus 30 Gauss in the containment volume.

A PLAN OF ACTION FOR THE EBT PROGRAM

On Table VIII is a plan of action showing the steps required to operate the EBT-S facility as an EFBT plasma. It should be noted that these changes are not irreversible, and indeed they could be made in such a way that it would be possible to operate the EBT-S plasma both with EFBT plasma generation and the input of ECRH power from the existing gyrotrons. With reasonable cooperation, these steps should be capable of being carried out in a few months.

Suppose that an EFBT plasma were successfully generated in the EBT-S facility, and produced number densities and ion temperatures substantially above those possible with the Elmo approach. On Table IX is shown a long-term research strategy for bootstrapping the EBT experiment into a much more interesting range of plasma

TABLE VIII

PLAN OF ACTION

1.) INSTALL DC POWER SUPPLY TO ENERGIZE ELECTRODE

2.) DISCONNECT/ISOLATE GYROTRONS AND ECRH SOURCES FROM EBT-S FACILITY

3.) FABRICATE & TEST BIASING ELECTRODE

4.) INSTALL BIASING ELECTRODE IN MIDPLANE OF ONE SECTOR

5.) INSTALL & TEST RF SOURCE FOR BOOTSTRAP PLASMA

6.) INSTALL/MODIFY VERTICAL MAGNETIC FIELD COILS

7.) DEMONSTRATE PLASMA GENERATION

parameters. Such may be sufficient to justify continuation of the EBT-program, appropriately modified. The first step would be to turn on the EFBT plasma and operate it in much the same way as we did at NASA-Lewis. There is no reason in principle why ECRH power could not be applied to the EFBT plasma, if needed. If the hot electron rings were needed for macroscopic stability, then ECRH power could be applied to generate hot electron rings. With the EFBT plasma and possibly the Elmo ECRH power applied to the plasma, one would then adjust the vertical magnetic field and other plasma parameters to maximize the plasma density and confinement time.When the plasma number density was maximized at number densities substantially above those achieved so far in the EBT-S experiment, one would then turn on the ion cyclotron resonant heating power and adjust the plasma parameters to maximize the number density, confinement time, and ion temperature in the ICRH-heated plasma. When this optimum was reached, one could turn off the ECRH, if used, and then the plasma would readjust itself to operate on the ICRH power input alone.

TABLE IX

RESEARCH STRATEGY USING EFBT PLASMA GENERATION

1.) TURN ON EFBT PLASMA

2.) TURN ON ECRH POWER, IF NEEDED

3.) MAXIMIZE DENSITY/CONFINEMENT TIME

4.) TURN ON ICRH POWER

5.) MAXIMIZE DENSITY, CONFINEMENT TIME, ION TEMPERATURE

6.) TURN OFF ECRH

7.) TURN OFF EFBT ELECTRODE

8.) WITHDRAW EFBT ELECTRODE

9.) PROCEED ON ICRH POWER ALONE

If this could be achieved, and if the radial electric fields were not necessary to macroscopic stability of the plasma, one could turn off the EFBT electrode, withdraw the EFBT electrode, and then proceed with the bumpy torus plasma on ICRH power alone. In the very long term, one could imagine heating a bumpy torus plasma to ignition conditions on ICRH power and then turning the ICRH power off when the plasma reached self-sustaining conditions.

ACKNOWLEDGEMENTS

Participation in this workshop and some of the results on electric field dominated plasmas has been suppored in part by contracts ORN N00014-80-C-0063 and AFOSR 81-0093.

REFERENCES

1. James F. Decker, Editor; An Evaluation of Alternate Magnetic Fusion Concepts-1977, DoE/ET-0047, May, 1978.

2. Roth, J. R.: Modification of Penning Discharge Useful in Plasma Physics Experiments. RSI 37, No. 8, Aug. 1966, pp. 1100-1101.

3. Roth, J. R.: Experimental Study of Spectral Index, Mode Coupling, and Energy Cascading in a Turbulent, Hot-Ion Plasma. Phys. of Fluids 14, No. 10, Oct. 1971, pp. 2193-2202.

4. Roth, J. R.: Origin of Hot Ions Observed in a Modified Penning Discharge. Phys. of Fluids 16, No. 2, 1973, pp. 231-236.

5. Roth, J. R.: Hot Ion Production in a Modified Penning Discharge. IEEE Trans. on Plasma Sci., 1, No. 1, 1973, pp. 34-45.

6. Roth, J. R.: Energy Distribution Functions of Kilovolt Ions in a Modified Penning Discharge. Plasma Physics 15, No. 10, October 1973, pp. 995-1005.

7. Roth, J. R.; Holmes, A. D.; Keller, T. A.; Krawczonek, W. M.: A A 12-Coil Superconducting "Bumpy Torus" Magnetic Facility for Plasma Research. IEEE Proc. of the 1972 Applied Superconductivity Conf., Annapolis, MD, May 1972, pp. 361-366.

8. Roth, J. R.; Holmes, A. D.; Keller, T. A.; and Krawczonek, W. M.: Performance of a 12-Coil Superconducting "Bumpy Torus" Magnet Facility. Proceedings of Technology of Controlled Thermonuclear Fusion Experiments and the Engineering Aspects of Fusion Reactors. Am. Nuclear Soc., 1974, pp. 409-425.

9. Roth, J. R.; Krawczonek, W. M.; Powers, E. J.; Kim, Y. C.; and Hong, J. Y.: Ion Confinement and Transport in a Toroidal Plasma with Externally Imposed Radial Electric Fields. NASA TP 1411, March 1979.

10. Roth, J. R.; "Ion Heating and Containment in an Electric Field Bumpy Torus (EFBT) Plasma," Paper G-4, Proceedings of the Conference on New Trends in Unconventional Approaches to Magnetic Fusion, Stockholm, Sweden, June 16-18, 1982, ISSN 0348-7644, Royal Institute of Technology, Stockholm, Sweden, B. Lehnert, Editor, (1982).

11. J. Reece Roth, Ion Heating and Containment in an Electric Field Bumpy Torus (EFBT) Plasma, Nuclear Instruments and Methods, Vol. 207 (1983) pp. 271-299.

12. Roth, J. R.; Gerdin, G. A.: Characteristics of the NASA Lewis Bumpy Torus Plasma Generated with High Positive or Negative Applied Potentials. Plasma Physics, Vol. 19, No. 5, 1977, pp. 423-446.

13. Richardson, R. W.: Determination of Electron Temperature in a Penning Discharge by the Helium Line Ratio Method. NASA TM X-71677, 1975.

14. Kambic G. X.: Determination of the Radial Potential Profile in the Modified Penning Discharge with a Heavy Ion Beam Probe. IEEE Trans. on Plasma Science, Vol. PS-4, No. 1, March 1976, pp. 1-5.

15. Roth, J. R.: Radial Electric Field and Potential Control in an Electric Field Bumpy Torus Plasma. Proceedings, Workshop on Ambipolar Potential Formation and Control in Bumpy Tori and Mirrors, May 11-12, 1981, Oak Ridge, Tennessee, Conf. 810511, p. 313 (1981).

16. Roth, J. R.: Anomalous Conductivity of an Electric Field Bumpy Torus Plasma. Conference Record, 1980 IEEE International Conference on Plasma Science, May 19-21, 1980, Madison, Wisconsin 80CH1544-6 NPS p. 141 (1980).

17. Roth, J. R.: Effects of Applied DC Radial Electric Fields on Particle Transport in a Bumpy Torus Plasma. IEEE Trans. on Plasma Science, Vol. PS-6, No. 1, June 1978, pp. 158-165.

18. Singh, Chandra M.; Krawczonek, Walter M; Roth, J. Reece; Hong, Jae Y; and Powers, Edward J.: Fluctuation Spectra in the NASA Lewis Bumpy Torus Plasma, NASA TP 1257, June 1978.

19. Roth, J. R.; Krawczonek, W. M.; Powers, E. J.; Kim, Y. C.; and Hong, J. Y.: Fluctuations and Turbulence in an Electric Field Bumpy Torus Plasma. Journal of Applied Physics, Vol. 52, No. 4, 2705-2713 (1981).

20. Powers, E. J.; Kim, Y. C.; Hong, J. Y.; Roth, J. R.; and Krawczonek, W. M.: A Fluctuation-Induced Plasma Transport Diagnostic Based Upon Fast-Fourier Transform Spectral Analysis, NASA TM-38932, May 1978.

21. Roth, J. R.; Krawczonek, W. M.; Powers, E. J.; Hong, J. Y.; and Kim, Y. C.: Inward Transport of a Toroidally Confined Plasma Subject to Strong Radial Electricl Fields. Phys. Rev. Lett., Vol. 40, 1450-1453, May 29, 1977.

22. Roth, J. R.; Krawczonek, W. M.; Powers, E. J.; Hong, J. Y.; and Kim, Y. C.: The Role of Fluctuation-Induced Transport in a Toroidal Plasma with Strong Radial Electric Fields. Plasma Physics, Vol. 23, No. 6, 509-514 (1981).

23. Kim, Y. C.; Powers, E. J.; Hong, J. Y: Roth, J. R.; and Krawczonek, W. M.: The Effect of a Weak Vertical Magnetic Field on Fluctuation-Induced Transport in a Bumpy Torus Plasma. Nuclear Fusion, Vol. 20, No. 2, 171-176 (1980).

24. Roth, J. R.: Radial Equilibrium and Force Balance in Electric Field Dominated Plasmas. APS Bulletin 26, p. 851 (1981).

25. Alexeff, I.; Roth, J. R.; "Stabilization of the Flute Instability by a D. C. Electric Field in Toroidal Plasmas," Proceedings, 1982 IEEE International Conference on Plasma Science, IEEE Cat. No. 82CH1770-7, p. 36 (1982).

26. Roth, J. R.; Hayman, P. W.; and Pastel, R. L.; "A Paired Comparison of High Frequency RF Emission from Two Configurations of Electric Field Dominated PLasma," Proceedings of the International Conference on Plasma Physics, Goteborg, Sweden, June 9-15, 1982 p. 250.

27. Roth, J. R.: The Electric Field Bumpy Torus Plasma as a Test Bed for Plasma-Wall Interaction Studies. Proceedings, Fourth Topical Meeting on the Technology of Controlled Nuclear Fusion, Paper E-11, October 14-16, 1980. Conf 801011, Vol. III, pp. 692-701 (1981).

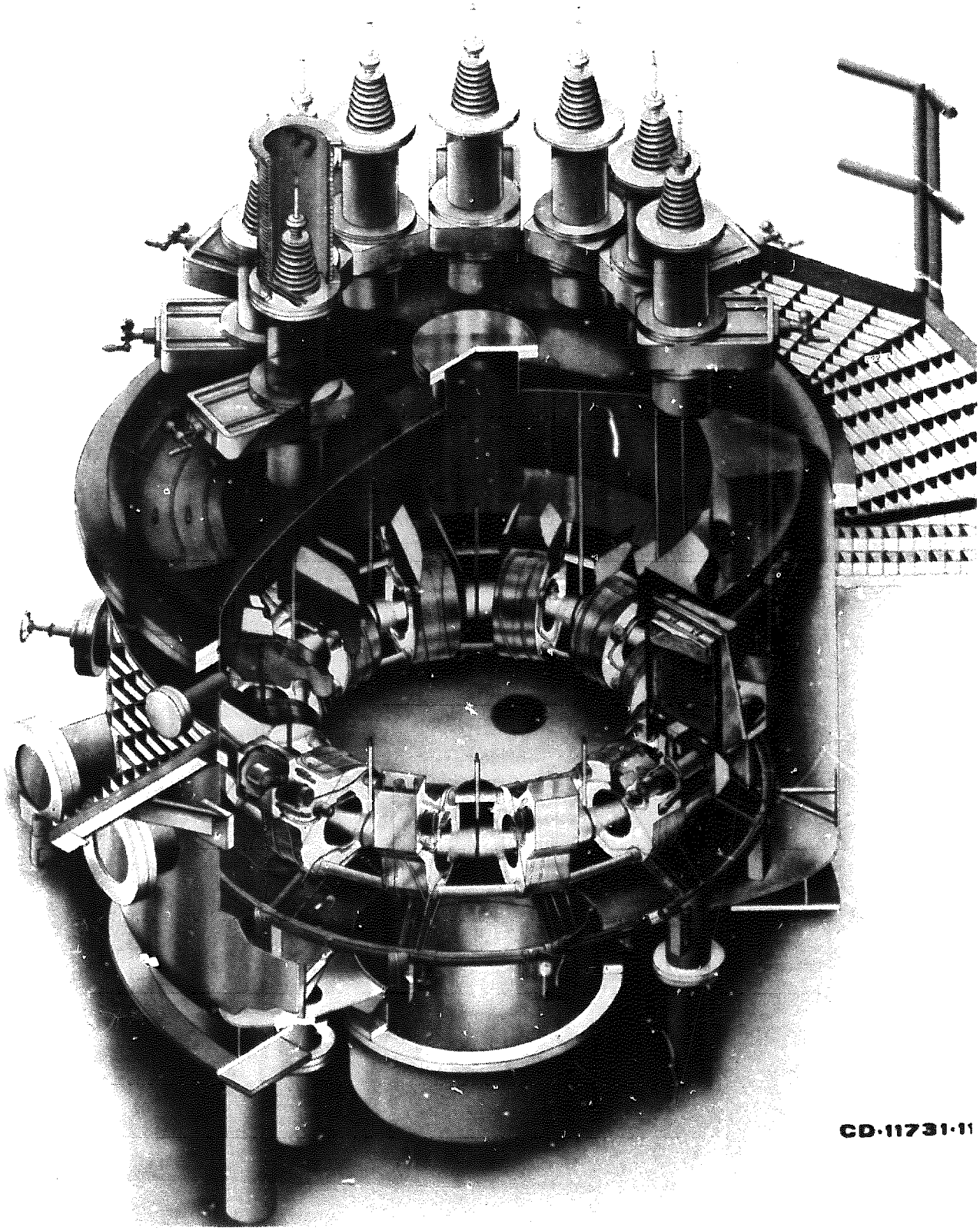

Figure 1. Isometric cutaway drawing of the NASA-Lewis Bumpy Torus Superconducting Magnet Facility.

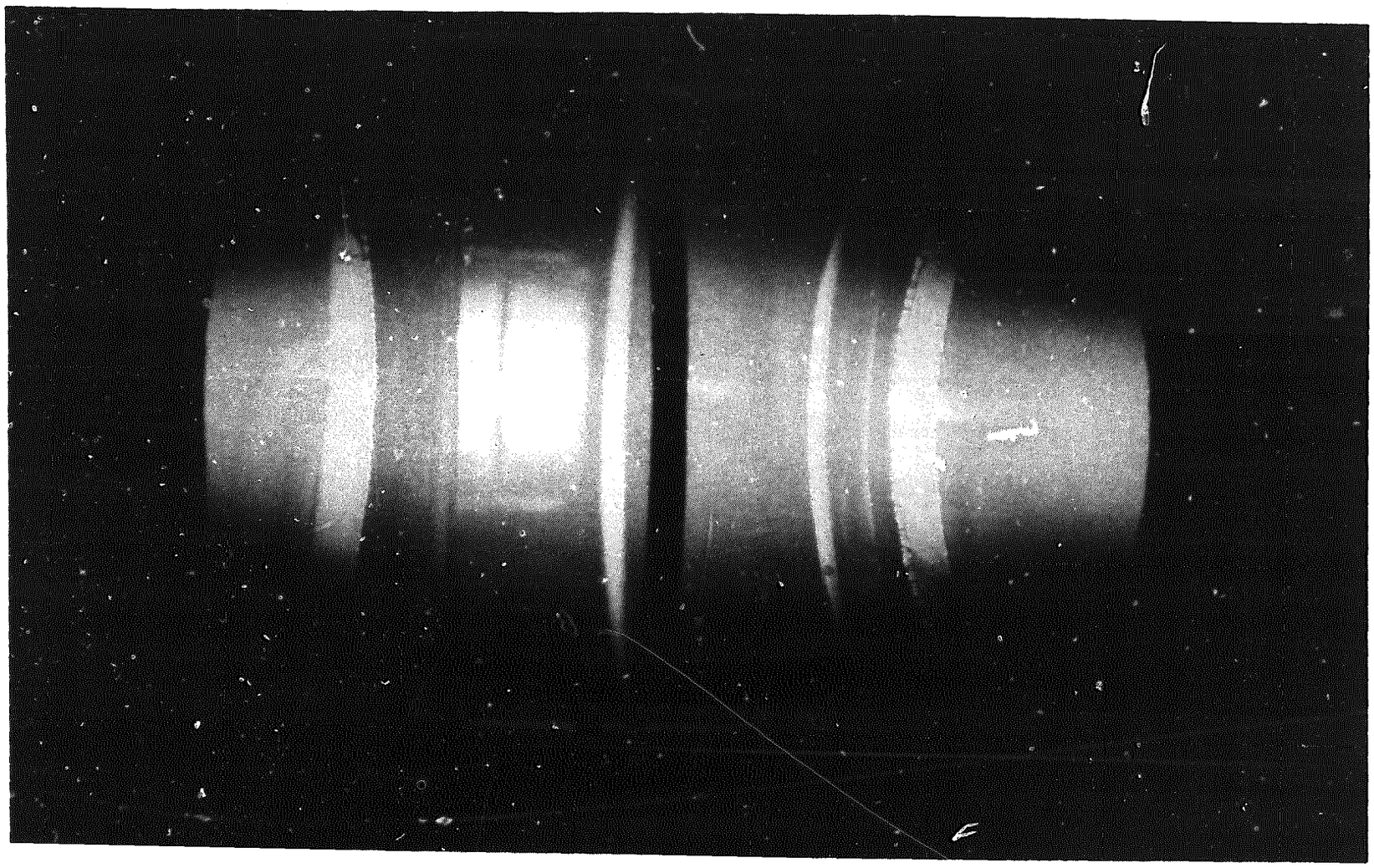

Figure 2. Photograph of the NASA-Lewis EFBT Plasma. The vertical structure in the center is the midplane electrode ring. Visible slightly to left of center is the sector at the opposite end of the major diameter.

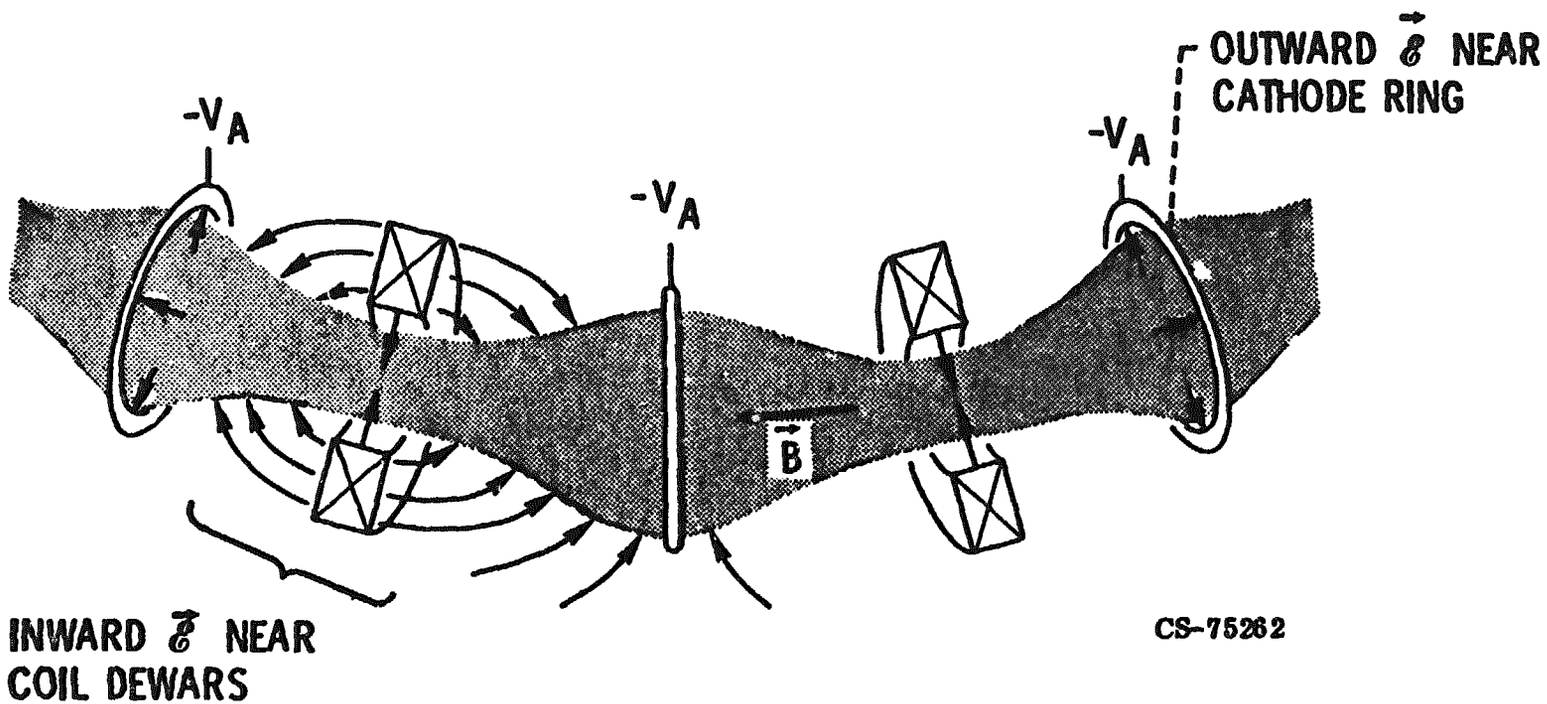

Figure 3. Electric field structure in the EFBT plasma with negative midplane electrodes. Each negative electrode acts like a Langmuir probe in ion saturation, and collects only ions.

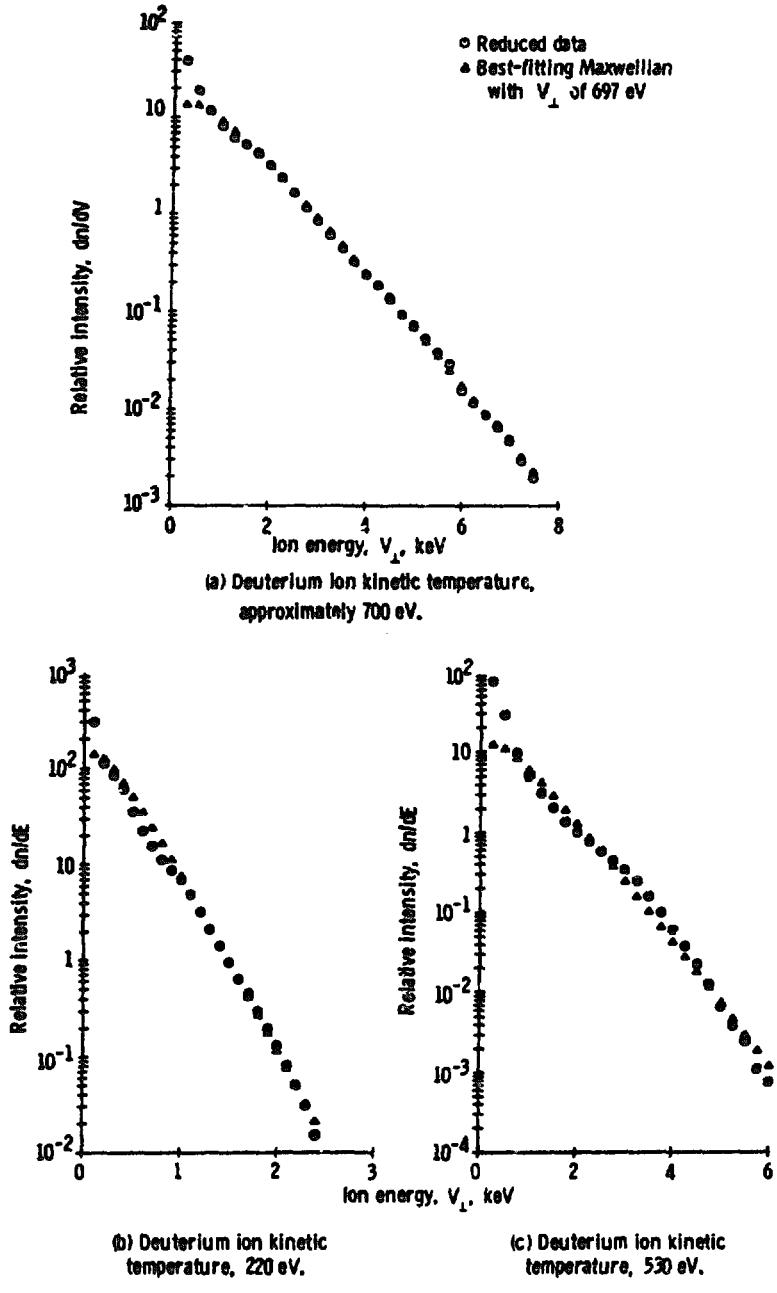

Figure 4. Characteristic examples of ion energy distribution functions from the EFBT Plasma.

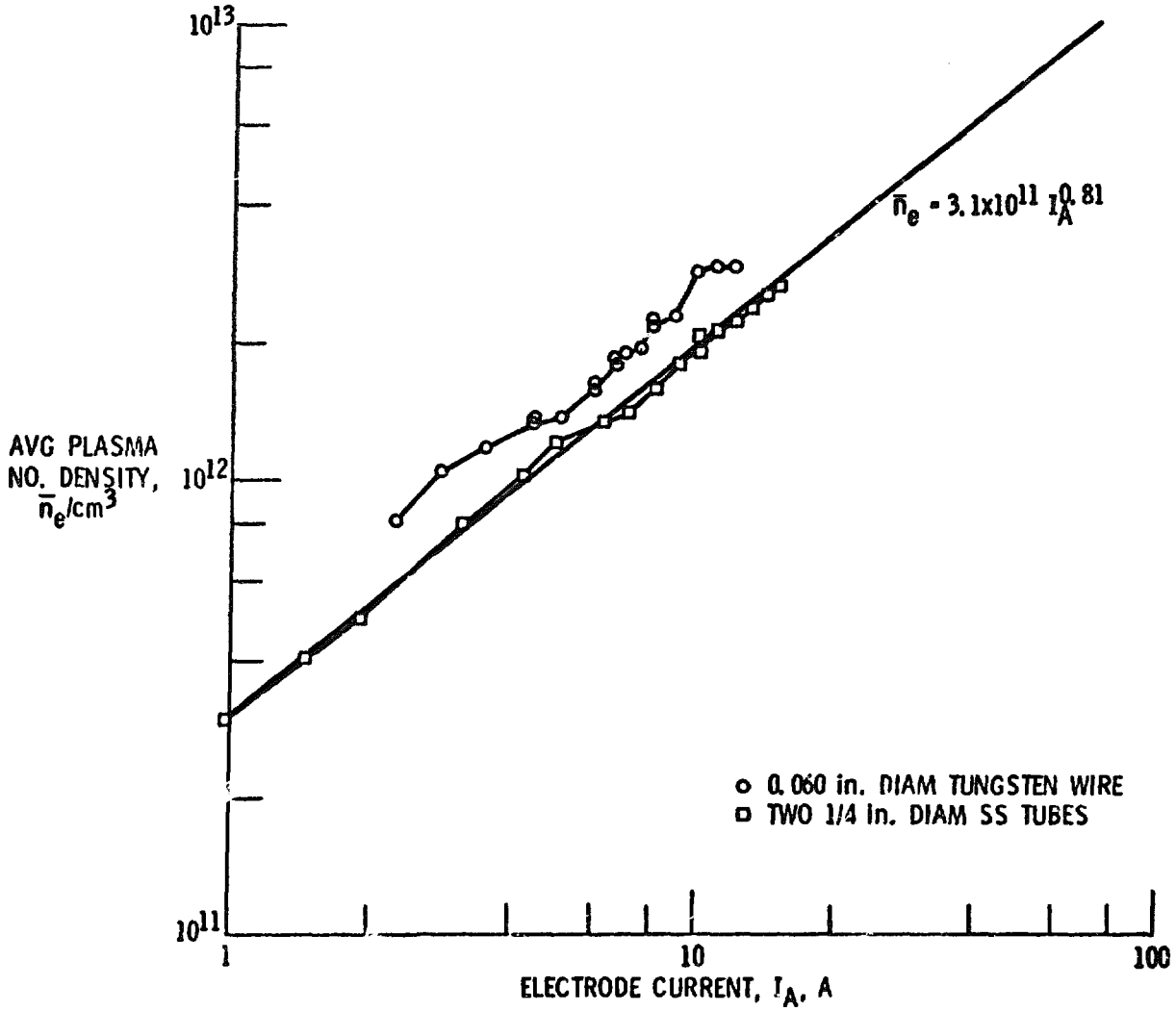

Figure 5. Scaling of the averge plasma number density with electrode current flowing to the biasing electrode ring. The maximum number density was limited only by provisions for cooling sheet metal surrounding the plasma.

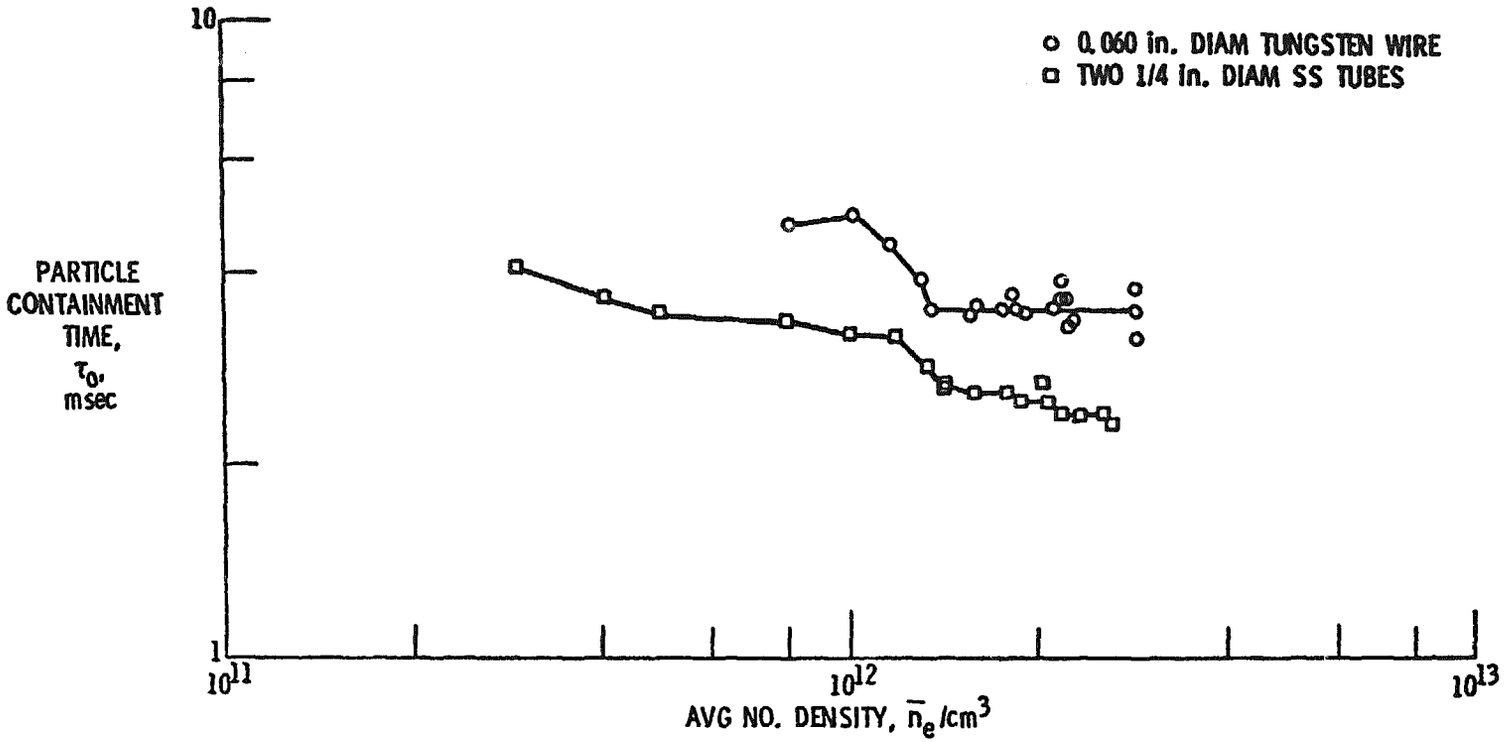

Figure 6. The average particle containment time as a function of the average particle number density. The containment times increased as the surface area of the biasing electrode in contact with the plasma decreased.

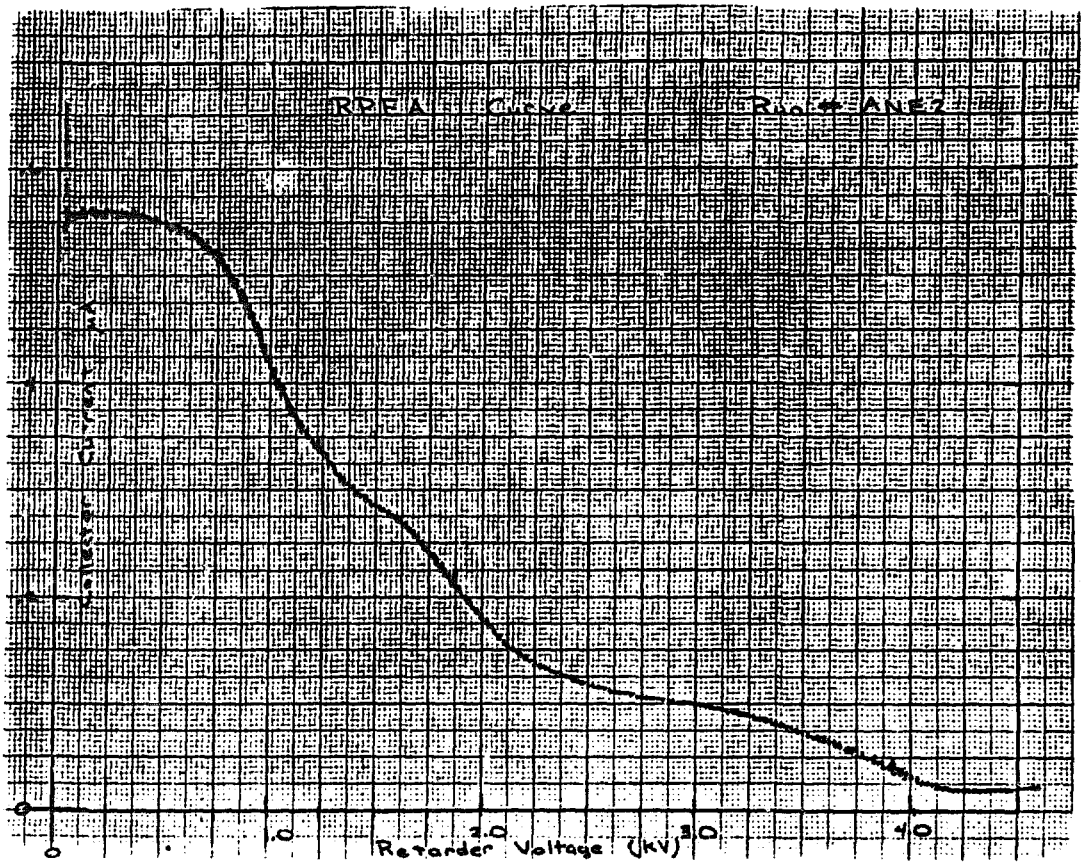

Figure 7a. A retarding potential energy analyzer curve from the UTK Plasma Science Laboratory, illustrating a thermalized distribution of ions from a modified Penning discharge.

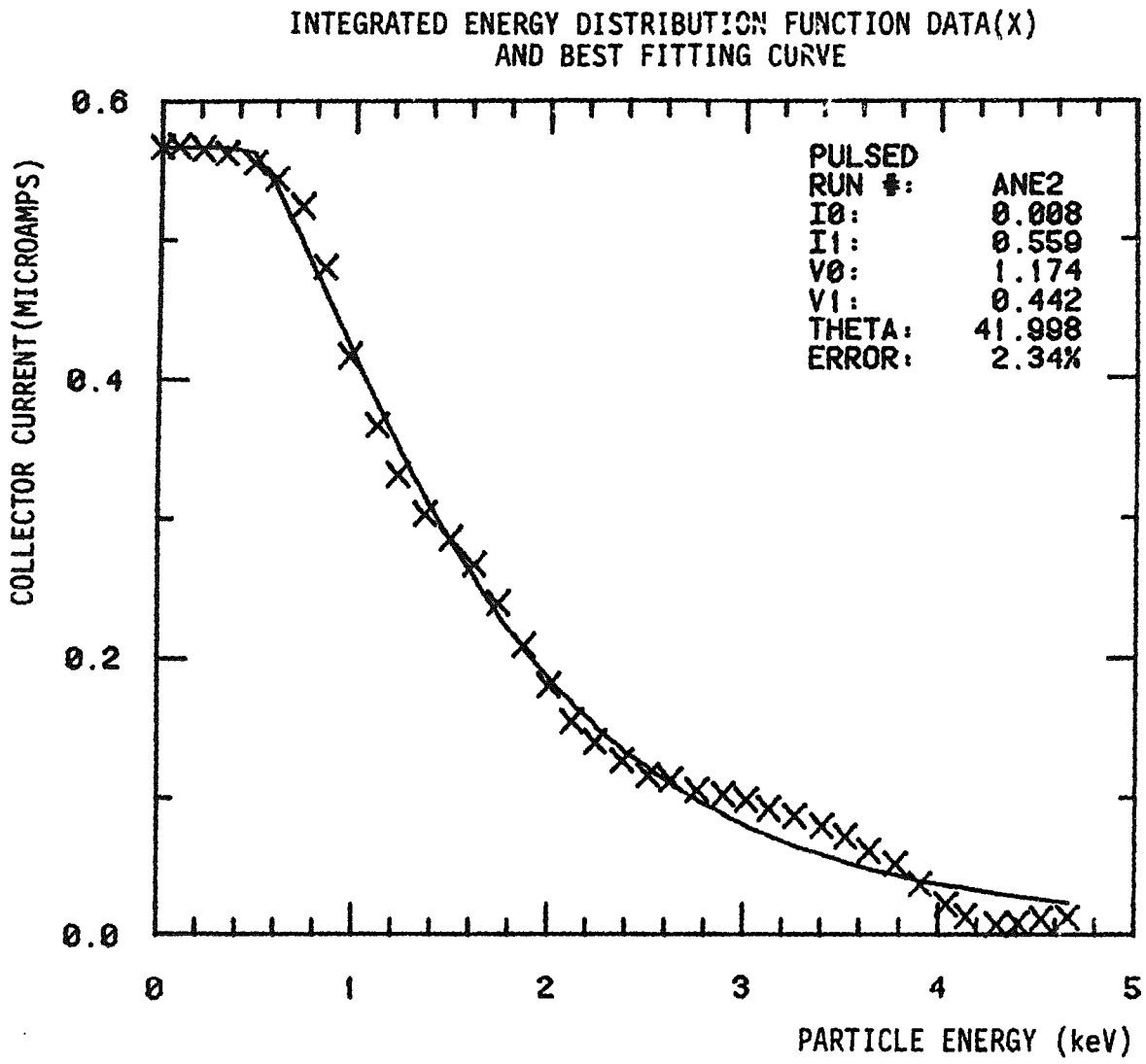

Figure 7b. **The best-fitting maxwellian distribution to the retarding potential curve of Figure 7a. The ion kinetic temperature in this case was about 400 eV and the plasma was floating at a potential of about 1200 volts.**

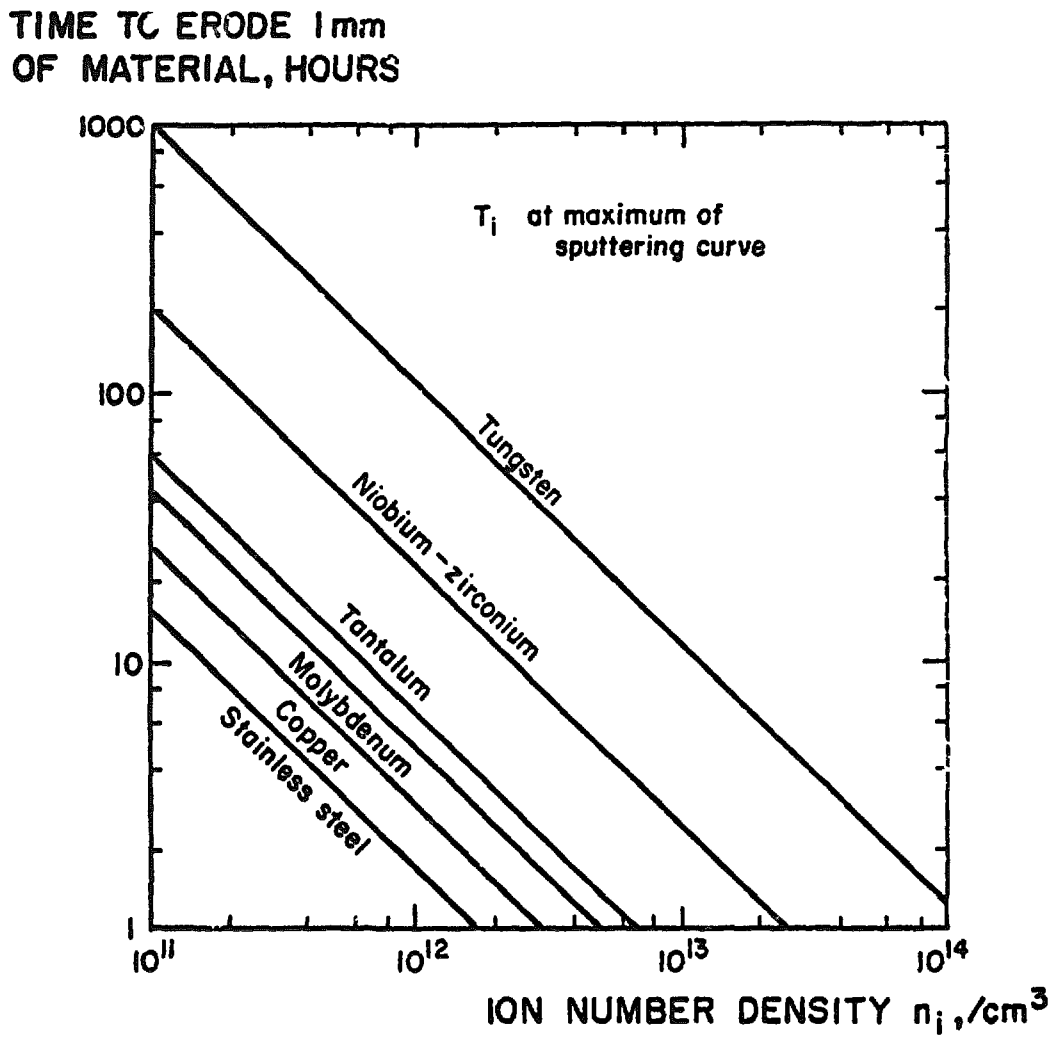

Figure 8. Time to erode one millimeter of material from candidate electrode materials for incident ion energies at the maximum of the sputtering curve.

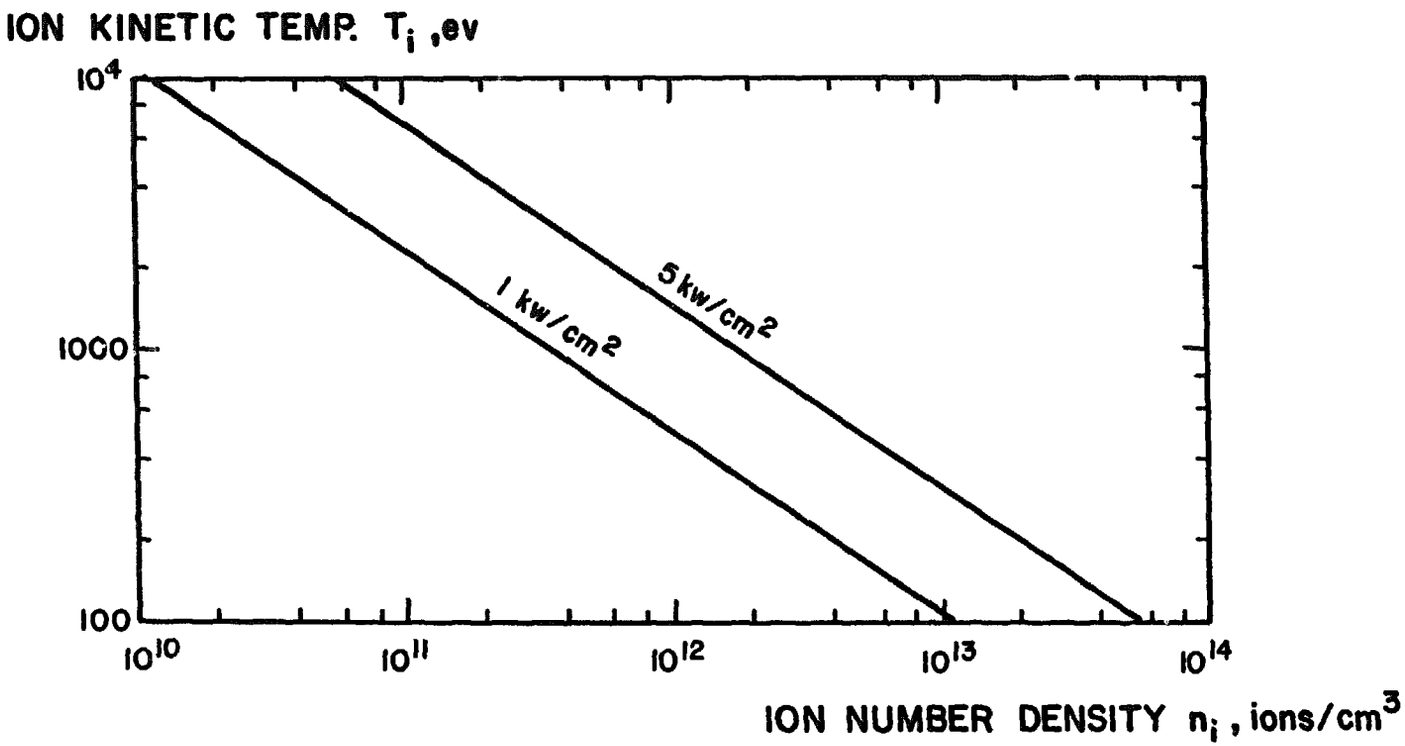

Figure 9. Combinations of ion kinetic temperature and ion number density which produce heat fluxes to a biasing electrode of 1 and 5 kilowatts per square centimeter, the approximate upper limit of water-cooled heat transfer technology.

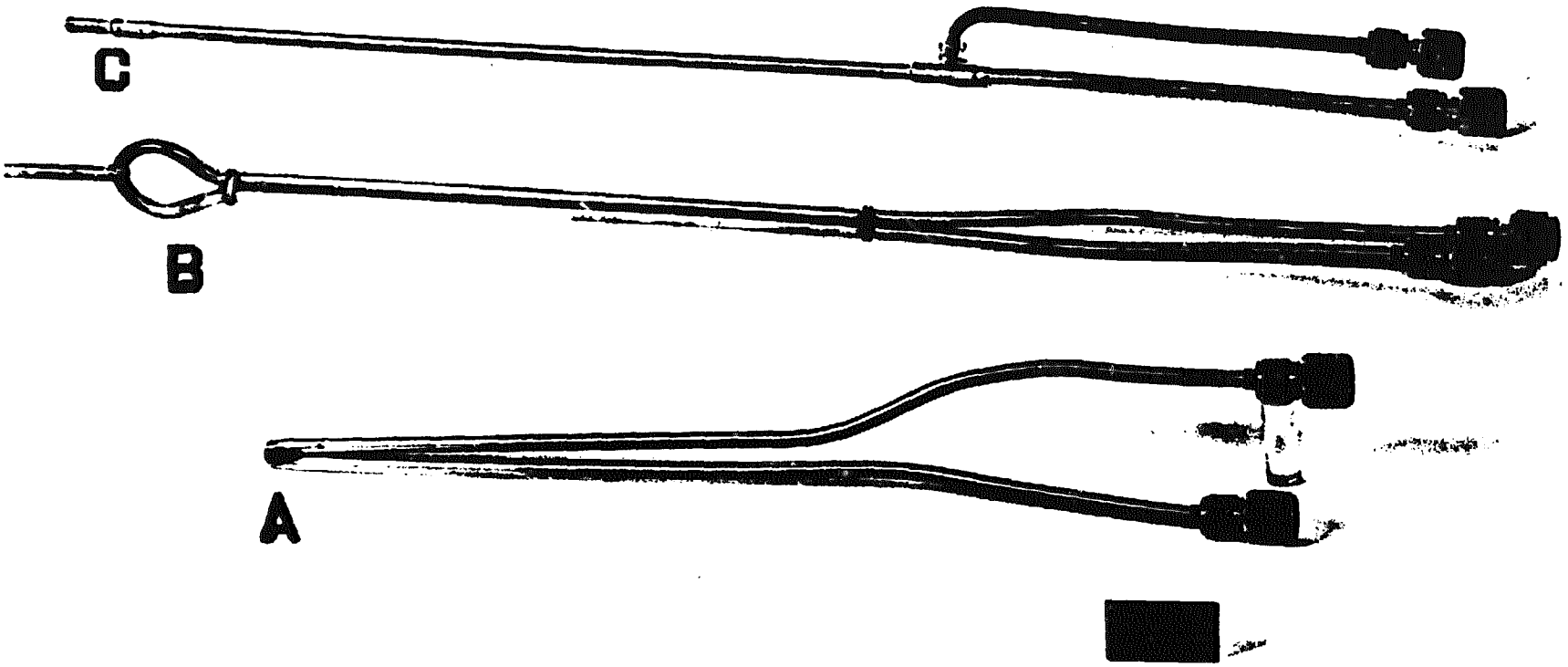

Figure 10. Various stainless steel electrode configurations inserted across the minor diameter of the plasma. All were water-cooled. Configuration A was inserted only to the equatorial plane of the plasma, halfway across the minor diameter.

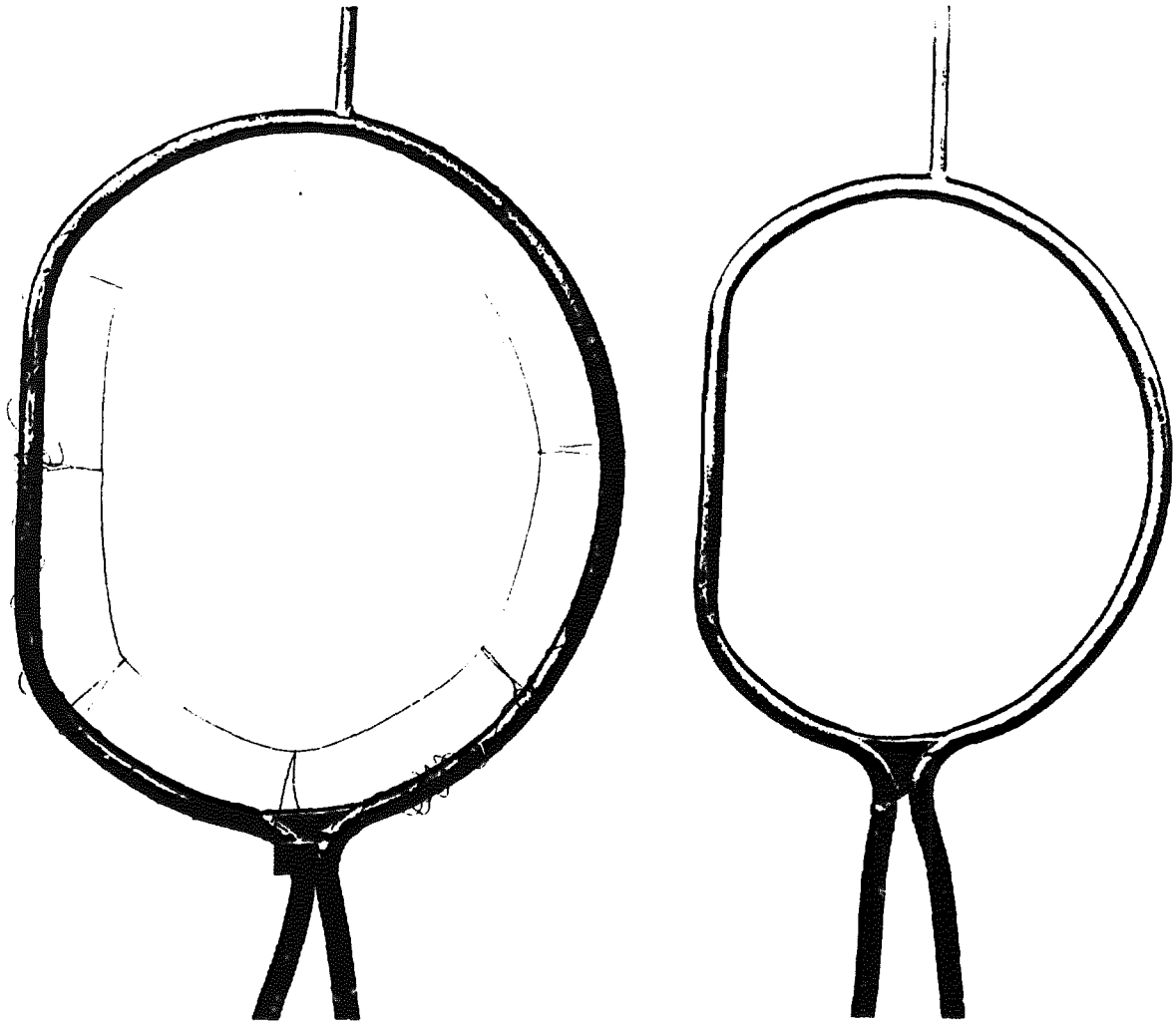

Figure 11. On the right is the standard water-cooled copper electrode ring configuration used for the EFBT plasma. On the left is a biasing electrode arrangement designed to eliminate the possibility of a water line rupture into the containment volume.

363/364

RF HEATING

Buildup and Sustainment of 10^{13} cm^{-3} Plasma by ICRF in RFC-XX

T. Sato, S. Okamura, K. Adati, T. Aoki, D.R. Baker*,
H. Fujita, H.R. Garner*, K. Hattori, S. Hidekuma,
T. Kawamoto, R. Kumazawa, Y. Okubo, and K. Uchino**

Institute of Plasma Physics, Nagoya University, Nagoya 464, Japan

*GA Technologies, Inc., San Diego, California 92138, USA
**Graduate School of Engineering Sciences, Kyushu University
Kasuga, Fukuoka 816, Japan

Abstract

A high density plasma is produced in the central section of RFC-XX by rf fields in the ion cyclotron frequency range. The magnetic field configuration of the central section is a solenoid or a mirror. An externally injected plasma or an ECH produced plasma is used as a start-up plasma. RF fields are applied to this plasma by a rotating type-III antenna to buildup a high density plasma and to sustain it. The rotating type-III antenna can excite the left-hand circularly ($m = -1$), the right-hand circularly ($m = +1$), or the linearly ($m = \pm 1$) polarized wave.

In general, the $m = +1$ excitation can produce higher density (up to 7×10^{13} cm^{-3}) and rather low ion temperature (30 - 50 eV) plasmas, and the $m = -1$ excitation can produce higher ion temperature (100 - 150 eV) and moderate density ($\sim 10^{13}$ cm^{-3}) plasmas. The plasma is sustained for the duration of the rf pulse and gas puffing ($\sim$50 ms).

This method is applicable to various kinds of magnetic fusion experimental devices.

§1. Introdution

Plasma production by radio-frequency fields is used for various plasma experimental devices. The frequency usually used is in the

range of the electron cyclotron frequency. Especially, the bumpy torus plasma has been made by a high power microwave source at the electron cyclotron frequency. The maximum density obtained[1] in the EBT-S device, however, is 2.5×10^{12} cm^{-3} which is less than the density expected by the condition, $\omega = \omega_{ce} = \omega_{pe}$. In the experiments of plasma heating by the slow or the fast hydromagnetic wave in the stellarators [2,3] in Princeton, the plasma was prepared for ohmic heating with 250 KHz rf pre-ionization. Nobody has used the rf power in the ion cyclotron frequency range to create and sustain the high density plasma.

Recently, the experiments on plasma production and sustainment using rf fields with the ion cyclotron frequency range have been performed on RFC-XX[4] and Phaedrus[5]. The plasmas can be sustained by only rf power for the rf pulse duration (20 - 30 ms) which is much longer than the plasma confinement time. Here, results of buildup and sustainment of 10^{13} cm^{-3} plasma by the rf power with the ion cyclotron frequency range in the RFC-XX device in the Institute of Plasma Physics, Nagoya University, are presented. The RFC-XX device has a magnetic field configuration of a long-uniform field (central section) terminated by spindle cusp fields (plug section). Two-line and two-point cusps are plugged by rf fields in the ion cyclotron frequency range. In this experiment, however, the rf plugging is not applied and only a rotating type-III antenna[6] setup in the central section is excited to produce the plasma.

§2. Experimental Set-up

A schematic diagram of RFC-XX with its diagnostics is shown in Fig.1. The distance between two field-null points is 2 m. The magnetic field strength in full operation is 2.1 T at the line cusp, 3.9 T at the point cusp, and 1.0 T at the central solenoidal section. After the modification, the distance between field-null points was elongated to 3 m, and the central section was changed to have a simple mirror, the magnetic field strength of which is 0.35 T at the midplane and 0.96 T at the mirror throat. To produce plasmas, an azimuthal array of four antenna elements, which we refer to as a rotating type-III antenna, is installed in the central section. The rf currents of opposite elements

are always driven in opposite phases, and the rf current of one set (top and bottom elements) has a phase difference δ relative to that of another set (right and left elements) as shown in Fig.2. By changing the phase difference, we can select the $m=-1$ mode (left-hand rotating), the $m=+1$ mode (right-hand rotating), or the $m=\pm 1$ mode (linearly oscillating). The rotating type-III antenna is excited by two 0.4-MW rf oscillators.

Hydrogen gas is fed from a gas box which has a slit round the plasma column in order to obtain azimuthal uniformity. The gas puffing rate is varied from 5 to 85 $\mathrm{Torr \cdot l \cdot sec^{-1}}$. For operation at low gas puffing rates, a low-density initial seed plasma is needed at the start-up phase. An external plasma produced by TPD-type plasma source or an ECH plasma produced in the region of the field-null point is used as the initial seed plasma. The microwave power for ECH is 500-W with 2 ms width and the frequency is 2.45-GHz.

§3. Experimental Results

(1) Plasma production in the solenoidal central section

An example of the time sequence and some plasma parameters in the case of the $m=-1$ excitation are shown in Fig.3. After the partial decay of the external plasma source, the rotating type-III antenna is excited with gas puffing. The plasma density increases again to its stationary value. The frequency is 13.7 MHz. The magnetic field strength in the central section is chosen to have the maximum values of line density and diamagnetic signal in the central section when the left-hand rotating wave is excited, so that the value of ω/ω_{ci} is restricted from 0.90 to 0.95. Figure 4 shows the line density and the diamagnetic signal versus the phase difference δ. The rf amplitude of each antenna is kept constant when δ is changed. The line density has the maximum value at $\delta=\pi/2$ $(m=+1)$, but the diamagnetic signal has the minimum value. On the contrary, the diamagnetic signal becomes maximum at $\delta=3\pi/2$ $(m=-1)$.

The line density increases with the gas puffing rate as shown in Fig.5. In the case of the m = -1 excitation, the line density saturates at the value of 0.35×10^{14} cm^{-2}. But the m = +1 excitation can produce very high density plasma ($nl = 2.5 \times 10^{14}$ cm^{-2}). The density above the cut-off value for 70-GHz microwave is measured by means of the laser scattering method. The net rf input power in this experiment is about 100 kW. The large gas puffing rate for the m = -1 mode gives rise to short energy confinement time which results from large charge exchange loss.

The radial density profile measured in the central section is almost flat within the diameter of the gas box for the m = -1 mode as shown in Fig.6(a). However, the radial density profile for the m = +1 mode shows a sharp high density peak with lower flat distribution as shown in Fig.6(b). The maximum density is attained to 7×10^{13} cm^{-3} when the line density is 2.5×10^{14} cm^{-2}. Azimuthal uniformity is checked by the five multi-grid energy analyzers set around the line cusp and they show that the deviation is within 20 %.

(2) Plasma production in the mirror central section

The modified device, RFC-XX-M, has a simple mirror field in the central section. The mirror field and the cusp field are connected with a uniform field region in which the rotating type-III antenna is set up as shown in Fig.7. The frequency is 7.0 MHz. Values of ω/ω_{ci} shown in this figure correspond to the cyclotron resonance point at which the slow wave excited with the condition of the indicated ω/ω_{ci} can be damped away. The value ω_{ci} is evaluated with the magnetic field strength B_a at the position of the antenna.

The line density and the diamagnetic signal measured at the mid-plane of the mirror are plotted against the phase difference of the rotating type-III antenna in Fig.8. For $B_a = 0.755$ T ($\omega/\omega_{ci} = 0.606$), the m = -1 mode can produce higher density and higher temperature plasma compared with the m = ±1 and the m = +1 modes. In the contrary, the m = +1 mode is more effective in producing high density plasma for a weak magnetic field, $B_a = 0.472$ T ($\omega/\omega_{ci} = 0.970$).

Figures 9 and 10 show the line density and the diamagnetic signal versus B_a and the gas puffing rate for the m = -1 mode. The optimum plasma production is obtained in the range from $B_a = 0.614$ T ($\omega/\omega_{ci} = 0.745$) to 0.802 T ($\omega/\omega_{ci} = 0.570$) for the gas puffing rate of 21 Torr·l·sec^{-1}. When the gas puffing rate increases, the line density increases to 1×10^{14} cm^{-2} which is approximately three times as much as that in the case of the solenoidal central section (cf. Fig.5). The line density and the diamagnetic signal are also shown against the anode voltage of the power amplifier triode in Fig.11 for the m = -1 mode. These quantities increase abruptly at the threshold value of the anode voltage, and then the line density keeps a constant value but the diamagnetic signal still increase linearly. The net rf input power is about 50 kW in this range. The threshold value can be reduced by increasing the initial seed plasma density. The radial distribution of atomic hydrogen is estimated by means of the measurement of radial profiles of H_α - line intensity and electron density. The result is shown in Fig.12 with the electron density distribution. The hydrogen atom density near the axis is of the order of 10^{10} cm^{-3} and is less than 20 % of that of outer region. This value is consistent with the fact that charge exchange is not the main energy loss channel of the plasma.

Figure 13 and 14 show the line density versus B_a and the gas puffing rate for the m = +1 mode. In contrast with the case of the m = -1 mode, the plasma can be produced in a wide range of the magnetic field strength. The dependence of gas puffing rate on the line density is almost similar to that in the case of the solenoidal central section (cf. Fig.5). The line density for larger gas puffing rates has the saturated value but this is caused by the cut-off of microwave signal, so the real line density must increase just like the case of the solenoidal central section.

For both cases of the m = -1 and +1 modes, the plasma can be sustained by rf power for the rf pulse duration up to 50 ms which is limited by the power supply.

§4. Conclusion

By using the rotating type-III antenna, high density plasmas are produced in the solenoidal central section of RFC-XX and in the mirror central section of RFC-XX-M. The frequency used is in the ion cyclotron frequency range. The TPD-plasma injected through one of the point cusps or the ECH plasma produced in the region of the field-null point is used as the initial seed plasma. After the decay of the seed plasma, the rotating type-III antenna is excited with gas puffing. The plasmas can be sustained for the duration of the rf pulse and gas puffing ($\sim$50 ms).

In the case of the m = -1 excitation, the line density obtained is 1×10^{14} cm^{-2} with the net rf input power of 50 kW. The radial distribution of the density is almost flat within the diameter of the gas box. The plasma density is about 10^{13} cm^{-3}. The ion temperature ranges from 100 to 150 eV. The hydrogen atom density near the axis is less than 20 % of that of outer region, so that this plasma is almost charge-exchange free.

In the case of the m = +1 excitation, the line density becomes 2.5×10^{14} cm^{-2}. The radial density profile shows sharp peak on the axis and the peak density is 7×10^{13} cm^{-3}. The ion temperature is less than 50 eV.

This method is applicable to not only linear devices but also vairous kinds of toroidal devices.

References

1) N.A. Uckan and EBT Group, Plasma Phys. 25 (1983) 129.
2) T.H. Stix and R.W. Palladino, Phys. Fluids 1 (1958) 446.
3) K. Chung and M.A. Rothman, Phys. Fluids 10 (1967) 2634.
4) R. Kumazawa et al., Plasma Physics and Controlled Fusion Research 1982 (Proc. 9th Int. Conf. Baltimore, 1982) Vol.I, IAEA, Vienna (1983) 565.
5) N. Hershkowitz et al., Plasma Physics and Controlled Fusion Research 1982 (Proc. 9th Int. Conf. Baltimore, 1982) Vol.I, IAEA, Vienna (1983) 553.
6) T. Watari et al., Nucl. Fusion 22 (1982) 1359.

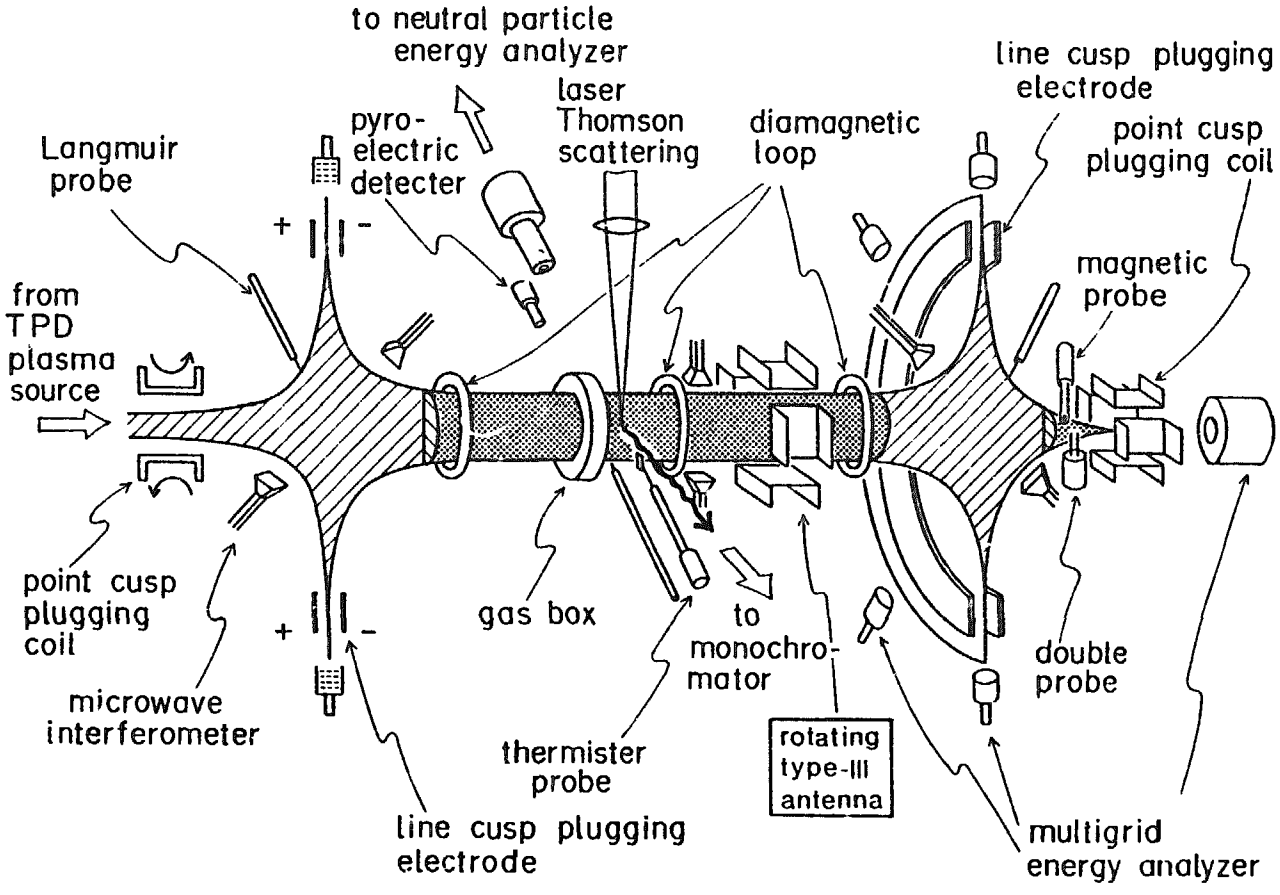

Fig.1 Schematic drawing and diagnostic system of RFC-XX.

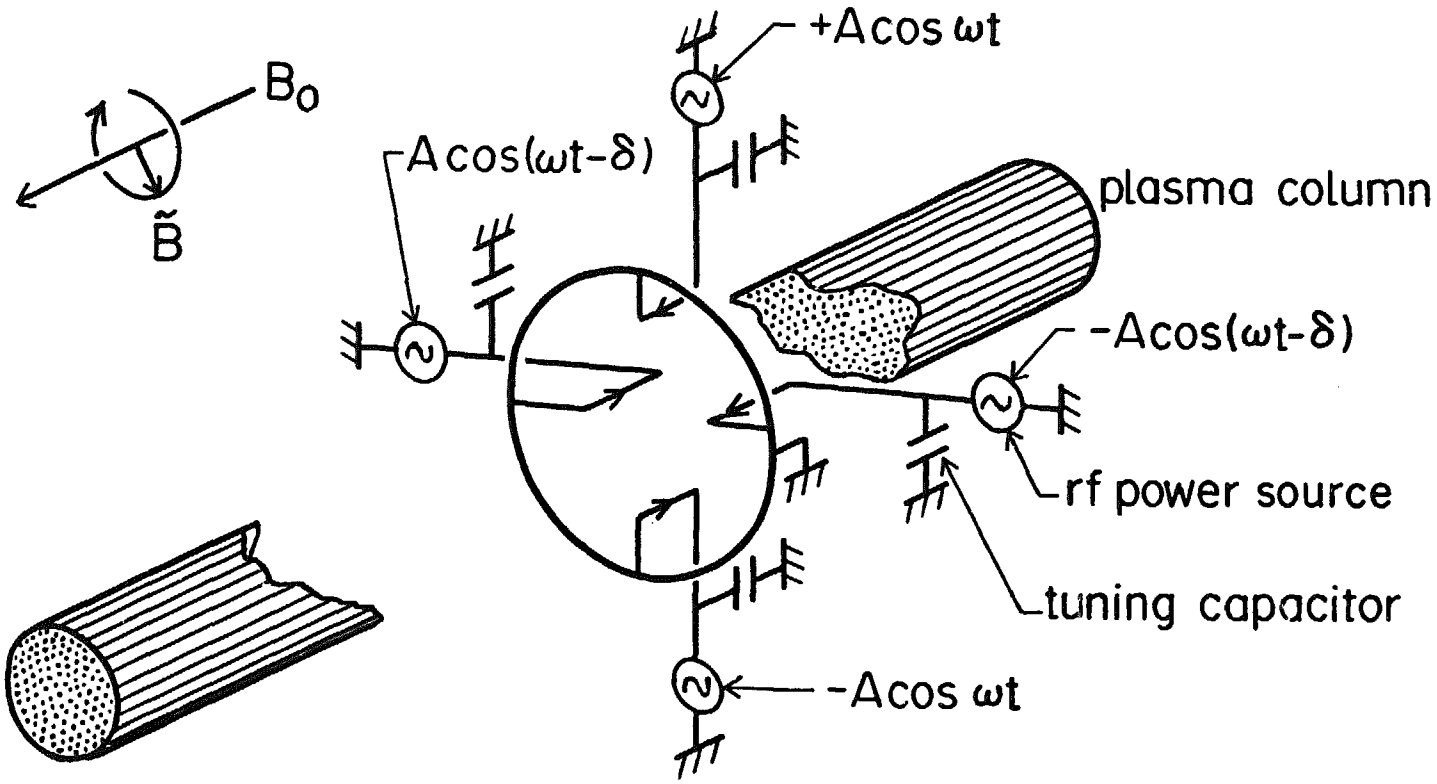

Fig.2 Schematic diagram of rotating type-III antenna.

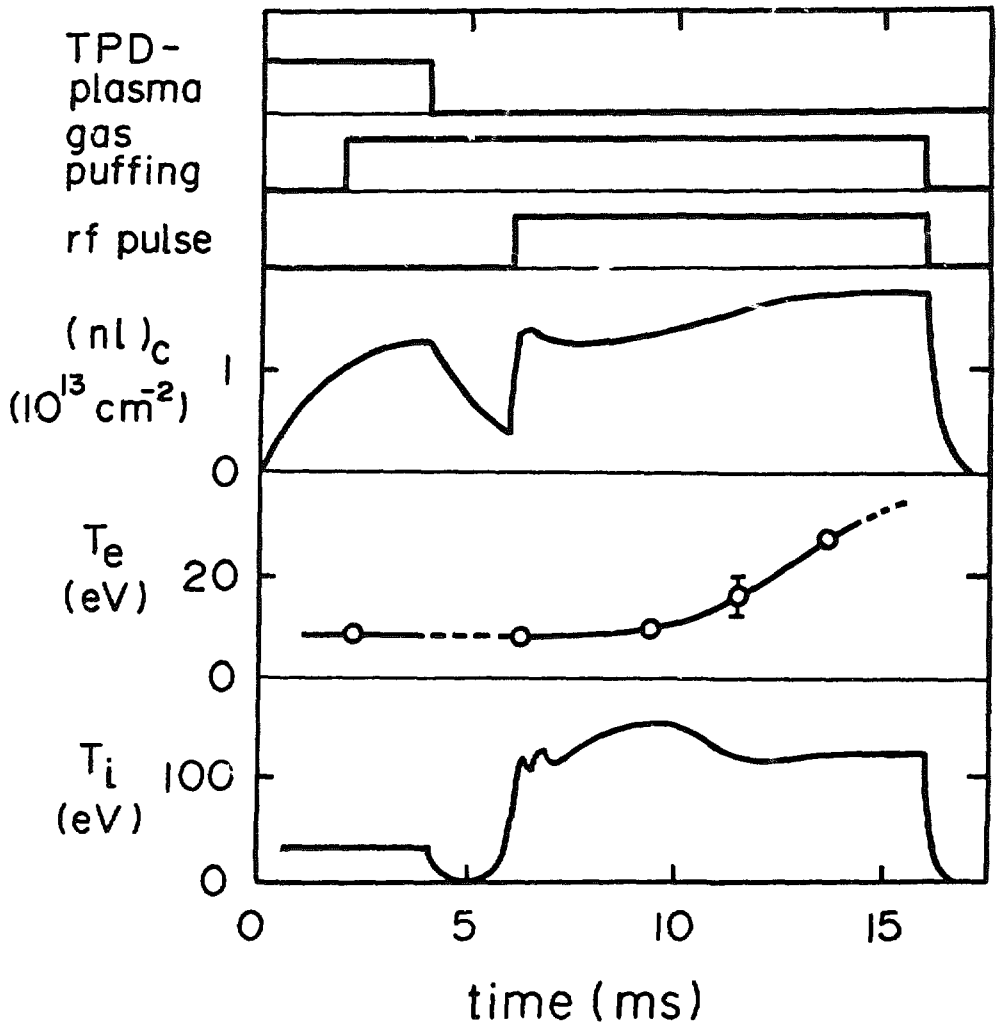

Fig.3 Time sequence and some plasma parameters in the case of the $m = -1$ mode, where $(nl)_c$ is the line density in the central section.

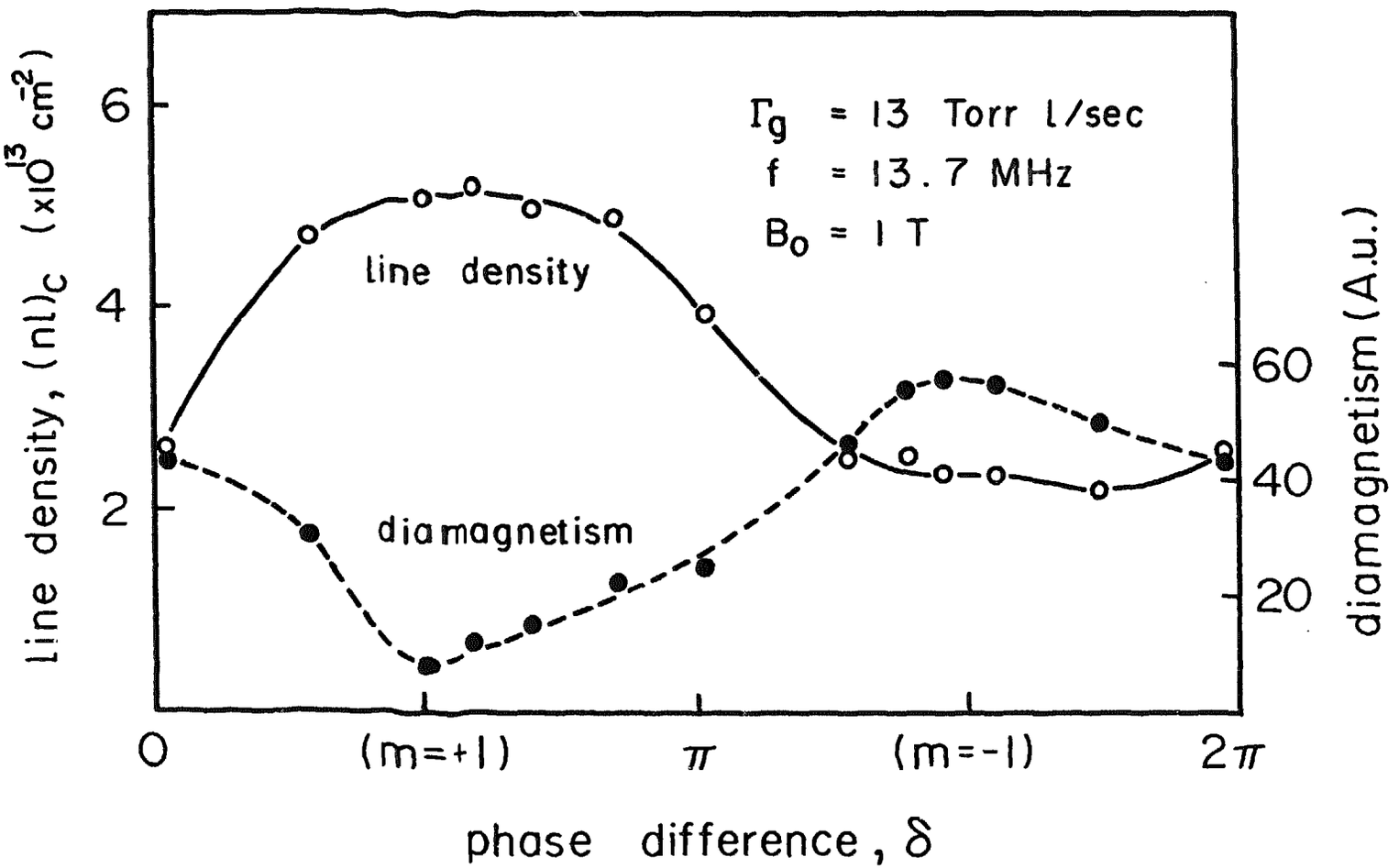

Fig.4 Line density and diamagnetic signal versus the phase difference, δ. Γ_g is the gas puffing rate and B_0 is the magnetic field strength in the solenoidal central section.

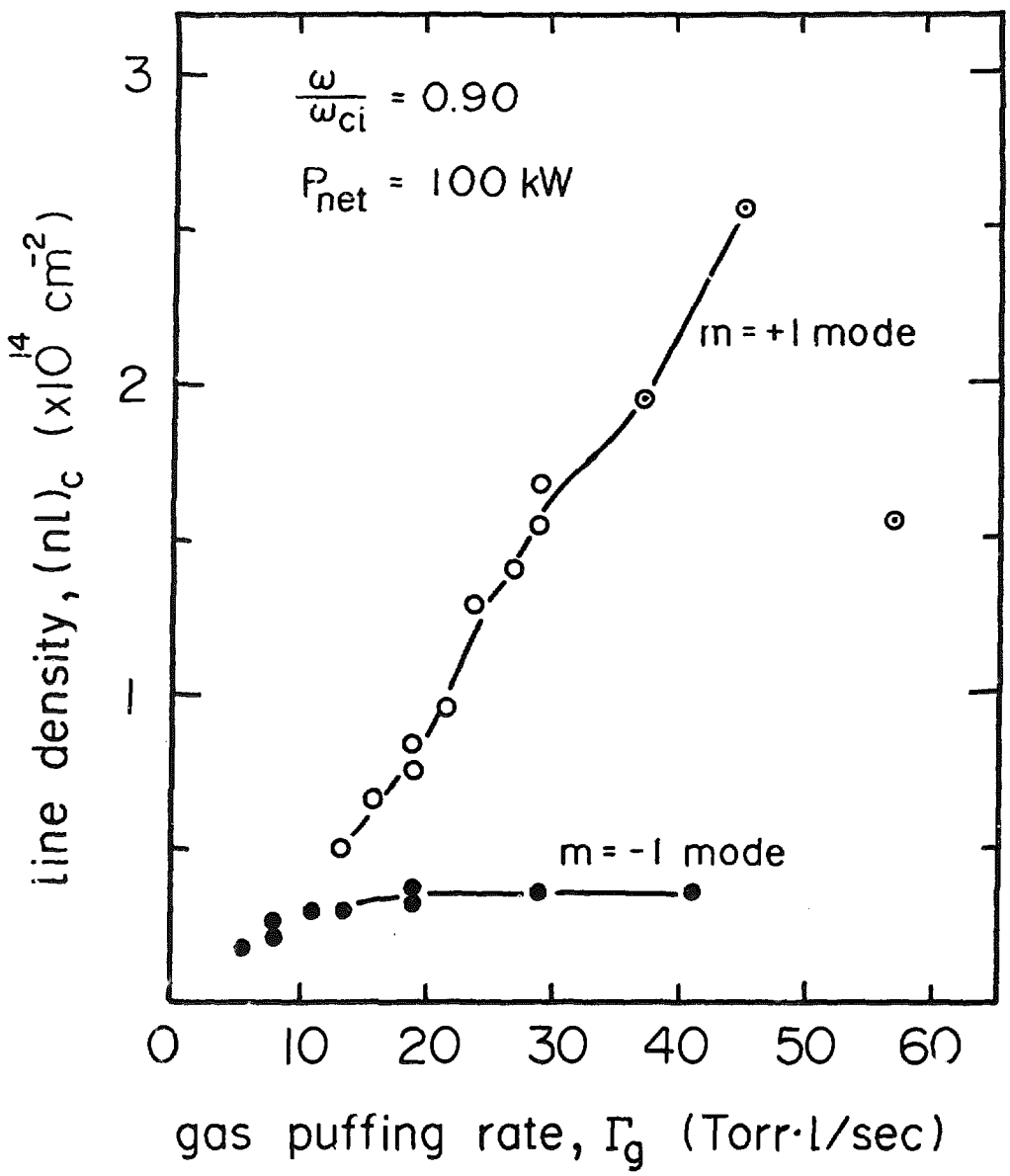

Fig.5 Line density versus the gas puffing rate for the m = +1 and the m = -1 modes. The net rf power, P_{net} is approximately 100 kW.

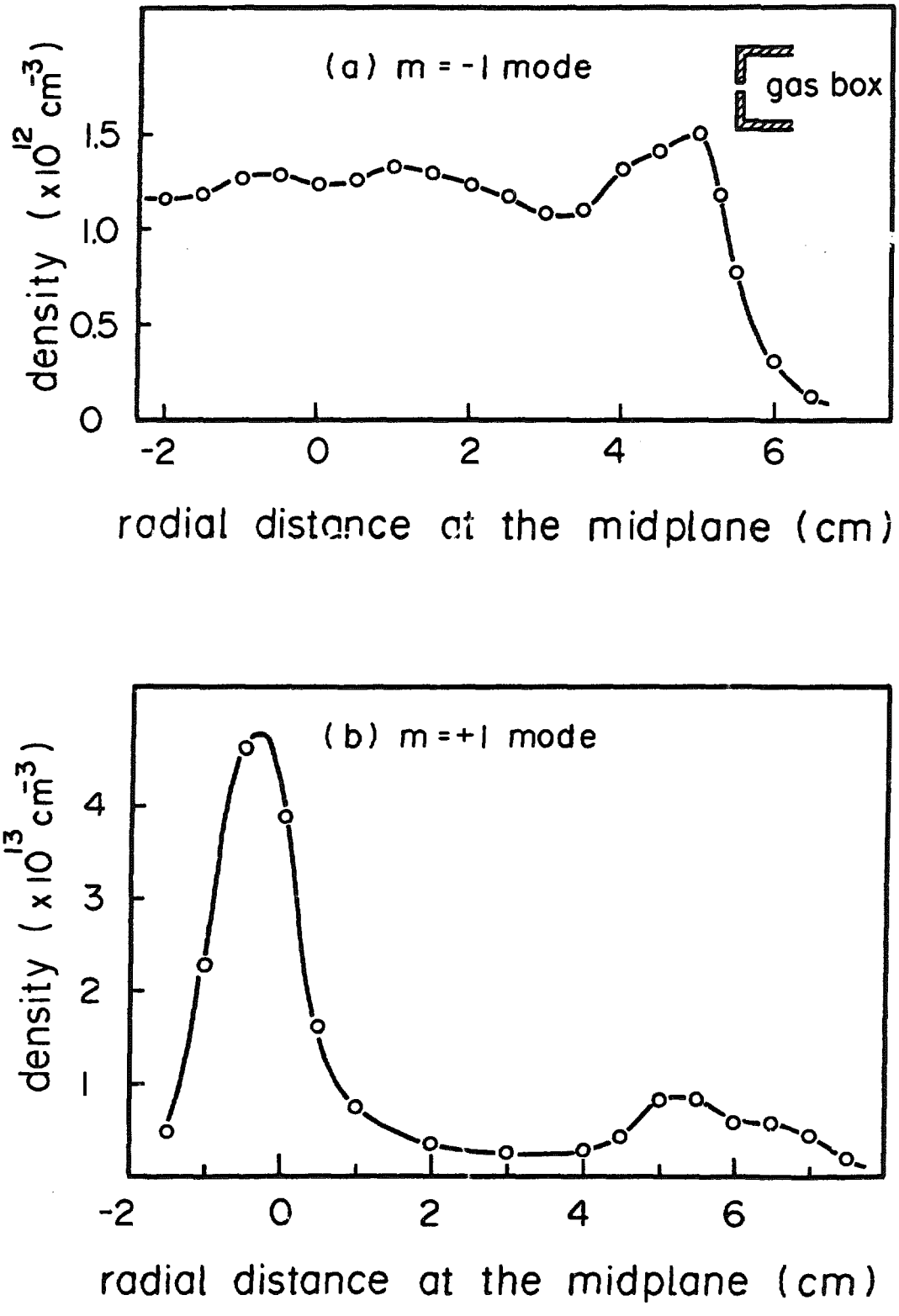

Fig.6 Radial density profiles measured in the central section for the m = -1 mode (a) and the m = +1 mode (b).

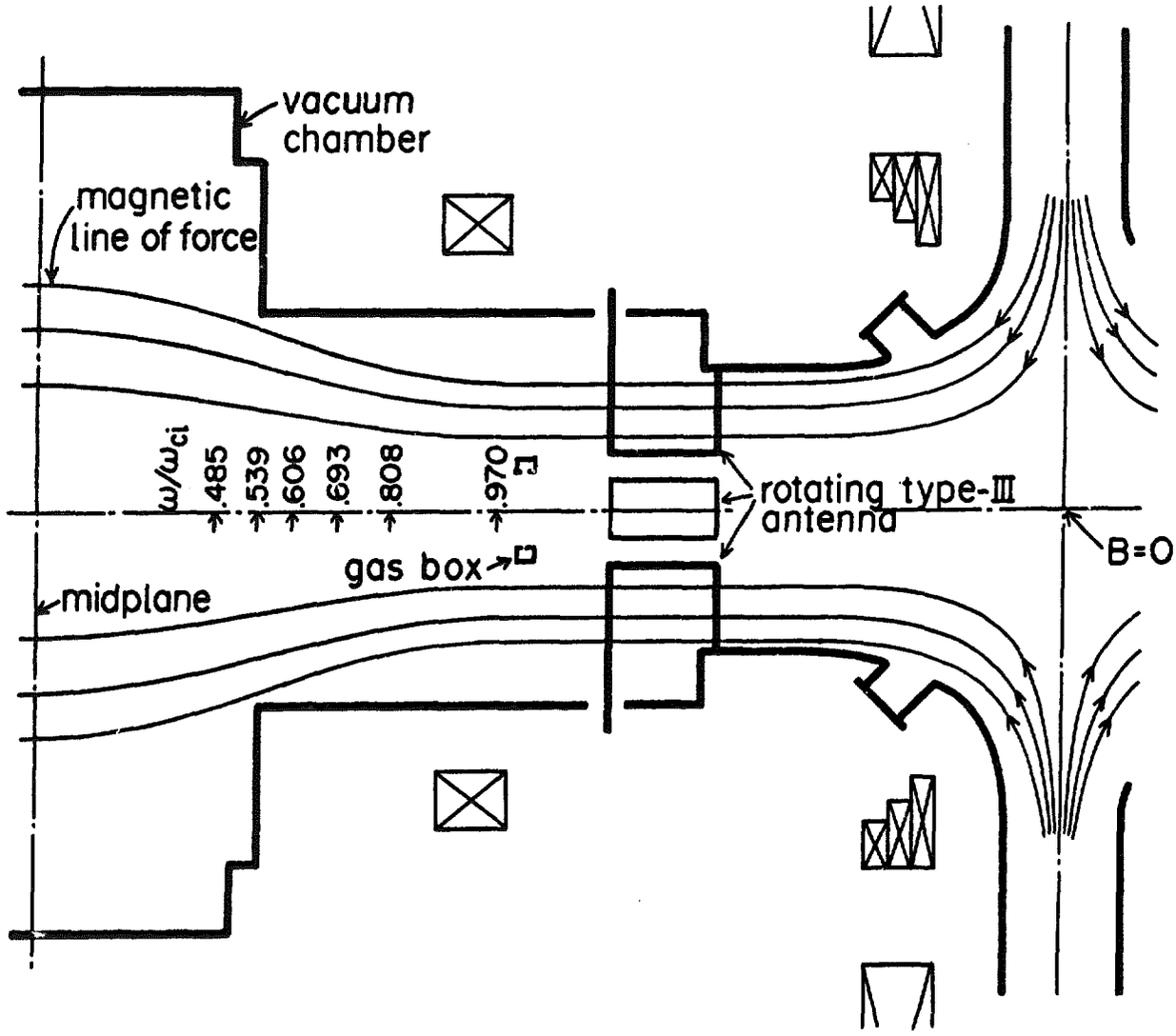

Fig.7 Schematic of the central section of RFC-XX-M.

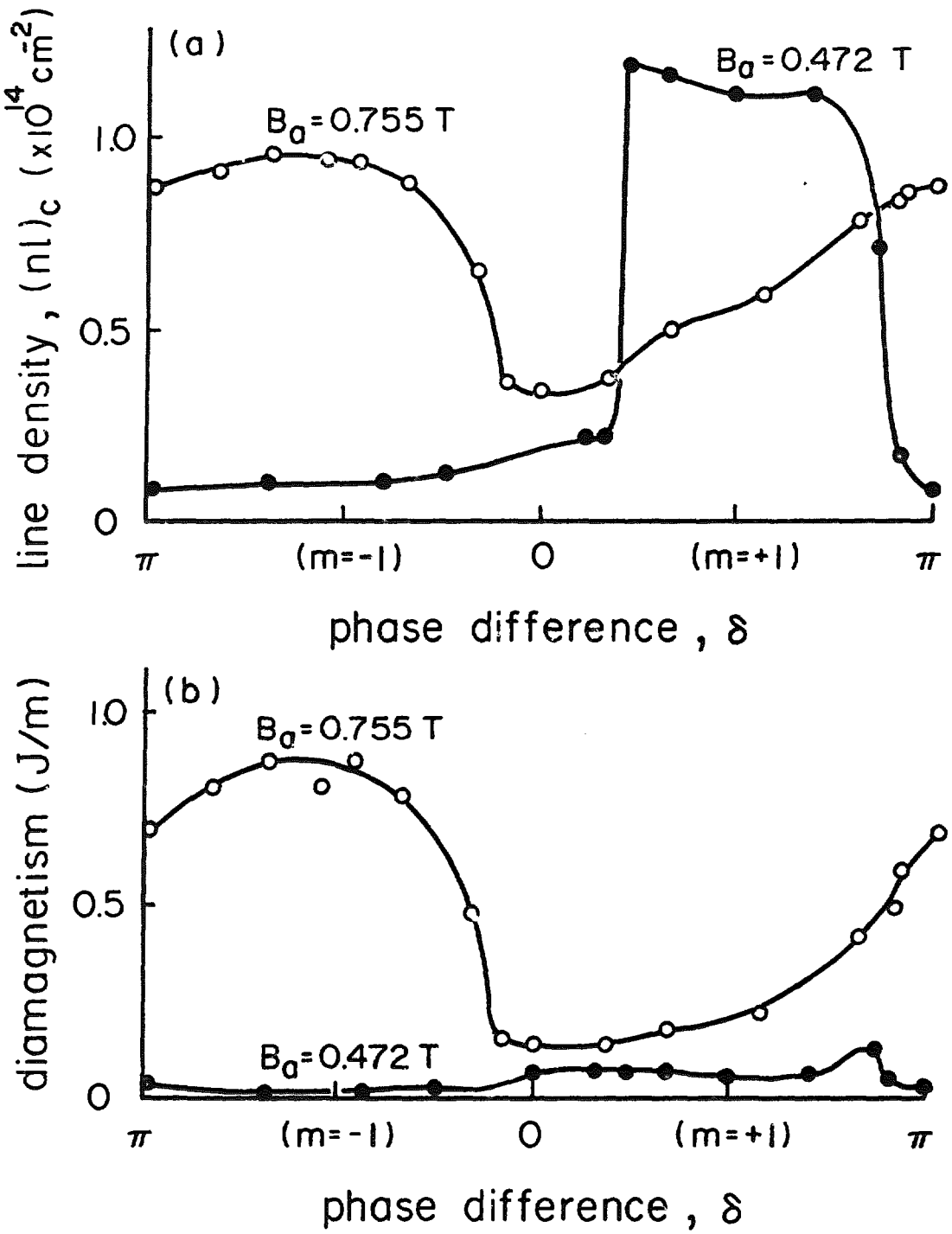

Fig.8 Line density(a) and diamagnetism(b) measured at the midplane versus the phase difference, δ, for a parameter of B_a.

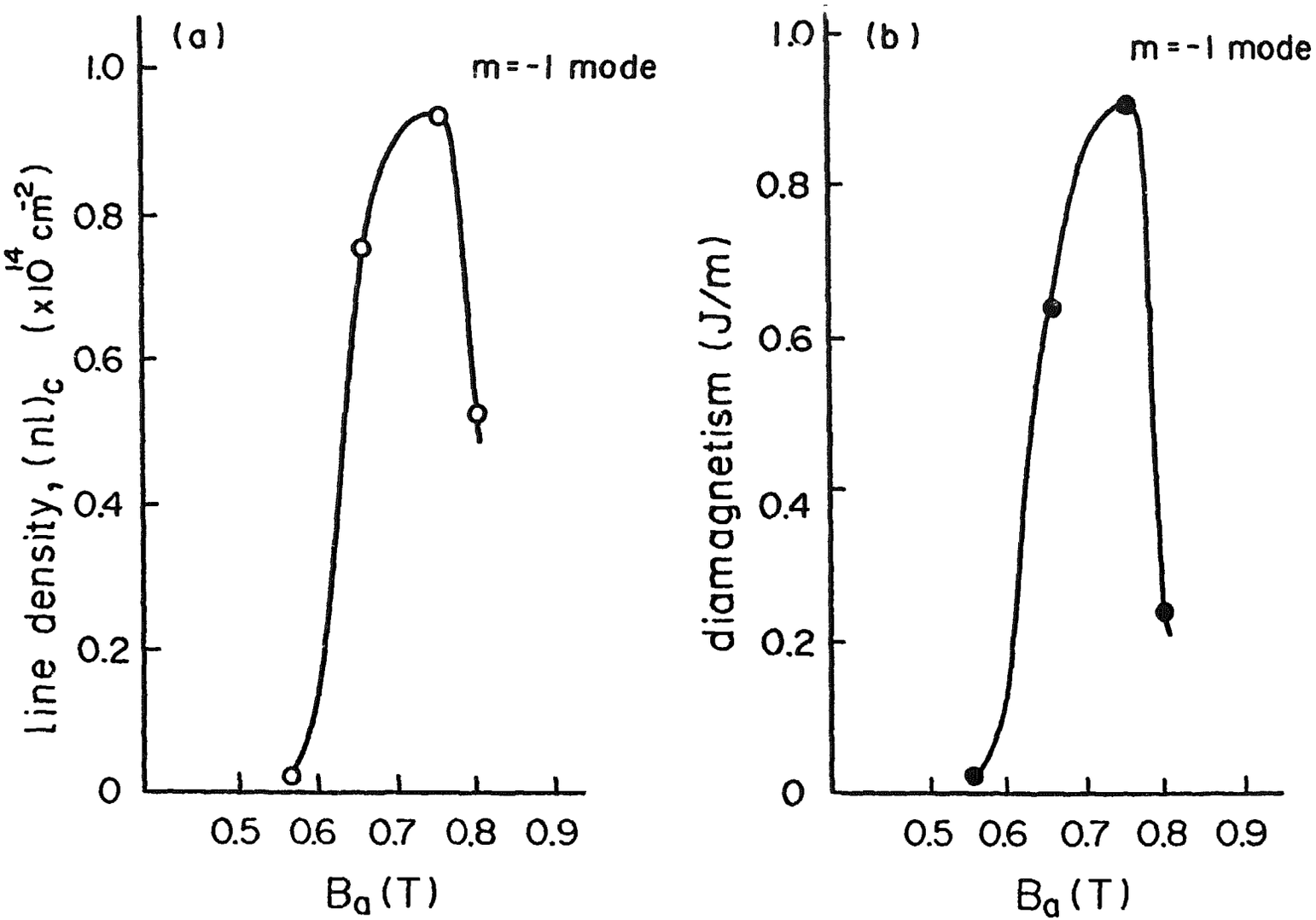

Fig.9 Line density(a) and diamagnetism(b) measured at the midplane versus B_a for the m = -1 mode. Gas puffing rate, Γ_g = 21 Torr·l/sec. Anode voltage of the power amplifier triode V_p = 18.5 kV.

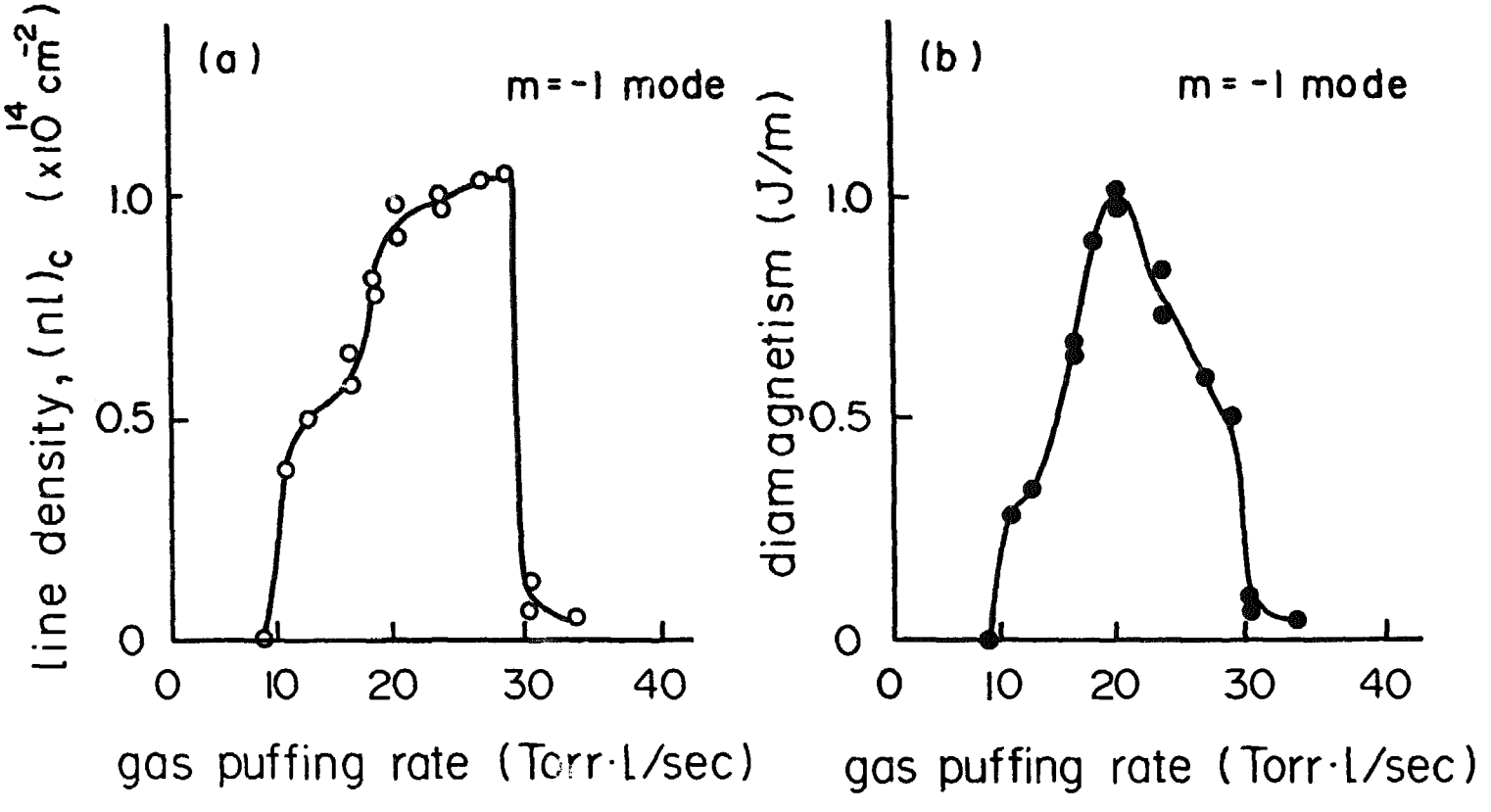

Fig.10 Line density(a) and diamagnetism(b) measured at the midplane versus gas puffing rate, Γ_g, for the m = -1 mode. $B_a = 0.755$ T. $V_p = 16$ kV.

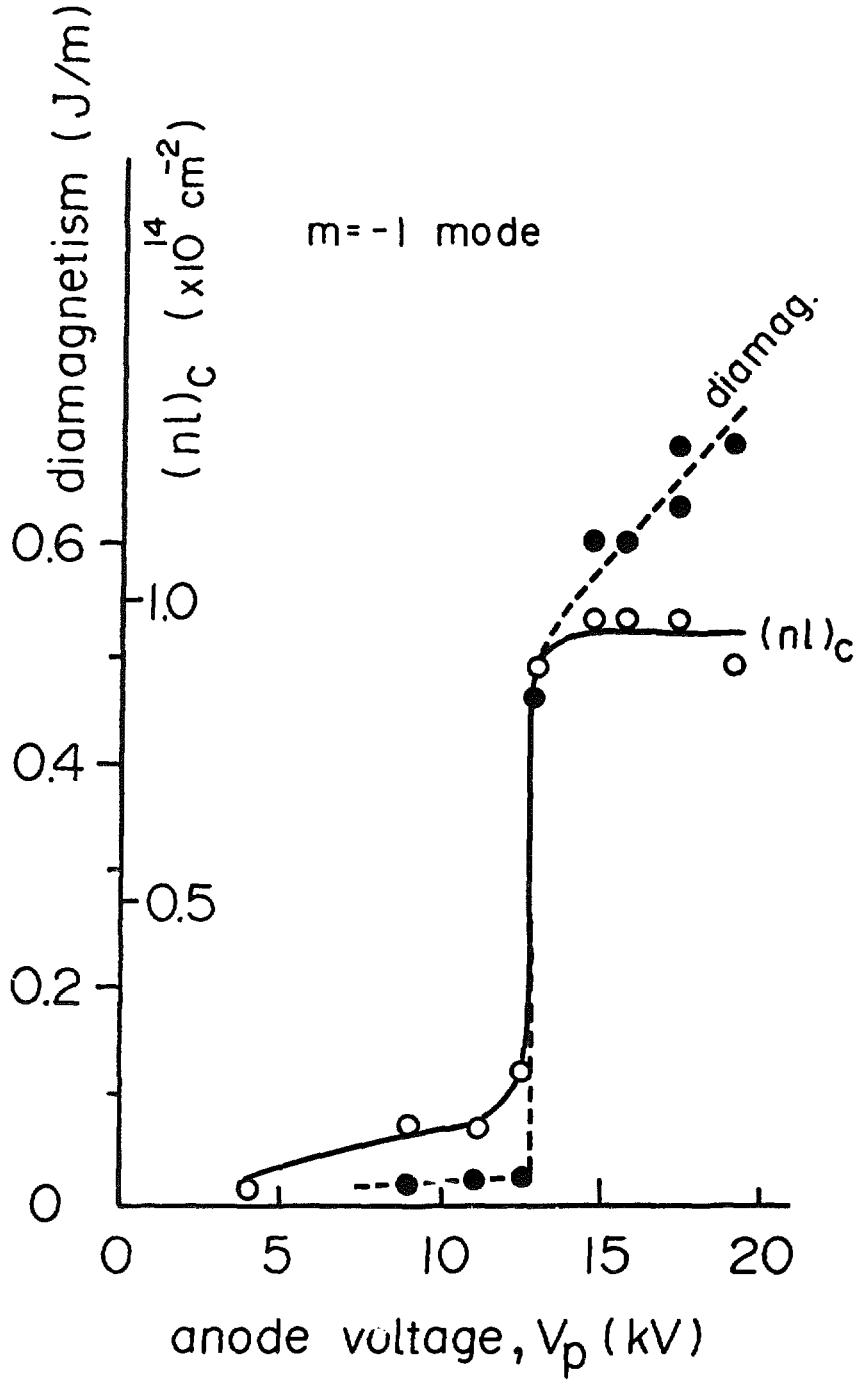

Fig.11 Line density and diamagnetism measured at the midplane versus anode voltage of the power amplifier triode, V_p, for the m = -1 mode. Γ_g = 21 Torr·l/sec. B_a = 0.755 T.

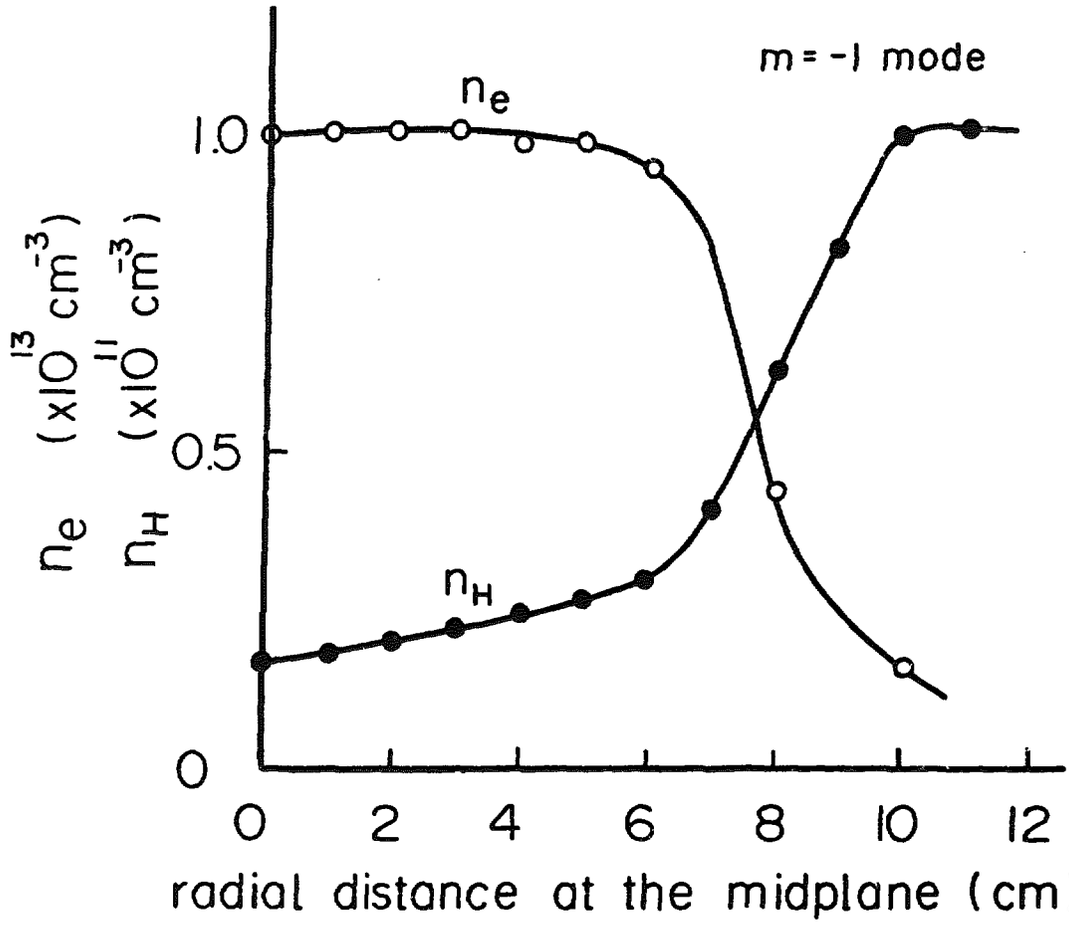

Fig.12 Radial distribution of hydrogen atom density, n_H, and electron density, n_e.

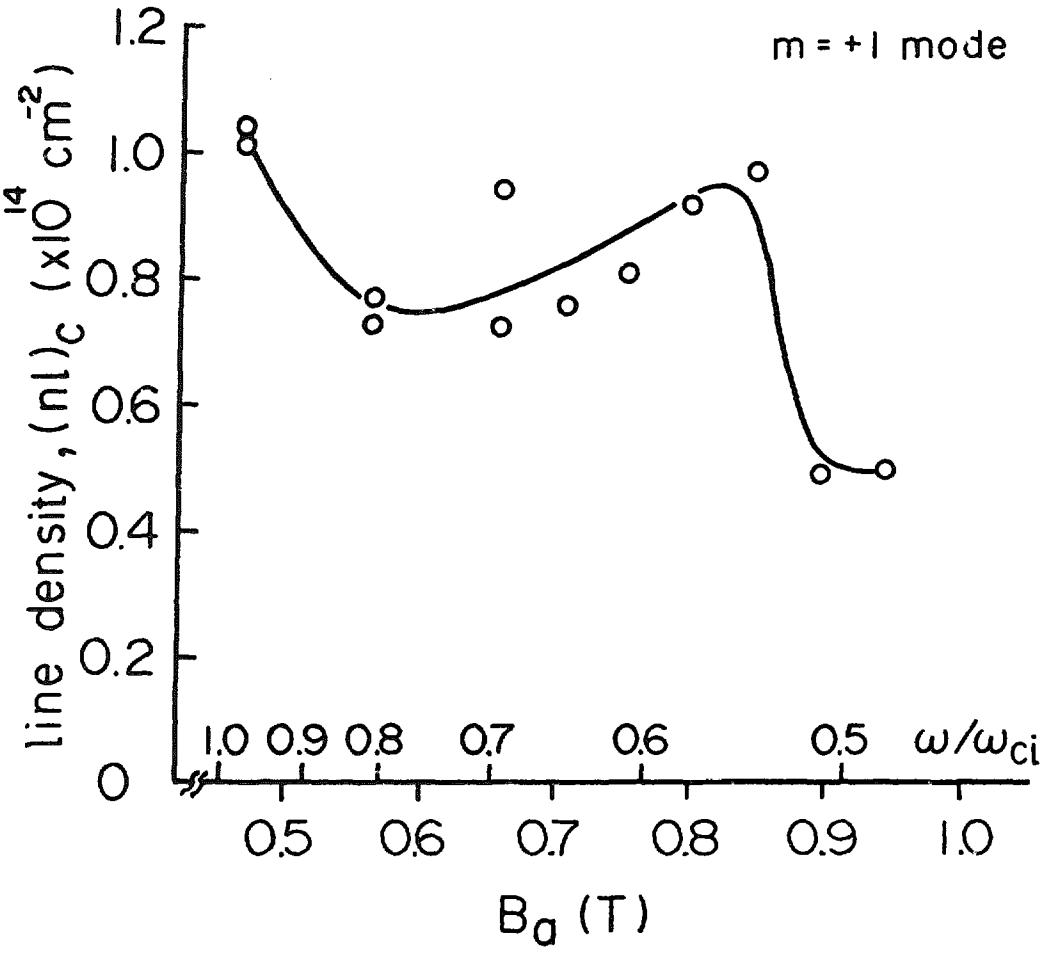

Fig.13 Line density measured at the midplane versus B_a for the m = +1 mode. Γ_g = 21 Torr·l/sec. V_p = 15 - 16 kV.

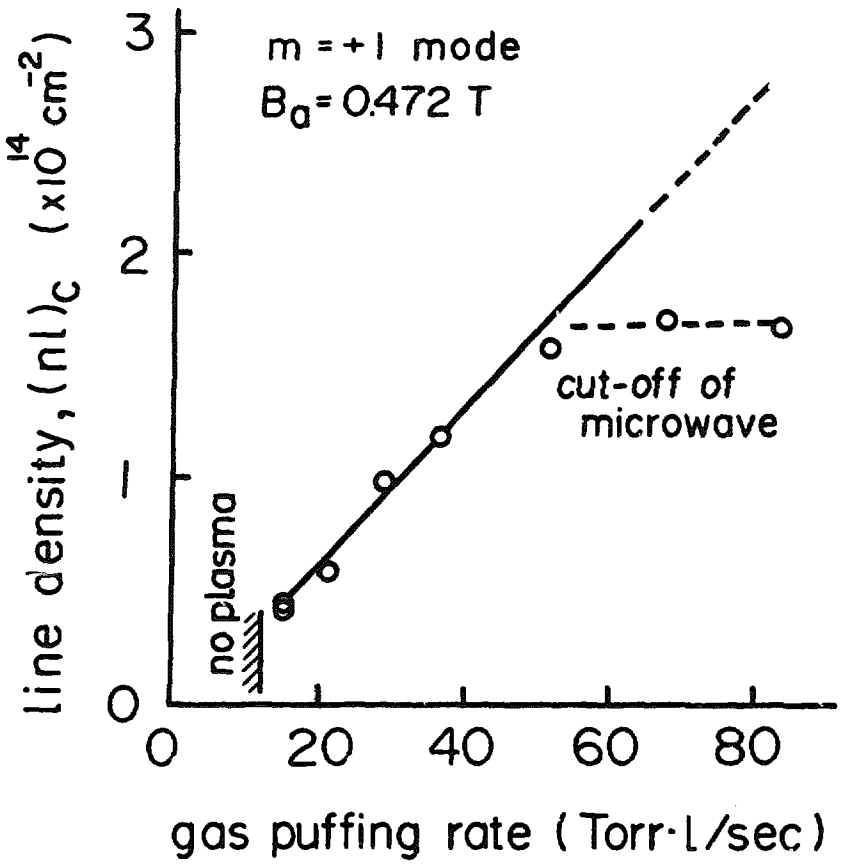

Fig.14 Line density measured at the midplane versus gas puffing rate for the m = +1 mode. B_a = 0.472 T. V_p = 16 kV.

EBT MICROWAVE DEPOSITION MODELING

S. Tamor
Science Applications, Inc.
La Jolla, California 92038

ABSTRACT

In view of the great importance of energy deposition calculations in evaluation of EBT performance, an investigation of such models is underway to determine the sensitivity of their predictions to details of the model and to plasma parameters. A multi region model has been formulated which is similar to, but not identical with, that proposed by Batchelor. The model can be used to simulate both start-up and steady state conditions. The most interesting result thus far obtained is the great sensitivity of the energy coupled to the plasma to assumed wall reflection conditions. The model is presented in some detail, and numerical results are discussed.

1. INTRODUCTION

Propagation and absorption of RF injected into the EBT cavity are so complex that exact calculation of the energy absorbed by the several plasma components is extraordinarily difficult. This difficulty is aggravated by the fact that the main core heating mechanism is by X-mode arriving at the fundamental resonance from the throat region, while in the typical configuration the throat is isolated from the RF source by the right-hand cutoff. There appear to be two mechanisms by which this effect can be circumvented. One is the tunneling of X-mode through the evanescent layer in the relatively low density surface plasma. The second mechanism relies upon mode mixing upon reflection whereby the O-mode, which can propagate freely into the throat region partially converts to X-mode on bouncing off the wall which is then strongly absorbed.

Batchelor[1] has suggested a method of modeling these processes which reduces calculation of energy absorption to a tractable problem. The

underlying idea is that the numerous wall reflections in the complex geometry cause the RF intensity to be nearly isotropic and slowly varying in space, except possibly near cutoffs and resonances. One can then break up the cavity into a finite number of regions in each of which the intensity is uniform and isotropic. Knowing the sources and sinks in each region, and the transmission, reflection , and absorption at each interface one can easily write down an energy balance equation for each region, leading to a finite set of algebraic equations for the intensities. This model has been applied to calculations of energy deposition into EBT-I and EBT-S.

Since results of these calculations are of considerable importance in evaluation of EBT energy confinement, it appears appropriate to make an independent evaluation of this model. Ideally, one would like to compare model predictions with an "exact" or at least presumably better calculation. Since the capability for such a calculation does not exist and would require serious effort to develop, one has to resort to the less rigorous method of formulating alternate models which appear properly to reflect the physics and to examine the sensitivity of the results to choice of the model as well as to the assumed parameters.

It must be stated at the outset that, in spite of strenuous efforts to avoid it, the model finally formulated is similar to Batchelor's in most major features. One reason for this is that it is very difficult to do any better. A second, and more positive, reason is that experience in calculation of transport of cyclotron radiation, for which detailed transport code is available, has shown that similar models do a quite creditable job in predicting energy flow in the plasma[2].

2. THE MODEL

Figure 1 is a schematic view of the EBT cavity showing the location of the resonant and right-hand cutoff surfaces. These surfaces are used to define the boundaries of three regions. Region I is that on the low field

side of the right-hand cutoff. Region II lies between the two surfaces, while Region III is the throat volume behind the fundamental resonance. In the low density surface plasma the two surfaces are very close together and the model assumes them to coincide. Figure 2 shows the locations of the plasma relative to these regions. The portion of the cutoff layer within the core plasma is assumed to be a perfect reflector for X-mode, while the resonant surface is assumed to totally absorb all X-mode incident from the high field side. With these assumptions, Region II is totally inaccessible to X-mode radiation. At the resonance-cutoff layer in the surface plasma the X-mode is assumed to be transmitted, reflected, or absorbed according to the theory of Budden tunneling for parallel stratification[1]. Also indicated is the locus of the second harmonic resonance in the core and surface plasmas.

The portions of the chamber walls bordering on regions I and III are labeled AI and AIII, respectively. Each of these can be assigned a reflection coefficient R_I and R_{III}. An isotropic power source of pure X- or pure O-mode can be located in Region I or Region III. Energy balance leads to a system of 5 simultaneous equations for the O-mode intensities in the three regions and the X-mode intensities in I and III. The included energy deposition mechanisms are:

1. Second harmonic X-mode absorption in the ring.

2. Total X-mode absorption at the fundamental resonance in the core.

3. Partial fundamental X-mode absorption in the surface plasma.

4. Second harmonic O-mode absorption in the ring.

5. Fundamental O-mode absorption in the core and surface plasmas.

6. Second harmonic X-mode absorption in the core and surface plasmas.

Items 4, 5, and 6 are not significant in modeling of present experimental machines but will not be negligible for reactor grade plasmas. The code produces results including all processes as well as the result of neglecting 4-6.

Parameters required for complete specification of the problem are:

Wall surface areas AI and AII.
Areas of the surfaces S_1, S_2, and S_3.
Ring surface area and thickness.
Areas of the second harmonic surface in the core and surface plasmas.
Temperatures and densities of the three plasma components.
A mode mixing coefficient for wall reflection.
Reflectivities of AI and AIII.
A characteristic scale length for gradients of B.

Fundamental O-mode and second harmonic X-mode absorption in the core and surface plasmas are calculated from the formulas of Engelmann and Curatolo[3] for pure inhomogeneity broadening averaged over angle. Ring absorption is calculated via an analytic fit to angle averaged absorption coefficients generated by a relativistic opacity code. Ring absorption can be calculated assuming an isotropic distribution or a bi-Maxwellian assuming $P_\perp/P_\parallel = 5$. Also the value of k_{real} entering into the absorption can be chosen to be appropriate to zero core plasma background or a background density of 10^{12} cm^{-3}.

Apart from the inclusion of a few additional knobs the model differs from Batchelor's in three respects:

(a) the precise definition of the three regions.

(b) allowing a separate O-mode intensity in each region.

(c) imperfect wall reflectivity.

The existing code cannot calculate the first pass ring absorption. If this is known or assumed it is easily incorporated as a small correction factor.

3. RESULTS

Runs were made for EBT-S parameters chosen to agree as closely as possible with those in Batchelor's paper[4]. The ring thickness was chosen to be 1.5 cm with a density of $3x10^{11}$. This choice leads to a $W_\perp$ in agreement with experiment. Since the ring is optically thin one can, except for a finite β correction, trade off ring density against volume with no effect on the final results. The surface plasma temperature is chosen to be 100 eV, and for most runs the mode mixing coefficient is set equal to 0.5.

Figure 3 displays the computed energy partition as a function of surface plasma density for pure X-mode injection. Due to strong mode mixing results for an O-mode source are essentially identical. Wall reflectivities were $R_{III} = 1.0$ and $R_I = 0.99990$. Since the results are sensitive to choices of S_1 and S_2 we cannot be certain that this is directly comparable to Batchelor's curve. On the other hand, exploration of a range of these parameters seems to indicate a definite tendency for the core heating to slightly exceed and the ring heating to be slightly less than Batchelor's. The discrepancy is too large to be accounted for by the first pass correction and, while parameters can be chosen to increase the ring absorption by ~ 50% this causes the core absorption to exceed the surface absorption for all values of surface plasma density. For the case shown the ring heating was calculated assuming zero cool background. A finite plasma density further decreases the ring absorption, while a bi-Maxwellian increases the absorption by a factor ~ 1.3. In all cases tinkering with the ring properties seems to move energy between the ring and surface plasmas with little effect upon the core heating.

The result of varying R_I with constant assumed plasma properties is shown in Figure 4. These results simulate the effect of degradation of

reflectivity due to wall penetrations and erosion. Because the radiation undergoes on the average many wall reflection before being absorbed in the plasma the reflectivity corrections are quite large. A wall loss of only a few percent per reflection can take up as much as 30% of the total RF input and could be an important effect in determination of plasma heating.

4. SUMMARY

An alternate multi-region RF energy deposition model similar, but not identical, to Batchelor's has been formulated. For high wall reflectivity the overall results are in general agreement with Batchelor's but with a tendency to predict slightly more core and less ring heating. This result is somewhat surprising since the present treatment of the O-mode would be expected to decrease the core heating. This discrepancy is not at present understood and may be due either to details of the model or simply to differing choice of parameters. A much more significant effect is that of imperfect wall reflectivity. Inclusion of wall losses dramatically decreases the energy available for plasma heating and may be a non-negligible contribution to the overall power balance.

ACKNOWLEDGMENT

This work was supported by the U.S. Department of Energy under contract DE-AC01-82-ER53126.

REFERENCES

1. D. B. Batchelor, Nucl. Fusion 21, 1615 (1981).

2. S. Tamor, "A Simple Fast Routine for Computation of Energy Transport by Synchrotron Radiation in Tokamaks and Similar Geometries," Science Application, Inc. Report SAI02381-189LJ (May 1981).

3. F. Engelmann and M. Curatolo, Nucl. Fusion 13, 497 (1973).

4. EBT-S Data Review, February 14-17, 1983. Paper #11.

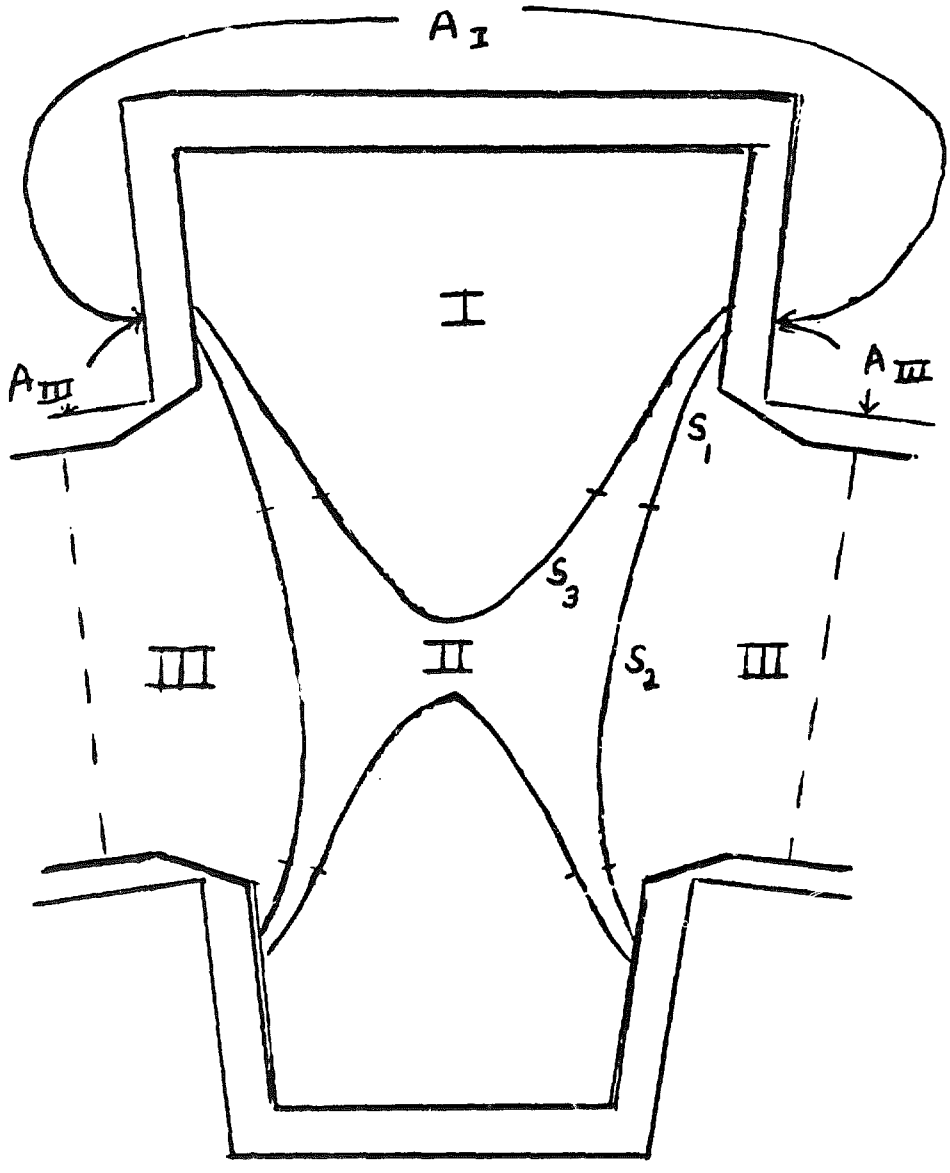

Figure 1. Schematic of EBT cavity showing the location of the fundamental resonance and right-hand cutoff. The three regions are shown, as well as, the wall areas A_I and A_{III} associated with each region.

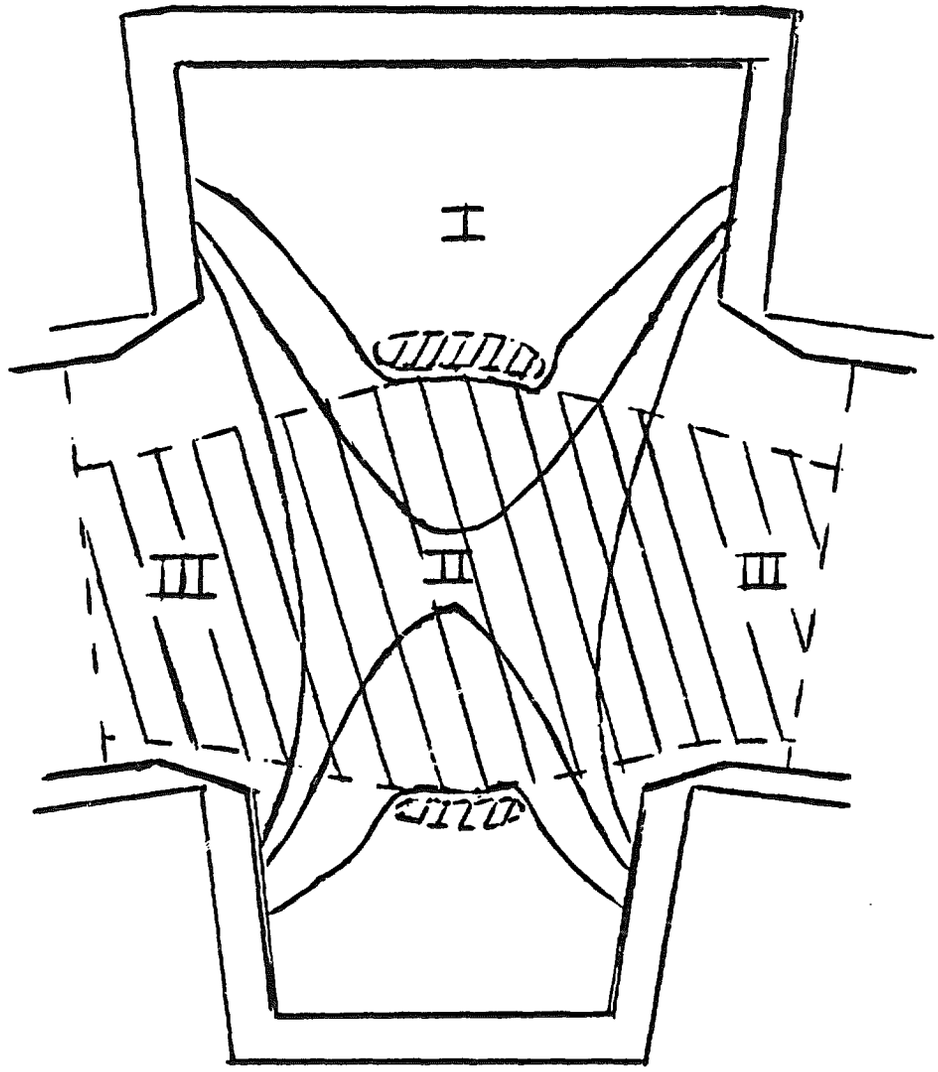

Figure 2. Schematic of an EBT cavity including location of core plasma, ring plasma and second harmonic resonant surface.

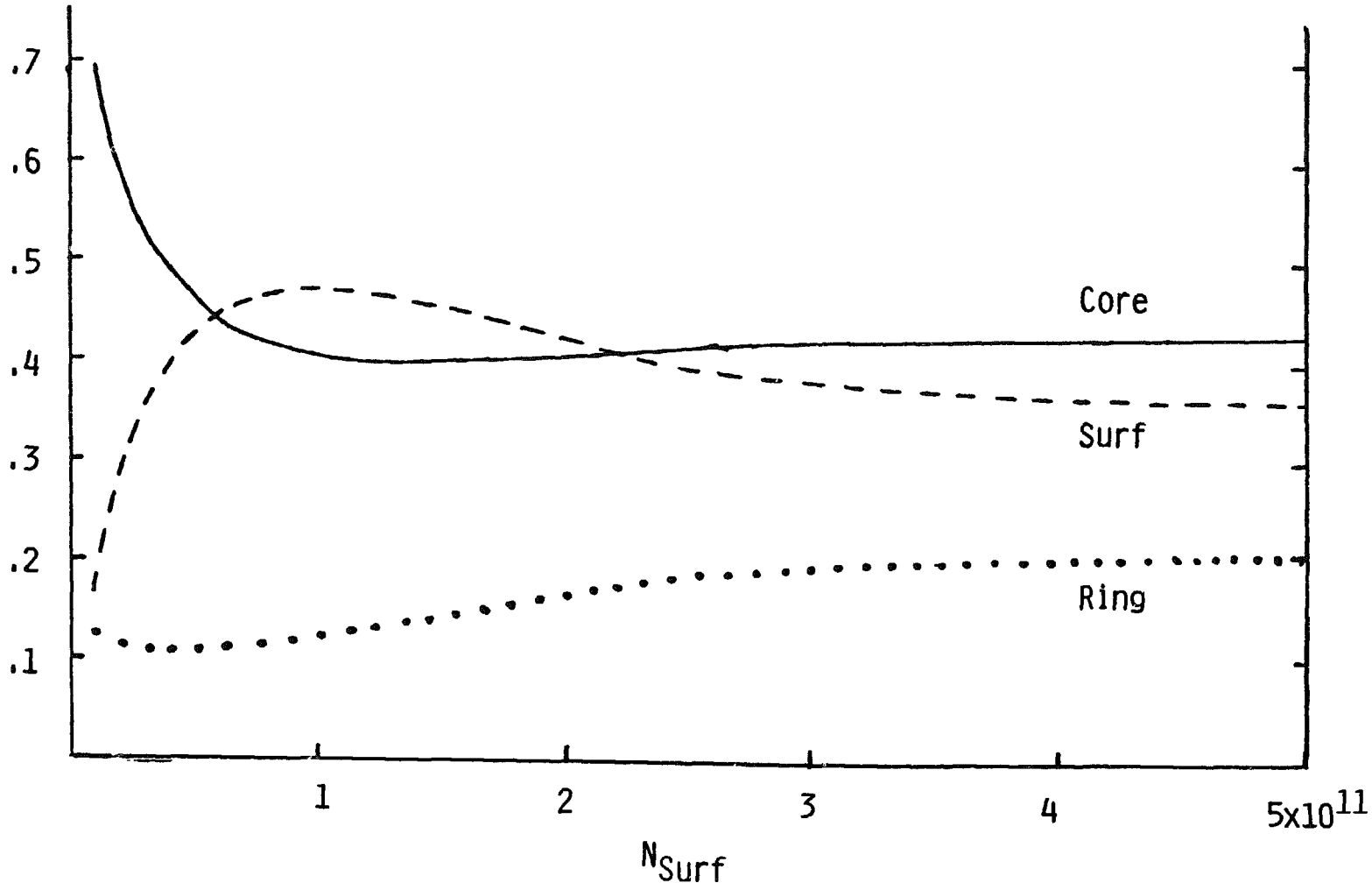

Figure 3. Energy partition among core, surface, and ring plasmas vs. surface plasma density for an X-mode source in Region I.

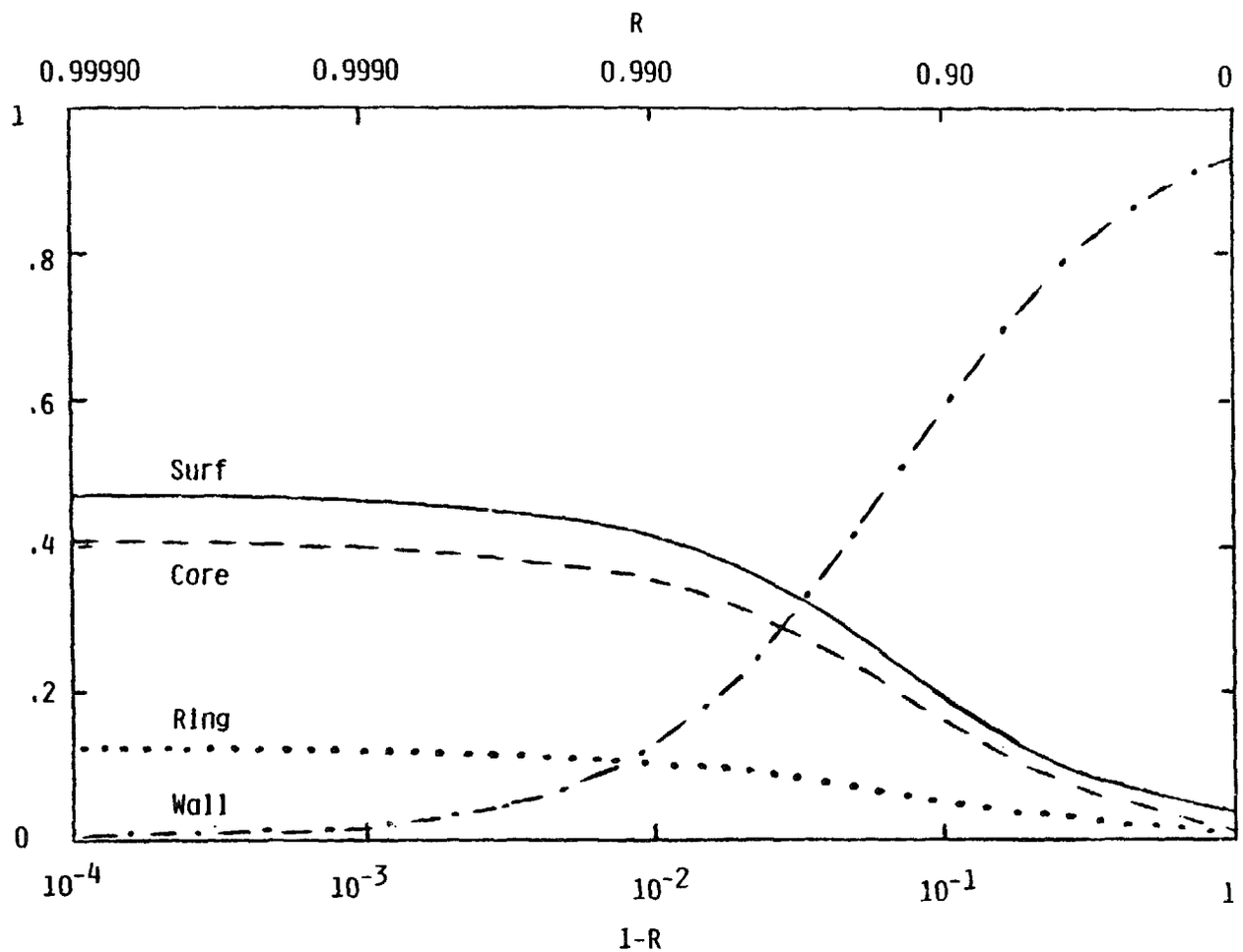

Figure 4. Energy absorbed in each plasma component and in wall as function of R_I. Surface density = 10^{11} cm^{-3}.

THEORETICAL ASPECTS OF THROAT LAUNCH MICROWAVE HEATING IN EBT-S

D. B. Batchelor, R. C. Goldfinger, D. A. Rasmussen,
and D. W. Swain
Oak Ridge National Laboratory
Oak Ridge, Tennessee 37830

Abstract

A simple radiation power balance model is used to gain insight into the role of antenna directivity and polarization control when throat launch is used to improve core heating efficiency and to separate ring heating from core heating. Ray tracing calculations are used to illustrate energy flow and absorption behavior for various throat launch positions and angles.

*Research sponsored by the Office of Fusion Energy, U. S. Department of Energy, under contract W-7405-eng-26 with the Union Carbide Corporation.

1. INTRODUCTION

To the extent that the core electron confinement in EBT is dominated by neoclassical transport processes, the core density and temperature are microwave power limited. Indeed, the neoclassical scaling $P_\mu \propto n^2 T^{-1/2}$ has been verified experimentally in EBT-S up to the maximum available power (200 kW at 28 GHz) provided the core plasma profiles are maintained constant through manipulation of the gas feed.[1] As discussed previously[2,8] and reiterated below, the present method of core heating in EBT-I and EBT-S is an indirect and very inefficient process. Therefore, it is anticipated that any method of core heating which substantially increases the function of available power deposited in the core plasma will result in improved plasma parameters.

A complicating factor is that high power tends to push EBT plasma into the unstable m-mode at low collisionalities. For example, at fixed microwave power, reducing neutral density in the collisionless regime is not observed to dramatically increase the plasma density as is expected on the basis of purely neoclassical theory.[3] Rather the density is found to decrease down to the T-M mode transition. This is currently intepreted as a result of ring density increasing with decreasing P_o to the point that core plasma density can no longer stabilize hot electron interchange modes. The unstable fluctuations in turn produce additional particle losses. With the present midplane microwave launch it is not possible to increase the power to the core without simultaneously heating the ring. If the heating of the rings and core could be separately controlled it might be possible to adjust the ring β to give optimum core confinement and thereby increase core pressure obtainable per watt of core heating.

Launching some of the microwave power in the high field (mirror throat) region offers the potential for achieving both of the above goals. By beaming the power to intersect the fundamental resonance at the center of the core plasma from the high field side, the fraction of power absorbed by the core can be increased about a factor of two, while the power absobed by the rings is decreased a factor of two

relative to midplane launching. If the power can be excited purely in the extraordinary mode and directed to the fundamental resonance at the core plasma, virtually all of the wave energy can be put into the core component with none going to the rings or surface plasma.

In Section 2 of this report, we review the current understanding of midplane launch microwave heating in EBT and use a radiation power balance model to estimate the fraction of power going to ring, core and surface plasma components. In Section 3, we use the power balance model to consider the effect on partitioning of wave power aassuming various degrees of polarization control and antenna directivity for throat launched microwaves. In Section 4, we examine three approaches to throat launch: (1) "snaking" the waveguide through the fundamental resonance and shooting to the opposite resonance [Fig. 1], (2) "snaking" the waveguide through the fundamental and shooting back to the same resonance [Fig. 2], and (3) launch from split coil [Fig. 3]. Ray tracing is used to give an indication of the power flow and absorption from the various assumed launch points.

2. ECH OF EBT DEVICES FROM THE MIDPLANE

The dominant feature of ECH wave propagation in EBT devices is the presence of the right hand cutoff for the extraordinary mode on the low magnetic field side of the fundamental resonance. The fundamental resonance, which strongly absorbs the extraordinary mode, is not accessible from the midplane. The ordinary mode, which propagates freely throughout the plasma, is only weakly absorbed at the densities and temperatures of EBT-I and EBT-S. On the other hand, because of strong gradients in $|\underline{B}|$ along field lines (i.e., magnetic beach) any extraordinary mode energy propagating from the high field side (mirror throat region) is totally absorbed at the fundamental resonance. Hence, the only significant core heating mechanism in EBT-I/S is extraordinary mode power propagating from the high field side. Because of the cutoff, this extraordinary mode power can only reach the high field region by indirect means such as conversion of ordinary mode to extraordinary mode at cavity walls in the high field

region or by Budden tunnelling. Strong absorption of the extraordinary mode at the fundamental resonance holds even for the low density surface plasma. The relevant parameter here is $\omega_{pe}^2/\Omega_e^2 > v_e/c$ where ω_{pe} = plasma frequency, Ω_e = electron cyclotron frequency and $v_e = (2T_e/m_e)^{1/2}$ = electron thermal speed. When this inequality is satisfied in a parallel stratified plasma, the absorption of the extrordinary mode is virtually complete from the high field side. Since $\omega_{pe}^2/\Omega_e^2 > V_e/c$ is well satisfied even in the surface plasma region, the ratio of power deposition $P_{core}/P_{surface}$ tends to follow the ratio of surface area of the fundamental resonance zone lying in the respective plasma component $S_{core}/S_{surface}$, assuming uniform power flux incident on the resonance layer. The core heating tends to be very inefficient because $S_{surface} > S_{core}$. Details of the various processes involved have been discussed elsewhere.[2,4,8]

Estimates of the power deposited in each of the three important plasma components (core, surface, annulus) can be obtained from a simple zero-dimensional radiation power balance model.[4,8] This model includes: ordinary and extraordinary mode absorption by the ring, core, and surface components; wall reflection and depolarization; and Budden tunnelling in a globally averaged way. Application of the model to midplane launch in EBT-I and EBT-S is described in the references above. Because the standard operating current of 7250A for the toroidal field coils in EBT-S compared to 5000A in EBT-I is somewhat less than the ratio of microwave frequencies (28 GHz/18 GHz) the fundamental and 2nd harmonic resonances are spatially displaced toward high field compared to EBT-I. The effect of the displacement is to reduce the areas of the resonant surfaces and to increase $S_{surface}/S_{core}$ (see Table 1 for numerical values).

Other parameters required for the model are the averages over incidence angle of the fraction of power absorbed from a ray in passing through one of the resonant surfaces, for each polarization. In the previous studies of EBT-I and EBT-S, these were obtained from extensive ray tracing calculations using a relativistic absorption model. We have assumed peak core density $n_e = 1 \times 10^{12}/cm^3$, peak core temperature T_e = 1 keV, peak annulus density $n_A = 5.0 \times 10^{11}/cm^3$ and

ring temperature T_A = 390 keV. These values are consistent with measured EBT-S parameters at 175 kW power level near the lower end of the T-mode, $P_o \sim 8 \times 10^{-6}$ Torr.[6,7]

Using these values in the power balance model, we find that the power launched from the midplane of EBT-S should be deposited in the various plasma components as follows:

$$P_{core} = 0.33\ P_{inj}^{mid} \qquad P_{surface} = 0.39\ P_{inj}^{mid} \qquad P_{Annulus} = 0.28\ P_{inj}^{mid}.$$

A few comments are in order concerning these results. One important untested assumption of the model is that the wave power flux in each mode is uniform throughout each region. In particular, the fundamental resonance zone is assumed to be uniformly illuminated by the extraordinary mode. Now the extraordinary mode in the high field region is presumably produced at the cavity walls by conversion of the ordinary mode upon reflection. Therefore, it is conceivable that the extraordinary mode power flux is greater on the outer portion of the resonance zone intercepted by the surface plasma than at the center The effect of this would be to increase $P_{surface}$ relative to P_{core} without affecting $P_{Annulus}$. The numbers quoted above should therefore be considered an upper bound on the fraction deposited in the core. Using the power balance model, it is possible to calculate the power flux on the cavity wall. This is a measure of the stored RF energy or equivalently, the cavity Q. We have calculated the power which should be coupled into a microwave calorimeter and have found good agreement with experiments. This indicates that the total rate of power dissipation predicted by the model is approximately correct, but it does not verify the correctness of the partitioning between the various plasma components.

3. POWER DEPOSITION OF THROAT LAUNCHED MICROWAVES

In order to maximize the power coupled to the core plasma and simultaneously minimize ring heating one should direct a narrow beam of radiation to the center of the plasma and polarize the radiation so as to excite only extraordinary mode waves. This would result in 100% of the power being deposited in the core with virtually none of it going to the surface or rings. Ordinary mode energy excited will be only weakly absorbed at the fundamental resonance. The remainder passes to the low field side and is deposited according to the ratios in Section 2 essentially as if it were launched from the midplane. Antenna directivity is very important because any extraordinary mode power beamed to the surface plasma is absorbed there.

We have used the power balance model to investigate the effect of polarization control and directivity on throat launched microwaves. For these calculations, the same surface areas and absorption parameters were used as for the midplane calculations of the previous section. That is, no attempt was made to account for improved plasma parameters due to the throat launched microwaves. Three cases were considered:

<u>CASE 1: No Directivity or Polarization Control</u>. It is assumed that 50% ordinary mode and 50% extraordinary mode is excited and that this power is randomized with respect to direction of propagation before being absorbed (i.e., the power is absorbed entirely according to the rules of the power balance model). We find

$$P_{core} = 0.38\ P_{inj}^{throat} \qquad P_{surface} = 0.47\ P_{inj}^{throat} \qquad P_{Annulus} = 0.15\ P_{inj}^{throat}$$

The fraction going to the core is increased slightly relative to midplane launch. The only significant difference from midplane launch is that about half as much power goes to the rings.

CASE 2: 100% Extraordinary Mode Excitation, But No Directivity. This case is very similar to Case 1 except that waves must take at least one wall bounce before converting to ordinary mode. The extraordinary mode energy density in the high field region is increased and leakage to the low field with associated ring heating is reduced. We find

$$P_{core} = 0.40\ P_{inj}^{throat} \qquad P_{surface} = 0.54\ P_{inj}^{throat} \qquad P_{Annulus} = 0.06\ P_{inj}^{throat}$$

CASE 3: 100% Beamed to Core, No Polarization Control. The case which seems most likely to be realized in practive is that the throat launched power is directed to the central portion of the fundamental resonance but that 50% extraordinary and 50% ordinary mode is excited. The result would be that the 50% in the extraordinary mode is absorbed immediately in the core at fundamental while the 50% ordinary mode passes to the midplane and is absorbed according to the ratios in Section 2. The resulting deposition is

$$P_{core} = 0.68\ P_{inj}^{throat} \qquad P_{surface} = 0.20\ P_{inj}^{throat} \qquad P_{Annulus} = 0.12\ P_{inj}.$$

All of the results from the power balance model are summarized in Table 2.

4. RAY TRACING CALCULATIONS

Although direct calculation of the radiation patterns into different modes by a given antenna structure is a very difficult problem for such a complex geometry as EBT, some insight into the propagation and absorption properties can be obtained simply by ray tracing from an assumed launch point.[7]

For these calculations we have assumed a bumpy cylinder equilibrium having plasma parameters appropriate for high power EBT-S operation $n_{e,max} = 2 \times 10^{12}/cm^3$, $T_{e,max} = 1$ keV, $f_\mu = 28$ Ghz. Ring

parameters do not enter; therefore, for simplicity, we have used vacuum magnetic fields.

Figure 4 shows extraordinary mode rays propagating in the equatorial plane at varying angles (10° increments) with respect to the z-axis. Also shown are magnetic field lines, the fundamental cyclotron and 2nd harmonic resonant layers, and the right hand cutoff. The launch point is on the left side of the coil case. Rays 1 thru 7 represent the case shown in Fig. 1 of shooting to the opposite resonance while rays 8 thru 16 represent the case shown in Fig. 2 of shooting back to the same resonance. Wave absorption is determined by integrating k_i along the ray path where k_i is determined from a non-relativisic expansion of the warm plasma dispersion relation.[7] The rays are terminated when 99% of the energy in the ray is absorbed or when the ray leaves the plasma (rays 6,7,8). As previously mentioned, the energy is completely absorbed near the fundamental resonance even in the low density surface region. It can be seen that the effect of refraction is to bend the rays toward the center of the plasma.

Figure 5 shows ordinary mode rays propagating from the same location as in Fig. 4. There is virtually no refraction for this case. The numbers on each ray indicate the fraction of power absorbed as the ray passes through the fundamental resonance. It can be seen that rays passing through the opposite resonance zone (rays 1-6) are essentially undamped while those passing through the near resonance do have substantial damping. The reason for the large difference is that the damping rate, k_i, for the ordinary mode increases as the angle between k and B increases and because the rays on the left are more nearly tangent to the resonant surface giving a longer path length in the resonant zone.

Figure 6 shows extraordinary mode rays launched from the coil plane. Again, we see the focusing effect of refraction and the total wave absorption which is characteristic of parallel stratified plasma. Figure 7 shows ordinary mode rays launched from the coil plane with the associated values of fractional absorption. The maximum absorption is much smaller than that seen in Fig. 5.

We are now in position to compare the three launch geometries discussed in the introduction. Shooting across to the opposite resonance (Fig. 1) would require only moderate antenna directivity to concentrate the wave energy at the plasma center. All extraordinary mode power launched between about 5° and 35° with respect to the z axis is absorbed in the core. On the other hand, the ordinary mode at these angles is not absorbed. The disadvantage of this geometry is the difficulty of exciting pure extraordinary mode at parallel or oblique angles to the magnetic field. For example, ray 3 of Fig. 4 is absorbed essentailly at the plasma center. This ray is launched with $\theta = = 10^{\circ}$ (θ = angle between $\hat{\underset{\sim}{k}}$ and $\underset{\sim}{B}$) and has electric field polarization $|E_+|^2 = 2 \times 10^{-6}$, $|E_-|^2 = 0.9996$, $|E_{\parallel}|^2 = 3 \times 10^{-4}$, where E_+, E_-, and $E_{\parallel}$ are the amplitudes of the left circular, right circular, and parallel components, respectively. Thus, the extraordinary mode is nearly right circularly polarized. A linearly polarized dominant mode waveguide or a circular waveguide carrying equal amplitudes of left and right circular polarization would tend to excite equal amplitudes of ordinary and extraordinary mode in the plasma. This situation corresponds essentially to Case 3 as discussed in the previous section.

To shoot back toward the near resonance as shown in Fig. 2 again does not seem to require high directivity. Rays 9 through 18 of Fig. 4 are totally absorbed by the core plasma although θ ranges from 80° to 170° (Ray 8, $\theta = 80^{\circ}$ is actually launched away from the resonance). The advantage of this geometry is that the waves are propagating nearly perpendicularly to $\underset{\sim}{B}$ and are therefore almost linearly polarized. For example, Ray 11 of Fig. 4 which is absorbed near the plasma center, has initial $\theta = 100^{\circ}$ and initial electric field polarization $|E_x|^2 = 0.021$, $|E_y|^2 = 0.971$, $|E_{\parallel}|^2 = 6 \times 10^{-4}$. A linearly polarized antenna with electric vector oriented perpendicular to $\underset{\sim}{B}$ could therefore excite a high fraction of extraordinary mode beamed to the plasma center. This is of course the ideal situation. In addition, any ordinary mode created would be more efficiently absorbed at these propagation angles (see Fig. 5). However, ordinary mode heating would probably be important only if the plasma density and temperature could be increased to give near 100% absorption.

One potential technological disadvantage of this geometry is that the fundamental resonance would cross the waveguide near to the antenna opening. Any plasma flowing into the waveguide could contribute to breakdown problems.

Finally, we consider launching from the coil plane, possibly through split mirrors. The same comments as above on antenna directivity apply here. And as in the case of shooting across to the opposite resonance, the ordinary mode absorption is negligeable. The difficulty of exciting pure extraordinary mode also arises. The initial polarization vector for Ray 5 of Fig. 6 is $|E_+|^2 = 0.137$, $|E_-|^2 = 0.746$, $|E_\parallel|^2 = 0.116$. Thus, we expect the performance for this approach to be as in Case 3 of the previous section. There might, however, be an advantage to this geometry if a suitable antenna could be designed having a null in the forward direction and side lobes steered to the plasma center. Then a single antenna and waveguide would suffice to heat two adjacent cavities.

5. CONCLUSIONS

Calculations with the power balance model show that if the microwave power is unpolarized but is beamed from high field to the plasma center, a factor of ~2 increase in core heating efficiency is expected. A possibly more important consideration is that ring heating can be reduced by a factor of about two. If beam directivity and excitation of nearly pure extraordinary mode can be achieved simultaneously, virtually 100% of the throat launched power can be deposited in the core plasma. If, contrary to assumption in the power balance model, the midplane launched power is not spread uniformly across the fundamental resonance surface but is concentrated on the outside, the value of 33% for present core heating efficiency may be a serious overestimate. In that case, the gain in core heating efficiency from throat launch without polarization control may be much higher than the factor of two mentioned above.

We have also used the RAYS code to examine various positions for throat launch. Antenna directivity requirements do not appear stringent since the core plasma portion of the fundamental resonance is a relatively big target. However, the polarization of the extraordinary mode varies from right circular to linear depending on angle of propagation. Therefore, the feasibility of exciting predominantly extraordinary mode may depend strongly on the antenna location and orientation.

Finally, our calculations show that little is gained in core heating efficiency from simply running a waveguide to the throat region, but not controlling directivity or polarization (Case 1 of Section 3). There is however some reduction in ring heating.

REFERENCES

[1]T. Uckan, et al., ORNL/TM-8117.

[2]D. B. Batchelor and R. C. Goldfinger, Nucl. Fusion 20, 403 (1980).

[3]E. F. Jaeger, C. L. Hedrick, and W. B. Ard, Phys. Rev. Lett. 43, 855 (1979).

[4]D. B. Batchelor, Nucl. Fusion 21, 1615 (1981).

[5]Hillis, Haste, Berry, ORNL/TM-8256.

[6]Hillis, ORNL/TM-8179.

[7]D. B. Batchelor and R. C. Goldfinger, ORNL/TM-6844.

[8]D. B. Batchelor, R. C. Goldfinger, and D. A. Rassmussen, ORNL/TM-8770 (1983), submitted to Phys. of Fluids.

TABLE 1

Numerical Values of Parameters Used in Power Balance Model

Definitions of these quantities are given in Ref. 4.

S^{I}_{Wall}	$= 3.3 \times 10^{3} cm^{2}$
S^{III}_{Wall}	$= 8.8 \times 10^{2} cm^{2}$
$S_{Surface}$	$= 938\ cm^{2}$
S_{core}	$= 632\ cm^{2}$
$S_{Annulus}$	$= 751\ cm^{2}$
S_{2nd}	$= 394\ cm^{2}$
S_{12}	$= 1.08 \times 10^{3}\ cm^{3}$
$\langle f \rangle_{x}^{Annulus}$	$= 0.081$
$\langle f \rangle_{o}^{Annulus}$	$= 9 \times 10^{-3}$
$\langle f \rangle_{x}^{2nd}$	$= 0.014$
$\langle f \rangle_{o}^{2nd}$	$= 0.0$
$\langle f \rangle_{o}^{1st}$	$= 0.06$
$\tau^{I} = \tau^{III}$	$= 0.5$
$\lvert T \rvert^{2}$	$= 0.05$

TABLE 2

Comparison of Variuos Power Launch Techniques in EBT-S

HEATING TECHNIQUE	P_{CORE}	$P_{SURFACE}$	$P_{ANNULUS}$
Midplane Launch (Present Method)	33%	39%	28%
Throat Launch (No directivity or Polarization control)	38%	47%	15%
Throat Launch (100% x-Mode)	40%	54%	6%
Throat Launch (100% beamed to core, 50% X-Mode/50% 0-Mode)	68%	20%	12%
Throat Launch (100% Beamed to Core, 100% X-mode)	100%	0	0

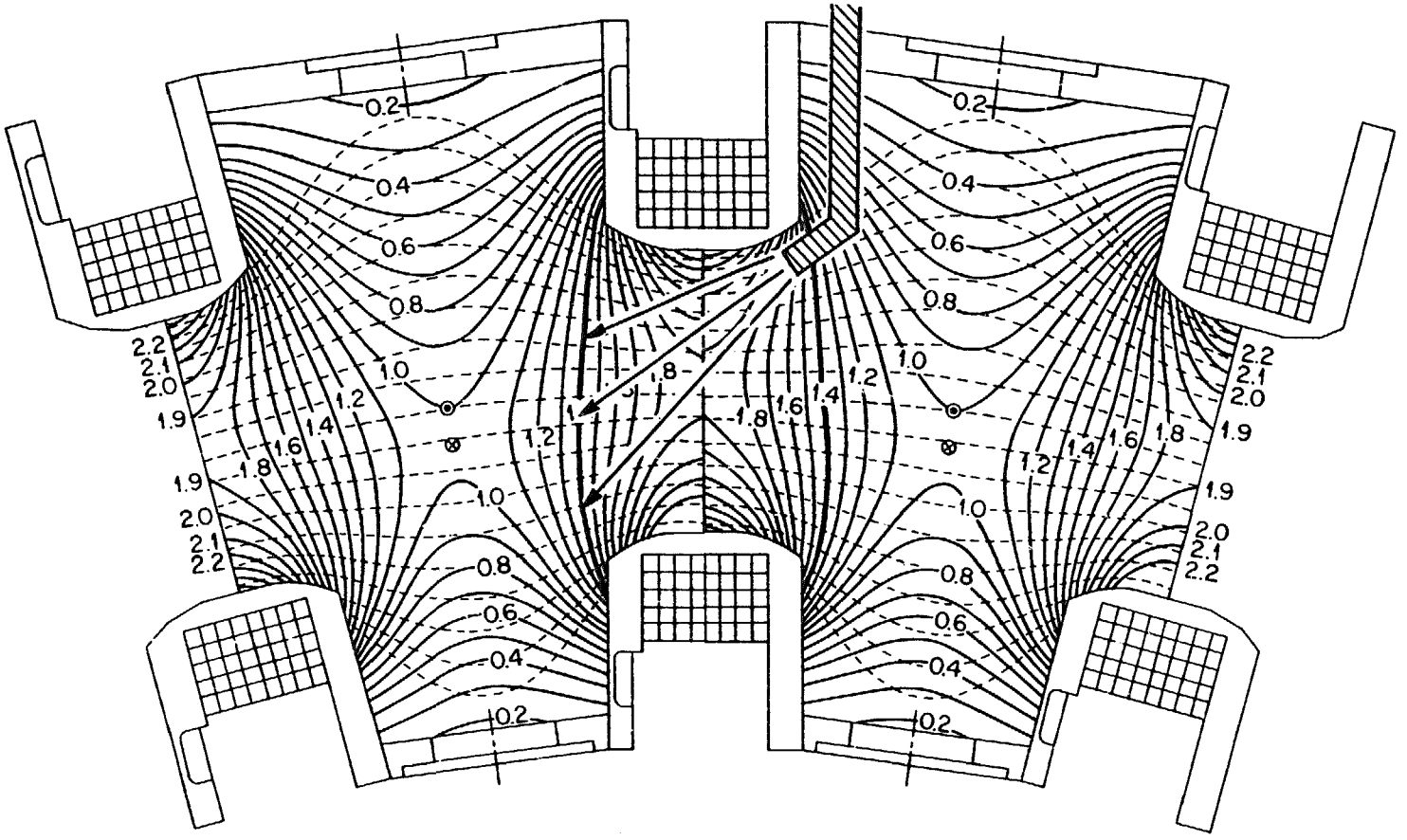

Fig. 1. Waveguide "snaked" through fundamental resonance shooting to opposite resonance.

ORNL-DWG 83-2446A FED

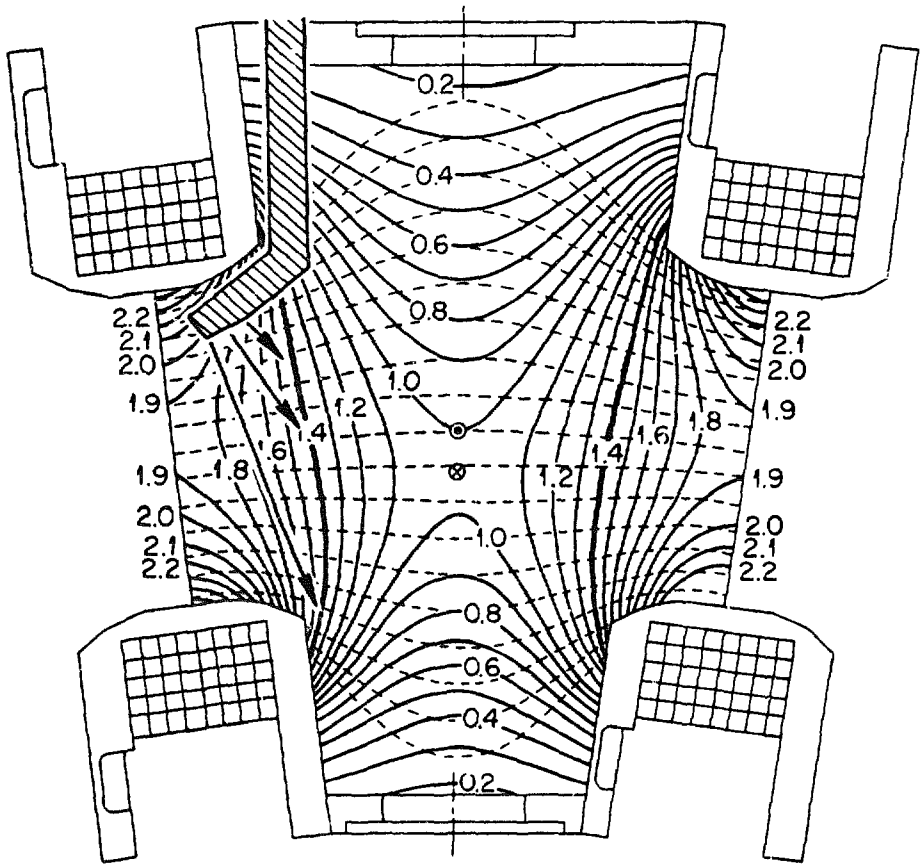

Fig. 2. Waveguide "snaked" through fundamental resonance shooting back to same resonance.

ORNL-DWG 83-2896 FED

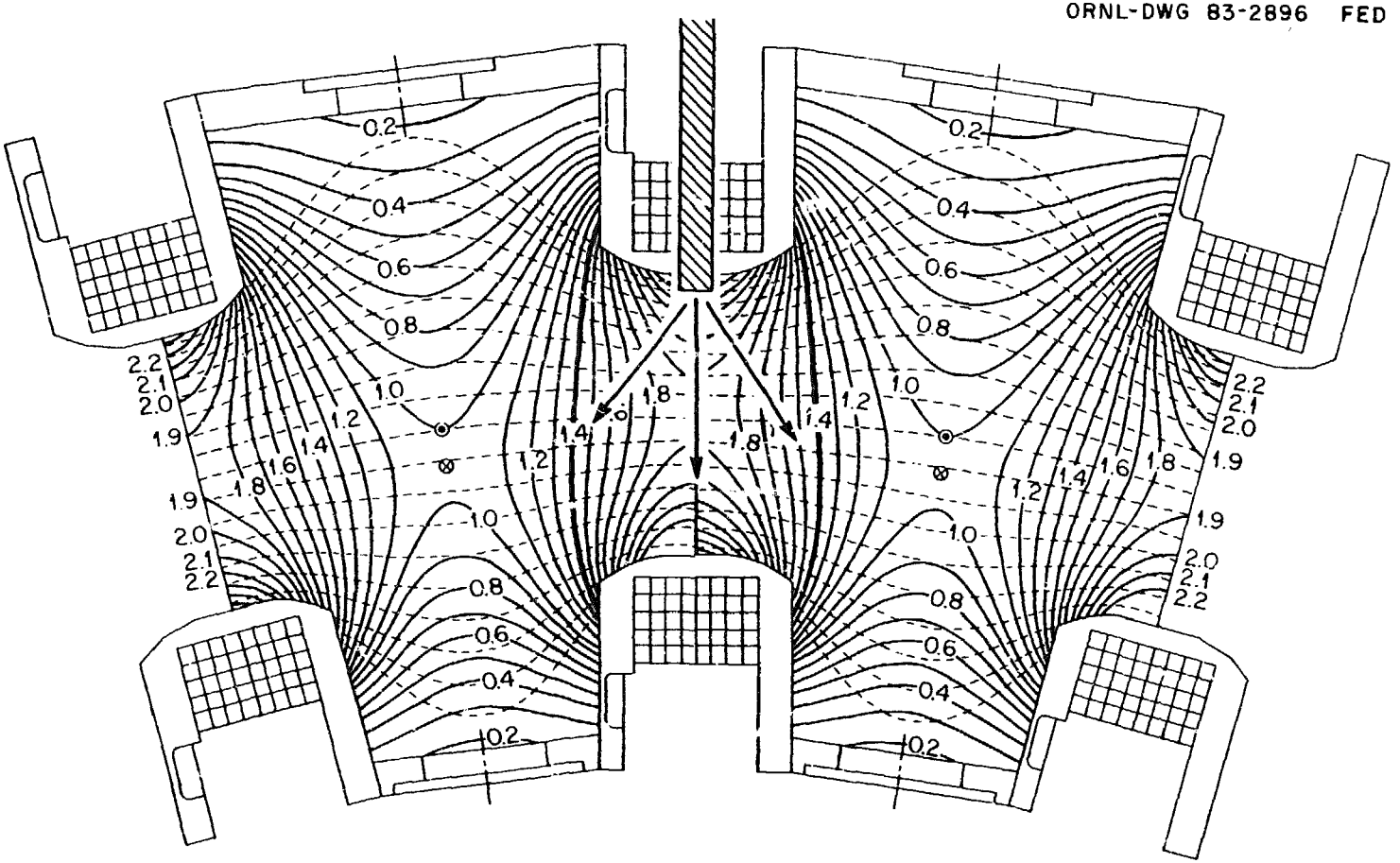

Fig. 3. Split Mirror Launch

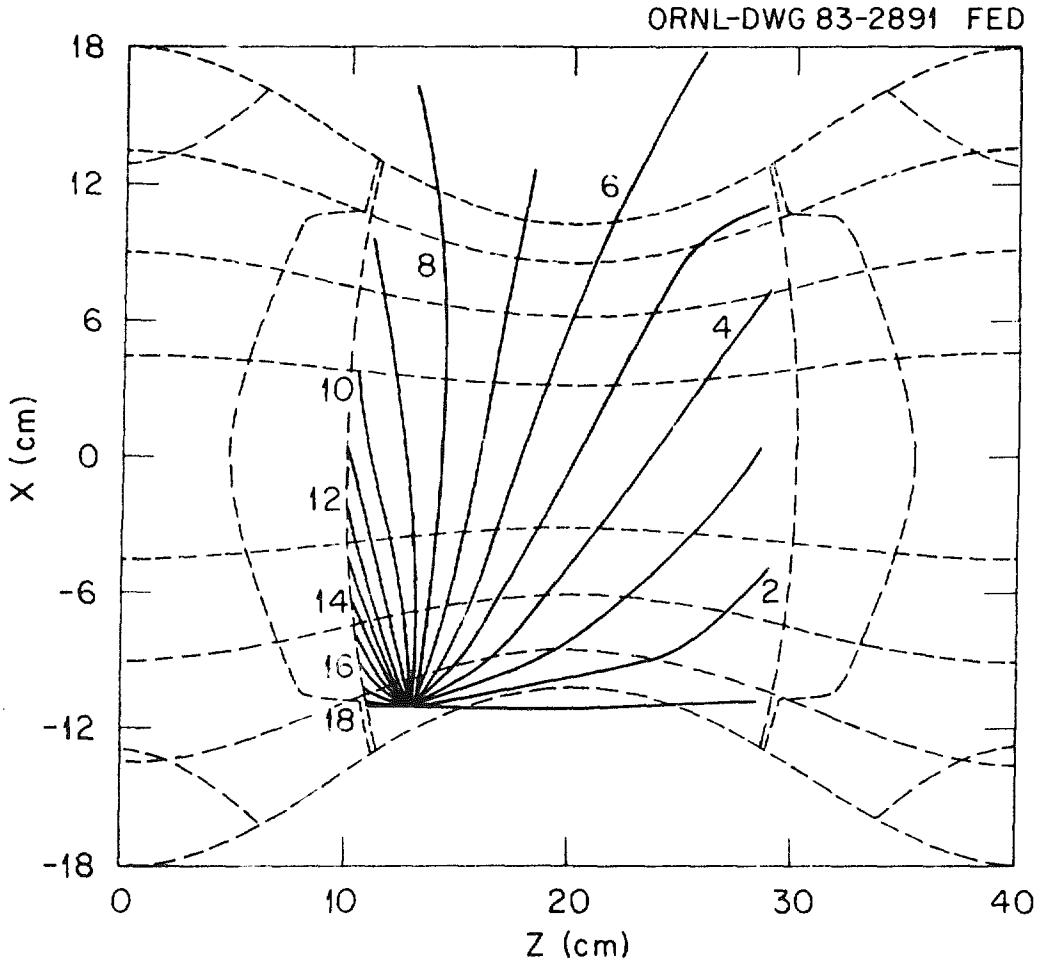

Fig. 4. Extraordinary mode rays launched from left side of coil case.

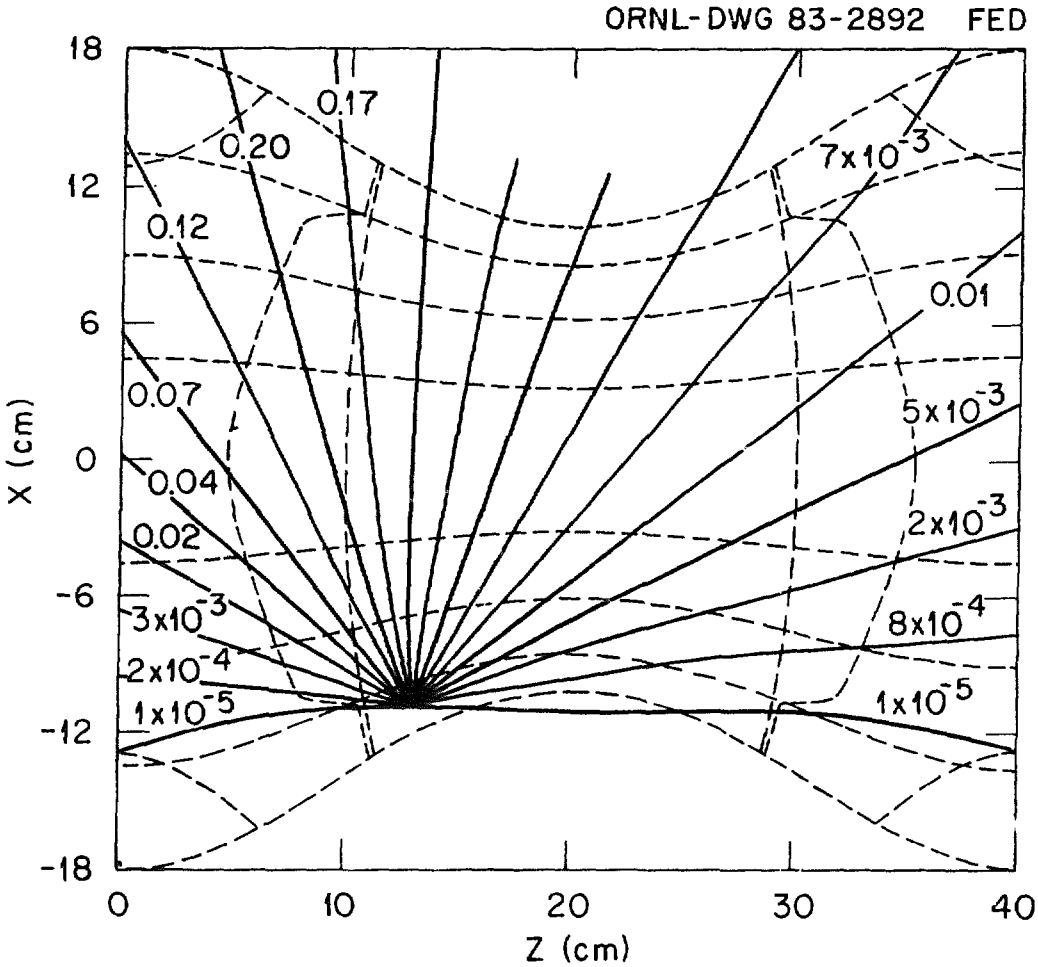

Fig. 5. Ordinary mode rays launched from left side of coil case.

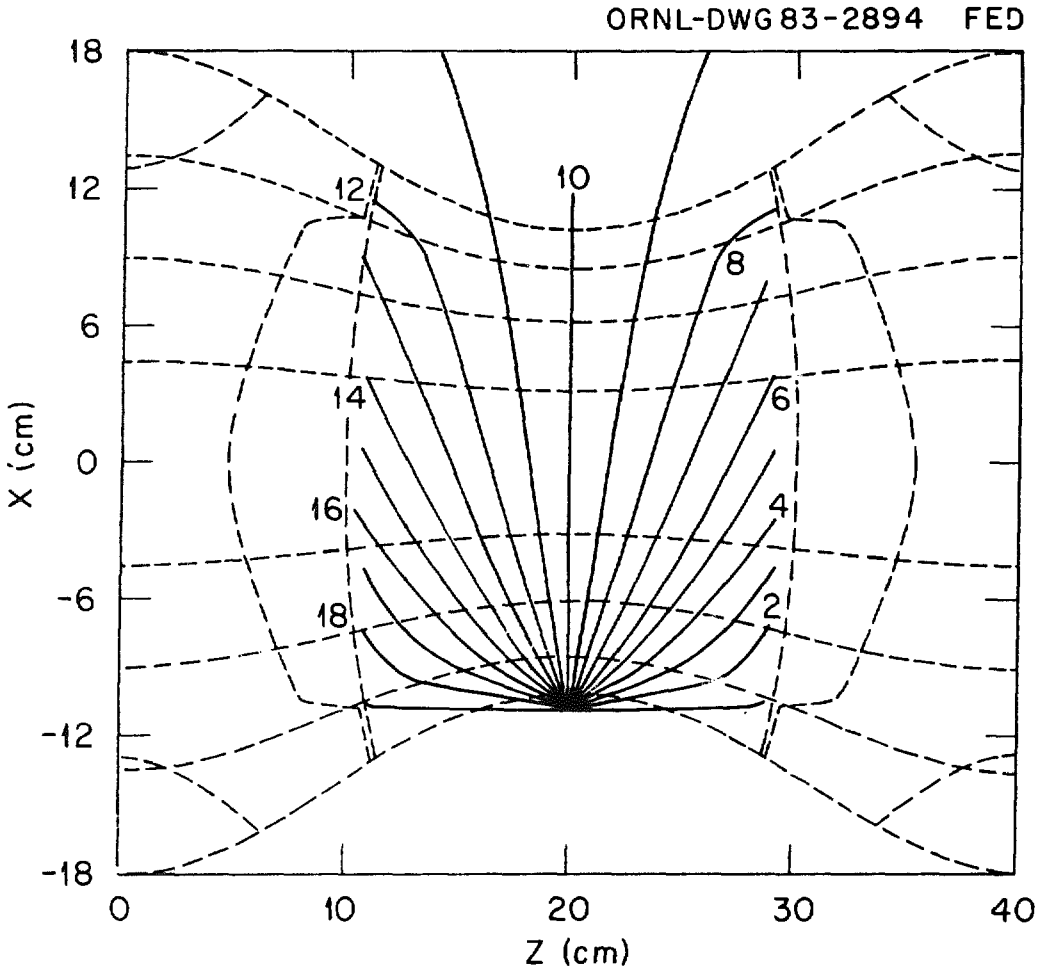

Fig. 6. Extraordinary mode launched from center of coil.

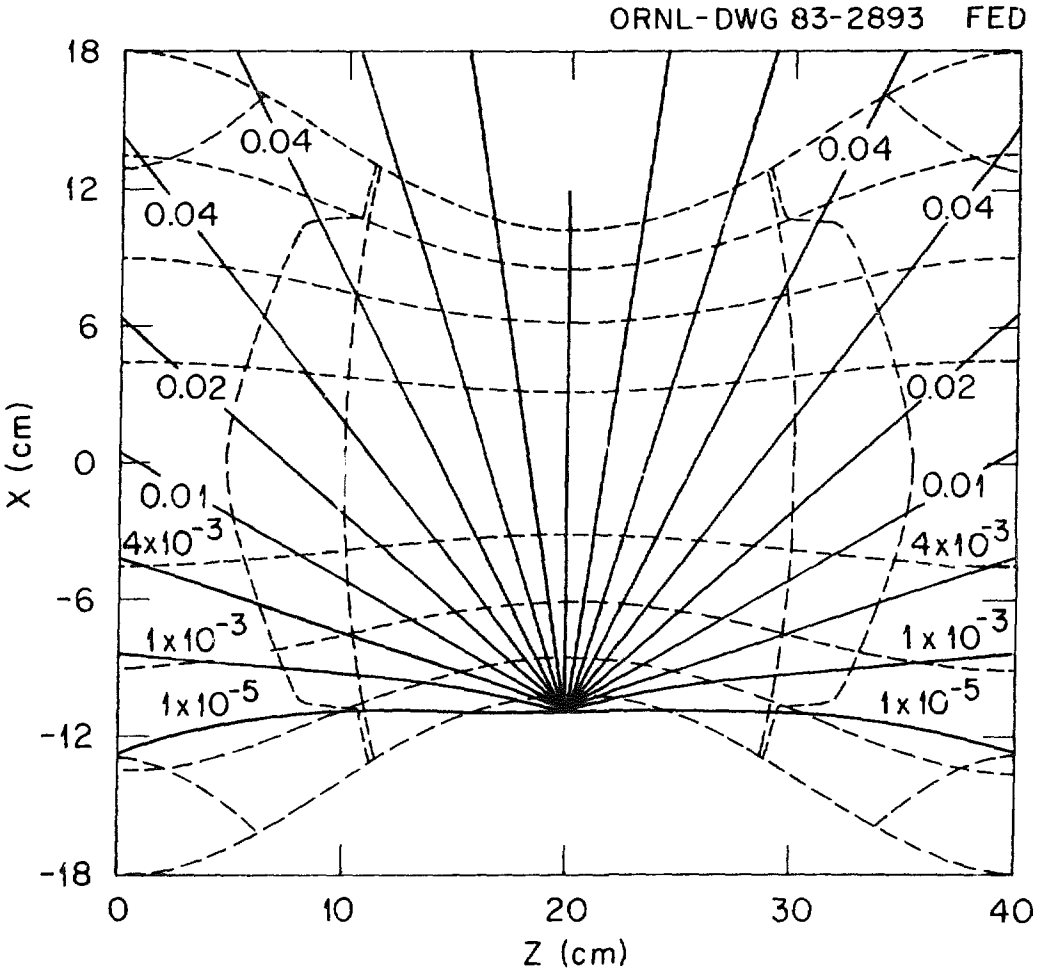

Fig. 7. Ordinary mode launched from center of coil.

415/416

RING PHYSICS

CONTROL OF ELMO RING BY USING SURMAC COILS IN ADVANCED EBT SYSTEMS

B. H. Quon

JAYCOR
2811 Wilshire Boulevard, Suite 690
Santa Monica, CA 90403

ABSTRACT

A scheme is proposed for control of the ELMO ring parameters in advanced higher field and larger scale length EBT Systems. This control can be achieved by the modification of the local axial scale length

$$L^{-1} = \left(\frac{1}{B}\frac{dB}{dz}\right)$$

using a Surmac coil[1] coaxial with the mirror [illegible]
located outside the ring and the core pla[illegible]
$\rho/L \simeq 0.05$ scaling[2] to hold, con[illegible]
operating the ring at the [illegible]
reactor. Sustain[illegible] [illegible]nis
technique [illegible]

****
Editor's Note: This paper, although presented at the workshop, has been withdrawn from the proceedings and therefore cannot be used for reference. — N. A. Uckan
****

[illegible]itional stabilizing
[illegible]nese effects include (1) the

$$\delta \int \frac{dl}{B} < 0$$

region between the ring and the cavity wall, and (2) confinement of a stable, cold plasma at the separatrix in the vicinity of the ring.[1]

---

[1]J. R. Ferron and A. Y. Wong, UCLA Plasma Physic Group Report #PPG 625, (1982).

[2]N. Uckan, Proc. 2nd Workshop on Hot Electron Ring Physics, San Diego, Conf. 811203 (1981), p. 361.

ON THE POSSIBILITY OF RINGS IN A MODULAR STELLARATOR*

James A. Rome, Jeffrey H. Harris, Billie Masden, and Vickie Lynch
Oak Ridge National Laboratory
Oak Ridge, Tennessee 37830

ABSTRACT

Combining the features of modular stellarators and EBT's opens new approaches to configurational optimization. A stellarator may not be stable at zero beta but may dig a well and become stable at finite beta when it enters the "second regime." The use of EBT-like rings has been proposed to provide stable access into this regime.[1] From [illegible] point of view, the average magnetic well near the [illegible] and slight shear, provided by a weak [illegible] significantly enhance the stab[illegible] of the properties of th[illegible] more sophisti[illegible] con[illegible]

****
Editor's Note: This paper, although presented at the workshop, has been withdrawn from the proceedings and therefore cannot be used for reference. — N. A. Uckan
****

[illegible]meless, [illegible] not a ring could [illegible]ellarator, it is necessary [illegible] $v_{\parallel}/v$ whose orbits reside on a $|B|$ [illegible]second harmonic of the electron cyclotron [illegible]s locus should be reasonably omnigenous with the flux [illegible]es. We will discuss our progress in calculating and understanding the feasibility of such configurations. One obvious starting point is to design a system based upon the EBT-S coils, keeping its mirror and aspect ratios.

---

*Research sponsored by the Office of Fusion Energy, U.S. Department of Energy, under contract W-7405-eng-26 with the Union Carbide Corporation.

[1]Private communication, H. P. Furth and A. H. Boozer.

REDUCTION OF MICROWAVE POWER REQUIREMENTS FOR EBT

S. Hamasaki, H. H. Klein, N. A. Krall, and J. L. Sperling
JAYCOR
San Diego, California 92138

Power requirements for EBT electron ring formation are calculated based on the assumption that the ring electrons originate as runaways accelerated by the first harmonic resonance of the extraordinary mode. The minimum power, P_μ, for startup is shown to scale roughly linearly with the background plasma density ($P_\mu \propto n_e$). On the other hand, the microwave power required to maintain the constant bulk electron temperature increases as the square of the plasma density ($P_\mu \propto n^2$). It is therefore suggested that more economical EBT operation in high density regimes ($n_e \simeq 10^{13}$-10^{14} cm^{-3}) can be obtained by utilizing alternate and less expensive power sources for bulk plasma heating, using the minimum required microwave power to start up the energetic electron annulus.

1. INTRODUCTION

A central feature of the bumpy torus concept is an annulus of relativistic electrons which stabilize the bulk plasma through their diamagnetic modification of the bumpy torus magnetic field in each mirror sector. Without the relativistic annuli, the bumpy torus could not contain a stable plasma.

The relativistic electron annulus is created through irradiation of plasma with microwaves. In this paper, the minimum microwave power required for startup is calculated based on the assumption that the ring electrons originate as runaways accelerated by the first harmonic resonance of the extraordinary mode. The minimum power density, P_μ, for startup is shown to scale (roughly) linearly with the background density, n ($P_\mu \propto n$). Microwave power is also to heat the bulk plasma

itself. The required power to operate the bulk T-mode plasma at a constant specified temperature seems to scale as $P_\mu \propto n^2$ in EBT experiments. It is therefore suggested that alternate and less expensive power sources for bulk plasma heating combined with the minimum required microwave power for annular electron heating may allow economical EBT operation in high density regimes ($n \sim 10^{13}$-10^{14} cm^{-3}).

2. CALCULATION OF MICROWAVE POWER REQUIREMENTS FOR ELECTRON RING STARTUP

2.1 RING STARTUP MODEL

The initial phase of EBT often starts with cold dense plasma (C-mode) immersed in a bath of microwave radiation. Because microwave absorption and particle collisionality are both velocity dependent, we can imagine that although electrons in the C-mode originally have a Maxwellian distribution, electrons of sufficiently high energy (in the tail of the Maxwellian) are heated more rapidly by ECRH than they are slowed down by collisions. This produces a small group of runaway electrons which can form the high energy population observed to form the EBT annulus as the fill pressure is reduced. The majority of the electrons will be heated gradually by ECRH, remaining in a nearly Maxwellian distribution, with the distribution shape dominated by collisions.

To quantify this idea, we divide the electrons into two groups even before startup, representing the C-mode distribution as

$$f = f_1 + f_2$$

$$f_1(v) = \frac{n_e}{\left(\pi v_{th}^2\right)^{3/2}} \exp\left(-\frac{v^2}{v_{th}^2}\right) H(v_c - v) \tag{1a}$$

$$f_2(v) = \frac{n_e}{\left(\pi v_{th}^2\right)^{3/2}} \exp\left(-\frac{v^2}{v_{th}^2}\right) H(v - v_c) \tag{1b}$$

where n_e and v_{th} are the total electron density and electron thermal velocity. H is a Heaviside function with a cut-off velocity of v_c left arbitrary for the moment, except that $f_1(v)$ represents the bulk of the C-mode plasma while $f_2(v)$ corresponds to the small number of (eventually) runaway electrons.

We assume the temperature of the bulk C-mode plasma ($T_c = \frac{1}{2} m v_{th}^2$) is in semi-equilibrium with an assumed microwave power, P_μ, and its density, n_e, is such that

$$P_\mu = \frac{3}{2} \frac{n_e T_c}{\tau_c} \tag{2}$$

The confinement time, τ_c, of the C-mode plasma has been calculated[1] based on flute interchange instability ($\tau_c \simeq 10^{-4}$-10^{-5} s).

We refer to Reference 1 for the details of the calculation. We only outline the calculation procedures here.

A. We assume that all the microwave power is transferred[2] from the port at the weak magnetic field region to the magnetic throat regions through reflections of ordinary mode from the walls of the devices. It is absorbed in the plasma through the first harmonic resonances of the extraordinary mode, into which the ordinary mode is converted by the multiple reflections from the wall. Based on this, we calculate the fraction of the energy absorbed in the tail electrons, using the quasilinear electron cyclotron heating equation.[3] This gives the heating rate, $dE/dt\big|_h$, of the tail electrons, f_2, for a given microwave power.

B. We then calculate the collisional drag rate, $dE/dt\big|_c$, on f_2 by the bulk plasma, f_1, as a function of boundary energy, E_c [$E_c = (m/2) v_c^2$]. In this calculation, we use the Fokker-Planck equation[3] in describing the collisional interaction of f_2 on f_1.

C. The net heating rate of tail electrons, f_2, for a given microwave power is obtained as

$$\frac{dE}{dt} = \left.\frac{dE}{dt}\right|_h - \left.\frac{dE}{dt}\right|_c \quad . \tag{3}$$

D. We calculate the electron crossing rate from below E_c to above E_c (in energy) due to the microwave heating, obtaining the tail electron density increase rate $dn_2/dt\big|_h$. We also estimate the initial leakage rate of tail electrons due to the poor confinement of the initial plasma as

$$\left.\frac{dn_2}{dt}\right|_L \simeq \frac{n_2}{\tau_c} \quad . \tag{4}$$

E. Now we obtain the net tail electron density increase rate as

$$\frac{dn_2}{dt} = \left.\frac{dn_2}{dt}\right|_h - \left.\frac{dn_2}{dt}\right|_c \quad . \tag{5}$$

F. We estimate the life time, τ_h, of runaway electrons (after surviving the initial leakage) from the estimated final temperature, T_h, which may be determined by nonadiabaticity in their magnetic moment.

G. We try to find a value of E_c for a given microwave power and a given background density which will satisfy the following two conditions: (1) the heating rate is big enough to satisfy $(dE/dt)\,\tau_h > T_h$ and (2) the density increase rate is big enough to satisfy the minimum β condition

$$T_h \left(\frac{dn_h}{dt}\,\tau_h\right) \frac{8\pi}{B_0^2} > \beta_{min} \quad . \tag{6}$$

H. The minimum microwave power required for the electron ring startup in a given density, n_e, is the smallest power that allows a cutoff energy, E_c, which satisfies the above two conditions.

2.2 CALCULATION RESULTS

One of the remarkable results of the calculation is that the power requirement for startup is roughly independent of magnetic field strength, B_o, and, therefore, also roughly independent of applied microwave frequency as long as the frequency allows the first harmonic resonances in the magnetic throat regions.

The heating rate, dE/dt, and the density increase rate, dn_h/dt, are roughly independent of B_o, or also the choice of field line over which we take the field line average, because the power is isotropically distributed and entirely absorbed in the first harmonic resonant region regardless of B_o. The minimum β condition is satisfied for roughly the same E_c and roughly the same microwave power for different EBT devices like NBT, EBT-1 or EBT-S because larger B_o usually gives a larger tail temperature, T_h, while the larger T_h means a larger life time, τ_h. Both effects, the increases in T_h and in τ_h, cancel the effect of the increase of B_o on minimum power requirements.

Therefore, the minimum microwave power is only a function of the background density, n_e. The result of our calculation is shown in Fig. 1. The minimum required power density to start up the ring is plotted against the background density, n_e, of the cold C-mode plasma. The required power density increases more nearly linearly than as the square of n_e. The empirical relation turns out to be

$$P_\mu = 1.75 \times 10^{-17}\, n_e^{1.28} \qquad (W/cm^3) \tag{7}$$

where n_e is in cm^{-3}.

2.3 COMPARISON WITH EXPERIMENTS

Experimentally, the transition from the C-mode to T-mode operation occurs at the knee point[4] of the line density, measured by the interferometer, with decreasing operating neutral pressure, P_o, and a fixed power, P_μ. It is not entirely clear that at this point the system

changes abruptly from an MHD-unstable to a stable state by the formation of rings. However, the system seems to become more stable so that the confinement time becomes longer, enhancing the plasma density at this C-T transition point. Experimental line densities[4] observed by interferometers at the C-T transition points are plotted as a function of total microwave power, P_μ, for various devices in Fig. 2.

Data for an individual device shows that the line density, $n\ell$, goes up with the microwave power, P_μ, linearly at first and quickly slows down. The trend of $n\ell$ with P_μ seems to be $n\ell \propto P_\mu^{1/2}$ as shown by dashed lines, over a fairly limited range of P_μ, for each device, EBT-S, EBT-1, and NBT-M. However, these devices have almost the same size and identical magnetic configurations. Using this fact to consider the trend of $n\ell$ with P_μ over a wider range of P_μ, the overall behavior of the line density, $n\ell$, is to increase roughly linearly with P_μ as shown by the solid line. In fact, $P_\mu \propto (n\ell)^{1.25}$. If we assume that roughly ℓ = constant, the required microwave power for C-T transitions depends almost in the same way on the background density, n_e, as we have calculated. This can be more clearly seen in Fig. 3. Here the background density, n_e, is plotted as a function of the minimum total microwave power, P_μ, calculated for ring startup and the experimental C-T transition points are also shown. In calculating P_μ from the power density, P_μ, shown in Fig. 1, the plasma volume ($V = 3.6 \times 10^5$ cm^3) is used and in calculating n_e from the C-T transition points shown in Fig. 2, the plasma size ℓ = 15 cm is used.

Our theoretical prediction of the minimum microwave power to start up the ring for a given n_e is roughly one-third of the experimental value of the microwave power for C-T transition. However, the functional dependence of P_μ on n_e is well predicted by the theory. The calculation assumes perfect efficiency of energy transfer from the microwave ports to the magnetic throat region ($\eta = 1$). A recent calculation by Tamor[5] indicates that the absorption of microwave energy by the irregularities of the wall can be enormous so that the efficiency of $\eta = 0.3$ may not be unreasonable at all. Also, the neoclassical zero-dimensional calculation[6] has consistently indicated that the actual power absorption by

plasma may be substantially smaller than the microwave power out of the microwave ports. Considering these elements, our calculated minimum microwave power density for startup may indeed be the bare net power necessary for direct absorption by the plasma.

One interesting observation in our startup calculation is that the actual microwave power used to extract the electron tail is only a small fraction of the total microwave power. The rest of the power went to heat the background electrons. Therefore, if we can deposit the microwave power directly in the tail, much less power is needed to start up the electron rings. Of course, in that case, it requires other means to heat up the plasma.

3. MICROWAVE POWER REQUIREMENTS FOR T-MODE OPERATIONS

3.1 NEOCLASSICAL SCALING

The majority of the microwave power absorbed by the bulk electrons heats up and maintains the plasma at its operating temperature. The scaling with plasma density of the microwave power for maintaining the steady state operating plasma temperature can be entirely different from the scaling law of the microwave power for the ring startup. The microwave power required for a steady state electron temperature is controlled by the loss mechanism of the bulk electrons.

Assuming the bulk electrons are lost neoclassically, we can obtain the scaling law as follows.

The particle balance equation is

$$n_e n_o \langle \sigma_i v \rangle = \frac{n_e}{\tau_p} \tag{8}$$

where σ_i is the ionization cross section, v is the electron velocity, $\langle\ \rangle$ is an average over the electron distribution, n_o is the neutral density, and τ_p is the particle confinement time.

The energy balance equation is

$$P_\mu = \frac{3}{2}\frac{n_e T_e}{\tau_E} \tag{9}$$

where τ_E is the energy confinement time. In the collisionless regimes of the neoclassical diffusions, τ_p and τ_E are proportional to the classical collision time

$$\tau_E \propto \tau_p \propto \frac{T_e^{3/2}}{n_e} \quad . \tag{10}$$

Also, when T is not too small, roughly we expect

$$\langle \sigma_i v \rangle \propto \frac{1}{T_e} \quad . \tag{11}$$

From Eqs. (8) through (11), we obtain the scaling laws as

$$T_e \propto \frac{P_\mu^{2/3}}{n_o^{4/3}} \tag{12}$$

$$n \propto \frac{P_\mu^{2/3}}{n_o^{1/3}} \quad . \tag{13}$$

The most relevant scaling law for our purpose is obtained by eliminating n_o from Eqs. (12) and (13) as

$$P_\mu \propto \frac{n_e^2}{T_e^{1/2}} \quad . \tag{14}$$

This law gives the microwave power scaling with the bulk electron density, n_e, to maintain a constant temperature, T_e. We see that the microwave power required for a constant temperature scales with square of the density, n^2.

3.2 EXPERIMENTAL INDICATIONS

So far there is very little experimental data for density and temperature in T-mode operation by Thomson scattering. On the other hand, the extensive available data[7] obtained by soft x-ray measurements is quite consistent[6] with the neoclassical diffusion model. Therefore, we are referring only to soft x-ray data in the following analysis. From the soft x-ray data,[7] we can plot the electron density, n_e, as a function of total power, P_μ, with a fixed electron temperature, T_e (by adjusting the neutral pressure, P_0). The result is shown in Fig. 4. The experimental data seems consistent with the scaling law $P_\mu \propto n^2$.

The "best" state (highest temperature) in T-mode operation is obtained at T-M transition points. The line densities measured by interferometer can be plotted as a function of the microwave power at T-M transition points. Here, we use the experimental data from various literature cited in Reference 4. In contrast to Fig. 2, which corresponds to C-T transition point, the microwave power, P_μ, seems to scale roughly with $(n\ell)^2$. This also indicates that the microwave power required for sufficient heating of the background electrons increases roughly proportional to square of the density.

4. ECONOMICAL EBT OPERATION

We have found that microwave power roughly proportional to the density, n_e, is required for starting up the electron rings. After startup, maintaining the rings should require less than the startup power. Therefore, the minimum power required for the sake of annular electron rings in EBT operation increases roughly proportionally with the plasma density, $P_\mu \propto n$.

We note, however, that the microwave power required to maintain a certain plasma temperature increases proportionally with the square of the density in the usual EBT operations, $P_\mu \propto n^2$. This means that much more microwave power will be required for maintaining the plasma temperature than for creating and maintaining the electron annulus in future high density ($n_e \simeq 10^{13}$-$10^{14}/cm^3$) EBT devices.

It is therefore suggested that an economical EBT operation in high density regimes can be obtained if we utilize an alternate and less expensive power source (e.g., ion cyclotron wave, neutral injections, or various beam heating) for bulk plasma heating and using only the minimum required microwave power to start up and maintain the energetic electron annulus.

REFERENCES

1. S. Hamasaki, N. A. Krall, and J. L. Sperling, JAYCOR Report J530-83-121 (1983); also N. A. Krall, JAYCOR Report J530-82-001 (1982).
2. D. B. Batchelor, Nucl. Fusion 21, 1615 (1981).
3. S. Hamasaki et al., Phys. Fluids 24, 1706 (1981).
4. EBT-S Data: T. Uckan, L. A. Berry, D. L. Hillis, and R. K. Richard, Oak Ridge Report ORNL/TM-8117. EBT-1 Data: R. J. Colchin, Proceedings of the Workshop, EBT Ring Physics, 529 (1979). NBT-1M Data: Data sheets presented at EBT Review Meeting at Oak Ridge (1983).
5. S. Tamor, Proceedings of this conference.
6. J. B. McBride, H. H. Klein, N. A. Krall, and C. L. Hedrick, JAYCOR Report J530-83-001 (1983).
7. D. L. Hillis, G. R. Haste, and L. A. Berry, Oak Ridge Report ORNL/TM-8256 (1982).

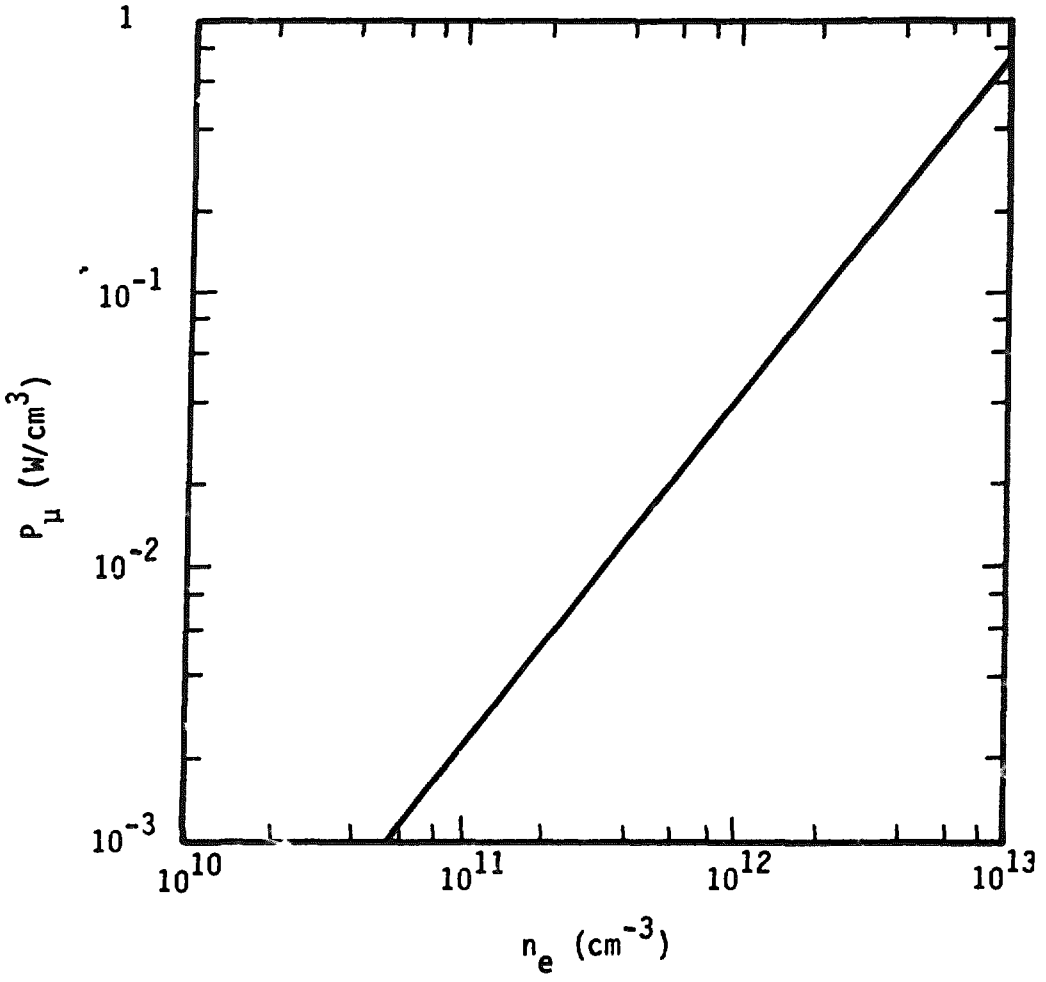

Fig. 1. The minimum microwave power density, P_μ, as a function of the background density, n_e.

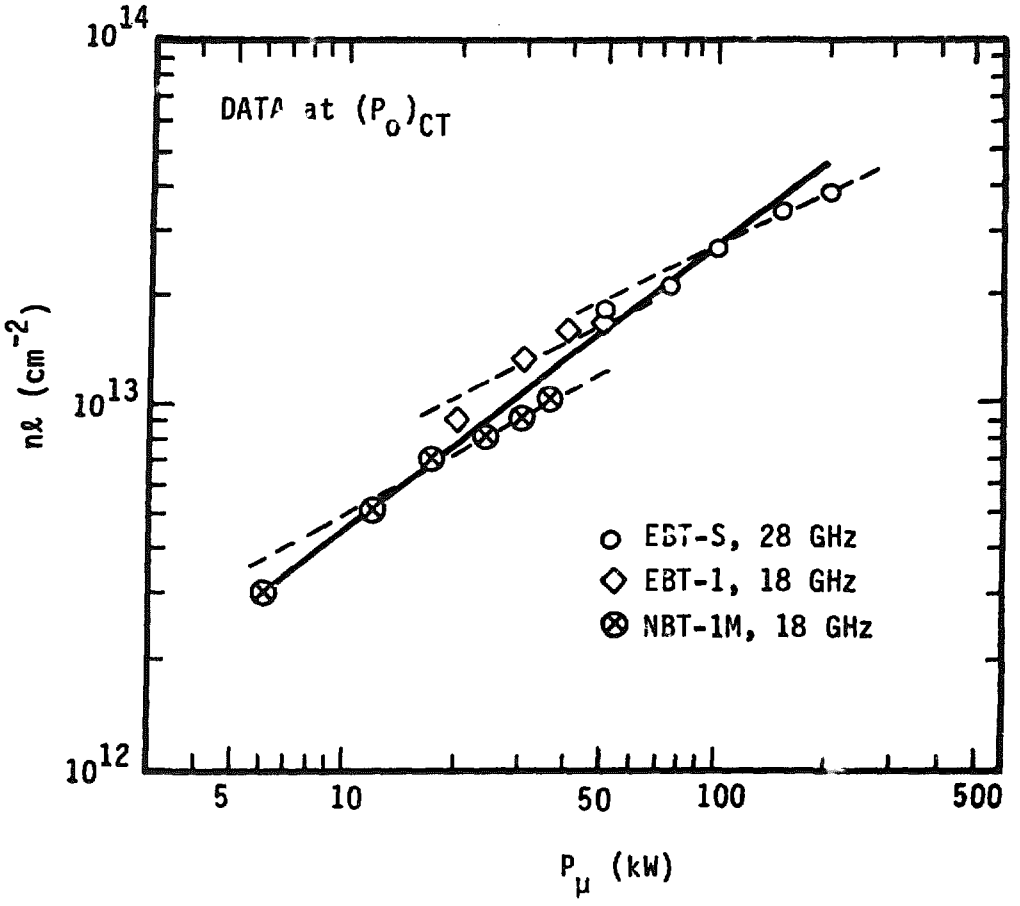

Fig. 2. Experimental data:[4] line density, $n\ell$, as a function of microwave power, P_μ, at the C-T transition points for various EBT devices.

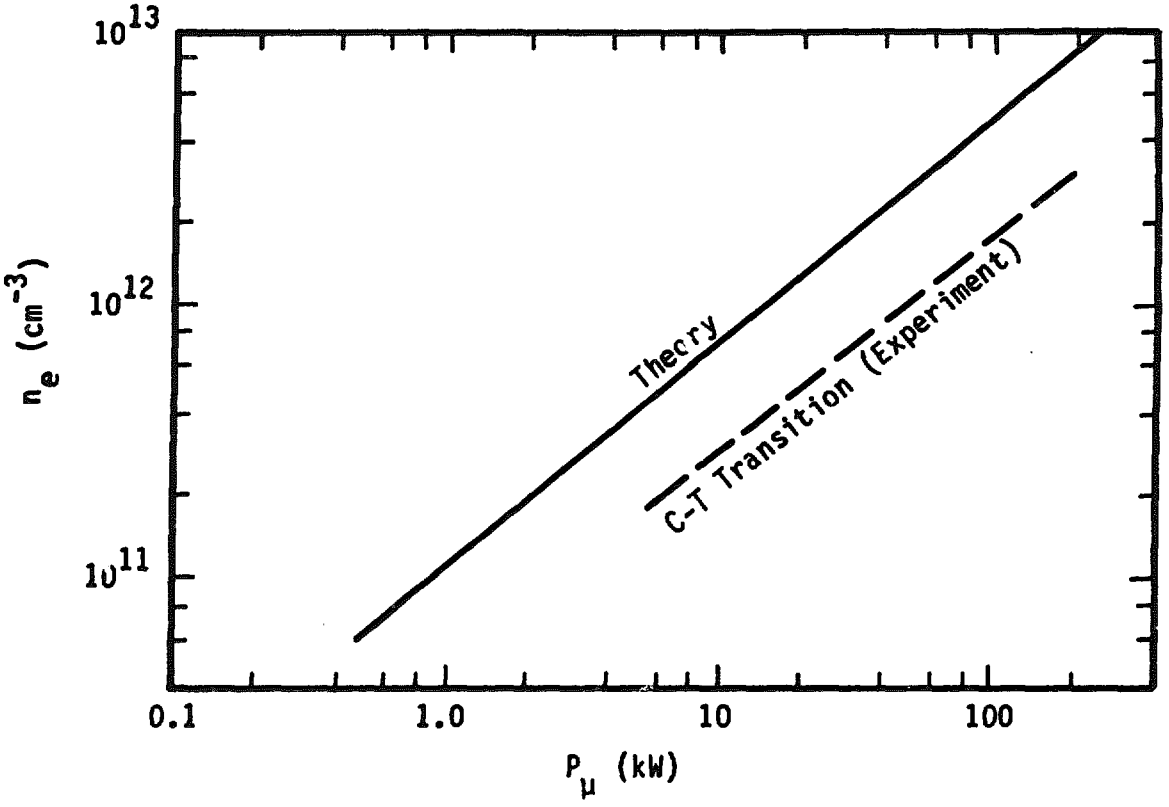

Fig. 3. Theoretical and experimental microwave power requirements for electron ring formation in various background densities, n_e.

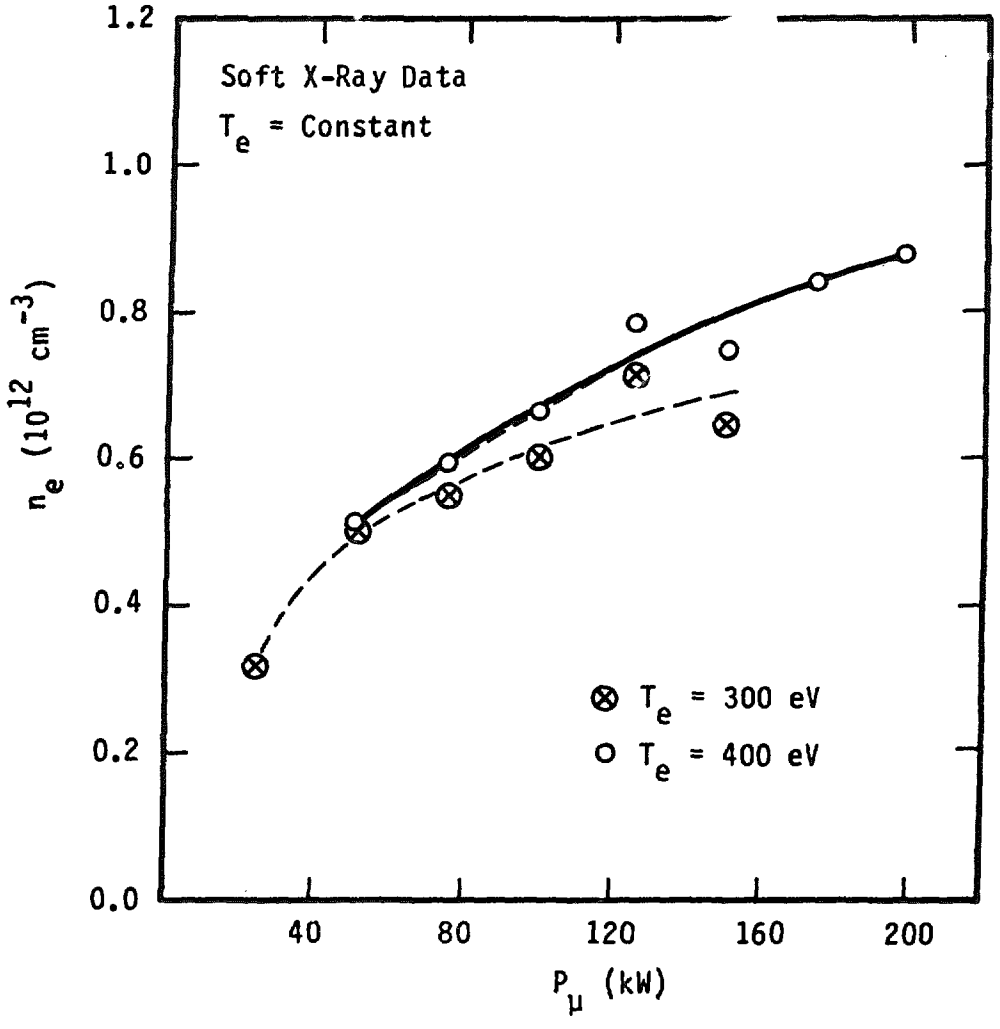

Fig. 4. Soft x-ray experimental data[7] in EBT-S: the electron density, n_e, as a function of the microwave power, P_μ, keeping the electron temperature, T_e, fixed.

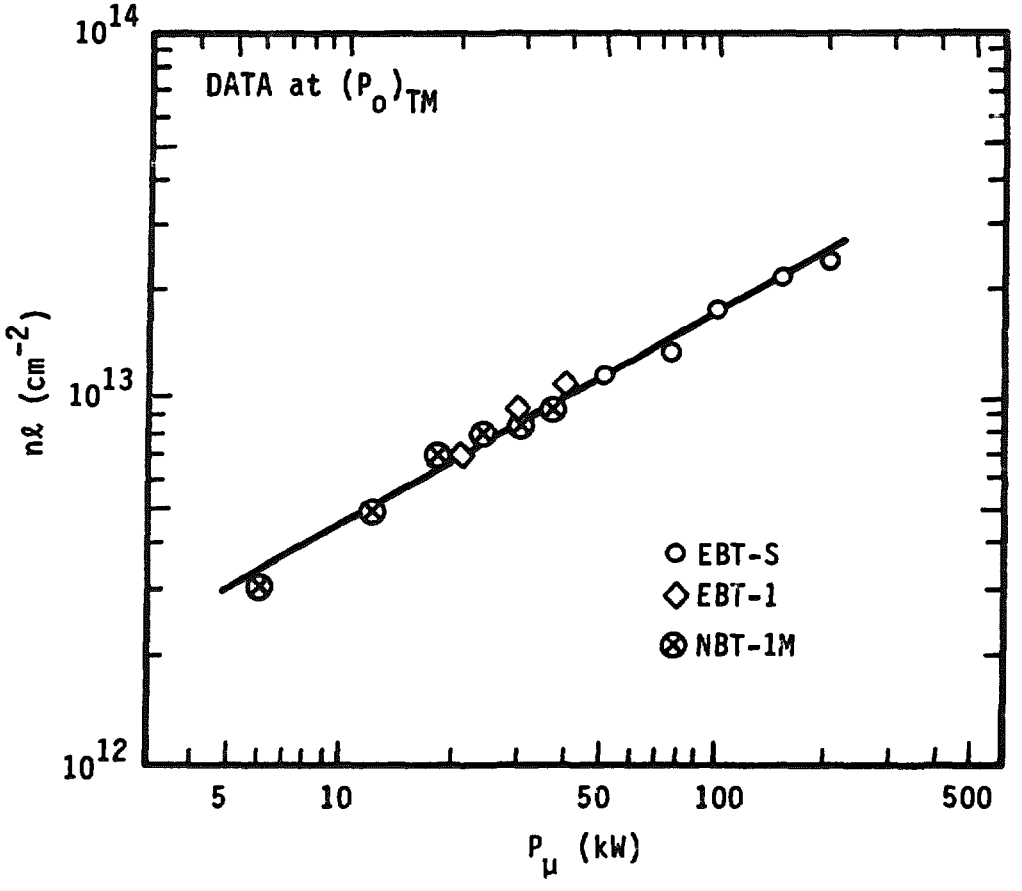

Fig. 5. Experimental data:[4] line density, $n\ell$, as a function of microwave power, P_μ, at the T-M transition points for various EBT devices.

AUTHOR INDEX

K. Adati, 365
T. Aoki, 365
W. B. Ard, 1, 99

D. R. Baker, 365
D. B. Batchelor, 395
L. A. Berry, 1
F. M. Bieniosek, 99
A. H. Boozer, 161

C. S. Chang, 273
J. L. Conlee, 117

R. A. Dandl, 37
R. J. Dannenmueller, 117
R. J. DeBellis, 117
C. F. Dillow, 117

M. G. Engquist, 167

H. Fujita, 365
M. Fujiwara, 71, 151

H. R. Garner, 365
G. Gibson, 1, 73
R. C. Goldfinger, 395
G. E. Guest, 37

K. Hamamatsu, 285
S. Hamasaki, 421
D. E. Hastings, 191
K. Hattori, 365
C. L. Hedrick, 55, 217
S. Hidekuma, 365
H. Hojo, 285

H. Ikegami, 1, 71, 179
H. F. Imster, 117

T. Kamimura, 71
T. Kammash, 237
R. J. Kashuba, 99
T. Kawamoto, 365
H. H. Klein, 421
N. A. Krall, 1, 19, 219, 421

R. Kumazawa, 365

D. K. Lee, 55

L. P. Mai, 73
M. Matsumoto, 318
J. B. McBride, 219
R. L. Miller, 37, 273

K. Nguyen, 237
K. Nishikawa, 285

S. Okamura, 365
Y. Okubo, 365
L. W. Owen, 55

J. F. Pipkins, 99
T. J. Poteat, 117

D. A. Rasmussen, 395
M. Rosenberg, 219
M. N. Rosenbluth, 167
J. R. Roth, 327

K. Sakai, 318
H. Sanuki, 261
T. Sato, 365
R. J. Schmitt, 99, 117
J. L. Sperling, 421
D. W. Swain, 395

S. Takeuchi, 318
S. Tamor, 385
S. T. Tsai, 167
A. Tsushima, 151

K. Uchino, 365
N. A. Uckan, 1

J. W. Van Dam, 167

T. Watanabe, 285
H. Weitzner, 1

S. Yoshikawa, 67

ATTENDANCE LIST

US-JAPAN WORKSHOP
ADVANCED BUMPY TORUS CONCEPTS

July 11-13, 1983
Rancho Santa Fe, California

William B. Ard
McDonnell Douglas Astronautics Co.
Fusion Science Department
Dept. 240, St. Louis Division
P.O. Box 516
St. Louis, MO 63166

Donald B. Batchelor
Oak Ridge National Laboratory
Bldg. 9201-2, MS-2
P.O. Box Y
Oak Ridge, TN 37830

Lee A. Berry
Oak Ridge National Laboratory
Bldg. 9201-2, MS-2
P.O. Box Y
Oak Ridge, TN 37830

Allen H. Boozer
Plasma Physics Laboratory
Princeton University
P.O. Box 451
Princeton, NJ 08544

Robert B. Campbell
Lawrence Livermore National Lab.
P.O. Box 5511
Livermore, CA 94550

Choong-Seock Chang
AMPC Inc.
2210-P Encinitas Blvd.
Encinitas, CA 92024

Guo-Liang Chen
Oak Ridge National Laboratory
Bldg. 9201-2, MS-2
P.O. Box Y
Oak Ridge, TN 37830

Michel Cotsaftis
JAYCOR
11011 Torreyana Road
P.O. Box 85154
San Diego, CA 92138

John O. Cowles
Office of Fusion Energy
ER-56 GTN
U.S. Department of Energy
Washington, DC 20545

Raphael A. Dandl
AMPC Inc.
2210-P Encinitas Blvd.
Encinitas, CA 92024

Steven O. Dean
Fusion Power Associates
2 Professional Drive, #249
Gaithersburg, MD 20879

Roy J. DeBellis
McDonnell Douglas Astronautics Co.
Fusion Science Department
Dept. E240, St. Louis Division
P.O. Box 516
St. Louis, MO 63166

Donald R. Dobrott
Science Applications Inc.
1200 Prospect Street
P.O. Box 2351
La Jolla, CA 92038

Wesley B. Downum
Oak Ridge National Laboratory
Bldg. 9201-2, MS-3
P.O. Box Y
Oak Ridge, TN 37830

Adel M. El Nadi
Oak Ridge National Laboratory
Bldg. 9201-2, MS 3
P.O. Box Y
Oak Ridge, TN 37830

Masami Fujiwara
Institute of Plasma Physics
Nagoya University
Nagoya 464, Japan

Gordon Gibson
Westinghouse Electric Corporation
Advanced Reactor Division
Waltz Mill Site
P.O. Box 158
Madison, PA 15663

N. Thomas Gladd
JAYCOR
11011 Torreyana Road
P.O. Box 85154
San Diego, CA 92138

Irvy Gledhill
Department of Physics
University of California-Los Angeles
405 Hilgard Avenue
Los Angeles, CA 90024

John C. Glowienka
Oak Ridge National Laboratory
Bldg. 9201-2, MS-2
P.O. Box Y
Oak Ridge, TN 37830

Heinz Goede
R1/2144
TRW Inc., Energy Development Group
One Space Park
Redondo Beach, CA 90278

Gareth E. Guest
AMPC Inc.
2210-P Encinitas Blvd.
Encinitas, CA 92024

Seishi Hamasaki
JAYCOR
11011 Torreyana Road
P.O. Box 85154
San Diego, CA 92138

Glenn R. Haste
Oak Ridge National Laboratory
Bldg. 9201-2, MS-2
P.O. Box Y
Oak Ridge, TN 37830

Daniel E. Hastings
Oak Ridge National Laboratory
Bldg. 9201-2, MS-2
P.O. Box Y
Oak Ridge, TN 37830

C. L. Hedrick
Oak Ridge National Laboratory
Bldg. 9201-2, MS-2
P.O. Box Y
Oak Ridge, TN 37830

Shinji Hiroe
Oak Ridge National Laboratory
Bldg. 9201-2, MS-2
P.O. Box Y
Oak Ridge, TN 37830

Hitoshi Hojo
Institute for Fusion Theory
Hiroshima University
Hiroshima, 730, Japan

Hideo Ikegami
Institute of Plasma Physics
Nagoya University
Nagoya, 464, Japan

Mark Iskra
R1/2144
TRW Inc., Energy Development Group
One Space Park
Redondo Beach, CA 90278

E. F. Jaeger
Oak Ridge National Laboratory
Bldg. 9201-2, MS-2
P.O. Box Y
Oak Ridge, TN 37830

Ronald J. Kashuba
McDonnell Douglas Astronautics Co.
Fusion Science Department
Dept. E240, St. Louis Division
P.O. Box 516
St. Louis, MO 63166

Nicholas A. Krall
JAYCOR
11011 Torreyana Road
P.O. Box 85154
San Diego, CA 92138

Norman H. Lazar
R1/2136
TRW Inc., Energy Development Group
One Space Park
Redondo Beach, CA 90278

Liang-Peng Mai
Westinghouse Electric Corporation
Advanced Reactors Division
Waltz Mill Site
P.O. Box 158
Madison, PA 15663

John B. McBride
Science Applications Inc.
1200 Prospect Street
P.O. Box 2351
La Jolla, CA 92038

Robert L. Miller
AMPC Inc.
2210-P Encinitas Blvd.
Encinitas, CA 92024

Khanh Nguyen
Dept. of Nuclear Engineering
North Campus
University of Michigan
Ann Arbor, MI 48109

Larry W. Owen
Oak Ridge National Laboratory
Bldg. 9104-2
P.O. Box Y
Oak Ridge, TN 37830

James F. Pipkins
McDonnell Douglas Astronautics Co.
Fusion Science Department
Dept. E240, St. Louis Division
P.O. Box 516
St. Louis, MO 63166

Bill H. Quon
JAYCOR
2811 Wilshire Blvd., Suite 690
Santa Monica, CA 90403

Marlene Rosenberg
JAYCOR
11011 Torreyana Road
P.O. Box 85154
San Diego, CA 92138

J. Reece Roth
Electrical Engineering Department
Room 409, Ferris Hall
University of Tennessee
Knoxville, TN 37996-2100

Thomas K. Samec
R1/2136
TRW Inc., Energy Development Group
One Space Park
Redondo Beach, CA 90278

Heiji Sanuki
Department of Physics
University of California-Los Angeles
405 Hilgard Avenue
Los Angeles, CA 90024

Teruyuki Sato
Institute of Plasma Physics
Nagoya University
Nagoya 464. Japan

Ray J. Schmitt
McDonnell Douglas Astronautics Co.
Fusion Science Department
Dept. E240, St. Louis Division
P.O. Box 516
St. Louis, MO 63166

Donald A. Spong
Oak Ridge National Laboratory
Bldg. 9201-2, MS-2
P.O. Box Y
Oak Ridge, TN 37830

V. Stefan
University of California at San Diego
Physics Department, B-019
La Jolla, CA 92093

Stephen Tamor
Science Applications Inc.
1200 Prospect Street
P.O. Box 2351
La Jolla, CA 92038

James A. Turner
Office of Fusion Energy
ER-56, GTN
U.S. Department of Energy
Washington, DC 20545

Nermin A. Uckan
Oak Ridge National Laboratory
Bldg. 9201-2, MS-3
P.O. Box Y
Oak Ridge, TN 37830

Taner Uckan
Oak Ridge National Laboratory
Bldg. 9201-2, MS-2
P.O. Box Y
Oak Ridge, TN 37830

James W. Van Dam
McDonnell Douglas Astronautics Co.
Fusion Science Department
Dept. E240, St. Louis Division
P.O. Box 516
St. Louis, MO 63166

Michael B. Voytilla
AMPC Inc.
2210-P Encinitas Blvd.
Encinitas, CA 92024

Harold Weitzner
New York University
Courant Institute
251 Mercer Street
New York, NY 10012

Shoichi Yoshikawa
Plasma Physics Laboratory
Princeton University
P.O. Box 451
Princeton, NJ 08544

US-JAPAN WORKSHOP

ADVANCED BUMPY TORUS CONCEPTS

July 11-13, 1983
Rancho Santa Fe, California

AGENDA

Monday, July 11, 1983

8:30 am	Welcome: R. L. Miller, Applied Microwave Concepts (AMPC) J. M. Turner, U. S. Department of Energy H. Ikegami, Japanese Ministry of Education
	Announcements: N. A. Uckan, Oak Ridge National Laboratory M. B. Voytilla, AMPC
	MAGNETICS - CLOSED FIELD LINE DEVICES — G. Gibson
9:00 am	R. L. Miller - "Drift Surface Studies of EBT Configurations with Noncircular Magnetic Coils"
9:30 am	L. W. Owen, et al. - "ELMO Bumpy Square"
10:00 am	Break
10:15 am	S. Yoshikawa - "Azimuthally Symmetric Mirrors Plus EBT Principles"
10:45 am	T. Kamimura, et al. - "Orbits Aspect of Advanced Bumpy Torus"
11:15 am	L. P. Mai and G. Gibson - "Magnetics of Innovative Bumpy Tori"
12:00	Lunch
	MAGNETICS - CLOSED FLUX-SURFACE DEVICES — W. B. Ard
1:30 pm	J. F. Pipkins, et al. - "Optimized Approaches to EBT's with Simple Circular Coils"
2:00 pm	R. J. Schmitt, et al. - "Preliminary Conceptual Design of a Twisted Racetrack EBT Device"
2:30 pm	Break
2:45 pm	A. Tsushima and M. Fujiwara - "Analytical Studies on Characteristics of New Bumpy Torus Configurations"

US-JAPAN WORKSHOP AGENDA CONT'D.

Monday, July 11, 1983 Cont'd.

3:15 pm	A. H. Boozer - "ELMO Snakey Torus"
3:45 pm	J. Van Dam - "Energetic Particles in Tokamaks: Stabilization of Ballooning Modes"
4:15 pm	Discussions

Tuesday, July 12, 1983

INTERPRETATION AND SUPPORTING THEORY — L. A. Berry

8:30 am	H. Ikegami - "Optimized Operation of Bumpy Torus"
9:00 am	D. E. Hastings - "Nonresonant Particles Transport for Bumpy Field Line Devices with Arbitrary Shaped Flux Surfaces"
9:30 am	C. L. Hedrick - "Comparison of Magnetic Equilibria and Low Frequency Stability for EBT and EBS"
10:00 am	Break
10:10 am	J. B. McBride et al. - "Wave Interactions with EBT Plasmas in the Magnetic Drift Frequency Range"
10:40 am	K. Nguyen and T. Kammash - "Stability Bounds for Ballooning Modes in EBT"
11:35 am	H. Sanuki - "Effects of Ambipolar Field on Low Frequency Fluctuations in Bumpy Tori"
12:00	Lunch

ELECTRIC FIELD ENHANCED CONFINEMENT — H. Weitzner

1:30 pm	C. S. Chang - "Plasma Confinement in Self-Consistent, One-Dimensional Transport Equilibria in the Collisionless-Ion Regime of EBT Operation"
2:00 pm	H. Hojo et al. - "ICRF Confinement and Stabilization of Torus Plasma"
2:30 pm	Break
2:45 pm	J. Reece Roth - "The Electric Field Bumpy Torus (EFBT) Concept: An Alternate Means of Plasma Production"

US-JAPAN WORKSHOP AGENDA CONT'D.

Tuesday, July 12, 1983 Cont'd.

	RF HEATING	H. Weitzner
3:15 pm	T. Sato et al. - "Buildup and Sustainment of 10^{13} cm^{-3} Plasma by ICRF in RFC-XX"	
3:45 pm	S. Tamor - "EBT Microwave Deposition Modeling"	
4:15 pm	D. B. Batchelor and R. C. Goldfinger - "Theoretical Aspects of Throat Launch Microwave Heating in EBT-S"	
Evening	Reception	

Wednesday, July 13, 1983

	ELMO RING PHYSICS	H. Ikegami
8:30 am	B. H. Quon - "Control of ELMO Ring by Using Surmac Coils in Advanced EBT Systems"	
9:00 am	J. A. Rome et al. - "On the Possibility of Rings in a Modular Stellarator"	
9:30 am	S. Hamasaki et al. - "Reduction of Microwave Power Requirements for EBT Electron Ring Production"	
10:00 am	Break	
10:15 am	Summary and Discussions	N. A. Krall
12:00	Lunch	